



HAL
open science

Design of flexible and nanostructured composites by combining Al³⁺ MOFs and graphene oxide for adsorption applications

Ali Saad

► **To cite this version:**

Ali Saad. Design of flexible and nanostructured composites by combining Al³⁺ MOFs and graphene oxide for adsorption applications. Material chemistry. Université Paris-Saclay, 2023. English. NNT : 2023UPAST019 . tel-04861198

HAL Id: tel-04861198

<https://theses.hal.science/tel-04861198v1>

Submitted on 2 Jan 2025

HAL is a multi-disciplinary open access archive for the deposit and dissemination of scientific research documents, whether they are published or not. The documents may come from teaching and research institutions in France or abroad, or from public or private research centers.

L'archive ouverte pluridisciplinaire **HAL**, est destinée au dépôt et à la diffusion de documents scientifiques de niveau recherche, publiés ou non, émanant des établissements d'enseignement et de recherche français ou étrangers, des laboratoires publics ou privés.

Design of flexible and nanostructured composites by combining Al^{3+} MOFs and graphene oxide for adsorption applications

Conception de composites flexibles et nanostructurés en associant des MOFs à base d' Al^{3+} et de l'oxyde de graphène pour des applications en adsorption

Thèse de doctorat de l'université Paris-Saclay

École doctorale n° 573, Interfaces : matériaux, systèmes, usages (INTERFACES)

Spécialité de doctorat : Chimie

Graduate School : Sciences de l'ingénierie et des systèmes

Référent : Université de Versailles-Saint-Quentin-en-Yvelines

Thèse préparée dans l'unité de recherche **Institut Lavoisier de Versailles (Université Paris-Saclay, UVSQ, CNRS)**, sous la direction de **Nathalie STEUNOU**, professeure, et la co-encadrement de **Clémence SICARD**, maitresse de conférences.

Thèse soutenue à Versailles, le 08 mars 2023, par

Ali SAAD

Composition du Jury

Membres du jury avec voix délibérative

Cédric BOISSIERE

Directeur de Recherche CNRS, Laboratoire de chimie de la matière condensée de Paris (LCMP)

Président

Bruno ALONSO

Directeur de Recherche CNRS, Institute Charles Gerhardt Montpellier (ICGM)

Rapporteur & Examineur

Aude DEMESSENCE

Chargée de recherche CNRS, IRCE Lyon

Rapporteur & Examinatrice

Darren BRADSHAW

Associate Professor, University of Southampton

Examineur

Nathalie GUILLOU

Chargée de recherche CNRS, Institut Lavoisier de Versailles (ILV)

Examinatrice

Christian SERRE

Directeur de Recherche CNRS, Institut des Matériaux Poreux de Paris (IMAP)

Examineur

Title : Design of flexible and nanostructured composites by combining Al^{3+} MOFs and graphene oxide for adsorption applications

Keywords : MOFs, graphene oxide, flexibility

Abstract : Despite the increasing number of works covering metal organic frameworks (MOFs) in the state of the art, the focus of literature is still oriented towards the discovery of novel MOF structures and examining their physico-chemical properties for applications. Yet, it should be taken into account that most MOFs reported till today are microporous in nature, which means they suffer limitations related to material properties and applications (e.g., adsorption and conversion of small guest molecules). To address this issue, the design of composites by combining MOFs with carbon-based materials has been developed and such materials can present interesting functional properties (i.e., more exposed reactive/ functional facets) and an induced hierarchical porosity (i.e., micro- and mesopores). Among the different carbon-based materials reported in literature, graphene oxide (GO) has proved to play an interesting role in directing the nucleation and growth of a few MOFs. Thus, the objective of this thesis was to develop novel nanostructured MOF/GO composites that combine the properties of GO (e.g., processability, electron conductivity, etc.) and porous Al^{3+} polycarboxylate MOF (e.g., crystallinity, porosity, etc.) through a synergistic manner. We have shown that these composites consist of the assembly of single crystal MOF nanowires and GO sheets. The nucleation and growth of such nanowires is directed by the self-assembly of GO sheets into GO nanoscrolls. The design of composites based on anisotropic MOF nanocrystals is quite challenging and has been rarely reported in literature. However, such composites are of interest in the domains of catalysis, sensing, gas transport, and electronics since the dimensionality and morphology of MOF crystals can impact the diffusion and the mass transport efficiency of analytes towards the catalytic and the adsorption sites of the MOF. The synthesis of such composites was optimized by tuning the different physico-chemical parameters of the synthesis. They were characterized by combining multiple characterization tools (PXRD, SEM, TEM, HAADF-STEM, electron diffraction, N_2 porosimetry, solid state NMR) while we have studied their formation mechanism by combining WAXS, PXRD, SEM and TEM experiments. We have also investigated their gas and liquid adsorption properties. A flexible behavior of such composites was evidenced while the pure MOF does not exhibit any dynamic behavior. The MOF present in the composite can exhibit a structural transition and thus switch between a large pore (lp) form and a narrow pore (np) form depending on the stimulus applied (solvents, temperature). These findings make it possible to further validate the role of GO as a structural directing agent of MOFs, and to build a better understanding on the dynamic behavior of MOFs.

Titre : Conception de composites flexibles et nanostructurés en associant des MOFs à base d' Al^{3+} et de l'oxyde de graphène pour des applications en adsorption

Mots clés : MOFs, oxyde de graphène, flexibilité

Résumé : Malgré le nombre croissant de travaux portant sur les matériaux hybrides poreux de type Metal Organic Frameworks (MOF) dans l'état de l'art, les recherches dans ce domaine portent essentiellement sur la découverte de nouvelles structures de MOF et l'étude de leurs propriétés physico-chimiques pour des applications. Cependant, la plupart des MOFs décrits jusqu'à aujourd'hui sont microporeux, et ces matériaux sont capables d'adsorber et de convertir des petites molécules, ce qui représente une limitation pour leurs applications potentielles en adsorption ou en catalyse. Pour améliorer les performances de ces matériaux, la conception de composites en combinant les MOFs avec des matériaux à base de carbone a été développée et ces matériaux peuvent présenter des propriétés fonctionnelles intéressantes et une porosité hiérarchique à différentes échelles (micro- et mésoporosité). Parmi les différents matériaux à base de carbone étudiés dans la littérature, l'oxyde de graphène (GO) s'est avéré jouer un rôle intéressant en contrôlant la nucléation et la croissance de certains MOFs. Ainsi, l'objectif de cette thèse était de développer de nouveaux composites MOF/GO nanostructurés qui combinent de manière synergique les propriétés du GO (e.g., mise en forme, conductivité électronique, etc.) et d'un polycarboxylate d' Al^{3+} poreux (e.g., cristallinité, porosité, etc.). Nous avons montré que ces composites consistent en l'assemblage de nanofils monocristallins de MOF et de feuillets de GO. Nous avons montré que la nucléation et la croissance de ces nanofils sont contrôlées par l'autoassemblage des feuilles de GO en nanoscrolls de GO. La conception de composites à base de nanocristaux de MOF anisotropes est assez difficile et a été rarement décrite dans la littérature. Pourtant, ces composites sont intéressants dans les domaines de la catalyse, de la détection, du transport de gaz et de l'électronique, car la dimensionnalité et la morphologie des cristaux de MOF peuvent avoir un impact sur la diffusion et l'efficacité du transport des analytes vers les sites catalytiques et d'adsorption du MOF. La synthèse de ces composites a été optimisée en ajustant les différents paramètres physico-chimiques de la synthèse. Ils ont été caractérisés en combinant plusieurs outils de caractérisation avancés (diffraction des rayons X sur poudre (DRX), MEB, MET, HAADF-STEM, diffraction électronique, porosimétrie de N_2 , RMN à l'état solide) tandis que nous avons étudié leur mécanisme de formation en combinant des expériences diffusion des rayons X, DRX, MEB et MET. Nous avons également étudié leurs propriétés d'adsorption de gaz et de liquides. Un comportement flexible de ces composites a été mis en évidence alors que le MOF pur ne présente aucun comportement dynamique. Nous avons observé que le MOF du composite peut présenter une transition structurale d'une forme larges pores (lp) à une forme petits pores (np) sous l'application de différents stimuli (solvants, température...). Ces résultats permettent de valider davantage le rôle du GO comme agent structurant des MOFs, et de mieux comprendre le comportement dynamique des MOFs.

ACKNOWLEDGMENTS

I would like to extend my heartfelt gratitude to all those who have supported and encouraged me throughout my four-years journey at Versailles. I would like to express my deep appreciation to my family, colleagues, and superiors who have provided me with opportunities for growth and development in my professional life. Your guidance, mentorship, and friendship have been instrumental in my success, and I am grateful for all that I have learned from each and every one of you.

I would like first to express gratitude to the members of my thesis committee, Dr. Bruno Alonso, Dr. Aude Demessence, Dr. Cédric Boissiere, Pr. Daren Bradshaw, Dr. Nathalie Guillou, and Pr. Christian Serre for accepting to be part of my PhD defense. Undoubtedly, their insightful comments and constructive criticism are instrumental in the development of my research and professional experience. I am specially thankful to Dr. Alonso and Dr. Demessence for their time and efforts in reviewing my manuscript.

Special thanks to the Université de Versailles Saint-Quentin-en-Yvelines (UVSQ) for the generous funding of the last two years of my PhD thesis following a very hard situation in my home country. Thanks particularly to Yves Dumont and Pascale Le Gall from the Interfaces doctorate School, Alexis Constantin and Fanny Duret.

Many thanks to the director of ILV, Pr. Emmanuel Magnier and the head of the MIM team, Pr. Emmanuel Cadot, for accepting me in their team and providing a healthy and professional working atmosphere.

I would like also to express my sincere appreciation and admiration to my two supervisors, Pr. Nathalie Steunou and Dr. Clémence Sicard. To my thesis director, Nathalie Steunou, I have always wanted to express how grateful I am to have passed this journey under your supervision. You were always supportive at the moral, educational, and even the financial level despite the many hardships that have encountered me (Lebanese economic crisis, COVID-19, family problems, ...). Your invaluable contributions to my growth as a researcher and a person are memorable. For me, you are a major reason behind the success of this work and my success as a person. I will always remember you as someone who left a big positive impact in my

ACKNOWLEDGMENTS

personal and professional life (I am not exaggerating!). To my thesis co-supervisor, Clémence Sicard, thank you first for providing me with the guidance, encouragement, and resources necessary (including the chocolates!) to complete this research. When I first came to France, I did not expect to build such a nice friendship with my superior. I have always told you that I appreciate much the impact you had on my development as a scientist, and the positive moral you have added to this PhD project which seemed impossible to accomplish at the beginning. Thank you, Nathalie and Clémence, for being very professional and very caring at the same time!

My special thanks to Dr. Nathalie Guillou, despite the fact that you were not officially part of my thesis supervision team, you have provided me a lot of your time and effort. You introduced me to the very broad world of crystallography, and you have played an irreplaceable role in this project. Thank you very much for your time, the collaborations, and your insightful ideas. It was a pleasure to work with you.

Many thanks to Dr. Thibaud Coradin for accepting to be part of my "comité de suivi de thèse". Thank you for your time and advice.

Many collaborations were built during this project, and I would like to mention and thank each of the collaborators from Versailles, France, and Europe.

From Versailles, many thanks to Dr. Mohamed Haouas for the valuable solid state NMR experiments and his patience during the discussions. Special thanks to both Dr. Nathalie Leclerc and Dr. Carine Livage for the TGA experiments and their very kind attitude in the lab. From the EPI team, thanks to Dr. Mathieu Frégnaux for the XPS experiments, and to Dr. Muriel Bouttemy for the fruitful SEM training sessions. Thanks also to Flavien Bourdreux for the in-situ FT-IR experiment and Aurelie Damond for her help with managing the BET apparatus. Thanks also to all the permanents at ILV for their kind assistance during these 4 years, many thanks to Dr. Clement Falaise, Dr. Eddy Dumas, Dr. Oliver Oms, Pr. Pierre Mialane, Dr. Anne Vallée, and others.

From France, many thanks to Dr. Frédéric Gobeaux (CEA Saclay) for the effective collaboration on the WAXS experiments and the nice scientific discussions. Thanks to Pr. Nicolas Menguy (Sorbonne Université) for his time on the microscope and the many experiments we have performed together. Thanks to Dr. Catherine de Villeneuve (Ecole Polytechnique, Palaiseau) for the very long AFM experiments. Many thanks also

to Dr. Erik Elkaim from the CRISTAL beamline at Synchrotron Soleil and for Dr. Benoît Baptiste for his help with the PDF experiments (Sorbonne Université). Thanks also to Dr. Thomas Devic for the productive discussions during the ECM33 conference.

I am especially thankful to the team of Pr. Stefan Kaskel in Germany for inviting me to Dresden and for their kind welcoming. Thank you for the very special in-situ XRD and BET coupled experiments and for all the insights on the field of flexible MOFs. Special appreciation to Dr. Volodymyr Bon for his time in performing the experiments and the fruitful long scientific discussions we had together. Thanks to Dr. Irena Senkovska for the rewarding discussions on DUT-5(Al) MOF, the structure she has personally developed.

I am also very grateful to my colleagues and friends at ILV for their camaraderie and support during my time here. I would like first to thank my colleagues from the MIM team. The seminars, delicious meals, crazy nights out, and our time on the green field are unforgettable. I am thankful for the lovely memories, unwavering support, and endless encouragement. Thank you very much Subha, Soumaya, Ioanna, Sanchari, Jonathan, Sri, Mai, Juan, Youven, Maxence, Melvin, Khaled, Cédric, Khadija, Sa, Dima, Sergiu, Mouhieddine, Fay, Somia, Lucie, Linda, and others. A big thank you also to my colleagues and friends from the organic team, Olfa, Mamour, Abdelilah, Thibault, Manon, Camille, Safa... and best of luck for the next generation Nour, Roa, Gabrielle, Jason, Mathilde, ...

Outside the lab, I would like finally to extend my deepest gratitude to my family and friends for their steady love and support. To my family, thanks to each of you for being my constant source of love and motivation. Your belief in me have made this accomplishment possible. To my friends, Hussein Mehidine, Olfa Zayenne, Jamal Darwish, Jana Hussein, Fatma Boukataya, Rawan Sayed, Hussein Shokor, Hussein Krecht, Abdallah Nasserredine, (and many others including the KLEY team!), your love, support, and understanding have been a source of strength and motivation during the challenging times.

Thank you all for playing a part in this special chapter of my life and for your invaluable contributions to my success.

Avec tous mes remerciements !

TABLE OF CONTENTS

GENERAL INTRODUCTION.....1

CHAPTER 1: An Overview on MOFs, Flexibility, and MOF/GO composites

1.1. INTRODUCTION	10
1.2. METAL ORGANIC FRAMEWORKS.....	11
1.2.1. Porous Coordination Polymers	11
1.2.2. Building Blocks of MOFs	14
1.2.3. Main Synthesis Protocols of MOFs.....	16
1.3. FLEXIBILITY IN MOFS.....	19
1.3.1. Flexibility modes.....	20
1.3.2. Breathing of MIL53(M) as a case study	21
1.3.3. MOFs Studied in this Work	26
1.3.4. Stimuli affecting flexibility in MOFs.....	31
1.4. MOF – GRAPHENE OXIDE COMPOSITES.....	42
1.4.1. Graphene and Graphene Oxide.....	43
1.4.2. From GO sheets to nanoscrolls	47
1.4.3. MOF/GO 1D nanostructures.....	52
1.5. CONCLUSION	62
1.6. REFERENCES.....	64

CHAPTER 2: Selection & Screening of MOF Candidates

2.1 INTRODUCTION	83
2.2 SELECTED MOF CANDIDATES AND THEIR COMPOSITES.....	85
2.2.1. Selection criteria for MOFs.....	85
2.2.2. Preparation strategy of MOF/GO composites.....	91
2.3 SCREENING OF SELECTED MOF CANDIDATES.....	94
2.3.1. CAU-10-H(Al).....	95
2.3.2. CAU-23(Al).....	99
2.3.3. DUT-5(Al).....	102
2.3.4. DUT-67(Zr).....	106
2.3.5. MOF-545(Zr).....	110
2.4 SCREENING CONCLUSIONS AND SELECTED CANDIDATE.....	112
2.5 REFERENCES.....	113

CHAPTER 3: DUT-5(Al) and DUT-5(Al)/GO

3.1	INTRODUCTION	120
3.2	DUT-5(Al) IN THE STATE OF THE ART	123
3.3	SYNTHESIS OPTIMIZATION OF DUT-5(Al)	125
3.3.1.	Reported synthesis of DUT-5(Al) under reflux.....	125
3.3.2.	Optimization of the reported synthesis.....	127
3.4	SYNTHESIS OPTIMIZATION OF DUT-5(Al)/GO.....	137
3.4.1.	Synthesis of DUT-5(Al)/GO with different molar ratios.....	137
3.4.2.	Optimization of DUT-5(Al)/GO synthesis.....	143
3.5	EXPLORING THE EFFECT OF GO ADDITION	161
3.5.1.	Effect of GO on reaction kinetics.....	162
3.5.2.	Effect of GO on final morphology.....	163
3.6	CONCLUSIONS AND PERSPECTIVES.....	170
3.7	REFERENCES.....	172

CHAPTER 4: Insights on the Induced Flexibility in the DUT-5(Al) Structure

4.1	INTRODUCTION	181
4.2	STATE OF THE ART: FLEXIBILITY OF DUT-5(Al).....	184
4.3	THE STRUCTURAL BEHAVIOR OF DUT-5(Al).....	185
4.4	ELUCIDATING STRUCTURES: TWO PHASES OF DUT-5(Al)/GO	191
4.4.1.	Rietveld Refinement of the two phases.....	193
4.4.2.	Characterization by Pair Distribution Function.....	195
4.5	STUDYING THE FLEXIBLE BEHAVIOR OF DUT-5(Al)/GO	197
4.5.1.	Effect of Temperature on the Flexibility of DUT-5(Al)/GO.....	197
4.5.2.	Effect of Solvent on the Flexibility of DUT-5(Al)/GO.....	202
4.5.3.	Effect of Gas Guest Molecules on Flexibility of DUT-5(Al)/GO.....	205
4.6	EFFECT OF SIZE AND MORPHOLOGY ON FLEXIBILITY	209
4.7	CONCLUSIONS AND PERSPECTIVES.....	212
4.8	REFERENCES.....	213

CONCLUSION & PERSPECTIVES.....218

ANNEXES.....225

GENERAL INTRODUCTION

During the last decades the interest in the design and synthesis of hybrid porous materials has grown enormously due to their potentiality in numerous industrial applications. Among the porous materials, Metal-organic frameworks (MOFs) are two-dimensional (2D) or three-dimensional (3D) porous coordination polymers constructed through the assembly of two building units: organic linkers (which are multidentate organic ligands) and inorganic nodes (which can be single atoms (cations) or (oxo)clusters (inorganic complexes), or chains). MOFs exhibit exceptional surface areas of up to 7800 m²/g, topological diversity, and high functional tunability.¹ Such properties added to the relative ease of MOF synthesis and their synthetic tailorability, made MOFs promising candidates in different applications such as gas storage/separation, sensing, catalysis, and biomedicine.²

Of interest, is combining MOFs with other supporting materials to yield composites combining the properties of the MOF and the supporting matrix. Among the different materials presented in literature, carbon-based materials provide interesting properties.³ The controllable integration of MOFs and carbon-based materials not only leads to a further improvement of single-phase MOFs in terms of stability and electrical conductivity, but also introduces a number of novel functionalities related to their texture (hierarchical porosity) and their morphology. These advantages enable the application of the resulting MOF-carbon composites beyond the fields of single-phase MOFs. Among the different reported carbon-based materials in literature, graphene oxide (GO) presents an exciting candidate.⁴ GO is an oxidized derivative of graphene; it is a single-layered material made of carbon, hydrogen, and oxygen molecules. These single layers are in forms of sheets which are decorated by different oxygen groups (epoxy, hydroxyl, carboxylic acid) on both sides. The double-sided decoration of GO sheets provides two main

advantages: it offers a polyaromatic dispersible platform for performing chemistry and establishes a 2D building block that can participate in the assembly of supramolecular hybrid structures at the nanoscale.⁵ Furthermore, the incorporated functional groups can be utilized to target specific applications (e.g., electronics, optics, energy storage, etc.).^{4,6} Lately, a growing research interest has been sparked in the interdisciplinary field of combining MOFs and GO. It has been shown that the synergistic effects between the two compounds can lead to the improvement of certain properties compared to the parent compounds (e.g., processability, chemical stability, electron conductivity, etc.). MOF/GO composites have been studied for various applications including innovative approaches as microwave adsorption (MSA) processes suitable for CO₂ capture,⁷ and wearable biosensor.⁸ They were also employed as electrode materials of supercapacitors (SCs),⁹ in biomedical applications,¹⁰ water treatment membranes,^{11,12} etc. Nevertheless, the combination of MOFs and GO have proved to play a role in the formation of nanostructured composites. Among those nanostructures, one-dimensional nanowires (NWs), nanotubes (NTs), and nanorods (NRs) have drawn significant attention, since the anisotropy of their crystal shape is prone to exposing functional or reactive crystal facets for optimal performance in applications such as catalysis and sensing.¹³ Their dimensionality can enhance the diffusion and mass-transport efficiency of analytes towards the catalytic and adsorption sites of the MOF. Still, this aim has always been a challenge as the relationship between the synthesis parameters (precursor concentrations, temperature, time, etc.) and the morphology of the MOF is difficult to predict.

Recently, some of our group have reported the use of graphene oxide (GO) as a structural directing agent for the formation of 1D MOF based single crystals.¹⁴ Precisely, MIL-69(Al) (Matériaux de l'Institut Lavoisier n°69) single crystalline nanowires (NWs) were formed using GO nanoscrolls as structure directing agents.¹⁴ MOF NWs are 1D nanostructures with diameters in the nanometer range and

lengths of up to a few centimeters. Their aspect ratio (length to diameter ratio) varies to a large extent and is significantly higher than that of nanorods (NRs). The concept of directing the growth of MOFs at the nanoscale has always been enticing. The objective of this PhD is to extend the approach for the design of MIL-69(Al)/GO to another composite. The importance of this approach lies in granting hierarchically porous MOF/GO composites with a specific microstructure that allows a homogeneous dispersion of MOF NWs in the GO matrix, without any agglomeration of MOF NPs or restacked GO layers. In addition, the formed microstructures combine the properties of the MOF (porosity and crystallinity) and those of GO (processibility, conductivity, etc.) via the synergistic effect between both.

This PhD thesis is divided into four main chapters:

The first chapter provides the state of art on the different topics covered in this PhD project. The chapter reviews the original and recent works in literature that discuss MOF chemistry, flexibility in MOFs, and MOF-graphene oxide composites, respectively. The first part of the chapter provides a brief introduction about MOF chemistry in general, while listing some recent reports and describing the global MOF market forecast in the next 3 years. The second part focuses on the distinct flexibility phenomena observed in MOFs. The different modes of flexibility in MOFs are described, with a case study on the MIL-53(Al) type MOFs. The third part of the chapter considers the importance of combining MOFs with graphene oxide (GO). An overview of graphene and graphene oxide is provided first. Then, the interesting ability of GO sheets to self-scroll into nanoscrolls is explained. Last, the formation, induced properties, and application of anisotropic MOF/GO composites is deliberated.

The second chapter discusses the screening of different MOF candidates for the selection of the best candidate to form MOF/GO anisotropic structures. The choice

of the different MOFs candidates is first justified. For each of the MOFs, both the reported and modified (if needed) synthesis are described. Afterwards, the design of MOF/GO composites is explained, and the characterization of both the MOFs and their corresponding composites will be presented. Finally, based on the results obtained by the different characterization techniques, DUT-5(Al) (Dresden University of Technology MOF n°5) was selected since the corresponding DUT-5/GO presents promising microstructural properties.

In the third chapter, following the selection of DUT-5(Al) as the best MOF candidate, directing the growth of small DUT-5(Al) nanoparticles into nanowires using GO is thoroughly investigated. The synthesis optimization of both DUT-5(Al) and DUT-5(Al)/GO is thoroughly discussed, and a panel of advanced characterizations techniques are presented. Finally, it was of huge importance to investigate the effect of GO on both the sample's final morphology and its formation kinetics. Interestingly, the results obtained in this chapter were accompanied by an observed structural flexibility.


The fourth chapter studies the observed dynamic behavior of DUT-5(Al) in DUT-5/GO composite in comparison to pure DUT-5(Al). The flexible behavior of DUT-5(Al) in the composite was studied under different stimuli (solvent and gas guest molecules, heating) and the response of the MOF was examined using various *in-situ* and *ex-situ* characterization techniques. The chapter emphasizes on understanding the relationship between the applied stimuli and the obtained dynamic behavior of the MOF in the composite. It also comments on the relationship between effect of crystallite size and morphology on the flexible behavior of DUT-5(Al) in the composite.

Lastly, the conclusions and perspectives of the PhD project are provided, along with annexes presenting different publications reported during this PhD including papers based on collaborative projects.

REFERENCE LIST

- (1) Yaghi, O. M.; Kalmutzki, M. J.; Diercks, C. S. Emergence of Metal-Organic Frameworks. In *Introduction to Reticular Chemistry*, John Wiley & Sons, Ltd, 2019; pp 1–27. <https://doi.org/10.1002/9783527821099.ch1>.
- (2) Safaei, M.; Foroughi, M. M.; Ebrahimpour, N.; Jahani, S.; Omid, A.; Khatami, M. A Review on Metal-Organic Frameworks: Synthesis and Applications. *TrAC Trends in Analytical Chemistry* **2019**, *118*, 401–425. <https://doi.org/10.1016/j.trac.2019.06.007>.
- (3) Xu, J.; Peng, Y.; Xing, W.; Ding, Z.; Zhang, S.; Pang, H. Metal-Organic Frameworks Marry Carbon: Booster for Electrochemical Energy Storage. *Journal of Energy Storage* **2022**, *53*, 105104. <https://doi.org/10.1016/j.est.2022.105104>.
- (4) Yu, W.; Sisi, L.; Haiyan, Y.; Jie, L. Progress in the Functional Modification of Graphene/Graphene Oxide: A Review. *RSC Advances* **2020**, *10* (26), 15328–15345. <https://doi.org/10.1039/D0RA01068E>.
- (5) Erickson, K.; Erni, R.; Lee, Z.; Alem, N.; Gannett, W.; Zettl, A. Determination of the Local Chemical Structure of Graphene Oxide and Reduced Graphene Oxide. *Adv. Mater.* **2010**, *22* (40), 4467–4472. <https://doi.org/10.1002/adma.201000732>.
- (6) Tarcan, R.; Todor-Boer, O.; Petrovai, I.; Leordean, C.; Astilean, S.; Botiz, I. Reduced Graphene Oxide Today. *J. Mater. Chem. C* **2020**, *8* (4), 1198–1224. <https://doi.org/10.1039/C9TC04916A>.
- (7) Muschi, M.; Devautour-Vinot, S.; Aureau, D.; Heymans, N.; Sene, S.; Emmerich, R.; Ploumistos, A.; Geneste, A.; Steunou, N.; Patriarche, G.; Weireld, G. D.; Serre, C. Metal–Organic Framework/Graphene Oxide Composites for CO₂ Capture by Microwave Swing Adsorption. *J. Mater. Chem. A* **2021**, *9* (22), 13135–13142. <https://doi.org/10.1039/D0TA12215G>.
- (8) Xiao, J.; Fan, C.; Xu, T.; Su, L.; Zhang, X. An Electrochemical Wearable Sensor for Levodopa Quantification in Sweat Based on a Metal–Organic Framework/Graphene Oxide Composite with Integrated Enzymes. *Sensors and Actuators B: Chemical* **2022**, *359*, 131586. <https://doi.org/10.1016/j.snb.2022.131586>.
- (9) Oh, H. J.; Kim, S. Preparation and Capacitive Property of Graphene Oxide Composite Supercapacitor Electrodes Functionalized by Fe-Based Metal–Organic Frameworks. *Carbon Lett.* **2022**, *32* (1), 273–283. <https://doi.org/10.1007/s42823-021-00300-y>.
- (10) Karimzadeh, Z.; Javanbakht, S.; Namazi, H. Carboxymethylcellulose/MOF-5/Graphene Oxide Bio-Nanocomposite as Antibacterial Drug Nanocarrier Agent. *Bioimpacts* **2019**, *9* (1), 5–13. <https://doi.org/10.15171/bi.2019.02>.
- (11) Qu, H.; Huang, L.; Han, Z.; Wang, Y.; Zhang, Z.; Wang, Y.; Chang, Q.; Wei, N.; Kipper, M. J.; Tang, J. A Review of Graphene-Oxide/Metal–Organic Framework Composites Materials: Characteristics, Preparation and Applications. *J. Porous Mater.* **2021**, *28* (6), 1837–1865. <https://doi.org/10.1007/s10934-021-01125-w>.

- (12) Yu, S.; Pang, H.; Huang, S.; Tang, H.; Wang, S.; Qiu, M.; Chen, Z.; Yang, H.; Song, G.; Fu, D.; Hu, B.; Wang, X. Recent Advances in Metal-Organic Framework Membranes for Water Treatment: A Review. *Science of The Total Environment* **2021**, *800*, 149662. <https://doi.org/10.1016/j.scitotenv.2021.149662>.
- (13) Saad, A.; Biswas, S.; Gkaniatsou, E.; Sicard, C.; Dumas, E.; Menguy, N.; Steunou, N. Metal–Organic Framework Based 1D Nanostructures and Their Superstructures: Synthesis, Microstructure, and Properties. *Chem. Mater.* **2021**, *33* (15), 5825–5849. <https://doi.org/10.1021/acs.chemmater.1c01034>.
- (14) Muschi, M.; Lalitha, A.; Sene, S.; Aureau, D.; Fregnaux, M.; Esteve, I.; Rivier, L.; Ramsahye, N.; Devautour-Vinot, S.; Sicard, C.; Menguy, N.; Serre, C.; Maurin, G.; Steunou, N. Formation of a Single-Crystal Aluminum-Based MOF Nanowire with Graphene Oxide Nanoscrolls as Structure-Directing Agents. *Angew. Chem. Int. Ed.* **2020**, *59* (26), 10353–10358. <https://doi.org/10.1002/ange.202000795>.



CHAPTER 1: An Overview on MOFs, Flexibility, and MOF/GO composites

TABLE OF CONTENTS

1.1. INTRODUCTION	10
1.2. METAL ORGANIC FRAMEWORKS	11
1.2.1. Porous Coordination Polymers	11
1.2.2. Building Blocks of MOFs	14
1.2.2.1. Organic building blocks	14
1.2.2.2. Inorganic building blocks.....	15
1.2.3. Main Synthesis Protocols of MOFs.....	16
1.3. FLEXIBILITY IN MOFS	19
1.3.1. Flexibility modes.....	20
1.3.2. Breathing of MIL53(M) as a case study	21
1.3.3. MOFs Studied in this Work	26
1.3.4. Stimuli affecting flexibility in MOFs.....	31
1.3.4.1. Effect of solvent on flexibility.....	32
1.3.4.2. Effect of crystallite size on flexibility.....	35
1.3.4.3. Effect of functionalization and post synthetic modifications	38
1.4. MOF – GRAPHENE OXIDE COMPOSITES	42
1.4.1. Graphene and Graphene Oxide.....	43
1.4.1.1. History.....	43
1.4.1.2. Properties of Graphene and GO	45
1.4.2. From GO sheets to nanoscrolls	47
1.4.2.1. Solvent induced self-scrolling	48
1.4.2.2. Nanoparticles induced self-scrolling	50
1.4.3. MOF/GO 1D nanostructures.....	52
1.4.3.1. Main preparation strategies.....	53
1.4.3.2. Induced physico-chemical properties	58
1.4.3.3. Applications of MOF/GO composites.....	59
1.5. CONCLUSION	62
1.6. REFERENCES	64

1.1. INTRODUCTION

Materials institute Lavoisier (MILs), iso-reticular metal–organic frameworks (IR-MOFs) and zeolitic metal–organic frameworks (ZMOFs) are all subclasses of metal–organic frameworks (MOFs) and examples of porous coordination polymers (PCMs).¹ Each of these materials has its own structure, concept for linkers, synthesis procedure and post-synthetic modifications. Undeniably, MOFs occupy a special position among other porous materials (zeolites, COFs, etc.) due to their high surface areas up to 7800 m²/g, topological diversity, and high functional tunability.² Owing to their high and tunable porosity as well as chemical diversity, metal–organic frameworks (MOFs) have shown great promise over the past two decades for a wide range of applications, including gas storage/separation, catalysis, and biomedicine. Nevertheless, to date, MOF nanoparticles (NPs) have mostly been obtained as polycrystalline powders or spherical nanocrystals while anisotropic MOFs nanocrystals have been less explored and are of interest in the fields of catalysis, sensing, and electronics. One of the main challenges for the practical application of MOFs is thus to control their crystal size, morphology, and multiscale porosity while developing adequate shaping strategies. Additionally, research has gone beyond the understanding of the fundamental aspects of MOF chemistry. The structural flexibility present in some MOFs has been a hot topic to address in the last two decades after its first prediction in 1998.³ Unlike rigid MOFs, MOFs with a robust and flexible structure have not yet been thoroughly understood. Such smart frameworks are intriguing for different research areas such as catalysis, adsorption, separation, etc. Hence, the idea of shaping MOFs at the nanoscale while inducing structural flexibility in their rigid structure could be an interesting research area to accentuate.

Chiefly, this chapter provides an insight on the different topics covered in this PhD project. The chapter reviews the original and recent works in literature that discuss MOF chemistry, flexibility in MOFs, and MOF-graphene oxide composites, respectively. The first part of the chapter provides a brief introduction about MOF chemistry in general, while listing some recent reports and describing the global MOF market forecast in the next 3 years. The second part focuses on the distinct flexibility phenomena observed in MOFs. The different modes of flexibility in MOFs are described, and the specific choice of the MIL-53(Al) type MOFs as a case study is justified. Besides, this part emphasizes on understanding the relationship between the applied stimuli and the obtained dynamic behavior of the MOFs. The third part of the chapter considers the importance of combining MOFs with graphene oxide (GO). An overview of graphene and graphene oxide is provided first. Then, the interesting ability of GO sheets to self-scroll into nanoscrolls is explained. Last, the formation, induced properties, and application of anisotropic MOF/GO composites is deliberated.

1.2. METAL ORGANIC FRAMEWORKS

1.2.1. Porous Coordination Polymers

MOFs are a class of porous coordination polymers (PCPs). To be more specific, they are inorganic-organic hybrid materials, with coordinative bonding formed by association of inorganic building units (i.e., metal centers, metal oxo-clusters or chains) with organic linkers holding at least two functional groups (**Figure 1-1**). The concept of combining a metal cluster to an organic ligand to form two- or three-dimensional MOFs has led to a wide variety of promising porous materials with tunable properties and different topologies.¹ Hundreds of thousands of MOFs have been synthesized.⁴ The field began to grow following seminal papers by Robson and co-workers in the 1990s,^{5,6} but the concept of MOFs was first introduced by Yaghi.⁷ The first two MOFs to be synthesized and reported appeared

CHAPTER 1: An Overview on MOFs, Flexibility, and MOF/GO composites

in 1999. Ian Williams and colleagues reported the synthesis of HKUST-1,⁸ and few months later Li et. al⁹ reported MOF-5 (i.e., IRMOF-1). These two works inspired the synthesis of thousands of MOFs annually, and the field was developed throughout the years by scientists like Kitagawa,¹⁰ Yaghi¹¹, Ferey,^{12,13} Hupp,¹⁴ Zhou,^{15,16} and several others¹⁷⁻²⁰. There is no universal terminology for MOFs. Some are named according to their structural type, for example Zeolitic Imidazolate Frameworks are named ZIFs as they have a similar topology to zeolites. Other MOFs are named with the initials of the university (or institute) where they were first synthesized (e.g., MIL for Matériaux de l'Institut Lavoisier; UiO for University of Oslo; DUT for Dresden University of Technology; etc.). Nowadays, the building of MOF architectures can include several types of metals. Besides, the organic linkers can be of different nature too. Most common ligands are usually carboxylates, phosphonates, sulfonates and nitrogen derivatives such as pyridines, cyanides and imidazole.^{7,9} An important part of the MOF architecture is the bridging network that connects the three-dimensional structure. This network is considered the backbone of the structure, it can be functionalized by amino, halogen, or sulfonic groups. Such modifications can be done before and/or after MOF synthesis depending on the desired application (pre-and post-synthesis modifications). The metallic center, linker and bridging network formed, are what leads mainly to the huge versatility of MOF structures.

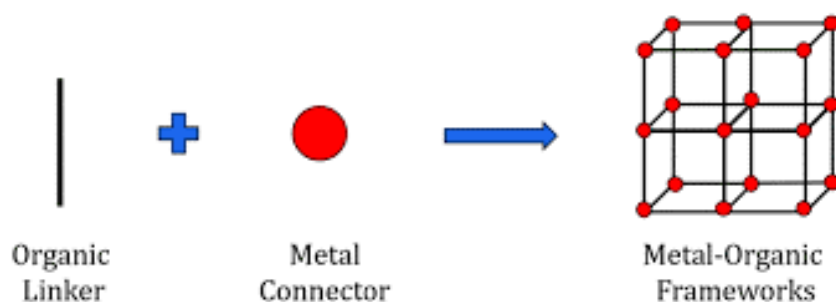


Figure 1-1. Schematic illustration of the construction of MOFs.

Notably, MOFs have endured their position as a hot research topic throughout the years due to their promising role in different applications. The state of the art is full

of daily released reports of MOFs in catalysis, gas storage, sensors, energy conversion, environmental remediation, drug delivery, etc.^{1,21} Nowadays, MOFs are getting more linked to industrial applications.²² For instance, a recent work by the group of Farha reported the use of UiO-66 as a polymer degrading catalyst that can break down plastic water bottles into its component parts.²³ The catalytic process can be done in 24 hours, has a yield of 98% under hydrogen and 81% under argon, and one of the obtained component parts (terephthalic acid (TA)) can be re-used in the synthesis of the MOF itself. Another example is the recent work done by the group of Kitagawa, the researchers reported an unprecedented work in which they were able to store acetylene, an industrial flammable gas, inside the pores of flexible MOF-508 and control its release while being accomplished at a temperature and pressure conditions suitable for industrial applications.²⁴ Furthermore, the Business Research Company published a 175 pages economic report this year, indicating that the technological advancement in material science is driving the MOF market into a 37% growth rate in the next 4 years (**Figure 1-2**).²⁵ The study covered main MOF manufacturers in the global MOF market like BASF SE, GS Alliance Co. Ltd, MOF Technologies Ltd, Mosaic materials LLC, Nanoshel LLC, novoMOF AG, Numat Technologies Inc, ProfMOF, and Promethean Particles Ltd. In their report, the authors discussed that despite the Covid-19 complications, the market size is expected to reach 743 million USD in 2026.²⁵



Figure 1-2: Global MOF market forecast for market size of 2021-2026 in million USD.²⁵

1.2.2. Building Blocks of MOFs

1.2.2.1. Organic building blocks

Concerning the organic building blocks, these blocks can be of different di-, tri- or poly-dentate ligands such as carboxylic acids, N-donor ligands (*e.g.*, imidazole and pyridine), sulfonates, and phosphonates (**Figure 1-3**).²⁶ Besides, the number and position of these anchoring groups can also be varied (*e.g.*, benzene-1,4-dicarboxylic acid (bdc), benzene-1,3,5-tricarboxylic acid (btc), benzene-1,2,4-tricarboxylic acid, and benzene-1,2,4,5-tetracarboxylic acid (btec), etc.). Most of the ligands employed in MOF synthesis are composed of aromatic rings, which grants rigidity and therefore stability to the structure. Generally, aromatic carboxylic acids are preferred as they provide strong ionocovalent bonds when coordinated with high valence metal ions (M^x-O-C ; $x \geq 3+$). This leads into the formation of well-defined inorganic blocks (metal clusters or chains), usually referred to as SBUs (Secondary Building Units), and thus, robust MOF structures.²⁶ In addition, as aromatic carboxylic acid ligands are ionic in nature, they generally provide neutral frameworks obviating the need for charge compensating counter-ions in the pores and thus diminishing the risk of framework collapsing after the evacuation/exchange of the counterions.²⁶ This great diversity leads to thousands of compounds with diverse properties/structures. For example, it is possible to vary the porosity of the MOFs in a tunable manner.²⁷ This has been specifically reported for MOFs based on aromatic dicarboxylic acid ligands leading to the IRMOFs, MIL-88, MIL-101, and UiO-66 reported series. In these series, by increasing the size of the spacer, the pore size and therefore the specific surface of the material could be controlled. It is thus possible to obtain micro- and mesoporous MOFs having similar structural types.²⁷

It is important to note that a combination of several ligands with different sizes and functionalities is possible and has been reported.^{28,29} Besides, the addition of functional groups to MOFs is interesting since it can change the framework's physicochemical characteristics.¹⁹ Such functionalities can provide specific interactions with targeted molecules (e.g., gas molecules, drugs, enzymes, etc.),^{19,30} tune certain properties (e.g., stability),³¹ and bring new functionalities (e.g., fluorescence, proton conductivity, catalytic properties).^{32,33}

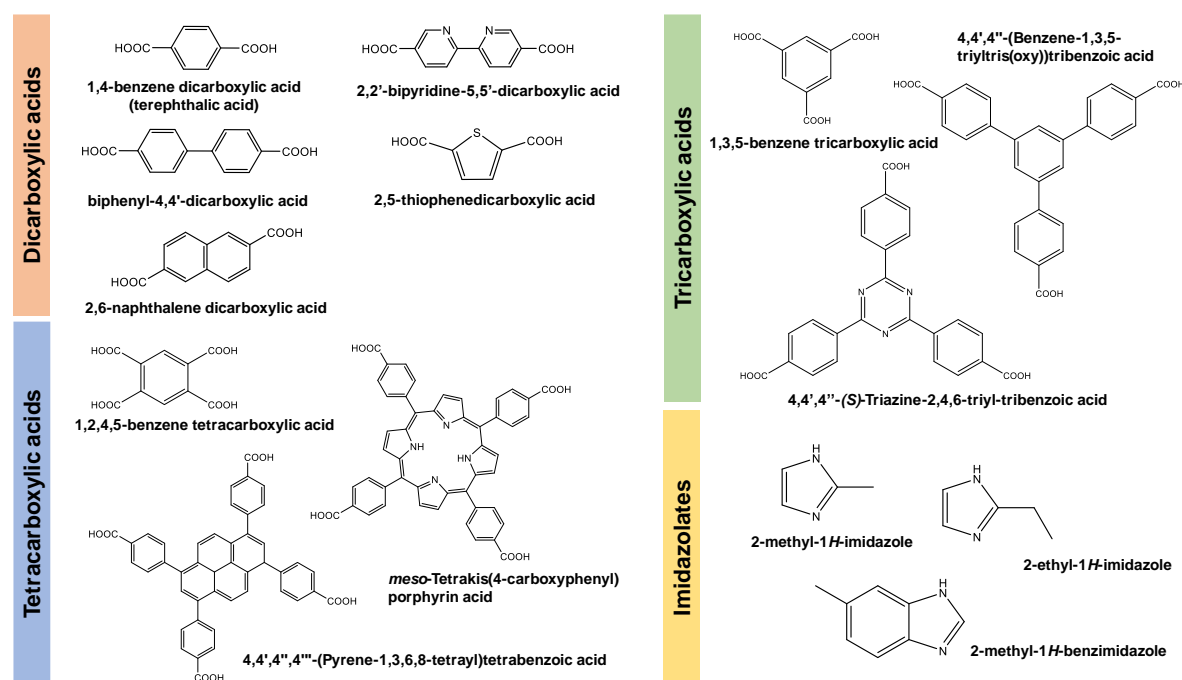


Figure 1-3. Examples of organic ligands used in MOF synthesis.

1.2.2.2. Inorganic building blocks

Regarding the inorganic building blocks, these blocks can be of various elements including transition metals (Zn^{2+} , Cu^{2+} , Fe^{3+} , Cr^{3+} , Ti^{4+} , Zr^{4+}), 3p metals (Al^{3+} , Ga^{3+} , In^{3+}), alkaline earth metals (Mg^{2+} , Ca^{2+}) or also lanthanides and actinides.^{34–36} They can either be single metal atoms, like in the case of ZIF-8, or metal oxo-clusters/metal chains, known as SBUs (**Figure 1-4, A**). Bimetallic and tri-metallic clusters,³⁷ including rare earth ones, can participate in the building of the frameworks as metal clusters or centers. Furthermore, different SBUs can be formed in the presence of polydentate organic ligands based on the nature of the metal

cation, its reactivity in solution, and the synthesis conditions (Figure 1-4).³⁵ It is possible to isolate some SBUs as molecular complexes (Cu_2O_{10} dimer,³⁸ μ_3 -oxo trimers,³⁹ and $\text{Zr}_6\text{O}_4(\text{OH})_4$ hexamers⁴⁰), whereas others are formed only in the presence of ligands during the MOF synthesis (e.g., 1D chains of trans-connected $\text{AlO}_4(\text{OH})_2$ octahedra).⁴¹ In general, the structural characteristics of a MOF are controlled by the synthetic conditions and the SBUs' geometry. Structures with higher chemical and thermal stability are obtained in the case of high-valence cations (M^{3+} , M^{4+}) and O complexing ligands as a result of the stronger metal-oxygen bonds formed.³⁵

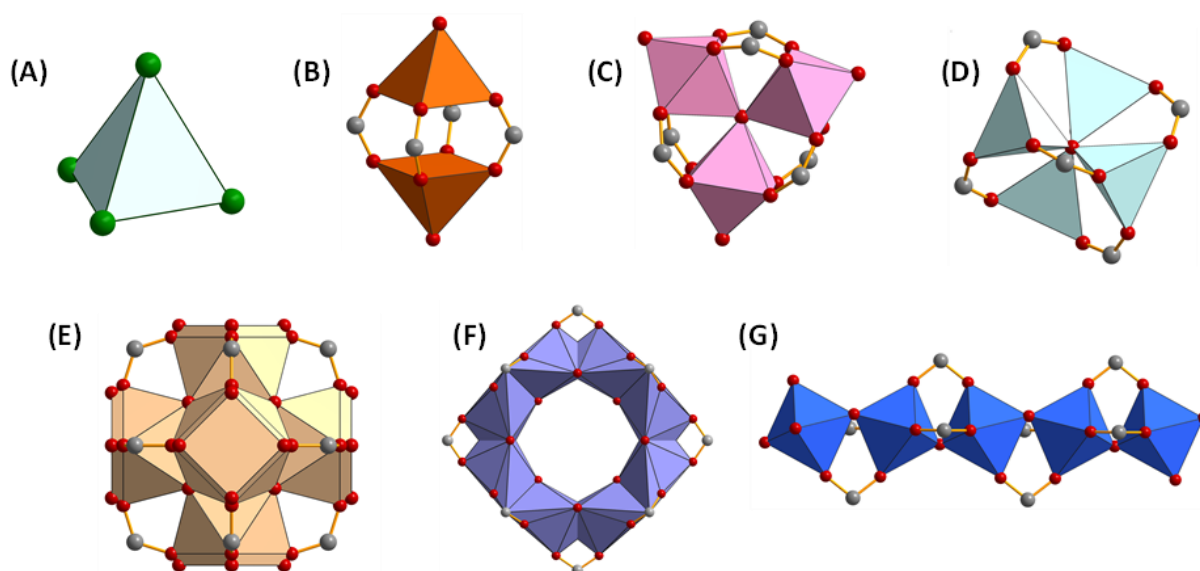


Figure 1-4. Common SBUs of MOFs. (A) Zn^{2+} ion of ZIF-8, connected with four N atoms of the ligands; (B) Cu_2O_{10} dimer of HKUST-1; (C) μ_3 -oxo trimer of MIL-100/101(Cr, Fe, Al); (D) Zn_4O tetramer of MOF-5 (or IR-MOF-1); (E) $\text{Zr}_6\text{O}_4(\text{OH})_4$ of UiO-66; (F) $\text{Ti}_8\text{O}_8(\text{OH})_4$ octamer of MIL-125 and (G) 1D $\text{AlO}_4(\text{OH})_2$ chain of MIL-53 (C atoms in grey, O atoms in red, N atoms in green).

1.2.3. Main Synthesis Protocols of MOFs

Mostly, MOFs reported in literature are synthesized by either hydro- or solvothermal syntheses (e.g., MIL-53, MIL-100, MIL-101, PCN-333, PCN-777, UiO-66, etc.). These reactions are based on heating the reactants (organic ligand and inorganic metal source) at a temperature higher than the boiling point of the organic solvent (water in case of hydrothermal synthesis) in a closed vessel under

an autogenous pressure. This approach allows the dissolution of usually insoluble aromatic ligands, increasing the reactivity of inert ions (e.g., Cr^{3+}), and favors crystallization.⁴² At the early stages, the aim of the synthesis in MOF research was to obtain single crystals allowing the resolution of the crystal structures. Later, the need for obtaining MOF nanoparticles for processing and applications has emerged, and alternative synthesis techniques like microwave synthesis appeared. Basically, it is possible to utilize microwave irradiation that allows homogenous heating throughout the sample with a high heating rate leading to an increased number of nucleation points, an accelerated crystallization processes, and formation of monodispersed nano-scaled materials. This synthesis approach is a subclass of (hydro)-solvothermal reactions and normally referred to as microwave-assisted (hydro)-solvothermal synthesis. The importance of this synthesis was first revealed in the case of MIL-100(Cr) which was synthesized in 96 hours at 220°C using conventional hydrothermal synthesis compared to 4 hours under microwave irradiation.^{43,44} Ever since, microwave assisted syntheses became the major approach to obtain nanoMOFs through very fast reactions (e.g., nanoMIL-101(Cr): 50 nm in 5 min; nanoMIL-101(Fe)-NH₂: 173 nm in 5 min; etc.).^{45,46} Lately, massive efforts have been made to move from (hydro)-solvothermal syntheses into more sustainable reactions under ambient pressure.⁴⁷ Therefore, room temperature and reflux MOF synthesis have also been widely reported.⁴⁷ This type of reactions is operated at various temperatures between room temperature and the boiling point of the solvent, and under ambient pressure. Performing reactions under ambient pressure allows a better control over the synthesis conditions and facilitates *in-situ* and *ex-situ* (e.g., sample extraction during synthesis) of the MOF formation. In addition, RT and reflux synthesis are more suitable for high-scale production, especially when nontoxic solvents are utilized. Some classic examples of MOFs synthesized under ambient pressure are MOF-5, HKUST-1, ZIF-8, MIL-100(Fe), MIL-96(Al), MIL-125(Ti)-NH₂, UiO-66(Zr), etc. Likewise, other synthetic

methods as mechanochemical⁴⁸, electrochemical⁴⁹, and sonochemical⁵⁰ have also been reported. Finally, after every MOF synthesis, it is vital to activate the MOF. This step consists of washing the MOF sample to remove any residual solvent molecules and/or impurities (e.g., unreacted ligands) in order to obtain highly porous materials.

In conclusion, an organic linker and an inorganic metal center are needed to synthesize a MOF. It is important during the synthesis process to find conditions that lead to the formation of robust SBUs, without the decomposition of the organic linker, and to yield a crystalline pure phase.⁴² To make sure that the desired phase can nucleate and grow, thermodynamic and kinetic parameters should be studied and satisfied, yet, MOF synthesis is commonly based on empirical trials. In addition, experimental and physico-chemical parameters are studied and analyzed too. Experimentally, the molar ratio of ligands to metals, nature of precursors, pH, solvent, etc. all play a vital role during synthesis. Similarly, the physico-chemical parameters: temperature, pressure and reaction time, are considered vital for the formation of the framework.^{1,42} Moreover, additives like acids, bases or modulator can be added to the mixture at a given time to favor MOF crystallization. Previously, HF has been widely used as a mineralizing agent as it favors the formation of well crystalline MOF phases. Yet, HF is a highly toxic and corrosive material. Efforts have been made lately to replace HF by other less toxic and less dangerous acids such as HCl, acetic acid (AcOH) or to avoid completely the use of modulators.¹

1.3. FLEXIBILITY IN MOFS

MOFs can be subjectively categorized as rigid or flexible materials. Originally, once the assembly of inorganic nodes with the organic linkers into a crystalline state occurs, rigid MOF structures are obtained. Rigid MOFs offer a permanent porosity and a robust network. Comparingly, frameworks with a flexible structure offer huge dynamicity as they respond to different physical and chemical stimuli (e.g., guest adsorption/ desorption, thermal, mechanical, etc.) allowing their utilization in different selectivity demanding applications (e.g., gas adsorption/ separation, sensors, etc.). MIL-53(Cr) was the first flexible MOF to be reported in literature in 2002,⁵¹ and few years later leading works exploiting dynamic and flexible MOFs started to appear.^{52,53} These works allowed a better understanding of the so-called third-generation MOFs that started to rise after its prediction in 1998.^{3,54} The first generation of porous coordination networks suffered a huge drawback in which the network collapses upon removal of solvent molecules.^{3,32,55} In contrast, the second generation did not suffer this drawback, the network remained intact after removal of guest molecules.^{3,32,55} Then, the third generation emerged, and it had the privilege of turning this drawback into a unique functional advantage through the proper selection and design of the building units and the structure **(Figure 1-5)**.⁵⁶ In fact, this last generation covers what is referred to today as flexible (or switchable) MOFs.

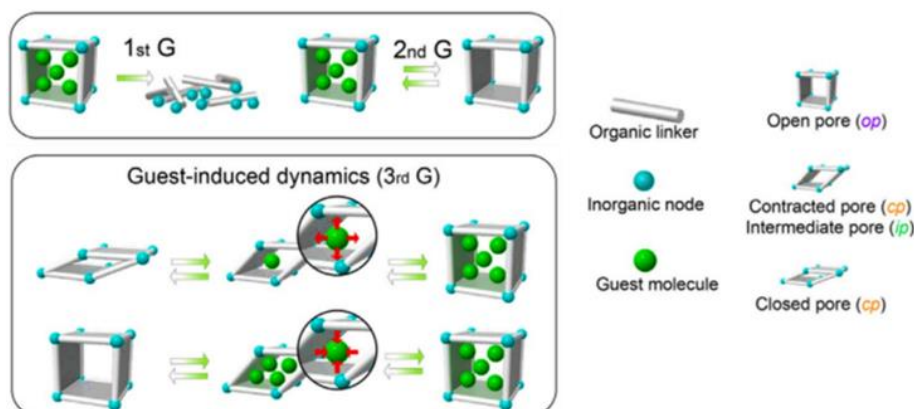


Figure 1-5: The three generations of MOFs and their structural behavior upon guest insertion/ removal. Reproduced from⁵⁴

1.3.1. Flexibility modes

Flexibility modes in MOFs were early classified into two classes by Bousquet *et al.* and Coudert *et al.*^{57,58} The first class includes phenomena that involve a change in the unit cell volume ($\Delta V \neq 0$), while the second includes those that do not ($\Delta V = 0$). Examples on class one include breathing effect (e.g., MIL-53),⁵⁹ swelling deformation (e.g., MIL-88),⁶⁰ and subnetwork displacement (e.g., $\text{Cu}_2(\text{bdc})_2(\text{bpy})$)^{61,56} The most common mode of flexibility in MOFs is breathing. It is referred to as the dynamic behavior of the MOF network in which a transition between two or more phases occurs (e.g., large and narrow pore phases). Second common mode is swelling which is described by the three-dimensional increase/decrease in unit cell volume without a change in its shape or space group. Regarding subnetwork displacement in flexible MOFs (**Figure 1-6, D**), this phenomenon can differ depending on the MOFs network type (i.e., catenated, interdigitated, or stacked layers network). All three types involve a change in the unit cell volume but with different dynamic behaviors. In fact, subnetwork displacement appears in MOFs which are built of 2D networks connected by weak forces. These subnets can drift, relocate, or shift to each other, allowing a big change in the unit cell and even giving rise to symmetrical modification. On the other side, the second class of flexible MOFs comprises MOFs that undergo a free linker rotation transition (**Figure 1-6, C**). Different to the previously mentioned three modes, linker rotation in flexible MOFs will not cause a change in the unit cell volume but rather a unified rotational motion of the linkers. A prototypical example of the second class is the linker rotation in ZIF-8 which was first discussed in 2011 by Fairen-Jimenez.⁶²

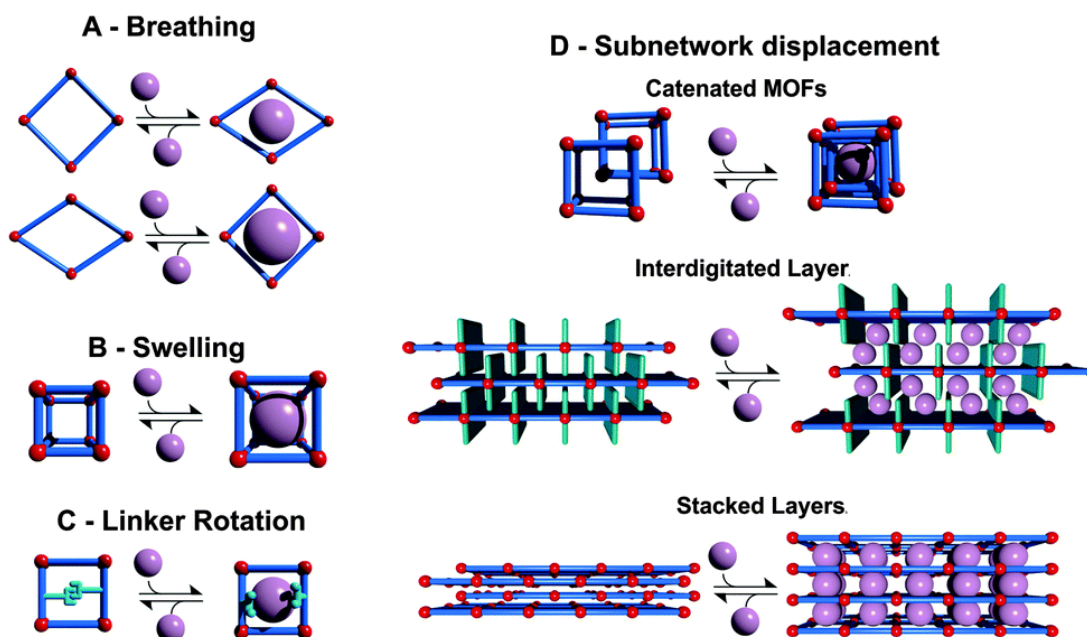


Figure 1-6: Two classes of flexibility in MOFs. Class 1 comprises change in unit cell volume ($\Delta V \neq 0$; A, B and D), while class 2 does not ($\Delta V = 0$; C). Retrieved from ⁵⁶

1.3.2. Breathing of MIL53(M) as a case study

Chiefly, the type of metal nodes involved and the way they coordinate with the linker molecules monitors the framework flexibility. The cooperation between both the organic linker and the inorganic node can lead to breathing (**Figure 1-6, A**); one of the most intriguing aspects of flexibility in MOFs. Breathing phenomenon could be defined as the reversible transition of MOFs through which a change in the unit cell volume occurs as a function of the displacement of atoms in response to specific stimuli (e.g., gas molecules, solvents, pressure). Indeed, the known characteristic distances and angles of the unit cell change and the crystallographic space groups of the two distinct phases can, but not necessarily, differ. Principally there is two main phases that occur during breathing: the large pore (lp) phase and the narrow pore (np) phase. In some reports, it is referred to as open pore (op) and closed pore (cp) phases. Besides, some reports use labels as high temperature (ht) and low temperature (lt) phase depending on the form of the pores at each temperature. Terminologies like very narrow pore (vnp) are used in MOFs with more than two distinct pore forms. The classic example of breathing in MOFs is the

MIL-53(M) family ($[M(\text{bdc})(\text{OH})]_n$ with $\text{bdc} = 1,4\text{-benzenedicarboxylate}$, and $M = \text{Cr},^{51,63} \text{Al},^{64} \text{Fe},^{59} \text{Ga},^{65} \text{Sc}^{66}$). The metal terephthalates MIL-53 series is well known for varying the shape and size of its pores based on certain stimuli (e.g., adsorption of polar molecules (CO_2 , H_2O) and linear hydrocarbons (except CH_4)). The unit cell volume can decrease by $\sim 40\%$ during the transition from (lp) to (np) depending on the adsorbed species (i.e., size, and bonding characteristics). Furthermore, the structure can undergo a reversible switching from (np) to (lp) when the loading of the adsorbates is increased. As mentioned, one of the first discussed case studies was MIL-53(Cr).⁵¹ This MOF presents a huge increase in the unit cell volume ($\Delta V = 473 \text{ \AA}^3$; $\sim 32\%$) when moving from the low temperature (lt) to the high temperature (ht) phase.^{51,63} The MOF is hydrated at low (room) temperature and present in its (lt) phase. At high temperatures, the pores are evacuated (ht), and the volume of the pores increases significantly. Of huge interest is understanding flexible behavior in MOFs. Considering the case of MIL-53(Cr), bdc is a rigid linker, hence the flexibility in the framework can be related to changes in the inorganic node or the angle between the SBU and the linker.⁶⁷ As shown in **(Figure 1-7)** below, no changes in the SBU that can justify the big increase in the unit cell volume were observed.^{51,63} Concerning the angles between the SBU and the organic ligand, it was stated that despite the transitional state (as-synthesized, ht, or lt) the O–Cr–O and Cr–O–Cr angles do not show any dramatic change **(Figure 1-7, b-d)**. However, a change in the dihedral angle between O–Cr–Cr–O and the O–C–O planes was observed indicating a breathing effect of the framework (177.5° for -as, 180° for -ht and 139° for -lt forms) **(Figure 1-7, e-f)**. In fact, the α dihedral angle is the measuring scale for the extent of this breathing where the most extended structure occurs upon a dihedral angle of 180° . In addition, hydrated pores lead to strong hydrogen bonds between the framework and the guest molecules. Yet, weak intermolecular interactions between water molecules and $\mu_2\text{-OH}$ of the framework can justify the structural transformation process upon hydration/dehydration.

Later, Parent and co-workers were able to visualize the breathing phenomenon of MIL-53(Cr) under water adsorption/ desorption and heating by recording in-situ electron diffraction patterns using an environmental transmission electron microscope.⁶⁸

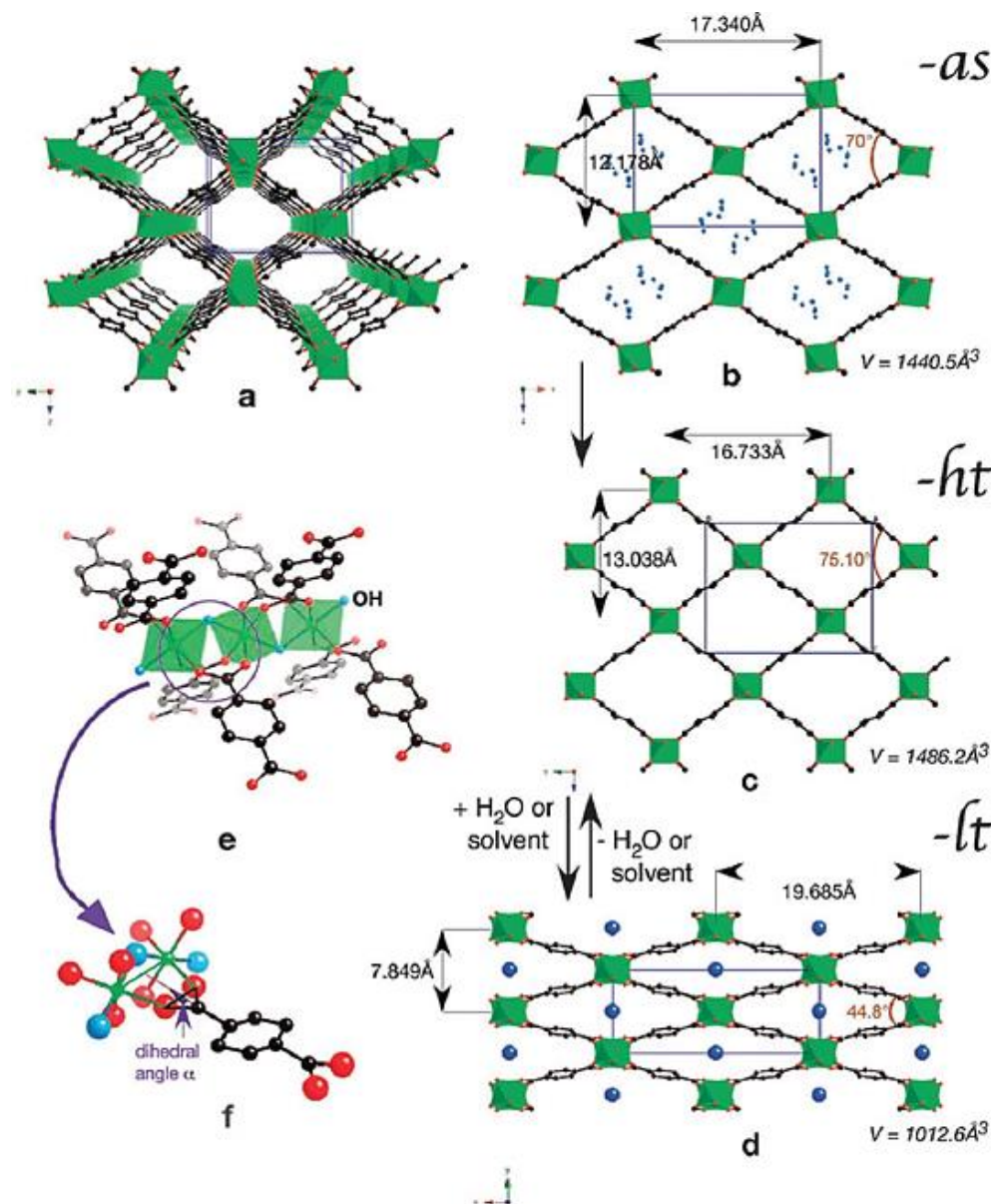


Figure 1-7. (a) Perspective view of MIL-53-ht; (b)–(d) Projection along the direction of the channels of: (b) MIL-53-as (with some atoms of the disordered terephthalic acid in blue), (c) MIL-53-ht, and (d) MIL-53-lt with variable parameters; (e), (f) Perspective views of the connection between the chromium chains and the terephthalate ions. Chromium octahedra are depicted in green, water molecules in dark blue, OH groups in pale blue, oxygen in red, and carbon in black. Retrieved from ⁶⁷

Another example is the MIL-53(Al). Compared to MIL-53(Cr), the pores are also filled with unreacted bdc ligands before activation. Yet, the main difference is that

MIL-53(Al) evolves into three phases in response to stimuli and not only two. Previously, it was assumed that MIL-53(Al) evolves into two phases after activation. A (lp) phase with an orthorhombic crystal system once the pores are evacuated at elevated temperature (**Figure 1-8, c**), and (np) phase with a smaller unit cell and monoclinic crystal system after hydration at room temperature (**Figure 1-8, a**). The transition between the two phases was explained by guest-host interactions between the imprisoned water and the carboxylate groups of the ligand. The hydrogen-bonding interactions between the water molecules trapped within the channels and the carboxylate groups of the BDC linkers lead to the rotation of the aluminum octahedra. In fact, this rotation of the octahedra towards the trapped water molecules causes the rhombic channels to contract due to the decrease of the α angle (bdc-Al-bdc).⁶⁴ Nevertheless, it was later reported that a third phase with also a monoclinic crystal structure, but a smaller unit cell, can occur under vacuum and in absence of any guest molecules and was referred to as the closed pore phase (cp) (**Figure 1-8, b**).⁶⁹ Afterwards, it was reported that the transition between the different phases of MIL-53(Al) can also occur under temperature or pressure.^{70,71} Hence, MIL-53(Al) is a prototypical example for which the breathing phenomenon is an intrinsic property that occurs due to various stimuli. Further work was recently done by Hoffman *et al.*⁷² to better understand the breathing behavior of MIL-53(Al). Through employing both vibrational spectroscopy (IR, Raman) and advanced computational techniques (static and dynamic DFT), Hoffman and co-workers defined a 'vibrational fingerprint' of the breathing effect occurring at the inorganic Al-OH backbone of the framework that allows differentiating the IR spectra of both the closed and large pore forms of the MOF. In addition, a collective 'trampoline' motion of the linkers to increase π - π interactions as the framework contracts upon cooling was displayed and discussed.⁷² Seoane *et al.* reported an interesting work in which they tracked the anisotropic expansion of the MIL-53(Al) in real time using environmental scanning

electron microscopy (ESEM). The authors considered the electron beam as a source of heating and then utilized this source to measure directly the changes in dimensions of individual crystals.⁷³

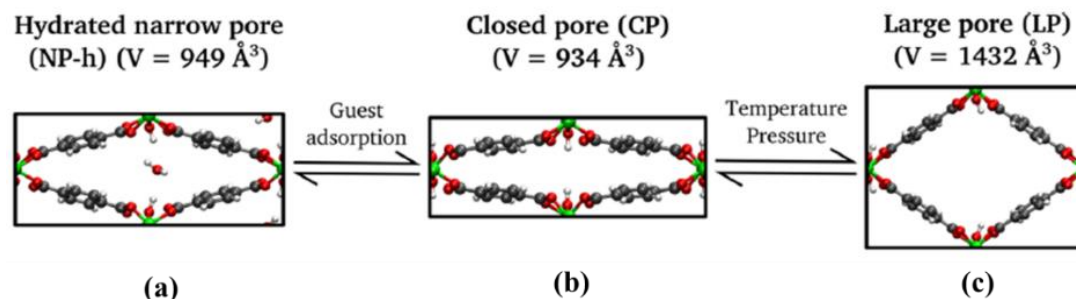


Figure 1-8. Illustration of the crystal structures of the distinct phases of MIL-53(Al): (a) narrow pore phase at RT, $\text{Al(OH)[O}_2\text{C-C}_6\text{H}_4\text{-CO}_2\text{]}\cdot\text{H}_2\text{O}$; (b) closed pore phase under vacuum, $\text{Al(OH)[O}_2\text{C-C}_6\text{H}_4\text{-CO}_2\text{]}$; (c) calcined form, $\text{Al(OH)[O}_2\text{C-C}_6\text{H}_4\text{-CO}_2\text{]}$ with empty channels. Adapted from ⁷².

In fact, MIL-53 has always been an appealing candidate to explore due to the vast variety of metals and linker derivatives that can form the structure. It was reported that the flexibility of the MIL-53(M) series depends on the metal nodes (**Table 1-1**).⁵⁶ For example, contrary to the other MIL-53 frameworks, iron and scandium-based frameworks show a contraction upon activation despite the fact that they are in their guest-free state. Comparably, aluminum, gallium, and chromium all show the same transition from large to narrow pore when hydrated after cooling at ambient conditions.

Table 1-1. Comparison of the unit cell volumes (\AA^3) of different flexible MIL-53 derivatives.

	MIL-53(Cr)	MIL-53(Al)	MIL-53(Fe)	MIL-53(Ga)	MIL-53(Sc)
Reference	51,63	64	59	65	66
V (-as form)	1440.6	1383.1	899.6	1434.1	1296.6
V (-ht form)	1486.1	1411.9	899.6	1479.7	902.5
V (-lt form)	1012.8	946.7	986.8	885.6	954.385
$\Delta V (V_{lp} - V_{np})$	473.3	465.2	87.2	594.1	51.885

Finally, it is worth mentioning that besides the famous MIL-53 family, other classical examples of flexible MOFs are MIL-88⁶⁰ and paddlewheel-based MOFs which have been employed in applications related to controllable release and separation.⁶⁷

1.3.3. MOFs Studied in this Work

As listed in **(Table 1-1)** above, exploiting different metals can lead to different dynamic behaviors in flexible MOFs. Yet, it should be of interest to understand the role of the cooperative effect of both the metal and the ligand in this flexibility. This objective can be achieved by comparing different isorecticular MOFs, which are MOFs with similar topologies but different organic ligands (e.g., MIL-69(Al) and DUT-5(Al)). Among the different aluminum MOFs with a similar “wine rack” MIL-53 type structure is the DUT-5(Al) framework.⁷⁴ Our interest in DUT-5(Al) arises from results obtained throughout this PhD project. In fact, via applying certain experimental conditions (**check chapter 4**), a flexibility behavior was detected in the rigid DUT-5(Al) framework. Originally, this MOF is known to be a permanently open rigid MOF, yet an interesting guest- and temperature-induced flexible behavior was observed during this PhD project.

To better understand this behavior, the focus of this section will be oriented towards reviewing the flexible behavior of Al³⁺-polycarboxylate based MOFs (Al-MOFs) reported in literature, with a similar structure to DUT-5(Al). To be more specific, the focus of this section is towards MOFs in which the coordination of Al³⁺ cations with polycarboxylate ligands forms 1D chain SBUs build up from μ_2 -hydroxo corner sharing octahedra (**Figure 1-4, g**).^{35,75} The combination of 1D chain SBU with linear dicarboxylate ligands leads most of the time to the formation of 3D structures with 1D channels. These channels could be of different architectures (e.g., triangular, rectangular, hexagonal, diamond shaped, etc.). Among the different Al-based MOFs reported in literature with such a structure, MIL-53(Al) and its isostructural series presents an attractive example. First, comparing different Al based MOFs of the MIL-53(M) family type structure helps better understand the relationship between flexibility and the coordination network of the MOF (**Figure 1-9**). Secondly, DUT-5(Al), which is the MOF studied throughout this PhD, belongs

to the same series. Lastly, it should be mentioned that MOFs based on aluminum and aromatic carboxylates occupy an exceptional position among the ever-increasing number of studied MOFs.^{76–78} Aluminum metal is the third most abundant element in the shallow earth, and it is commercially available at a low cost. Al-MOFs present a good performance in the sorption, separations, purification of water and air, heterogeneous catalysis, and sensing.^{76–78} These properties make aluminum an interesting building block for MOFs. Compared to MOFs with divalent d-block metals (e.g., Zn^{2+} , Cu^{2+}) and trivalent f-block (e.g., lanthanides), the trivalent Al^{3+} ion has been a promising candidate for building different coordination frameworks with a low density and notably high thermal or physicochemical stability.^{75,76}

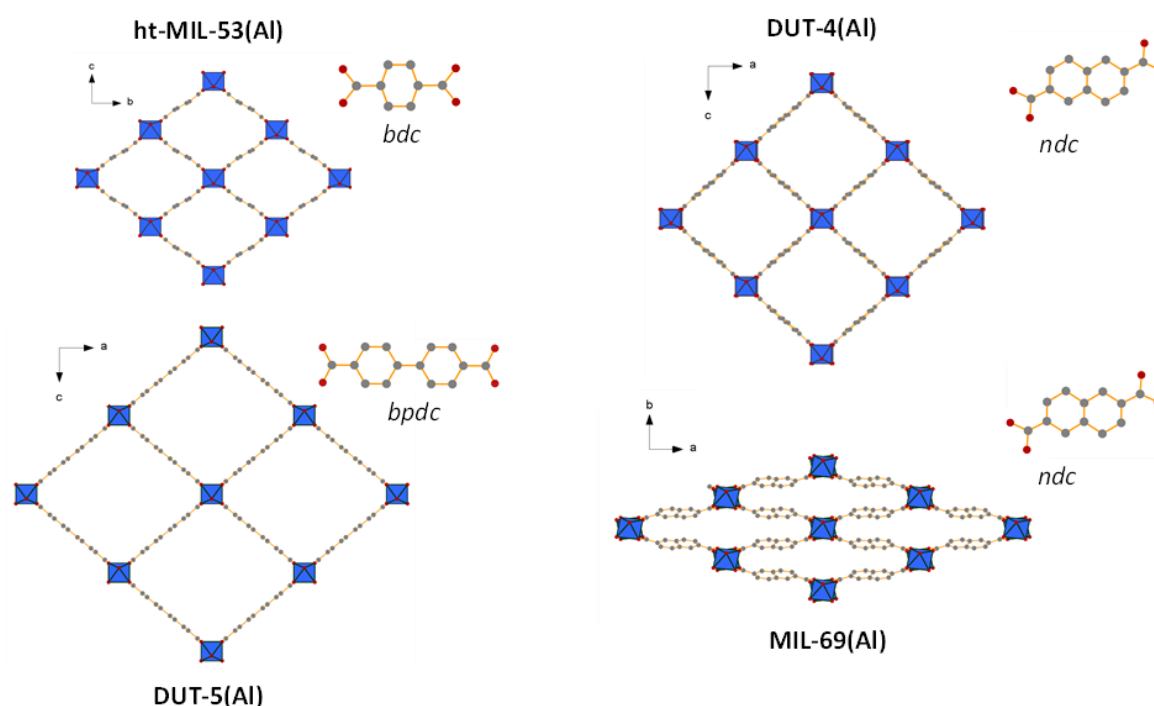


Figure 1-9. Topological view along the channels of MIL-53(Al) and its isoreticular series with the corresponding ligands: DUT-4(Al), DUT-5(Al), and MIL-69(Al). Dark blue polyhedra represent $\{AlO_6\}$ octahedra, while grey and red present C and O atoms, respectively.

As observed in literature, despite the intrinsic flexible property of MIL-53(Al), this flexibility is not transferred in a hereditary manner into its isorecticular MOFs or MOFs with a similar wine rack structure. It should always be remembered that the metal-ligand coordination of the MOF plays a key role in achieving flexibility and it has been the hot spot of early-stage research on this topic. As an example, when terephthalic acid in flexible MIL-53(Al) is replaced by 2,6-naphthalenedicarboxylic acid, the MIL-69(Al) MOF is obtained with a rigid structure made of 1D channels of $2.7 \times 19.4 \text{ \AA}$.⁷⁹ This rigidity could be explained by the strong π - π interactions between the ligands that do not allow the pore opening after dehydration.⁷⁵ Similarly, DUT-4(Al) which is the open porous version of the non-porous MIL-69(Al), with 1D rectangular channels of $8.5 \times 8.5 \text{ \AA}$, is also recognized as a rigid framework.⁷⁴ Likewise, DUT-5(Al) which is isorecticular to DUT-4(Al), and possesses the same inorganic building units of MIL-53(Al), is known in literature to have a rigid framework with a permanent porosity and 1D channels of $11.1 \times 11.1 \text{ \AA}$.⁷⁴ Another MOF with the MIL-53 type structure is the patented MIL-53(Al)-FA (FA: Fumaric Acid), or Basolite A520 as commercially referred to by BASF and Sigma-Aldrich.⁸⁰ The coordination of fumaric acid with the 1D Al-chains yields a non-flexible MOF with microporous channels of $5.7 \times 6.0 \text{ \AA}$. However, a MOF with the MIL-53(Al) type structure which exhibits a distinct flexibility behavior exists. For instance, CAU-13(Al) (CAU: Christian-Albrechts-Universität) with 1,4-cyclohexanedicarboxylic acid as a ligand, shows a linker rotation induced flexibility behavior. Ligands are coordinated in the a,a and e,e conformations while the pores are empty, once xylenes are adsorbed, they all convert to the e,e conformation causing the framework to breath **(Figure 1-10)**.^{81,82}

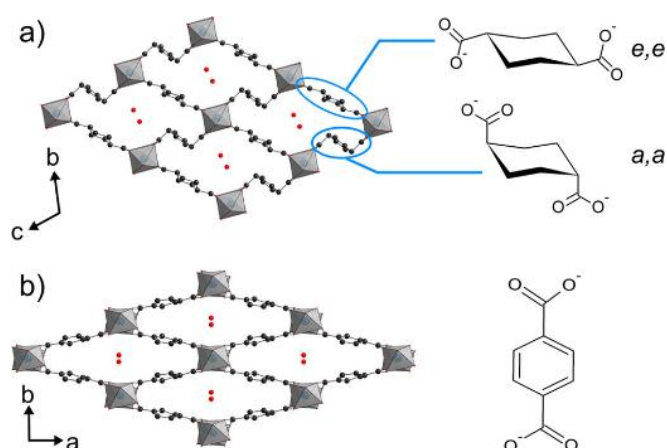


Figure 1-10. Crystal structures and formula of the incorporated linkers of (a) CAU-13-H₂O and (b) MIL-53(Al) (np). AlO₆ polyhedra are presented in gray, carbon atoms in black, and oxygen in red. On the right, the linkers present in the structures of CAU-13 and MIL-53 are shown: (a) e,e-CDC²⁻ and a,a-CDC²⁻; (b) BDC²⁻.⁸²

Other MOFs with the MIL-53(Al) type structures include MIL-118(Al),⁸³ MIL-121(Al),⁸⁴ MIL-122(Al),⁸⁵ and NOTT-300(Al)⁸⁶ but they will not be further discussed.

Of our interest in this PhD project is to extensively study the work done on DUT-5(Al). Of special importance in the field of MOFs is utilizing highly extended linkers in order to prepare isorecticular analogues with superior porosity.²⁷ As known, the replacement of the parent ligand by another extended one can yield MOFs with isostructural topologies, higher porosities, and different properties that depend on the employed ligands.²⁷ DUT-5(Al) was first reported by Senkovska and co-workers as an extended form of the MIL-53 structure.⁷⁴ The bdc linker used in the synthesis of MIL-53 was replaced by biphenyl-4,4'-dicarboxylate (bpdc). This MOF is built from Al³⁺ metal centers and bpdc organic ligand. It consists of Al-OH inorganic chains that are connected by the organic linkers to form a 3D structure. Each inorganic chain is connected to other four neighboring chains (**Figure 1-11**). This coordination results in the formation of diamond shaped micropores (channels) that extend in one direction. The effect of the extended linker can be shown through the distance between the aluminum centers in neighboring chains. In case of DUT-5(Al) they are separated by 19.24 and 22.94 Å compared to 16.73 and 13.04 Å in case of MIL-53(Al). To our knowledge, in contrast to MIL-53, DUT-5 has always

been synthesized as a rigid permanently open structure with no breathing effect.⁸⁷ Nevertheless, its vanadium analogue, CMOC-2, have shown a pressure induced flexibility behavior that was later applied in separating hydrocarbon mixtures.^{88,89} Besides, a mixed metal approach was followed for DUT-5(Al), and it allowed the transition between the large and narrow phases more rapidly, at lower pressures.⁹⁰ The COMOC-2(V)/DUT-5(Al) reported by Depauw exhibited a pressure induced flexibility in which two distinct (lp) phases and a (np) one are presented. The authors noticed that the transition between the (lp) and (np) phases is faster with increasing the Al content in the mixed metal framework.⁹⁰ Hence, it can be stated that tailoring the breathing behavior in COMOC-2(V) is possible through (Al) doping. Indeed, the mixed metal approach was also previously applied for MIL-53 type structures. Additionally, a DUT-5 variant using 2-phenylpyridine-5,4'- dicarboxylate (dcpyp) was reported by Dau *et al.* The dcpyp ligand is a derivative of bpdc. The MOF variant showed the same chemical and thermal stability of the parent MOF, but the flexibility of this framework was no further discussed in literature.⁹¹

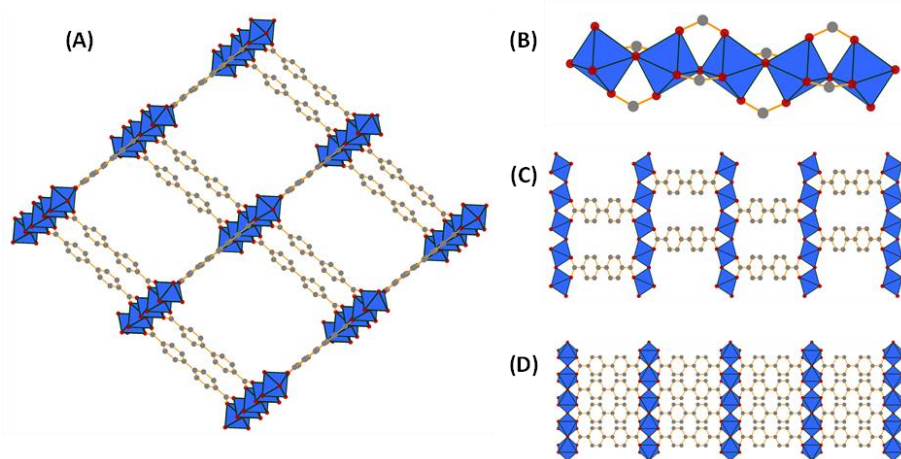


Figure 1-11. (A) View along the channels of DUT-5(Al); (B) 1D $\text{AlO}_4(\text{OH})_2$ chain of DUT-5(Al); (C) view along (a) axis; (D) view along (c) axis. Blue polyhedra represent $\{\text{AlO}_6\}$ octahedra, while grey and red present C and O atoms, respectively.

Hence, these works further validate the role of the frameworks coordination network in monitoring the flexibility of the structure. Not only the rigidity of the linker, but also the metal nodes involved, and the way they coordinate with the

employed linkers, play a vital role in controlling MOFs flexibility. In addition, it was shown that in case of DUT-5(Al) and its analogue COMOC-2, the functionalization of the MOF ligands with diverse groups (i.e., NO₂, NH₂, SO₂) did not affect the flexibility of the framework, however it yielded some interesting properties (e.g., higher CO₂ capacity in case of SO₂-COMOC-2 at low pressure).

1.3.4. Stimuli affecting flexibility in MOFs

Flexibility in MOFs was always correlated to the guest molecules inside the pores (presence/ absence by removal).³² Nonetheless, physical, or chemical stimuli have been considered necessary to trigger dynamic behaviors in MOFs. Evidently, a structurally responsive crystalline material towards external stimuli is a non-rigid one, or in other words, a flexible material. Fischer, Kaskel, and co-workers⁵⁶ defined flexible MOFs as "materials that combine the crystalline order of the underlying coordination network with cooperative structural transformability attaining the ability to respond to physical and chemical stimuli of various kinds in a tunable fashion by molecular design, which does not exist for other known solid-state materials". The various kinds of stimuli include guest adsorption/ desorption, photochemical, thermal, and mechanical stimuli. Coudert⁹² and Fischer⁵⁶ summarized and reviewed different recent examples of flexible MOFs based on the various mechanisms mentioned above. As an example, photo-responsive flexible MOFs were stated in literature and were mainly discussed for targeted encapsulation and sensing applications.^{15,93,94} Furthermore, thermosensitive flexible MOFs were also discussed based on the responsive behavior of their organic ligands. The ligands respond to heat through either the rotation of the aromatic rings or the movement of the dangling side chains which affects the form of the linker and induces flexibility in the framework.⁹⁵⁻⁹⁹ Nevertheless, MOFs also possess other flexible properties such as sub-net sliding and linker rotation which are not constantly accompanied by a crystallographic phase transition.⁶⁷ Alarmingly, till today there is no clear theory that can provide a full understanding

of the key parameters for flexibility in MOFs or predict its occurrence. Yet, some empirical rules have been formulated based on previously recorded experimental data by G. Ferey and C. Serre.⁶⁷ As an example, one of these rules concerns the metal clusters with ditopic carboxylates; the inorganic brick should have a mirror plane with the carboxylates ordered in symmetrical position around it to observe a breathing phenomenon.

1.3.4.1. Effect of solvent on flexibility

A very recent example on dynamic MOFs is the work done by the group of Jancik. Recently, the group has reported a new flexible MOF with a guest-selective transition between (op) and (cp) phase.¹⁰⁰ The MOF labelled as CCIQS-1 consists of three interpenetrated subnetworks of $[\text{Sc}_3(\mu_3\text{-O})\text{-(H}_2\text{O)}_2\text{(OH)}(\mu\text{-O}_2\text{CR)}_6]$ nodes interconnected by 4,4'-(9,10-anthracenediyl)dibenzoate ligands (**Figure 1-12, A**). This connection led to the formation of both hydrophilic and hydrophobic channels inside the MOF structure. It was observed that upon removal of certain solvents from the pores, the hydrophobic channels contract, while the 1D hydrophilic ones stay open. This results in a low affinity toward non-polar guests (e.g., toluene, cyclohexene, and hexane) and justifies the fact that only certain solvents can reopen the pores of the MOF after being closed. In fact, CCIQS-1 displays a selective response to the adsorbate, where the (cp) to (op) transition is only triggered by solvents with a large molecular size and moderated polarity (e.g., MeOH, DMF, acetone, and TH). However this transition is absent when using solvents at the extremities of the scale of polarities (e.g., H₂O and hexane) (**Figure 1-12, B**).¹⁰⁰ Hence, the obtained results can be explained by the interplay between the strength of the guest-host interactions and both the polarity and the molecular size of the guest. It is worth mentioning that among the non-polar solvents, only 1-hexene can reopen the closed pores of CCIQS-1 (**Figure 1-12, C**). This selective behavior towards 1-hexene can be explained by the π - π interactions between the pore walls and hexene molecules. Therefore, the kinetic diameter, polarity, and double bond

pg. 32

of 1-hexene triggered the rapid reopening of MOF pores and offered it a selective response compared to other non-polar solvents.

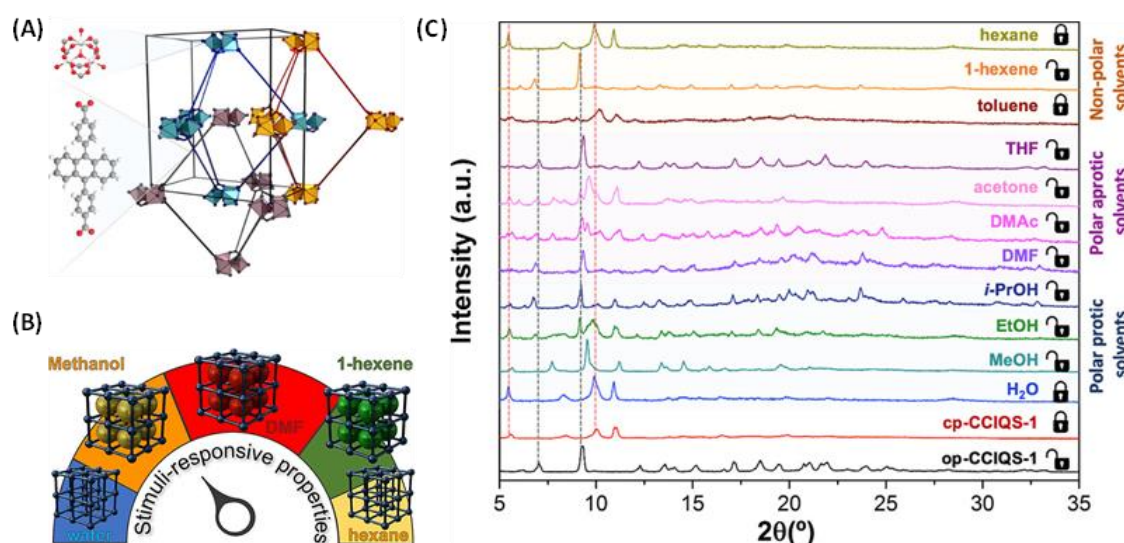


Figure 1-12: (A) Identification of the relative position of the three independent subnetworks in the unit cell; (B) Selective response to different guests; (C) PXRD patterns of (cp) CCIQS-1 samples exposed to different solvents for re-opening. Reproduced from ¹⁰⁰

Table 1-2. Physical properties of some guest solvents. ¹⁰⁰

Guest	Polarity (E_N^T)	Kinetic diameter (Å)
H ₂ O	1	2.96
MeOH	0.762	3.8
EtOH	0.654	4.3
i-PrOH	0.617	4.7
DMF	0.386	5.5
DMAc	0.377	~5.8
acetone	0.355	4.6
THF	0.207	4.86
toluene	0.099	5.85
1-hexene	0.052	4.2
hexane	0.009	4.3

This structure-property relationship can be further validated through analyzing the work done by Kundu *et al.*¹⁰¹ The authors discussed the solvent-induced changes in the particle size and in the structural transition between the (lp) and (vnp) phases of MIL-53(Al)-NH₂ and MIL-53(Al)-OH. The solvent induced changes were based on tuning the water/DMF ratio for the synthesis of MIL-53 samples. The breathing

behavior of these MOF samples was studied by high-pressure methane (CH_4) sorption tests. Upon increasing the CH_4 partial pressure, a structural transition from the very narrow pore (vnp) to the np and lp forms of MIL-53(Al)- NH_2 and MIL-53(Al)-OH is observed (**Figure 1-13**). It was shown that increasing the DMF concentration in the reaction mixture decreases the MOF particle size and increases the stability of the (lp) phases in both MIL-53(Al) MOFs (**Figure 1-13**). For example, the (lp) in MIL-53- NH_2 (with 0% DMF) is reached typically at a pressure above 98 bar under CH_4 sorption. When the DMF content in the synthesis solution was increased to 40%, this (lp) was reached at a pressure of 80 bar only. To highlight the importance of this solvent induced control over the porous phases in MIL-53(Al), it is important to relate the DMF concentration to the amount of deliverable gas that can be stored in the MOF. As shown in (**Figure 1-13, right a-b**), increasing the DMF content in the water synthesis solution from 0 to 20 vol.% led to a 33% increase in the deliverable CH_4 capacity. Similar results were obtained for MIL-53(Al)-OH in which the increase in the DMF volume in synthesis solution from 20 to 40% increased the amount of adsorbed CH_4 at 20 bar by almost 85%.

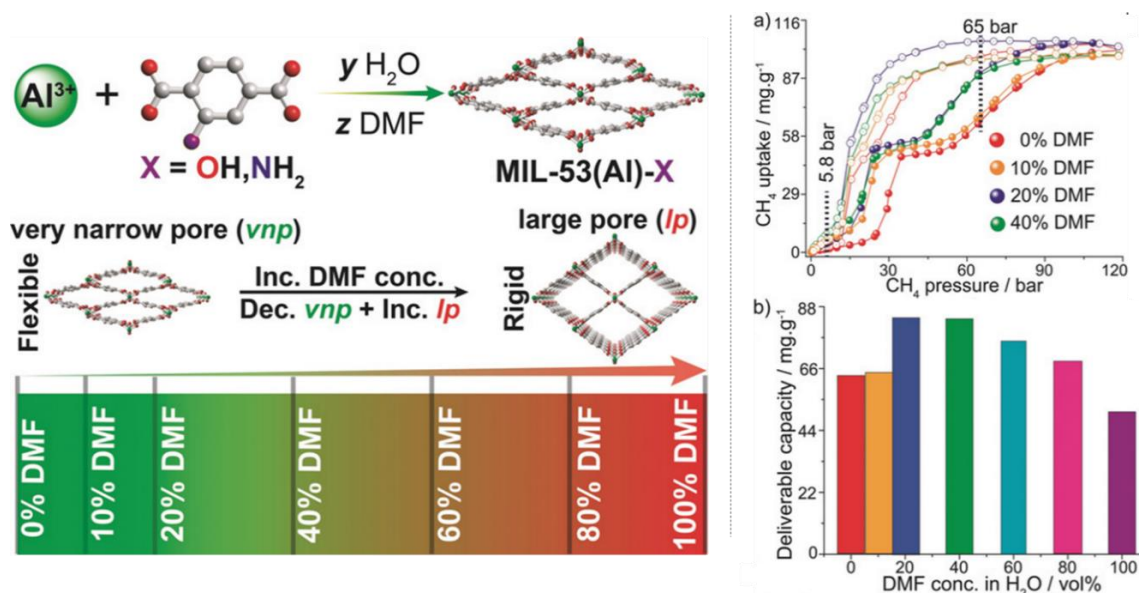


Figure 1-13. The general method of synthesizing flexible MOFs by increasing the DMF concentration (left). a) CH_4 excess isotherms of MIL-53(Al)- NH_2 samples at 298 K (filled=adsorption; empty=desorption); b) deliverable capacity (5.8–65 bar) as a function of DMF concentration (right). Reproduced from ¹⁰¹

Nevertheless, it should be taken into consideration that this increase in DMF content has also led into downsizing the MOF crystals, which in accordance with the results mentioned in the next section, can restrain the flexible nature of the MOF. Hence, the interplay between the solvent and particle size makes it hard to conclude on one effect on flexibility. Thus, the next section will discuss the effect of crystallite size on flexibility.

1.3.4.2. Effect of crystallite size on flexibility

Many reports have linked flexibility in MOFs to the crystallite size and morphology. It was found that in many cases, the downsizing of MOF crystals can lead to a hindered flexibility. These findings have mostly been evidenced by N₂ physisorption studies, where the presence of a gating, breathing, gate shifting, and negative gas adsorption (NGA) phenomena can reveal the occurrence of phase transitions as summarized by Erhling (**Figure 1-15**).¹⁰² A typical example on the size dependent flexibility in MOFs is the pillared layer MOF DUT-8(Ni).^{103–105} DUT-8(Ni) is a flexible MOF consisting of Ni₂-paddle wheels (PWs), bridged by 2,6-naphthalene dicarboxylate (2,6-ndc) ligands to form 2D layers. The Ni₂-PWs are interconnected by 1,4-diazabicyclo[2,2,2]-octane (dabco) ligands into a 3D [Ni₂(2,6-ndc)₂(dabco)]_n framework.¹⁰⁶ Once guest molecules are removed, the op structure of DUT-8(Ni) transforms into the cp structure.¹⁰⁷ The reverse transition into op phase occurs through the adsorption of guest species like N₂ at 77 K. The unit cell volume difference of cp and op phases is ~ 250%.¹⁰⁸

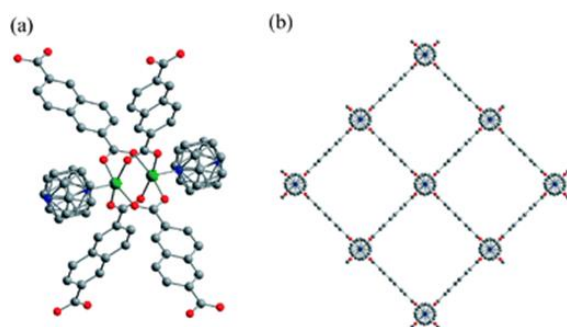


Figure 1-14. (a) Paddle wheel-unit, (b) the view on the structure along c (Ni: green, O: red, N: blue, C: gray).¹⁰⁶

In fact, this MOF can be obtained as a rigid material when synthesized as submicron sized crystals (<500 nm) and flexible when synthesized as micron sized.^{109,110} As shown in **(Figure 1-15, A)** for DUT-8(Ni) micron sized crystals, a step wise isotherm characterized by an hysteresis between the adsorption and desorption branch is indicative of a gating process and thus a transition from (cp) to (lp) (in purple) form of the MOF. However, when downsizing the MOF crystals to the nanoscale, a type I isotherm (in orange) indicating a rigid (op) phase is presented. A similar rigidification of the MOF framework while decreasing the MOF particle size was observed for DUT-98(Zr).¹¹¹ Similarly for MIL-53(Al)-NH₂, in **(Figure 1-15, B)** an (op)-(cp)-(op) transition can be observed in purple, indicating a breathing behavior, which also turns into a type I isotherm indicating an (op) phase when the MOF particle is downsized.¹¹² Comparably, DUT-49(Cu) is known to undergo a negative gas adsorption (NGA) in which the gas expelled from the pores of the MOF due to contraction under certain pressures.¹¹³ The isotherm of DUT-49(Cu) presented in **(Figure 1-15, C)** also describes an (op)-(cp)-(op) transition but with a negative step following the first transition and hysteresis (NGA phenomenon). Yet, reducing the particle size below 1 μ m reveals a type Ib isotherm as shown in orange. Nevertheless, DUT-49(Cu) presents a particular case, the same experiments done under a stronger reacting guest (n-butane instead of N₂) can lead to a colossal contraction even in nanoparticles.¹¹³ In case of n-butane, a decrease in the amount of released gas in NGA is proportional to the decrease of particle size. Another example is ZIF-8 in which the decrease of the crystal size leads to an increase in the gate opening pressure and hysteresis dimension, in other terms, a suppression in the responsivity to stimuli is observed **(Figure 1-15, D)**.¹¹⁴ On the contrary, and from a mechanical point of view, Tiba and co-workers discussed an increase in the flexibility of ZIF-8.¹¹⁵

However, it was also shown that the decrease in MOFs particle size can increase guest induced flexibility in some coordination frameworks. In 2016, the group of Kitagawa reported a coordination framework that exhibits an induced flexibility on adsorption once downsized.¹¹⁶ $\text{Fe}(\text{py})_2[\text{Pt}(\text{CN})_4]$ was observed to exhibit no gas uptake of EtOH vapor under adsorption as a bulk, however when downsized into 16 nm MOF thin film, a form of gate opening was observed (**Figure 1-15, E**). The absence of flexibility on adsorption in bulk material was explained by the prevented access of guest molecules by the strong π - π stacking between the pyridine ligands. Once downsized, these interactions between the framework layers are weaker (reduced number of ligands at the outermost surface) and the guest molecules could access the pores in an easier manner leading to a gate-opening phenomenon.¹¹⁶

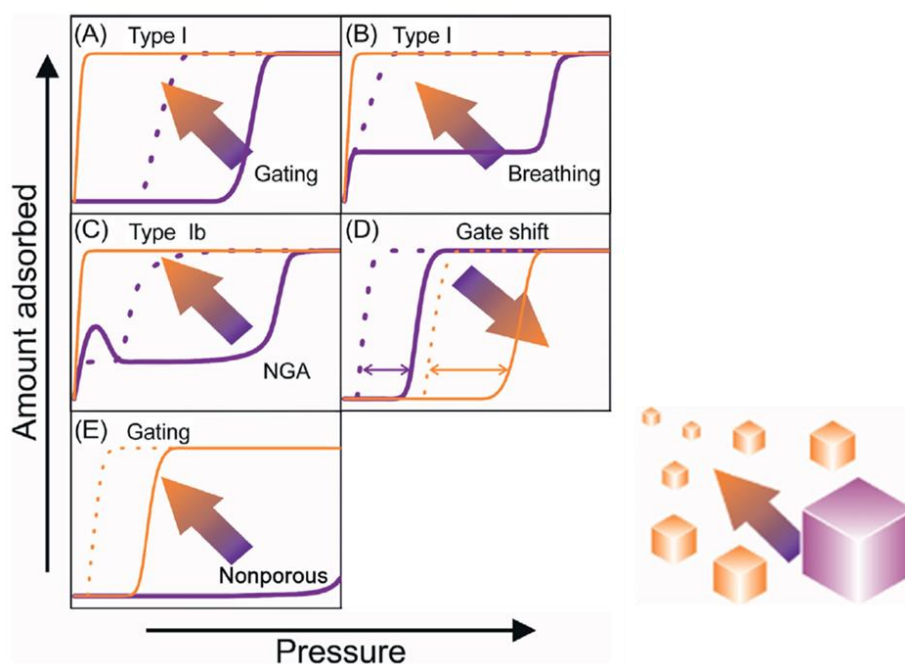


Figure 1-15. Prototypical gas adsorption isotherms showing the impact of downsizing MOF crystal size on structural flexibility (purple: before downsizing; orange: after downsizing; unbroken line: adsorption; broken line: desorption). Reproduced from ¹⁰²

To date, there is no clear explanation for the effect of particle size on flexibility in MOFs. In fact, even though models addressing size-dependent flexibility in MOFs are yet to be further developed, Erhling and co-workers suggested some

hypotheses that can explain the energetics involved in this type of flexibility.^{102,117}

According to authors, it is important to understand the solid-phase thermodynamics and kinetics involved in the phase transformation (e.g., from (lp) to (np)). These factors are system dependent and the effect of their magnitude on the system depends on the composition of the material and the stimuli involved.

1.3.4.3. Effect of functionalization and post synthetic modifications on flexibility

The functionalization of MOF ligands has proven to affect the flexibility of the MOF and has been tested both theoretically and experimentally on several MOFs (e.g., MIL-53 and MIL-88).^{118,119} In fact, this topic was the hotspot of the early-stage research on flexible MOFs. In 2010, Devic *et al.* synthesized a series of the flexible MIL-53(Fe) based on bdc derivatives with various groups (–Cl, –Br, –CF₃, –COOH, –CH₃, –NH₂, –OH) where it was observed that the dynamic behavior of each was selectively correlated with the guest–framework interaction.¹¹⁸ This showed the significant effect of the functionalization groups attached on the initial pore opening (size and shape) and the selective adsorption of liquid guests through the existence of specific guest–framework interactions. One year later, Horcajada *et al.* reported similar results for the swelling MIL-88(Fe) MOF.¹¹⁹ Functional groups with different sizes and numbers were introduced onto the phenyl rings of the bdc ligand of MIL-88B and the bpdc ligand of MIL-88D (**Figure 1-16**). It was observed that a decrease in the breathing amplitude is proportional to the size of the functional group and the number of such groups per ligand, leading sometimes to a permanent porosity for nitrogen after complete activation of the samples. Moreover, it was noted that the linker functionalization strongly facilitates the swelling behavior in liquid phase, including an unexpected breathing in nonpolar solvents. This ease in swelling following the linkers functionalization was attributed to the modifying the energetics of the host–guest/intraframework interactions and/or by lowering the initial diffusion barrier of the guest.

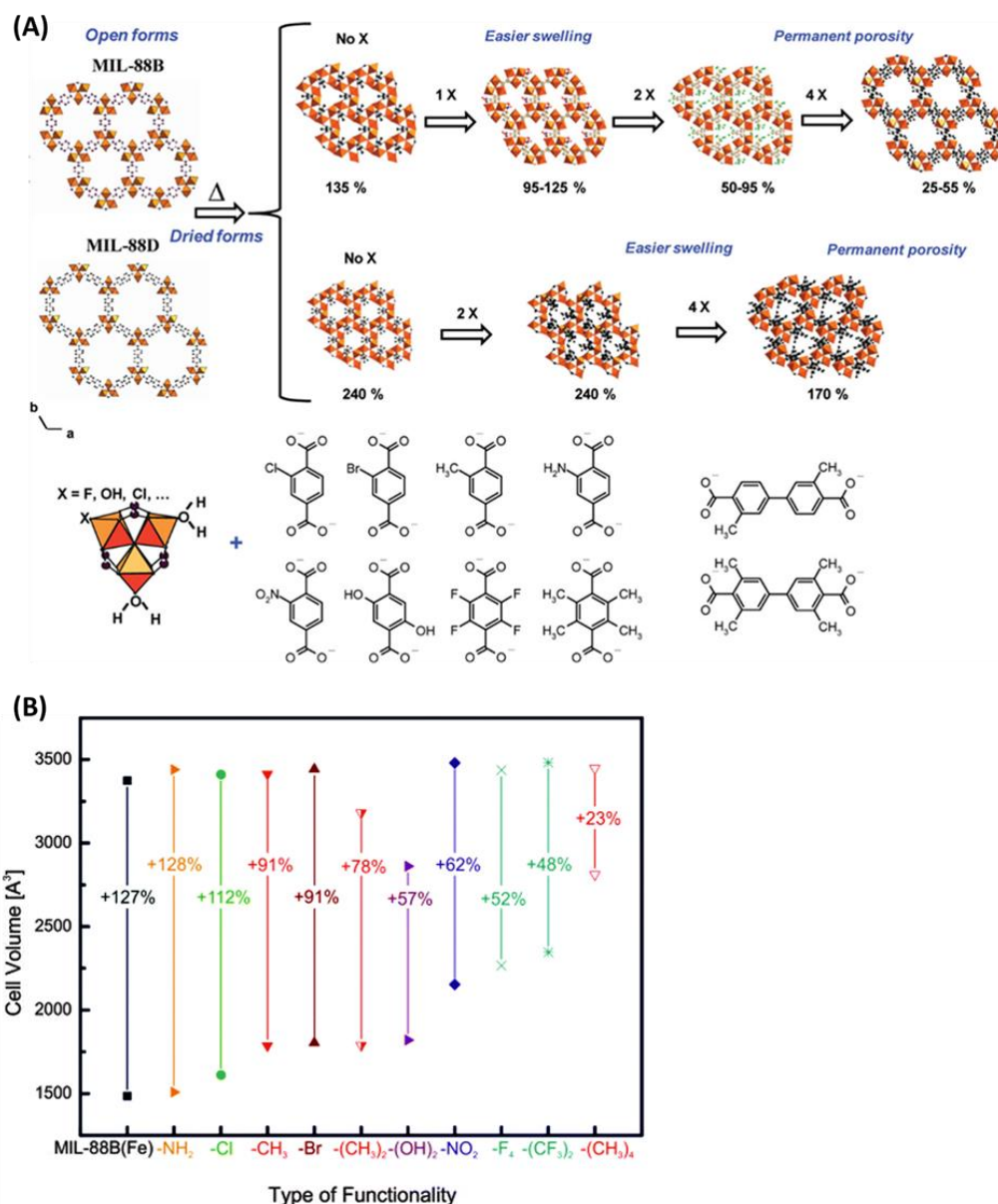


Figure 1-16: (A) Swelling of MIL-88B and D modified solids as a function of the number of functional groups X. Amplitudes of swelling are given in % ($=100 \times (V_{op} - V_{dry})/V_{dry}$) below each crystal structure. μ_3 -oxo-centered trimer of iron(III) octahedra (left bottom) and functionalized linkers (right bottom). Metal polyhedra, carbon, oxygen, and fluorine are in orange, black, red, and green, respectively. **(B)** Evolution of the cell volumes during the swelling of MIL-88B(Fe), based on the functionalities added at the bdc benzene core.^{56,119}

Similarly, it was shown in many works that the post-synthetic modifications of MOFs can affect their dynamic behavior.¹²⁰ An interesting work by Xu and co-workers described a reversible and controllable conversion of a UiO-type Zr-MOF between two distinct structures (rigid and flexible) via post synthetic modification.¹²¹ Originally, the rigid $[Zr_6O_4(OH)_4(sbdc)_6]_n$ where (sbdc = 4,4'-stilbenedicarboxylate) is presented **(Figure 1-17, 1)**. The post-synthetic

bromination of the alkene moiety in sbdc led to the formation of $[\text{Zr}_6\text{O}_4(\text{OH})_4(\text{brbdc})_6]_n$ where (brbdc = meso-4,4'-(1,2-dibromoethane-1,2-diyl)dibenzoate) which is flexible (**Figure 1-17, 2**). The C-C single bond obtained from a previously double bond via bromination is rotatable. This allows $[\text{Zr}_6\text{O}_4(\text{OH})_4(\text{brbdc})_6]_n$ to reversibly convert between a crystalline and non-crystalline structure via the release/ recovery of guest molecules.¹²¹ In addition, owing to the structural flexibility of $[\text{Zr}_6\text{O}_4(\text{OH})_4(\text{brbdc})_6]_n$, it was able to capture many bulky guest molecules (porphyrin and phthalocyanine derivatives, etc.) that were much larger than the opening of the pristine non-flexible framework.¹²¹

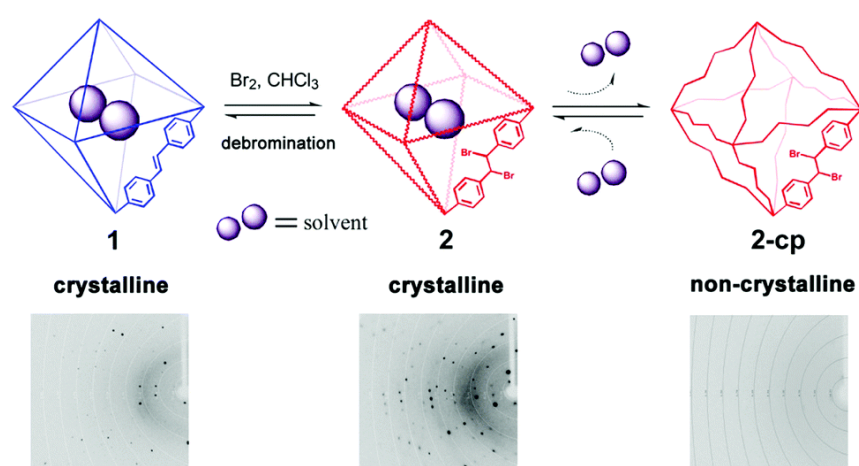


Figure 1-17: Post synthetic modification of UiO-type Zr MOF.¹²¹

Furthermore, Rollins and co-workers have shown very recently that it is possible to stabilize the large pore phase in a flexible MIL-53(Al) analogue, via chemical cross-linking.¹²² $\text{Al}(\text{OH})\text{dmtpd}c$ ($\text{dmtpd}c^{2-} = 2',5'$ -dimethyl-[1,1':4',1''-terphenyl]-4,4''-dicarboxylate) is a terphenyl-expanded variant of MIL-53(Al) with a pore size of 17 Å. Typically, this MOF partially closes upon removal of guest molecules, however, when $\text{H}_4\text{tpdc-XL}$ cross-linkers were added between the ligands, the MOF was locked in its open pore phase (**Figure 1-18**).¹²² While $\text{Al}(\text{OH})\text{dmtpd}c$ partially closes upon guest evacuation, the installation of the synthesized H_4tpdc ligands as simple cross-linkers between ligands effectively locks the pores in the open form with a $S_{\text{BET}} = 1870 \text{ m}^2/\text{g}$.

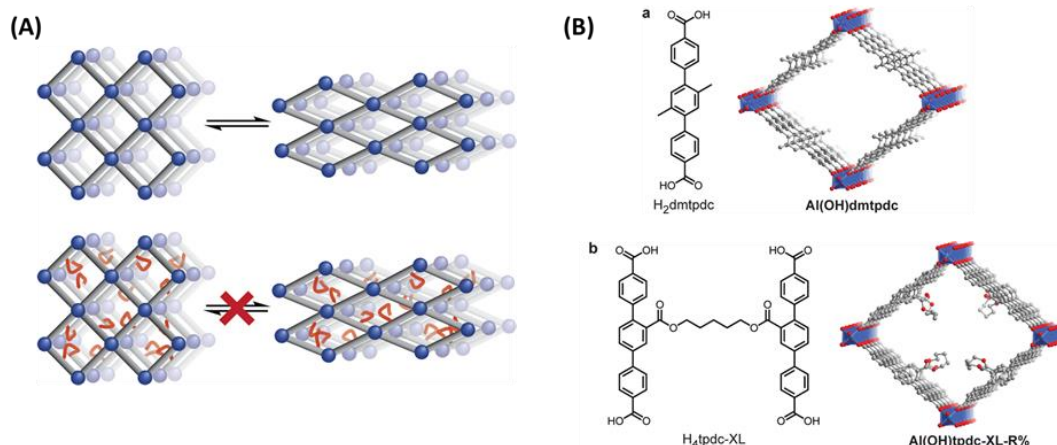


Figure 1-18: (A) Overview of chemical cross-linking strategy to induce pore rigidification in flexible frameworks. (B) Modeled structures of the terphenyl expanded MIL-53(Al) frameworks (a) Al(OH)dmtfdc and (b) synthesized Al(OH)tpdc-XL-R%. R% refers to the % of cross-linked ligand struts in the framework. Reproduced from ¹²²

To conclude, structural transitions in MOFs can be associated to their building units and their cooperative role, external stimuli (e.g., heating, pressure, etc.), and guest-host interactions (e.g., solvent exchange, adsorption/ desorption of guest molecules, etc.). Besides, the response of the flexible framework to the same stimuli can vary from one MOF to another. Finally, flexible MOFs typically require a bistable framework that can switch between two stability minima in response to specific stimuli, however it is worth highlighting that recently multi-stable systems with a repeatable switchability between the different minima are emerging. A recent example is the work reported by the group of Kaskel covering DUT-8(Ni) that adopts a configurationally disturbed series of disordered states in the presence of specific guests (**Figure 1-19**).¹¹⁷

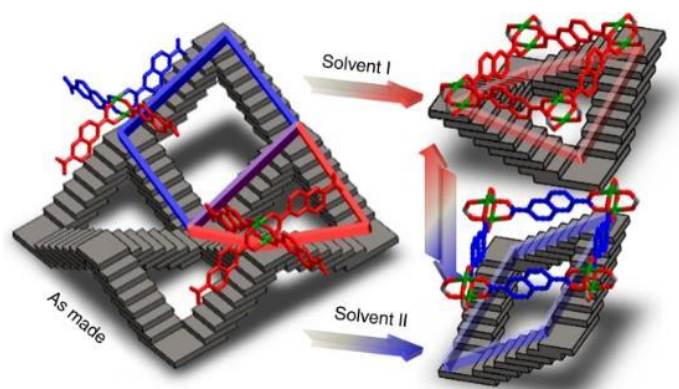


Figure 1-19: Simplified illustration of the configurationally disturbed series of DUT-8(Ni) disordered states in the presence of specific guests.¹¹⁷

1.4. MOF – GRAPHENE OXIDE COMPOSITES

The low electrical conductivity, and sometimes the limited chemical, thermal, and/or mechanical stability are considered major challenges in the field of MOFs. Literature attempted to address these problems through the focus on functionalization and post-synthetic modifications of MOFs, exploring the connectivity of their SBUs, and the design of MOF-based composites.¹²³ Among the different composites reported, the combination of MOFs with carbon-based materials, in particular graphene oxide (GO), has proven to play an important role in yielding multifunctional composites that hold the properties of the MOF (i.e., porosity and crystallinity), and the properties of the supporting matrix (i.e., mechanical-chemical stability, processability, etc.) **(Figure 1-20)**. This synergistic effect between the MOF and GO elects MOF/GO based composites as promising materials due to their several functional properties (e.g., controlled porosity, selectivity, conductivity, mechanical stability, etc.). In addition, as MOFs are mostly obtained in the form of polycrystalline powders, with micron-sized particles, GO has been reported to play an important role as a structural directing agent of MOFs that can yield anisotropic single crystals.¹²⁴ This could be of interest in many fields like catalysis, sensing, adsorption, and electronics. Hence, the combination of MOF and GO could play a vital role in overcoming limitations concerning control over the crystal size, morphology, and multiscale porosity of MOF materials via adequate shaping strategies.

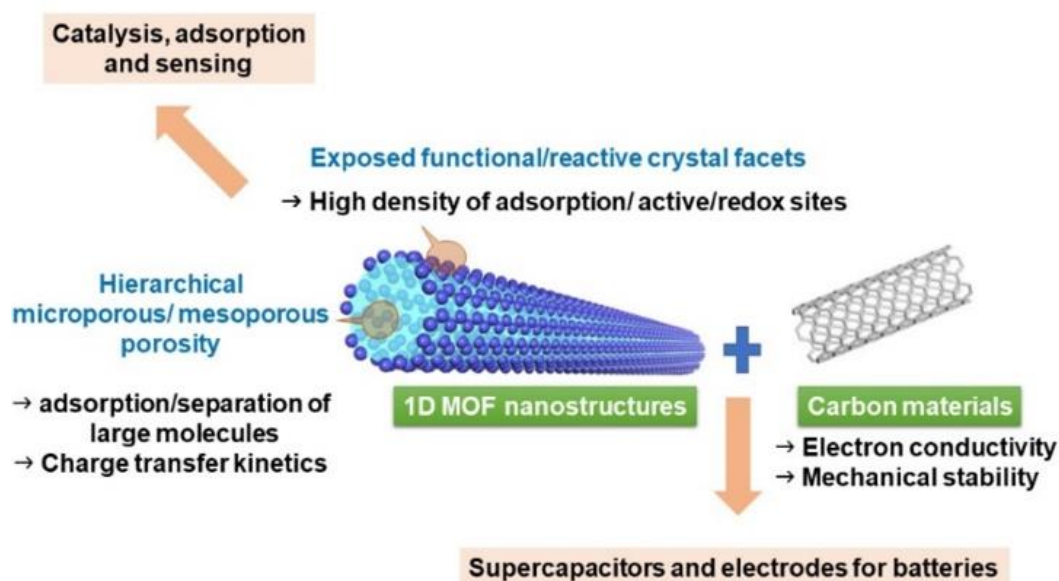


Figure 1-20. Schematic representation of the relationship between the structural and physico-chemical properties of 1D MOF nanostructures and their potential applications. ¹²⁵

1.4.1. Graphene and Graphene Oxide

At the beginning of this chapter, MOFs were briefly introduced. Furthermore, their flexible behaviors were discussed while highlighting our interest in the MIL-53 structure type series. In this section, we have introduced the importance of combining MOFs with GO briefly. Hence, herein, a brief overview of graphene and graphene oxide will be provided before discussing the combination of MOFs and GO. This section of the chapter will cover the chronological development of graphene and graphene oxide. Next, the physico-chemical and morphological properties of GO will be discussed.

1.4.1.1. History

The interest of the scientific community in graphene and its derivatives goes back to the 19th century. In 1859, Benjamin Brodie recognized that thermally reduced graphite oxide has a curious layered nature and reported the atomic weight of graphite.¹²⁶ The isolation of graphene sheets from graphite first sparked in the early 1960s by Boehm and co-workers who first identified these sheets using TEM and X-ray diffraction.¹²⁷ One decade later, monolayers of graphite were first deposited

on other materials.¹²⁸ Nevertheless, the term graphene was first utilized in 1987 to describe a single sheet of graphite and in some papers to describe carbon nanotubes.¹²⁹ Scientists knew that the one atom thick 2D crystal graphene existed, however no procedure for extracting it from graphite was reported. In 2004, an experiment by Geim and Novoselov allowed the extraction of a thermodynamically stable one atom thick piece of graphene from a graphite crystal for the first time using a scotch tape and then transferring these layers to a silicon substrate.¹³⁰ This experiment allowed later the isolation of graphene sheets and a better understanding of their physico-chemical properties, and granted the two scientists the noble prize in physics.^{131,132} Hence, graphene could be described as a flat single layer of carbon atoms tightly packed into a 2D honeycomb lattice. It is a building block for graphitic materials of all other dimensionalities. It can be wrapped up into 0D buckyballs, rolled into 1D nanotubes or stacked into 3D graphite (**Figure1-21**).¹³²

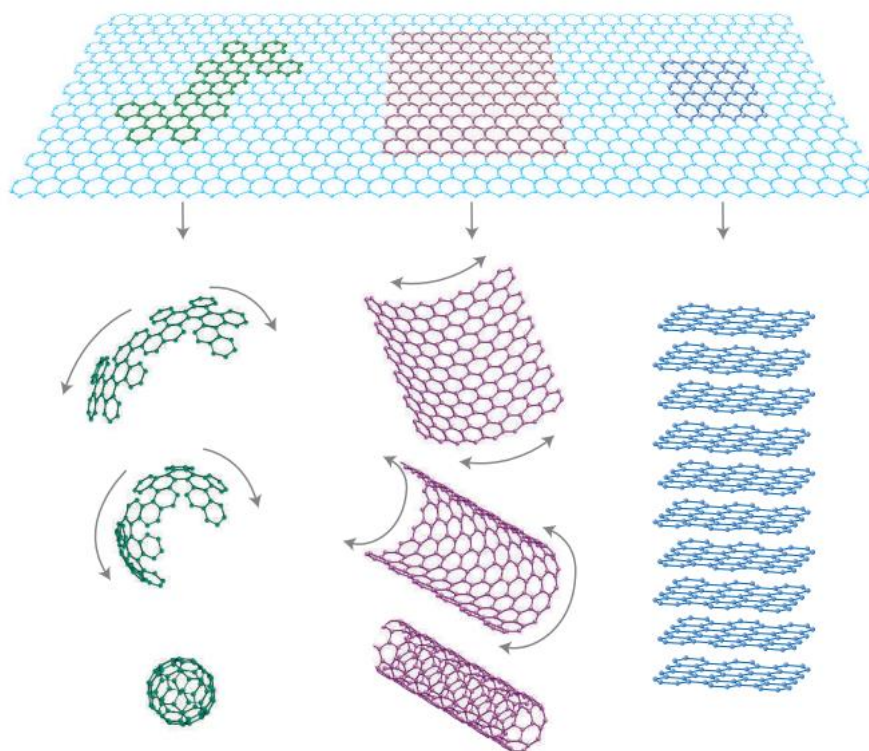


Figure1-21. A monolayer of graphene being wrapped up into 0D buckyballs (green), rolled into 1D nanotubes (purple) or stacked into 3D graphite (blue). Retrieved from ¹³²

1.4.1.2. Properties of Graphene and GO

The exceptional physico-chemical properties, tunability, and immense potential for many applications have elected graphene as an intense research topic for a long period of time. A vast number of publications have been reported covering graphene and its derivatives in fields related to chemistry, physics, and material science.^{133,134} Graphene possesses very interesting properties. It has a theoretical specific area of $2630 \text{ m}^2.\text{g}^{-1}$, a thermal conductivity of $5000 \text{ Wm}^{-1}\text{K}^{-1}$ and an optical transmittance of around 97.7%, in addition to a good electrical conductivity and high intrinsic electron mobility.¹³⁵ Graphene oxide (GO) and reduced graphene oxide (rGO) are the two graphene derivatives that have constantly shown a great potential in numerous applications.¹²³ GO is generally obtained from graphite using strong oxidizing agents, based on Hummers' method.¹³⁶ The oxidization takes place in a mixture solution made of concentrated sulfuric acid, sodium nitrate and potassium permanganate. After oxidative exfoliation, a GO sheet covered with three main oxygen functionalities is obtained: Hydroxyl and epoxy on the basal planes and carboxylic acid on the edges. The oxygenated groups and the co-existence of both ionic and aromatic sp^2 domains provide interesting possibilities such as covalent or metallic bindings.¹³⁷ GO is amphiphilic. It contains hydrophilic functional groups but is locally hydrophobic in the hydrocarbon regions.

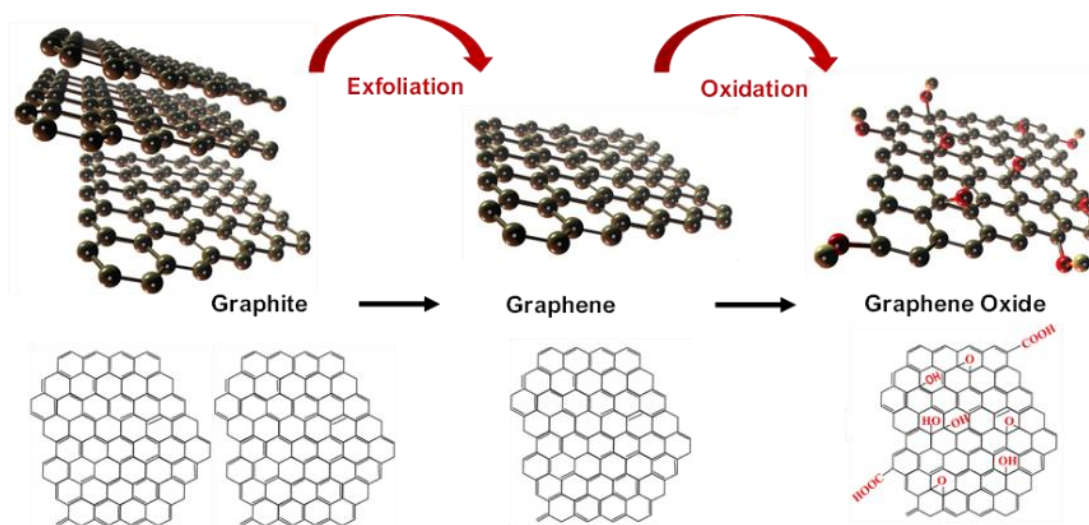


Figure 1-22. 2D and 3D schematic illustrations of graphite, graphene, and graphene oxide.

Compared to graphene, GO adds a lot of value to the possible applications. For example, the hydrophobic nature and impermeability of graphene to water, prevent its application in photocatalysis, adsorption, and membrane separations. The less hydrophobic nature of GO induced by the polar groups present on the lattice make it as a desirable alternative of graphene. GO is considered as a semi-conductive material with a lower electron conductivity than graphene. This character is due to the disrupted sp^2 bonding networks in addition to the defects present in its crystalline network. These defects are mainly due to the strong oxidizing agents, such as potassium permanganate, usually used in the synthesis of GO.¹³⁸ Once the GO is partially reduced, the oxygen content in the GO sheet is decreased, and the electrical conductivity increases. In fact, the value of the electrical conductivity depends on the degree of GO reduction. Highly reduced rGO is almost a super electron conductor, just like pure graphene. The reduction of GO into rGO could be achieved thermally, chemically, or electrochemically.¹³⁸

As well, the chemical reactivity and dispersibility of GO, added to the full-open nature of the sheets, allows the functionalization of both the two-sided basal planes and the edges. The double-sided decoration of GO sheets provides two main advantages; it offers a polyaromatic solution dispersible platform for performing chemistry and establishes a 2D building block that can participate in the assembly of supramolecular hybrid structures at the nanoscale.¹³⁷ Furthermore, the incorporated functional groups can be utilized to target specific applications (e.g., electronics, optics, energy storage, etc.).^{133,138} The functionalization of GO sheet can be performed via covalent and non-covalent bonding and have been nicely reviewed by Yu *et al.*¹³³ The different oxygen functionalities (carboxyl, epoxy, hydroxyl, etc.), besides the defects, act as chemically reactive oxygen species for the functionalization of the different sites. It is expected that the reaction of nucleophiles with epoxy groups is sterically hindered compared to that with

carboxylic acids. Considering non-covalent functionalization, it can be achieved via π - π stacking or van der Waals interactions on the sp^2 grids.

1.4.2. From GO sheets to nanoscrolls

The rolling of 2D GO sheets in a spiral like geometry can form 1D open-end scrolls in the nano-regime known as GO nanoscrolls (GONs) (**Figure1-21**). These scrolls possess properties comparable to that of GO sheets, however they provide an enhanced functionality through the exposed reactive facets accompanied by a more accessible inner wall area. It can be said that the covalent sp^2 C-C bonds and remarkably high length-to-diameter ratio help GONs exhibit improved properties. In fact, such morphology provides a porous structure with an increased surface to volume ratio and a tunable inter-planar distance between the layers compared to plane sheets. As recently reviewed by Sontakke and Purkait, the formation of GO nanoscrolls from GO sheets can be obtained through several methods.¹³⁹ The rolling of GO sheets into GO nanoscrolls can be spontaneous under certain conditions (driven self-scrolling), or via synthetic techniques (e.g., ultrasonication). The first report to discuss the fabrication of GO nanoscrolls and applying them in supercapacitors was via lyophilization.¹⁴⁰ GO nanoscrolls were then fabricated using synthesis techniques like ultra-sonication and microwave irradiation.^{139,141} Recently, vortex fluidic devices (VFD), molecular combing, and the Langmuir-Blodgett (LB) method have all been reported for forming GO nanoscrolls.^{139,142} Nevertheless, the focus of this work will be oriented towards the self-scrolling of GO sheets into GO nanoscrolls driven by solvents, nanoparticles, or both.

Generally speaking, the scroll formation is controlled by two opposite energetic influences. The bending of the GO sheet is accompanied by an increase in the elastic energy, while van der Waals and other interactions (π - π stacking, H bonding) in certain regions of the GO sheet will reduce the free energy. Still, a minimum energy barrier for the initial curling should be overcome for the scrolling

to occur. Theoretically, Wallace and Shao have shown that one way to overcome the torsional bending's energy barrier is to utilize defects/ vacancies on the GO sheet to allow local stress relaxation around these sites. These sites will be later stabilized by the van der Waals interaction in the curled regions.¹⁴³

1.4.2.1. Solvent induced self-scrolling

The solvent induced scrolling of GO can be explained by the inhomogeneous distribution of polar/nonpolar groups in a dispersion.¹⁴⁴ For example, when GO is dispersed in a mixture of solvents (e.g., DMF and water), due to its amphiphilic nature, GO tends to reduce the interaction with some solvent molecules at certain areas in the GO sheet. For instance, the oxygen functionalities present at particular areas of the GO sheet would prefer to interact with water and lessen the interaction with DMF molecules. This leads to an instable dispersion that in turn drives the initial scrolling of GO sheets which prefer to curl onto themselves rather than coagulate in solution.¹⁴⁴ In fact, this behavior is comparable to the solvent dependent self-assembly of amphiphilic polymers (e.g., surfactants). Besides, it should be mentioned that the π - π interactions in the overlap region of GO sheets cause the free energy in the system to decrease, which in turn compensates the gained energy from bending. These phenomena were explained by Tang *et al.* where they reported that in presence of "unfavorable" solvents, GO prefers to self-scroll rather than interact with solvent molecules.¹⁴⁴ The approach developed by Tang was based on adding DMF, in a dropwise manner, to a GO in water suspension leading to the formation of GO scrolls (**Figure 1-23, A**). Moreover, when the DMF content was increased, the already formed scrolls acted as a template for other sheets to self-scroll, via van der Waals interactions, forming spindle shaped scrolls out of the originally formed GO cylinders (**Figure 1-23, B**).

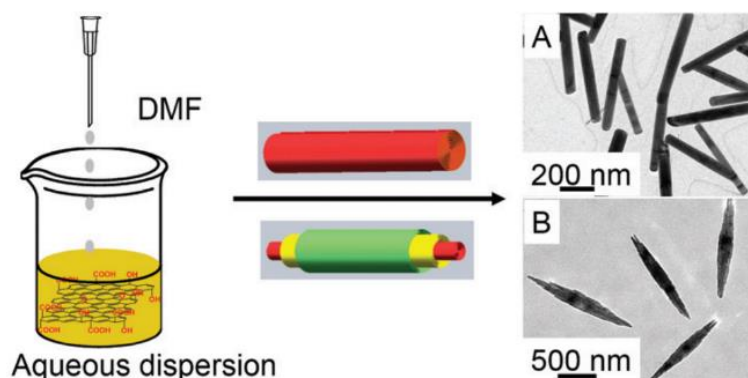


Figure 1-23. Illustration of the self-assembly of GO sheets to form nanoscrolls induced by adding DMF dropwise, and TEM images of the scrolls. Retrieved from ¹⁴⁴

Moreover, to better understand the effect of solvent properties on the scrolling process of GO, Tang and co-workers studied the solvent induced formation of GO nanoscrolls in distinct solvents. Both protic (methanol, ethanol, isopropyl alcohol, acetic acid, and isobutyric acid) and aprotic (pyridine, DMF) solvents were used to form GO dispersions. Basically, they dispersed GO sheets in the different solvents via sonication for 2 hours at a 40 kHz frequency and 200 W power density. This sonication resulted in a sedimentation in which the formation of GO nanoscrolls (GONs) happened. The obtained results were analyzed by different characterization techniques, and it was observed that the length, diameter, and yield of the obtained nanoscrolls depended mainly on the dipole moment and Hansen solubility parameters of the solvent, and the ζ potential of GO in the different suspensions.¹⁴⁵ Thus, it was concluded that the formation of large GO scrolls is facilitated by solvents with a smaller dipole moment and suspensions with a less negative ζ potential of GO.

1.4.2.2. Nanoparticles induced self-scrolling

Aside from solvent induced self-scrolling of GO sheets, the formation of GONs can be driven by the modification of the GO surface by nanoparticles. As known, the surface of a GO sheet is full of oxygen functionalities. Groups like carboxyl, carbonyl, hydroxyl, and epoxide are used for the coordination and stabilization of metal cations. Hence, it is possible to obtain metal (oxo)clusters on the surface of the GO sheet through adding metal precursors gradually into a GO suspension, the added metals are coordinated by the functional groups and then the growth of the metal clusters occurs.¹⁴⁶ In 2012, Wang *et al.* were the first to demonstrate the concept of scrolling GO sheets into nanoscrolls via nanoparticle aggregation.¹⁴⁷ Wang added a silver nitrate solution into a GO suspension in a dropwise manner which led to the Ag⁺ ions being coordinated by the oxygen functionalities at the edge of the GO sheet which induces the growth of metal clusters (**Figure 1-24, A**). The suspension was then sonicated and Ag decorated sheets were obtained, and the bending occurred.¹⁴⁷ The bending phenomenon was explained by different factors. First, the van der Waal interactions between the adjacent silver nanoparticles causes their propagation towards each other, this leads to the simultaneous rolling of the GO sheets. In addition, as explained in the case of the solvent-induced scrolling, the π - π interactions in the overlap region of GO sheets supports the bending of GO in order to compensate the energy lost in the system. Therefore, silver nanoparticles are observed to be firmly wrapped by the rolled GO sheet (**Figure 1-24, B-b**). The formation mechanism of GONs via NPs aggregation was well defined by Wang and later confirmed by different works.¹³⁹ For instance, both Wang *et al.* and Gai *et al.* performed recently a similar study with silver cyanide and silver nitrate, respectively.^{148,149}

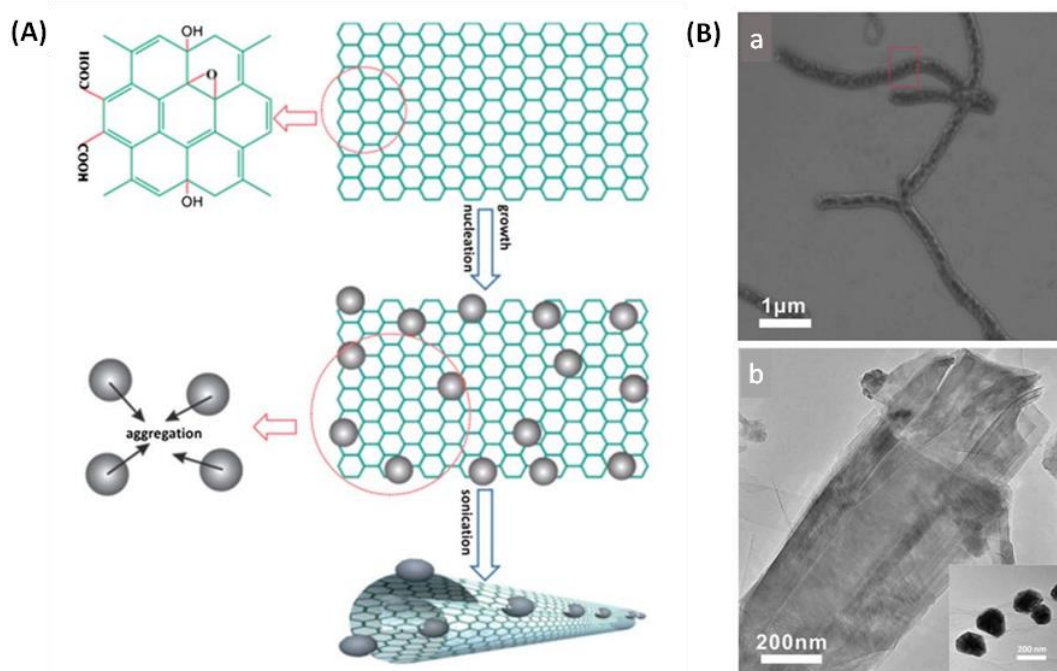


Figure 1-24. (A) Schematic diagram shows the rolling process of the inorganic particle-decorated GO sheet. The aggregation of inorganic nanoparticles leads to the formation of hybrid nanoscrolls. (B) (a) SEM image of rolled Ag-decorated GO sheets (Ag-GO hybrid nanoscrolls). (b) TEM image of the fabricated nanoscrolls. The space between the rolls is obvious, indicating that the nanoscrolls is from the rolling of 2D sheets. The TEM image in the inset shows that the nanoparticles are tightly wrapped by the rolled GO sheet. The inset is from (a), red square. Adapted from ¹⁴⁷

Similarly, Sharifi and co-workers successfully turned nitrogen doped sheets of rGO into nanoscrolls via decorating the sheets with magnetic $\gamma\text{-Fe}_2\text{O}_3$ nanoparticles.¹⁵⁰ The strong dipole moment of these maghemite nanoparticles, in addition to their strong interaction with nitrogen functionalities at the lattice of N-rGO lead to a strong adsorption at the nitrogen defects directing the formation of scrolls (**Figure 1-25**). A part of the novelty of this work is that the nanoscrolls' formation process is completely reversible. When the maghemite nanoparticles were removed, the nanoscrolls return to the open sheets form.¹⁵⁰

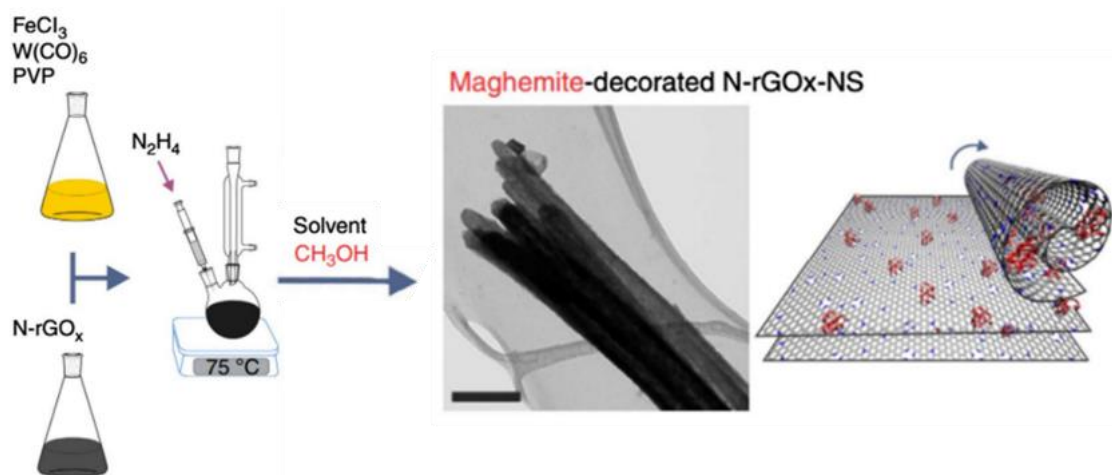


Figure 1-25. Schematic process of the adsorption of iron oxide nanoparticles and formation of maghemite-decorated N-RGO nanoscrolls. Reproduced from ¹⁵⁰

In conclusion, it can be concluded that both the solvent induced self-assembly, and the nanoparticles assisted nanoscrolls formation are simple and energy efficient. Nanoparticles driven self-assemblies have shown to offer a reversible pathway and a good yield, however they suffer from a limited de-agglomeration ability that encourages the formation of aggregates at the surface of GO. Whereas solvent induced techniques are easier and cheaper as the cost of metals is absent. Even though both fabrication methods lack a full control over size, yet they are considered efficient, cheap, and simple compared to other methods (e.g., ultrasonication, lyophilization, molecular combing, etc.).

1.4.3. MOF/GO 1D nanostructures

Of interest in this PhD work is organic template-directed synthesis of 1D MOF tubular nanostructures, more specifically nanowires. Based on a review we recently published; various (bio)organic templates were used to direct the synthesis of 1D tubular-structured MOFs (e.g., graphene oxide, polycarbonate membranes, bacteria, etc.).¹²⁵ In addition to the template types, different depositions methods (solution-based deposition, electrodeposition, etc.) were used to coat the template with the MOF precursors or with MOF preformed particles. This templating strategy is thus a versatile approach even if the morphology and size of the MOF

nanostructures are limited by the dimensions of the templates. Graphene and graphene oxide (GO) were among the different materials used for the fabrication of MOF NWs.^{124,151}

1.4.3.1. Main preparation strategies

In 2010, Jahan and co-workers used benzoic acid-functionalized graphene (BFG) as a structure-directing agent of MOF-5 NW.¹⁵¹ MOF-5 presents a cubic 3D porous structure by assembling tetramers of Zn tetrahedra and bdc ligands.⁹ Due to the low density of carboxylate groups on the basal plane of GO and thus the expected limited metal-chelation capability of GO, the basal planes of GO were functionalized with benzoic acid functions with a high density.¹⁵¹ Indeed, such carboxylate groups that possess bridging bidentate coordination ability are prone to react with the Zn^{2+} cations and thus induce strong MOF-5/BFG interactions and a high degree of framework connectivity. In the second step, BFG was heated at reflux with the precursors of MOF-5 (zinc nitrate/ bdc) in DMF, following the same protocol as that of MOF-5 synthesis. The microstructure of the resulting NWs consists of the stacking of MOF-5 nanocrystals with a [220] growth direction and intercalated graphene sheets periodically distributed along the NWs, as shown by coupling multiple techniques (PXRD, SEM, TEM, SAED, micro-raman spectroscopy) **(Figure 1-26)**.¹⁵¹ Hence, this work demonstrated that BFG is not only a structure-directing agent of 1D MOF-5 NW but also as an integral component of the MOF-5 framework **(Figure 1-27)**.¹⁵¹ These BFG/MOF-5 NWs have a uniform shape and their diameter of ~300 nm is consistent with the average diameter of the BFG sheets, in agreement with the structure-directing effect of BFG. Finally, it was shown that these BFG sheets impart new electrical properties such as a photoelectric transport property.¹⁵¹

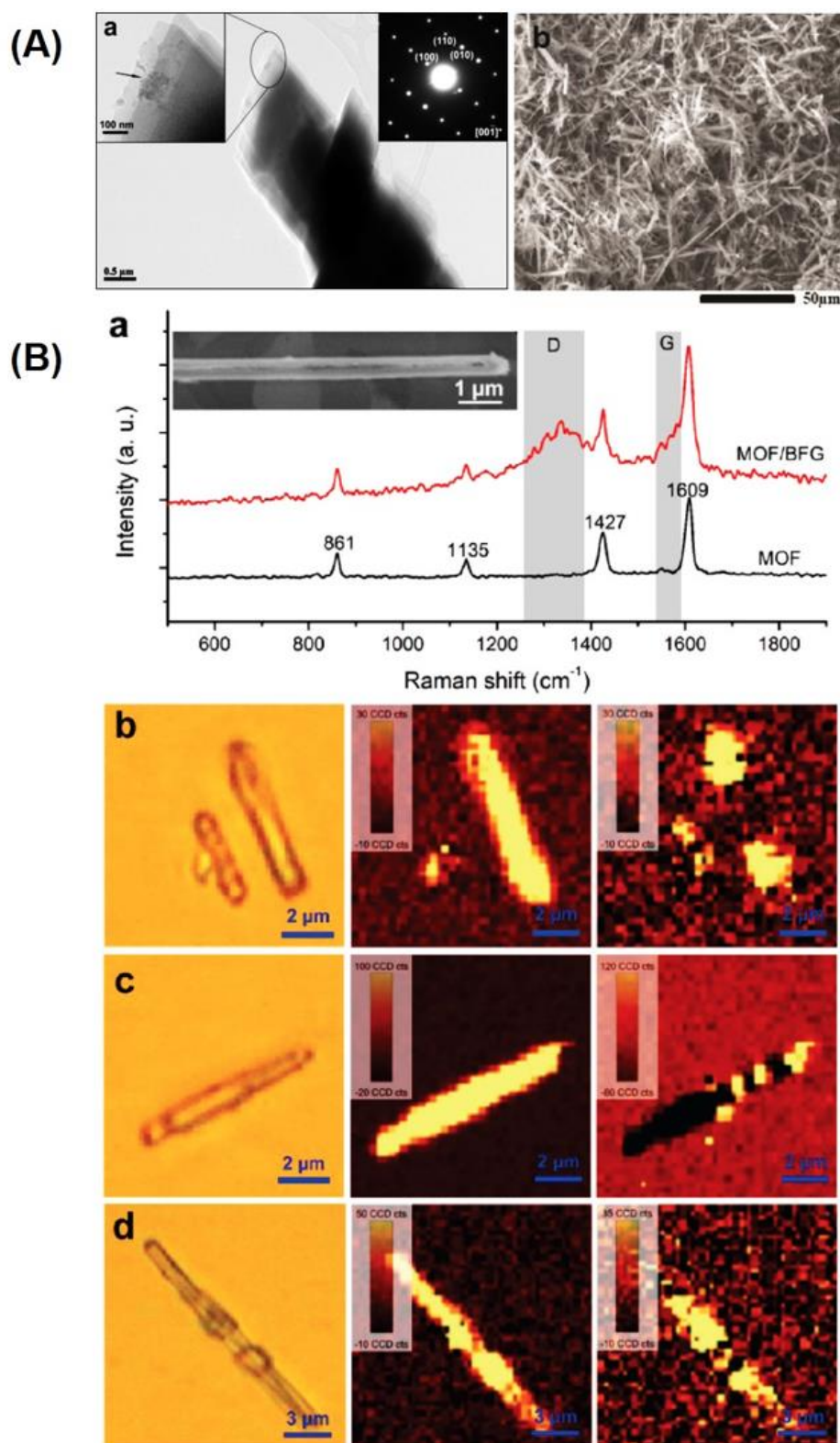


Figure 1-26. (A) (a) TEM images of MOF/BFG (5 wt.%) NW. The upper-left insert shows magnified image and the arrow inside indicates BFG flake. The upper-right insert shows SAED pattern; (b) SEM image of MOF/BFG (5 wt.%) NW; (B) (a) Raman spectra of MOF-5 and MOF/BFG (5 wt.%). Insert shows SEM image of an individual MOF/BFG NW. (b-d) Raman mapping of MOF/BFG NWs. Left: optical image. Medium: Raman maps integrated by Raman band at 1609 cm⁻¹. Right: Raman maps integrated by D band of graphene.¹⁵¹

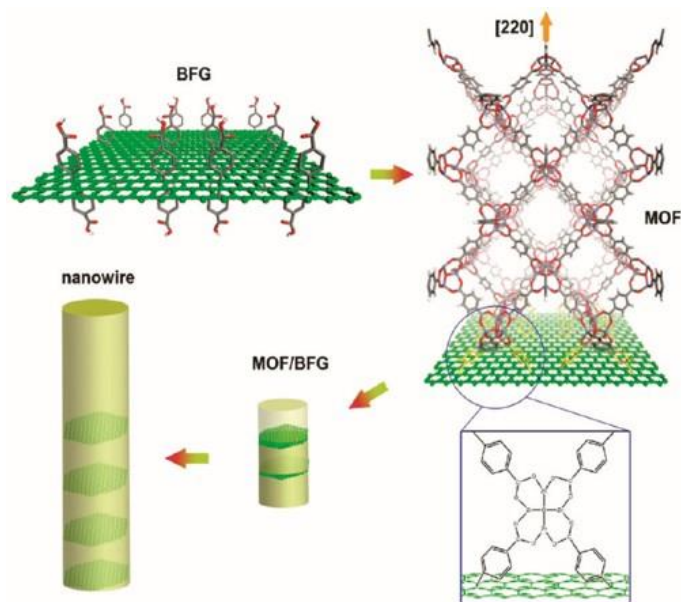


Figure 1-27. Scheme of proposed bonding between functionalized graphene and MOF-5 via -COOH groups along [220] direction and the assembly into NW structure.¹⁵¹

Previously in our group, the synthesis of single-crystal NWs of the microporous Al^{3+} dicarboxylate MIL-69(Al) MOF by using GO nanoscrolls as structure-directing agents, has been reported.¹²⁴ MIL-69(Al)/GO NWs were formed by mixing GO and the precursors of MIL-69(Al) (i.e., Al^{3+} salts, NaOH and 2,6 ndc) under reflux. As shown by combining complementary characterization tools (PXRD, TEM, SAED, SEM, N_2 porosimetry), these NWs present a core-shell porous microstructure with lengths up to 2 μm and aspect ratio up to 20. Their average diameter of 70 ± 20 nm is close to that of the GO nanoscrolls, which is in line with the templating role of GO. Note that this morphology contrasts strongly with that of polydisperse MIL-69(Al) NPs. According to SAED, each NW corresponds to a single-crystal of MIL-69(Al) and was found to preferentially grow along the [001] crystallographic direction which is parallel to the chain axis of the corner-sharing Al^{3+} octahedra in the structure of MIL-69(Al).¹²⁴ The interplay between multimodal characterization techniques and molecular modeling tools was exploited to unravel their mechanism of formation which involves a mutual recognition between GO and MIL-69(Al).¹²⁴ GO directs the formation of the MOF while conversely, the MOF drives the structuring of GO (**Figure 1-28**). The formation of MIL-69(Al) seeds, the

self-scrolling of GO sheets and the subsequent anisotropic growth of MIL-69(Al) NWs in the inner cavity of GO nanoscrolls were mainly mediated by specific GO sheets/MOF interactions, thereby limiting the crystal growth of MOF on certain facets (**Figure 1-28**).¹²⁴ In the first stages of the growth process, the internal surface of GO nanoscrolls was decorated by numerous MIL-69(Al) nanorods (NRs) and NPs whose further growth and assembly were constrained in a confined space. This may drive the crystalline growth orientation in a direction parallel to the NW axis, gradually forming primary smaller aligned NWs (**Figure 1-29**).¹²⁴ Such mechanism can involve redissolution-crystallization steps owing to the highly reversible nature of coordination bonds of the MOF network. Finally, the lateral aggregation or crystallite fusion of these small NWs led to one single crystalline NW and this last step may proceed either through Ostwald ripening or the oriented attachment mechanism as previously reported for the anisotropic growth of inorganic nanocrystals or biomineralization systems.¹⁰⁹ In comparison to the pure MIL-69(Al) NPs, this MIL-69(Al)/GO composite presents a higher electrical conductivity.

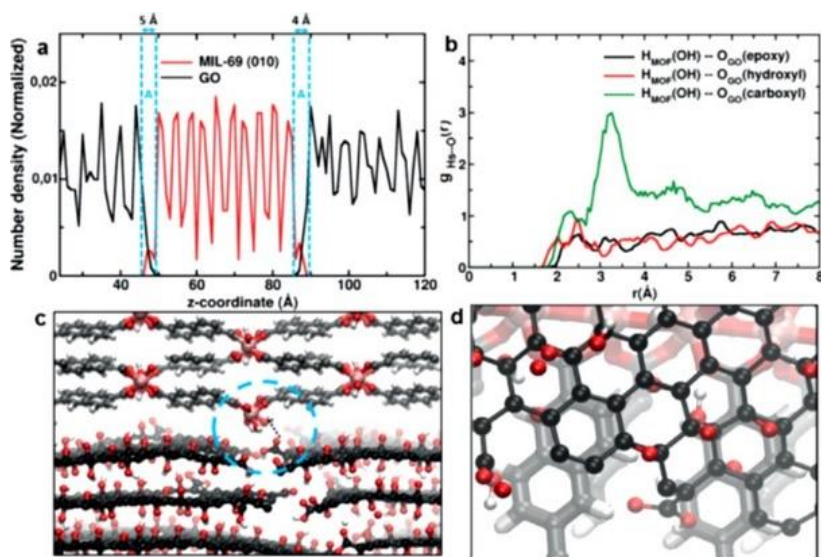


Figure 1-28. MIL-69(Al)(010)/GO model. a) Representation of the normalized atomic density showing the interfacial region denoted A. b) Radial distribution functions calculated between H_{OH} of MIL-69(Al) and the different O atoms of the functional groups of GO. c) Illustrative snapshot showing the main interactions between the edge carboxylic acid groups of GO and H_{OH} of MIL-69(Al). d) Snapshot showing preferential π-π like interactions at the MIL-69(Al)(010)/GO interface. Color schemes are GO layers: C black, O red, H white; MIL-69(010): C gray, Al pink, O red, H white.¹²⁴

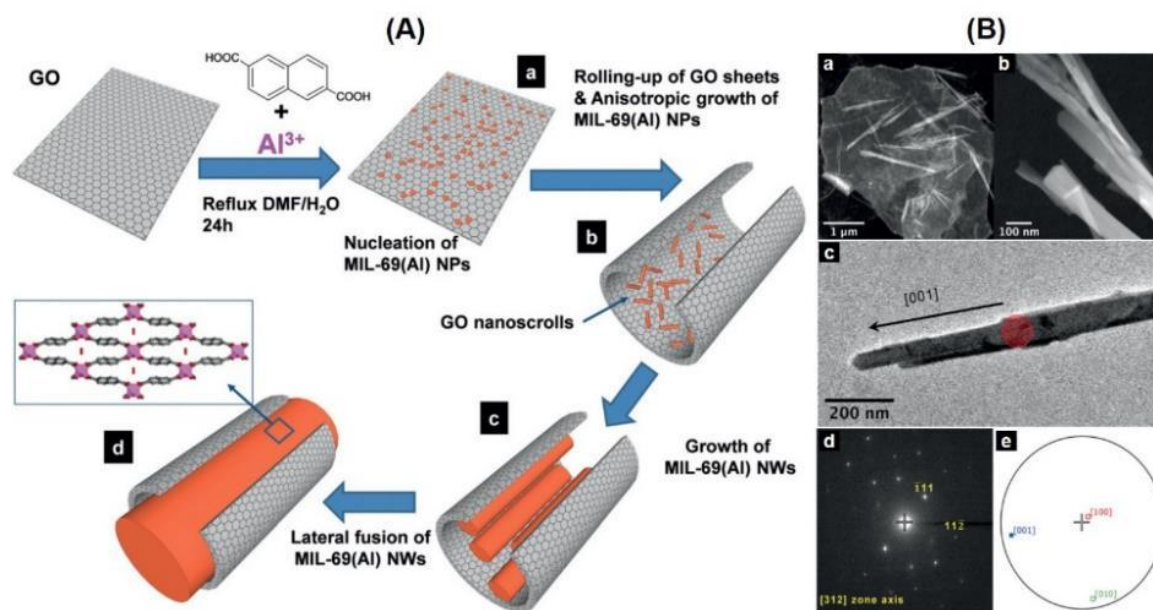


Figure 1-29. (A) Summary of the main stages of the MIL-69(Al) NWs formation; (B) a), b) STEM-HAADF images, c) TEM-BF image of MIL-69(Al) NWs; d) SAED of the area highlighted by the red circle in (c). The stereographic projection (e) that is related to the crystallographic orientation deduced from (d) indicates unambiguously that the crystal growth proceeds along the [001] direction.¹²⁴

Based on these results, the structuring of MOF by using GO nanoscrolls can thus be considered as a valuable approach to integrate MOFs into GO without any agglomeration of MOFs NPs or restacked GO layers while imparting electron transport properties. Yet, despite the interesting results obtained in terms of morphology and crystallinity, the MIL-69(Al)/GO composite obtained in this work still suffers of a very low BET surface area (125 m²/g) which can affect its application. Therefore, our aim in this PhD is to extend the concept applied to MIL-69(Al) into other MOFs with a higher permanent porosity and further prove the role of GO directing the growth of MOF materials. This will be further discussed in detail in **chapter 2** of this PhD project.

1.4.3.2. Induced physico-chemical properties

Recently, several works have reviewed the topic of MOF/GO nanocomposites.^{123,153–155} In their reviews, they used multiple citations to prove the undebatable role of GO addition in enhancing the stability, processability, and porosity of MOFs. In fact, the multiple oxygen functionalities in GO interact with the metal ions in the MOF leading to the formation of new inter-particle spaces at the interface between the MOF and GO. These spaces are created through the enhanced dispersion forces, suppressed aggregation, and the structural directing role of GO.¹⁵³ The induced physico-chemical properties in MOF/GO composites include chemical stability, enhanced electrical conductivity, thermal stability, electron-beam resistance, etc.

For instance, the stability of MOF/GO composites in water is enhanced by the coordination binding of oxygen functionalities (hydroxyl, epoxy, carboxylic acid) of GO with the metal sites of the MOF.¹⁵⁶ This coordination prevents the adsorption of water through creating a hydrophobic barrier of carbon rings around the open metal centers, which in turn can prevent the hydrolysis of the MOF coordination bonds.¹⁵⁶ As mentioned earlier, GO possess an amphiphilic character. Despite the fact that GO has many polar groups, the presence of distorted layers of graphene with huge aromaticity confers it the ability to expel water. Examples of MOF/GO composites that showed promising stability in water include MOF-5/GO, ZIF-8/GO, and HKUST-1/GO.¹⁵⁴ Except for the recent work on conductive MOFs,^{157–159} MOFs have typically an insulating character. This character is due to the insulating organic linkers, and the metal ions with overlapping p and d orbitals. On the other side, numerous carbon-based materials are typically good electrical conducting materials, especially graphene. As GO can chemically bind to the MOF, or even be a building block during the assembly of the composite, it can provide new electron conducting pathways. For example, MOF/GO composites has been employed as

sensors, supercapacitors, and in batteries.^{160–162} In terms of thermal stability, GO is thermally stable up to 220°C.¹⁶³ Yet, it was shown in some cases that the combination of MOFs with GO can enhance the thermal stability of GO.¹⁶⁴ In addition, the presence of carbonaceous materials leads to the efficient dissipation of electrostatic charges leading to an enhanced electron beam resistance in the MOF/GO composite compared to the pure MOF.¹⁶⁵ Indeed, it is worth mentioning that introducing GO into a MOF has shown a promising synergistic effect in different applications. This effect rises from the unique interfacial structures and leads to enhanced properties.^{166–168}

Moreover, despite the continuous development in the field of MOFs, these materials have been mostly reported as microporous polycrystalline powders or spherical nanoparticles. Thus, they suffer of application limitation related to material properties and applications (e.g., adsorption and conversion of small guest molecules). The combination of MOFs with GO has allowed forming anisotropic nanostructured composites that expose functional or reactive crystal facets for optimal performance in applications such as catalysis and sensing.¹²⁵ In addition, these nanostructured MOF based composites enhance the diffusion and mass-transport efficiency of analytes towards the catalytic and adsorption sites of the MOF. Finally, the induced physico-chemical properties of combining MOFs with GO are further explained in the next section where some recent examples on the application of MOF/GO composites are provided.

1.4.3.3. Applications of MOF/GO composites

MOF/GO composites have been employed in different applications ranging from batteries, supercapacitors, and sensors to gas and water treatment.^{160–162,169} For instance, the intrinsic low electrical conductivity of most MOFs is a main limitation for the development of highly performing electrochemical devices. Several strategies have been employed to improve the electrical conductivity of MOFs

including their combination with conductive carbon-based materials like graphene and graphene oxide.^{160–162,169} Besides, due to the electrochemically active metal sites of the MOF, and the enhanced conductivity of GO, MOF/GO composites were employed as efficient electro- or photocatalysts. It is expected that MOF/GO composites which are 1D-oriented can show great interest in such applications due to the enhanced electron transport properties in specific directions.^{160–162} Aside from electrochemical and energy storage related applications, MOF/GO composites have been utilized in gas separation and adsorption applications.^{1,154} For instance, Li *et al.* reported a ZIF-8/GO membrane with a high hydrogen permeance and a remarkable H₂/CO₂ selectivity of 106.¹⁷⁰ The membrane showed no traces of thermal degradation after 400 hours at 30–150°C under a gas feed.¹⁷⁰ In terms of gas adsorption, it was seen in several reports that combining MOFs with GO can lead to an increase in the adsorption capacity. Petit *et al.* have shown that the adsorption capacity of ammonia in HKUST-1/GO is double that of parent MOF alone.¹⁷¹ Varghese *et al.* also showed that Cu-BTC MOF/GO adsorbents allow hydrogen gas storage at RT with a ~60% increase in H₂ capacity compared to pure MOF.¹⁷² Furthermore, as a part of the GRAMOFON European project, some of us with others have shown that the MIL-91(Ti)/GO composite could be used as an efficient adsorbent for microwave swing adsorption (MSA) processes.¹⁷³ Indeed, in post-combustion industrial processes, the use of adsorbents usually involves pressure swing adsorption (PSA) or thermal swing adsorption (TSA) processes. The latter consists of using steam or hot gas sent into the separation column during the desorption step to regenerate the material through thermal transfer between the steam/hot gas and the adsorbent. However, it requires a uniform and fast heating rate of the material in the separation column. Unfortunately, MOFs exhibit very low thermal conductivities, and the use of TSA is associated with slow desorption kinetics, which limits the practical use of MOFs despite their suitable adsorption properties. Therefore, there is a need to find more efficient alternative

desorption processes that would decrease the energy penalty related to the material regeneration. Among reported innovative desorption processes, the use of microwave irradiation, called microwave swing adsorption (MSA), has proven to lead to faster CO₂ release compared to conventional heating on solid adsorbents such as GO. In this study, it was shown that the MIL-91(Ti)/GO combines a good CO₂ adsorption and good electron conductivity and thus could be used as an efficient adsorbent for MSA. The work on MOF/GO has initially started in my group at Versailles in this context of the European GRAMOFON project.

In addition to gas separation membranes, liquid filtration membranes based on layer by layer assembled GO have a remarkable permeability, chemical stability, and molecular selectivity.¹⁷⁴ Combining a MOF with GO can help control the layer spacing in GO while providing accessible channels.¹⁵¹ Such properties help yield membranes with an increased hydrophilicity and enhanced water transport.¹⁷⁵ Sui *et al.* have proved this through a simulation study where MOFs were used to modulate the permeability of GO by controlling the interlayer spacing between the sheets.¹⁷⁶ Finally, it is worth mentioning that MOF/GO composites have been employed in distinct fields like biomedical applications¹⁷⁷, epoxy resins¹⁷⁸, and others. For example, Zhang *et al.* recently reported a bi-metallic (Zn/Cu) MOF/GO composite as a nano-hybrid for improving fire safety of epoxy. The samples showed an excellent thermal stability. Only 2 wt.% of composite were enough to reach 30 wt.% reduction in peak heat release rate, and an amplified ultimate oxygen index (LOI) of epoxy resin composite from 23.4 to 29%.¹⁶⁴ Karimzadeh *et al.* combined MOF-5, GO, and carboxymethylcellulose (CMC) biopolymer to design a drug nanocarrier that can be used in antibacterial drug delivery systems.¹⁷⁷ The designed MOF/GO can efficiently load and release tetracycline.

1.5. CONCLUSION

This chapter provided a brief bibliographic and fundamental background comprising MOFs, flexibility in MOFs, and MOF/GO composites. The high porosity, stability, and synthetic tunability of MOFs designate them as favored candidates for different applications (catalysis, adsorption, separations, etc.). This was further validated by the huge increase in their market forecast that is expected to reach 743 million USD in the next three years.²⁵ Nonetheless, MOFs still present some limitations as they are mostly obtained as polycrystalline powders that are difficult to process. To address these limitations, literature has discussed combining MOFs with carbon-based materials for forming composites with enhanced physico-chemical properties and specific microstructure.¹²⁵ In particular, MOF/GO composites have attracted a lot of attention due to the synergic effects between the two materials, leading to enhanced properties compared to the separate components. The addition of GO to MOFs leads to a better processability, chemical stability, electron conductivity, and other properties which make MOF/GO composites interesting candidates for different applications (gas storage, separation membranes, supercapacitors, etc.). For instance, as a part of the GRAMOFON European project, it was recently shown that combining MIL-91(Ti) with GO have led to maximizing CO₂ capture effectiveness as well as reducing cost, time and energy needed for its desorption and regeneration process.¹⁷³ The MIL-91(Ti)/GO took advantage of the good adsorption properties of the MOF and the electron conductivity of GO. Moreover, the combination of MOFs with GO has also proved to produce anisotropic nanostructures with a specific microstructure and an induced hierarchical porosity.¹²⁴ Shaping MOFs into anisotropic composites leads to enhanced physico-chemical properties and processability.¹²⁵ For instance, some of us have shown that it is possible to form single crystalline MIL-69(Al) based NWs using GO nanoscrolls as a structural directing agent.

Based on the provided discussions, the objective of this PhD project is to extend the approach applied to the MIL-69(Al)/GO to another composite. The importance of this approach lies in granting hierarchically porous MOF/GO composites with a specific microstructure that allows a homogeneous dispersion of MOF NWs in the GO matrix, without any agglomeration of MOF NPs or restacked GO layers. As well, the formed microstructures will benefit from the properties of the MOF (porosity and crystallinity) and GO (processibility, conductivity, etc.) via the synergistic effect between both. Additionally, throughout this chapter, we have shown our interest in flexible MOFs with the MIL-53(M) type structure, namely DUT-5(Al). It was highlighted that DUT-5(Al) has always been referred to as an open rigid MOF in literature. Though, in the following chapters of this manuscript, it will be shown that it was possible to induce flexibility into this previously well-known rigid MOF structure while shaping it into an anisotropic structure using GO as a structural directing agent.

The next chapter of this manuscript will discuss the screening of different MOFs leading to our selected candidate for designing an anisotropic MOF/GO composite.

1.6. REFERENCES

- (1) Safaei, M.; Foroughi, M. M.; Ebrahimpour, N.; Jahani, S.; Omid, A.; Khatami, M. A Review on Metal-Organic Frameworks: Synthesis and Applications. *TrAC Trends in Analytical Chemistry* **2019**, *118*, 401–425. <https://doi.org/10.1016/j.trac.2019.06.007>.
- (2) Yaghi, O. M.; Kalmutzki, M. J.; Diercks, C. S. Emergence of Metal-Organic Frameworks. In *Introduction to Reticular Chemistry*, John Wiley & Sons, Ltd, 2019; pp 1–27. <https://doi.org/10.1002/9783527821099.ch1>.
- (3) Kitagawa, S.; Kondo, M. Functional Micropore Chemistry of Crystalline Metal Complex-Assembled Compounds. *BCSJ* **1998**, *71* (8), 1739–1753. <https://doi.org/10.1246/bcsj.71.1739>.
- (4) Altintas, C.; Avci, G.; Daglar, H.; Nemati Vesali Azar, A.; Erucar, I.; Velioglu, S.; Keskin, S. An Extensive Comparative Analysis of Two MOF Databases: High-Throughput Screening of Computation-Ready MOFs for CH₄ and H₂ Adsorption. *J. Mater. Chem. A* **2019**, *7*(16), 9593–9608. <https://doi.org/10.1039/C9TA01378D>.
- (5) Hoskins, B. F.; Robson, R. Design and Construction of a New Class of Scaffolding-like Materials Comprising Infinite Polymeric Frameworks of 3D-Linked Molecular Rods. A Reappraisal of the Zinc Cyanide and Cadmium Cyanide Structures and the Synthesis and Structure of the Diamond-Related Frameworks [N(CH₃)₄][Cu^IZn^{II}(CN)₄] and Cu^I[4,4',4'',4'''-Tetracyanotetraphenylmethane]BF₄.XC₆H₅NO₂. *J. Am. Chem. Soc.* **1990**, *112*(4), 1546–1554. <https://doi.org/10.1021/ja00160a038>.
- (6) Robson, R.; Abrahams, B. F.; Batten, S. R.; Gable, R. W.; Hoskins, B. F.; Liu, J. Crystal Engineering of Novel Materials Composed of Infinite Two- and Three-Dimensional Frameworks. In *Supramolecular Architecture*, Bein, T., Ed.; American Chemical Society: Washington, DC, 1992; Vol. 499, pp 256–273. <https://doi.org/10.1021/bk-1992-0499.ch019>.
- (7) Yaghi, O. M.; Li, G.; Li, H. Selective Binding and Removal of Guests in a Microporous Metal–Organic Framework. *Nature* **1995**, *378*(6558), 703–706. <https://doi.org/10.1038/378703a0>.
- (8) Chui, S. S. A Chemically Functionalizable Nanoporous Material [Cu₃(TMA)₂(H₂O)₃]_n. *Science* **1999**, *283*(5405), 1148–1150. <https://doi.org/10.1126/science.283.5405.1148>.
- (9) Li, H.; Eddaoudi, M.; O’Keeffe, M.; Yaghi, O. M. Design and Synthesis of an Exceptionally Stable and Highly Porous Metal-Organic Framework. *Nature* **1999**, *402*(6759), 276–279. <https://doi.org/10.1038/46248>.
- (10) Kitagawa, S.; Uemura, K. Dynamic Porous Properties of Coordination Polymers Inspired by Hydrogen Bonds. *Chemical Society Reviews* **2005**, *34* (2), 109–119. <https://doi.org/10.1039/B313997M>.
- (11) Ockwig, N. W.; Delgado-Friedrichs, O.; O’Keeffe, M.; Yaghi, O. M. Reticular Chemistry: Occurrence and Taxonomy of Nets and Grammar for the Design of Frameworks. *Acc. Chem. Res.* **2005**, *38*(3), 176–182. <https://doi.org/10.1021/ar020022l>.
- (12) Férey, G. Hybrid Porous Solids: Past, Present, Future. *Chemical Society Reviews* **2008**, *37*(1), 191–214. <https://doi.org/10.1039/B618320B>.

- (13) Férey, G.; Mellot-Draznieks, C.; Serre, C.; Millange, F. Crystallized Frameworks with Giant Pores: Are There Limits to the Possible? *Acc. Chem. Res.* **2005**, *38* (4), 217–225. <https://doi.org/10.1021/ar040163i>.
- (14) Jeong, N. C.; Samanta, B.; Lee, C. Y.; Farha, O. K.; Hupp, J. T. Coordination-Chemistry Control of Proton Conductivity in the Iconic Metal–Organic Framework Material HKUST-1. *J. Am. Chem. Soc.* **2012**, *134* (1), 51–54. <https://doi.org/10.1021/ja2110152>.
- (15) Park, J.; Yuan, D.; Pham, K. T.; Li, J.-R.; Yakovenko, A.; Zhou, H.-C. Reversible Alteration of CO₂ Adsorption upon Photochemical or Thermal Treatment in a Metal–Organic Framework. *J. Am. Chem. Soc.* **2012**, *134* (1), 99–102. <https://doi.org/10.1021/ja209197f>.
- (16) Li, J.-R.; Zhou, H.-C. Bridging-Ligand-Substitution Strategy for the Preparation of Metal–Organic Polyhedra. *Nature Chem* **2010**, *2* (10), 893–898. <https://doi.org/10.1038/nchem.803>.
- (17) Plonka, A. M.; Banerjee, D.; Woerner, W. R.; Zhang, Z.; Nijem, N.; Chabal, Y. J.; Li, J.; Parise, J. B. Mechanism of Carbon Dioxide Adsorption in a Highly Selective Coordination Network Supported by Direct Structural Evidence. *Angewandte Chemie International Edition* **2013**, *52* (6), 1692–1695. <https://doi.org/10.1002/anie.201207808>.
- (18) Chapman, K. W.; Halder, G. J.; Chupas, P. J. Pressure-Induced Amorphization and Porosity Modification in a Metal–Organic Framework. *J. Am. Chem. Soc.* **2009**, *131* (48), 17546–17547. <https://doi.org/10.1021/ja908415z>.
- (19) Wang, Z.; M. Cohen, S. Postsynthetic Modification of Metal–Organic Frameworks. *Chemical Society Reviews* **2009**, *38* (5), 1315–1329. <https://doi.org/10.1039/B802258P>.
- (20) Clearfield, A. Unconventional Metal Organic Frameworks: Porous Cross-Linked Phosphonates. *Dalton Transactions* **2008**, *0* (44), 6089–6102. <https://doi.org/10.1039/B807676F>.
- (21) Sheta, S. M.; El-Sheikh, S. M. Nanomaterials and Metal-Organic Frameworks for Biosensing Applications of Mutations of the Emerging Viruses. *Analytical Biochemistry* **2022**, 114680. <https://doi.org/10.1016/j.ab.2022.114680>.
- (22) Severino, M. I.; Gkaniatsou, E.; Nouar, F.; Pinto, M. L.; Serre, C. MOFs Industrialization: A Complete Assessment of Production Costs. *Faraday Discuss.* **2021**, *231* (0), 326–341. <https://doi.org/10.1039/D1FD00018G>.
- (23) Wu, Y.; Wang, X.; Kirlikovali, K. O.; Gong, X.; Atilgan, A.; Ma, K.; Schweitzer, N. M.; Gianneschi, N. C.; Li, Z.; Zhang, X.; Farha, O. K. Catalytic Degradation of Polyethylene Terephthalate Using a Phase-Transitional Zirconium-Based Metal–Organic Framework. *Angewandte Chemie International Edition* **2022**, *61* (24), e202117528. <https://doi.org/10.1002/anie.202117528>.
- (24) Bonneau, M.; Lavenn, C.; Zheng, J.-J.; Legrand, A.; Ogawa, T.; Sugimoto, K.; Coudert, F.-X.; Reau, R.; Sakaki, S.; Otake, K.; Kitagawa, S. Tunable Acetylene Sorption by Flexible Catenated Metal–Organic Frameworks. *Nat. Chem.* **2022**, *14* (7), 816–822. <https://doi.org/10.1038/s41557-022-00928-x>.

CHAPTER 1: An Overview on MOFs, Flexibility, and MOF/GO composites

- (25) *Metal-Organic Framework Global Market Report 2021: COVID-19 Implications and Growth*. <https://www.reportlinker.com/p06151378/Metal-Organic-Framework-Global-Market-Report-COVID-19-Implications-And-Growth.html> (accessed 2022-04-29).
- (26) Yaghi, O. M.; Kalmutzki, M. J.; Diercks, C. S. Building Units of MOFs. In *Introduction to Reticular Chemistry*, John Wiley & Sons, Ltd, 2019; pp 57–81. <https://doi.org/10.1002/9783527821099.ch3>.
- (27) Eddaoudi, M.; Kim, J.; Rosi, N.; Vodak, D.; Wachter, J.; O’Keeffe, M.; Yaghi, O. M. Systematic Design of Pore Size and Functionality in Isorecticular MOFs and Their Application in Methane Storage. *Science* **2002**, *295* (5554), 469–472. <https://doi.org/10.1126/science.1067208>.
- (28) Liu, B.; Zhou, H.-F.; Hou, L.; Wang, Y.-Y. Functionalization of MOFs via a Mixed-Ligand Strategy: Enhanced CO₂ Uptake by Pore Surface Modification. *Dalton Transactions* **2018**, *47* (15), 5298–5303. <https://doi.org/10.1039/C8DT00502H>.
- (29) Yu, G.-H.; Yang, C.-L.; Zhao, H.-L.; Yu, A.-X.; Zhang, G.; Du, D.-Y.; Su, Z.-M. Mixed-Linker Strategy for the Construction of Metal–Organic Framework Combined with Dyes toward Alcohol Detection. *Inorg. Chem.* **2022**, *61* (13), 5318–5325. <https://doi.org/10.1021/acs.inorgchem.2c00023>.
- (30) Islamoglu, T.; Goswami, S.; Li, Z.; Howarth, A. J.; Farha, O. K.; Hupp, J. T. Postsynthetic Tuning of Metal–Organic Frameworks for Targeted Applications. *Acc. Chem. Res.* **2017**, *50* (4), 805–813. <https://doi.org/10.1021/acs.accounts.6b00577>.
- (31) Ding, M.; Cai, X.; Jiang, H.-L. Improving MOF Stability: Approaches and Applications. *Chemical Science* **2019**, *10* (44), 10209–10230. <https://doi.org/10.1039/C9SC03916C>.
- (32) Kitagawa, S.; Kitaura, R.; Noro, S. Functional Porous Coordination Polymers. *Angewandte Chemie International Edition* **2004**, *43* (18), 2334–2375. <https://doi.org/10.1002/anie.200300610>.
- (33) Hao, J.; Xu, X.; Fei, H.; Li, L.; Yan, B. Functionalization of Metal–Organic Frameworks for Photoactive Materials. *Advanced Materials* **2018**, *30* (17), 1705634. <https://doi.org/10.1002/adma.201705634>.
- (34) Dolgoplova, E. A.; Rice, A. M.; Shustova, N. B. Actinide-Based MOFs: A Middle Ground in Solution and Solid-State Structural Motifs. *Chemical Communications* **2018**, *54* (50), 6472–6483.
- (35) Devic, T.; Serre, C. High Valence 3p and Transition Metal Based MOFs. *Chemical Society Reviews* **2014**, *43* (16), 6097–6115. <https://doi.org/10.1039/C4CS00081A>.
- (36) Gorai, T.; Schmitt, W.; Gunnlaugsson, T. Highlights of the Development and Application of Luminescent Lanthanide Based Coordination Polymers, MOFs and Functional Nanomaterials. *Dalton Transactions* **2021**, *50* (3), 770–784. <https://doi.org/10.1039/D0DT03684F>.
- (37) Sahiner, N.; Demirci, S.; Yildiz, M. Preparation and Characterization of Bi-Metallic and Tri-Metallic Metal Organic Frameworks Based on Trimesic Acid and Co(II), Ni(II), and Cu(II) Ions. *Journal of Elec Materi* **2017**, *46* (2), 790–801. <https://doi.org/10.1007/s11664-016-4969-4>.

- (38) Zhou, C.-F.; Chen, X.-H.; Huang, Y.-X.; Pan, Y.; Mi, J.-X. Rational Design of $(\text{NH}_4)\text{Cu}[\text{PO}_4]$ with a Spin Gapped, Distorted Honeycomb Layer. *European Journal of Inorganic Chemistry* **2020**, *2020* (14), 1286–1292. <https://doi.org/10.1002/ejic.201901284>.
- (39) Surblé, S.; Serre, C.; Mellot-Draznieks, C.; Millange, F.; Férey, G. A New Isoreticular Class of Metal-Organic-Frameworks with the MIL-88 Topology. *Chemical communications* **2006**, No. 3, 284–286.
- (40) Dahlman, C. J.; DeCrescent, R. A.; Venkatesan, N. R.; Kennard, R. M.; Wu, G.; Everest, M. A.; Schuller, J. A.; Chabynyc, M. L. Controlling Solvate Intermediate Growth for Phase-Pure Organic Lead Iodide Ruddlesden–Popper $(\text{C}_4\text{H}_9\text{NH}_3)_2(\text{CH}_3\text{NH}_3)_{n-1}\text{Pb}_n\text{I}_{3n+1}$ Perovskite Thin Films. *Chemistry of Materials* **2019**, *31* (15), 5832–5844.
- (41) Kalmutzki Markus J.; Hanikel Nikita; Yaghi Omar M. Secondary Building Units as the Turning Point in the Development of the Reticular Chemistry of MOFs. *Science Advances* **2018**, *4* (10). <https://doi.org/10.1126/sciadv.aat9180>.
- (42) Stock, N.; Biswas, S. Synthesis of Metal-Organic Frameworks (MOFs): Routes to Various MOF Topologies, Morphologies, and Composites. *Chem. Rev.* **2012**, *112* (2), 933–969. <https://doi.org/10.1021/cr200304e>.
- (43) Férey, G.; Serre, C.; Mellot-Draznieks, C.; Millange, F.; Surblé, S.; Dutour, J.; Margiolaki, I. A Hybrid Solid with Giant Pores Prepared by a Combination of Targeted Chemistry, Simulation, and Powder Diffraction. *Angewandte Chemie* **2004**, *116* (46), 6456–6461. <https://doi.org/10.1002/ange.200460592>.
- (44) Jhung, S.-H.; Lee, J.-H.; Chang, J.-S. Microwave Synthesis of a Nanoporous Hybrid Material, Chromium Trimesate. *Bulletin of the Korean Chemical Society* **2005**, *26* (6), 880–881. <https://doi.org/10.5012/bkcs.2005.26.6.880>.
- (45) Demessence, A.; Horcajada, P.; Serre, C.; Boissière, C.; Grosso, D.; Sanchez, C.; Férey, G. Elaboration and Properties of Hierarchically Structured Optical Thin Films of MIL-101 (Cr). *Chemical communications* **2009**, No. 46, 7149–7151.
- (46) Horcajada, P.; Chalati, T.; Serre, C.; Gillet, B.; Sebrie, C.; Baati, T.; Eubank, J. F.; Heurtaux, D.; Clayette, P.; Kreuz, C. Porous Metal–Organic-Framework Nanoscale Carriers as a Potential Platform for Drug Delivery and Imaging. *Nature materials* **2010**, *9* (2), 172–178.
- (47) Tranchemontagne, D. J.; Hunt, J. R.; Yaghi, O. M. Room Temperature Synthesis of Metal-Organic Frameworks: MOF-5, MOF-74, MOF-177, MOF-199, and IRMOF-0. *Tetrahedron* **2008**, *64* (36), 8553–8557. <https://doi.org/10.1016/j.tet.2008.06.036>.
- (48) Główniak, S.; Szczeńsiak, B.; Choma, J.; Jaroniec, M. Mechanochemistry: Toward Green Synthesis of Metal–Organic Frameworks. *Materials Today* **2021**, *46*, 109–124. <https://doi.org/10.1016/j.mattod.2021.01.008>.
- (49) Zhang, X.; Wan, K.; Subramanian, P.; Xu, M.; Luo, J.; Fransaer, J. Electrochemical Deposition of Metal–Organic Framework Films and Their Applications. *Journal of Materials Chemistry A* **2020**, *8* (16), 7569–7587. <https://doi.org/10.1039/D0TA00406E>.

- (50) Vaitsis, C.; Sourkouni, G.; Argirusis, C. Metal Organic Frameworks (MOFs) and Ultrasound: A Review. *Ultrasonics Sonochemistry* **2019**, *52*, 106–119. <https://doi.org/10.1016/j.ultsonch.2018.11.004>.
- (51) Serre, C.; Millange, F.; Thouvenot, C.; Noguès, M.; Marsolier, G.; Louër, D.; Férey, G. Very Large Breathing Effect in the First Nanoporous Chromium(III)-Based Solids: MIL-53 or $\text{Cr}^{\text{III}}(\text{OH})\cdot\text{O}_2\text{C}-\text{C}_6\text{H}_4-\text{CO}_2\cdot\text{HO}_2\text{C}-\text{C}_6\text{H}_4-\text{CO}_2\text{H}_x\cdot\text{H}_2\text{O}_y$. *J. Am. Chem. Soc.* **2002**, *124* (45), 13519–13526. <https://doi.org/10.1021/ja0276974>.
- (52) Seo, J.; Matsuda, R.; Sakamoto, H.; Bonneau, C.; Kitagawa, S. A Pillared-Layer Coordination Polymer with a Rotatable Pillar Acting as a Molecular Gate for Guest Molecules. *J. Am. Chem. Soc.* **2009**, *131* (35), 12792–12800. <https://doi.org/10.1021/ja904363b>.
- (53) Beurroies, I.; Boulhout, M.; Llewellyn, P. L.; Kuchta, B.; Férey, G.; Serre, C.; Denoyel, R. Using Pressure to Provoke the Structural Transition of Metal–Organic Frameworks. *Angewandte Chemie International Edition* **2010**, *49* (41), 7526–7529. <https://doi.org/10.1002/anie.201003048>.
- (54) Krause, S.; Hosono, N.; Kitagawa, S. Chemistry of Soft Porous Crystals: Structural Dynamics and Gas Adsorption Properties. *Angewandte Chemie International Edition* **2020**, *59* (36), 15325–15341. <https://doi.org/10.1002/anie.202004535>.
- (55) Yaghi, O. M.; O’Keeffe, M.; Ockwig, N. W.; Chae, H. K.; Eddaoudi, M.; Kim, J. Reticular Synthesis and the Design of New Materials. *Nature* **2003**, *423* (6941), 705–714. <https://doi.org/10.1038/nature01650>.
- (56) Schneemann, A.; Bon, V.; Schwedler, I.; Senkovska, I.; Kaskel, S.; A. Fischer, R. Flexible Metal–Organic Frameworks. *Chemical Society Reviews* **2014**, *43* (16), 6062–6096. <https://doi.org/10.1039/C4CS00101J>.
- (57) Bousquet, D.; Coudert, F.-X.; Fossati, A. G. J.; Neimark, A. V.; Fuchs, A. H.; Boutin, A. Adsorption Induced Transitions in Soft Porous Crystals: An Osmotic Potential Approach to Multistability and Intermediate Structures. *J. Chem. Phys.* **2013**, *138* (17), 174706. <https://doi.org/10.1063/1.4802888>.
- (58) Coudert, F.-X.; Boutin, A.; Fuchs, A. H.; Neimark, A. V. Adsorption Deformation and Structural Transitions in Metal–Organic Frameworks: From the Unit Cell to the Crystal. *J. Phys. Chem. Lett.* **2013**, *4* (19), 3198–3205. <https://doi.org/10.1021/jz4013849>.
- (59) Millange, F.; Guillou, N.; I. Walton, R.; Grenèche, J.-M.; Margiolaki, I.; Férey, G. Effect of the Nature of the Metal on the Breathing Steps in MOFs with Dynamic Frameworks. *Chemical Communications* **2008**, *0* (39), 4732–4734. <https://doi.org/10.1039/B809419E>.
- (60) Mellot-Draznieks, C.; Serre, C.; Surblé, S.; Audebrand, N.; Férey, G. Very Large Swelling in Hybrid Frameworks: A Combined Computational and Powder Diffraction Study. *J. Am. Chem. Soc.* **2005**, *127* (46), 16273–16278. <https://doi.org/10.1021/ja054900x>.
- (61) Sakata, Y.; Furukawa, S.; Kondo, M.; Hirai, K.; Horike, N.; Takashima, Y.; Uehara, H.; Louvain, N.; Meilikhov, M.; Tsuruoka, T.; Isoda, S.; Kosaka, W.; Sakata, O.; Kitagawa, S. Shape-Memory Nanopores Induced in Coordination Frameworks by Crystal Downsizing. *Science* **2013**, *339* (6116), 193–196. <https://doi.org/10.1126/science.1231451>.

- (62) Fairen-Jimenez, D.; Moggach, S. A.; Wharmby, M. T.; Wright, P. A.; Parsons, S.; Düren, T. Opening the Gate: Framework Flexibility in ZIF-8 Explored by Experiments and Simulations. *J. Am. Chem. Soc.* **2011**, *133* (23), 8900–8902. <https://doi.org/10.1021/ja202154j>.
- (63) Millange, F.; Serre, C.; Férey, G. Synthesis, Structure Determination and Properties of MIL-53as and MIL-53ht: The First Cr III Hybrid Inorganic–Organic Microporous Solids: $\text{Cr}^{\text{III}}(\text{OH})\cdot\text{O}_2\text{C}-\text{C}_6\text{H}_4-\text{CO}_2\cdot\text{HO}_2\text{C}-\text{C}_6\text{H}_4-\text{CO}_2\text{H}_x$. *Chemical Communications* **2002**, *0* (8), 822–823. <https://doi.org/10.1039/B201381A>.
- (64) Loiseau, T.; Serre, C.; Huguenard, C.; Fink, G.; Taulelle, F.; Henry, M.; Bataille, T.; Férey, G. A Rationale for the Large Breathing of the Porous Aluminum Terephthalate (MIL-53) Upon Hydration. *Chemistry – A European Journal* **2004**, *10* (6), 1373–1382. <https://doi.org/10.1002/chem.200305413>.
- (65) Volkringer, C.; Loiseau, T.; Guillou, N.; Férey, G.; Elkaïm, E.; Vimont, A. XRD and IR Structural Investigations of a Particular Breathing Effect in the MOF-Type Gallium Terephthalate MIL-53(Ga). *Dalton Trans.* **2009**, No. 12, 2241–2249. <https://doi.org/10.1039/B817563B>.
- (66) S. Mowat, J. P.; R. Seymour, V.; M. Griffin, J.; P. Thompson, S.; Z. Slawin, A. M.; Fairen-Jimenez, D.; Düren, T.; E. Ashbrook, S.; A. Wright, P. A Novel Structural Form of MIL-53 Observed for the Scandium Analogue and Its Response to Temperature Variation and CO_2 Adsorption. *Dalton Transactions* **2012**, *41* (14), 3937–3941. <https://doi.org/10.1039/C1DT11729G>.
- (67) Férey, G.; Serre, C. Large Breathing Effects in Three-Dimensional Porous Hybrid Matter: Facts, Analyses, Rules and Consequences. *Chemical Society Reviews* **2009**, *38* (5), 1380–1399. <https://doi.org/10.1039/B804302G>.
- (68) Parent, L. R.; Pham, C. H.; Patterson, J. P.; Denny, M. S.; Cohen, S. M.; Gianneschi, N. C.; Paesani, F. Pore Breathing of Metal–Organic Frameworks by Environmental Transmission Electron Microscopy. *J. Am. Chem. Soc.* **2017**, *4*.
- (69) Liu, Y.; Her, J.-H.; Dailly, A.; Ramirez-Cuesta, A. J.; Neumann, D. A.; Brown, C. M. Reversible Structural Transition in MIL-53 with Large Temperature Hysteresis. *J. Am. Chem. Soc.* **2008**, *130* (35), 11813–11818. <https://doi.org/10.1021/ja803669w>.
- (70) Nevjestić, I.; Depauw, H.; Gast, P.; Tack, P.; Deduytsche, D.; Leus, K.; Van Landeghem, M.; Goovaerts, E.; Vincze, L.; Detavernier, C.; Van Der Voort, P.; Callens, F.; Vrielinck, H. Sensing the Framework State and Guest Molecules in MIL-53(Al) via the Electron Paramagnetic Resonance Spectrum of V^{IV} Dopant Ions. *Phys. Chem. Chem. Phys.* **2017**, *19* (36), 24545–24554. <https://doi.org/10.1039/C7CP04760F>.
- (71) G. Yot, P.; Boudene, Z.; Macia, J.; Granier, D.; Vanduyfhuys, L.; Verstraelen, T.; Speybroeck, V. V.; Devic, T.; Serre, C.; Férey, G.; Stock, N.; Maurin, G. Metal–Organic Frameworks as Potential Shock Absorbers: The Case of the Highly Flexible MIL-53(Al). *Chemical Communications* **2014**, *50* (67), 9462–9464. <https://doi.org/10.1039/C4CC03853C>.
- (72) Hoffman, A. E. J.; Vanduyfhuys, L.; Nevjestić, I.; Wieme, J.; Rogge, S. M. J.; Depauw, H.; Van Der Voort, P.; Vrielinck, H.; Van Speybroeck, V. Elucidating the Vibrational Fingerprint of the Flexible Metal–Organic Framework MIL-53(Al) Using a Combined Experimental/Computational Approach. *J. Phys. Chem. C* **2018**, *122* (5), 2734–2746. <https://doi.org/10.1021/acs.jpcc.7b11031>.

CHAPTER 1: An Overview on MOFs, Flexibility, and MOF/GO composites

- (73) Seoane, B.; Sorribas, S.; Mayoral, Á.; Téllez, C.; Coronas, J. Real-Time Monitoring of Breathing of MIL-53(Al) by Environmental SEM. *Microporous and Mesoporous Materials* **2015**, *203*, 17–23. <https://doi.org/10.1016/j.micromeso.2014.10.016>.
- (74) Senkovska, I.; Hoffmann, F.; Fröba, M.; Getzschmann, J.; Böhlmann, W.; Kaskel, S. New Highly Porous Aluminium Based Metal-Organic Frameworks: Al(OH)(Ndc) (Ndc=2,6-Naphthalene Dicarboxylate) and Al(OH)(Bpdc) (Bpdc=4,4'-Biphenyl Dicarboxylate). *Microporous and Mesoporous Materials* **2009**, *122* (1), 93–98. <https://doi.org/10.1016/j.micromeso.2009.02.020>.
- (75) Loiseau, T.; Volkringer, C.; Haouas, M.; Taulelle, F.; Férey, G. Crystal Chemistry of Aluminium Carboxylates: From Molecular Species towards Porous Infinite Three-Dimensional Networks. *Comptes Rendus Chimie* **2015**, *18* (12), 1350–1369. <https://doi.org/10.1016/j.crci.2015.08.006>.
- (76) Samokhvalov, A. Aluminum Metal–Organic Frameworks for Sorption in Solution: A Review. *Coordination Chemistry Reviews* **2018**, *18*.
- (77) Wu, T.; Prasetya, N.; Li, K. Recent Advances in Aluminium-Based Metal-Organic Frameworks (MOF) and Its Membrane Applications. *Journal of Membrane Science* **2020**, *615*, 118493. <https://doi.org/10.1016/j.memsci.2020.118493>.
- (78) Ge, L.; Ge, T.; Wang, R. Facile Synthesis of Al-Based MOF and Its Applications in Desiccant Coated Heat Exchangers. *Renewable and Sustainable Energy Reviews* **2022**, *157*, 112015. <https://doi.org/10.1016/j.rser.2021.112015>.
- (79) Loiseau, T.; Mellot-Draznieks, C.; Muguerra, H.; Férey, G.; Haouas, M.; Taulelle, F. Hydrothermal Synthesis and Crystal Structure of a New Three-Dimensional Aluminum-Organic Framework MIL-69 with 2,6-Naphthalenedicarboxylate (Ndc), Al(OH)(Ndc)·H₂O. *C. R. Chim.* **2005**, *8* (3), 765–772. <https://doi.org/10.1016/j.crci.2004.10.011>.
- (80) Leung, E.; Muller, U.; Trukhan, N.; Mattenheimer, H.; Cox, G.; Blei, S. Process for Preparing Porous Metal-Organic Frameworks Based on Aluminum Fumarate. US 8,524,932, 2013.
- (81) Niekel, F.; Ackermann, M.; Guerrier, P.; Rothkirch, A.; Stock, N. Aluminum-1,4-Cyclohexanedicarboxylates: High-Throughput and Temperature-Dependent in Situ EDXRD Studies. *Inorg. Chem.* **2013**, *52* (15), 8699–8705. <https://doi.org/10.1021/ic400825b>.
- (82) Niekel, F.; Lannoeye, J.; Reinsch, H.; Munn, A. S.; Heerwig, A.; Zizak, I.; Kaskel, S.; Walton, R. I.; de Vos, D.; Llewellyn, P.; Lieb, A.; Maurin, G.; Stock, N. Conformation-Controlled Sorption Properties and Breathing of the Aliphatic Al-MOF [Al(OH)(CDC)]. *Inorg. Chem.* **2014**, *53* (9), 4610–4620. <https://doi.org/10.1021/ic500288w>.
- (83) Volkringer, C.; Loiseau, T.; Guillou, N.; Férey, G.; Haouas, M.; Taulelle, F.; Audebrand, N.; Margiolaki, I.; Popov, D.; Burghammer, M.; Riekkel, C. Structural Transitions and Flexibility during Dehydration–Rehydration Process in the MOF-Type Aluminum Pyromellitate Al₂(OH)₂[C₁₀O₈H₂] (MIL-118). *Crystal Growth & Design* **2009**, *9* (6), 2927–2936. <https://doi.org/10.1021/cg900276g>.

- (84) Volkringer, C.; Loiseau, T.; Guillou, N.; Férey, G.; Haouas, M.; Taulelle, F.; Elkaim, E.; Stock, N. High-Throughput Aided Synthesis of the Porous Metal–Organic Framework-Type Aluminum Pyromellitate, MIL-121, with Extra Carboxylic Acid Functionalization. *Inorg. Chem.* **2010**, *49* (21), 9852–9862. <https://doi.org/10.1021/ic101128w>.
- (85) Volkringer, C.; Loiseau, T.; Guillou, N.; Férey, G.; Elkaim, E. Syntheses and Structures of the MOF-Type Series of Metal 1,4,5,8,-Naphthalenetetracarboxylates $M_2(OH)_2[C_{14}O_8H_4]$ (Al, Ga, In) with Infinite Trans-Connected M–OH–M Chains (MIL-122). *Solid State Sciences* **2009**, *11* (8), 1507–1512. <https://doi.org/10.1016/j.solidstatedsciences.2009.05.017>.
- (86) Yang, S.; Ramirez-Cuesta, A. J.; Schröder, M. Inelastic Neutron Scattering Study of Binding of Para-Hydrogen in an Ultra-Microporous Metal–Organic Framework. *Chemical Physics* **2014**, *428*, 111–116. <https://doi.org/10.1016/j.chemphys.2013.11.004>.
- (87) Millange, F.; Walton, R. I. MIL-53 and Its Isoreticular Analogues: A Review of the Chemistry and Structure of a Prototypical Flexible Metal–Organic Framework. *Israel Journal of Chemistry* **2018**, *58* (9/10), 1019–1035. <https://doi.org/10.1002/ijch.201800084>.
- (88) Liu, Y.-Y.; Couck, S.; Vandichel, M.; Grzywa, M.; Leus, K.; Biswas, S.; Volkmer, D.; Gascon, J.; Kapteijn, F.; Denayer, J. F. M.; Waroquier, M.; Van Speybroeck, V.; Van Der Voort, P. New VIV-Based Metal–Organic Framework Having Framework Flexibility and High CO₂ Adsorption Capacity. *Inorg. Chem.* **2013**, *52* (1), 113–120. <https://doi.org/10.1021/ic301338a>.
- (89) Couck, S.; Van Assche, T. R. C.; Liu, Y.-Y.; Baron, G. V.; Van Der Voort, P.; Denayer, J. F. M. Adsorption and Separation of Small Hydrocarbons on the Flexible, Vanadium-Containing MOF, COMOC-2. *Langmuir* **2015**, *31* (18), 5063–5070. <https://doi.org/10.1021/acs.langmuir.5b00655>.
- (90) Depauw, H.; Nevjestić, I.; Wang, G.; Leus, K.; Callens, F.; Canck, E. D.; Buysser, K. D.; Vrielinck, H.; Voort, P. V. D. Discovery of a Novel, Large Pore Phase in a Bimetallic Al/V Metal–Organic Framework. *J. Mater. Chem. A* **2017**, *5* (47), 24580–24584. <https://doi.org/10.1039/C7TA08103K>.
- (91) Dau, P. V.; Kim, M.; Garibay, S. J.; Münch, F. H. L.; Moore, C. E.; Cohen, S. M. Single-Atom Ligand Changes Affect Breathing in an Extended Metal–Organic Framework. *Inorg. Chem.* **2012**, *51* (10), 5671–5676. <https://doi.org/10.1021/ic202683s>.
- (92) Coudert, F.-X. Responsive Metal–Organic Frameworks and Framework Materials: Under Pressure, Taking the Heat, in the Spotlight, with Friends. *Chem. Mater.* **2015**, *27* (6), 1905–1916. <https://doi.org/10.1021/acs.chemmater.5b00046>.
- (93) Yanai, N.; Uemura, T.; Inoue, M.; Matsuda, R.; Fukushima, T.; Tsujimoto, M.; Isoda, S.; Kitagawa, S. Guest-to-Host Transmission of Structural Changes for Stimuli-Responsive Adsorption Property. *J. Am. Chem. Soc.* **2012**, *134* (10), 4501–4504. <https://doi.org/10.1021/ja2115713>.
- (94) Luo, F.; Fan, C. B.; Luo, M. B.; Wu, X. L.; Zhu, Y.; Pu, S. Z.; Xu, W.-Y.; Guo, G.-C. Photoswitching CO₂ Capture and Release in a Photochromic Diarylethene Metal–Organic Framework. *Angewandte Chemie* **2014**, *126* (35), 9452–9455. <https://doi.org/10.1002/ange.201311124>.

CHAPTER 1: An Overview on MOFs, Flexibility, and MOF/GO composites

- (95) Henke, S.; Schneemann, A.; Wütscher, A.; Fischer, R. A. Directing the Breathing Behavior of Pillared-Layered Metal–Organic Frameworks via a Systematic Library of Functionalized Linkers Bearing Flexible Substituents. *J. Am. Chem. Soc.* **2012**, *134* (22), 9464–9474. <https://doi.org/10.1021/ja302991b>.
- (96) Zhang, J.-P.; Chen, X.-M. Optimized Acetylene/Carbon Dioxide Sorption in a Dynamic Porous Crystal. *J. Am. Chem. Soc.* **2009**, *131* (15), 5516–5521. <https://doi.org/10.1021/ja8089872>.
- (97) Henke, S.; Fischer, R. A. Gated Channels in a Honeycomb-like Zinc–Dicarboxylate–Bipyridine Framework with Flexible Alkyl Ether Side Chains. *J. Am. Chem. Soc.* **2011**, *133* (7), 2064–2067. <https://doi.org/10.1021/ja109317e>.
- (98) Fernandez, C. A.; Thallapally, P. K.; McGrail, B. P. Insights into the Temperature-Dependent “Breathing” of a Flexible Fluorinated Metal–Organic Framework. *ChemPhysChem* **2012**, *13* (14), 3275–3281. <https://doi.org/10.1002/cphc.201200243>.
- (99) Horcajada, P.; Salles, F.; Wuttke, S.; Devic, T.; Heurtaux, D.; Maurin, G.; Vimont, A.; Daturi, M.; David, O.; Magnier, E.; Stock, N.; Filinchuk, Y.; Popov, D.; Riekkel, C.; Férey, G.; Serre, C. How Linker’s Modification Controls Swelling Properties of Highly Flexible Iron(III) Dicarboxylates MIL-88. *J. Am. Chem. Soc.* **2011**, *133* (44), 17839–17847. <https://doi.org/10.1021/ja206936e>.
- (100) de J. Velásquez-Hernández, M.; López-Cervantes, V. B.; Martínez-Ahumada, E.; Tu, M.; Hernández-Balderas, U.; Martínez-Otero, D.; Williams, D. R.; Martis, V.; Sánchez-González, E.; Chang, J.-S.; Lee, J. S.; Balmaseda, J.; Ameloot, R.; Ibarra, I. A.; Jancik, V. CCIQS-1: A Dynamic Metal–Organic Framework with Selective Guest-Triggered Porosity Switching. *Chem. Mater.* **2022**, *34* (2), 669–677. <https://doi.org/10.1021/acs.chemmater.1c03388>.
- (101) Kundu, T.; Wahiduzzaman, M.; Shah, B. B.; Maurin, G.; Zhao, D. Solvent-Induced Control over Breathing Behavior in Flexible Metal–Organic Frameworks for Natural-Gas Delivery. *Angewandte Chemie* **2019**, *131* (24), 8157–8161. <https://doi.org/10.1002/ange.201902738>.
- (102) Ehrling, S.; Miura, H.; Senkovska, I.; Kaskel, S. From Macro- to Nanoscale: Finite Size Effects on Metal–Organic Framework Switchability. *Trends in Chemistry* **2021**, *3* (4), 291–304. <https://doi.org/10.1016/j.trechm.2020.12.012>.
- (103) Ehrling, S.; Senkovska, I.; Bon, V.; Evans, J. D.; Petkov, P.; Krupskaya, Y.; Kataev, V.; Wulf, T.; Krylov, A.; Vtyurin, A.; Krylova, S.; Adichtchev, S.; Slyusareva, E.; Weiss, M. S.; Büchner, B.; Heine, T.; Kaskel, S. Crystal Size versus Paddle Wheel Deformability: Selective Gated Adsorption Transitions of the Switchable Metal–Organic Frameworks DUT-8(Co) and DUT-8(Ni). *J. Mater. Chem. A* **2019**, *7* (37), 21459–21475. <https://doi.org/10.1039/C9TA06781G>.
- (104) Abylgazina, L.; Senkovska, I.; Engemann, R.; Ehrling, S.; Gorelik, T. E.; Kavooosi, N.; Kaiser, U.; Kaskel, S. Impact of Crystal Size and Morphology on Switchability Characteristics in Pillared-Layer Metal–Organic Framework DUT-8(Ni). *Frontiers in Chemistry* **2021**, *9*.
- (105) J. Thompson, M.; L. Hobday, C.; Senkovska, I.; Bon, V.; Ehrling, S.; Maliuta, M.; Kaskel, S.; Düren, T. Role of Particle Size and Surface Functionalisation on the Flexibility Behaviour of Switchable Metal–Organic Framework DUT-8(Ni). *Journal of Materials Chemistry A* **2020**, *8* (43), 22703–22711. <https://doi.org/10.1039/D0TA07775E>.

- (106) Klein, N.; Herzog, C.; Sabo, M.; Senkovska, I.; Getzschmann, J.; Paasch, S.; R. Lohe, M.; Brunner, E.; Kaskel, S. Monitoring Adsorption-Induced Switching by ^{129}Xe NMR Spectroscopy in a New Metal–Organic Framework $\text{Ni}_2(2,6\text{-Ndc})_2(\text{Dabco})$. *Physical Chemistry Chemical Physics* **2010**, *12* (37), 11778–11784. <https://doi.org/10.1039/C003835K>.
- (107) Bon, V.; Kavoosi, N.; Senkovska, I.; Kaskel, S. Tolerance of Flexible MOFs toward Repeated Adsorption Stress. *ACS Appl. Mater. Interfaces* **2015**, *7* (40), 22292–22300. <https://doi.org/10.1021/acsami.5b05456>.
- (108) Bon, V.; Klein, N.; Senkovska, I.; Heerwig, A.; Getzschmann, J.; Wallacher, D.; Zizak, I.; Brzhezinskaya, M.; Mueller, U.; Kaskel, S. Exceptional Adsorption-Induced Cluster and Network Deformation in the Flexible Metal–Organic Framework DUT-8(Ni) Observed by in Situ X-Ray Diffraction and EXAFS. *Phys. Chem. Chem. Phys.* **2015**, *17* (26), 17471–17479. <https://doi.org/10.1039/C5CP02180D>.
- (109) Miura, H.; Bon, V.; Senkovska, I.; Ehrling, S.; Watanabe, S.; Ohba, M.; Kaskel, S. Tuning the Gate-Opening Pressure and Particle Size Distribution of the Switchable Metal–Organic Framework DUT-8(Ni) by Controlled Nucleation in a Micromixer. *Dalton Transactions* **2017**, *46* (40), 14002–14011. <https://doi.org/10.1039/C7DT02809A>.
- (110) Kavoosi, N.; Bon, V.; Senkovska, I.; Krause, S.; Atzori, C.; Bonino, F.; Pallmann, J.; Paasch, S.; Brunner, E.; Kaskel, S. Tailoring Adsorption Induced Phase Transitions in the Pillared-Layer Type Metal–Organic Framework DUT-8(Ni). *Dalton Transactions* **2017**, *46* (14), 4685–4695. <https://doi.org/10.1039/C7DT00015D>.
- (111) Krause, S.; Bon, V.; Du, H.; Dunin-Borkowski, R. E.; Stoeck, U.; Senkovska, I.; Kaskel, S. The Impact of Crystal Size and Temperature on the Adsorption-Induced Flexibility of the Zr-Based Metal–Organic Framework DUT-98. *Beilstein J. Nanotechnol.* **2019**, *10*, 1737–1744. <https://doi.org/10.3762/bjnano.10.169>.
- (112) Dai, Z.; Lee, D. T.; Shi, K.; Wang, S.; Barton, H. F.; Zhu, J.; Yan, J.; Ke, Q.; Parsons, G. N. Fabrication of a Freestanding Metal Organic Framework Predominant Hollow Fiber Mat and Its Potential Applications in Gas Separation and Catalysis. *J. Mater. Chem. A* **2020**, *8* (7), 3803–3813. <https://doi.org/10.1039/C9TA11701F>.
- (113) Krause, S.; Bon, V.; Senkovska, I.; Töbrens, D. M.; Wallacher, D.; Pillai, R. S.; Maurin, G.; Kaskel, S. The Effect of Crystallite Size on Pressure Amplification in Switchable Porous Solids. *Nat Commun* **2018**, *9* (1), 1573. <https://doi.org/10.1038/s41467-018-03979-2>.
- (114) Watanabe, S.; Ohsaki, S.; Hanafusa, T.; Takada, K.; Tanaka, H.; Mae, K.; Miyahara, M. T. Synthesis of Zeolitic Imidazolate Framework-8 Particles of Controlled Sizes, Shapes, and Gate Adsorption Characteristics Using a Central Collision-Type Microreactor. *Chemical Engineering Journal* **2017**, *313*, 724–733. <https://doi.org/10.1016/j.cej.2016.12.118>.
- (115) Tiba, A. A.; Tivanski, A. V.; MacGillivray, L. R. Size-Dependent Mechanical Properties of a Metal–Organic Framework: Increase in Flexibility of ZIF-8 by Crystal Downsizing. *Nano Lett.* **2019**, *19* (9), 6140–6143. <https://doi.org/10.1021/acs.nanolett.9b02125>.

CHAPTER 1: An Overview on MOFs, Flexibility, and MOF/GO composites

- (116) Sakaida, S.; Otsubo, K.; Sakata, O.; Song, C.; Fujiwara, A.; Takata, M.; Kitagawa, H. Crystalline Coordination Framework Endowed with Dynamic Gate-Opening Behaviour by Being Downsized to a Thin Film. *Nature Chem* **2016**, *8* (4), 377–383. <https://doi.org/10.1038/nchem.2469>.
- (117) Ehrling, S.; Reynolds, E. M.; Bon, V.; Senkovska, I.; Gorelik, T. E.; Evans, J. D.; Rauche, M.; Mendt, M.; Weiss, M. S.; Pöppel, A.; Brunner, E.; Kaiser, U.; Goodwin, A. L.; Kaskel, S. Adaptive Response of a Metal–Organic Framework through Reversible Disorder–Disorder Transitions. *Nat. Chem.* **2021**, *13* (6), 568–574. <https://doi.org/10.1038/s41557-021-00684-4>.
- (118) Devic, T.; Horcajada, P.; Serre, C.; Salles, F.; Maurin, G.; Moulin, B.; Heurtaux, D.; Clet, G.; Vimont, A.; Grenèche, J.-M.; Ouay, B. L.; Moreau, F.; Magnier, E.; Filinchuk, Y.; Marrot, J.; Lavalley, J.-C.; Daturi, M.; Férey, G. Functionalization in Flexible Porous Solids: Effects on the Pore Opening and the Host–Guest Interactions. *J. Am. Chem. Soc.* **2010**, *132* (3), 1127–1136. <https://doi.org/10.1021/ja9092715>.
- (119) Horcajada, P.; Salles, F.; Wuttke, S.; Devic, T.; Heurtaux, D.; Maurin, G.; Vimont, A.; Daturi, M.; David, O.; Magnier, E.; Stock, N.; Filinchuk, Y.; Popov, D.; Riekkel, C.; Férey, G.; Serre, C. How Linker’s Modification Controls Swelling Properties of Highly Flexible Iron(III) Dicarboxylates MIL-88. *J. Am. Chem. Soc.* **2011**, *133* (44), 17839–17847. <https://doi.org/10.1021/ja206936e>.
- (120) Qian, B.; Chang, Z.; Bu, X.-H. Functionalized Dynamic Metal–Organic Frameworks as Smart Switches for Sensing and Adsorption Applications. *Top Curr Chem (Z)* **2020**, *378* (1), 5. <https://doi.org/10.1007/s41061-019-0271-2>.
- (121) Xu, X.; Yang, F.; Chen, S.-L.; He, J.; Xu, Y.; Wei, W. Dynamic Behaviours of a Rationally Prepared Flexible MOF by Postsynthetic Modification of Ligand Struts. *Chem. Commun.* **2017**, *53* (22), 3220–3223. <https://doi.org/10.1039/C7CC00230K>.
- (122) Rollins, D. S.; Geary, J.; Wong, A. H.; Xiao, D. J. Stabilizing Large Pores in a Flexible Metal–Organic Framework via Chemical Cross-Linking. *Chem. Commun.* **2022**. <https://doi.org/10.1039/D2CC04829A>.
- (123) Muschi, M.; Serre, C. Progress and Challenges of Graphene Oxide/Metal–Organic Composites. *Coordination Chemistry Reviews* **2019**, *387*, 262–272. <https://doi.org/10.1016/j.ccr.2019.02.017>.
- (124) Muschi, M.; Lalitha, A.; Sene, S.; Aureau, D.; Fregnaud, M.; Esteve, I.; Rivier, L.; Ramsahye, N.; Devautour-Vinot, S.; Sicard, C.; Menguy, N.; Serre, C.; Maurin, G.; Steunou, N. Formation of a Single-Crystal Aluminum-Based MOF Nanowire with Graphene Oxide Nanoscrolls as Structure-Directing Agents. *Angew. Chem. Int. Ed.* **2020**, *59* (26), 10353–10358. <https://doi.org/10.1002/ange.202000795>.
- (125) Saad, A.; Biswas, S.; Gkaniatsou, E.; Sicard, C.; Dumas, E.; Menguy, N.; Steunou, N. Metal–Organic Framework Based 1D Nanostructures and Their Superstructures: Synthesis, Microstructure, and Properties. *Chem. Mater.* **2021**, *33* (15), 5825–5849. <https://doi.org/10.1021/acs.chemmater.1c01034>.
- (126) Brodie, B. On the Atomic Weight of Graphite. *Phil. Trans.* **1859**, *149*, 249–259. <https://doi.org/10.1098/rstl.1859.0013>.

- (127) Boehm, H. P.; Clauss, A.; Fischer, G. O.; Hofmann, U. Das Adsorptionsverhalten sehr dünner Kohlenstoff-Folien. *Z. Anorg. Allg. Chem.* **1962**, *316* (3–4), 119–127. <https://doi.org/10.1002/zaac.19623160303>.
- (128) Berkman, S.; Park, F. Vapor Deposition Apparatus with Pyrolytic Graphite Heat Shield. 6.
- (129) Marcus, B.; Soubeyroux, J. L.; Touzain, Ph. In-Situ Diffraction Study of Electrochemical Intercalation of Potassium Solvated by Tetrahydrofuran into Graphite. Observation of a Fractional Stage $n = 4/3$. In *Chemical Physics of Intercalation*; Legrand, A. P., Flandrois, S., Eds.; NATO ASI Series; Springer US: Boston, MA, 1987; pp 375–378. https://doi.org/10.1007/978-1-4757-9649-0_24.
- (130) Novoselov, K. S.; Geim, A. K.; Morozov, S. V.; Jiang, D.; Zhang, Y.; Dubonos, S. V.; Grigorieva, I. V.; Firsov, A. A. Electric Field Effect in Atomically Thin Carbon Films. *Science* **2004**, *306* (5696), 666–669. <https://doi.org/10.1126/science.1102896>.
- (131) Novoselov, K. S.; Geim, A. K.; Morozov, S. V.; Jiang, D.; Katsnelson, M. I.; Grigorieva, I. V.; Dubonos, S. V.; Firsov, A. A. Two-Dimensional Gas of Massless Dirac Fermions in Graphene. *Nature* **2005**, *438* (7065), 197–200. <https://doi.org/10.1038/nature04233>.
- (132) Geim, A. K.; Novoselov, K. S. The Rise of Graphene. *Nature Mater* **2007**, *6* (3), 183–191. <https://doi.org/10.1038/nmat1849>.
- (133) Yu, W.; Sisi, L.; Haiyan, Y.; Jie, L. Progress in the Functional Modification of Graphene/Graphene Oxide: A Review. *RSC Advances* **2020**, *10* (26), 15328–15345. <https://doi.org/10.1039/D0RA01068E>.
- (134) Lee, X. J.; Hiew, B. Y. Z.; Lai, K. C.; Lee, L. Y.; Gan, S.; Thangalazhy-Gopakumar, S.; Rigby, S. Review on Graphene and Its Derivatives: Synthesis Methods and Potential Industrial Implementation. *Journal of the Taiwan Institute of Chemical Engineers* **2019**, *98*, 163–180. <https://doi.org/10.1016/j.jtice.2018.10.028>.
- (135) Zhu, Y.; Murali, S.; Cai, W.; Li, X.; Suk, J. W.; Potts, J. R.; Ruoff, R. S. Graphene and Graphene Oxide: Synthesis, Properties, and Applications. *Adv. Mater.* **2010**, *22* (35), 3906–3924. <https://doi.org/10.1002/adma.201001068>.
- (136) Hummers, W. S.; Offeman, R. E. Preparation of Graphitic Oxide. *J. Am. Chem. Soc.* **1958**, *80* (6), 1339–1339. <https://doi.org/10.1021/ja01539a017>.
- (137) Erickson, K.; Erni, R.; Lee, Z.; Alem, N.; Gannett, W.; Zettl, A. Determination of the Local Chemical Structure of Graphene Oxide and Reduced Graphene Oxide. *Adv. Mater.* **2010**, *22* (40), 4467–4472. <https://doi.org/10.1002/adma.201000732>.
- (138) Tarcan, R.; Todor-Boer, O.; Petrovai, I.; Leordean, C.; Astilean, S.; Botiz, I. Reduced Graphene Oxide Today. *J. Mater. Chem. C* **2020**, *8* (4), 1198–1224. <https://doi.org/10.1039/C9TC04916A>.
- (139) Sontakke, A. D.; Purkait, M. K. A Brief Review on Graphene Oxide Nanoscrolls: Structure, Synthesis, Characterization and Scope of Applications. *Chemical Engineering Journal* **2021**, *420*, 129914. <https://doi.org/10.1016/j.cej.2021.129914>.

CHAPTER 1: An Overview on MOFs, Flexibility, and MOF/GO composites


- (140) Fan, T.; Zeng, W.; Niu, Q.; Tong, S.; Cai, K.; Liu, Y.; Huang, W.; Min, Y.; Epstein, A. J. Fabrication of High-Quality Graphene Oxide Nanoscrolls and Application in Supercapacitor. *Nanoscale Res Lett* **2015**, *10* (1), 192. <https://doi.org/10.1186/s11671-015-0894-3>.
- (141) Amadei, C. A.; Stein, I. Y.; Silverberg, G. J.; Wardle, B. L.; Vecitis, C. D. Fabrication and Morphology Tuning of Graphene Oxide Nanoscrolls. *Nanoscale* **2016**, *8* (12), 6783–6791. <https://doi.org/10.1039/C5NR07983G>.
- (142) Alharbi, T. M. D.; Harvey, D.; Alsulami, I. K.; Dehbari, N.; Duan, X.; Lamb, R. N.; Lawrance, W. D.; Raston, C. L. Shear Stress Mediated Scrolling of Graphene Oxide. *Carbon* **2018**, *137*, 419–424. <https://doi.org/10.1016/j.carbon.2018.05.040>.
- (143) Wallace, J.; Shao, L. Defect-Induced Carbon Nanoscroll Formation. *Carbon* **2015**, *91*, 96–102. <https://doi.org/10.1016/j.carbon.2015.04.012>.
- (144) Tang, B.; Xiong, Z.; Yun, X.; Wang, X. Rolling up Graphene Oxide Sheets through Solvent-Induced Self-Assembly in Dispersions. *Nanoscale* **2018**, *10* (8), 4113–4122. <https://doi.org/10.1039/C7NR08415C>.
- (145) Tang, B.; Yun, X.; Xiong, Z.; Wang, X. Formation of Graphene Oxide Nanoscrolls in Organic Solvents: Toward Scalable Device Fabrication. *ACS Appl. Nano Mater.* **2018**, *1* (2), 686–697. <https://doi.org/10.1021/acsanm.7b00160>.
- (146) Liu, H.; Le, T.; Zhang, L.; Xu, M. Carbon Nanoscrolls: Synthesis and Applications. *J Mater Sci: Mater Electron* **2018**, *29* (22), 18891–18904. <https://doi.org/10.1007/s10854-018-0074-1>.
- (147) Wang, X.; Yang, D.-P.; Huang, G.; Huang, P.; Shen, G.; Guo, S.; Mei, Y.; Cui, D. Rolling up Graphene Oxide Sheets into Micro/Nanoscrolls by Nanoparticle Aggregation. *J. Mater. Chem.* **2012**, *22* (34), 17441. <https://doi.org/10.1039/c2jm32810k>.
- (148) Wang, W.; Gai, Y.; Xiao, D.; Zhao, Y. A Facile and General Approach for Production of Nanoscrolls with High-Yield from Two-Dimensional Nanosheets. *Sci Rep* **2018**, *8* (1), 15262. <https://doi.org/10.1038/s41598-018-33709-z>.
- (149) Gai, Y.; Wang, W.; Xiao, D.; Tan, H.; Lin, M.; Zhao, Y. Reversible Conversion between Graphene Nanosheets and Graphene Nanoscrolls at Room Temperature. *RSC Adv.* **2018**, *8* (18), 9749–9753. <https://doi.org/10.1039/C8RA00475G>.
- (150) Sharifi, T.; Gracia-Espino, E.; Reza Barzegar, H.; Jia, X.; Nitze, F.; Hu, G.; Nordblad, P.; Tai, C.-W.; Wågberg, T. Formation of Nitrogen-Doped Graphene Nanoscrolls by Adsorption of Magnetic γ -Fe₂O₃ Nanoparticles. *Nat Commun* **2013**, *4* (1), 2319. <https://doi.org/10.1038/ncomms3319>.
- (151) Jahan, M.; Bao, Q.; Yang, J.-X.; Loh, K. P. Structure-Directing Role of Graphene in the Synthesis of Metal–Organic Framework Nanowire. *J. Am. Chem. Soc.* **2010**, *132* (41), 14487–14495. <https://doi.org/10.1021/ja105089w>.
- (152) Sturm (née Rosseeva), E. V.; Cölfen, H. Mesocrystals: Structural and Morphogenetic Aspects. *Chem. Soc. Rev.* **2016**, *45* (21), 5821–5833. <https://doi.org/10.1039/C6CS00208K>.

- (153) Uflyand, I. E.; Naumkina, V. N.; Zhinzhiro, V. A. Nanocomposites of Graphene Oxide and Metal-Organic Frameworks. *Russ J Appl Chem* **2021**, *94* (11), 1453–1468. <https://doi.org/10.1134/S107042722111001X>.
- (154) Qu, H.; Huang, L.; Han, Z.; Wang, Y.; Zhang, Z.; Wang, Y.; Chang, Q.; Wei, N.; Kipper, M. J.; Tang, J. A Review of Graphene-Oxide/Metal–Organic Framework Composites Materials: Characteristics, Preparation and Applications. *J Porous Mater* **2021**, *28* (6), 1837–1865. <https://doi.org/10.1007/s10934-021-01125-w>.
- (155) Mazlan, N. A.; Butt, F. S.; Lewis, A.; Yang, Y.; Yang, S.; Huang, Y. The Growth of Metal–Organic Frameworks in the Presence of Graphene Oxide: A Mini Review. *Membranes* **2022**, *12* (5), 501. <https://doi.org/10.3390/membranes12050501>.
- (156) Szczeńniak, B.; Choma, J.; Jaroniec, M. Gas Adsorption Properties of Hybrid Graphene-MOF Materials. *Journal of Colloid and Interface Science* **2018**, *514*, 801–813. <https://doi.org/10.1016/j.jcis.2017.11.049>.
- (157) Wang, J.; Hu, H.; Lu, S.; Hu, J.; Zhu, H.; Duan, F.; Du, M. Conductive Metal and Covalent Organic Frameworks for Electrocatalysis: Design Principles, Recent Progress and Perspective. *Nanoscale* **2022**, *14* (2), 277–288. <https://doi.org/10.1039/D1NR06197F>.
- (158) Niu, L.; Wu, T.; Chen, M.; Yang, L.; Yang, J.; Wang, Z.; Kornyshev, A. A.; Jiang, H.; Bi, S.; Feng, G. Conductive Metal–Organic Frameworks for Supercapacitors. *Advanced Materials* **2022**, *n/a* (n/a), 2200999. <https://doi.org/10.1002/adma.202200999>.
- (159) Xie, L. S.; Skorupskii, G.; Dincă, M. Electrically Conductive Metal–Organic Frameworks. *Chem. Rev.* **2020**, *120* (16), 8536–8580. <https://doi.org/10.1021/acs.chemrev.9b00766>.
- (160) Xu, J.; Peng, Y.; Xing, W.; Ding, Z.; Zhang, S.; Pang, H. Metal-Organic Frameworks Marry Carbon: Booster for Electrochemical Energy Storage. *Journal of Energy Storage* **2022**, *53*, 105104. <https://doi.org/10.1016/j.est.2022.105104>.
- (161) Wang, K.; Hui, K. N.; San Hui, K.; Peng, S.; Xu, Y. Recent Progress in Metal–Organic Framework/Graphene-Derived Materials for Energy Storage and Conversion: Design, Preparation, and Application. *Chem. Sci.* **2021**, *12* (16), 5737–5766. <https://doi.org/10.1039/D1SC00095K>.
- (162) Peng, Y.; Xu, J.; Xu, J.; Ma, J.; Bai, Y.; Cao, S.; Zhang, S.; Pang, H. Metal-Organic Framework (MOF) Composites as Promising Materials for Energy Storage Applications. *Advances in Colloid and Interface Science* **2022**, *307*, 102732. <https://doi.org/10.1016/j.cis.2022.102732>.
- (163) Najafi, F.; Rajabi, M. Thermal Gravity Analysis for the Study of Stability of Graphene Oxide–Glycine Nanocomposites. *Int Nano Lett* **2015**, *5* (4), 187–190. <https://doi.org/10.1007/s40089-015-0154-7>.
- (164) Zhang, J.; Li, Z.; Qi, X.; Zhang, W.; Wang, D.-Y. Size Tailored Bimetallic Metal-Organic Framework (MOF) on Graphene Oxide with Sandwich-like Structure as Functional Nano-Hybrids for Improving Fire Safety of Epoxy. *Composites Part B: Engineering* **2020**, *188*, 107881. <https://doi.org/10.1016/j.compositesb.2020.107881>.

CHAPTER 1: An Overview on MOFs, Flexibility, and MOF/GO composites

- (165) Alihosseini, M.; Ghasemi, S.; Ahmadkhani, S.; Alidoosti, M.; Esfahani, D. N.; Peeters, F. M.; Neek-Amal, M. Electronic Properties of Oxidized Graphene: Effects of Strain and an Electric Field on Flat Bands and the Energy Gap. *J. Phys. Chem. Lett.* **2022**, *13* (1), 66–74. <https://doi.org/10.1021/acs.jpcllett.1c03286>.
- (166) Bae, C.; Jeong, G.; Park, S.; Kim, Y.; Gu, M.; Kim, D.; Kim, J. Synergistic Effect of MIL-101/Reduced Graphene Oxide Nanocomposites on High-Pressure Ammonia Uptake. *ACS Omega* **2022**, *7*(20), 17144–17150. <https://doi.org/10.1021/acsomega.2c00741>.
- (167) Yang, Y.; Zan, J.; Shuai, Y.; Yang, L.; Zhang, L.; Zhang, H.; Wang, D.; Peng, S.; Shuai, C. In Situ Growth of a Metal–Organic Framework on Graphene Oxide for the Chemo-Photothermal Therapy of Bacterial Infection in Bone Repair. *ACS Appl. Mater. Interfaces* **2022**, *14* (19), 21996–22005. <https://doi.org/10.1021/acsami.2c04841>.
- (168) Firouzjaei, M. D.; Shamsabadi, A. A.; Aktij, S. A.; Seyedpour, S. F.; Sharifian Gh., M.; Rahimpour, A.; Esfahani, M. R.; Ulbricht, M.; Soroush, M. Exploiting Synergetic Effects of Graphene Oxide and a Silver-Based Metal–Organic Framework To Enhance Antifouling and Anti-Biofouling Properties of Thin-Film Nanocomposite Membranes. *ACS Appl. Mater. Interfaces* **2018**, *10* (49), 42967–42978. <https://doi.org/10.1021/acsami.8b12714>.
- (169) Shinde, S. K.; Kim, D.-Y.; Kumar, M.; Murugadoss, G.; Ramesh, S.; Tamboli, A. M.; Yadav, H. M. MOFs-Graphene Composites Synthesis and Application for Electrochemical Supercapacitor: A Review. *Polymers* **2022**, *14* (3), 511. <https://doi.org/10.3390/polym14030511>.
- (170) Li, Y.; Liu, H.; Wang, H.; Qiu, J.; Zhang, X. GO-Guided Direct Growth of Highly Oriented Metal–Organic Framework Nanosheet Membranes for H₂/CO₂ Separation. *Chem. Sci.* **2018**, *9*(17), 4132–4141. <https://doi.org/10.1039/C7SC04815G>.
- (171) Petit, C.; Mendoza, B.; Bandoz, T. J. Reactive Adsorption of Ammonia on Cu-Based MOF/Graphene Composites. *Langmuir* **2010**, *26* (19), 15302–15309. <https://doi.org/10.1021/la1021092>.
- (172) Varghese, A. M.; Reddy, K. S. K.; Karanikolos, G. N. An In-Situ-Grown Cu-BTC Metal–Organic Framework / Graphene Oxide Hybrid Adsorbent for Selective Hydrogen Storage at Ambient Temperature. *Ind. Eng. Chem. Res.* **2022**, *61* (18), 6200–6213. <https://doi.org/10.1021/acs.iecr.1c04710>.
- (173) Muschi, M.; Devautour-Vinot, S.; Aureau, D.; Heymans, N.; Sene, S.; Emmerich, R.; Ploumistos, A.; Geneste, A.; Steunou, N.; Patriarche, G.; Weireld, G. D.; Serre, C. Metal–Organic Framework/Graphene Oxide Composites for CO₂ Capture by Microwave Swing Adsorption. *J. Mater. Chem. A* **2021**, *9* (22), 13135–13142. <https://doi.org/10.1039/D0TA12215G>.
- (174) Thebo, K. H.; Qian, X.; Zhang, Q.; Chen, L.; Cheng, H.-M.; Ren, W. Highly Stable Graphene-Oxide-Based Membranes with Superior Permeability. *Nat Commun* **2018**, *9* (1), 1486. <https://doi.org/10.1038/s41467-018-03919-0>.

- (175) Yu, S.; Pang, H.; Huang, S.; Tang, H.; Wang, S.; Qiu, M.; Chen, Z.; Yang, H.; Song, G.; Fu, D.; Hu, B.; Wang, X. Recent Advances in Metal-Organic Framework Membranes for Water Treatment: A Review. *Science of The Total Environment* **2021**, *800*, 149662. <https://doi.org/10.1016/j.scitotenv.2021.149662>.
- (176) Sui, X.; Ding, H.; Yuan, Z.; Leong, C. F.; Goh, K.; Li, W.; Yang, N.; D'Alessandro, D. M.; Chen, Y. The Roles of Metal-Organic Frameworks in Modulating Water Permeability of Graphene Oxide-Based Carbon Membranes. *Carbon* **2019**, *148*, 277–289. <https://doi.org/10.1016/j.carbon.2019.03.049>.
- (177) Karimzadeh, Z.; Javanbakht, S.; Namazi, H. Carboxymethylcellulose/MOF-5/Graphene Oxide Bio-Nanocomposite as Antibacterial Drug Nanocarrier Agent. *Bioimpacts* **2019**, *9*(1), 5–13. <https://doi.org/10.15171/bi.2019.02>.
- (178) Haeri, Z.; Ramezanzadeh, B.; Ramezanzadeh, M. Recent Progress on the Metal-Organic Frameworks Decorated Graphene Oxide (MOFs-GO) Nano-Building Application for Epoxy Coating Mechanical-Thermal/Flame-Retardant and Anti-Corrosion Features Improvement. *Progress in Organic Coatings* **2022**, *163*, 106645. <https://doi.org/10.1016/j.porgcoat.2021.106645>.



CHAPTER 2: Selection & Screening of MOF Candidates

TABLE OF CONTENTS

2.1 INTRODUCTION	83
2.2 SELECTED MOF CANDIDATES AND THEIR COMPOSITES	85
2.2.1. Selection criteria for MOFs.....	85
2.2.1.1. Polycarboxylate aromatic ligands	85
2.2.1.2. Al/Zr based MOFs	87
2.2.1.3. Reflux synthesis	88
2.2.1.4. Synthesis in a mixture of solvents.....	89
2.2.1.5. Selected MOF candidates	90
2.2.2. Preparation strategy of MOF/GO composites	91
2.3 SCREENING OF SELECTED MOF CANDIDATES.....	94
2.3.1. CAU-10-H(Al)	95
2.3.1.1. Synthesis of pure MOF	95
2.3.1.2. Addition of GO to the synthesis	96
2.3.1.3. Characterization results.....	97
2.3.2. CAU-23(Al).....	99
2.3.2.1. Synthesis of pure MOF	99
2.3.2.2. Addition of GO to the synthesis	100
2.3.2.3. Characterization results.....	100
2.3.3. DUT-5(Al)	102
2.3.3.1. Synthesis of pure MOF.....	102
2.3.3.2. Addition of GO to the synthesis	103
2.3.3.3. Characterization results.....	103
2.3.4. DUT-67(Zr)	106
2.3.4.1. Synthesis of pure MOF	106
2.3.4.2. Synthesis of MOF/GO.....	107
2.3.4.3. Characterization results.....	108
2.3.5. MOF-545(Zr)	110
2.3.5.1. Synthesis of pure MOF	110
2.3.5.2. Synthesis of MOF/GO.....	110
2.3.5.3. Characterization results.....	111
2.4 SCREENING CONCLUSIONS AND SELECTED CANDIDATE	112
2.5 REFERENCES	113

2.1 INTRODUCTION

Forming anisotropic MOF nanocrystals is of huge importance in the domains of catalysis, sensing, gas transport, and electronics.¹ For instance, the dimensionality and morphology of MOF crystals can impact the diffusion and the mass transport efficiency of analytes towards the catalytic and the adsorption sites of the MOF. Yet, to date, MOFs have largely been produced as polycrystalline powders or spherical nanocrystals.^{2,3} Controlling their crystal size, shape, and multiscale porosity while creating suitable shaping procedures is one of the major barriers for the practical application of MOFs.¹ Anisotropic materials have not yet received enough attention in literature as the aim of MOF research was historically more oriented towards obtaining novel MOF structures. Later, MOF science was oriented towards obtaining MOF nanoparticles for processing and applications which was less complicated than exploring anisotropic materials which generally require a higher degree of control over the different synthetic parameters (reaction kinetics, solvents, etc.). Nowadays, one of the strategies recently emerging in literature for designing anisotropic MOF crystals consists of combining MOFs with different carbon-based materials (polymers, graphene, graphene oxide, carbon nanotubes, etc.).⁴ As discussed in **chapter 1**, the use of GO nanoscrolls as structural directing agents has led to the formation of anisotropic single crystal MIL-69(Al) based NWs.⁵ Following this approach, it could be possible to obtain hierarchically porous MOF/GO composites with a specific microstructure that allows a homogeneous dispersion of MOF NWs in the GO matrix, without any agglomeration of MOF NPs or restacked GO layers.⁵ Certainly, the work done on MIL-69(Al) is unprecedented from a conceptual point of view. However, this work suffered a major limitation in which the final product (MIL-69(Al)/GO) presented a low porosity, thereby affecting its use in many applications.

CHAPTER 2: Selection & Screening of MOF Candidates

As observed in **(Figure 2-1)**, adding GO to MIL-69(Al) has led to a hierarchically porous structure that was not obtained in case of the pure MOF.⁵ This can be deduced from the hysteresis of the type IIb N₂ isotherm which is absent in case of the pure MOF. Yet, the final product (MIL-69(Al)/GO) exhibited a low porosity with a $S_{\text{BET}} = 125 \text{ m}^2/\text{g}$.⁵ Note that the pure hydrated MIL-69(Al) has a low surface area ($S_{\text{BET}} = 320 \text{ m}^2/\text{g}$) due to the narrow pores ($2.7 \times 13.6 \text{ \AA}$), and this surface area further decreased after adding GO.⁶ Such results impact the utilization of the MOF based composite in future applications. Hence, it would be of huge interest to expand the reported concept of forming anisotropic MOF crystals on other MOFs with higher porosity. In this PhD project, one of our objectives was to extend the concept applied to MIL-69(Al) into a MOF with a higher permanent porosity and to prove the reliability of this approach in which GO can be employed as a structural directing agent of MOFs.

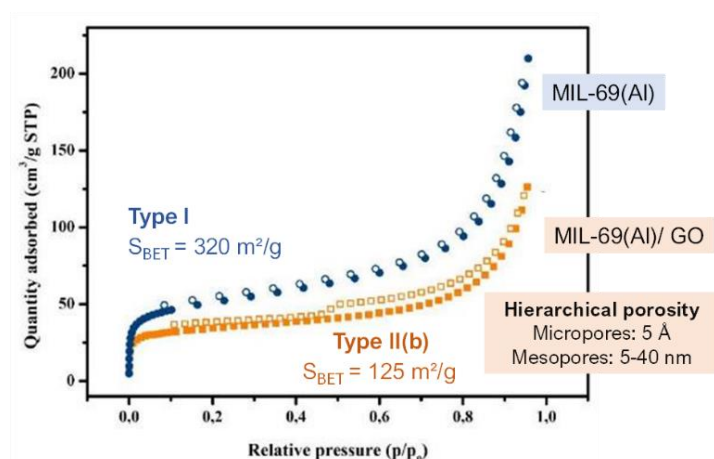


Figure 2-1: N₂ physisorption isotherms of MIL-69(Al) MOF and MIL-69(Al)/GO composite.⁵

To achieve this goal, the work done on MIL-69(Al) was thoroughly studied, and a group of MOFs was chosen based on the results obtained with MIL-69(Al) for an initial screening of the best candidate for further studies.⁵ The selection of MOFs and the preparation strategy of their corresponding composites will be discussed in the next section of this chapter. First, the MOFs selection criteria will be explained, and the selected MOFs will be then listed. Secondly, the preparation approach of the different MOF/GO composites will be discussed.

In the next part of the chapter, the screening of the selected MOFs will be reviewed. For each of the selected MOFs, both the reported and modified (if needed) synthesis will be described. Afterwards, the design of the MOF/GO composite will be explained, and the characterization of both the MOFs and their corresponding composites will be presented. MOFs and MOF/GO composites included in this chapter were mainly characterized by powder X-ray diffraction (PXRD), Fourier-transform infrared (FT-IR) spectroscopy and scanning electron microscopy (SEM). Finally, based on the results obtained by the different characterization techniques, the last part of this chapter will discuss the MOF/GO composite with the most promising results and the intended plan for the coming chapters.

2.2 SELECTED MOF CANDIDATES AND THEIR COMPOSITES

The criteria for the selection of MOF candidates and the strategy for designing their corresponding composites in presence of GO is discussed in this section.

2.2.1. Selection criteria for MOFs

To meet the objective of extending the concept applied to MIL-69(Al) into MOFs of higher porosity, only MOFs with higher surface areas ($S_{\text{BET}} \geq 600 \text{ m}^2/\text{g}$) were considered. Then, the selection criteria were focused on targeting polycarboxylate aromatic Al/Zr based MOFs which can be obtained under reflux in DMF, water, or a mixture of the two solvents. The reason for those criteria is detailed below.

2.2.1.1. Polycarboxylate aromatic ligands

Generally speaking, the bidentate and bridging coordination mode of the carboxylate group make aromatic polycarboxylates ligands an interesting choice for MOFs synthesis. More importantly, the presence of carboxylate groups offers the potential of forming strong ionocovalent bonds when combined with high valent metals, leading to stable structures. Herein, the presence of rigid aromatic groups is considered essential for the later design of MOF/GO anisotropic

CHAPTER 2: Selection & Screening of MOF Candidates

structures. This assumption is based on observations related to the MIL-69(Al)/GO case. It was concluded based on both theoretical and experimental results that the formation of MIL-69(Al) based NWs involved the GO arrangement at the (010) surface of MIL-69(Al) in a manner that allows π - π stacking interactions.⁵ The naphthalene ligand of MIL-69(Al) lies parallel to the aromatic ring of GO (**Figure 2-2**), which reinforces the affinity between the MOF and GO, and limits the growth of the (010) crystal facets of MIL-69 crystal.⁵ These predictions are in accordance with the experimentally observed growth of MIL-69(Al) based NWs along the [001] direction. Such result suggests that π - π stacking interactions through the polyaromatic rings of naphthalene are presumably involved in the formation of MIL-69(Al) NWs. Additionally, it should be noted that other interactions involving the OH groups of MIL-69(Al) and the oxygen functions of GO (COOH, OH, epoxide) were revealed by molecular modeling and were found stronger for the (010) crystal facets in comparison to (001) crystal facets.⁵ Moreover, one can assume that polyaromatic ligands can provide better interactions for shaping MOF/GO composites than single aromatic ones. Finally, it is worth mentioning that the polycarboxylate aromatic ligands offer the chance of examining the impact of ligand functionalization on the design process of MOF/GO anisotropic structures which is also of our interest.

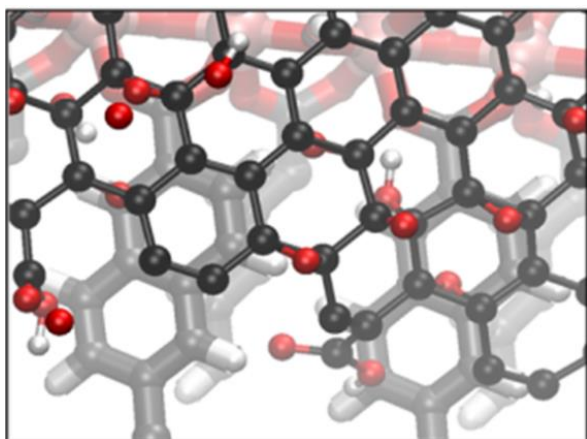


Figure 2-2. Snapshot showing preferential π - π like interactions at the MIL-69(Al)(010)/GO interface. The snapshot was based on the molecular modeling of the MIL-69(Al)(010)/GO composite. Color schemes of GO layers: C black, O red, H white; and of MIL-69(010): C grey, Al pink, O red, H white.⁵

2.2.1.2. Al/Zr based MOFs

Aluminum and zirconium polycarboxylate MOFs were desired due to their high stability as function of the high oxidation states of their respective cations (Al^{3+} , Zr^{4+}).⁷ Moreover, Al^{3+} and Zr^{4+} possess a low toxicity, and they both present Lewis acid properties which are of interest in applications like catalysis and adsorption. Compared to MOFs with divalent d-block metals (e.g., Zn^{2+} , Cu^{2+}) and trivalent f-block (e.g., lanthanides), the tri- and tetravalent (Al^{3+} , Zr^{4+}) ions have been a promising candidate for building different coordination frameworks with a low density and notably high thermal or physicochemical stability.⁷ Besides, Al^{3+} and Zr^{4+} offer higher reactivity when compared with some cations of similar valency (e.g., Al^{3+} is more reactive than the inert Cr^{3+}). Furthermore, the good thermal stability combined with high densities of accessible reactive sites make Al/Zr based MOFs good candidates for several applications (e.g., catalysis, separations, etc.).⁸ In addition, the local environment of Al based MOFs can be easily probed by ^{27}Al solid-state NMR which can be of interest for the optimization of composites. As the aim of this project is to later combine the selected MOFs with GO, solid-state NMR allows characterizing the organic moieties and investigating the inorganic SBUs without any thermal treatments. Such treatments are required for other characterization techniques (i.e., thermogravimetric analysis) and generally lead to the reduction of the GO sheet.⁹ This will be further shown in the coming chapters. Finally, it is worth mentioning that Al/Zr based MOFs have received a lot of attention in hierarchical porosity¹⁰ and many applications of interest such as catalysis,⁸ gas storage and separation,¹¹ adsorption of organics,¹² and others.^{2,3}

2.2.1.3. Reflux synthesis

Typically, conventional hydro- and solvothermal synthesis are the mostly used techniques for the preparation of MOFs. These techniques require elevated temperatures and pressures in closed system, and they clearly suffer the need of special apparatus and blindness of reaction process monitoring. In comparison, reflux is considered as a rapid, less expensive, and observable alternative synthesis approach that allows monitoring reaction processes. Reflux offers softer conditions than hydro/solvothermal conditions and allows to control the diameter of MOF nanoparticles, which is of our huge interest. With this in mind, several MOFs have been reported under reflux.^{2,3} Due to the poor solubility of most synthetic MOF ligands in water, reflux synthesis provides the advantage of elevating the reaction temperatures to promote their dissolution without the huge increase in the pressure noted in hydrothermal synthesis. Furthermore, our objective in this project is adding graphene oxide to the selected MOFs for designing MOF based anisotropic composites. Reports have shown that only reflux allows the homogeneous mixing of GO and the MOF under stirring and heating without strongly reducing the GO sheet. Such GO reduction may partially lead to the removal of the oxygen groups of GO (carboxylate, OH, epoxide), thereby affecting the interactions at the interface between the MOF and GO.⁵ In contrast, the high pressure and temperature in the closed vessels used in solvothermal techniques are prone to reduce GO and thus affect the interactions at the interface. Similarly, submitting GO to microwave radiations is not safe or convenient. Microwave assisted synthesis leads to a huge emission of heat which is also followed by the reduction of the GO sheet.¹³

2.2.1.4. Synthesis in a mixture of solvents

Of our huge interest in this project is to select MOFs that can be synthesized in a mixture of water/DMF or later optimized in that manner. Many reports in literature have shown the effect of the synthesis solution on the scrolling of GO sheets. It was shown that the scrolling of GO sheets is promoted in a mixture of solvents.¹⁴⁻¹⁶ In fact, this was also observed for the formation of the MIL-69(Al) NWs.⁵ The solvent induced scrolling of GO can be explained by the inhomogeneous distribution of polar/nonpolar groups in a GO sheets.¹⁴ This was thoroughly explained in **chapter 1**. For example, when GO is dispersed in a mixture of solvents (e.g., DMF and water), due to its amphiphilic nature, GO tends to reduce the interaction with some solvent molecules at certain areas in the GO sheet. For instance, the oxygen functionalities present at particular areas of the GO sheet would prefer to interact with water and lessen the interaction with DMF molecules. This leads to an instable dispersion that in turn drives the initial scrolling of GO sheets which prefer to curl onto themselves rather than coagulate in solution.¹⁴ In fact, this behavior is comparable to the self-assembly process via solvent control that have been widely reported for amphiphilic surfactants and polymers. Besides, it should be mentioned that the Van der Waals and π - π interactions taking place in the GO nanoscrolls are prone to decrease the free energy of the system, which in turn compensates the gained energy from bending. These phenomena were explained by Tang *et al.* where they reported that in presence of "unfavorable" solvents, GO prefers to self-scroll rather than interact with solvent molecules.¹⁴

2.2.1.5. Selected MOF candidates

Five MOFs that meet the mentioned criteria were studied during this PhD project with the aim of producing anisotropic MOF/GO composites: CAU-10-H(Al),^{17,18} CAU-23(Al),¹⁹ DUT-5(Al),^{20,21} DUT-67(Zr),^{22,23} and MOF-545(Zr)^{24,25}. **Table 2-1** below provides a brief overview of the selected MOFs. The five listed MOFs have all been published during the last two decades. The synthesis of these MOFs was adjusted to reflux synthesis for the reasons mentioned above. The reported, and optimized (if needed), protocols of each MOF are stated in this section. CAU-23(Al),¹⁹ DUT-5(Al),²¹ and MOF-545(Zr)²⁵ were reproduced using previously reported reflux protocols. The synthesis of CAU-10-H(Al),¹⁸ and DUT-67(Zr)²³ was optimized under reflux based on previous reports using conventional solvothermal techniques.

Table 2-1: Summary of the molecular formula, reactants, and the reported synthesis method and solvent for each of the five MOFs.

MOF Name	Molecular formula	Employed ligand	Synthesis method	Synthesis solvent	ref.
CAU-10-H(Al) (dry)	Al(OH)(C ₈ H ₄ O ₄) C ₈ H ₅ O ₅ Al	isophthalic acid (1,3-H ₂ BDC)	reflux, solvothermal	DMF, water	17,18
CAU-23(Al) (dry)	Al(OH)(C ₆ H ₂ O ₄ S) C ₆ H ₃ O ₅ SAI	sodium thiophene dicarboxylate (Na ₂ TDC)	reflux	water	19
DUT-5(Al)	Al ₄ (OH) ₄ (bpdc) ₄ C ₅₆ H ₃₆ O ₂₀ Al ₄	4,4'biphenyldicarboxylic acid (bpdc)	reflux	DMF	20,21
DUT-67(Zr)	Zr ₆ O ₈ (tdc) ₄ (OAc) ₂ Zr ₆ C ₂₈ H ₁₆ O ₂₈ S ₄	thiophene dicarboxylic acid (H ₂ TDC)	microwave, solvothermal	DMF, acetic acid (modulator)	22,23
MOF-545(Zr)	Zr ₆ O ₈ (H ₂ O) ₈ (TCPP) ₂ Zr ₆ C ₉₆ H ₆₈ O ₃₂ N ₈	Porphyrin (TCPP-H ₂)	reflux, solvothermal	DMF	24,25

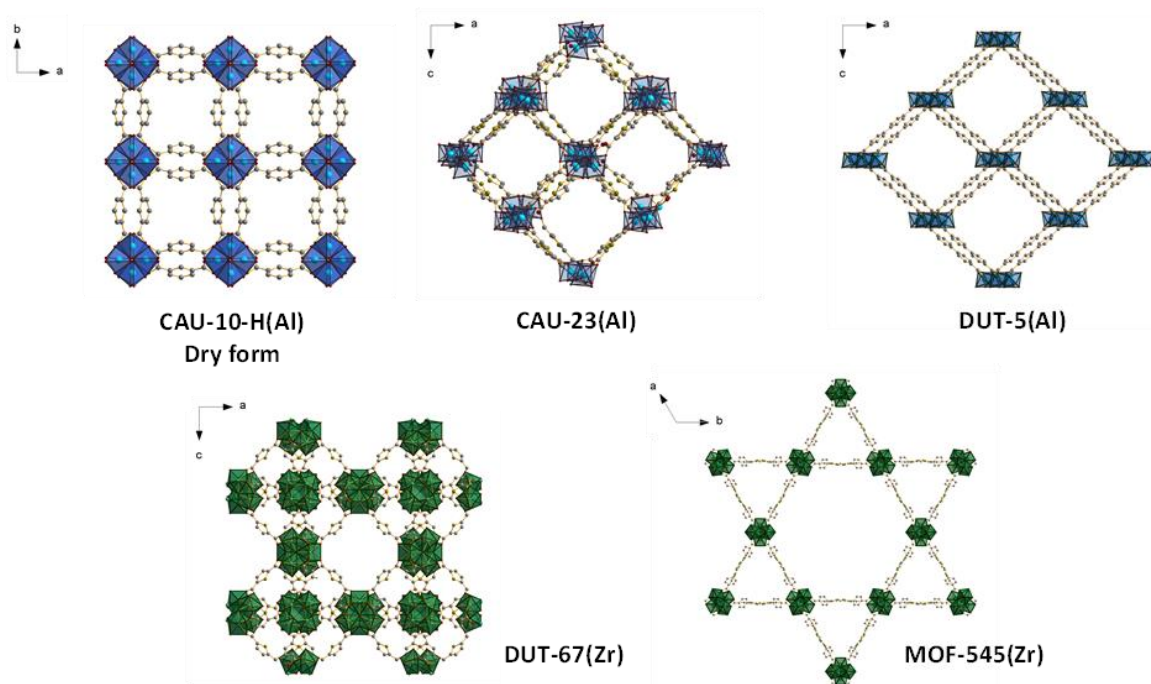


Figure 2-3: Illustration of MOFs studied in this chapter. Blue polyhedra represent $\{AlO_6\}$ octahedra, while green polyhedra represent $\{Zr_6O\}$ polyhedra. Light green, yellow, light blue, green, grey, and red atoms present N, S, Al, Zr, C, and O atoms, respectively. Bonds between atoms are in light orange. Graphics were produced by software Diamond from cif-files with CCDC code 1454067 for (CAU-10-H(Al)), 1878820 for (CAU-23(Al)), 691979 for (DUT-5(Al)), 902898 for (DUT-67(Zr)), and 893545 for (MOF-545(Zr)).

2.2.2. Preparation strategy of MOF/GO composites

Following the selection of the five MOF candidates, the preparation strategy for adding graphene oxide to their synthesis was established. In this project, a trial-and-error approach will be followed where calculated amounts of graphene oxide are added to the different MOFs. These relative amounts of GO were decided based on previous observations of the MIL-69(Al)/GO system.⁵ In fact, it was concluded from the work done by Muschi *et al.* that the GO content in the MOF/GO composite strongly impacts the formation of GO nanoscrolls, that act as structural directing agent for the formation of MIL-69(Al) NWs.⁵ For instance, it was observed that MIL-69(Al)/GO NWs are only formed with a GO content between 20-30 wt.% at which GO Archimedean nanoscrolls with a diameter of 70-100 nm are formed (**Figure 2-4**).⁵ Note that the width of the final MIL-69(Al) NWs is also close to 70 nm, thereby

suggesting the role of GO nanoscrolls as structural directing agent of the MOF. Therefore, it was critical to control the GO content in our synthesis.

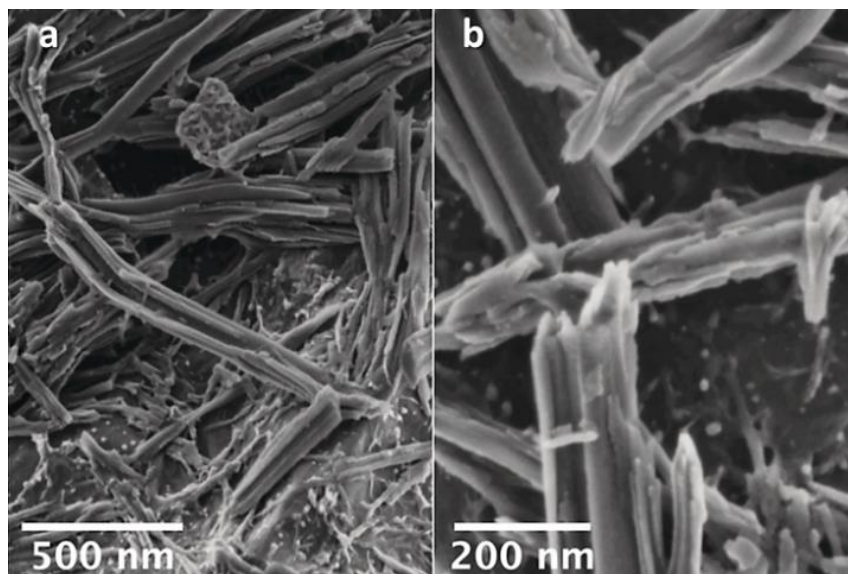


Figure 2-4: SEM of MIL-69/GO showing the formation of Archimedean nanoscrolls.⁵

In the mentioned publication, the GO content in the MIL-69(Al)/GO composite was controlled through an Al/GO ratio calculated from the mass of $\text{Al}(\text{NO}_3)_3 \cdot 9\text{H}_2\text{O}$ precursor used in the synthesis.⁵ (Eq. 2-1) below was used, and it was concluded that following an Al/GO ratio between 4.5 and 9 will yield the desired results.

$$r \left(\frac{\text{Al}}{\text{GO}} \right) = \frac{\text{mass of metal precursor}}{\text{mass of GO}} = 4.5 - 9 \quad \text{(Equation 2-1)}$$

Nevertheless, this approach cannot be followed to control the GO content of the different MOFs selected in this PhD project. The five selected MOFs have different metal precursors (Al, Zr). In addition, shifting towards calculations based on molar ratios is not possible as graphene oxide is a non-stoichiometric compound, and it has no specific molecular weight. Hence, we recalculated the ratios obtained in case of MIL-69(Al) while considering only the metal (no counter ions or water molecules were taken into consideration). Initially, 2.25 g (6 mmol) of $\text{Al}(\text{NO}_3)_3 \cdot 9\text{H}_2\text{O}$ and 8.34 g of GO slurry (3 wt.% in water) were used for the synthesis of MIL-69(Al)/GO NWs.

Hence, based on these values, the $r(\text{Al}/\text{GO})$ followed in the MIL-69(Al)/GO project can be recalculated as follows:

$$m_{\text{Al}} = n_{\text{Al}(\text{NO}_3)_3 \cdot 9\text{H}_2\text{O}} \times \text{MW}_{\text{Al}} = (6 \times 10^{-3}) \times 27 = 0.162 \quad \text{(Equation 2-2)}$$

$$r \left(\frac{\text{Al}}{\text{GO}} \right) = \frac{m_{\text{Al}}}{m_{\text{GO}}} = \frac{0.162}{0.03 \times 8.34} = 0.65 \quad \text{(Equation 2-3)}$$

Concerning the Zr MOFs selected, the same approach was followed. However, as the molecular weight of Zr is almost 3.38 times higher than that of Al ($\text{MW}_{\text{Zr}} = 91$, $\text{MW}_{\text{Al}} = 27$ g/mol), the previously calculated r value for Al-based MOFs was multiplied by this factor:

$$r \left(\frac{\text{Zr}}{\text{GO}} \right) = \frac{m_{\text{Zr}}}{m_{\text{GO}}} = 0.65 \times 3.38 = 2.19 \quad \text{(Equation 2-4)}$$

Therefore, in this PhD project, to monitor the GO content in the desired MOF based composites, the amount of GO (2.5 wt.% in water) that will be added to the synthesis was calculated in such a way that yields a metal/GO ratio of around 0.6-0.7 and 2-2.2 for Al- and Zr-based MOFs, respectively. In the next part of the chapter, these calculations will be used as a starting point for the design of the different MOF/GO composites.

2.3 SCREENING OF SELECTED MOF CANDIDATES

The screening of the different selected samples will be based on the observed experimental results. Only crystalline MOF/GO composites that consist in the presence of crystalline and anisotropic nanostructures inherent of the parent MOF will be considered. Hence, the different synthesis protocols for every MOF/GO composite will be listed in this section. The calculations used to control the GO content in the composite will be stated for each case. It should be mentioned that the same source and batch of GO slurry was used in all syntheses (2.5 wt.% water, Graphenea UK). After listing the synthesis protocols for each MOF and its corresponding composite, their characterization will be presented and discussed. PXRD and FT-IR spectroscopy were employed to verify that each of the selected MOFs is present in its designed composite. Once confirmed, SEM was used to check the presence of elongated nanocrystals. Hence, each characterization section in this part is divided into two parts: structural characterization (PXRD, FT-IR spectroscopy), and morphological one (SEM).

Powder X-ray diffraction (PXRD) patterns were recorded at room temperature (ILV, Versailles) using a Siemens D5000 diffractometer with a $\theta/2\theta$ geometry, and a step length of 0.02° . Measurements were done in different 2θ ranges depending on each sample. Concerning Fourier transform infrared (FT-IR) spectra, they were recorded on a 6700 FT-IR Nicolet spectrophotometer (ILV, Versailles) using the diamond ATR technique. The spectra were recorded on solid compounds and ATR correction was applied. All scanning electron microscopy (SEM) images have been recorded on a JEOL JSM-7001F microscope using gold-coated samples. Studying the change in morphology after the addition of GO to the different MOFs is critical in this project. In fact, microscopic techniques are the sole techniques to study such phenomena. SEM was employed to study the presence/ absence of any structural directing

effect of GO on the MOFs. Concerning the listed figures, the metal polyhedra are presented in blue and green for Al MOFs and Zr MOFs, respectively.

2.3.1. CAU-10-H(Al)

2.3.1.1. Synthesis of pure MOF

CAU-10-H(Al) synthesis was recently reported under reflux.¹⁸ However, the employed reactant amount was extremely high for the later incorporation of a reasonable amount of GO. The reported synthesis employs 7.7g (22.5 mmol) of $(\text{Al}_2\text{SO}_4)_3$ which would require the addition of 75 g of GO later. Hence, it was necessary to scale down the reported reflux synthesis. Yet, the scaling down failed, so another reported synthesis by Reinsch *et al.*¹⁷ under solvothermal conditions was considered and performed under reflux conditions.

Initially, a mixture of 200 mg of isophthalic acid (1,3- H_2BDC) (1.20 mmol), 800 mg of $\text{Al}_2(\text{SO}_4)_3 \cdot 18\text{H}_2\text{O}$ (1.20 mmol), 1 mL of DMF, and 4 mL of H_2O were added into a Teflon-lined steel-autoclave in an oven for 12 h at 135°C .¹⁷ Herein, we were able to upscale the reported synthesis by a factor of 3 using reflux synthesis. The same synthesis protocol was used with few modifications concerning reaction time. Therefore, in a mixture of DMF and water, 3 and 12 mL respectively, 600 mg of 1,3- H_2BDC (3.6 mmol) were dissolved under stirring and sonication at room temperature. Then, 2.4 g of $\text{Al}_2(\text{SO}_4)_3 \cdot 18\text{H}_2\text{O}$ (3.6 mmol) were added to the solution. The homogenous solution was then put under reflux for 24 hours at 140°C . After being cooled, the product was centrifuged and washed twice in 25 mL water, and once in a solution of NaOH (2M, 25 mL water). It was then dried overnight at 100°C .

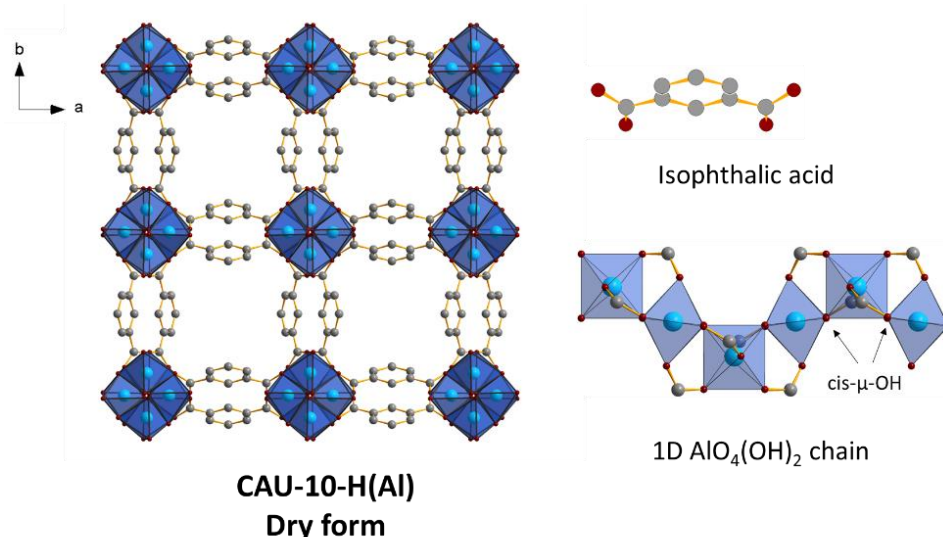


Figure 2-5: The 3D framework structure exhibiting square shaped one-dimensional channels of CAU-10-H(Al) is presented on the left. The organic ligand (bdc), and the inorganic building unit, a fourfold helical chain of cis vertex-sharing AlO₆ polyhedra, are presented on the right. Blue polyhedra represent {AlO₆} octahedra, while light blue, grey and red present Al, C, and O atoms, respectively.

2.3.1.2. Addition of GO to the synthesis

The amount of GO added to the synthesis of CAU-10-H(Al) was calculated based on (eq. 2-3) discussed earlier, hence:

$$m_{\text{Al}} = n_{\text{Al}_2(\text{SO}_4)_3 \cdot 18\text{H}_2\text{O}} \times 2 \times \text{MW}_{\text{Al}} = (3.6 \times 10^{-3}) \times 2 \times 27 = 0.19 \text{ g}$$

$$r \left(\frac{\text{Al}}{\text{GO}} \right) = \frac{m_{\text{Al}}}{m_{\text{GO}}} = \frac{0.19}{0.025 \times m_{\text{GO slurry}}} = 0.65$$

So, the amount of GO slurry added to the synthesis:

$$m_{\text{GO slurry}} = 11.7 \text{ g}$$

Hence, 11.7 g of GO slurry were dissolved in the solvent mixture via stirring and ultra-sonication in a water bath for 3 minutes. 600 mg of 1,3-H₂BDC were then added under stirring at RT for 10 minutes. Once well dissolved, 2.4 g of Al₂(SO₄)₃·18H₂O were added to the solution. The solution was then refluxed for 24 hours at 140°C. After being cooled down to room temperature, it was washed 3 times with 25 mL water and dried overnight at 100°C.

2.3.1.3. Characterization results

As mentioned before, structural characterization techniques were employed first. Hence, CAU-10(Al) and CAU-10(Al)/GO were first characterized by PXRD, and FT-IR spectroscopy. Promising results were obtained. **(Figure 2-6, A)** below shows that the PXRD patterns of the pure CAU-10-H(Al) and CAU-10-H(Al)/GO are both in agreement with the pattern calculated from the crystal structure of CAU-10-H(Al) in literature.²⁶ The MOF is present in the composite, and no loss of crystallinity was observed after the addition of GO. The characteristic Bragg peaks of CAU-10-H(Al) were all observed in the composite. Concerning the FT-IR spectroscopy results, the same coordination environment is present in the pure MOF and the composite. CAU-10-H(Al) and CAU-10-H(Al)/GO both present the characteristic bands of the asymmetric ($\nu_{as}(\text{COO})$) = 1552 cm^{-1} and symmetric ($\nu_s(\text{COO})$) = 1402 cm^{-1} stretching vibrations of the coordinating carboxylate groups.²⁷ Yet, an extra band is present in the case of CAU-10-H(Al)/GO at 1710 cm^{-1} . This band is attributed to the free carboxylic acid of the unreacted 1,3-H₂BDC ligand.

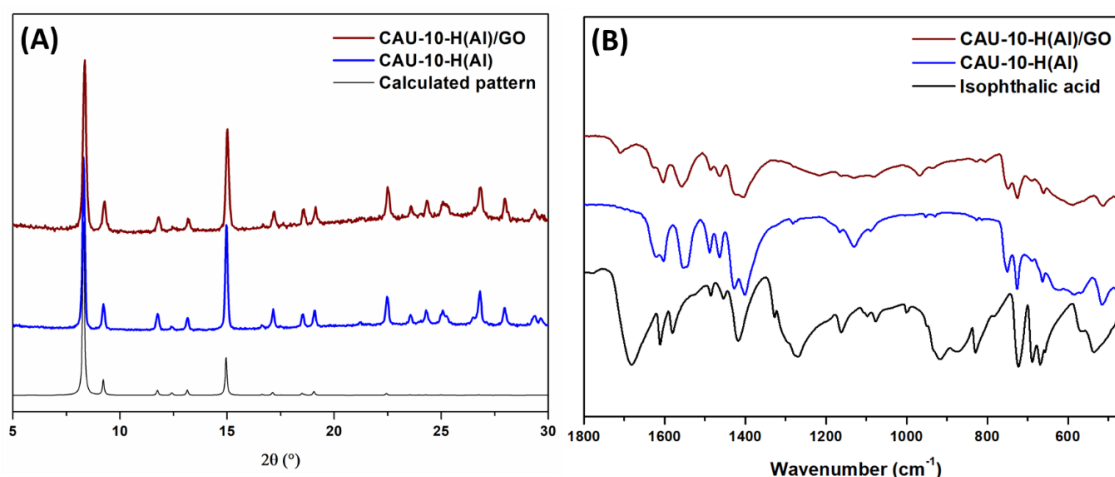


Figure 2-6: (A) PXRD patterns of calculated and synthesized CAU-10-H(Al), and synthesized CAU-10-H(Al)/GO. (B) FT-IR spectra of TDC, CAU-10-H(Al), and CAU-10-H(Al)/GO.

Based on the favorable results obtained by PXRD and FT-IR spectroscopy, CAU-10-H(Al) and CAU-10-H(Al)/GO were further characterized by SEM. CAU-10-H(Al) synthesized under reflux is homogeneous and monodisperse showing MOF particles with a diameter in the range of 240-290 nm **(Figure 2-7, A-B)**. Following

CHAPTER 2: Selection & Screening of MOF Candidates

the addition of GO, it can be shown that the CAU-10-H(Al)/GO is less monodisperse, and it is composed of an assembly of GO sheets and MOF particles with a diameter reaching few micrometers (**Figure 2-7, C-D**). The particle size in case of the composite is hugely polydisperse and several GO aggregated sheets can be observed. In fact, the increase in particle size from less than 300 nm to few micrometers after the addition of GO can be partly explained by the formation of aggregates of GO sheets.

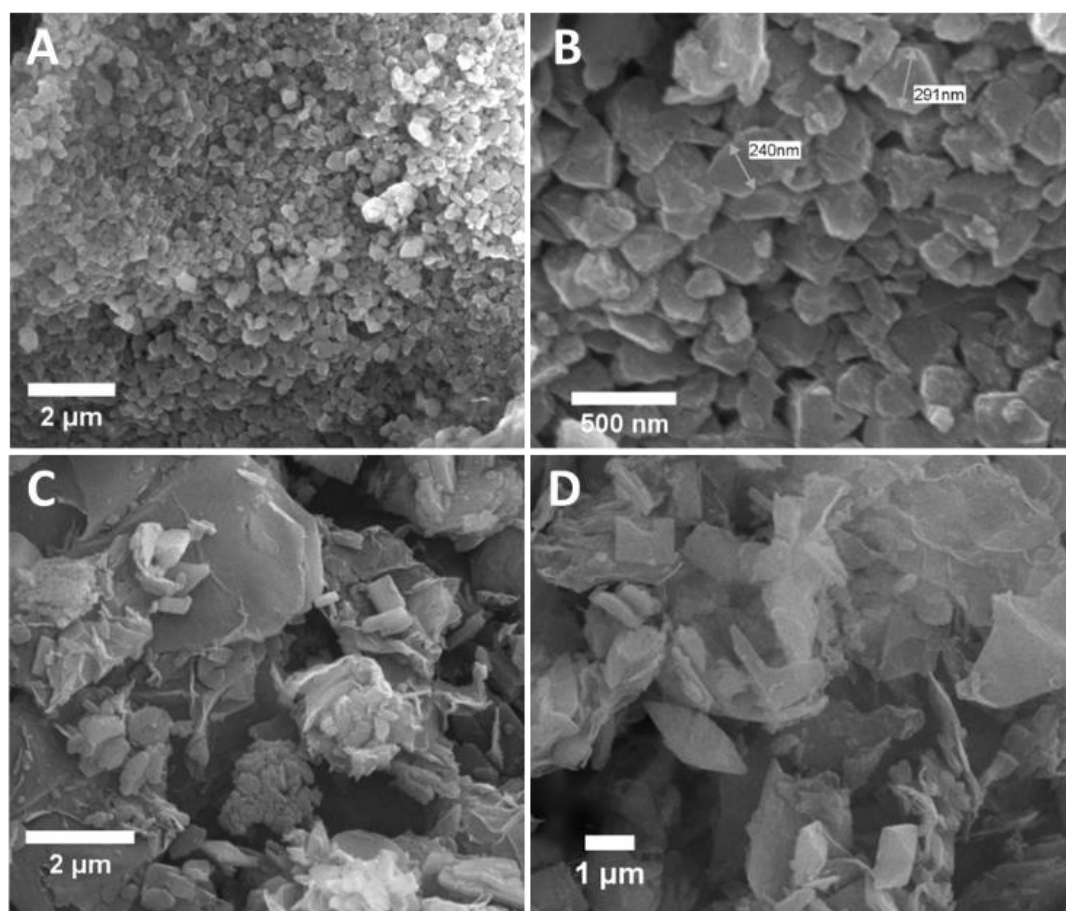


Figure 2-7: SEM images of pure CAU-10-H(Al) (A-B), and CAU-10-H(Al)/GO (C-D).

Thus, despite obtaining the crystalline CAU-10-H(Al) phase in presence of GO, the high heterogeneity of CAU-10-H(Al)/GO composite suggests that much more optimizations would be required in order to obtain the desired results.

2.3.2. CAU-23(Al)

2.3.2.1. Synthesis of pure MOF

Concerning CAU-23(Al), its synthesis was reported by Lenzen *et al.* under reflux.¹⁹ Following the reported protocol, CAU-23(Al) was synthesized using AlCl_3 and NaAlO_2 as metal sources, and sodium thiophen dicarboxylate (Na_2TDC) as a linker. First, 4.3 g (25 mmol) of the commercially available 2,5-thiophenedicarboxylic acid (H_2TDC) was deprotonated through mixing with 2.0 g (50 mmol) sodium hydroxide in 100 mL distilled water. Secondly, two aqueous solutions were prepared. The first one is an 18.75 mL aqueous aluminum chloride AlCl_3 solution (1 mol/L, 18.75 mmol) and the second one is a 12.5 mL aqueous sodium aluminate NaAlO_2 solution (0.5 mol/L, 6.25 mmol). The two solutions were added to the solution of Na_2TDC . The mixture was stirred and put under reflux at 100°C for 6 hours, then it was centrifuged and washed with 200 mL of water under reflux to remove any traces of sodium chloride solution. Finally, it was dried at 100°C for 4 hours.

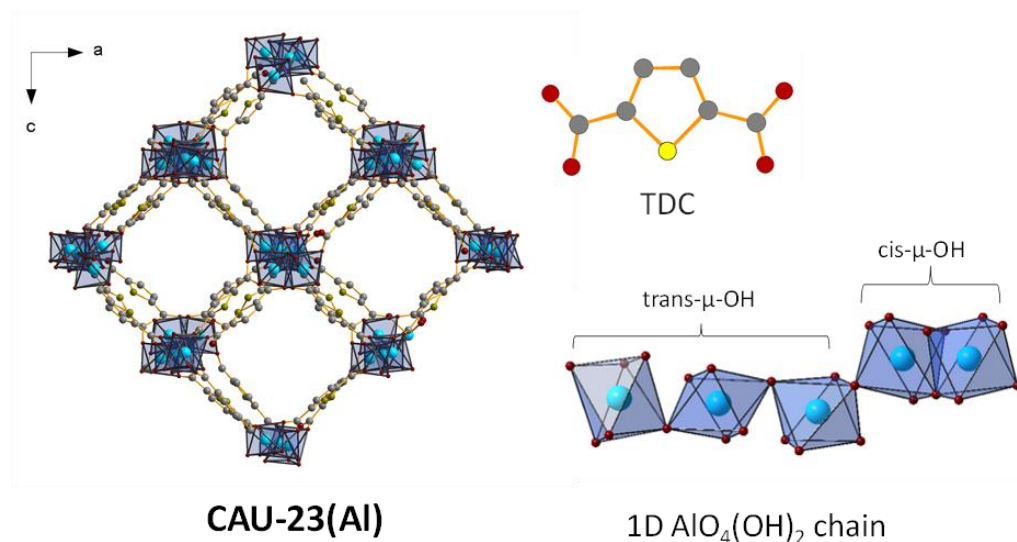


Figure 2-8: The 3D framework structure of CAU-23(Al) exhibiting square shaped one-dimensional channels is presented on the left. The organic ligand (TDC), and the inorganic building unit, a cis and trans corner-sharing AlO_6 polyhedra, are presented on the right. Straight trans and helix cis. Blue polyhedra represent $\{\text{AlO}_6\}$ octahedra, while light blue, yellow, grey, and red present Al, S, C, and O atoms, respectively.

2.3.2.2. Addition of GO to the synthesis

Following the same calculation approach as before would yield 43 g of needed GO slurry as shown in the calculation below. This amount of GO is not feasible; the calculated value was therefore later divided by 10.

$$m_{\text{Al}} = n_{\text{Al}} \times MW_{\text{Al}} = (25 \times 10^{-3}) \times 27 = 0.675$$

$$r \left(\frac{\text{Al}}{\text{GO}} \right) = \frac{m_{\text{Al}}}{m_{\text{GO}}} = \frac{0.675}{0.025 \times m_{\text{GO slurry}}} = 0.65$$

So, the amount of GO slurry that needs to be added to the synthesis:

$$m_{\text{GO slurry}} = 43 \text{ g}$$

Thus, 4.30 g H₂TDC (25 mmol) were mixed with 2.0 g (50 mmol) of sodium hydroxide in 100 mL distilled water until a clear yellow solution of Na₂TDC was obtained. 4.3 g of GO slurry were added, and the solution was stirred and then sonicated for 3 minutes. Then two aqueous solutions of AlCl₃ and NaAlO₂ were prepared as mentioned before. All three solutions are then mixed and stirred under reflux conditions overnight, and then centrifuged, washed in water, then put under reflux in 200 mL of water at 100°C overnight.

2.3.2.3. Characterization results

As observed in **(Figure 2-9, A)**, the PXRD pattern of CAU-23(Al) is in accordance with the calculated one from the CAU-23(Al) crystal structure in literature.¹⁹ Yet, the PXRD patterns of CAU-23(Al) and CAU-23(Al)/GO do not resemble each other. Despite obtaining a crystalline phase, CAU-23(Al)/GO revealed a completely different crystallographic structure. Hence, it can be concluded that CAU-23(Al) is not well identified in the composite, and thus it was not further considered for morphological study by SEM. Besides, it can be assumed that the results obtained herein can be attributed to the huge amounts of GO needed in this synthesis. In addition, the particularity of the present synthesis of CAU-23(Al) based on the

addition of two metal precursors can also explain the difficulty to form CAU-23(Al) in the presence of GO.

Regarding the recorded FT-IR spectra, the same coordination environment is observed for both CAU-23(Al) and CAU-23(Al)/GO (**Figure 2-9, B**). The characteristic bands of the asymmetric ($\nu_{as}(\text{COO})$) = 1605 and 1577 cm^{-1} and symmetric ($\nu_s(\text{COO})$) = 1396 cm^{-1} stretching vibrations of the carboxylate group are present in both samples. Yet, by comparing the FT-IR spectrum of the synthesized Na_2BDC free ligand to that of CAU-23(Al) and CAU-23(Al)/GO, it can be noted that both the MOF and MOF/GO present traces of unreacted BDC ligands. This is shown by the presence of the absorption band at 1690 cm^{-1} that can be assigned to the free carboxylic acid of the unreacted $\text{Na}_2\text{-BDC}$ ligand. A weak band at 1690 cm^{-1} is present in both CAU-23(Al) and CAU-23(Al)/GO.

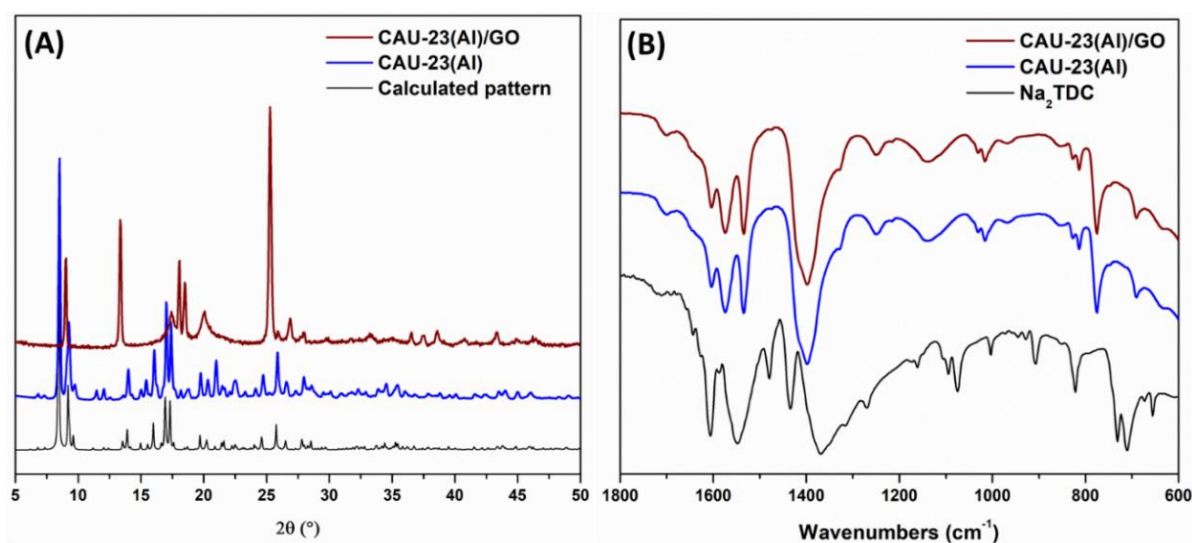


Figure 2-9: (A) PXRD patterns of calculated and synthesized CAU-23(Al), and synthesized CAU-23(Al)/GO. (B) FT-IR spectra of TDC, CAU-23(Al), and CAU-23(Al)/GO.

2.3.3. DUT-5(Al)

2.3.3.1. Synthesis of pure MOF

DUT-5(Al) was first reported by Senkowska *et al.* via a solvothermal approach in 2009.²⁰ Then, 6 years later Gotthardt *et al.* reported a new protocol using reflux and functionalized ligands.²¹ Herein, we followed the protocol reported by Gotthardt *et al.* First, 136 mg (0.54 mmol) of 4,4'-biphenyldicarboxylic acid (bpdc) were dissolved in 20 mL of DMF at 120°C in a round bottom flask under reflux. A change in color from white to colorless was observed after 10 minutes, showing the complete dissolution of the organic linker. Then, 262.6 mg (0.70 mmol) of $\text{Al}(\text{NO}_3)_3 \cdot 9\text{H}_2\text{O}$ were dissolved in 5 mL of DMF and added to the round bottom flask containing the organic linker solution. The solution was put under reflux for 24 hours, where it turned turbid white again after 15-20 minutes. The solution was then collected, centrifuged at a rate of 12500 rpm for 10 minutes, and washed 3 times with ethanol (25 mL). After washing, the produced MOF was then dried at 130°C overnight.

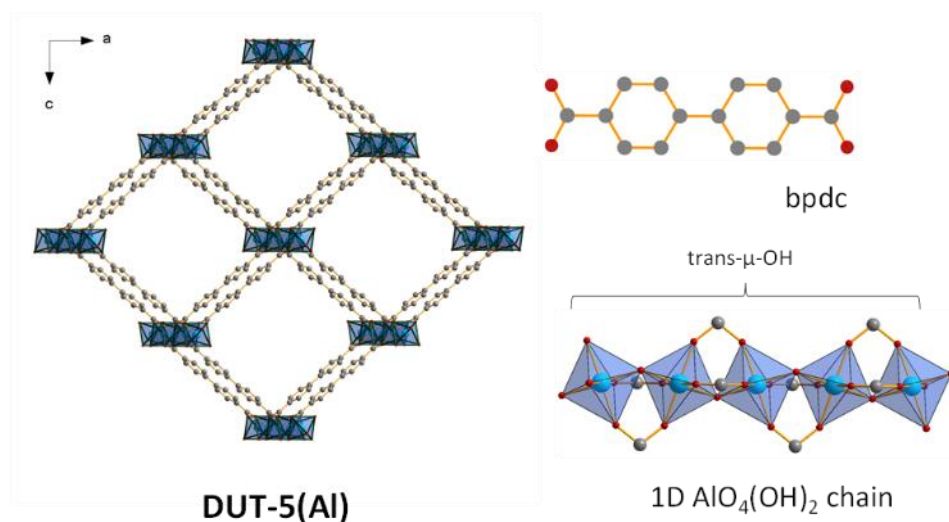


Figure 2-10: The 3D framework structure of DUT-5(Al) exhibiting square shaped one-dimensional channels is presented on the left. The organic ligand (bpdc), and the inorganic building unit, a trans corner-sharing AlO_6 polyhedra, are presented on the right. Blue polyhedra represent $\{\text{AlO}_6\}$ octahedra, while light blue, grey, and red present Al, C, and O atoms, respectively.

2.3.3.2. Addition of GO to the synthesis

The amount of GO added to the synthesis of DUT-5(Al) was calculated as follows:

$$m_{\text{Al}} = n_{\text{Al}(\text{NO}_3)_3 \cdot 9\text{H}_2\text{O}} \times MW_{\text{Al}} = (0.7 \times 10^{-3}) \times 27 = 0.019$$

$$r \left(\frac{\text{Al}}{\text{GO}} \right) = \frac{m_{\text{Al}}}{m_{\text{GO}}} = \frac{0.019}{0.025 \times m_{\text{GO slurry}}} = 0.65$$

So, the amount of GO slurry added to the synthesis: $m_{\text{GO slurry}} = 1.17 \text{ g}$

Hence, 1.17 g of GO slurry was dispersed in a solution of 25 mL DMF. The dispersion was stirred and then sonicated for few minutes. Then, 136 mg (0.54 mmol) of bpdC were added and a change in color from dark black to grey is observed after its dissolution. 262.6 mg of $\text{Al}(\text{NO}_3)_3 \cdot 9\text{H}_2\text{O}$ (0.70 mmol) were then added. The solution was put under reflux for 24 hours and was then collected, centrifuged, and washed 3 times with ethanol (25 mL). The composite was dried at room temperature overnight.

2.3.3.3. Characterization results

For DUT-5(Al), remarkable results were obtained by PXRD (**Figure 2-11, A**). Despite the broadening observed in the characteristic Bragg peaks of the DUT-5(Al) in the composite, the patterns of DUT-5(Al) and DUT-5(Al)/GO are both in agreement with the calculated pattern. The major characteristic Bragg peaks of DUT-5(Al) at 6.01, 12.05, and 14.15° were all observed in the composite. Generally, the broadening of PXRD peaks can arise from two sources, either instrumental or/sample related.^{28,29} Instrumental broadening can arise from technical issues (energy bandwidth, size and divergence of the incoming X-ray beam, detector acceptance, point spread function and resolution, etc.).³⁰ On the other side, the sample contribution could be due to strain and/or crystallite size.^{28,29} Concerning strain related broadening, it is triggered by the presence of strains within a certain volume of a diffracting crystal.^{28,31} These lattice strains can arise from several factors like the anisotropic crystallite shape, dislocations (unexpected change in the

CHAPTER 2: Selection & Screening of MOF Candidates

arrangement of atoms), etc.^{31,32} Concerning size related broadening, Scherrer's equation can be followed:

$$d = \frac{k\lambda}{\beta \cos\theta}$$

where d is the crystallite size of a material, λ is the wavelength of the X-ray; β is the integral breadth of the diffraction peak; θ is the diffraction angle; and k is constant.

The crystallite size and peak width are inversely proportional. Thus, a decrease in the crystallite domain will lead to a broadening in the PXRD peaks.^{28,29} Yet, despite the observed broadening, it can be concluded that the MOF is present in the crystalline composite.

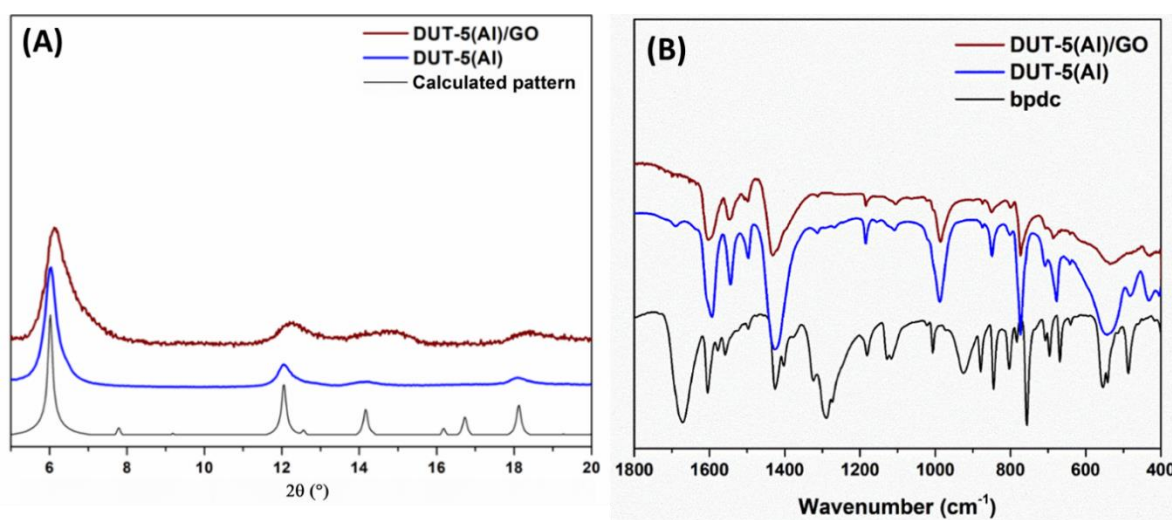


Figure 2-11: (A) PXRD patterns of calculated and synthesized DUT-5(Al), and synthesized DUT-5(Al)/GO. (B) FT-IR spectra of bpdc, DUT-5(Al), and DUT-5(Al)/GO.

On the other side, the recorded FT-IR spectra exclude the presence of residual free unreacted bpdc linker. By comparing the FT-IR spectra of the free bpdc ligand to that of the MOF and MOF/GO, no unreacted ligands were observed. The band at 1670 cm^{-1} corresponding to the free carboxylic acid of unreacted bpdc is absent in both DUT-5(Al) and DUT-5(Al)/GO. Moreover, the FT-IR spectra of both DUT-5(Al) and DUT-5(Al)/GO composite are in accordance. The bands in the range of $1608\text{--}1570\text{ cm}^{-1}$ represent the asymmetric stretching vibrations of the carboxylate group ($\nu_{\text{as}}(\text{C-O})$), while those at 1430 and 1364 cm^{-1} can be ascribed to the symmetric

vibrations ($\nu_s(\text{C-O})$).³³ The bands at 1542 and 775 cm^{-1} correspond to the vibrations of the aromatic C=C and the Al–O, respectively.³⁴ A small band is observed in the case of the pure MOF at 1687 cm^{-1} which is attributed to the presence of traces of DMF in the sample.

From a morphological point of view, the recorded SEM images show that the pure DUT-5(Al) consist in the presence of monodisperse circular disks with a diameter of about 350–450 nm (**Figure 2-12, A-B**). Yet, of interest was the results obtained after the addition of GO to the synthesis. As presented in (**Figure 2-12, C-D**), the addition of GO resulted in the formation of some elongated structures. (**Figure 2-12, C**) clearly shows the formation of a long rod like particles. However, at such stage, it is not possible to know whether these particles correspond to DUT-5(Al), GO nanoscrolls or a mixture of both. On the other hand, (**Figure 2-12, D**) clearly shows the presence of some GO nanoscrolls in the sample. The formed nanoscrolls are marked by a red dashed rectangles. These results are thus very promising since GO nanoscrolls, that are structure directing agents of MOF nanowires, can be formed in the synthesis conditions of DUT-5. Although DUT-5 nanowires were not clearly identified in this preliminary experiment, the GO nanoscrolls and DUT-5 crystals were concomitantly formed and we can thus expect that an optimization of this protocol can be attempted.

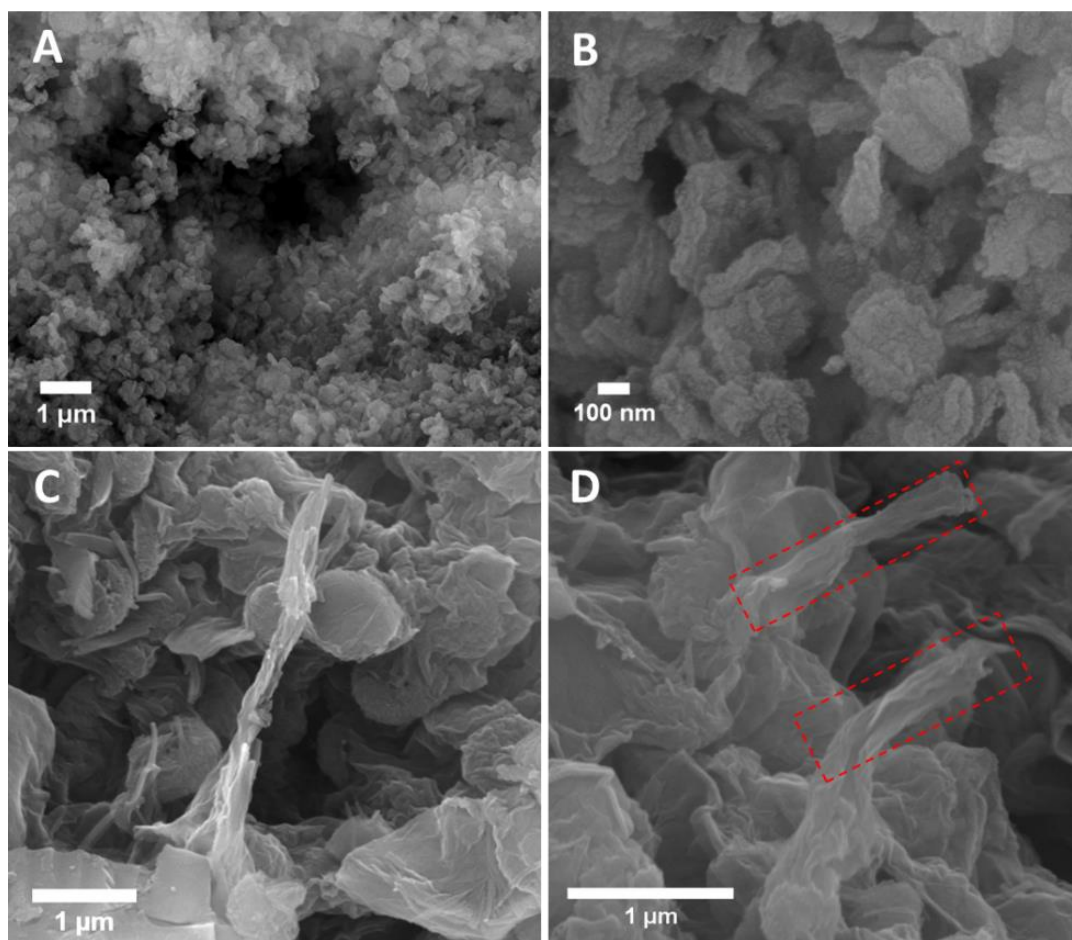


Figure 2-12: SEM images of pure DUT-5(Al) (A-B), and DUT-5(Al)/GO (C-D). The dashed red rectangles present the formation of GO scrolls.

2.3.4. DUT-67(Zr)

2.3.4.1. Synthesis of pure MOF

The synthesis of DUT-67(Zr) was initially reported by Reinsch *et al.* using a microwave assisted synthesis.²³ This MOF was synthesized in a mixture of solvents and has proven to be scalable up to 40 times,²³ therefore it was an interesting candidate to consider. Initially, a mixture of 458 mg H₂TDC (2.66 mmol), 1.288 g ZrOCl₂·8H₂O (4 mmol), water (10 mL), and acetic acid (10 mL) was heated in a microwave at 95°C for 1 h under stirring.²³ Herein, we reproduced the mentioned synthesis protocol under reflux. Hence, in 20 mL solution of water and glacial acetic acid (10 mL each), 458 mg of H₂TDC were dissolved under stirring and heating at 90°C. Then, 1.28 g of ZrOCl₂·8H₂O were added and stirred under heating for 5

minutes. The homogeneous solution was put under reflux for 1 hour. The final product was then centrifuged, washed twice by 15 mL of a sodium acetate solution (0.1 M), and twice with 15 mL of water. Finally, it was dried at 95°C overnight.

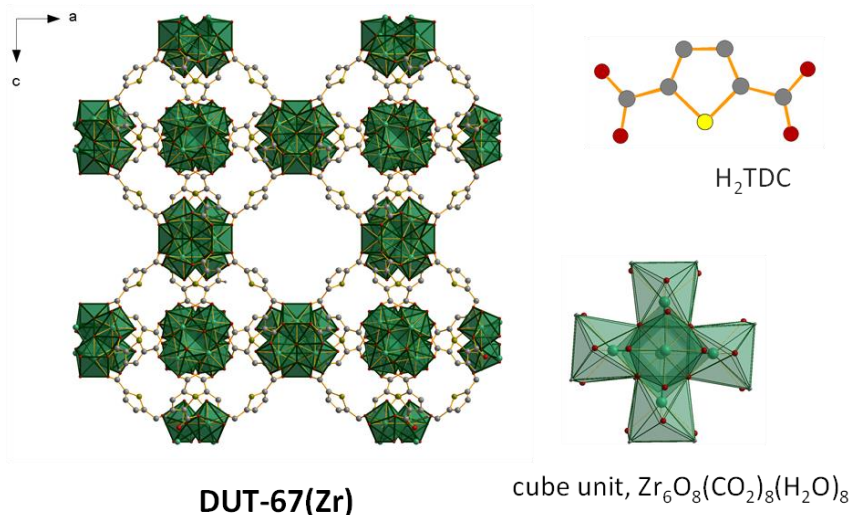


Figure 2-13: DUT-67(Zr) with a view along the channels is presented on the left. The organic building block (TDC) and the inorganic building block, $\{Zr_6O_8\}$ polyhedra are presented on the right. ZrO polyhedra in green, sulfur atoms in yellow, oxygen in red, and carbon in grey.

2.3.4.2. Synthesis of MOF/GO

The amount of GO added to the synthesis of DUT-67(Zr) was calculated as follows:

$$m_{Zr} = n_{ZrOCl_2 \cdot 8H_2O} \times MW_{Zr} = (4 \times 10^{-3}) \times 91 = 0.364$$

$$r \left(\frac{Zr}{GO} \right) = \frac{m_{Zr}}{m_{GO}} = \frac{0.364}{0.025 \times m_{GO \text{ slurry}}} = 2.19$$

So, the amount of GO slurry added to the synthesis: $m_{GO \text{ slurry}} = 6.7 \text{ g}$

Hence, 6.7 g of GO slurry was added to the 20 mL solution of water and acetic acid, stirred, and then sonicated for few minutes. To the GO dispersion, 458 mg of H_2TDC were added and well dissolved. Then, 1.288 g of $ZrOCl_2 \cdot 8H_2O$ were added and stirred at 90°C. The homogeneous solution was then put under reflux for 24 hours. The final product was washed twice by 15 mL of a sodium acetate solution (0.1 M), and twice by 15 mL of water. Finally, it was dried at 100°C overnight.

2.3.4.3. Characterization results

DUT-67(Zr)/GO showed encouraging results once characterized by PXRD and FT-IR spectroscopy. The PXRD patterns of synthesized DUT-67(Zr) and DUT-67(Zr)/GO are in accordance with the calculated PXRD pattern of DUT-67(Zr). No loss in crystallinity or change in peaks positions was seen after the addition of GO. DUT-67(Zr) is present in the composite. The major characteristic Bragg peaks of DUT-67(Zr) at 6.44, 7.87, and 9.09° were all detected in the composite. Concerning the recorded FT-IR spectra, the spectra of DUT-67(Zr) and DUT-67(Zr)/GO are in accordance. The bands at 1577 and 1384 cm^{-1} represent the characteristic asymmetric ($\nu_{\text{as}}(\text{COO})$) and symmetric ($\nu_{\text{s}}(\text{COO})$) stretching vibrations of the carboxylate group, respectively.³⁵ Yet, by comparing the spectrum of free ligand to that of DUT-67(Zr) and DUT-67(Zr)/GO, it can be observed that the free carboxylic acid bands of unreacted TDC at 1660 and 1690 cm^{-1} are present in the MOF but absent in the composite. Thus, some unreacted TDC ligands are present in the case of DUT-67(Zr). One can assume that these bands were absent in case of the DUT-67(Zr)/GO composite as the composite was refluxed for 24 hours while the MOF was only refluxed for 1 hour. So, 1 hour of synthesis under reflux is not enough for all TDC ligands to be coordinated.

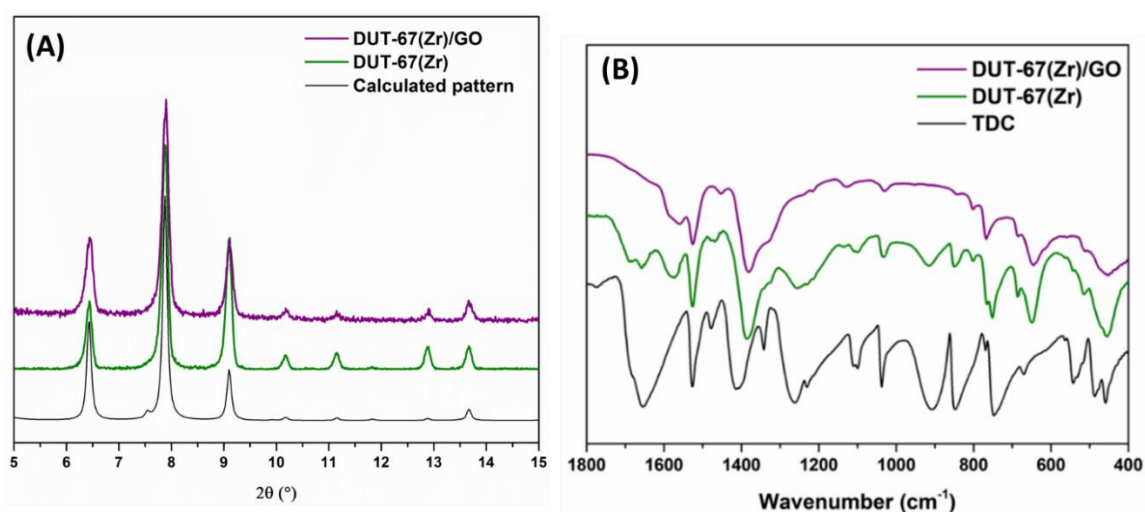


Figure 2-14: (A) PXRD patterns of calculated and synthesized DUT-67(Zr), and synthesized DUT-67(Zr)/GO. (B) FT-IR spectra of 2,5-thiophenedicarboxylic acid (H_2TDC), DUT-67(Zr), and DUT-67(Zr)/GO.

Moreover, despite the successful formation of both DUT-67(Zr) and DUT-67(Zr)/GO under reflux, no structural directing effect of GO on DUT-67(Zr) was observed by SEM. In case of the pure MOF (**Figure 2-15, A-B**), a sample consisting of monodisperse nanoparticles with a diameter ranging from 110 to 160 nm was obtained. After adding GO, the particle size increased by almost 500 nm. This increase can be related to an aggregation phenomenon between the GO layers and MOF particles. The comparison between (**Figure 2-15, A**) and (**Figure 2-15, C**) can clearly show the presence of GO layers covering DUT-67(Zr) particles, along with some aggregates forming in certain parts of the sample as marked by a dashed red rectangle (**Figure 2-15, C**).

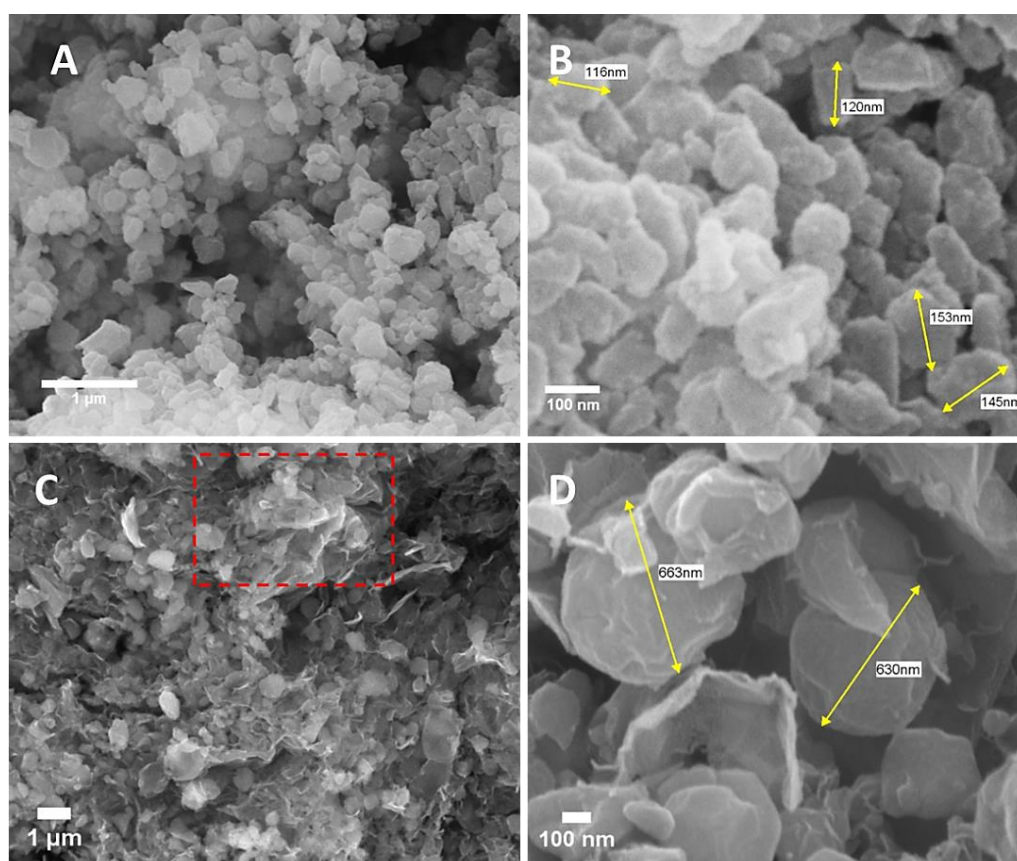


Figure 2-15: SEM images of pure DUT-67(Zr) (A-B), and DUT-67(Zr)/GO (C-D). The dashed red rectangle in C presents the aggregation of GO in certain spots of the sample.

2.3.5. MOF-545(Zr)

2.3.5.1. Synthesis of pure MOF

MOF-545(Zr) was synthesized following a reported protocol by Paille and co-workers under reflux.²⁵ In a round bottom flask, 65 mg of TCPP-H₂ (0.086 mmol) and 325 mg of ZrOCl₂·8H₂O (1.0 mmol) were mixed in 80 mL of DMF. Once dissolved, 2.5 mL of dichloroacetic acid were added, and the solution turned green. The mixture was then put under reflux for 15 hours and allowed to cool down at room temperature. After centrifugation, the sample was washed under reflux in a mixture of 25 mL DMF and 2.5 mL of 1 M HCl for 2 hours. The sample was centrifugated, washed with DMF and acetone, then soaked in acetone overnight. Finally, the sample was collected, washed with acetone and diethyl ether, and dried overnight at 90°C.

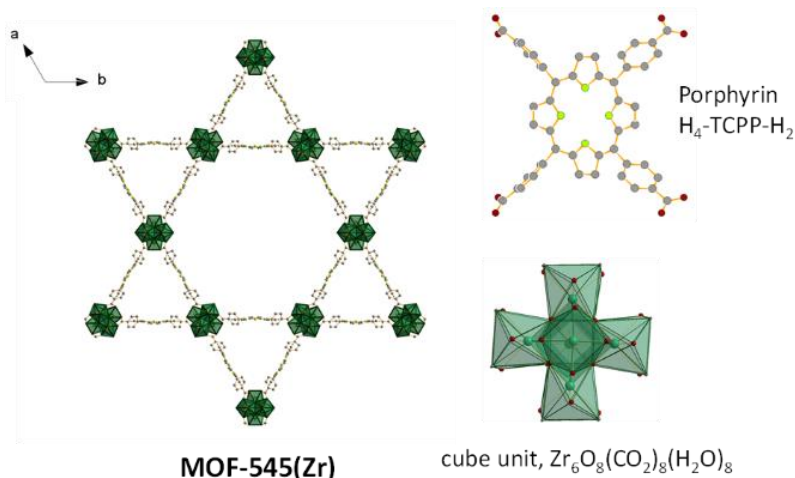


Figure 2-16: MOF-545(Zr) with view along the channels is presented on the left. The organic building block (porphyrin) and the inorganic building block, cube unit, $Zr_6O_8(CO_2)_8(H_2O)_8$ are presented on the right. ZrO polyhedra in green, oxygen atoms in red and C atoms in grey.

2.3.5.2. Synthesis of MOF/GO

The amount of GO added to the synthesis of MOF-545(Zr) was calculated:

$$m_{Zr} = n_{ZrOCl_2 \cdot 8H_2O} \times MW_{Zr} = (1 \times 10^{-3}) \times 91 = 0.091$$

$$r \left(\frac{Zr}{GO} \right) = \frac{m_{Zr}}{m_{GO}} = \frac{0.091}{0.025 \times m_{GO \text{ slurry}}} = 2.19$$

So, the amount of GO slurry added to the synthesis: $m_{GO \text{ slurry}} = 1.66 \text{ g}$

In a round bottom flask, 65 mg of TCPP-H₂ (0.086 mmol) and 325 mg of ZrOCl₂·8H₂O (1.0 mmol) were well mixed in 80 mL of DMF. Once well dissolved, 2.5 mL of dichloroacetic acid were added, the solution turned green. 1.66 g of GO slurry was added to the solution, stirred, and then sonicated for 3 min. The mixture was then put under reflux overnight at 130°C and allowed to cool down at room temperature. After centrifugation, the sample was washed under reflux in a mixture of 25 mL DMF and 2.5 mL of 1M HCl for 2hrs. The sample was centrifugated again, washed with DMF and acetone, then soaked in acetone overnight. The sample was then collected, washed with acetone and diethyl ether, and dried overnight at 90°C.

2.3.5.3. Characterization results

As observed below, the PXRD pattern of synthesized MOF-545(Zr) is in agreement with the calculated one. However, following the addition of GO, a completely amorphous structure was obtained (**Figure 2-17, A**). Concerning FT-IR spectroscopy, the same coordination environment was present in MOF-545(Zr) and MOF-545(Zr)/GO. Both samples present the characteristic bands of the porphyrin-based MOF.³⁶ The C=C and C-N stretching vibrations are presented at 1580 and 1370 cm⁻¹, while the N-H and C-H bending vibrations are presented at 970 and 860 cm⁻¹ respectively (**Figure 2-17, B**). However, based on the results obtained by PXRD, MOF-545(Zr) was not considered for further study by SEM.

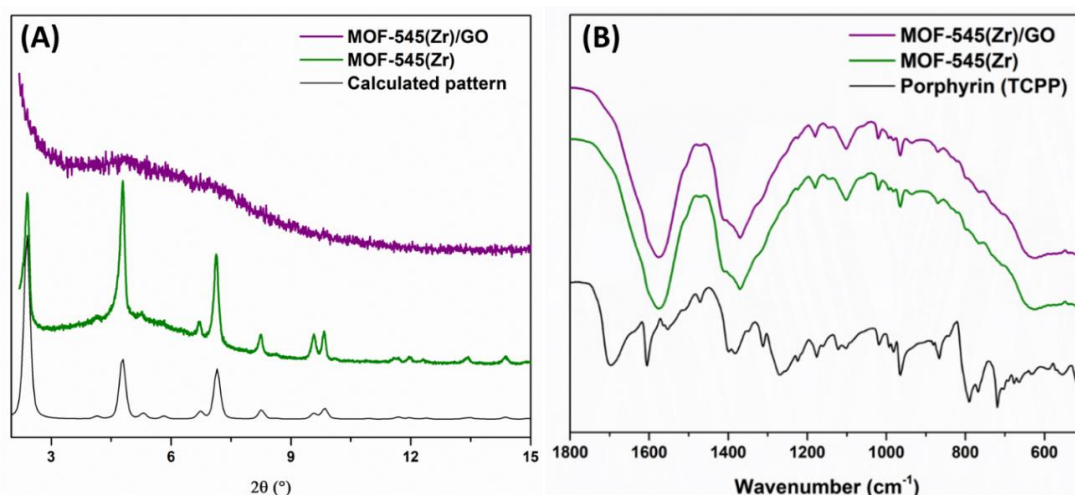


Figure 2-17: (A) PXRD patterns of calculated and synthesized MOF-545(Zr), and synthesized MOF-545(Zr)/GO. (B) FT-IR spectra of porphyrin (TCPP), MOF-545(Zr), and MOF-545(Zr)/GO.

2.4 SCREENING CONCLUSIONS AND SELECTED CANDIDATE

Based on the work previously done on MIL-69(Al)/GO, five MOFs were selected and tested for controlling their morphology using GO as a structural directing agent. These MOFs are CAU-10-H(Al), CAU-23(Al), DUT-5(Al), DUT-67(Zr), and MOF-545(Zr). First, it should be mentioned that all the five MOFs were successfully synthesized under reflux according to the reported and modified protocols discussed in the previous sections. As shown by the respective PXRD patterns, all the calculated and synthesized MOF patterns are in agreement. In addition, the recorded FT-IR spectra of the synthesized MOFs are consistent with the reported ones in literature. In most cases, they showed negligible, or completely absent, traces of unreacted ligands or remaining solvents. Yet, as no thermogravimetric analysis (TGA) and N₂ physisorption analysis was performed nor provided in this chapter, it is not possible to comment on the purity of the formed MOFs. Concerning the composites, CAU-23(Al)/GO and MOF-545(Zr) were excluded as the PXRD patterns of the composites did not present the characteristic Bragg peaks of the parent MOFs. However, it should be mentioned that only one metal/GO ratio was tested for the two MOFs, it is possible that different results could be obtained using other ratios. This was not further tested during this PhD as the aim here was to screen the selected candidates based on primary results. On the other side, CAU-10-H(Al)/GO, DUT-5(Al)/GO, and DUT-67(Zr)/GO all presented promising results when characterized by PXRD and FT-IR spectroscopy. Thus far, once characterized by scanning electron microscopy, DUT-5(Al)/GO was the only sample to present some favorable results. The addition of GO to DUT-5(Al) led to the formation of some elongated particles (i.e., GO nanoscrolls, elongated rod like particles) that were not observed in the case of the pure MOF.

The results obtained in the case of DUT-5(Al)/GO are of vast interest. Such results can help further understand, and extend, the concept of using GO as a structural

directing agent of MOFs which was previously applied to MIL-69(Al). Nevertheless, the synthesized composite is not monodispersed and homogeneous material. Particles of different size and morphology were present in the recorded SEM images. In addition, the employed characterization techniques were not sufficient to further verify the role of GO in this shaping process. Hence, based on the listed results, the next chapter will cover the synthesis optimization and the employment of added characterization techniques.

2.5 REFERENCES

- (1) Saad, A.; Biswas, S.; Gkaniatsou, E.; Sicard, C.; Dumas, E.; Menguy, N.; Steunou, N. Metal–Organic Framework Based 1D Nanostructures and Their Superstructures: Synthesis, Microstructure, and Properties. *Chem. Mater.* **2021**, *33* (15), 5825–5849. <https://doi.org/10.1021/acs.chemmater.1c01034>.
- (2) Safaei, M.; Foroughi, M. M.; Ebrahimipoor, N.; Jahani, S.; Omid, A.; Khatami, M. A Review on Metal–Organic Frameworks: Synthesis and Applications. *TrAC Trends in Analytical Chemistry* **2019**, *118*, 401–425. <https://doi.org/10.1016/j.trac.2019.06.007>.
- (3) Li, Y.; Wen, G.; Li, J.; Li, Q.; Zhang, H.; Tao, B.; Zhang, J. Synthesis and Shaping of Metal–Organic Frameworks: A Review. *Chem. Commun.* **2022**, *58* (82), 11488–11506. <https://doi.org/10.1039/D2CC04190A>.
- (4) Feng, L.; Wang, K.-Y.; Powell, J.; Zhou, H.-C. Controllable Synthesis of Metal–Organic Frameworks and Their Hierarchical Assemblies. *Matter* **2019**, *1* (4), 801–824. <https://doi.org/10.1016/j.matt.2019.08.022>.
- (5) Muschi, M.; Lalitha, A.; Sene, S.; Aureau, D.; Fregnaux, M.; Esteve, I.; Rivier, L.; Ramsahye, N.; Devautour-Vinot, S.; Sicard, C.; Menguy, N.; Serre, C.; Maurin, G.; Steunou, N. Formation of a Single-Crystal Aluminum-Based MOF Nanowire with Graphene Oxide Nanoscrolls as Structure-Directing Agents. *Angew. Chem. Int. Ed.* **2020**, *59* (26), 10353–10358. <https://doi.org/10.1002/ange.202000795>.
- (3) Loiseau, T.; Mellot-Draznieks, C.; Muguerra, H.; Férey, G.; Haouas, M.; Taulelle, F. Hydrothermal Synthesis and Crystal Structure of a New Three-Dimensional Aluminum–Organic Framework MIL-69 with 2,6-Naphthalenedicarboxylate (Ndc), Al(OH)(Ndc)·H₂O. *C. R. Chim.* **2005**, *8* (3), 765–772. <https://doi.org/10.1016/j.crci.2004.10.011>.
- (7) Devic, T.; Serre, C. High Valence 3p and Transition Metal Based MOFs. *Chemical Society Reviews* **2014**, *43* (16), 6097–6115. <https://doi.org/10.1039/C4CS00081A>.
- (8) Yang, D.; Gates, B. C. Elucidating and Tuning Catalytic Sites on Zirconium- and Aluminum-Containing Nodes of Stable Metal–Organic Frameworks. *Acc. Chem. Res.* **2021**, *54* (8), 1982–1991. <https://doi.org/10.1021/acs.accounts.1c00029>.

CHAPTER 2: Selection & Screening of MOF Candidates

- (9) Hoffmann, H. C.; Debowski, M.; Müller, P.; Paasch, S.; Senkovska, I.; Kaskel, S.; Brunner, E. Solid-State NMR Spectroscopy of Metal–Organic Framework Compounds (MOFs). *Materials (Basel)* **2012**, *5* (12), 2537–2572. <https://doi.org/10.3390/ma5122537>.
- (10) Feng, L.; Yuan, S.; Zhang, L.-L.; Tan, K.; Li, J.-L.; Kirchon, A.; Liu, L.-M.; Zhang, P.; Han, Y.; Chabal, Y. J.; Zhou, H.-C. Creating Hierarchical Pores by Controlled Linker Thermolysis in Multivariate Metal–Organic Frameworks. *J. Am. Chem. Soc.* **2018**, *140* (6), 2363–2372. <https://doi.org/10.1021/jacs.7b12916>.
- (11) Brandt, P.; Xing, S.-H.; Liang, J.; Kurt, G.; Nuhnen, A.; Weingart, O.; Janiak, C. Zirconium and Aluminum MOFs for Low-Pressure SO₂ Adsorption and Potential Separation: Elucidating the Effect of Small Pores and NH₂ Groups. *ACS Appl. Mater. Interfaces* **2021**, *13* (24), 29137–29149. <https://doi.org/10.1021/acsami.1c06003>.
- (12) Mogale, R.; Akpomie, K. G.; Conradie, J.; Langner, E. H. G. Dye Adsorption of Aluminium- and Zirconium-Based Metal Organic Frameworks with Azobenzene Dicarboxylate Linkers. *Journal of Environmental Management* **2022**, *304*, 114166. <https://doi.org/10.1016/j.jenvman.2021.114166>.
- (13) Barman, B. K.; Nanda, K. K. Ultrafast-Versatile-Domestic-Microwave-Oven Based Graphene Oxide Reactor for the Synthesis of Highly Efficient Graphene Based Hybrid Electrocatalysts. *ACS Sustainable Chem. Eng.* **2018**, *6* (3), 4037–4045. <https://doi.org/10.1021/acssuschemeng.7b04398>.
- (14) Tang, B.; Xiong, Z.; Yun, X.; Wang, X. Rolling up Graphene Oxide Sheets through Solvent-Induced Self-Assembly in Dispersions. *Nanoscale* **2018**, *10* (8), 4113–4122. <https://doi.org/10.1039/C7NR08415C>.
- (15) Tang, B.; Yun, X.; Xiong, Z.; Wang, X. Formation of Graphene Oxide Nanoscrolls in Organic Solvents: Toward Scalable Device Fabrication. *ACS Appl. Nano Mater.* **2018**, *1* (2), 686–697. <https://doi.org/10.1021/acsanm.7b00160>.
- (16) Tang, B.; Gao, E.; Xiong, Z.; Dang, B.; Xu, Z.; Wang, X. Transition of Graphene Oxide from Nanomembrane to Nanoscroll Mediated by Organic Solvent in Dispersion. *Chem. Mater.* **2018**, *30* (17), 5951–5960. <https://doi.org/10.1021/acs.chemmater.8b02083>.
- (17) Reinsch, H.; van der Veen, M. A.; Gil, B.; Marszalek, B.; Verbiest, T.; de Vos, D.; Stock, N. Structures, Sorption Characteristics, and Nonlinear Optical Properties of a New Series of Highly Stable Aluminum MOFs. *Chem. Mater.* **2013**, *25* (1), 17–26. <https://doi.org/10.1021/cm3025445>.
- (18) Lenzen, D.; Bendix, P.; Reinsch, H.; Fröhlich, D.; Kummer, H.; Möllers, M.; Hügenell, P. P. C.; Gläser, R.; Henninger, S.; Stock, N. Scalable Green Synthesis and Full-Scale Test of the Metal–Organic Framework CAU-10-H for Use in Adsorption-Driven Chillers. *Advanced Materials* **2018**, *30* (6), 1705869. <https://doi.org/10.1002/adma.201705869>.
- (19) Lenzen, D.; Zhao, J.; Ernst, S.-J.; Wahiduzzaman, M.; Ken Inge, A.; Fröhlich, D.; Xu, H.; Bart, H.-J.; Janiak, C.; Henninger, S.; Maurin, G.; Zou, X.; Stock, N. A Metal–Organic Framework for Efficient Water-Based Ultra-Low-Temperature-Driven Cooling. *Nat Commun* **2019**, *10* (1), 3025. <https://doi.org/10.1038/s41467-019-10960-0>.

- (20) Senkovska, I.; Hoffmann, F.; Fröba, M.; Getzschmann, J.; Böhlmann, W.; Kaskel, S. New Highly Porous Aluminium Based Metal–Organic Frameworks: Al(OH)(Ndc) (Ndc=2,6-Naphthalene Dicarboxylate) and Al(OH)(Bpdc) (Bpdc=4,4'-Biphenyl Dicarboxylate). *Microporous and Mesoporous Materials* **2009**, *122* (1), 93–98. <https://doi.org/10.1016/j.micromeso.2009.02.020>.
- (21) Gotthardt, M. A.; Grosjean, S.; Brunner, T. S.; Kotzel, J.; Gänzler, A. M.; Wolf, S.; Bräse, S.; Kleist, W. Synthesis and Post-Synthetic Modification of Amine-, Alkyne-, Azide- and Nitro-Functionalized Metal–Organic Frameworks Based on DUT-5. *Dalton Trans.* **2015**, *44* (38), 16802–16809. <https://doi.org/10.1039/C5DT02276B>.
- (22) Bon, V.; Senkovska, I.; Baburin, I. A.; Kaskel, S. Zr- and Hf-Based Metal–Organic Frameworks: Tracking Down the Polymorphism. *Crystal Growth & Design* **2013**, *13* (3), 1231–1237. <https://doi.org/10.1021/cg301691d>.
- (23) Reinsch, H.; Waitschat, S.; Chavan, S. M.; Lillerud, K. P.; Stock, N. A Facile “Green” Route for Scalable Batch Production and Continuous Synthesis of Zirconium MOFs. *European Journal of Inorganic Chemistry* **2016**, *2016* (27), 4490–4498. <https://doi.org/10.1002/ejic.201600295>.
- (24) Morris, W.; Voloskiy, B.; Demir, S.; Gándara, F.; McGrier, P. L.; Furukawa, H.; Cascio, D.; Stoddart, J. F.; Yaghi, O. M. Synthesis, Structure, and Metalation of Two New Highly Porous Zirconium Metal–Organic Frameworks. *Inorg. Chem.* **2012**, *51* (12), 6443–6445. <https://doi.org/10.1021/ic300825s>.
- (25) Paille, G.; Gomez-Mingot, M.; Roch-Marchal, C.; Lassalle-Kaiser, B.; Mialane, P.; Fontecave, M.; Mellot-Draznieks, C.; Dolbecq, A. A Fully Noble Metal-Free Photosystem Based on Cobalt-Polyoxometalates Immobilized in a Porphyrinic Metal–Organic Framework for Water Oxidation. *J. Am. Chem. Soc.* **2018**, *140* (10), 3613–3618. <https://doi.org/10.1021/jacs.7b11788>.
- (26) Fröhlich, D.; Pantatosaki, E.; Kolokathis, P. D.; Markey, K.; Reinsch, H.; Baumgartner, M.; Veen, M. A. van der; Vos, D. E. D.; Stock, N.; Papadopoulos, G. K.; Henninger, S. K.; Janiak, C. Water Adsorption Behaviour of CAU-10-H: A Thorough Investigation of Its Structure–Property Relationships. *J. Mater. Chem. A* **2016**, *4* (30), 11859–11869. <https://doi.org/10.1039/C6TA01757F>.
- (27) Solovyeva, M. V.; Shkatulov, A. I.; Gordeeva, L. G.; Fedorova, E. A.; Krieger, T. A.; Aristov, Y. I. Water Vapor Adsorption on CAU-10- X: Effect of Functional Groups on Adsorption Equilibrium and Mechanisms. *Langmuir* **2021**, *37* (2), 693–702. <https://doi.org/10.1021/acs.langmuir.0c02729>.
- (28) Holder, C. F.; Schaak, R. E. Tutorial on Powder X-Ray Diffraction for Characterizing Nanoscale Materials. *ACS Nano* **2019**, *13* (7), 7359–7365. <https://doi.org/10.1021/acsnano.9b05157>.
- (29) Saleh, T. A. Chapter 7 - Structural Characterization of Hybrid Materials. In *Polymer Hybrid Materials and Nanocomposites*; Saleh, T. A., Ed.; Plastics Design Library; William Andrew Publishing, 2021; pp 213–240. <https://doi.org/10.1016/B978-0-12-813294-4.00005-4>.
- (30) Guinebretière, R.; Boule, A.; Masson, O.; Dauger, A. Instrumental Aspects in X-Ray Diffraction on Polycrystalline Materials. *Powder Diffraction* **2005**, *20* (4), 294–305. <https://doi.org/10.1154/1.2136890>.

CHAPTER 2: Selection & Screening of MOF Candidates

- (31) Koker, M. K. A.; Welzel, U.; Mittemeijer, E. J. Measurement of X-Ray Diffraction-Line Broadening Induced by Elastic Mechanical Grain Interaction. *J Appl Crystallogr* **2014**, *47* (1), 391–401. <https://doi.org/10.1107/S1600576713032202>.
- (32) Muhammed Shafi, P.; Chandra Bose, A. Impact of Crystalline Defects and Size on X-Ray Line Broadening: A Phenomenological Approach for Tetragonal SnO₂ Nanocrystals. *AIP Advances* **2015**, *5* (5), 057137. <https://doi.org/10.1063/1.4921452>.
- (33) Kurisingal, J. F.; Li, Y.; Sagynbayeva, Y.; Chitumalla, R. K.; Vuppala, S.; Rachuri, Y.; Gu, Y.; Jang, J.; Park, D.-W. Porous Aluminum-Based DUT Metal-Organic Frameworks for the Transformation of CO₂ into Cyclic Carbonates: A Computationally Supported Study. *Catalysis Today* **2020**, *352*, 227–236. <https://doi.org/10.1016/j.cattod.2019.12.038>.
- (34) Zhou, Y.; Li, J.; Zhang, J.; Chen, Y.; Yao, T.; Chen, A.; Xiang, M.; Chen, Z.; Wu, Z. Dye Promoted Electron Transfer in DUT-5/BiVO₄ Heterojunction for Organic Pollutants Degradation. *Materials Research Bulletin* **2022**, *150*, 111740. <https://doi.org/10.1016/j.materresbull.2022.111740>.
- (35) Liu, H.-X.; Liu, T.-T.; Huang, T.; Fang, Z.-B.; Li, L.; Yin, Q.; Cao, R.; Gong, X.-Q.; Liu, T.-F. Trace of Molecular Doping in Metal–Organic Frameworks: Drastic Change in the Electronic Band Structure with a Preserved Topology and Porosity. *J. Mater. Chem. A* **2020**, *8* (25), 12370–12377. <https://doi.org/10.1039/D0TA03905E>.
- (36) Yu, K.; Won, D.-I.; Lee, W. I.; Ahn, W.-S. Porphyrinic Zirconium Metal-Organic Frameworks: Synthesis and Applications for Adsorption/Catalysis. *Korean J. Chem. Eng.* **2021**, *38* (4), 653–673. <https://doi.org/10.1007/s11814-020-0730-z>.



CHAPTER 3: DUT-5(AI) and DUT-5(AI)/GO

TABLE OF CONTENTS

3.1 INTRODUCTION	120
3.2 DUT-5(Al) IN THE STATE OF THE ART	123
3.3 SYNTHESIS OPTIMIZATION OF DUT-5(Al).....	125
3.3.1. Reported synthesis of DUT-5(Al) under reflux.....	125
3.3.2. Optimization of the reported synthesis	127
3.3.2.1. Optimization approach	127
3.3.2.2. Characterization of the optimized sample	129
3.3.2.3. Kinetic study on the optimized sample	133
3.4 SYNTHESIS OPTIMIZATION OF DUT-5(Al)/GO	137
3.4.1. Synthesis of DUT-5(Al)/GO with different molar ratios.....	137
3.4.2. Optimization of DUT-5(Al)/GO synthesis.....	143
3.4.2.1. Addition of water to the synthesis.....	143
3.4.2.2. Optimization of reactants concentration	146
3.4.2.3. Tuning the reaction time.....	148
3.4.2.4. Studying the MOF content inside DUT-5(Al)/GO-336.....	154
3.4.2.5. Studying the adsorption properties of DUT-5(Al)/GO-336	160
3.5 EXPLORING THE EFFECT OF GO ADDITION.....	161
3.5.1. Effect of GO on reaction kinetics.....	162
3.5.2. Effect of GO on final morphology	163
3.5.2.1. Obtained morphology in presence of GO	164
3.5.2.2. Morphology of DUT-5(Al)-336.....	167
3.6 CONCLUSIONS AND PERSPECTIVES.....	170
3.7 REFERENCES	172

3.1 INTRODUCTION

1D MOFs based nanotubes (NTs) and nanowires (NWs) with different composition, microstructure (length, diameter), and organization levels have been prepared following different synthetic protocols in literature (**Figure 3-1**).¹ While the use of soft (e.g., biological templates, surfactants, etc.) or hard templates (e.g., graphene, metal oxides, silica, etc.) has been revealed fruitful for the production of 1D MOF nanostructures, the number of MOF NWS and NTs produced in solution without any structure directing agents is however limited at the present time.¹ This may be partly due to the key challenge in MOF synthesis to control the structure and the morphology of the material that will be formed in specific experimental conditions.



Figure 3-1: Schematic illustrations of the different strategies used to prepare tubular MOF-based nanostructures and superstructures.¹

For numerous MOFs, the relationship between the synthetic parameters (precursors concentrations, temperature, time, etc.) and the structure/morphology of the MOF is hard to predict, such that the synthesis of MOF with a tailored crystal morphology is typically accomplished on the basis of trial and error, rather than a rational design. It is worth noting that significant progress on the formation mechanisms of MOFs was

achieved through *in situ* and time-resolved studies of MOF crystallization and growth performed by using a broad range of complementary experimental (scattering methods, microscopies and spectroscopies) and simulation techniques.² This valuable approach reported for a variety of MOFs has clearly shown that the processes of MOF nucleation and growth are highly-system specific and proceed through diverse mechanisms (monomer addition, dissolution-recrystallization, solid-phase transformations, etc.).² Although SEM and/or TEM experiments were generally performed to study the formation of MOFs NWs and NTs, time-resolved and *in situ* studies with the combination of multiple advanced characterization techniques would certainly provide insight into the anisotropic growth of MOF nanocrystals. This difficulty to predict the crystalline growth of MOFs as well as their structural evolution during synthesis is also related to the surface structure of MOFs nanocrystals which is much more complex and heterogeneous than other materials such as oxides due to the presence of a wide diversity of surface functional groups (organic linker, metal cations, surface defects, coordinating water molecules).³

In the previous chapter, the screening of five MOF candidates was described, and the selection of DUT-5(Al) as the best candidate was justified by the different characterization techniques employed. Herein, our objective is to successfully shape DUT-5(Al) nanoparticles into 1D nanowires using a hard template i.e., graphene oxide. To achieve this goal, a thorough synthesis optimization process had to be followed while considering several works in the state of the art. We have experimentally observed in **chapter 2** that DUT-5 could be formed in the presence of GO and the resulting composite contain elongated nanostructures within other particles and aggregates. However, it is of huge importance to complete the characterization of the parent DUT-5 (and the DUT-5/GO composite) as the fundamental characterization techniques (i.e., PXRD, FT-IR spectroscopy, SEM) used do not allow to ascertain the

CHAPTER 3: DUT-5(Al) and DUT-5(Al)/GO

purity of these samples. Thus, a brief summary of the state of the art covering DUT-5(Al) will be first discussed. Then, DUT-5(Al) will be characterized by additional techniques, and based on the obtained results, the synthesis of the pure MOF will be further optimized. Once the synthesis of DUT-5(Al) was successfully optimized, GO was added to the synthesis, and directing the growth of small nanoparticles into nanowires was thoroughly investigated. Finally, it was of huge importance to investigate the effect of GO on both the sample's final morphology and its formation kinetics.

Lastly, it is worth noting that most of the synthesis and characterization techniques applied in this PhD project will be described in this chapter. MOFs have always been synthesized and characterized through definite strategies.^{4,5} Herein, the employed characterization techniques include: powder X-ray diffraction (PXRD), Fourier transform infrared spectroscopy (FT-IR), thermogravimetric analysis (TGA), nitrogen gas physisorption, scanning and transmission electron microscopy (SEM, TEM, STEM), selected area electron diffraction (SAED), x-ray energy dispersive scattering (XEDS), X-ray photoelectron spectroscopy (XPS), and ²⁷Al solid-state NMR, etc.

3.2 DUT-5(Al) IN THE STATE OF THE ART

DUT-5(Al) was first reported in 2009 by Senkowska and co-workers as an extended form of the MIL-53(Al) structure.⁶ The benzene-1,4-dicarboxylate (bdc) linker used in the synthesis of MIL-53(Al) was replaced by biphenyl-4,4'-dicarboxylate (bpdc). DUT-5(Al) is built from Al^{3+} metal centers and bpdc organic ligand. It consists of Al-OH inorganic chains that are connected by the organic linkers to form a 3D structure. Each inorganic chain is connected to four neighboring chains (**Figure 3-2**). This coordination results in the formation of diamond shaped micropores (channels) that extend in one direction. The effect of the extended linker can be shown through comparing the distance between the aluminum centers in neighboring chains. In case of DUT-5(Al) they are separated by 19.24 and 22.94 Å compared to 13.04 and 16.73 Å in case of MIL-53(Al).

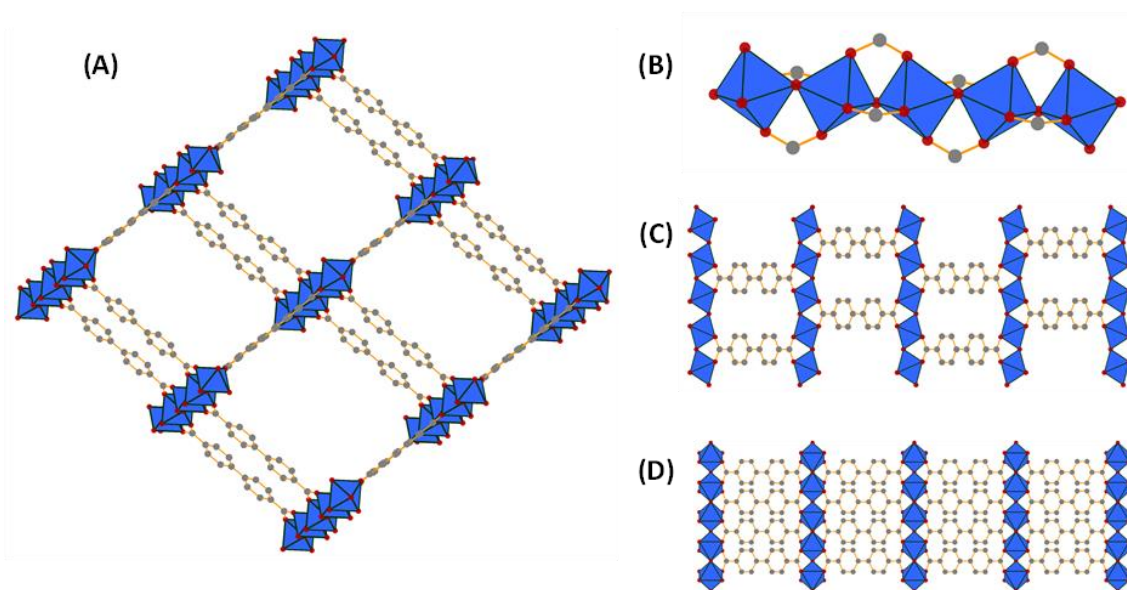


Figure 3-2. (A) View along the channels of DUT-5(Al); (B) 1D $\text{AlO}_4(\text{OH})_2$ chain of DUT-5(Al); (C) view along (a) axis; (D) view along (c) axis. Blue polyhedra represent $\{\text{AlO}_6\}$ octahedra, while grey and red present C and O atoms, respectively.

DUT-5(Al) was much discussed in literature.⁷ For instance, Couck *et al* reported isorecticular DUT-5- SO_2 using 4,4'-bibenzoic acid-2,2'-sulfone.⁸ The sulfone functionalization of DUT-5 revealed a selective behavior towards the adsorption of

alkanes as well as a preferred adsorption of benzene over hexanes which was justified by the decreased pore size and the stronger confinement effect inside the pores.⁸ Halis *et al*/reported DUT-5-NH₂ and DUT-5-NO₂ analogues using 2-amino- and 2-nitro-4,4'-biphenyldicarboxylic acid during the framework synthesis.⁹ The analogues also possessed a high permanent porosity and thermal stability. Dau *et al*/reported a DUT-5 variant using 2-phenylpyridine-5,4'-dicarboxylate (dcpyp), a derivative of bpdc, which showed the same chemical and thermal stability of the parent MOF.¹⁰ One year later, Liu and co-workers reported a DUT-5 vanadium analogue called CMOC-2(V). This analogue attracted attention as it showed a flexible behavior under pressure that was not previously observed in the parent DUT-5(Al).^{11,12} Gotthardt *et al*/later reported the synthesis of functionalized DUT-5 by using either bpdc ligands modified with additional amino, alkyne, azide or nitro groups or a mixture of modified bpdc (MIXMOF).¹³ This functionalization allowed tuning the frameworks properties by controlling the number of functional groups used (i.e., ratio of functionalized to unfunctionalized ligands). It was noted that the thermal stability of the different frameworks decreases with increasing the functionalization degree.¹³ The MIXMOFs approach was recently utilized by Yildiz *et al*/to obtain DUT-5(Al)-type frameworks with an enhanced porosity and a good distribution of catalytically active sites within the framework structure.¹⁴ The post-synthetic modification of the different MIXMOFs allowed constructing DUT-5 structures with immobilized Co²⁺, Mn²⁺ and Mn³⁺ complexes inside the framework as single sites for heterogenous catalysis. In addition to the mixed linker approach described for DUT-5, it is worth mentioning that a mixed metal approach was also reported.¹⁵ The COMOC-2(V)/DUT-5(Al) was reported by Depauw *et al*/ and similarly to CMOC-2(V), this material has shown an interesting flexible behavior under pressure.

3.3 SYNTHESIS OPTIMIZATION OF DUT-5(Al)

This part of the chapter will deal with the thorough characterization and synthesis optimization of DUT-5(Al).

3.3.1. Reported synthesis of DUT-5(Al) under reflux

The synthesis of DUT-5(Al) under reflux was based on a previously reported protocol by Gotthardt *et al.*¹³ The fundamental characterization techniques employed in **chapter 2** (i.e., PXRD, FT-IR spectroscopy, SEM) have shown that the synthesis of DUT-5(Al) was successful. Herein, additional characterization techniques were employed to better describe the DUT-5(Al) sample and evaluate its purity. For instance, **(Figure 3-3)** below shows the recorded HAADF-STEM (High angle annular dark field in the scanning transmission electron microscopy mode) image of DUT-5(Al) particles and the corresponding STEM-XEDS (X-ray energy dispersive spectrometer coupled with the STEM mode) elemental mapping. DUT-5(Al) consist in the presence of monodisperse circular disks with a diameter of about 350-450 nm. As shown by XEDS, these particles consist of the elements constituting DUT-5(Al) namely carbon (in red), oxygen (in orange), and aluminum (in yellow). However, at the surface of such circular disks, small particles (90-120 nm) are made of the Al and O elements while C element is not present, thereby excluding the presence of DUT-5(Al) for such particles. One can assume that these particles correspond presumably to Al oxides or hydroxide (i.e., Al_2O_3) forming at the surface of the DUT-5(Al) nanoparticles.

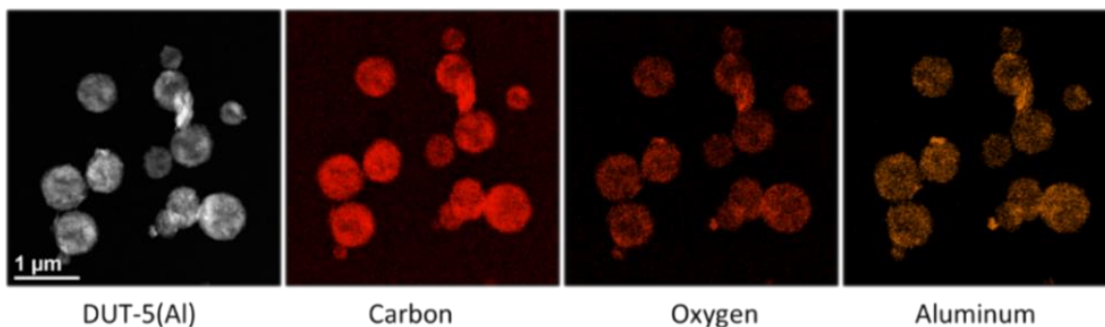
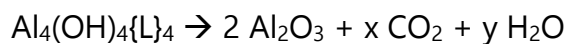


Figure 3-3: Scanning transmission electron microscopy (STEM) coupled with XEDS mapping analysis of DUT-5(Al).

CHAPTER 3: DUT-5(Al) and DUT-5(Al)/GO

To further confirm this assumption, TGA experiments were performed under oxygen gas under a rate of 5°C/min until 700°C. DUT-5(Al) has the following molecular formula: $C_{56}H_{36}O_{20}Al_4$, corresponding to $[Al_4(OH)_4\{L\}_4]$ where L represents the bpdc ligand $[OOC-C_6H_4-C_6H_4-COO]$. Considering the combustion of DUT-5(Al) under oxygen, the following reaction will be obtained:



Hence, the theoretical amount of residual Al_2O_3 from in the DUT-5(Al) structure is :

$$\% (Al_2O_3) = 2 \times \frac{MW_{Al_2O_3}}{MW_{DUT-5}} = 2 \times \frac{102}{1136} = 18 \% \quad \text{(Equation 3-1)}$$

In other words, any residual amount at 700 °C above 18 %wt. indicates an excess of aluminum oxide. It is reported that for DUT-5(Al), a weight loss between 40 and 260°C is attributed to the loss of 1.8 DMF and 3.5 H_2O molecules per aluminum atom, and the combustion of bpdc ligand starts at around 430°C.⁶ Hence, as shown in **(Figure 3-4)**, DUT-5(Al) synthesized following a metal/ligand ratio of 1.3 shows the presence of 20.5% of Al_2O_3 , 6% of water and DMF, and 73.5% of ligands. Yet, to be compared with the theoretically calculated value of 18%, the theoretically calculated value should consider the same amount of solvent. So, based on simple mathematical calculations:

$$100\% \text{ MOF (0\% solvent)} \rightarrow 18\%$$

$$94\% \text{ MOF (6\% solvent)} \rightarrow x$$

$$\text{then, } x = \frac{94}{100} \times 18 = 16.9\% \quad \text{(Equation 3-2)}$$

DUT-5(Al) with 6% solvent content is theoretically supposed to have 16.9 % Al_2O_3 . Compared to the 20.5% that were obtained experimentally, around 4 wt.% of extra Al_2O_3 are present in the sample composition. Thus, the assumed formation of aluminum oxide on the surface of the DUT-5(Al) particles is possible, and the optimization of the MOF synthesis is required in order to enhance the purity of the MOF sample.

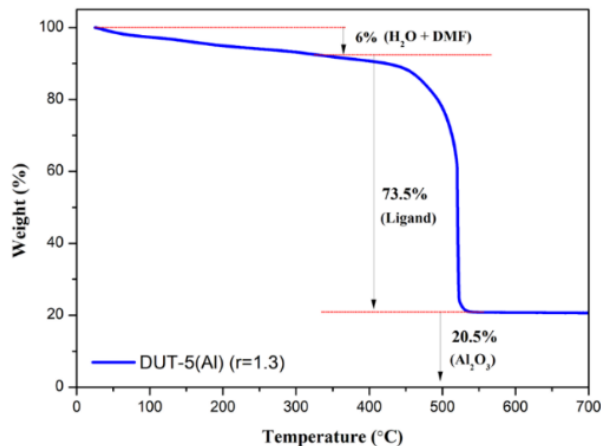


Figure 3-4: TGA curve of DUT-5(Al) synthesized using a molar metal to ligand ratio of 1.3.

Therefore, after employing some additional characterization techniques (i.e., STEM-XEDS, TGA), it was shown that an additional amount of aluminum oxide (presumably Al_2O_3) is formed on the surface of DUT-5(Al) particles, and these undesired oxides correspond to almost 4 wt.% of the sample. Therefore, it can be concluded that the reported synthesis by Gotthardt *et al*/needs to be further optimized in order to obtain DUT-5 with a high purity.

3.3.2. Optimization of the reported synthesis

3.3.2.1. Optimization approach

The reported synthesis of DUT-5(Al) was performed with an excess of $r = \text{metal/ligand ratio} = 1.3$. To decrease the amount of oxide, we can try to decrease the $r = \text{Al/ligand molar ratio}$ and thus perform the synthesis with an equimolar r ratio. Working with an equal r ratio can help the aluminum cations coordinate entirely with bpdc to form the MOF. Thus, the synthesis was optimized by decreasing the r ratio gradually from a ratio of 1.3 to 1 (i.e., $r = 1.2; 1.1; 1$). Interestingly, following this approach and using the same calculation method followed above (**Eq. 3-1 and 3-2**), the performed TGA experiments (**Figure 3-5**), revealed that the lower the metal to ligand ratio, the less undesired aluminum oxide is formed in the sample.

CHAPTER 3: DUT-5(Al) and DUT-5(Al)/GO

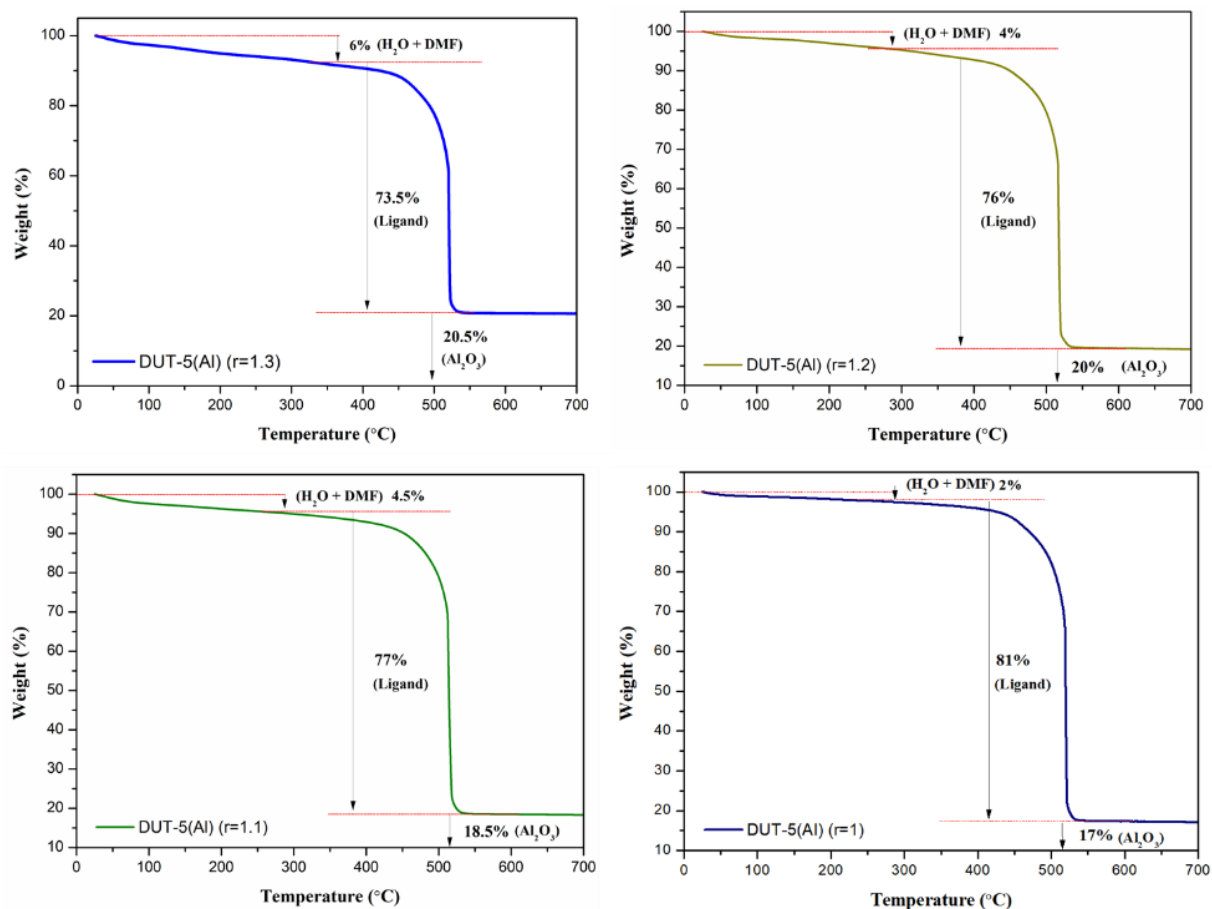


Figure 3-5: TGA results presenting the different MOF compositions while decreasing the metal/ligand ratio from 1.3 into 1 by a value of 0.1.

As shown in **(Figure 3-5)** above, the synthesis of DUT-5(Al) using a ratio of 1 presents an experimental value of 17 wt.% Al_2O_3 . Following the same calculations used before, the sample with 2 wt. % of solvent is expected to have a value of x .

$$x = \frac{98}{100} \times 18 = 17.6\%$$

According to the calculated and experimentally obtained values (17.6 and 17% respectively), less than 1% of aluminum oxide are present in the MOF. This value can be attributed to experimental error margins or even small traces of aluminum oxide present in the sample. Thus, this metal to ligand ratio will be preferred for the synthesis of DUT-5(Al). Therefore, to avoid the presence of any extra Al_2O_3 in DUT-5(Al), it was

re-synthesized using the following protocol: 170 mg (0.70 mmol) of 4,4'-biphenyldicarboxylic acid (bpdc) were dissolved in 20 mL of DMF at 120°C. A change in color from white to colorless was observed after 10 minutes, ensuring the complete dissolution of the bpdc linkers. Then, 0.70 mmol (262.6 mg) of $\text{Al}(\text{NO}_3)_3 \cdot 9\text{H}_2\text{O}$ were dissolved in 5 mL of DMF and added to the round bottom flask containing the organic linker solution. The solution was refluxed for 24 hours and turned turbid white after 15 min. It was then collected, centrifuged, and washed 3 times with ethanol (25 mL) at a rate of 12500 rpm for 10 min each. After washing, the produced MOF was then dried at 100°C overnight.

3.3.2.2. Characterization of the optimized sample

DUT-5(Al) synthesized with a metal to ligand ratio of 1 was fully characterized. All the employed characterization results are listed in this section. **(Figure 3-6)** shows that there is no difference in the data collected by PXRD and FT-IR spectroscopy after changing the molar ratios. Both samples are crystalline and in agreement with the calculated pattern from the DUT-5(Al) crystal structure in literature. The major characteristic Bragg peaks of DUT-5(Al) at 6.01, 12.05, and 14.15° were all observed in the optimized sample **(Figure 3-6, A)**. Besides, no change in the coordination environment was evidenced by FT-IR spectroscopy while changing the molar ratios. The characteristic bands are present in both samples. The bands in the range 1608–1570 cm^{-1} represents the asymmetric stretching vibrations of the carboxylate group ($\nu_{\text{as}}(\text{C-O})$), while those at 1430 and 1364 cm^{-1} can be ascribed to the symmetric vibrations ($\nu_{\text{s}}(\text{C-O})$) **(Figure 3-6, B)**.

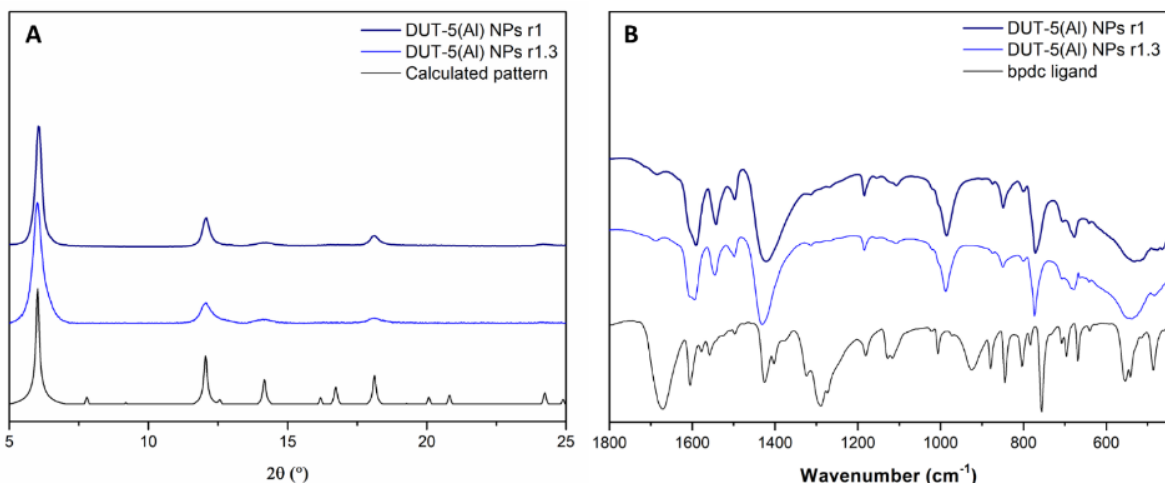


Figure 3-6: (A) PXRD patterns of calculated and synthesized DUT-5(Al) with different metal/ligand ratios. (B) FT-IR spectra of bpdC ligand and DUT-5(Al) synthesized with different metal/ligand ratios.

DUT-5(Al) synthesized using a metal/ligand ratio of 1 was as well characterized by different microscopic techniques. As shown in **(Figure 3-7)**, STEM-XEDS elemental mapping shows different results from those observed before optimization in **(Figure 3-3)**, all elements (C, O, Al) are homogeneously distributed in the entire particles, showing the absence of any additional Al or O on the particles surface. This further validates the results obtained by TGA. Besides, it should be noted that SAED experiments were performed **(Figure 3-7, C)**, and the electron diffraction pattern of DUT-5(Al) nanoparticles presented rings with different interplanar spaces showing that the formed MOF particles are polycrystalline in nature. It is worth noting that the interplanar distances observed in **(Figure 3-7, C)** at 14.7, 7.35, and 4.90 Å correspond to the (1,0,1), (2,0,2), and (3,0,3) reflections of the crystalline DUT-5(Al) structure, respectively.

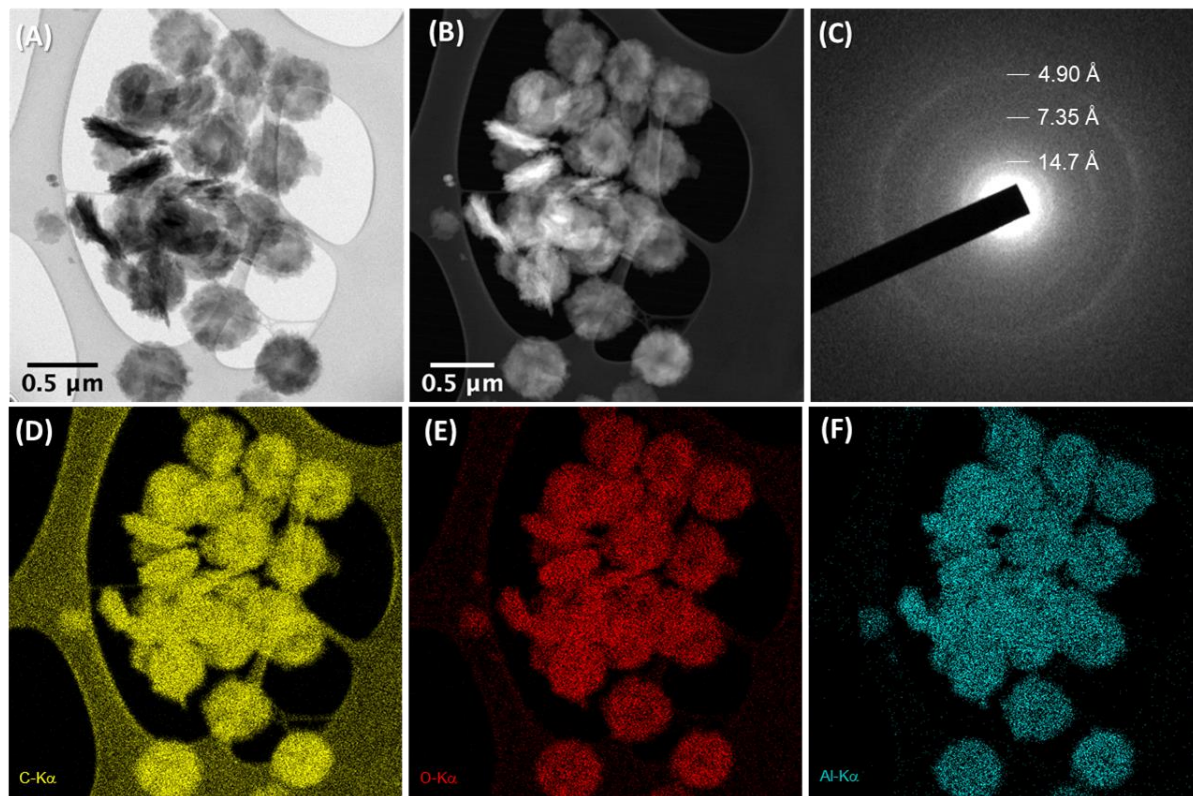


Figure 3-7: TEM observations of DUT-5(Al) synthesized with a metal/ ligand molar ratio of 1. TEM bright field (A) and STEM-HAADF (B) images and Selected Area Electron Diffraction (SAED) pattern (C). (D – E) STEM-XEDS elemental maps.

Furthermore, SEM and HAADF-STEM images collected show that changing the molar ratios did not affect the morphology of the DUT-5 particles. As shown in **(Figure 3-9)**, the nano-disks of DUT-5 with a diameter of 350-450 nm consist of an assembly of small nanorods with a diameter less than 50 nm.

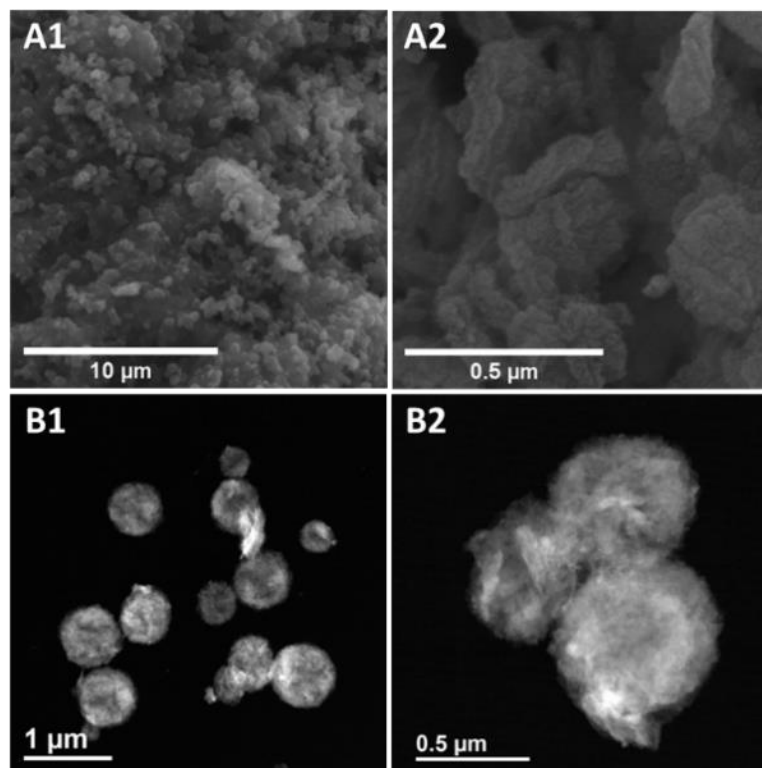


Figure 3-8: SEM (A1-A2) and HAADF-STEM (B1-B2) images of DUT-5(Al) NPs synthesized by metal/ligand ratio 1.3.

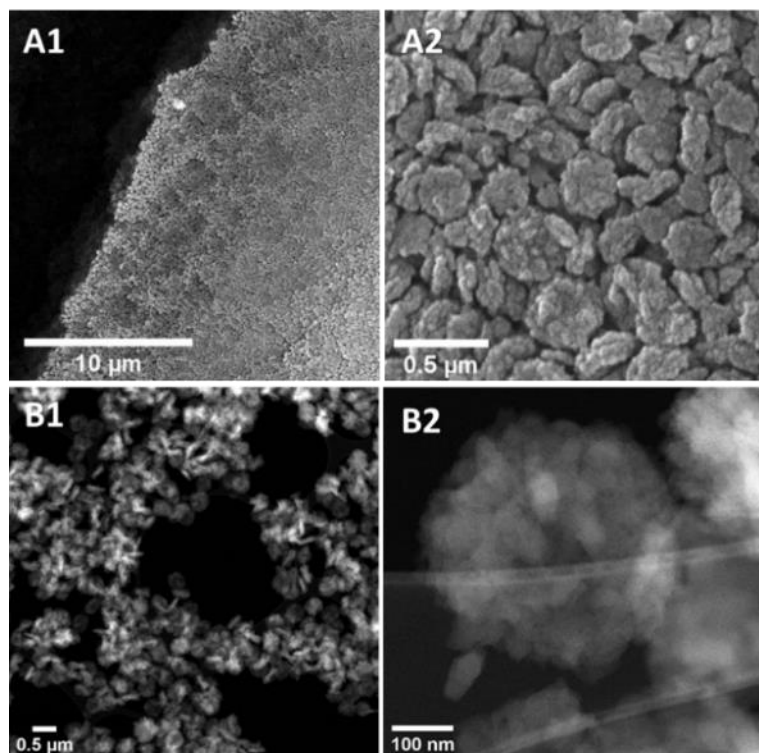


Figure 3-9: SEM (A1-A2) and HAADF-STEM (B1-B2) images of DUT-5(Al) NPs synthesized by metal/ligand ratio 1.

Furthermore, N₂ physisorption measurements were performed on both samples (**Figure 3-10**). The samples were both activated at 160 °C overnight, then N₂ physisorption measurements were performed on 35 mg of each sample. Even though both samples presented a type I isotherm typical of a microporous material, the obtained BET surface areas were different. DUT-5(Al) synthesized with a metal/ligand ratio of 1, revealed a higher BET surface area than that synthesized with a ratio of 1.3 (1950 > 1700 m²/g). These observations are in accordance with the results obtained by TGA and STEM-XEDS. In fact, the sample prepared at r=1.3 contains an amount of non-porous Al₂O₃ that can also limit the accessibility to the pores of the DUT-5(Al).

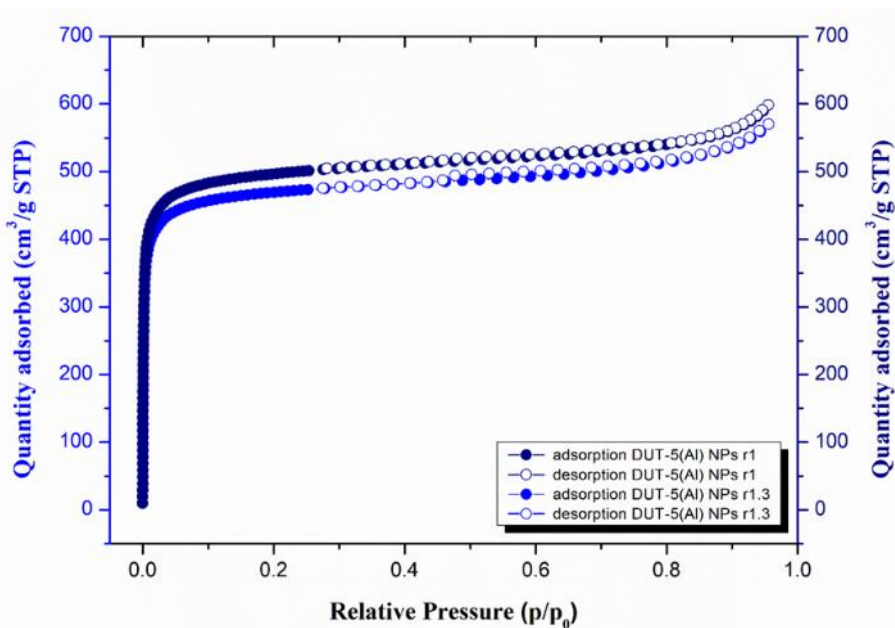


Figure 3-10: N₂ physisorption isotherms of DUT-5(Al) NPs synthesized by metal/ligand ratios of 1 and 1.3.

3.3.2.3. Kinetic study on the optimized sample

Additionally, the kinetics of formation of DUT-5(Al) nanoparticles were studied using wide angle X-ray scattering (WAXS) experiments. WAXS was performed on as synthesized DUT-5(Al) sample with a metal/ligand ratio of 1 in DMF solution using SWING beamline at Synchrotron Soleil (in collaboration with F. Gobeaux, CEA). As

displayed in **(Figure 3-11)**, the WAXS pattern of DUT-5(Al) after 24 hours of synthesis is presented in yellow. This pattern displays the characteristic Bragg peaks of the DUT-5(Al) structure. The WAXS pattern of the material obtained after only 1 hour of synthesis (in blue) also displays the peaks of DUT-5(Al), while additional peaks corresponding to the organic bpdc ligand are also present. After 2 hours of synthesis (in orange), the reflections of the organic linker are not anymore observed. Hence, it can be assumed that the growth of the MOF crystals starts after 1 hr of synthesis only, however, almost 2 hours are needed for all the ligands to coordinate. This was further validated by images recorded using an optical microscope. As shown in **(Figure 3-12)**, elongated micron sized particles corresponding to the 4 4'-biphenyl dicarboxylic acid ligands are still present after 1 hour of synthesis, however they are absent in the final product after 24 hours.

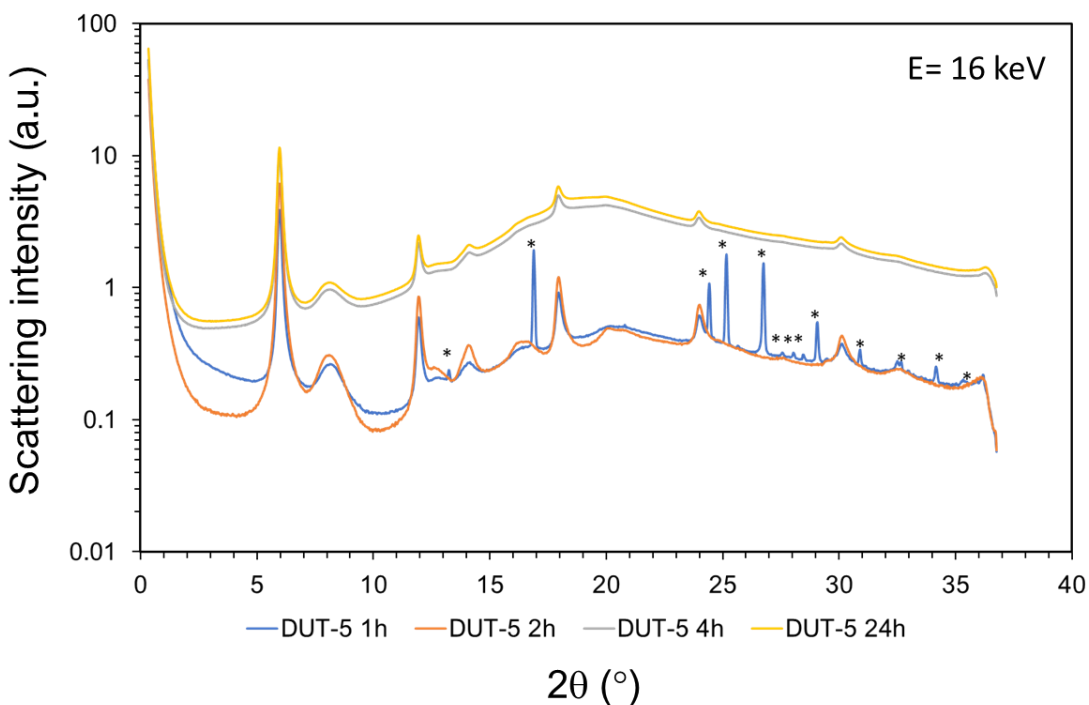


Figure 3-11: Wide angle X-ray scattering data recorded on SWING beamline at Synchrotron Soleil. The crystalline peaks correspond to the bpdc ligand are marked by asterisk.

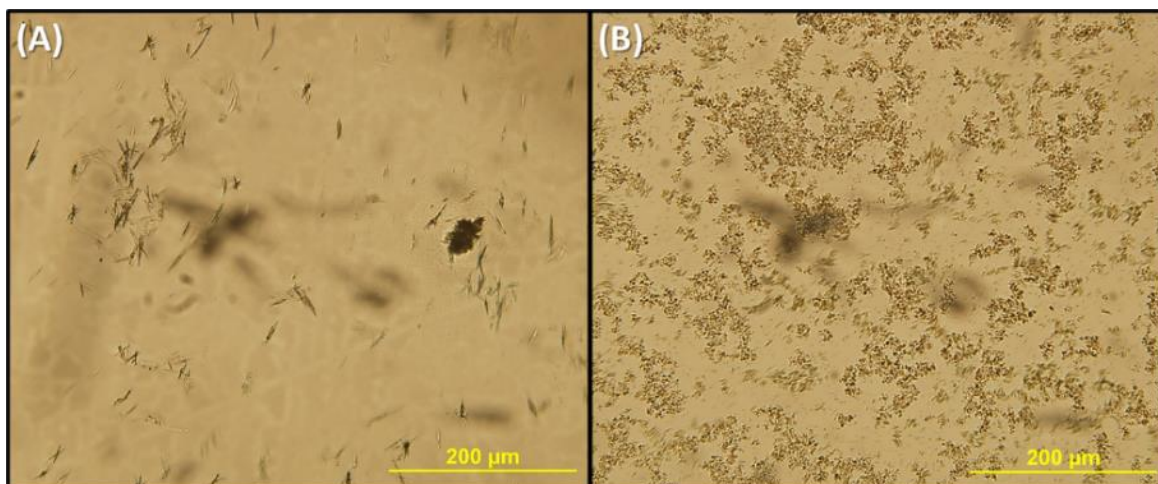


Figure 3-12: Optical images of DUT-5(Al) extracted after 1 hr (A), and 24 hours of synthesis (B).

Moreover, the data recorded via WAXS experiments were further analyzed to study the formation and growth of DUT-5(Al) crystals. First, WAXS *ex-situ* measurements were performed through sample extractions at different reaction times, where the reaction was quenched by cooling at room temperature (**Figure 3-13**). Then the scattering data was plotted in the form of peak intensity of the scattering vector at 0.43 \AA^{-1} as a function of reaction time after fitting the first peak (**Figure 3-14, A**). Secondly, a Lorentzian fit was applied to the plotted data, and a correlation length extracted from the full width at half maximum (FWHM) of the first peak and the reaction time was established. The analysis of the first peak have shown that the peak intensity stops to increase after 10 hours of synthesis (**Figure 3-14, A**). On the other hand, the correlation length which can be related to the crystallite size was equal to a constant value of around 45-50 nm after a reaction lime of 3 hours (**Figure 3-14, B**). Thus, it can be concluded that the crystallite domain of DUT-5(Al) (i.e., diameter of the particle) can reach a maximum value of approximately 50 nm. However, the intensity of the peaks keeps growing up to 10 hours of synthesis. Such results imply that the crystallite domain reaches a maximum value of 50 nm after 3 hours, while the formation of additional DUT-5 (Al) particles (formation of nuclei followed by their growth) continues up to 10 hours of synthesis.

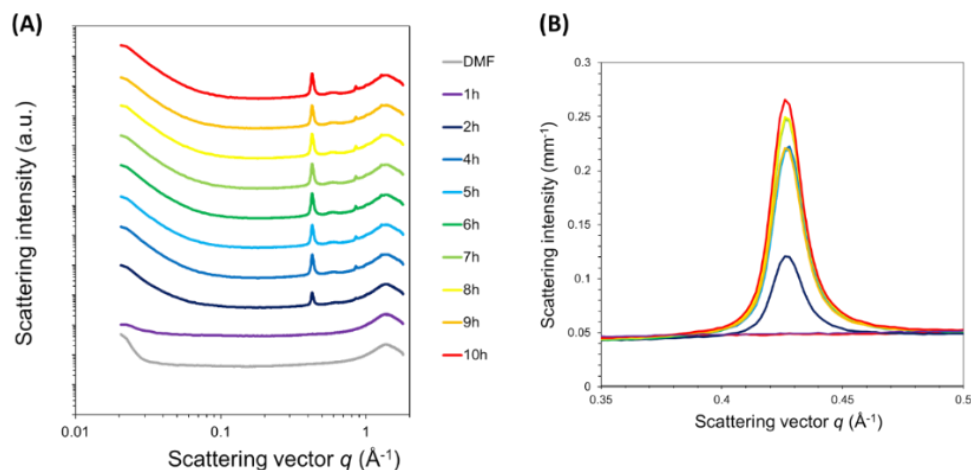


Figure 3-13: (A) WAXS fit of the formation and growth of DUT-5(Al) crystals. (B) Zoom in on the growth of the first peak between a scattering vector of 0.35 and 0.5 \AA^{-1} .

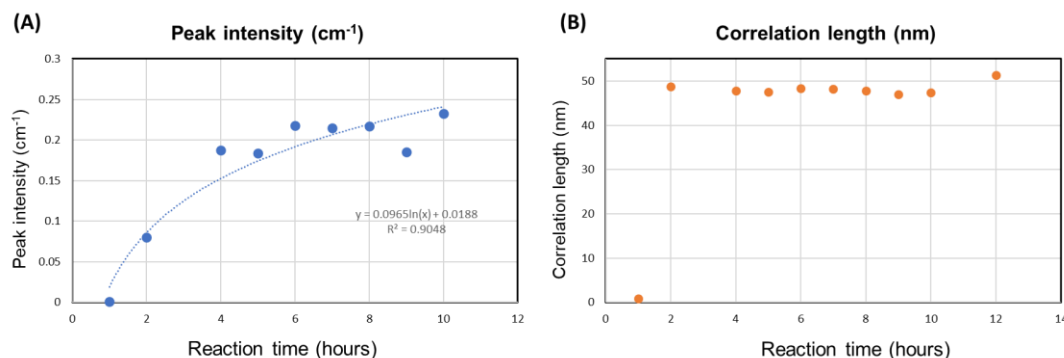


Figure 3-14: Lorentzian fit based on the peak analysis of recorded WAXS data of DUT-5(Al) extractions for a 24-hour synthesis. (A) Peak intensity as a function of reaction time. (B) Correlation length revealing the increase in crystallite size as a function of reaction time.

In conclusion, it was shown through TEM-XEDS and TGA techniques that the tuning of the reactants molar ratio was crucial to optimize the synthesis of the DUT-5(Al) without any Al_2O_3 . Both SEM HADDF-STEM and WAXS revealed that DUT-5(Al) are made of disk-like aggregates with a diameter of 350-500 nm consisting in the assembly of nanorods with a diameter of 50 nm. Finally, wide angle X-ray scattering helped study the kinetics of the DUT-5(Al) formation and growth in the synthesis suspension. It was concluded that the formation of the MOF crystals starts after 1 hour of synthesis, and these crystals grow in size until they reach an average size of 50 nm after 3 hours. Besides, the formation of additional MOF crystals continues up to 10 hours of synthesis, reaching the same average crystallite size of 45-50 nm.

3.4 SYNTHESIS OPTIMIZATION OF DUT-5(Al)/GO

It was anticipated that the optimized synthesis protocol of DUT-5(Al) should be followed for the preparation of composites in the presence of GO. Hence, in this section, DUT-5(Al)/GO was synthesized following optimized conditions (i.e., metal/ligand ratio of 1) and characterized to ensure the absence of extra Al₂O₃. Moreover, we have shown in **chapter 2** that the addition of GO to DUT-5(Al) led to promising composites with anisotropic particles, but these composites suffer from a poor homogeneity (check **chapter 2**). Herein, an experimental plan for optimizing the synthesis of a monodisperse composite will be detailed.

3.4.1. Synthesis of DUT-5(Al)/GO with different molar ratios

Based on the results obtained for DUT-5(Al), it was expected that Al₂O₃ will be also present in the composite if synthesized using the same reported metal/ligand ratio of 1.3. Nevertheless, it was not possible to perform TGA in the presence of GO. Indeed, the thermal treatment of graphene oxide (> 200°C) under oxygen atmosphere leads to its reduction involving the removal of oxygen functions and the creation of sp² carbon groups.^{16,17} At higher temperature, graphene oxide is completely degraded by combustion. The thermal treatment of GO is thus accompanied by an significant gas (CO₂ and H₂O) release that can damage the TGA apparatus.^{16,17} Therefore, as previously mentioned in **chapter 2**, solid-state NMR spectroscopy was used to evaluate the purity of the synthesized samples without any technical constraints.

Hence, DUT-5(Al)/GO previously synthesized with a molar metal/ligand ratio of 1.3 and characterized (by PXRD, FT-IR spectroscopy, and SEM), was further investigated by ²⁷Al solid-state NMR spectroscopy (in collaboration with M. Haouas, ILV). The 1D MAS spectrum of DUT-5(Al)/GO (**Figure 3-15a**) showed different more or less resolved resonances, and to gain resolution, a 2D multi-quantum magic-angle

spinning (MQMAS) ^{27}Al NMR experiment was performed. The MQMAS sequence suppresses the second order quadrupolar interaction in dimension 1 of the 2D map (**Figure 3-15b**). This experiment has allowed the identification of different Al sites with great precision. The extraction of both the isotropic chemical shifts (δ_{iso}) and quadrupolar parameters (C_Q and η_Q) of the ^{27}Al NMR signals enabled to describe the local environment of these Al sites, in particular their coordination number, degree of disorder, and relative symmetry. Three main signals were identified with distinct NMR parameters, S1: δ_{iso} 59.1 ppm, C_Q 3.5 MHz, $\eta_Q = 0$, S2: 10.5 ppm, C_Q 3.5 MHz, $\eta_Q = 0$, and S3: 16.4 ppm, C_Q 11.1 MHz, $\eta_Q = 0.1$, indicating the presence of different Al species. In a second step, spectral decomposition of the 1D MAS NMR spectrum was conducted considering these parameters to provide quantitative analysis. Good consistency between experimental and simulated spectra could be obtained using the MQMAS data except for δ_{iso} of S3 who deviates to ca. 10 ppm to provide an acceptable fit. The isotropic chemical shift of S3 is not determined accurately due to the line broadening and overlapping signals and should therefore range from 7 to 16 ppm. Nevertheless, and most importantly, this resonance signal S3 with a large quadrupolar coupling constant C_Q 10-11 MHz corresponds to a typical Al-carboxylate MOF such as the DUT-5(Al).¹⁸ It is in good agreement with the DUT-5(Al) structure where each aluminum metal center is in a hexacoordinated environment, bonded to four oxygen atoms from the carboxylate of ligands and two oxygen atoms from the bridged-hydroxide groups.^{6,19} On the other hand, the NMR signals S1 and S2 at 59.1 and 10.5 ppm should correspond to the tetrahedral and octahedral Al sites in unreacted Al_2O_3 , respectively.²⁰ Based on the recorded data, 56 mol.% of total Al are present as aluminum oxide in the sample. This value corresponds to almost 18.6 wt.% of Al_2O_3 .

This value is calculated as follows:

$$m(\text{Al}_2\text{O}_3) = \frac{n_{\text{Al}}}{2} \times \text{MW}_{(\text{Al}_2\text{O}_3)} = \frac{0.56}{2} \times 102 = 28.6 \text{ g}$$

$$m(\text{MOF}) = n_{\text{Al}} \times \text{MW}_{(\text{MOF})} = 0.44 \times 284 = 125 \text{ g}$$

Therefore, the wt. % of Al_2O_3 is

$$m = \frac{m(\text{Al}_2\text{O}_3)}{m(\text{Al}_2\text{O}_3) + m(\text{MOF})} = \frac{28.6}{28.6 + 125} = 18.6 \text{ wt.}\%$$

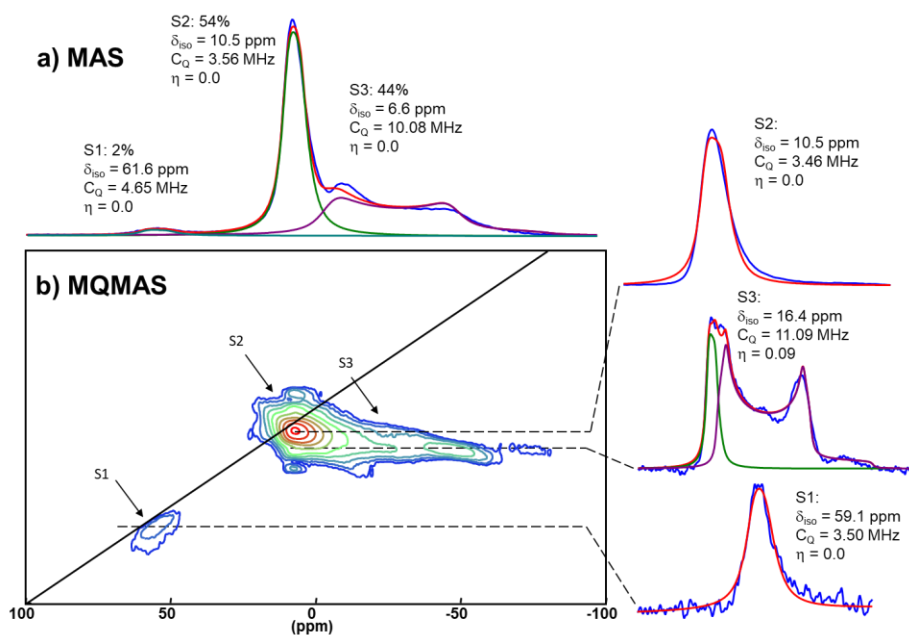


Figure 3-15: a) 1D ^{27}Al MAS and b) ^{27}Al MQMAS NMR spectra of DUT-5(Al)/GO synthesized using a molar ratio metal/ligand of 1.3. Extraction of the three components (S1, S2, and S3) along the isotropic dimension 2 with signal simulation (red line).

Hence, the same optimization approach applied for DUT-5(Al) was followed, and the reactants molar ratio was reduced to a value of 1. The same synthesis protocol developed in **chapter 2** was used with just varying the ligand content to reach a metal/ligand ratio of 1. First, 1.167 g of GO slurry was dissolved in a solution of 25 mL DMF, stirred, and sonicated for a few minutes. Then, 170 mg (0.70 mmol) of 4,4'-biphenyldicarboxylic acid (bpdc) were added and under stirring. A change in color from dark black to grey is observed. Then, 262.6 mg (0.70 mmol) of $\text{Al}(\text{NO}_3)_3 \cdot 9\text{H}_2\text{O}$ were then added and the solution was then put under reflux for 24 hours.

CHAPTER 3: DUT-5(Al) and DUT-5(Al)/GO

After changing the synthesis reactant ratios, the composite was first characterized by PXRD and FT-IR spectroscopy. As shown in **(Figure 3-16)**, compared to the previously obtained results with a metal/ ligand ratio of 1.3, there was no major change in the structure of the composite. Concerning PXRD results, despite the observed broadening after the addition of GO, the characteristic Bragg peaks of DUT-5(Al) at 6.01, 12.05, and 14.15° were all observed in the composite **(Figure 3-16, A)**. As explained in **chapter 2**, this broadening in the PXRD peaks can be attributed to a smaller crystallite size or some micro strains in the composite. Similarly, the FT-IR characteristic bands ($\nu_{as}(C-O)$) = 1608–1570 cm^{-1} and ($\nu_s(C-O)$) = 1430 and 1364 cm^{-1} were present in both the pure MOF and the composite **(Figure 3-16, B)**. Yet, traces of unreacted bpdc were observed in the composite synthesized using a reactants molar ratio of 1. This was concluded from the small band observed at 1670 cm^{-1} corresponding to the carboxylic acid group of unreacted bpdc ligand.

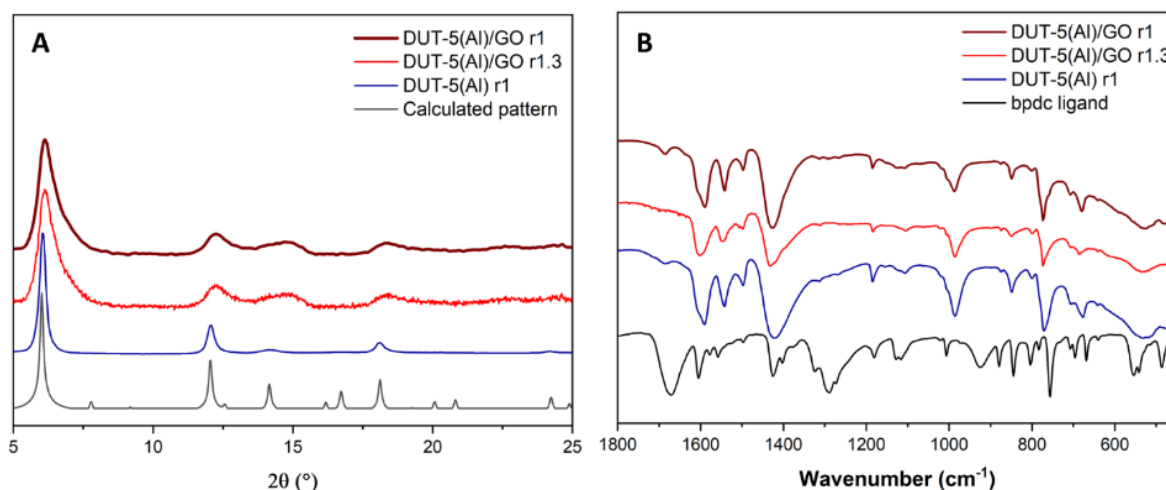


Figure 3-16: (A) PXRD patterns of calculated and synthesized DUT-5(Al), and DUT-5(Al)/GO synthesized with different metal/ligand ratios. (B) FT-IR spectra of bpdc ligand, DUT-5(Al), and DUT-5(Al)/GO synthesized with different metal/ligand ratios.

The sample was also characterized by ^{27}Al MAS NMR spectroscopy to evaluate the presence of impurities (Al oxide). **Figure 3-17** shows the ^{27}Al MAS spectrum of DUT-5(Al)/GO synthesized using a molar ratio metal/ligand of 1. As it can be seen, the

spectrum shows two main signals in the chemical shift range of 10 to 3 ppm. The signal at δ_{iso} 3.2 ppm corresponds to DUT-5(Al), while that at 8.8 ppm is attributed to the formation of some aluminum oxide.^{6,19} Note that the MOF Al signal exhibits a severe line shape distortion of its second order quadrupolar pattern, most likely due to distributed Al sites with various C_Q , and an average value of 10 MHz can be estimated from a rough simulation (**Figure 3-17**). This may reflect site defects in the MOF network or inhomogeneity in the MOF-GO composite. From a quantitative point of view, the composite synthesized with a metal/ligand ratio of 1 presents 91 mol.% of the total Al as MOF, compared to only 44 mol.% in case of synthesis using a ratio of 1.3. This value corresponds to only 2 wt.% of undesired Al_2O_3 . Thus, ^{27}Al MAS NMR analysis revealed that a high purity MOF-based composite can be prepared using a metal/ligand ratio of 1.

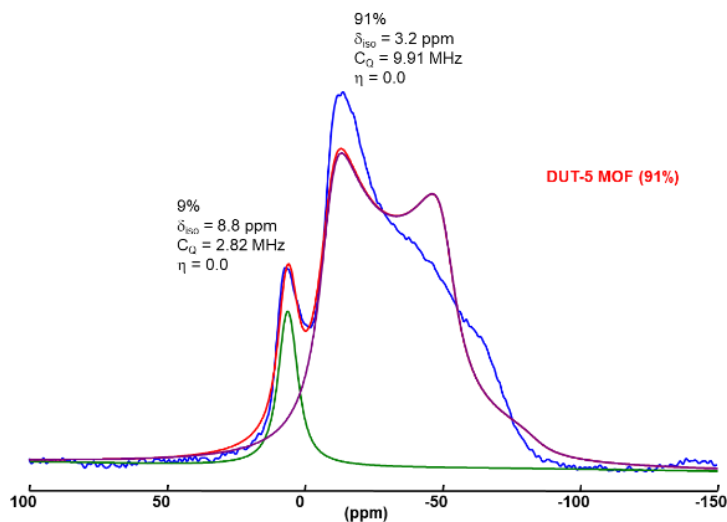


Figure 3-17: 1D- ^{27}Al MAS 20 kHz NMR spectrum of DUT-5(Al)/GO synthesized using a molar ratio metal/ligand of 1.

Besides, it was critical to ensure that elongated structures can still be observed in the composite after changing the synthesis conditions. Nevertheless, the results obtained by SEM mainly showed a highly heterogenous and polydisperse sample. Some micron-sized spherical particles covered with GO sheets were observed (**Figure 3-18, A**), as

CHAPTER 3: DUT-5(Al) and DUT-5(Al)/GO

well as a few elongated structures at rare location in the sample (**Figure 3-18, B**). Therefore, the objective of shaping DUT-5(Al) NPs into MOF NWs using GO was not achieved at that stage. Despite successfully avoiding the formation of undesired aluminum oxide, further synthesis optimization is required for the design of anisotropic DUT-5(Al)/GO nanostructures.

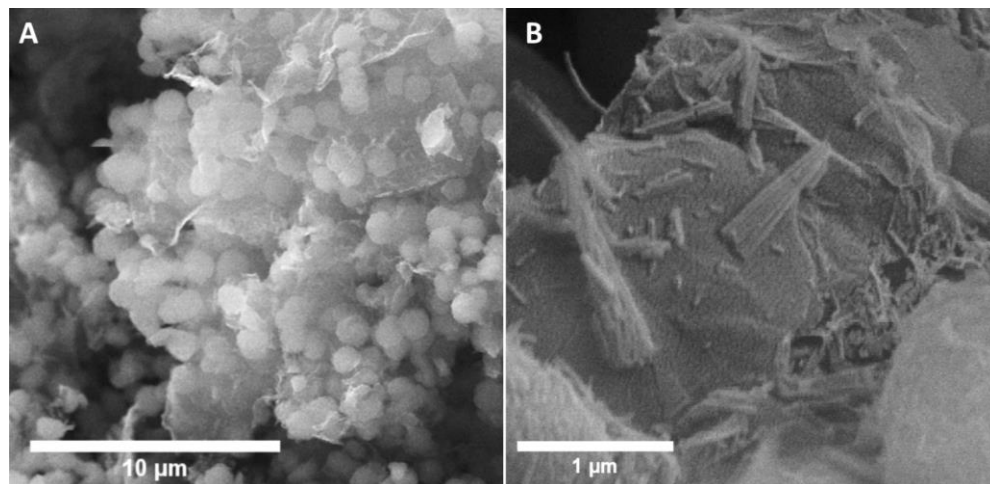


Figure 3-18: SEM images of DUT-5(Al)/GO with no aluminum oxide using a metal to ligand molar synthesis ratio of 1.

In conclusion, a DUT-5(Al)/GO composite with a high purity could be prepared by tuning the Al/bpdc molar ratio. This composite was characterized by combining multiple techniques (PXRD, FT-IR and ^{27}Al MAS NMR). However, the analysis of its morphology by SEM revealed that this composite is highly heterogeneous since it is made of particles of different size and morphology while the presence of nanowires could not be detected despite the presence of a few elongated particles. At that stage, the synthesis conditions used for the preparation of this composite did not allow any control of the morphology of the DUT-5(Al) particles in this composite. One of the reasons is that no GO nanoscrolls were also evidenced in the composite by SEM. Therefore, GO sheets are not able to drive the structuration of DUT-5(Al) into nanowires. The synthesis of this composite still needs further optimization in order to induce the structuration of DUT-5(Al) crystals driven by GO nanoscrolls.

3.4.2. Optimization of DUT-5(Al)/GO synthesis

In this section, the optimization strategy followed to further optimize the synthesis of DUT-5(Al)/GO is discussed. This optimization was mandatory as our goal of forming anisotropic structures was not yet achieved.

3.4.2.1. Addition of water to the synthesis

As previously explained in **chapter 1**, based on reports in literature, the self - scrolling of GO could be initiated in a mixture of solvents.²¹⁻²⁴ Hence, to further assist the restrained scrolling in the tested DUT-5(Al)/GO samples, the addition of water in the synthesis protocol was tested. Many works in the state of the art have shown that adding DMF to an aqueous solution can initiate the scrolling of GO sheets.²⁴ Among these works, the most recent one is related to the design of MIL-69(Al)/GO NWs.²⁵ In this PhD project, the addition of water was tested using a high DMF/water ratio (i.e., low water content). The 4,4'-biphenyldicarboxylic acid (bpdc) ligands used in the synthesis of DUT-5(Al) possess a good solubility in alcohols (i.e., methanol, ethanol) and several organic solvents (DMF, DEF), yet bpdc is not very soluble in water. The optimization approach followed in this project was based on testing a high DMF/H₂O ratio of v:v = 9/1 to ensure the complete dissolution of the ligand, and gradually increasing the water content if needed. Generally, the synthesis of Al-MOFs in water leads to a competing formation of metal oxides/ hydroxides (e.g., Al₂O₃). The synthesis of these Al based MOFs is commonly performed under slightly acidic conditions to avoid the competitive formation of the MOF and the metal oxide/hydroxide. Indeed, the precipitation of Al(OH)₃ in aqueous solution is typically observed in the pH range between 5 and 10 as shown in **(Figure 3-19)**.²⁶ Yet, it should be considered that the addition of acids leads to the protonation of the carboxylate ligands used in the synthesis and thus hinders the solubilization of the ligands. Hence, to enhance the solubilization of the organic linker, the synthesis of the composite was performed

CHAPTER 3: DUT-5(Al) and DUT-5(Al)/GO

under reflux. Besides, in the presence of an organic solvent like DMF, the solubilization of the ligands is promoted while the formation of $\text{Al}(\text{OH})_3$ is limited.²⁷ So instead of using a reaction temperature of 120°C under reflux, the synthesis temperature was increased to 150°C.

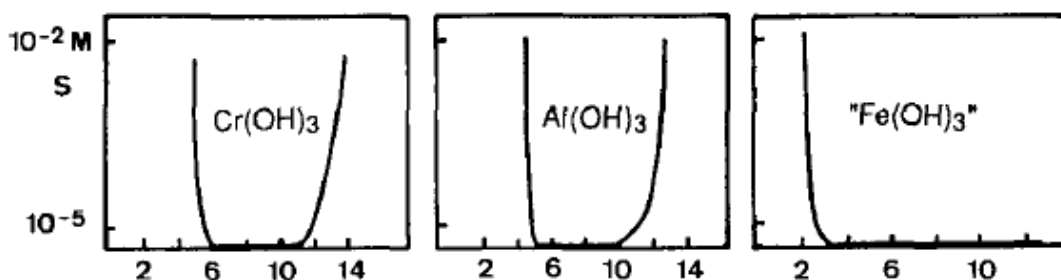


Figure 3-19: Precipitation diagram of Cr(III), Al(III), and Fe(III).²⁶

DUT-5(Al)/GO composites were synthesized under various solvent ratios and characterized by PXRD, FT-IR spectroscopy, and SEM to study the effect of the nature of solvents and the solvent ratios on the crystalline structure of DUT-5 as well as the microstructural properties and the morphology of the DUT-5(Al) based composite. The first optimization trial was performed in a solution of 22.5 mL DMF and 2.5 mL water (DMF/H₂O, v:v = 9/1) using the same synthesis protocol discussed above. Hence, 1.167 g of GO slurry was dissolved in a 25 mL solution of DMF and water, stirred, and sonicated for few minutes. Then, 170 mg of 4,4'-biphenyldicarboxylic acid (bpdc) (0.70 mmol) were added and under stirring. 262.6 mg of $\text{Al}(\text{NO}_3)_3 \cdot 9\text{H}_2\text{O}$ (0.70 mmol) were then added and the solution was then put under reflux for 24 hours.

As observed in the PXRD pattern in **(Figure 3-20, A)**, unfortunately, using the mentioned solvent ratios, an amorphous composite was obtained. This was explained by the strong band observed in the composite at 1670 cm^{-1} , corresponding to the carboxylic acid group of unreacted bpdc ligand as observed by FT-IR spectroscopy in **(Figure 3-20, B)**.

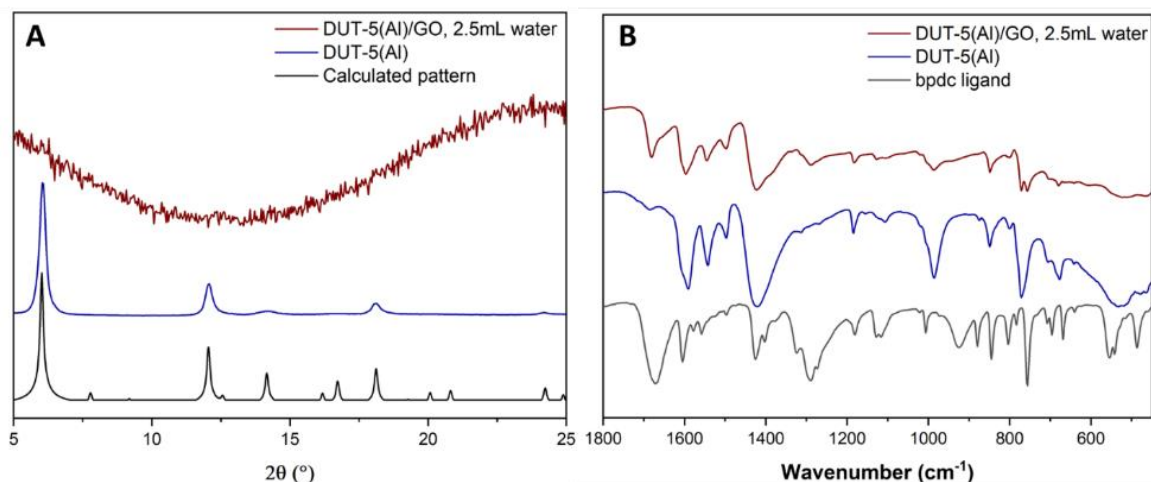


Figure 3-20: (A) PXRD patterns of calculated and synthesized DUT-5(Al) and DUT-5(Al)/GO after the addition of 2.5/25 mL water to the synthesis. (B) FT-IR spectra of bpdc ligand, DUT-5(Al), and DUT-5(Al)/GO after this addition of water.

Yet, the samples were characterized by SEM to verify if there is any effect of water addition on the sample from a morphological point of view. As observed in **(Figure 3-21)**, in comparison to the sample synthesized in pure DMF **(Figure 3-18)**, the addition of 10 vol.% water to the synthesis led to the formation of monodisperse microspheres of 1 μm in diameter resulting from the aggregation of self-arranged nanorods with length ranging between 150 and 300 nm. These microspheres coexist with nanorods of length up to 400 nm **(Figure 3-21, right)**.

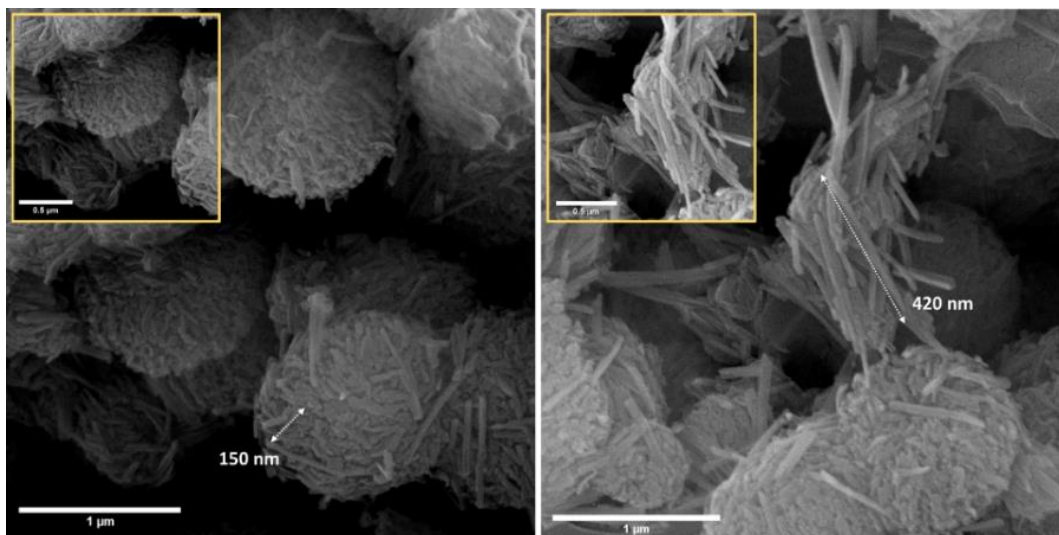


Figure 3-21: SEM images of DUT-5(Al)/GO synthesized in a 25 mL mixture of DMF/ H₂O v:v= 9/1.

Furthermore, it should be noted that the observed morphology is comparable to that observed in case of the pure DUT-5(Al) nanoparticles. As shown previously, DUT-5(Al) consist of aggregates made of nanorods but with a smaller diameter 40-50 nm (**Figure 3-8 and 3-9**). Moreover, the morphology of the aggregates in DUT-5/GO composites and pure DUT-5 is different. DUT-5/GO consist of spheroidal aggregates while DUT-5 is made of disk-shaped aggregates. Despite its amorphous nature, this composite presents interesting microstructural features related to the presence of anisotropic particles. However, we need to optimize the crystallinity of the MOF.

3.4.2.2. Optimization of reactants concentration

To obtain a crystalline composite, it was important to further optimize the synthesis. As seen by FT-IR spectroscopy a large amount of unreacted ligand was presented in the sample, suggesting its partial dissolution during the synthesis. Hence, the synthesis was performed in diluted conditions, in order to favor the bpdc dissolution. So, the reactants were diluted by a factor of two. The synthesis of DUT-5(Al)/GO was repeated in a mixture of 45 mL DMF and 5 mL water (DMF/H₂O, v:v = 9/1), while keeping the same amount of GO slurry, bpdc ligand, and aluminum salt. Thus, 1.167 g of GO slurry was dissolved in a solution of 50 mL DMF and water, stirred, and sonicated for few minutes. Then, 170 mg of 4,4'-biphenyldicarboxylic acid (bpdc) (0.70 mmol) were added and under stirring. 262.6 mg of Al(NO₃)₃·9H₂O (0.70 mmol) were then added and the solution was then put under reflux for 24 hours. As shown in (**Figure 3-22**), characterization by PXRD and FT-IR spectroscopy revealed much improved results after dilution.

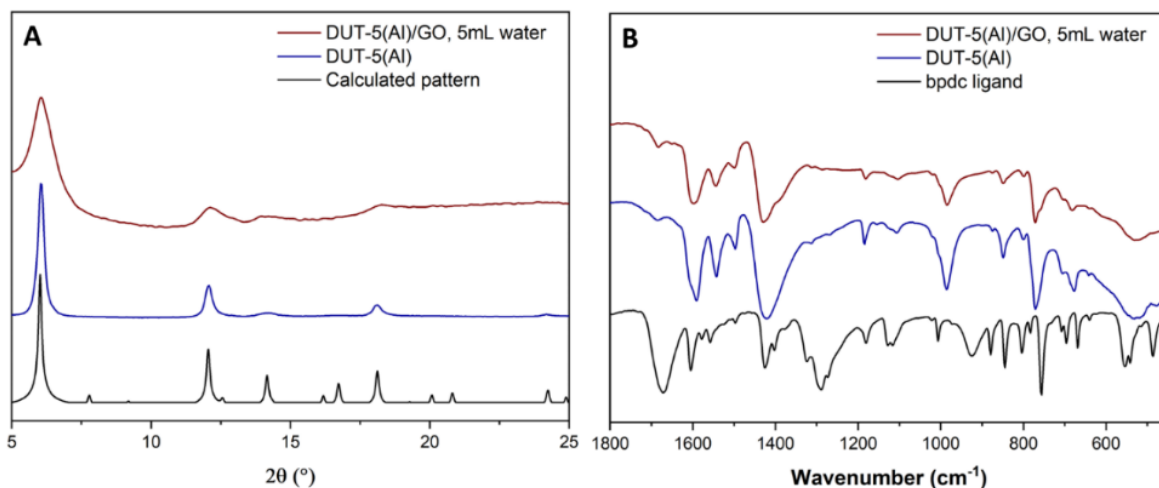


Figure 3-22: (A) PXRD patterns of calculated DUT-5(Al), synthesized DUT-5(Al), and DUT-5(Al)/GO after dilution by two in a mixture of DMF/ H₂O v:v= 9/1. (B) FT-IR spectra of bpdc ligand, DUT-5(Al), and DUT-5(Al)/GO after dilution by two in a mixture of DMF/ H₂O v:v= 9/1.

A crystalline sample is obtained whose experimental PXRD pattern is in good agreement with the calculated pattern of pure DUT-5(Al). Despite being much wider, the characteristic Bragg peaks of DUT-5(Al) at 6.01, 12.05, and 14.15° were all observed in the composite. Besides, a small amount of unreacted ligands was observed by FT-IR spectroscopy as shown by the small band at 1670 cm⁻¹ corresponding to the unreacted carboxylic acid of the free bpdc ligand. Nevertheless, it should be mentioned that the obtained PXRD profile was not very reproducible. Two out of five syntheses yielded crystalline samples, while other samples are amorphous as shown by PXRD. Yet, the chosen crystalline DUT-5(Al)/GO sample was characterized by SEM in order to study the impact of the reactants dilution on the morphology of the DUT-5(Al) based composite. For instance, interesting results were obtained by SEM. Once again, the presence of a mixture of solvents led to the formation of well-defined elongated structures (**Figure 3-21 and 3-23**). Besides, GO nanoscrolls can be clearly visualized on (**Figure 3-23**) thereby showing the positive effect of the solvent nature and reactants concentration on the scrolling process of GO. After dilution, despite keeping the same solvents ratio (i.e., DMF/ H₂O v:v= 9/1), the increase of DMF content in a solution of DMF/water led to the formation of more elongated structures. As

CHAPTER 3: DUT-5(Al) and DUT-5(Al)/GO

discussed in **chapter 1**, this is in accordance with results previously reported by Tang *et al.*²¹ GO layers do not assemble into nanoscrolls in water alone, and the addition of DMF is needed to induce this scrolling effect. Nevertheless, it cannot be established at this stage whether these observations are only related to the change in solvent composition, or also the diluted concentration of GO and/or the reactants in the composite.

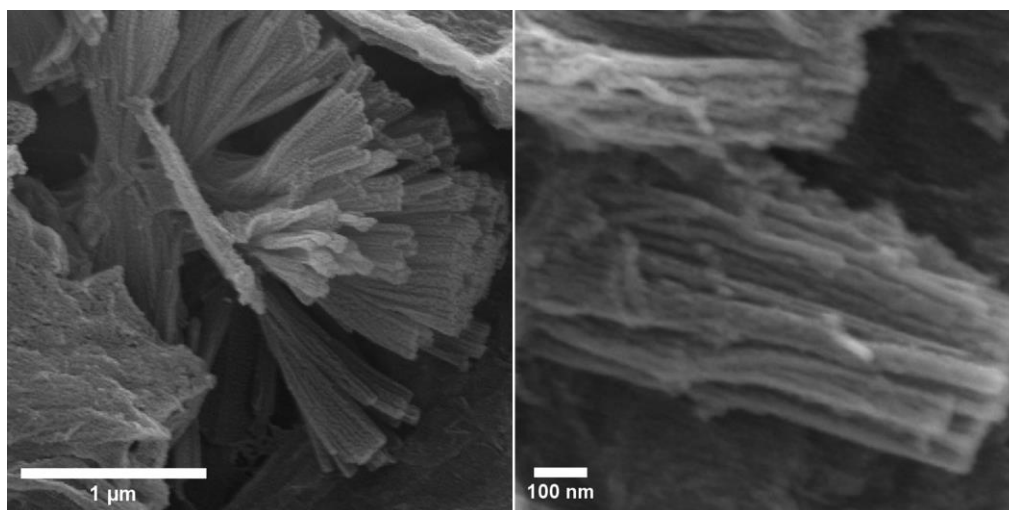


Figure 3-23: SEM images of DUT-5(Al)/GO synthesized in a 50 mL mixture of DMF/ H₂O v:v= 9/1.

Hence, it can be concluded that the addition of water to the synthesis solution has led to promising results in terms of DUT-5 morphology. The use of a water-DMF mixture as solvent favors the scrolling of GO. It is worth mentioning that the DMF/H₂O ratio with a v:v= 9/1 was not changed as it was not possible to form a crystalline composite with higher quantities of water or form anisotropic structures with a lower one.

3.4.2.3. Tuning the reaction time

Despite the promising results obtained in terms of morphology, the synthesis of DUT-5(Al)/GO in a 50 mL solution of DMF/water (v:v= 9/1) suffered from a major drawback in terms of synthesis reproducibility. The synthesis of the composite under reflux for 24 hours was not very reproducible. Hence, it is essential to study the

formation and growth process of this composite to better understand its formation and optimize the reproducibility of the synthesis. To achieve this goal, an *ex-situ* kinetic study was performed on the DUT-5(Al)/GO synthesis. The composite was put under reflux for 14 days in order to study its formation kinetics. Sample extractions were done at several intervals and were characterized both in suspension (by WAXS) and in the solid state (by PXRD, FT-IR spectroscopy, and TEM).

- **Ex-situ study of (as) synthesized sample in suspension**

The kinetic study of DUT-5(Al)/GO synthesis was performed using Wide Angle X-ray Scattering (WAXS). Sample extractions were performed throughout the 14 days of synthesis, and WAXS was performed on the as synthesized DUT-5(Al)/GO samples in synthesis suspension. As shown in **(Figure 3-24)**, the collected data was plotted and show the evolution of WAXS patterns with time. The recorded scattering data was then plotted in the form of the first peak intensity of the scattering vector at 0.43 \AA^{-1} as a function of reaction time **(Figure 3-25, A)**. Indeed, it can be observed that the intensity of the first peak kept increasing with the reaction time. It first increases rapidly up to 168 hours (7 days), and then more slowly, almost reaching a plateau after 264 hours (11 days) **(Figure 3-25, A)**. The evolution of the first peak intensity is then used to establish a correlation between the peaks FWHM and reaction time, thereby allowing the evaluation of crystallite domain size as a function of the reaction time. Thus, it can be observed through the plotted correlation length that the crystallite domain size (diameter of the MOF particle) increases rapidly reaching an average size of 50 nm after 168 hours, and then it increases more slowly reaching almost a range of 50-55 nm after 264 hours **(Figure 3-25, B)**. Thus, based on these experimental observations, the crystallite domain of DUT-5(Al)/GO can reach a maximum average size of 50-55 nm, yet the MOF continues to form (i.e., the number of MOF crystals keeps increasing) up to 11 days as the intensity of the first peak keeps increasing till then.

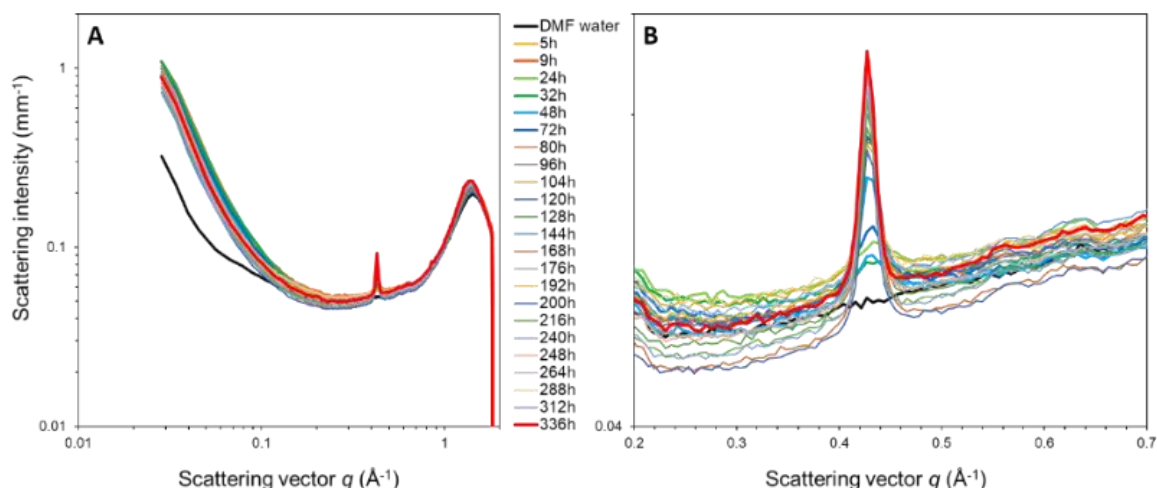


Figure 3-24: Ex-situ WAXS kinetic study of DUT-5(Al)/GO characterized in synthesis suspension. (A) Data plot, (B) Zoom in on the evolution of the first peak as a function of reaction time.

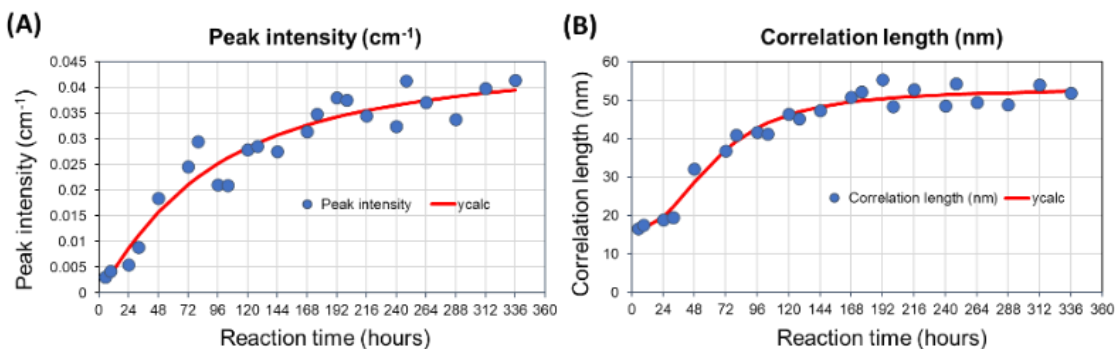


Figure 3-25: Lorentzian fit based on the peak analysis of recorded WAXS data for DUT-5(Al)/GO extractions for 14 days synthesis. (A) Peak intensity as a function of reaction time. (B) Correlation length revealing the increase in crystallite size as a function of reaction time.

It is of interest to compare the results obtained for the DUT-5/GO composite, to those obtained in case of the pure DUT-5 synthesized in pure DMF. In case of pure DUT-5(Al) (see Figure 3-14), the intensity of the first peak does not evolve after 10 hours of synthesis only. The crystallite domain of DUT-5(Al) reaches a maximum size of 50 nm that did not increase at a longer reaction time (Figure 3-14, B). In comparison, 168 hours were needed in case of the composite to reach the same size of 50 nm, and the crystallite domains kept growing with increasing the reaction time until they reached a fixed size of around 50-55 nm after 11 days of synthesis. Hence, despite presenting the same size of the crystallite domain (50-55 nm), it can be clearly shown

that the formation kinetics of DUT-5(Al) are affected by the modified synthesis conditions and the addition of GO. In the case of DUT-5(Al)/GO composite, a longer reaction time is required to induce the crystallization of DUT-5(Al) in comparison to pure DUT-5(Al).

- **Ex-situ study of washed and dried sample extractions**

A similar *ex-situ* kinetic study was performed using PXRD, FT-IR spectroscopy, and TEM. However, herein the extracted samples were characterized as powders after being washed and dried. The synthesis of DUT-5(Al)/GO under reflux was started, and 5 mL of sample were extracted at different intervals of the reaction. 5 mL of sample were centrifuged and washed 3 times with 5 mL of ethanol. Then, 1 mL of each sample was diluted for TEM measurements, while the 4 mL of sample were dried for 1 hour at 100 °C to perform PXRD and FT-IR measurements. Considering the structural characterization of DUT-5(Al)/GO, it was observed that a crystalline pattern started to be observed after 48 hours of synthesis (**Figure 3-26, A**). This explains the previous reproducibility issues faced when considering a 24 hours synthesis. The same results were obtained by FT-IR spectroscopy (**Figure 3-26, B**). The characteristic bands of DUT-5(Al) ($\nu_{\text{as}}(\text{C-O}) = 1608\text{--}1570\text{ cm}^{-1}$ and ($\nu_{\text{s}}(\text{C-O}) = 1430$ and 1364 cm^{-1}) start to appear after 48 hours only. The recorded data led to other critical conclusions. For the PXRD pattern of the the dried sample, the peak at $2\theta = 6.01^\circ$, corresponding to the (1,0,1) reflection, is shifted to a higher angle in comparison to the calculated pattern of DUT-5. In particular, the shift in the first peak is related to the diameter of the microporous tunnel of DUT-5. This phenomenon was not observed for the as-synthesized samples that were characterized as dispersed powders in suspension by WAXS. In fact, according to Bragg's law, a shift of the first PXRD peak to higher angle is ascribed to the contraction of the studied framework. Such phenomenon can be

potentially explained by a flexibility behavior of DUT-5(Al). These results will be the subject of the **next chapter** of the manuscript.

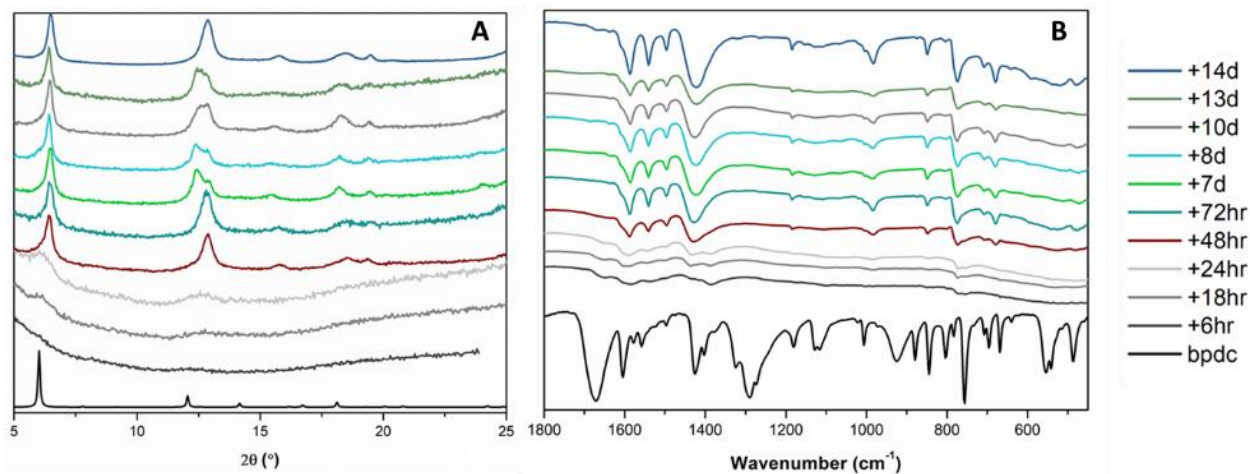


Figure 3-26: (A) Ex-situ PXRD patterns DUT-5(Al) calculated pattern and DUT-5(Al)/GO extracted at different intervals during synthesis and washed with ethanol. (B) Ex-situ FT-IR spectra of bpdC ligand and DUT-5(Al)/GO extracted and washed at different intervals during synthesis.

Moreover, as mentioned above, the different extracted samples were characterized by TEM (**Figure 3-27**). From a microscopic point of view, images collected by TEM presented very interesting results. GO sheets cover most of the particles during the first 2 days of synthesis. It was observed that the DUT-5(Al)/GO composite starts to grow in form of elongated structures after 18 hours of synthesis only. First, the elongated structures are obtained in the form of bundles. Similar bundles of tubular structures were shown earlier when the composite was synthesized in 24 hours only (**Figure 3-23, right**). Then, these elongated structures keep growing in length until the bundles start to separate after 48 hours. Remarkably, it can be observed that the length of the particles keeps growing with the increase of reaction time. For instance, the length of these particles increased from 1-2 μm in 24 hours to 4-5 μm in 48 hours (**Figure 3-27**). This length kept increasing with the increase in reaction time until it reached almost a value of 9-10 μm after 14 days of synthesis.

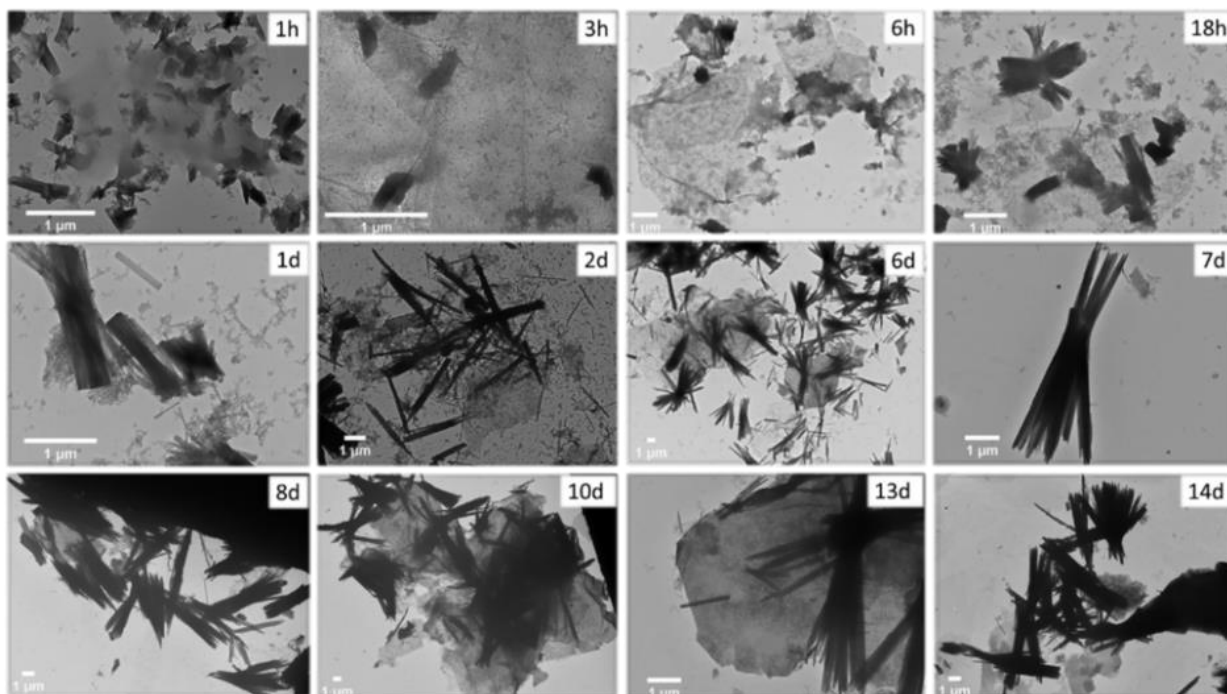


Figure 3-27: TEM images of DUT-5(Al)/GO extracted at different intervals during a 14-days reflux synthesis. All images are plot at a scale of 1 μm . Insert: reaction time.

Therefore, it can be concluded that through controlling the reaction time, it was possible to control the size of the obtained elongated particles. It was possible to obtain longer crystallites by increasing the reaction time. Moreover, based on experimental observations by WAXS, it was deduced that the crystallite size reaches a fixed size of 50-55 nm after 12 days of synthesis (**Figure 3-25**), however, TEM images show much bigger particles that can reach few micrometers (**Figure 3-27**). Thus, it could be assumed that the crystallite size of 50-55 nm deduced from the WAXS corresponds to the particle's diameter and not the length. Such results are of huge interest as it could indicate that the same crystallite of DUT-5(Al) (50-55 nm) increased in length in a confined direction using GO. Finally, by calculating the aspect ratio (i.e., length divided by width) of the obtained elongated structures, it can be stated that the DUT-5(Al)/GO obtained after 14 days presents an aspect ratio much higher than 20 and such nanoparticle thus corresponds to nanowires (NWs). Most of the NWs obtained after 2 weeks of synthesis has an average length of 6-8 μm and a diameter

of 70-90 nm. Therefore, it can be stated that the DUT-5(Al)/GO NWs obtained following 2 weeks of reflux present the optimized DUT-5(Al) based composite. First, 1.167 g of GO slurry was dissolved in a solution of 50 mL solution (45mL DMF + 5mL water), stirred, and sonicated for few minutes. Then, 170 mg of 4,4'-biphenyldicarboxylic acid (bpdc) (0.70 mmol) were added and under stirring. 262.6 mg of $\text{Al}(\text{NO}_3)_3 \cdot 9\text{H}_2\text{O}$ (0.70 mmol) were then added and the solution was then put under reflux for 336 hours (14 days) at 150 °C. This sample will be referred to as DUT-5(Al)/GO-336.

3.4.2.4. Studying the MOF content inside DUT-5(Al)/GO-336

Following the promising results obtained, it was important to study the chemical composition of the obtained DUT-5(Al)/GO-336 NWs. Among the methods used to characterize MOF/GO composites, X-ray photoelectron spectroscopy (XPS) appears particularly relevant as it gives access to both the elemental composition and the chemical environments of the elements detected at the sample surface. Here, XPS analyses were performed to highlight the interactions between the MOF and the GO, as well as stating the amount of MOF inside the composite. Thus, the surface elemental composition and the oxidation states of pure GO, pure DUT-5(Al) NPs, and DUT-5(A)/GO were studied by XPS (in collaboration with M. Fregnaud, ILV). Prior to the measurements, all samples were pressed to form pellets using KBr. Pure GO was characterized in its normal conditions as a slurry without any heat treatment. **(Figure 3-28)** shows the XPS survey spectra obtained on DUT-5(Al) NPs, GO and DUT-5(Al)/GO-336 composite.

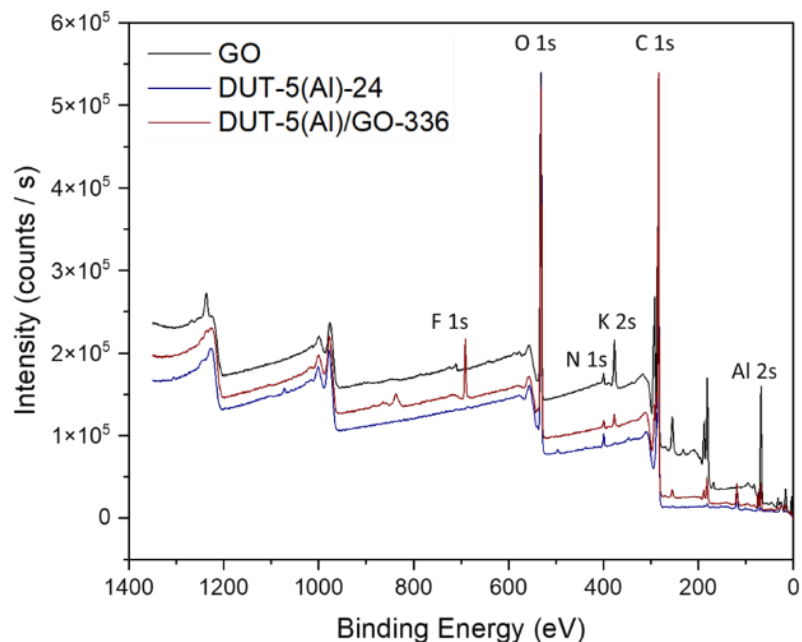


Figure 3-28: XPS survey spectra of GO (black), DUT-5(Al) NPs (dark blue), and DUT-5(Al)/GO-336 (brown).

The XPS survey spectrum of GO sample is dominated by the presence of the chemical elements C and O by their main spectral signatures C 1s and O 1s, at the respective binding energies of 285 and 532 eV. Traces of S 2p and Fe 2p are visible at 168 and 711 eV. For DUT-5(Al), the XPS survey analysis reveals, as expected, the major presence of C, O and Al by the detection of C 1s, O 1s and Al 2s at 284, 531 and 119 eV. Traces of Na 1s, Cl 2p and Si 2p are evidenced at 1072, 198 and 101 eV. The XPS survey spectrum of DUT-5(Al)/GO-336 consists of photopeaks that can be assigned respectively to DUT-5(Al) (C 1s, O 1s, and Al 2s), GO (C 1s and O 1s) and an extra peak at 691 eV attributed to F1s. For the three samples, N 1s, K 2s and Br 3d core levels are systematically detected at 400, 377 and 68 eV, respectively. The presence of nitrogen on the surface is associated with residual DMF while K and Br in the 1:1 ratio are attributed to the KBr used in forming sample pellets for technical purposes. Fluorine is evidenced in the composite and is attributed to some impurities as the element is not present in any synthesis precursor. **(Table 3-1)** summarizes the XPS chemical composition in the three samples obtained from the survey spectra analysis.

Table 3-1: XPS chemical composition of GO, DUT-5(Al) and DUT-5(Al)/GO-336 in atomic %.

Elements	GO	DUT-5(Al)	DUT-5(Al)/GO-336
C 1s	58.3	67.3	58.2
O 1s	25.9	26.1	28.1
Br 3d	7.7	0.17	1.5
Al 2s	0	4.4	5.0
K2s	6.6	0.3	1.8
N 1s	1.6	1.7	1.3
F 1s	0	0	4.2

The C 1s core level spectra of GO, DUT-5(Al) NPs, and DUT-5(Al)/GO-336 composite are presented in **(Figure 3-29)**. The C1s signal of the DUT-5(Al)/GO-336 composite is dominated by the DUT-5(Al) signature. Both the MOF and MOF/GO show two main peaks at 288.5 and 284.5 eV. These peaks are attributed to O-C=O groups and sp^2 carbons (C=C aromatic) of the bpdc linker, respectively **(Figure 3-29)**.²⁸ On the other side, GO, also shown in **(Figure 3-29)**, clearly shows a different signal in comparison to DUT-5(Al) and DUT-5(Al)/GO-336 in the C 1s region. It presents a peak at 284.5 eV attributed to sp^2 carbon and a contribution at 286.3 eV, attributed to C-O species of the graphene oxide. **(Table 3-2)** summarizes the observed chemical bonds in the C 1s region for the MOF, GO and composite samples. Thus, it can be assumed that GO was partially reduced during the synthesis of this composite. The reduction of GO into graphene could be expected since the samples were exposed to a high temperature of 150 °C for 14 days of synthesis. This was further validated by the fact that it was not possible to fit the XPS spectrum of MOF/GO composite by considering a linear combination of MOF and GO. This is mainly due to the absence of CO bonds (expected contribution at 286.3 eV) in the C 1s spectrum of the composite. Interestingly, the XPS spectrum of the composite can be fitted by a linear combination of DUT-5(Al) and graphene, assuming a MOF content of 96 wt.%.

The envelope obtained by the linear combination of graphene and DUT-5(Al) spectra considering 4 wt.% of graphene is presented in **(Figure 3-29)**.

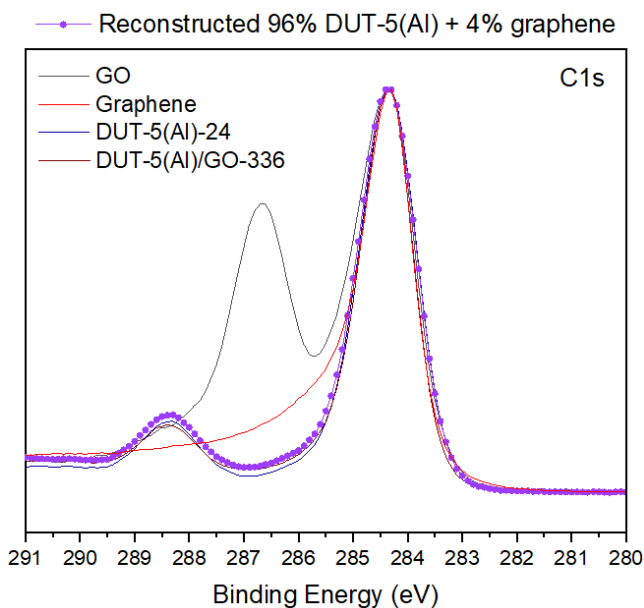


Figure 3-29: XPS high-resolution spectra (C1s region) of GO (grey), graphene (red), DUT-5(Al) NPs (dark blue), and washed DUT-5(Al)/GO-336 (brown). The linear combination of GO and DUT-5(Al) spectra considering 4 wt.% graphene content is displayed in purple.

It is worth noting that in case of the as-synthesized DUT-5(Al)/GO-336, the XPS spectrum of the composite can be fitted by a linear combination of DUT-5(Al) and graphene spectra, assuming a MOF content of 90 wt.%. The envelope obtained by the linear combination of graphene and DUT-5(Al) spectra considering 10 wt.% of graphene is presented in **(Figure 3-30)**. When compared to experimental ratios, as mentioned in **chapter 2**, an Al/GO ratio of 65 wt.% was used during the composite synthesis.

$$r \left(\frac{\text{Al}}{\text{GO}} \right) = \frac{m_{\text{Al}}}{m_{\text{GO}}} = \frac{0.019}{0.025 \times m_{\text{GO slurry}}} = 0.65$$

By simple calculation, an Al/GO ratio of 0.65 corresponds to 87 wt.% of MOF content in the composite, which is in full agreement with the MOF content evaluated by XPS.

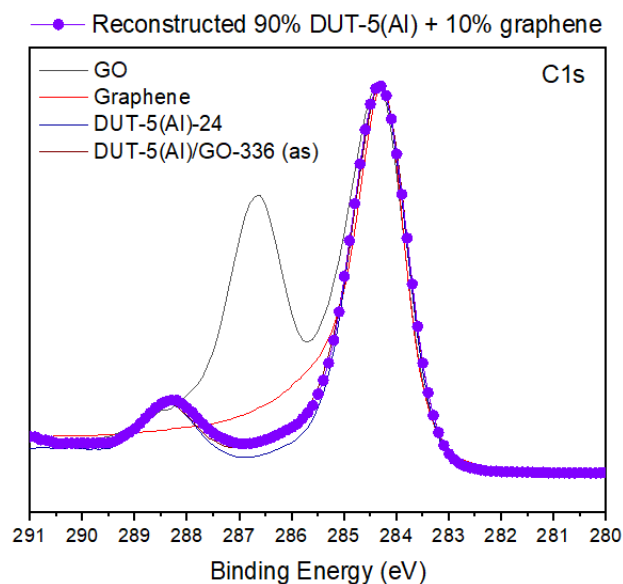


Figure 3-30: XPS high-resolution spectra (C1s region) of GO (grey), graphene (red), DUT-5(Al) NPs (dark blue), and as synthesized DUT-5(Al)/GO-336 (brown). The linear combination of GO and DUT-5(Al) spectra considering 10 wt.% graphene content is displayed in purple.

Table 3-2: Chemical environments observed in C 1s region for GO, DUT-5(Al), and DUT-5(Al)/GO.

Samples	Assignment	E _B (eV)
GO	C 1s C=C aromatic	284.5
	C 1s C-O	286.3
DUT-5(Al)	C 1s C=C aromatic	284.5
	C 1s O-C=O	288.5
DUT-5(Al)/GO-336	C 1s C=C aromatic	284.5
	C 1s O-C=O	288.5

In addition, O 1s spectral region for the three sample was also investigated. For the pure MOF, the O 1s signal is dominated by a main contribution at 531.6 eV related to C=O. In the case of GO, the O1s peak is centered at 532.9 eV corresponding to the C-OH. The feature at 532.9 eV, characteristic of GO, was not observed in DUT-5(Al)/GO-336 which tends to confirm that GO was reduced during the synthesis. Such results are in good agreement with the previous results obtained on the C 1s data (Figure 3-29 and 3-30). The position of the main O1s peak in the composite is also consistent

with the previous observations. Indeed, it is close in binding energy from the MOF signature which confirms that the MOF is in large excess in the composite, and it dominates in the XPS signal. In conclusion, the XPS experiments performed on GO, DUT-5(Al) NPs, and DUT-5(Al)/GO-336 confirm the successful synthesis of the MOF based composite. Also, based on these experiments, it was concluded that the DUT-5(Al) content in the DUT-5(Al)/GO-336 composite is 90 wt.%, and almost 6 wt.% of GO are lost after washing the sample resulting 96 wt.% of DUT-5(Al) in the composite.

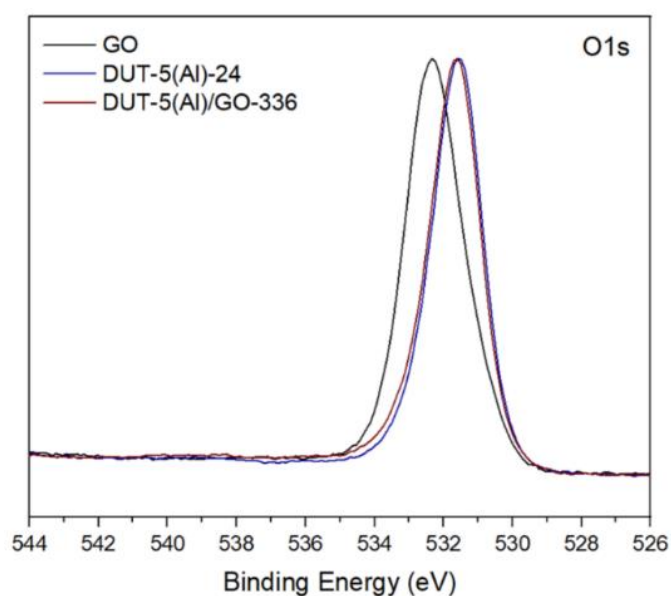


Figure 3-31: XPS high-resolution spectra (O1s region) of GO (black), DUT-5(Al) NPs (dark blue), and DUT-5(Al)/GO (brown).

Table 3-3: Main chemical environments observed in the O 1s core level spectrum of GO, DUT-5(Al), and DUT-5(Al)/GO-336.

Samples	Assignment	E _B (eV)
GO	O 1s C-OH	532.9
DUT-5(Al)	O 1s C=O	531.6
DUT-5(Al)/GO-336	O 1s C=O	531.6

3.4.2.5. Studying the adsorption properties of DUT-5(Al)/GO-336 under N₂

As mentioned in **chapter 2**, one of the objectives of this PhD project is to extend the concept applied to MIL-69(Al) into MOFs with a higher permanent porosity. It was explained that despite the successfully induced hierarchical porosity in the MIL-69(Al) structure following the addition of GO, it still suffered a low porosity characterized by a BET surface area of 125 m²/g.²⁵ Hence, of interest is to study the porosity of the designed DUT-5(Al)/GO-336 NWs, and to compare it with the previously reported MIL-69(Al)/GO. Thus, N₂ physisorption measurements were performed on DUT-5(Al) and DUT-5(Al)/GO-336. The samples were activated at 160 °C overnight, then N₂ physisorption measurements were performed on 35 mg of each sample.

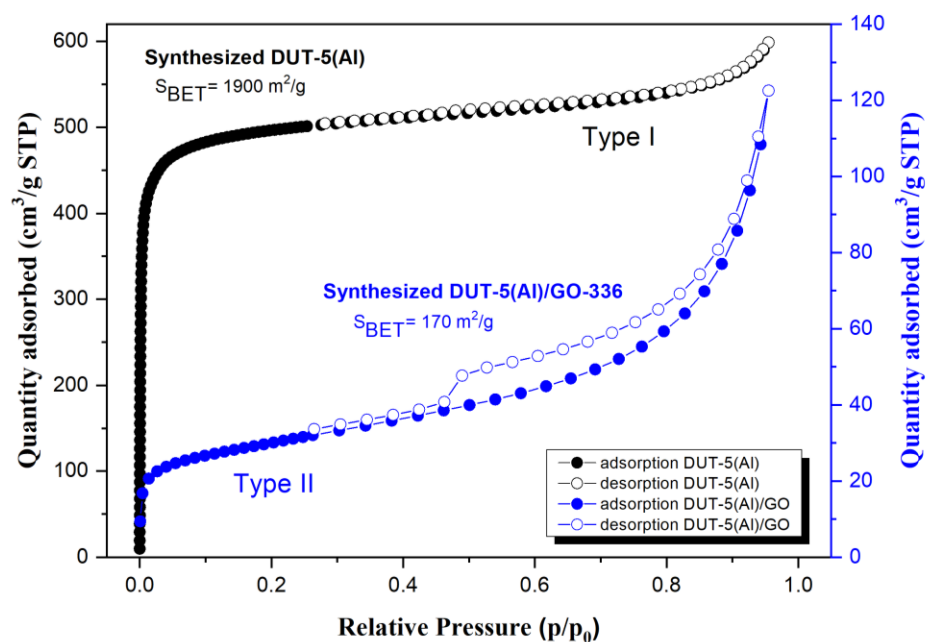


Figure 3-32: N₂ physisorption isotherms of DUT-5(Al) MOF and DUT-5(Al)/GO-336 composite.

As shown in **(Figure 3-32)**, similar to the MIL-69(Al) case, the addition of graphene oxide into DUT-5(Al) has led to a hierarchically porous structure that was not observed in case of the pure MOF. This can be deduced from the hysteresis of the type IIb N₂ isotherm which is absent in case of the pure DUT-5(Al). Moreover, once again, a huge

drop in the BET surface area of the MOF is observed after the addition of GO. The BET surface area of DUT-5(Al) dropped from 1900 to 170 m²/g. Regardless of the fact that DUT-5(Al) has much larger tunnels compared to MIL-69(Al), (11.1×11.1 Å) compared to (2.7×13.6 Å), respectively, the DUT-5(Al)/GO presented a very close surface area to that of MIL-69(Al)/GO. To exclude the weight percentage of the nonporous GO (i.e., 4 wt. %), the adsorption isotherm of DUT-5(Al)/GO-336 was normalized to the weight of the MOF only, giving a normalized BET area close to ~1824 m² g⁻¹. This value is significantly higher than the experimental BET area of the composite and the low porosity of the composite cannot be fully explained by the presence of GO itself. This low porosity may arise from a peculiar microstructure of the composite since the GO sheets at the surface of MOF particles may hinder the accessibility of N₂ to the MOF tunnels. Moreover, we have observed a closure of the DUT-5(Al) tunnels once the composite is dried and activated.

3.5 EXPLORING THE EFFECT OF GO ADDITION

In spite of the promising results obtained, it should be highlighted that the results obtained in case of DUT-5(Al)/GO-336 cannot be directly compared with those obtained for DUT-5(Al). Different synthetic procedures were followed in the two cases. DUT-5(Al) was synthesized in 25 mL DMF for 24 hours, while DUT-5(Al)/GO-336 was synthesized in a 50 mL mixture of water and DMF for 336 hours. The two synthesis protocols differ in the employed solvent(s), reactants concentration, synthesis duration, and presence of GO. Therefore, it is difficult to conclude on a possible influence of GO on the formation and growth of DUT-5 nanowires. It was thus necessary to synthesize pure DUT-5(Al) by using the synthetic conditions used for the preparation of the DUT-5/GO-336 composites (excluding the presence of GO).

3.5.1. Effect of GO on reaction kinetics

DUT-5(Al) was synthesized under reflux for 14 days in a mixture of DMF and water without GO. An early reaction time study was then performed where samples were extracted every 10 minutes during the first hour of the synthesis and were characterized by WAXS. As shown in **(Figure 3-33)**, remarkably the obtained results were different from those obtained for both DUT-5(Al) synthesized by 24 hours reflux in DMF, and those obtained in presence of GO via reflux for 14 days in water and DMF.

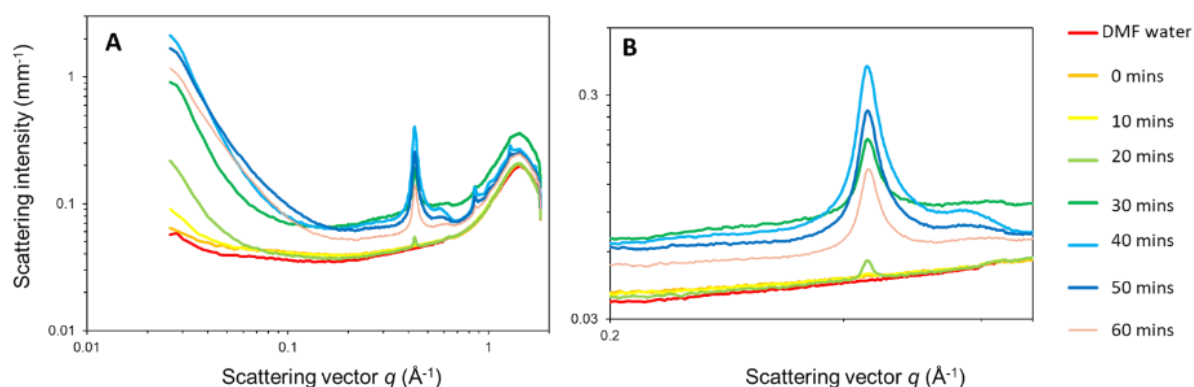


Figure 3-33: Early reaction times study by WAXS of DUT-5(Al) characterized in synthesis suspension. (A) Data plot, (B) Stacking of plotted to observe evolution in crystallinity as a function of time.

In the absence of GO, it was observed that the formation of DUT-5(Al) occurs after 30 minutes of synthesis only. As shown in **(Figure 3-33)**, the first peak of DUT-5(Al) at a scattering vector of 0.43 \AA^{-1} starts to appear after 30 minutes of synthesis. On the other hand, in the presence of GO, it was observed that the formation starts after 48 hours of synthesis. Besides, in case of DUT-5(Al) synthesized in DMF for 24 hours, it was observed that the organic ligand was still observed after 1 hour of synthesis, and the MOF ligands are completely coordinated after 2 hours. Thus, three different results were obtained following three different synthetic protocols. **(Table 3-4)** below summarizes the obtained results while mentioning the followed synthesis conditions.

Table 3-4. Summary of the effect of the different synthesis conditions on the formation kinetics of DUT-5(Al) crystals.

Sample label	Synthesis time	Synthesis solution	Formation time
DUT-5(Al)-24	24 hours	25 mL DMF	2 hours
DUT-5(Al)/GO-336	336 hours (14 days)	45 mL DMF + 5 mL water	48 hours
DUT-5(Al)-336	336 hours (14 days)	45 mL DMF + 5 mL water	30 minutes

By comparing the results summarized in **(Table 3-4)**, the formation of DUT-5(Al) crystals in a 50 mL mixture occurred faster than that in 25 mL DMF. This could be attributed to a faster dissolution and diffusion of the bpdc ligand in dilute conditions, leading to a faster formation of DUT-5(Al). In addition, the presence of water in case of DUT-5(Al)-336 can enhance the formation of Al chains as the presence of water is required for the hydrolysis and condensation of Al. Concerning the results obtained in the presence of GO, it can be concluded that the presence of GO led to a significant increase in the required time for the formation of DUT-5(Al) ($t = 48$ hr compared to $t \leq 2$ hr). This can be attributed to the fact that the coordinative oxygen functions of GO sheets can also interact with Al^{3+} cations at the beginning of the reaction and thus compete with bpdc linkers for Al. Besides, the presence of GO can lead to a slower diffusion of the bpdc linkers, leading to a slower formation.

3.5.2. Effect of GO on final morphology

Similarly, it was highly important to understand the templating role of GO in the formation of DUT-5(Al) based NWs. Therefore, DUT-5(Al)-336 and DUT-5(Al)/GO-336 were both characterized by several microscopic techniques (SEM, STEM-HAADF, SAED, and TEM). In fact, several batches of DUT-5(Al)-336 and DUT-5(Al)/GO-336 were synthesized and characterized to assess the reproducibility and homogeneity of the different samples.

3.5.2.1. Obtained morphology in presence of GO

Concerning the DUT-5(Al)/GO-336 composite, all synthesized batches were homogenous and presented the same morphology of long well-defined NWs when characterized by SEM, STEM-HAADF, and TEM (**Figure 3-34 and 3-35**). Almost all NWs have a similar diameter of (70-90 nm), and their length can reach up to 8-10 μm .

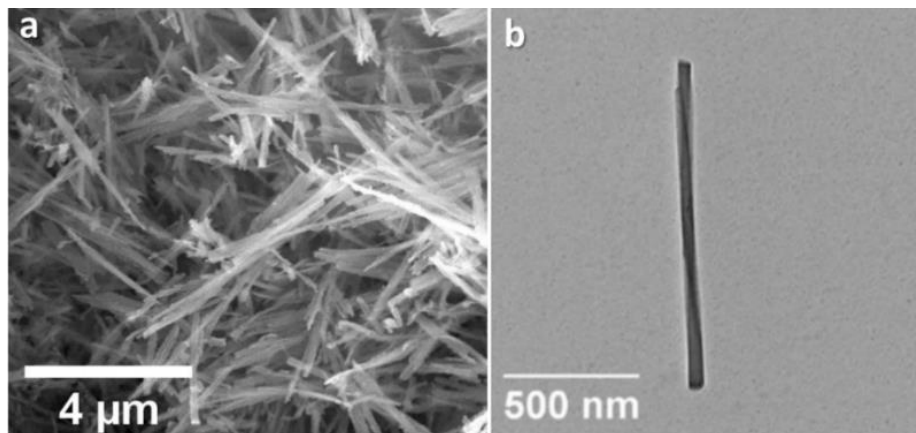


Figure 3-34: (a) SEM image of DUT-5(Al)/GO-336NWs and (b) TEM images of one isolated DUT-5(Al)/GO-336 NW.

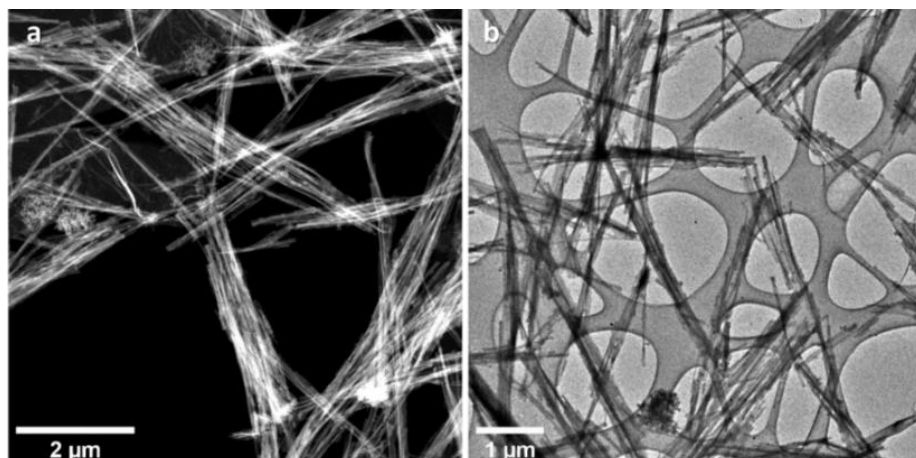


Figure 3-35: (a) STEM-HAADF and (b) TEM images of DUT-5(Al)/GO-336 NWs.

As well, when characterized by selected area electron diffraction (SAED), the DUT-5(Al) based composite showed that each nanowire corresponds to a single crystal of DUT-5(Al) growing along the [010] direction. This crystallographic direction is parallel to the chain axis of Al^{3+} octahedra of DUT-5(Al) (**Figure 3-36**) meaning that each nanowire

grows along the direction of the DUT-5 tunnels. Interestingly, this result is in accordance with observations reported in case of MIL-69(Al)/GO.²⁵ According to SAED, the MIL-69(Al)/GO composite is composed of single crystal MIL-69(Al) nanowires growing along the [001] direction which is parallel to the direction of Al chains in MIL-69(Al). Such results tend to indicate the structural directing role of GO.

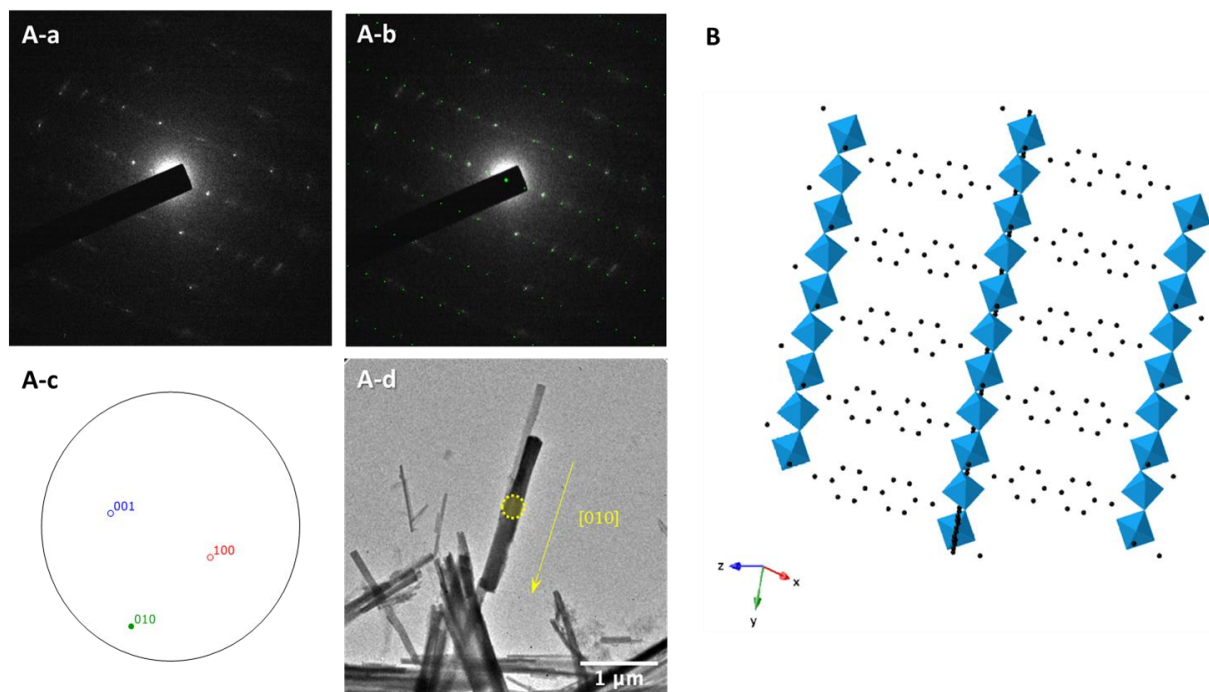


Figure 3-36: A-a experimental SAED of the DUT-5(Al)/GO-336 nanowire shown in A-d. A-b calculated SAED corresponding to the [1 -1 1] zone axis. The stereographic projection (A-c) that is related to the crystallographic orientation deduced from (A-a, b) indicates that the crystal growth proceeds along the [010] direction. (A-d) represents TEM bright field image of the NW; the elongation direction is also indicated. (B) Graphical presentation of DUT-5(Al) along [1 -1 1].

In addition, SAED patterns were recorded at different locations of the sample to ensure the homogeneity of the sample. **(Figure 3-37)** shows that DUT-5(Al) single crystals were observed in different locations of the sample.

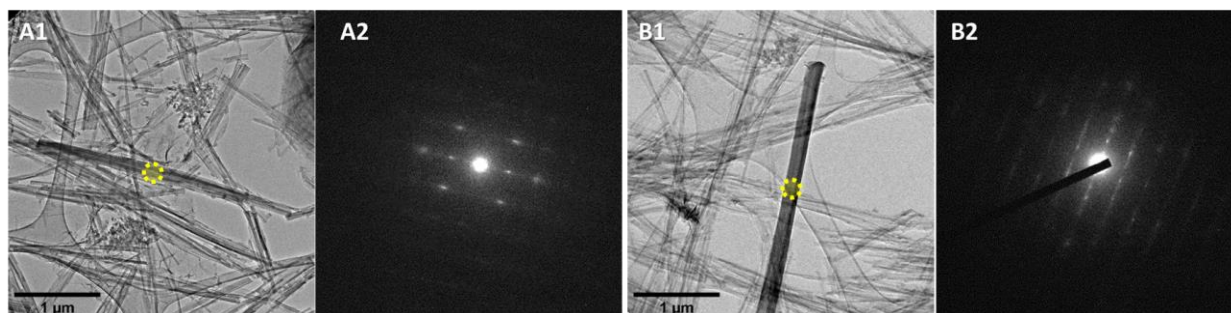


Figure 3-37: SAED patterns obtained at additional locations A and B in DUT-5(Al)/GO-336.

Moreover, the synthesized nanowires were analyzed by STEM-XEDS. The obtained results show that no impurities were observed by XEDS as only the elements constructing the MOF structure were observed and homogeneously distributed (i.e., carbon, aluminum, and oxygen).

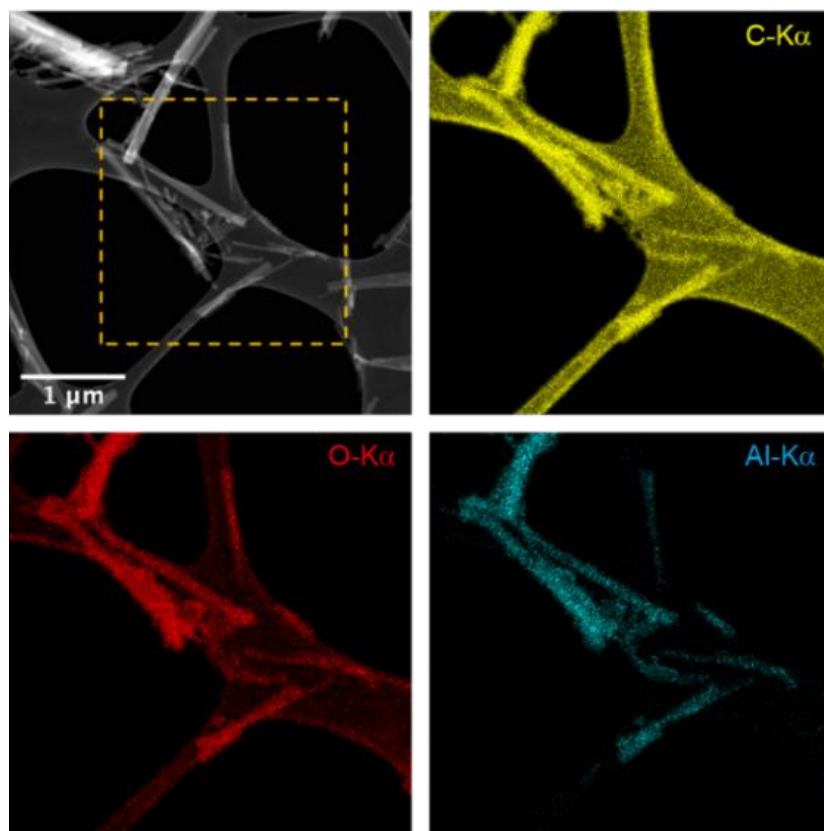


Figure 3-38: STEM-HAADF images of DUT-5(Al)/GO-336 and STEM-XEDS elemental mapping.

3.5.2.2. Morphology of DUT-5(Al)-336

On the other hand, DUT-5(Al)-336 samples were heterogenous. In most of the cases the obtained samples were made of two kinds of particles: spherical nanoparticles and elongated structures (**Figure 3-39, B**). Yet, the relative amount of each kind was not similar in the different batches. The spherical nanoparticles are built of self-arranged small nanoparticles. The sphere diameter is 500-700 nm. Concerning the elongated structures, they have a similar diameter to that of DUT-5(Al)/GO-336 NWs (70-90 nm), yet they are a little shorter (2-4 μm). Remarkably, when these elongated structures were isolated and characterized by SAED, they also presented a single crystalline structure, yet they are clearly less crystalline compared to the DUT-5(Al)/GO-336 NWs.

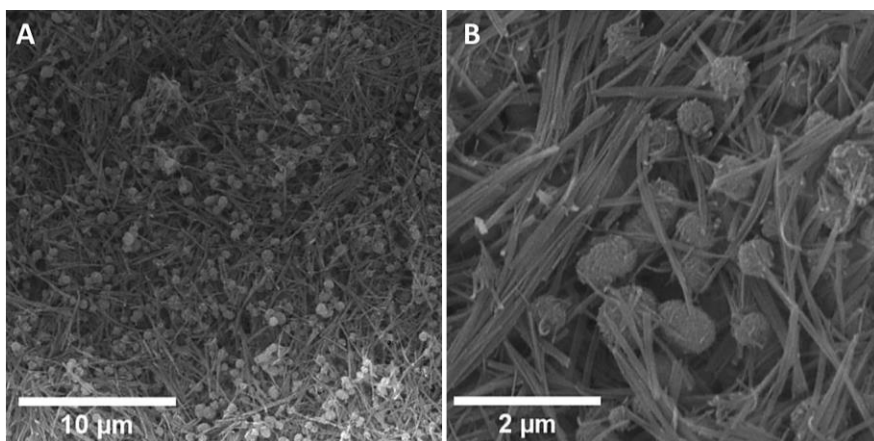


Figure 3-39: SEM images of DUT-5(Al)-336 showing both elongated structures and spherical arrangements.

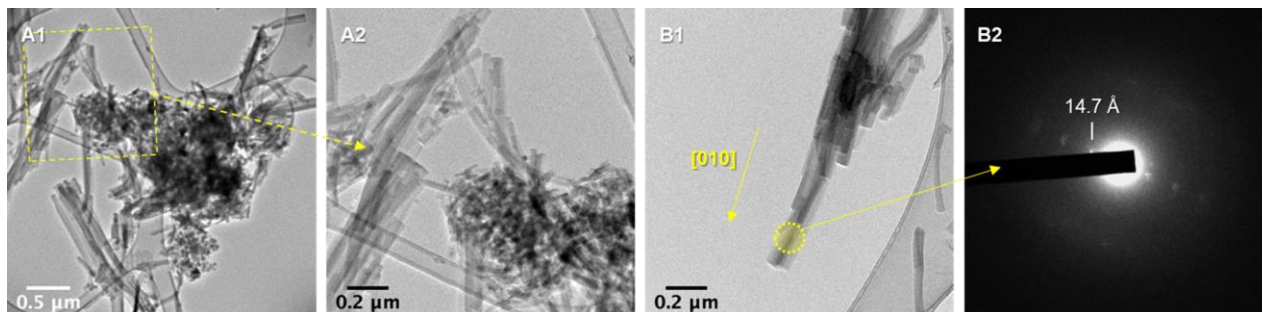


Figure 3-40: (A) TEM-BF images of DUT-5(Al)-336 showing both elongated structures and spherical arrangements. (B1) TEM-BF image of an elongated NW of DUT-5(Al)-336 and (B2) corresponding SAED. From the presence of the 101 reflections, it can be deduced that the elongation direction of the NW is [010].

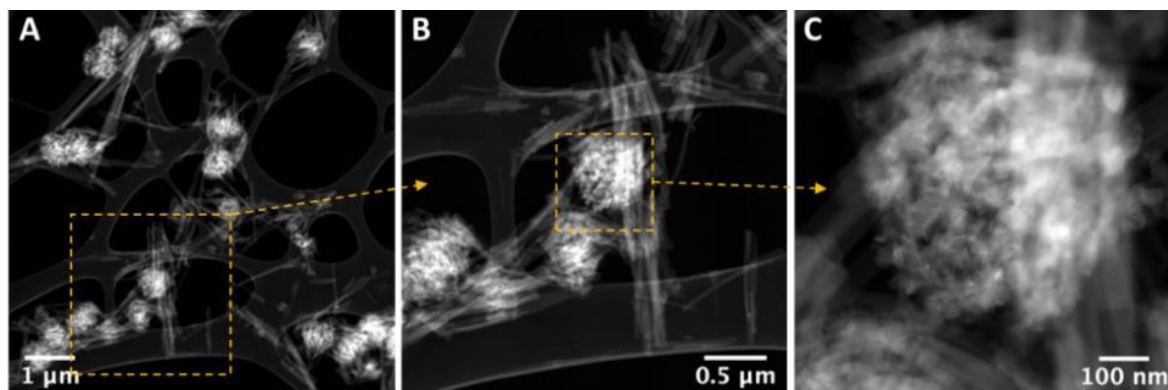


Figure 3-41: STEM-HAADF images of DUT-5(Al)-336 revealing the morphological heterogeneity of the sample.

Similarly to the case of the composite, DUT-5(Al)-336 was analyzed by STEM-XEDS and the obtained results show that no impurities were observed as only the elements constructing the MOF structure were observed (i.e., carbon, aluminum, and oxygen).

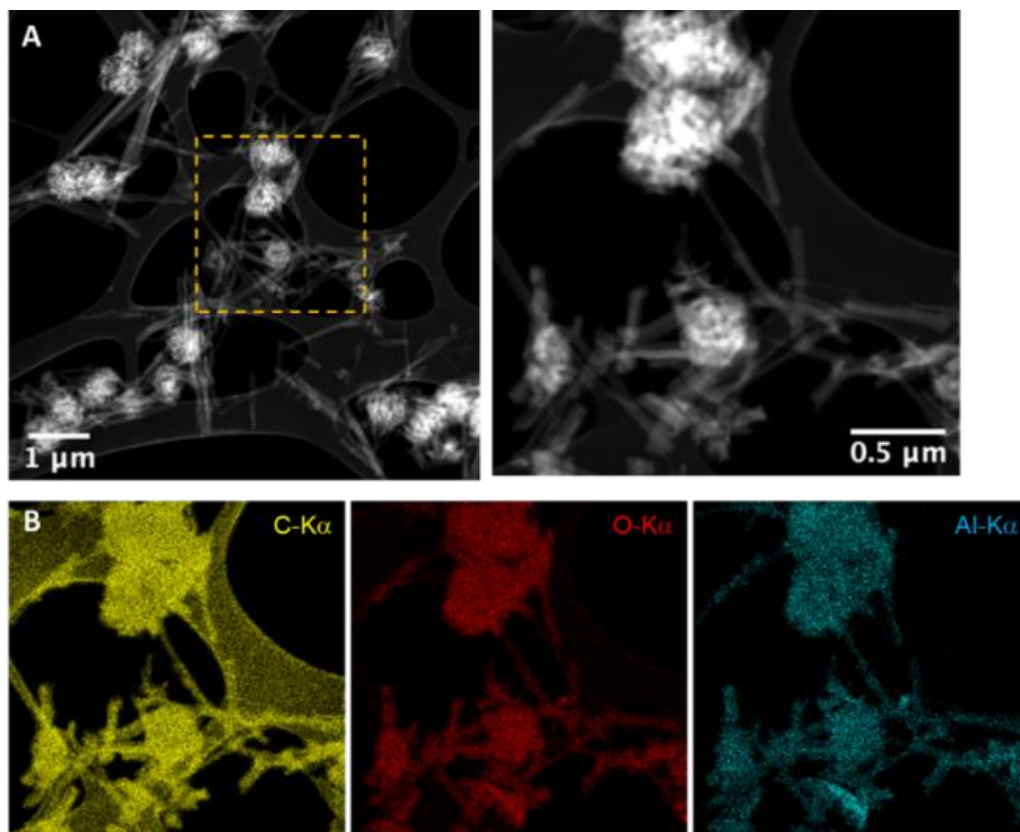


Figure 3-42: (A) STEM-HAADF images of DUT-5(Al)-336 and (B) STEM-XEDS elemental maps.

In summary, DUT-5(Al)/GO-336 presents only one dimensionality of NWs with an average length of 6-8 μm and a diameter of 70-90 nm. In comparison, despite the fact that the synthesis of DUT-5(Al) in the absence of GO presented some elongated structures, the samples were highly polydisperse and less crystalline (**Figure 3-39 to 3-41**). Not only DUT-5(Al)-336 presented two different kinds of particles (self-arranged spheres and elongated fibers) but also it suffered difficulties in terms of reproducibility where the relative amount of each kind was not similar in the different batches. The elongated structures showed similar diameter to that of DUT-5(Al)/GO-336 NWs (70-90 nm), yet they are a little shorter (2-4 μm). Therefore, it can be thus concluded that GO played an undeniable role as a structure directing agent for the formation of 1D DUT-5(Al) based single crystals of NWs (**Figure 3-34 to 3-38**).

Additionally, based on the obtained results, it can be assumed that the same formation mechanism reported for MIL-69(Al) could take place here.²⁵ Thus, it is a stepwise formation mechanism where the nucleation of DUT-5(Al) NPs occurs at the surface of the GO sheets first, then the self-scrolling of the GO happens. This self-scrolling is accompanied with the anisotropic growth of the MOF NPs which keep growing into NWs that laterally fuse forming a single NW inside a GO scroll (**Figure 3-43**).

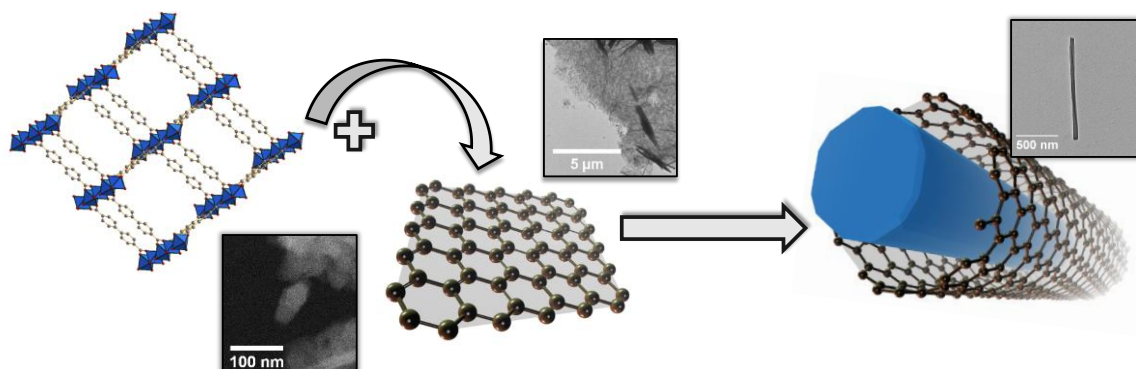


Figure 3-43: Graphical abstract of the structural directing effect of GO on the DUT-5(Al) MOF.

3.6 CONCLUSIONS AND PERSPECTIVES

In this chapter, it was shown through utilizing different characterization techniques that the reported reflux synthesis of DUT-5(Al) in literature needs to be further modified. The employed techniques (i.e., TEM, XEDS, TGA, and solid-state NMR spectroscopy) have revealed the presence of relatively high quantities (7 %wt.) of unreacted Al₂O₃ in the final DUT-5(Al) sample. Herein, we have shown that it was possible to avoid the formation of the undesired metal oxides through tuning the reactants ratio into an equimolar ratio of 1. This control over the reactants ratio allowed the formation of pure crystalline DUT-5(Al) samples. Similar results were obtained in case of DUT-5(Al)/GO. Nevertheless, the recorded SEM images for the optimized DUT-5(Al)/GO revealed that the composite lacked morphological homogeneity, and the elongated particles were only observed in few locations of the sample. Hence, the synthesis of DUT-5(Al)/GO was further optimized in order to obtain the desired anisotropic monodisperse DUT-5(Al) based nanostructures. Following a thorough optimization strategy, it was possible to form a monodisperse composite of single crystal DUT-5(Al) based NWs. The optimization strategy was based on different factors established on sample analysis and reports in literature. For instance, the presence of a mixture of solvents (water and DMF) has proven crucial for the formation of elongated nanostructures in our sample. This was widely discussed in previous reports,²¹⁻²⁴ among which is the MIL-69(Al) case.²⁵ In addition, based on experimental observations, it was concluded that the concentration of the reactants and the reaction time employed are also essential for the formation of crystalline well-defined NWs. Furthermore, the different characterizations demonstrated that the particles reveal an anisotropic growth, thanks presumably to specific interactions between the MOF and the GO sheets. The employed microscopic techniques (i.e., SAED) have revealed that the obtained single crystal MOF based NWs all grow along the [0 1 0] direction which

is the direction of the MOF channels and is in agreement with MIL-69(Al) based nanowires. Moreover, *ex-situ* studies have revealed that the formation and growth of the composite requires much longer time (48 hours) compared to the pure MOF (0.5-2 hours), and that it is possible to increase the length of the obtained wires via increasing the reaction time (from 1-2 μm in 24 hours to 4-5 μm in 48 hours).

Moreover, based on the obtained results, it was important to validate the role of GO in the formation process of DUT-5(Al) based NWs, and to understand whether the optimized synthesis conditions or GO affected the reaction kinetics and the final morphology of the composite. Therefore, the synthesis conditions used for DUT-5(Al)/GO were conducted in the absence of GO. The obtained DUT-5(Al) samples were heavily heterogenous as they presented a mixture of NPs and elongated particles. Moreover, the observed elongated particles were of different dimensions and presented a low crystallinity, contrary to the highly monodisperse DUT-5(Al)/GO made of single crystal NWs with a similar aspect ratio and dimensions.

In conclusion, it was shown that the concept applied to MIL-69(Al) could be extended to another MOF. It was possible to shape MOF nanoparticles into MOF based NWs by simply using GO as a structural directing agent. Finally, unexpected flexibility was observed in the synthesized DUT-5(Al)-336 and DUT-5(Al)/GO-336 samples. To our knowledge, no reports in literature discussed an experimentally observed flexible behavior in the DUT-5(Al) framework. These results will be the focus of **chapter 4** which will discuss the induced flexible behavior in DUT-5(Al).

3.7 REFERENCES

- (1) Saad, A.; Biswas, S.; Gkaniatsou, E.; Sicard, C.; Dumas, E.; Menguy, N.; Steunou, N. Metal–Organic Framework Based 1D Nanostructures and Their Superstructures: Synthesis, Microstructure, and Properties. *Chem. Mater.* **2021**, *33* (15), 5825–5849. <https://doi.org/10.1021/acs.chemmater.1c01034>.
- (2) Van Vleet, M. J.; Weng, T.; Li, X.; Schmidt, J. R. In Situ, Time-Resolved, and Mechanistic Studies of Metal–Organic Framework Nucleation and Growth. *Chem. Rev.* **2018**, *118* (7), 3681–3721. <https://doi.org/10.1021/acs.chemrev.7b00582>.
- (3) McGuire, C. V.; Forgan, R. S. The Surface Chemistry of Metal–Organic Frameworks. *Chem. Commun.* **2015**, *51* (25), 5199–5217. <https://doi.org/10.1039/C4CC04458D>.
- (4) Yuan, S.; Feng, L.; Wang, K.; Pang, J.; Bosch, M.; Lollar, C.; Sun, Y.; Qin, J.; Yang, X.; Zhang, P.; Wang, Q.; Zou, L.; Zhang, Y.; Zhang, L.; Fang, Y.; Li, J.; Zhou, H.-C. Stable Metal–Organic Frameworks: Design, Synthesis, and Applications. *Advanced Materials* **2018**, *30* (37), 1704303. <https://doi.org/10.1002/adma.201704303>.
- (5) Safaei, M.; Foroughi, M. M.; Ebrahimipour, N.; Jahani, S.; Omid, A.; Khatami, M. A Review on Metal–Organic Frameworks: Synthesis and Applications. *TrAC Trends in Analytical Chemistry* **2019**, *118*, 401–425. <https://doi.org/10.1016/j.trac.2019.06.007>.
- (6) Senkovska, I.; Hoffmann, F.; Fröba, M.; Getzschmann, J.; Böhlmann, W.; Kaskel, S. New Highly Porous Aluminium Based Metal–Organic Frameworks: Al(OH)(Ndc) (Ndc=2,6-Naphthalene Dicarboxylate) and Al(OH)(Bpdc) (Bpdc=4,4'-Biphenyl Dicarboxylate). *Microporous and Mesoporous Materials* **2009**, *122* (1), 93–98. <https://doi.org/10.1016/j.micromeso.2009.02.020>.
- (7) Millange, F.; Walton, R. I. MIL-53 and Its Isostructural Analogues: A Review of the Chemistry and Structure of a Prototypical Flexible Metal–Organic Framework. *Israel Journal of Chemistry* **2018**, *58* (9/10), 1019–1035. <https://doi.org/10.1002/ijch.201800084>.
- (8) Couck, S.; Liu, Y.-Y.; Leus, K.; Baron, G. V.; Van der Voort, P.; Denayer, J. F. M. Gas Phase Adsorption of Alkanes, Alkenes and Aromatics on the Sulfone-DUT-5 Metal Organic Framework. *Microporous and Mesoporous Materials* **2015**, *206*, 217–225. <https://doi.org/10.1016/j.micromeso.2014.11.028>.
- (9) Halis, S.; Reimer, N.; Klinkebiel, A.; Lüning, U.; Stock, N. Four New Al-Based Microporous Metal–Organic Framework Compounds with MIL-53-Type Structure Containing Functionalized Extended Linker Molecules. *Microporous and Mesoporous Materials* **2015**, *216*, 13–19. <https://doi.org/10.1016/j.micromeso.2015.01.030>.
- (10) Dau, P. V.; Kim, M.; Garibay, S. J.; Münch, F. H. L.; Moore, C. E.; Cohen, S. M. Single-Atom Ligand Changes Affect Breathing in an Extended Metal–Organic Framework. *Inorg. Chem.* **2012**, *51* (10), 5671–5676. <https://doi.org/10.1021/ic202683s>.
- (11) Liu, Y.-Y.; Couck, S.; Vandichel, M.; Grzywa, M.; Leus, K.; Biswas, S.; Volkmer, D.; Gascon, J.; Kapteijn, F.; Denayer, J. F. M.; Waroquier, M.; Van Speybroeck, V.; Van Der Voort, P. New VIV-Based Metal–

- Organic Framework Having Framework Flexibility and High CO₂ Adsorption Capacity. *Inorg. Chem.* **2013**, *52* (1), 113–120. <https://doi.org/10.1021/ic301338a>.
- (12) Couck, S.; Van Assche, T. R. C.; Liu, Y.-Y.; Baron, G. V.; Van Der Voort, P.; Denayer, J. F. M. Adsorption and Separation of Small Hydrocarbons on the Flexible, Vanadium-Containing MOF, COMOC-2. *Langmuir* **2015**, *31* (18), 5063–5070. <https://doi.org/10.1021/acs.langmuir.5b00655>.
- (13) Gotthardt, M. A.; Grosjean, S.; Brunner, T. S.; Kotzel, J.; Gänzler, A. M.; Wolf, S.; Bräse, S.; Kleist, W. Synthesis and Post-Synthetic Modification of Amine-, Alkyne-, Azide- and Nitro-Functionalized Metal–Organic Frameworks Based on DUT-5. *Dalton Trans.* **2015**, *44* (38), 16802–16809. <https://doi.org/10.1039/C5DT02276B>.
- (14) Yildiz, C.; Kutonova, K.; Oßwald, S.; Titze-Alonso, A.; Bitzer, J.; Bräse, S.; Kleist, W. Post-Synthetic Modification of DUT-5-Based Metal Organic Frameworks for the Generation of Single-Site Catalysts and Their Application in Selective Epoxidation Reactions. *ChemCatChem* **2020**, *12* (4), 1134–1142. <https://doi.org/10.1002/cctc.201901434>.
- (15) Depauw, H.; Nevjestić, I.; Wang, G.; Leus, K.; Callens, F.; Canck, E. D.; Buysser, K. D.; Vrielinck, H.; Voort, P. V. D. Discovery of a Novel, Large Pore Phase in a Bimetallic Al/V Metal–Organic Framework. *J. Mater. Chem. A* **2017**, *5* (47), 24580–24584. <https://doi.org/10.1039/C7TA08103K>.
- (16) Stankovich, S.; Dikin, D. A.; Piner, R. D.; Kohlhaas, K. A.; Kleinhammes, A.; Jia, Y.; Wu, Y.; Nguyen, S. T.; Ruoff, R. S. Synthesis of Graphene-Based Nanosheets via Chemical Reduction of Exfoliated Graphite Oxide. *Carbon* **2007**, *45* (7), 1558–1565. <https://doi.org/10.1016/j.carbon.2007.02.034>.
- (17) Azizighannad, S.; Mitra, S. Stepwise Reduction of Graphene Oxide (GO) and Its Effects on Chemical and Colloidal Properties. *Sci Rep* **2018**, *8* (1), 10083. <https://doi.org/10.1038/s41598-018-28353-6>.
- (18) Haouas, M.; Taulelle, F.; Martineau, C. Recent Advances in Application of ²⁷Al NMR Spectroscopy to Materials Science. *Progress in Nuclear Magnetic Resonance Spectroscopy* **2016**, *94–95*, 11–36. <https://doi.org/10.1016/j.pnmrs.2016.01.003>.
- (19) Obeso, J. L.; López-Olvera, A.; Flores, C. V.; Martínez-Ahumada, E.; Paz, R.; Viltres, H.; Islas-Jácome, A.; González-Zamora, E.; Balmaseda, J.; López-Morales, S.; Vera, M. A.; Lima, E.; Ibarra, I. A.; Leyva, C. Methylene Blue Adsorption in DUT-5: Relatively Strong Host-Guest Interactions Elucidated by FTIR, Solid-State NMR, and XPS. *Journal of Molecular Liquids* **2022**, *368*, 120758. <https://doi.org/10.1016/j.molliq.2022.120758>.
- (20) Xu, S.; Jaegers, N. R.; Hu, W.; Kwak, J. H.; Bao, X.; Sun, J.; Wang, Y.; Hu, J. Z. High-Field One-Dimensional and Two-Dimensional ²⁷Al Magic-Angle Spinning Nuclear Magnetic Resonance Study of θ-, δ-, and γ-Al₂O₃ Dominated Aluminum Oxides: Toward Understanding the Al Sites in γ-Al₂O₃. *ACS Omega* **2021**, *6* (5), 4090–4099. <https://doi.org/10.1021/acsomega.0c06163>.
- (21) Tang, B.; Xiong, Z.; Yun, X.; Wang, X. Rolling up Graphene Oxide Sheets through Solvent-Induced Self-Assembly in Dispersions. *Nanoscale* **2018**, *10* (8), 4113–4122. <https://doi.org/10.1039/C7NR08415C>.

CHAPTER 3: DUT-5(AI) and DUT-5(AI)/GO

- (22) Tang, B.; Yun, X.; Xiong, Z.; Wang, X. Formation of Graphene Oxide Nanoscrolls in Organic Solvents: Toward Scalable Device Fabrication. *ACS Appl. Nano Mater.* **2018**, *1* (2), 686–697. <https://doi.org/10.1021/acsnm.7b00160>.
- (23) Tang, B.; Gao, E.; Xiong, Z.; Dang, B.; Xu, Z.; Wang, X. Transition of Graphene Oxide from Nanomembrane to Nanoscroll Mediated by Organic Solvent in Dispersion. *Chem. Mater.* **2018**, *30* (17), 5951–5960. <https://doi.org/10.1021/acs.chemmater.8b02083>.
- (24) Sontakke, A. D.; Purkait, M. K. A Brief Review on Graphene Oxide Nanoscrolls: Structure, Synthesis, Characterization and Scope of Applications. *Chemical Engineering Journal* **2021**, *420*, 129914. <https://doi.org/10.1016/j.cej.2021.129914>.
- (25) Muschi, M.; Lalitha, A.; Sene, S.; Aureau, D.; Fregnaux, M.; Esteve, I.; Rivier, L.; Ramsahye, N.; Devautour-Vinot, S.; Sicard, C.; Menguy, N.; Serre, C.; Maurin, G.; Steunou, N. Formation of a Single-Crystal Aluminum-Based MOF Nanowire with Graphene Oxide Nanoscrolls as Structure-Directing Agents. *Angew. Chem. Int. Ed.* **2020**, *59* (26), 10353–10358. <https://doi.org/10.1002/ange.202000795>.
- (26) Jolivet, J. *De La Solution à l'oxyde-2e ED: Chimie Aqueuse Des Cations Métalliques-Synthèse de Nanostructures Chimie Aqueuse Des Cations Métalliques Synthèse de Nanostructures.*; EDP sciences, 2016.
- (27) Devic, T.; Serre, C. High Valence 3p and Transition Metal Based MOFs. *Chemical Society Reviews* **2014**, *43* (16), 6097–6115. <https://doi.org/10.1039/C4CS00081A>.
- (28) Zhou, Y.; Li, J.; Zhang, J.; Chen, Y.; Yao, T.; Chen, A.; Xiang, M.; Chen, Z.; Wu, Z. Dye Promoted Electron Transfer in DUT-5/BiVO₄ Heterojunction for Organic Pollutants Degradation. *Materials Research Bulletin* **2022**, *150*, 111740. <https://doi.org/10.1016/j.materresbull.2022.111740>.

MATERIALS & METHODS

Powder X-ray diffraction (PXRD). The pattern of supramolecular hybrid compounds was scanned at room temperature by using a Siemens D5000 diffractometer with a $\Theta/2\Theta$ geometry in the range $2\Theta = 5\text{--}40^\circ$ with a step length of 0.02° .

Fourier transform infrared (FT-IR). Spectra were recorded on a 6700 FT-IR Nicolet spectrophotometer, using the diamond ATR technique. The spectra were recorded on solid compounds and ATR correction was applied.

Thermal gravimetric analysis (TGA). To determine water and organic contents, a Mettler Toledo TGA/DSC 1, STARe System apparatus was used under oxygen flow ($50\text{ mL}\cdot\text{min}^{-1}$) at a heating rate of $5\text{ }^\circ\text{C}\cdot\text{min}^{-1}$ up to $700\text{ }^\circ\text{C}$. UV-Visible spectroscopy.

Scanning electron microscopy (SEM) images have been recorded on a JEOL JSM-7001F microscope equipped with an X-ray energy-dispersive spectrometry (EDX) detector with a X-Max SDD (Silicon Drift Detector) by Oxford using gold-coated samples.

Energy-dispersive X-ray spectroscopy (EDX). EDX measurements were performed using an SEMFEG (scanning electron microscope enhanced by a field emission gun) equipment (JSM 7001-F, Jeol). The measures were acquired with an SDD XMax 50 mm² detector and the Aztec (Oxford) system working at 15 kV and 10 mm working distance. The quantification is realized with the standard library provided by the constructor using $L\alpha$ lines.

X-ray Photoelectron Spectroscopy (XPS) Prior surface analysis, pure and composite compounds (powders) were pressed to form pellets. X-ray Photoelectron Spectroscopy (XPS) measurements were carried out using a Thermofisher Scientific Escalab 250xi spectrometer with a monochromated Al-K α X-ray source ($h\nu = 1486.6\text{ eV}$). High energy resolution spectral windows of interest were recorded with a $650\text{ }\mu\text{m}$ spot size. The photoelectron detection was performed using a constant analyzer energy (CAE) mode (10 eV pass energy) and a 0.1 eV energy step. The use of low-energy electron and ion flood gun was necessary to perform the analysis. Quantification was performed using the Thermofisher Scientific Advantage© software.

CHAPTER 3: DUT-5(Al) and DUT-5(Al)/GO

Chemical compositions were obtained from the C1s, O1s, Al2p peak areas after a Shirley type background subtraction and considering "AlThermo1" sensitivity factor library. The proportions of MOF and graphene in the composite was estimated by a linear combination of reference spectrum (pure MOF and pure graphene).

Transmission electron microscopy (TEM) characterization, samples were prepared by depositing one droplet of the colloidal suspension onto a carbon-coated copper grid and left to dry in air. TEM observations were performed using a JEOL 2010 Transmission Electron Microscope operating at 200 kV. In order to avoid beam damage on very sensitive MIL-69(Al)/GO samples, low voltage TEM observations were also carried out at IMPMC (Paris, France) on a JEOL JEM 2100 transmission electron microscope operating at 60 kV and equipped with a LaB6 emitter and a Gatan US2000 CCD camera. High-angle annular dark field imaging in scanning transmission electron microscope mode (STEM-HAADF) and X-ray energy-dispersive spectroscopy (XEDS) mapping experiments were performed on a JEOL JEM 2100F microscope installed at IMPMC (Paris, France), operating at 200 kV, equipped with a field emission gun, a JEOL detector with an ultrathin window allowing detection of light elements and a scanning TEM (STEM) device, which allows Z-contrast imaging in HAADF mode.

Nuclear magnetic resonance (NMR). The ^{27}Al solid state NMR spectra were recorded on an Avance Bruker 500 NMR spectrometer operating at static magnetic field of 11.7 T, corresponding to Larmor frequencies of 130MHz for ^{27}Al . The samples were packed in 2.5- or 4-mm outer diameter rotors. The ^{27}Al single-pulse NMR spectra were recorded using 1.6 μs ($\pi/12$ flip angle) pulse durations with recycle delays set to 0.1 s for ^{27}Al .

Wide angle X-ray scattering (WAXS). WAXS measurements were acquired on a laboratory device (LIONS-NIMBE CEA, Saclay, France) at 1.542 Å (Cu source) under vacuum with a Xeuss 2.0 apparatus (Xenocs). The displayed q -range from 2.10^{-2} to 1 \AA^{-1} was attained with a single sample-to-detector distance of 33 cm. The latter was calibrated with Silver Behenate and the detector count was normalized by direct beam measurements. The samples were inserted in

glass capillaries (diameter 1 mm, wall thickness 0.1 mm, WJM-Glas). The data were recorded by a two-dimensional Pilatus 1 M detector (Dectris). Acquisition times were 60 min. The treatment of the 2D images and of the resulting scattering profiles was performed using pySAXS (<https://pypi.org/project/pySAXS/>). Standard procedures were applied to subtract background scattering and to normalize the intensities [Linder]. The diffraction peaks were fitted using SASView (www.sasview.org).

Figure 3-11 was obtained on the SWING beamline of the SOLEIL synchrotron (Saint-Aubin, France). The scattering vector range q of $2 \times 10^{-3} \text{ \AA}^{-1}$ to 2.5 \AA^{-1} was obtained with an energy of 16 keV and two sample-to-detector distances (6 and 0.50 m for the SAXS and the wide-angle X-ray scattering ranges, respectively). The data were recorded by a two-dimensional Eiger 4 M (Dectris) detector. Data reduction was performed using Foxtrot software (Xenocs). The sample were placed in 1-mm diameter glass capillaries sealed with wax.


P. Linder, in Neutrons (Eds: P. Linder, T. Zemb), Elsevier, Amsterdam 2002, Ch. 2.

Acknowledgements

We thank David Carrière for SAXS-WAXS measurements performed on the SWING beamline (SOLEIL Synchrotron) during the BAG 20201118.

This work benefited from the use of the SasView application (<http://www.sasview.org>), originally developed under NSF award DMR-0520547. SasView contains code developed with funding from the European Union's Horizon 2020 research and innovation programme under the SINE2020 project, grant agreement no. 654000

Optical microscopy Microscope Olympus BX41 équipé d'une caméra numérique DP70 (12,5 millions de pixels) (+ polariseur et analyseur)



CHAPTER 4: Insights on the Induced Flexibility in the DUT-5(AI) Structure

TABLE OF CONTENTS

4.1 INTRODUCTION	181
4.2 STATE OF THE ART: FLEXIBILITY OF DUT-5(Al)	184
4.3 THE STRUCTURAL BEHAVIOR OF DUT-5(Al)	185
4.4 ELUCIDATING STRUCTURE: TWO PHASES OF DUT-5(Al)/GO	191
4.4.1. Rietveld Refinement of the Two Phases	193
4.4.2. Characterization by Pair Distribution Function	196
4.5 STUDYING THE FLEXIBLE BEHAVIOR OF DUT-5(Al)/GO	198
4.5.1. Effect of Temperature on the Flexibility of DUT-5(Al)/GO	198
4.5.1.1. Ex-situ PXRD under heating	198
4.5.1.2. In-situ FT-IR spectroscopy under heating.....	199
4.5.2. Effect of Solvent on the Flexibility of DUT-5(Al)/GO	203
4.5.3. Effect of Gas Guest Molecules on Flexibility of DUT-5(Al)/GO.....	206
4.6 EFFECT OF SIZE AND MORPHOLOGY ON FLEXIBILITY	210
4.7 CONCLUSIONS AND PERSPECTIVES.....	213
4.8 REFERENCES	214

4.1 INTRODUCTION

In the previous chapter, we have shown that it was possible to obtain anisotropic DUT-5(Al) based nanostructures either by tuning synthesis conditions or via using GO as a structural directing agent. It was observed that anisotropic nanostructures obtained in presence of GO (DUT-5(Al)/GO-336) were more well-defined and homogenous than those obtained without it (DUT-5(Al)-336) (**Figure 4-1, B-C**). While DUT-5(Al)/GO-336 consists of an assembly of monodisperse nanowires of 70-90 nm in diameter and length up to 8 μm , DUT-5(Al)-336 is made of spherical or elongated aggregates constructed by the assembly of rod-like particles with a high size distribution. However, while the PXRD pattern of DUT-5(Al)-24 nanoparticles is fully consistent with that of the calculated pattern of DUT-5(Al), the PXRD pattern of both DUT-5(Al)/GO-336 and DUT-5(Al)-336, once washed in ethanol and dried, are different. In particular, we can notice a shift of the first reflection (1,0,1) to a higher angle indicating a contraction of the MOF framework. This flexibility behavior was not evidenced for the pure DUT-5(Al)-24 nanoparticles. Compared to the other two samples, DUT-5(Al)-24 mainly differs in its final morphology, both DUT-5(Al)-336 and DUT-5(Al)/GO-336 present anisotropic particles that are absent in this sample. Therefore, there is a high interest to investigate the flexibility behavior of both DUT-5(Al)-336 and DUT-5(Al)/GO-336, and to examine if this difference in morphology of the samples affects the structural behavior of the framework.

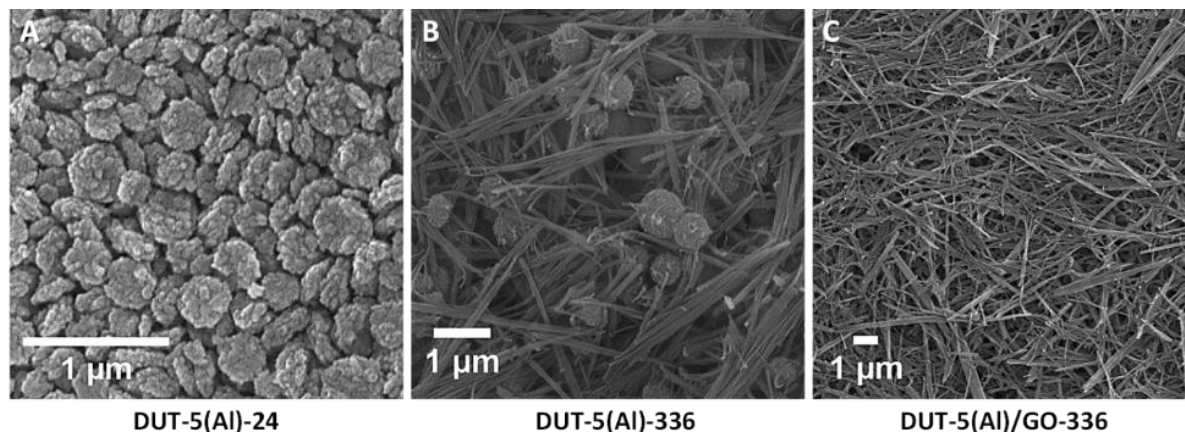


Figure 4-1: SEM images of (A) DUT-5(Al)-24 self-arranged nanoparticles, (B) DUT-5(Al)-336 with elongated particles, and (C) DUT-5(Al)/GO nanowires.

According to Bragg's law, the XRD peaks shift if the interplanar spacing changes between the successive Bragg planes, indicating a change in the lattice parameters of the unit cell. Herein, the observed shift in the first reflection (1,0,1) at $2\theta = 6.01^\circ$ is to the higher angle, signifying a contraction of the studied framework and thus a decrease in the unit cell volume (**Figure 4-2**). Hence, the obtained results present a structural contraction in the DUT-5(Al)-336 and DUT-5(Al)/GO-336 frameworks which can exhibit a potential flexible behavior. The interest in examining this behaviour is further reinforced by the fact that DUT-5(Al) is isorecticular to MIL-53(Al),¹ which is a well-known MOF for performing structural transitions between two distinct phases: large pore (lp) and narrow pore (np). In fact, many works in literature refer to DUT-5(Al) as a rigid permanent large pore (lp) phase MOF.¹ Both DUT-5(Al) and MIL-53(Al) have the same 3D network with lozenge-shape channels built by assembling 1D chains of Al^{3+} octahedra and ditopic organic linkers. Despite the fact that flexibility is not transferred in a hereditary manner between isorecticular MOFs, the potential flexible behavior of DUT-5(Al)-336 and DUT-5(Al)/GO-336 is of huge interest as to our knowledge no reports in literature have previously discussed any experimentally observed structural transition in the DUT-5(Al) structure or in any MOF/GO composite in general.

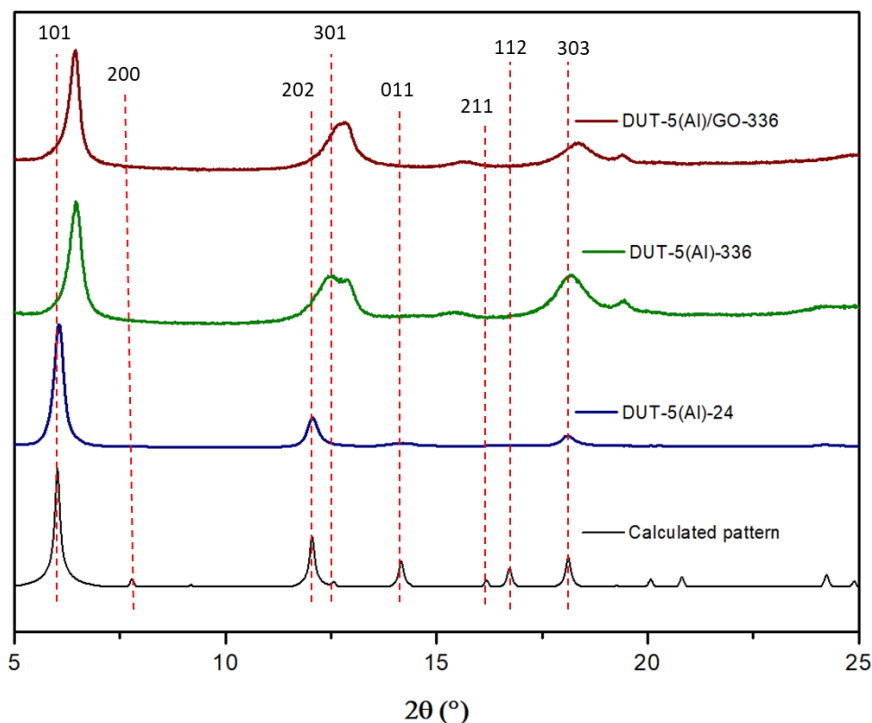


Figure 4-2: PXRD patterns of calculated DUT-5(Al) pattern, DUT-5(Al)-24, DUT-5(Al)-336, and DUT-5(Al)/GO-336.

This chapter will provide first a brief summary covering the flexibility of DUT-5(Al) in literature. Secondly, in order to understand the reasons behind the observed peak shift in the PXRD patterns of DUT-5(Al)-336 and DUT-5(Al)/GO-336 (**Figure 4-2**), the obtained results will be further analyzed. Based on this analysis, the third part of the chapter will comment on the possible flexible behavior while covering the advanced characterization of DUT-5(Al)-24, DUT-5(Al)-336, and DUT-5(Al)/GO-336 in response to different physical and chemical stimuli (e.g., heating, solvent exchange, gas adsorption, etc.).

4.2 STATE OF THE ART: FLEXIBILITY OF DUT-5(Al)

Flexible MOFs have been defined as “materials that combine the crystalline order of the underlying coordination network with cooperative structural transformability attaining the ability to respond to physical and chemical stimuli of various kinds in a tunable fashion by molecular design”.² Stimuli-responsive flexible MOFs are still at the forefront of porous materials research due to their vast potential for various applications, such as storage and separation, sensing, and guest capture and release.^{3,4} While flexible MOFs switching between two or more well-defined crystalline phases have been widely explored in literature,⁵⁻⁷ to date, no work in literature has discussed any experimentally observed flexible behavior of the DUT-5(Al) structure. Interestingly, Hoffman and co-workers have recently discussed theoretically the possibility of inducing flexibility in MOFs with the MIL-53(Al) structure type (i.e., DUT-4(Al), DUT-5(Al), MIL-47(V), etc.) based on the connectivity between chains of Al³⁺ octahedra with different organic linkers.⁸ This study was focused on different MOFs including DUT-5(Al) based on bpdc ligand.⁹ Compared to other MOFs, this theoretical study concluded that DUT-5(Al) is characterized by a large entropy difference between the large (lp) and close pore (cp) phases, the entropy being larger for the lp phase.⁸ However, the strong dispersion interactions between neighbouring bpdc linkers energetically favour the cp phase. In fact, the electronic energy difference between the lp and cp phase is so large that the cp is thermodynamically more stable and a transition to the lp phase should only be possible at high temperature. There is a discrepancy between the results deduced from this theoretical study and the experimental observations since DUT-5(Al) and its functionalized analogues were only described as a rigid and large pore form.

Still, it should be mentioned that COMOC-2(V) which is the vanadium analogue of DUT-5(Al) have shown a pressure induced flexibility behavior that was later applied in separating hydrocarbon mixtures.^{10,11} Soon after, a mixed metal approach was reported for DUT-5(Al) synthesis, which yielded the COMOC-2(V)/DUT-5(Al) and a transition between the (lp) and (np) phases of the previously discussed COMOC-2(V) was found at lower pressures.¹² It was noticed that the transition between the two phases is faster (at lower pressures) with increasing the Al content in the mixed metal framework.¹² Hence, it was concluded that tailoring the breathing behavior in COMOC-2(V) is possible through (Al) doping. Based on the listed information, the results obtained in this project are unprecedented and of huge importance.

4.3 THE STRUCTURAL BEHAVIOR OF DUT-5(Al)

As previously shown in **chapter 3**, when the three synthesized samples were washed with ethanol, dried at 100°C, and characterized by PXRD, the peaks of the PXRD patterns of both DUT-5(Al)-336 and DUT-5(Al)/GO-336 NWs were shifted in comparison to the calculated pattern of DUT-5(Al). As explained earlier, the first (1,0,1) reflection at $2\theta = 6.01^\circ$ is shifted to a higher angle, which is consistent with a contraction of the DUT-5(Al) framework and thus a decrease in its unit cell volume. In contrast, no shift of the reflections was observed for DUT-5(Al)-24 NPs (**Figure 4-3, A**), meaning that the PXRD pattern of such nanoparticles is in full agreement with the calculated pattern. Moreover, when the three samples were characterized as synthesized in suspension by Wide Angle X-ray Scattering (WAXS), they all exhibited the same profiles (**Figure 4-3, B**).

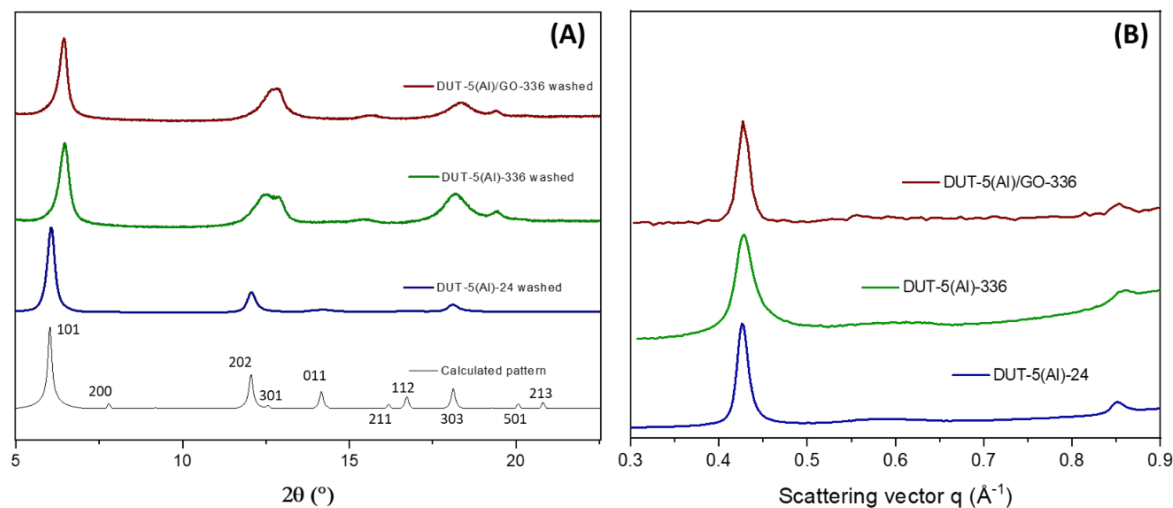


Figure 4-3: (A) PXRD patterns of calculated pattern, DUT-5(Al)-24 DUT-5(Al)-336, and DUT-5(Al)/GO-336; (B) WAXS profiles of DUT-5(Al)-24 DUT-5(Al)-336, and DUT-5(Al)/GO-336.

The main difference between the PXRD and WAXS measurements is the sample preparation: in the former the samples are in the powder form whereas in the latter they are in suspension. One can assume that the shift observed only in PXRD patterns could be due to the fact that the samples were washed and dried before characterization. In contrary, the samples characterized by WAXS were characterized directly as synthesized in suspension, thus the pore content was not modified (i.e., dried or exchanged by another solvent).

Table 4-1. Summary of the different samples, synthesis conditions, and observed dynamic behaviors under different conditions of DUT-5(Al) based structures.

Sample	Synthesis time	Synthesis solution	Shape	Contraction shown by characterization	
				as synthesized in suspension by WAXS	after washing and drying by PXRD
DUT-5(Al)-24	24 hours	DMF	NPs	Not observed	Not observed
DUT-5(Al)/GO-336	336 hours (14 days)	DMF/water	NWs	Not observed	Observed
DUT-5(Al)-336	336 hours (14 days)	DMF/water	aggregates of nanorods	Not observed	Observed

To ascertain the assumed effect of the pore content on the observed dynamic behaviors, it was required to characterize the samples after synthesis without performing any solvent exchange (i.e., without washing). Thus, the samples were characterized as synthesized after being dried at room temperature (RT) by PXRD. As shown in **(Figure 4-4)**, DUT-5(Al)-24 presented no difference in its PXRD pattern whether washed or not. This result was expected as this sample did not previously reveal any difference neither by WAXS nor PXRD **(Figure 4-3)**, and the first (1,0,1) reflection is observed at $2\theta = 6.01^\circ$. On the other side, both DUT-5(Al)-336 and DUT-5(Al)/GO-336 presented a different PXRD pattern. At low angles, it can be clearly shown that two reflections are observed at $2\theta = 6.01$ and 6.44° instead of one well-defined peak at 6.01° . Interestingly, this other peak at 6.44° is observed in the contracted washed samples **(Figure 4-4)**. This suggests that both DUT-5(Al)-336 and DUT-5(Al)/GO-336 are a mixture of the large pore form and contracted form (narrow pore) of DUT-5(Al). This conclusion can be further validated by the reflection forming at 12.83° , which is only present in the case of the contracted sample **(Figure 4-4)**.

Thus, DUT-5(Al)-24 is formed as a rigid and large pore form, while both DUT-5(Al)-336 and DUT-5(Al)/GO-336 presented a mixture of phases (large pore and narrow pore) when characterized as synthesized (dried at RT) without any solvent exchange. Thus, it can be stated that the drying of DUT-5(Al)-336 and DUT-5(Al)/GO-336 at room temperature was enough to induce some contraction in their framework. Furthermore, when characterized by WAXS in synthesis suspension, the pore content did not change and thus the different materials remained in their (lp) phase **(Figure 4-3, B)**. These results suggest a critical role of the pore content on the dynamic behavior of the two materials. Indeed, it is well known that the flexibility behavior of MOFs can be driven by host-guest interactions.

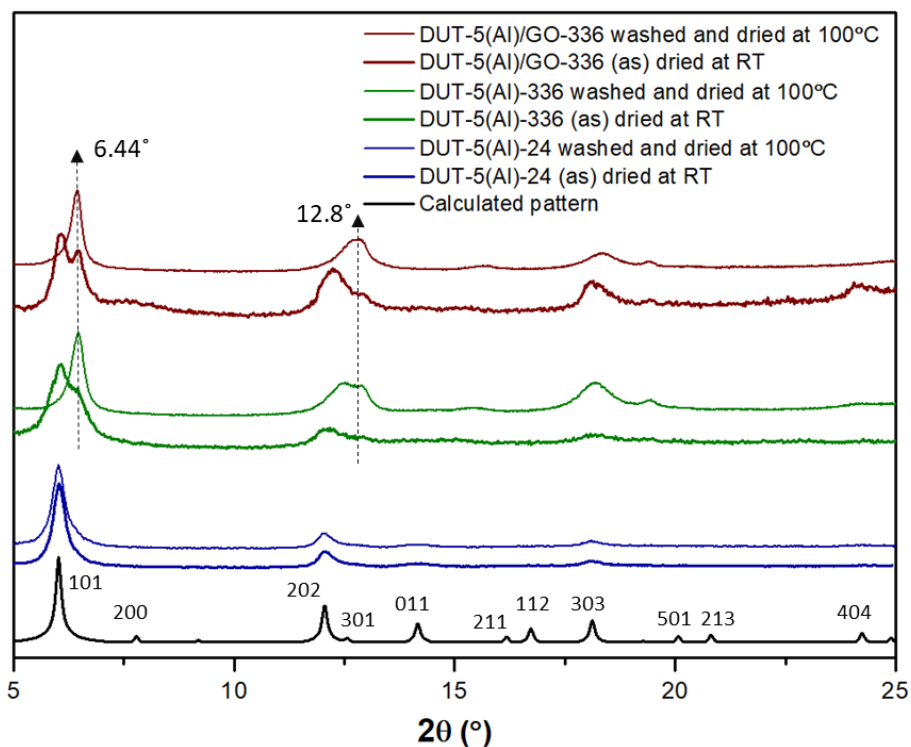


Figure 4-4: Calculated PXRD pattern of DUT-5(Al) and experimental PXRD patterns of DUT-5(Al)-24, DUT-5(Al)-336, and DUT-5(Al)/GO-336 characterized as synthesized without being washed (in bold); and after being washed with ethanol and dried overnight at 100°C (in thin).

It is worth noting that both DUT-5(Al)-336 and DUT-5(Al)/GO-336 showed almost a similar PXRD pattern of a distinct contracted phase, when both were washed by ethanol, and dried at 100°C overnight (**Figure 4-4**). In other terms, the two samples showed the same degree of contraction. This suggests that both materials have reached their maximum contraction after washing with ethanol and drying at 100 °C. To validate this assumption, the samples were synthesized, centrifuged, and characterized by PXRD without being allowed to completely dry at room temperature (i.e., wet state). Thus, the pore content of the different samples was not allowed to be strongly altered.

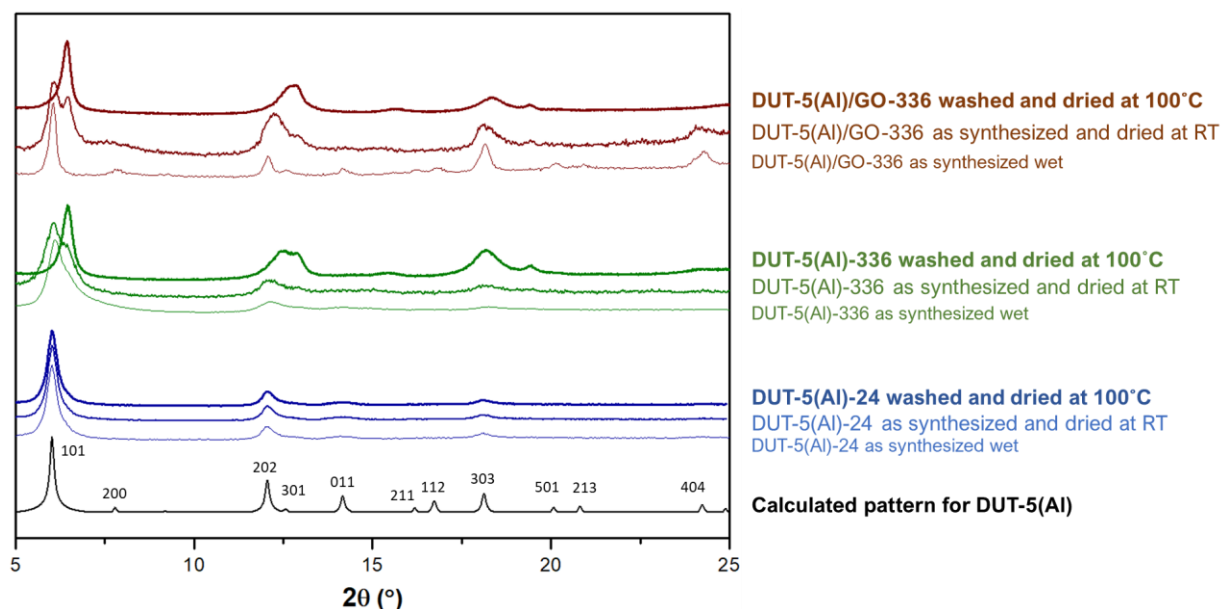


Figure 4-5: Calculated PXRD pattern of DUT-5(Al) and experimental PXRD patterns of DUT-5(Al)-24, DUT-5(Al)-336, and DUT-5(Al)/GO-336 characterized in different conditions (wet, dried at RT, and dried at 100 °C).

Remarkably, the PXRD patterns of the as-synthesized wet DUT-5(Al)-336 and DUT-5(Al)/GO-336 did not reveal any shift in their PXRD peak positions compared to the calculated pattern of DUT-5(Al) (**Figure 4-5**). Such results suggest the absence of any contraction behavior. Indeed, the three samples presented the main characteristic Bragg peaks of DUT-5(Al) at 6.01, 12.05, and 14.15°. This result is of huge importance as it further validates the role of the pore content on the structural dynamic behavior of DUT-5(Al)-336 and DUT-5(Al)/GO-336. In fact, while the DUT-5(Al) in both DUT-5(Al)-336 and DUT-5(Al)/GO-336 is present as the large pore form just after synthesis, drying the samples at RT is enough to start a contraction in their framework. This suggests that a progressive contraction of the DUT-5(Al) takes place upon drying for both DUT-5(Al)-336 and DUT-5(Al)/GO-336 as both the large pore and narrow pore forms can coexist depending on their drying state.

Yet, in comparison to the PXRD pattern of the as-synthesized DUT-5(Al)/GO-336, the PXRD pattern of the as-synthesized DUT-5(Al)-336 displays much broader reflections

(Figure 4-5). This reveals that DUT-5(Al)-336 presents a lower coherence length due to higher micro-strains (crystallographic disorder) and/or crystallite size effects than that of DUT-5(Al)/GO-336. Furthermore, based on experimental interpretations, the Bragg peaks positions in the PXRD pattern of as-synthesized DUT-5(Al)-336 varied significantly from one sample to another. Thus, it was very hard to control the dynamic behavior in case of DUT-5(Al)-336. Therefore, the following part of the chapter will mainly focus on the thorough characterization of the DUT-5(Al)/GO-336 while studying its response to different chemical and physical stimuli.

In summary, DUT-5(Al)-24 demonstrated a rigid behavior that was not affected by the different tests performed. In comparison, the set of data provided in this section revealed that the structural transition in the DUT-5(Al)-336 and DUT-5(Al)/GO-336 samples is strongly dependent on the pore content of these materials. Likewise, the characterization by WAXS has revealed no form of structural transition as the pore content of the different materials was not modified. The as-synthesized DUT-5(Al)-336 and DUT-5(Al)/GO-336 consist of the DUT-5(Al) in its large pore form. On the other hand, drying the two samples at RT was enough to induce the gradual contraction from the large pore form towards the narrow pore form. This was observed by the presence of both forms in their respective PXRD patterns (**Figure 4-5**). Nevertheless, the complete transition to the narrow pore form was achieved for both DUT-5(Al)-336 and DUT-5(Al)/GO-336 through solvent exchange in ethanol, followed by their complete drying overnight at 100°C. Therefore, based on these results, the next step was to determine the unit cell parameters of both the large and narrow pore forms of DUT-5(Al) which is the purpose of the next part in this chapter. Moreover, the possibility of switching between the two distinct phases in a controllable manner will be studied.

4.4 ELUCIDATING THE STRUCTURE: THE TWO PHASES OF DUT-5(Al)/GO

In this section, we will provide a full study covering the results obtained in presence of GO. As discussed, better results were observed in case of the composite. First, in absence of GO, the crystallinity of the sample was lower and the PXRD pattern of the as-synthesized DUT-5(Al)-336 was not always reproducible. Secondly, as elaborated in the previous chapter, despite the fact that anisotropic structures were obtained in both DUT-5(Al)-336 and DUT-5(Al)/GO-336, single crystalline homogenous materials were only obtained in presence of GO. Finally, to our knowledge, no flexible MOF based anisotropic composites have been yet published in literature. Therefore, it would be of huge interest to extensively study this system. **(Figure 4-6)** below shows the results obtained in case of DUT-5(Al)/GO NWs in comparison to the calculated pattern and rigid NPs of DUT-5(Al).

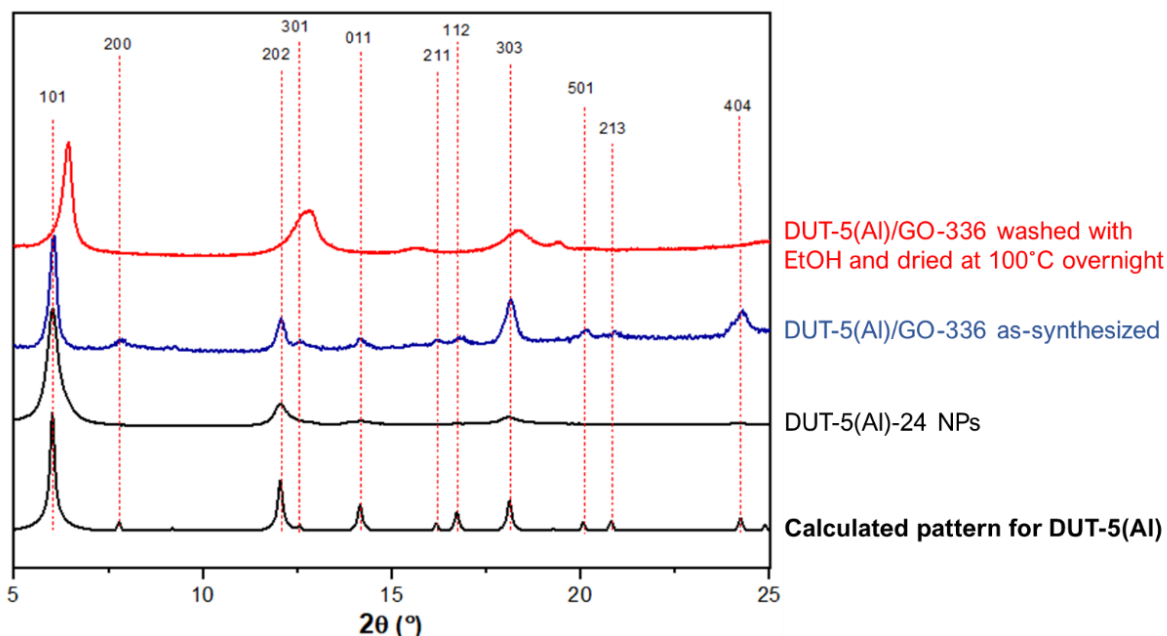


Figure 4-6: PXRD of calculated DUT-5(Al) pattern, rigid DUT-5(Al)-24 NPs, and DUT-5(Al)/GO-336 as synthesized and when washed by ethanol and dried at 100°C.

It can be clearly stated that there are two distinct phases that can occur in the DUT-5(Al)/GO-336 sample. The first phase is the large pore (lp) phase corresponding to the as-synthesized sample before contraction (**Figure 4-6, blue**), and the narrow pore phase (np) corresponding to the contracted sample (**Figure 4-6, red**). Thus, before studying the possibility of switching between the two phases in a controllable manner, it is of huge interest to determine the unit cell parameters of each phase. It should be noted that throughout this section, the (lp) phase of DUT-5(Al)/GO-336 will be marked in blue, while the (np) is in red.

Hence, to obtain the maximum information on both the large pore (lp) and narrow pore (np) phases of DUT-5(Al)/GO-336, the three samples shown in (**Figure 4-6**) were characterized by synchrotron X-ray diffraction. High resolution powder diffraction data were measured at SOLEIL Synchrotron on the Cristal beamline (in collaboration with E. Elkaim, SOLEIL, and B. Baptiste, IMPMC, Sorbonne Université) in order to undertake a Rietveld analysis and, taking into account to the low crystalline quality of the samples, to combine it with the Pair Distribution Function (PDF) analysis. The rigid DUT-5(Al)-24 NPs sample was used as a reference of the (lp) phase for comparison. Thus, each sample was filled in a capillary, and measurements were performed at three points in each capillary to ensure the homogeneity of the samples. As shown in (**Figure 4-7**), each sample presented reproducible and identical XRD pattern whatever the area of sample exposed to X-ray beam. In comparison to the calculated DUT-5(Al) pattern, a clear shift of the reflections is observed in case of DUT-5(Al)/GO-336 once washed with ethanol and dried at 100°C, as previously shown.

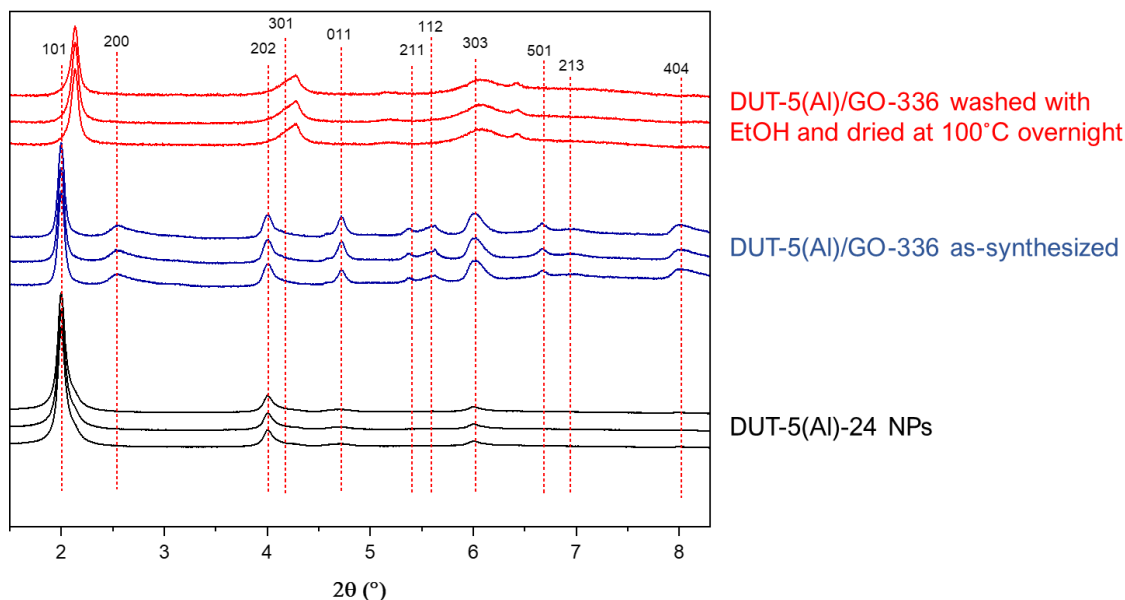


Figure 4-7: Synchrotron XRD patterns recorded at three different points in each capillary containing one of the following samples: DUT-5(Al)-24 in black, as-synthesized DUT-5(Al)/GO-336 in blue and washed in red. Observed patterns were compared to calculated one from literature. ($\lambda = 0.513607 \text{ \AA}$)

Indeed, major changes are observed in the PXRD pattern of the washed composite. The reflections in the PXRD pattern are not only shifted but are also significantly broader for the washed DUT-5(Al)/GO-336 in comparison to the as-synthesized DUT-5(Al)/GO-336. This broadening can be attributed to some induced micro-strains that may result from the changes in the unit cell parameters. Yet, to ascertain such assumption, it was necessary to determine the unit cell parameters of the two phases and study the changes.

4.4.1. Rietveld Refinement of the Two Phases

Thus, in collaboration with N. Guillou at ILV, the extraction of the peak positions, pattern indexing, and Rietveld refinements were all carried out with the TOPAS program (**Figure 4-8**). The atomic coordinates of the reported structural model of DUT-5(Al) were used, and only the unit cell parameters of DUT-5(Al)/GO-336 phases were refined, while keeping the orthorhombic *Imma* space group.⁹

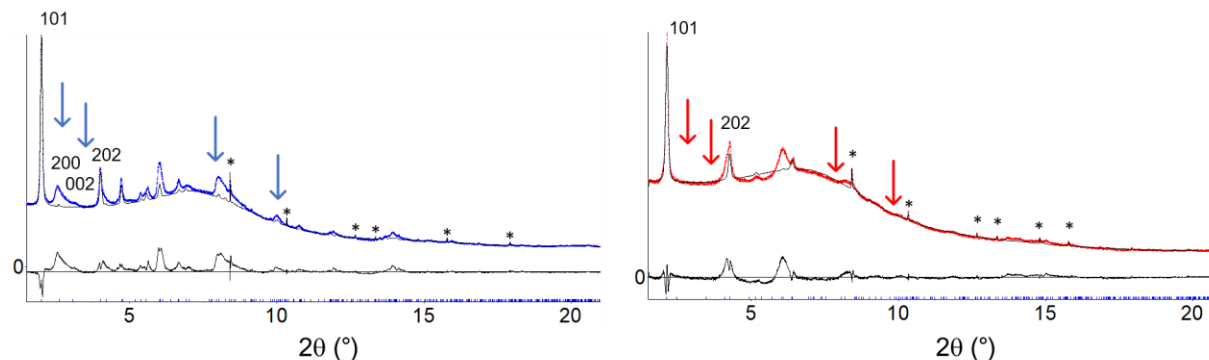


Figure 4-8: Final Rietveld plots of the as synthesized (left) and washed (right) DUT-5(Al)/GO NWs showing observed pattern in blue, calculated in red, and difference curves in black ($\lambda=0.5136 \text{ \AA}$). The asterisk describe the CaSO_4 found in the samples.

By comparing the two phases, it can be clearly seen that the (lp) (i.e., as-synthesized DUT-5(Al)/GO-336) phase presents numerous sharp ($h0h$) reflections indicating a good crystallinity for this sample in this direction. However, one can notice that the series of ($h00$) and ($00l$) reflections are very broad (**Figure 4-8, blue arrows**). Likewise, by observing the pattern of the (np) phase, it can be shown that only the $h0h$ reflections are present while the $h00$ and $00l$ become broader and almost disappear. To better understand these results, the different reflections were thoroughly examined. For instance, the fact that (002) and (200) are broad and (101) reflection is thin suggests that the diagonal of the (100) and (001) planes is fixed, and its value is $d= [(a^2c^2)/(c^2+a^2)]^{1/2}$. This value is calculated based on the interplanar distance of a lattice plane with Miller indices (hkl) of an orthorhombic space group:

$$\frac{1}{d^2} = \frac{h^2}{a^2} + \frac{k^2}{b^2} + \frac{l^2}{c^2}$$

The value of the interplanar distances for the (lp) phase is $d_{lp}=14.665 \text{ \AA}$, while for the (np) it is $d_{np}= 13.852 \text{ \AA}$. Yet, even though this d value is constant for each phase, a distribution of the a and c values is still present. For example, for the as-synthesized sample, we can imagine some domains with $a_x = 22.66$ that leads to $c_x = 19.23 \text{ \AA}$, and domains with $a_y = 23.82$ that leads to $c_y = 18.61 \text{ \AA}$, etc. For the washed sample, this

phenomenon is even more marked: The contraction of the unit cell leads to a more important distribution of a and c since (002) and (200) reflections have totally disappeared. One can also assume that such results suggest the presence of microstrains along the a and c axes, which are not present along the (101) axis. Another assumption could be related to the different behavior in the different domains of the crystal. Different pore opening/narrowing may be occurring in the different domains, as a form of correlated disorder. These assumptions are still under investigation with our collaborators. In addition, in case of the contracted (np) phase, a shortening in the b parameter was observed and confirmed by the shifting of the small (011) reflection marked by a red arrow (**Figure 4-8**) from $d = 6.245$ to 5.718 \AA^{-1} . This resulted in too short Al-O distances and to overcome this limitation, the structural model was optimized in order to have consistent Al-O distances of 1.9 \AA .

The structural models of the two phases are shown in (**Figure 4-9**), where the three-unit cell axes revealed a variation in their value. The b - and c -axes presented 8.8 and 11.5% losses in their values, respectively. On the contrary, the a -axis presented a 5.5% increase. Moreover, almost 15% loss of original unit cell volume occurred after contraction (lp \rightarrow np), the unit cell volume of DUT-5(Al)/GO-336 decreased from $2880(9)$ to $2461(17) \text{ \AA}^3$ ($\Delta V = 419 \text{ \AA}^3$). Moreover, the calculated contracted model presented a shortening in the Al-Al distance from $3.302(2)$ to $3.03(2) \text{ \AA}$. Thus, to go further in our interpretation, the materials were also characterized by pair distribution function (PDF), which includes both Bragg and diffusion scatterings.

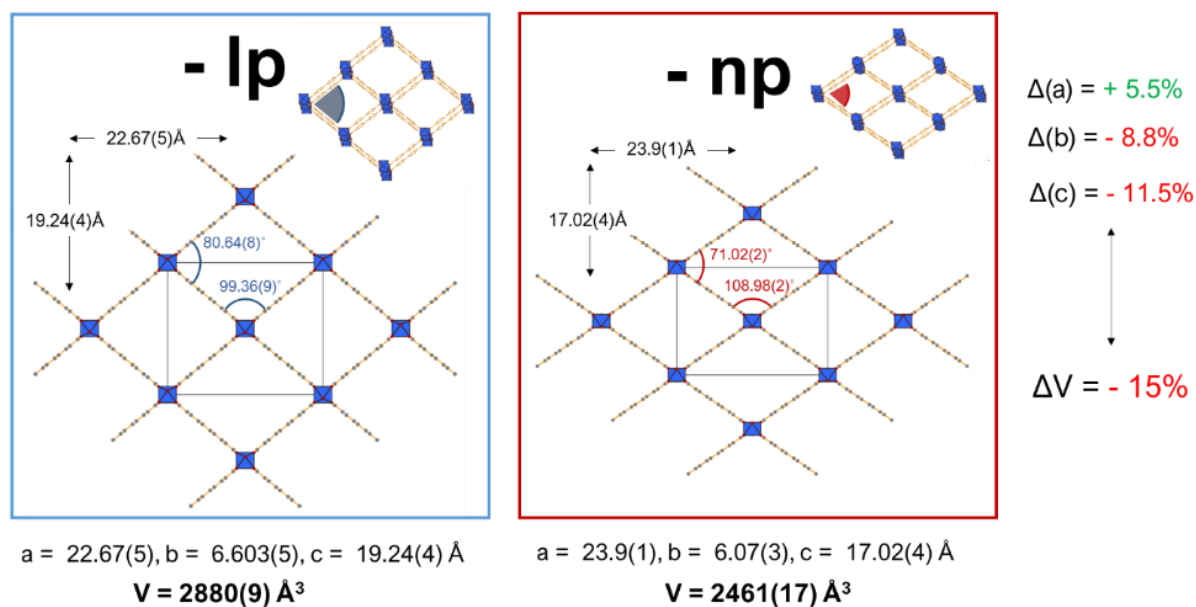


Figure 4-9: Comparison of the (lp) and (np) phases of DUT-5(Al)/GO-336 refined from synchrotron XRD data.

4.4.2. Characterization by Pair Distribution Function

PDF is a method which allows to obtain the interatomic distances between the different elements in the material. Thus, it would be possible to study the presence of any contraction or disorder in the structure based on the change of the distance between the different elements in the (lp) and (np) phases of DUT-5(Al)/GO-336. **(Figure 4-10)** presents the observed PDF of the pure MOF (DUT-5(Al)-24) as well as DUT-5(Al)/GO composites (as-synthesized or (lp) and washed or (np)), based on the experimental data recorded at synchrotron Soleil (beamline CRISTAL).

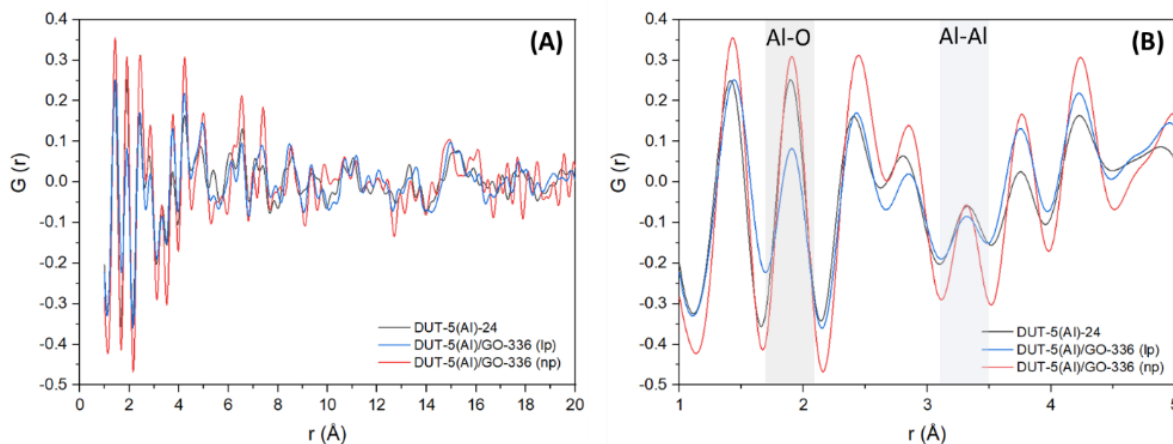


Figure 4-10: Observed PDF analyses (A) of DUT-5(Al)-24, as-synthesized (lp) and washed (np) DUT-5(Al)/GO-336. (B) Zoom on the peaks between $r = 1-5 \text{ \AA}$ to investigate the short-range order in the Al chains.

By investigating the short-range order in the chains of Al^{3+} octahedra (**Figure 4-10, B**), the PDF analysis of DUT-5(Al)-24 and both DUT-5(Al)/GO-336 composites are in accordance. For all samples, the PDF data show peaks at the same atom-pair distances, which corroborates similar local Al environments within the Al chains of the different samples. The PDF profiles of the as-synthesized and washed DUT-5(Al)/GO-336 are almost identical (**Figure 4-10, B**). These results are not in line with a contraction of the DUT-5 b axis in the washed DUT-5(Al)/GO-336 (np form) observed by PXRD, which inevitably leads to a shortening of the Al-Al distance from 3.3 to 3.0 Å. The Al-O and Al-Al interatomic distances were found to be 1.9 and 3.3 Å, respectively for all samples. Surprisingly, these results were not in accordance with the structural model obtained from the Rietveld refinement (**Figure 4-9**). Yet, it can be assumed that the difference in the obtained results is due to the techniques. XRD mainly probes the crystalline phase in a material while PDF, which includes total scattering, not only probes the crystalline phase with a long-range order but also the amorphous one. In other words, PDF considers the amorphous and the crystalline part of the sample. Moreover, given the low crystallinity of the np form, we cannot exclude that the b parameter has diverged and/or that the *Imma* space group is not preserved. These results may also

suggest that further work is needed to achieve the correct unit cell parameters. Unfortunately, this work is not completed yet and will not be added in this manuscript.

4.5 STUDYING THE FLEXIBLE BEHAVIOR OF DUT-5(Al)/GO

Following these findings, it was important to study the possibility of switching between the two phases, or only from one phase to another, in a controllable manner. Indeed, literature has focused on the presence/absence of guest molecules in MOF pores as crucial for inducing flexible behaviors.¹³ Thus, this part of chapter will study the effects of temperature, solvent exchange, and gas adsorption on the flexible behavior of DUT-5(Al).

4.5.1. Effect of Temperature on the Flexibility of DUT-5(Al)/GO

As concluded in **section 4.3**, the pore content strongly affects the behavior of the materials. Thus, one way to control the shift from the (lp) to the (np) phase would be through evacuating the pores of DUT-5(Al)/GO-336. This could be simply achieved via heating the sample. The effect of temperature on the dynamic behavior of DUT-5(Al)/GO-336 was studied by *ex-situ* PXRD under heating, and *in-situ* FT-IR spectroscopy.

4.5.1.1. Ex-situ PXRD under heating

The as-synthesized DUT-5(Al)/GO-336 was characterized by PXRD, then it was heated at 100°C for different intervals of time. The sample was then *ex-situ* characterized by PXRD after each heating.

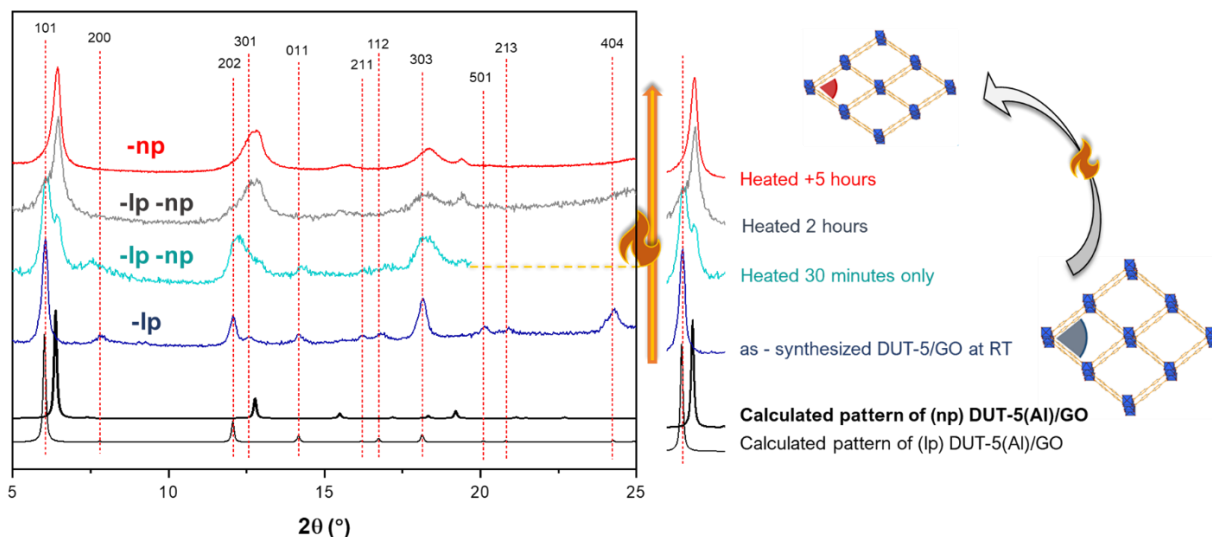


Figure 4-11: PXRD patterns of DUT-5(Al)/GO heated for different intervals in comparison to the calculated pattern of the (lp) and (np) phase of DUT-5(Al)/GO.

Remarkably, as shown in **(Figure 4-11)**, the sample transforms gradually from the (lp) to the (np) phase just by increasing the heating time. Furthermore, interestingly it can be observed that after 5 hours of heating at 100 °C, the same degree of contraction than the composite obtained after washing in ethanol and heating at 100 °C overnight can be achieved. Therefore, it can be deduced that the structural transition between the (lp) and (np) phase in the DUT-5(Al) based composite does not require any drastic conditions and can be achieved via different means.

4.5.1.2. In-situ FT-IR spectroscopy under heating

In addition to PXRD, FT-IR spectroscopy can be used to study the change in certain chemical bonds accompanied with the contraction in the MOF framework. Indeed, the contraction of MOF framework leads to changes in some chemical bonds that are reflected in the FT-IR spectra.¹⁴ Works in literature have discussed the impact of structural transition from the (lp) to the (np) phases on chemical bonds.¹⁴ For instance, a combined experimental and theoretical investigation assigned several bands of MIL-53(Al) as sensitive to its pore dimensions.¹⁵ Some examples are, the $\nu_{as}(\text{COO}^-)$ at 1573

and 1504 cm^{-1} (for the np) and 1596 and 1511 cm^{-1} (for the lp); and $\delta(\text{COO}^-)$ at 848 cm^{-1} (np) and 852 cm^{-1} (lp). Moreover, the flexible MIL-53(Al) was also studied by high resolution synchrotron IR specular reflectance spectroscopy.¹⁶ It was reported that the peak at 1600 cm^{-1} is shifted to 1585 cm^{-1} when shifting from the (lp) to the (np) of MIL-53(Al), and these changes were supported by *ab initio* DFT calculations. The sensitivity of bands around 1400 cm^{-1} (carboxylate symmetric stretching vibration) and 980 cm^{-1} (OH group deformation band) was also illustrated.¹⁶ Thus, to further validate the effect of heating on the contraction of DUT-5(Al)/GO-336, *in-situ* FT-IR spectroscopy was performed in collaboration with F. Bourdeux at ILV (**Figure 4-12**). As-synthesized DUT-5(Al)/GO-336 was characterized wet and upon heating from RT to $400\text{ }^\circ\text{C}$ ($2^\circ\text{C}/\text{min}$) while recording the FT-IR spectra each 10 mins, so every $+20\text{ }^\circ\text{C}$. In correlation to the results obtained by PXRD (**Figure 4-11**), DUT-5(Al)/GO-336 is prone to shrink under heating. Thus, the first FT-IR spectrum at RT in dark blue represents the wet as-synthesized sample corresponding to the (lp) phase, while the spectrum at $400\text{ }^\circ\text{C}$ in light blue corresponds to the (np) one (**Figure 4-12, B**). A gradual conversion from the (lp) to (np) phase of DUT-5(Al)/GO-336 under heating is observed, in accordance with the PXRD results. By observing the different bands of the composite spectrum, it can be shown that some bands disappeared while others are shifted. Besides the band at 985 cm^{-1} increased in intensity.

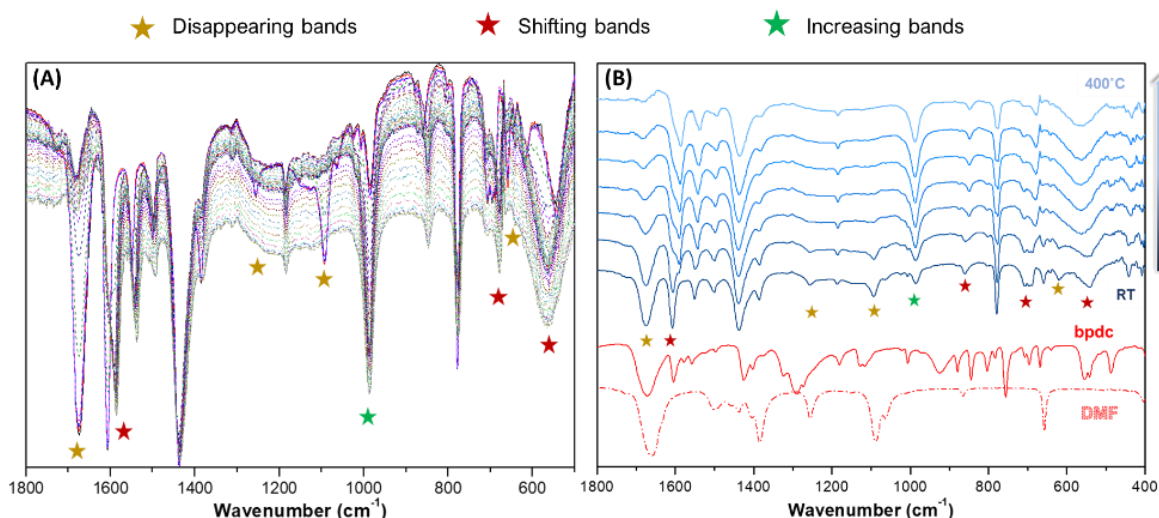


Figure 4-12: (A) *In-situ* FT-IR spectroscopy performed on as-synthesized DUT-5(Al)/GO-336 via heating from RT to 400 °C (2°/min) (B) stacking of selected spectra to reveal the transformation of spectrum under heating.

Concerning the disappearing bands (labelled with a yellow star), first, it can be seen clearly that the bands at 1673, 1257, 1093, and 670 cm⁻¹ decreased with time until they almost disappeared. These bands correspond to the C=O stretching, C-N asymmetric stretching, CH₃ rocking, and O=C-N stretching mode of DMF, respectively.¹⁷ Knowing that the boiling point of DMF is 153 °C, the disappearance of these absorption bands can be clearly explained by the DMF removal upon heating.

Concerning the shifting bands (labelled with a red star), **(Table 4-2)** summarizes the observed shift of representative vibration bands. The absorption bands at 1608 and 860 cm⁻¹, representing the $\nu_{as}(\text{C-O})$ and $\delta(\text{COO}^-)$, both shifted under heating to lower wavenumbers of 1587 and 843 cm⁻¹, respectively.¹⁶ As discussed above, the same shifts of $\nu_{as}(\text{C-O})$ (1600 to 1585 cm⁻¹) and $\delta(\text{COO}^-)$ (852 to 848 cm⁻¹) were considered as an indication of a contraction in MIL-53(Al).¹⁶ Also, the bands at 708 and 685 cm⁻¹ split and shift into 712 and 679 cm⁻¹, respectively. The bands in this region correspond to $\nu_{as}(\text{Al-O-Al})$,¹⁴ and their splitting in opposite directions is certainly due to a change in the local environment of Al sites. This change in the Al environment can be either related to a change in the bond angles, or the coordination environment. According

CHAPTER 4: Insights on the Induced Flexibility in the DUT-5(Al) Structure

to literature, such behavior indicates distortion of the framework, in agreement with the broadening of the PXRD peaks after contraction.¹⁴ Besides, the absorption band at 540 shifted to a higher wavenumber of 562 cm^{-1} under heating. A huge shift ($\Delta\nu = -22 \text{ cm}^{-1}$) was observed. It was not possible to assign this band, it would be of huge interest to later study it for demonstrating a fingerprint of contraction in the DUT-5(Al) based framework.

Table 4-2: Shifting of the representative vibration modes (in cm^{-1}) of the (lp) and (np) of DUT-5(Al)/GO-336 based on experimental observations.

mode	(lp)	(np)	$\Delta\nu$
$\nu_{\text{as}}(\text{C}-\text{OO})$	1608	1587	21
$\delta(\text{COO}^-)$	860	843	17
$\nu_{\text{as}}(\text{Al}-\text{O}-\text{Al})$	708	712	-4
$\nu_{\text{as}}(\text{Al}-\text{O}-\text{Al})$	685	679	6
signature band	540	562	-22

Finally, the OH group deformation band ($\delta(\text{OH})$) at 985 cm^{-1} showed an increase in its intensity with the increase in temperature. Titov *et al*/reported a similar result in case of MIL-53(Al) where the band intensity around 980 cm^{-1} increased with the increase in the applied pressure. The authors suggested that the increase intensity in this bands corresponds to decrease in (lp) content, as suggested from DFT calculations.¹⁶

In conclusion, it was shown in this section, that the shift between the (lp) and (np) is possible and controllable via heating at 100 °C. Both PXRD and FT-IR spectroscopy have shown a gradual transformation from the (lp) to the (np) of DUT-5(Al)/GO-336 via increasing the heating time. It would be of huge interest to combine experimental results obtained by FT-IR with theoretical studies¹⁸ (e.g., DFT calculations) in order to be able to assign a fingerprint of each phase.

4.5.2. Effect of Solvent on the Flexibility of DUT-5(Al)/GO

Several reports in literature have shown that the pore evacuation can lead to a contraction in the framework (e.g., MIL-53(Sc)¹⁹, MIL-53(Fe)²⁰, etc.). In most of these reports, this phenomenon is accompanied with a critical role of the guest-host interactions on the studied system. The effect of guest-host interactions on the phase transformations in MOFs can be observed through solvent exchange, gas adsorption/desorption, etc. Herein, our interest was to study the effect of different solvents on the dynamic behavior of DUT-5(Al)/GO. In addition, such study holds potential for testing the “flexible” nature of our sample via examining the re-opening of the contracted pores via solvent exchange.

Thus, DUT-5(Al)/GO-336 was synthesized, washed by different solvents, and characterized by PXRD without allowing the samples to completely dry. It was important to characterize the samples slightly wet in order to validate the role of the solvent at RT. Different solvents were tested i.e., dichloromethane (DCM), acetone, methanol, ethanol, water, and DMF. As observed in **(Figure 4-13)**, most solvents led to the contraction of the framework except for DMF and water. Ethanol, acetone, and DCM all revealed the same effect on the structure. DUT-5(Al)/GO-336 demonstrated a clear (np) phase when washed with these 3 solvents. In case of methanol, despite the fact that it resulted in a similar behavior, a mixture of the lp and np phases was observed. This suggests that the guest-host interactions with methanol are not enough to induce a complete transition to the np phase. When washed with DMF, DUT-5(Al)/GO-336 remains in its lp form, suggesting no effect of DMF on the contraction of the framework. Interestingly, when washed with water, DUT-5(Al)/GO-336 presented a new form which is intermediate between the lp and np phase. Such intermediate phases were observed previously in literature (e.g., the (lp), (np), and closed pore (cp) phases of MIL-53(Al)).¹⁸ However, this result was not further studied

in this PhD due to lack of time. Moreover, it is worth mentioning that all samples were characterized by SEM after washing, and no effect on morphology by changing the solvents was observed.

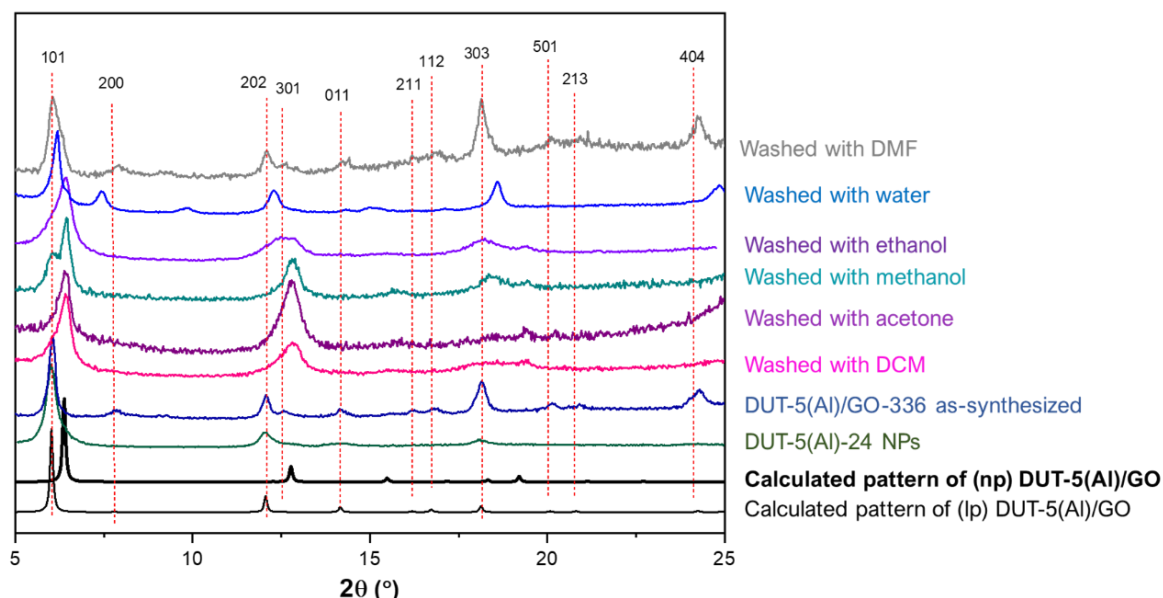


Figure 4-13: PXRD patterns of calculated DUT-5(Al), DUT-5(Al)-24, and DUT-5(Al)/GO-336 as-synthesized and washed with different solvents.

To further study the effect of solvents on the structural behavior of DUT-5(Al)/GO-336, the ability of different solvents to re-open the contracted pores was tested. Thus, DUT-5(Al)/GO-336 was synthesized and washed with ethanol in order to obtain its np phase. The same solvents tested in **(Figure 4-13)** were all tested to re-open the pores of DUT-5(Al)/GO-336. In most cases, the different peaks in PXRD patterns did not shift back to the 2θ angles of the lp form. Only DMF presented some interesting results. As shown in **(Figure 4-14)**, once the contracted sample was soaked in DMF and then re-characterized by PXRD, the DUT-5 in the composite evolved to its lp form. Then, after the composite was heated, a closure of the MOF channels occurred again. These results demonstrate the ability of DUT-5(Al)/GO-336 to switch between the (lp) and (np) form of DUT-5 simply via using ethanol, DMF, and heating.

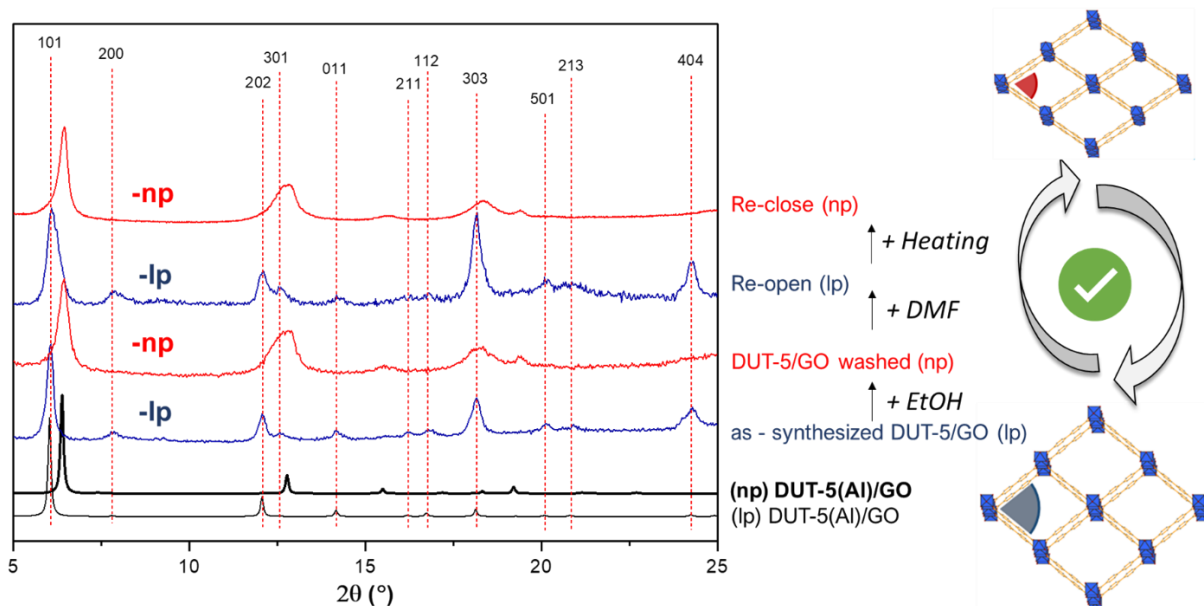


Figure 4-14: PXRD study of the switching between the (lp) and (np) of DUT-5(Al)/GO-336 using ethanol, DMF, and heating. Observed patterns are compared to the calculated (lp) and (np) phase of DUT-5(Al)/GO.

Based on the mentioned results, it can be concluded that the flexibility in the DUT-5(Al) based composite is based on guest-host interactions and can be induced either by the evacuation of the pores under heating or by solvent exchange with different solvents (ethanol, acetone, DCM). Moreover, a special intermediate phase was observed when the sample was washed with water. Furthermore, it was possible to switch between the (lp) and (np) using simple procedures as ethanol washing, soaking in DMF, and heating. These results clearly state the flexible character of the DUT-5(Al)/GO-336 composite.

4.5.3. Effect of Gas Guest Molecules on Flexibility of DUT-5(Al)/GO

Framework flexibility is one of the most important characteristics of MOFs, which is not only interesting, but also useful for a variety of applications. Designing, tailoring, or controlling framework flexibility of MOFs is usually much more difficult than studying static structural features such as the framework topology and pore size/shape. Nevertheless, some strategies have been developed for controlling the flexibility of MOFs and the corresponding properties. The in-depth understanding of the relationship between framework flexibility and guest loading is now possible. Among these strategies, the gas induced transformation monitored by *in-situ* XRD is of huge interest.^{6,21,22} Previous studies performed on DUT-49 in literature have shown that adsorption-induced transitions occur at temperatures close to the respective boiling point of the adsorbate. Thus, in this PhD project, we have performed a study on the effect of two different gases: CO₂ (195 K) and n-butane (273 K) on the flexible behavior of both DUT-5(Al)-336 and DUT-5(Al)/GO-336 in collaboration with V. Bon and S. Kaskel at TU Dresden. The smaller kinetic diameter of the CO₂ molecule (3.30 Å) compared to Ar (3.40 Å) and N₂ (3.64 Å) together with the higher boiling temperature (195 vs. 77 K) facilitates the diffusion of the gas into narrow micropores (size < 5 Å). In addition, compared to the CO₂ sorption experiments performed at 273 or 298 K, running the experiment at 195 K allows complete filling of the micropores at 100 kPa.²² Similarly, concerning the choice of n-butane (273 K), the adsorption of n-butane at 273 K has shown a flexible behavior on different MOFs (e.g., DUT-49(Cu), DUT-13(Zn), etc.) due to its high adsorption enthalpy.^{6,21} This flexible behavior of such MOFs was evidenced by combining *in-situ* PXRD and adsorption/desorption isotherms at low partial pressure characterized by multiple steps and hysteresis.^{6,21}

As shown in **(Figure 4-15)**, DUT-5(Al)-336 and DUT-5(Al)/GO-336 powders in the np form exhibited similar reversible CO₂ isotherms at low partial pressure characteristic of microporous material with no flexibility as deduced from the lack of any steps or hysteresis. In contrast, the physisorption of n-butane at 273K reveals the flexible behavior of these materials since stepwise isotherms with hysteresis were observed as previously reported for other flexible MOFs such as DUT-8(M) (M= Ni, Co), MIL-53(Al)-NH₂, and DUT-98(Zr). One can assume that the high adsorption enthalpy of n-butane associated to its higher kinetic diameter (i.e., kinetic diameters of n-butane and CO₂ are 4.3 and 3.3 Å respectively) can trigger the phase transition from the np form to the lp form. Note that the breathing effect is apparently higher for DUT-5(Al)/GO-336 in comparison to DUT-5(Al)-336 since the hysteresis between the adsorption and desorption branch is much larger.

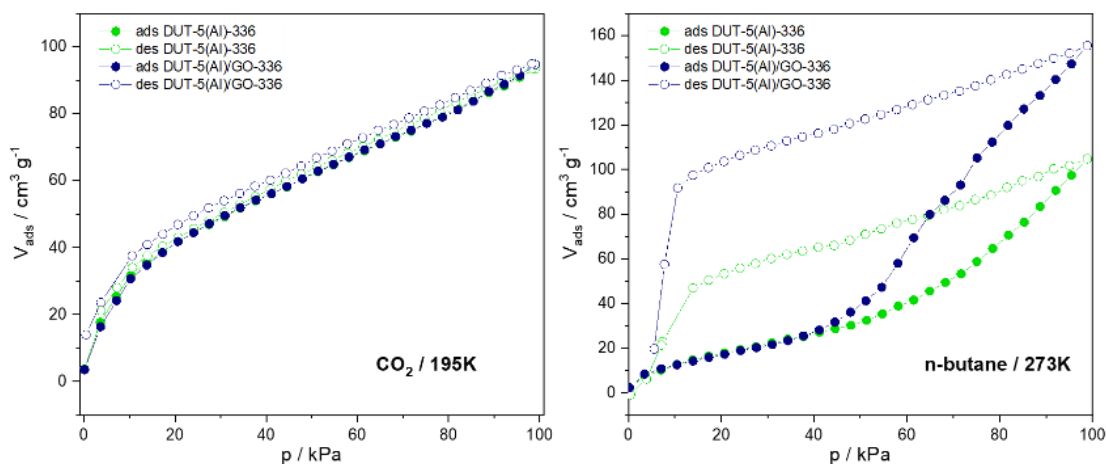


Figure 4-15: Physisorption isotherms of DUT-5(Al)-336 (in green) and DUT-5(Al)/GO-336 (in blue) under CO₂ at 195 K and n-butane at 273 K.

Thus, the adsorption of n-butane in those materials was considered for an in-depth study of the flexible behavior of DUT-5(Al)-336 and DUT-5(Al)/GO-336. The n-butane physisorption isotherms at 273 K were recorded with *in-situ* XRD measurement. **(Figure 4-16)** and **(Figure 4-17)** show the results obtained for DUT-5(Al)-336 and DUT-5(Al)/GO-336, respectively.

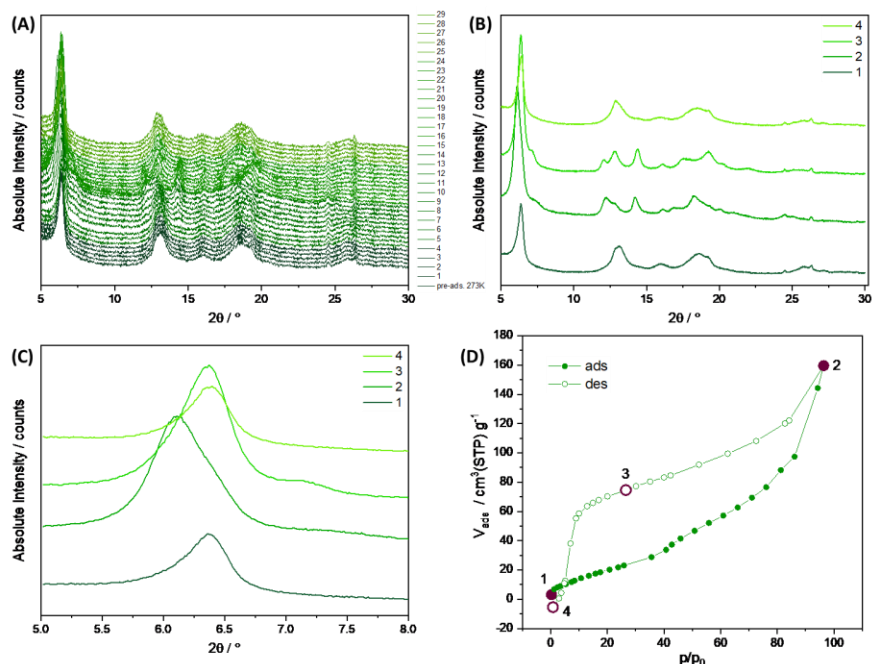


Figure 4-16: (A) *In-situ* PXRD of DUT-5(AI)-336 during the adsorption and desorption of n-butane at 273 K, (B) Selected patterns presenting a flexible behavior with a focus on the shift in first (101) peak (C). (D) n-butane physisorption isotherm at 273 K. At the n-butane partial pressures labelled in the isotherm (points 1, 2, 3, 4) were simultaneously recorded PXRD patterns presented in Figure (B)-(C).

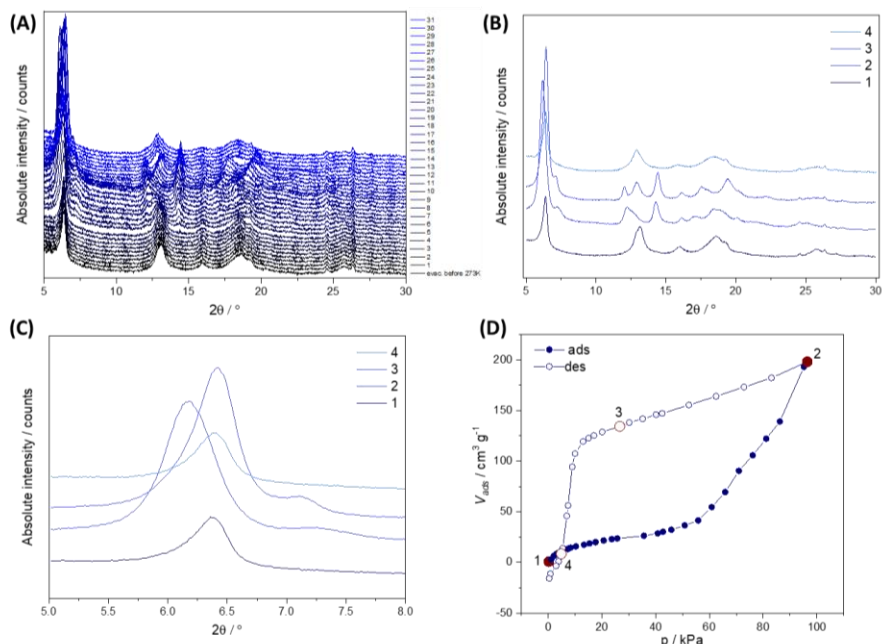


Figure 4-17: (A) *In-situ* PXRD of DUT-5(AI)/GO-336 during the adsorption and desorption of n-butane at 273 K, (B) Selected patterns presenting a flexible behavior with a focus on the shift in first peak(C). (D) n-butane physisorption isotherm at 273 K. At the n-butane partial pressures labelled in the isotherm (points 1, 2, 3, 4) were simultaneously recorded PXRD patterns presented in Figure (B)-(C).

As shown in **(Figure 4-16, C)** and **(Figure 4-17, C)**, both samples presented phase transitions at selected n-butane partial pressures. The opening and closure of the MOF pore in both DUT-5(Al)-336 and DUT-5(Al)/GO-336 and thus the lp-np phase transition was confirmed in the PXRD patterns. PXRD patterns were recorded at specific partial pressures identified in the n-butane isotherm (points 1, 2, 3 and 4 of **(Figure 4-16 and 4-17, D)**). It was possible to determine the pressure at which n-butane triggers a phase transition in the two flexible samples **(Table 4-3)**.

Table 4-3: Presentation of different pressures at which the adsorption/desorption of n-butane resulted in a flexible behavior in the DUT-5(Al)-336 (green) and DUT-5(Al)/GO-336 (blue).

Sample name	Pressure (kPa)	2θ (°)	Phase
DUT-5(Al)-336	Evacuated (1)	6.37	np1
	96.41 (2)	6.16	lp1
	26.5 (3)	6.46	np2
	0.47 (4)	6.38	lp2
DUT-5(Al)/GO-336	Evacuated (1)	6.38	np1
	96.76 (2)	6.11	lp1
	10.2 (3)	6.52	np2
	4.8 (4)	6.39	lp2

Knowing that the samples were first in their (np) phase, the first phase transition corresponds to the opening of the pores at almost 96-97 kPa in both samples. Thus, there is a shift from (np1) to (lp1). Interestingly, during n-butane desorption, when the n-butane partial pressure decreases, both DUT-5(Al)-336 (at 26.5 kPa) and DUT-5(Al)/GO-336 (at 10.2 kPa) recontracts moving from (lp1) to (np2). Further desorption leads to a reopening of the pores of DUT-5(Al)-336 (at 0.47 kPa) and DUT-5(Al)/GO-336 (at 4.8 kPa). Though, by comparing the diffracting angle of the first peak in the two samples, it can be deduced that following the second desorption step, the samples almost return to their original (np1) state. In other terms, np1 and lp2 correspond to the same phase **(Figure 4-18)**. These results suggest a gradual transition between the np and lp phases in both DUT-5(Al)-336 and DUT-5(Al)/GO-336.

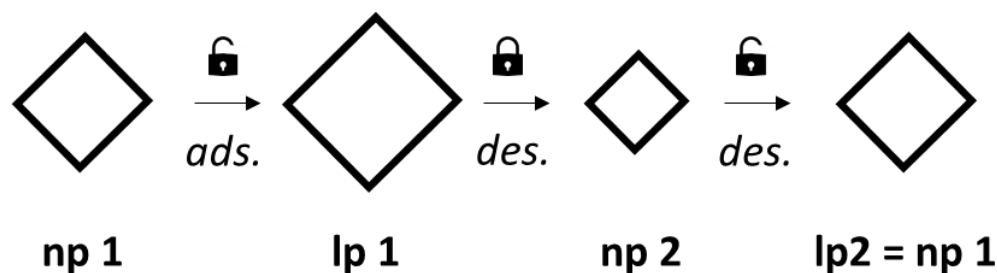


Figure 4-18: Graphical illustration of the 3-step structural transition observed in DUT-5(Al)-336 and DUT-5(Al)/GO-336 under n-butane (273 K) physisorption. Closed lock presents framework contraction while open lock presents opening of the pores.

Finally, it should be noted that some negative desorption points were observed in both samples at very low pressure of $P/P_o < 10$ kPa (**Figure 4-16 and 4-17, D**). It is not clear yet if this is a special phenomenon or if it is related to technical and operating conditions. This observation is still under study and investigation.

4.6 EFFECT OF SIZE AND MORPHOLOGY ON FLEXIBILITY

In 2013, a pioneering work by Kitagawa *et al*/discussed the so called “shape memory effect” presented by a new structural transition behavior that was absent before downsizing the MOF crystals of the flexible $\text{Cu}_2(\text{bdc})_2(\text{bpy})$ (bdc=1,4-benzenedicarboxylate and bpy=4,4'-bipyridine) framework.²³ Years later, many works in literature have mentioned the relationship between the crystallite size and morphology of a material, and its flexible behavior (check **chapter 1**).²⁴⁻³⁰ In particular, it was found that in many cases the downsizing of MOF crystals can lead to a hindered flexibility. A typical example on the size dependent flexibility in MOFs is the pillared layer MOF DUT-8(Ni).²⁴⁻²⁶ In fact, this MOF can be obtained as a rigid material when synthesized as submicron sized crystals (<500 nm) and flexible when synthesized as micron sized particles.^{27,28} A similar rigidification of the MOF framework while downsizing was observed for DUT-98(Zr).²⁹ Likewise for MIL-53(Al)-NH₂, the breathing

behavior involving a (op)-(cp)-(op) transition evolves to a rigid op phase when the diameter of the MOF crystal decreased.³⁰

It has been made clear in this chapter that no flexible behavior was observed in case of DUT-5(Al)-24 despite the different stimuli tested (i.e., heating, and solvent exchange) while both DUT-5(Al)-336 and DUT-5(Al)/GO-336 have shown a flexible behavior. One significant difference between DUT-5(Al)-24 and the other two samples is the absence of micron-sized elongated particles. Some of DUT-5(Al)-336 and all of DUT-5(Al)/GO-336 are made of micron-sized particles. Based on the mentioned reports from literature, one can assume that this difference in crystallite size and morphology between the three samples can explain the absence of flexibility in DUT-5(Al)-24, and the full control over switchability between the (lp) and (np) DUT-5(Al)/GO-336 (**Figure 4-19**). As mentioned earlier, there is a large polydispersity in the crystals morphology of DUT-5(Al)-336 depending on the synthesis batch. This may also explain the difficulty to obtain a reproducible flexible behavior for this sample. To our knowledge, no work in literature have yet discussed the relationship between shape anisotropy of MOFs and their flexibility. Knowing that the anisotropy observed in our samples is along the aluminum chains of the MOF (**chapter 3**, SAED experiments), one can assume that the observed flexible behavior can be attributed to the fact that DUT-5(Al) may favor ligand-ligand interactions along this direction. This assumption could be validated by the theoretical studies performed by Hoffman *et al*, which concluded that the adjacent bpdc ligands of the DUT-5(Al) framework thermodynamically favor a (cp) phase which allows strong dispersion interactions between them.⁸

CHAPTER 4: Insights on the Induced Flexibility in the DUT-5(Al) Structure

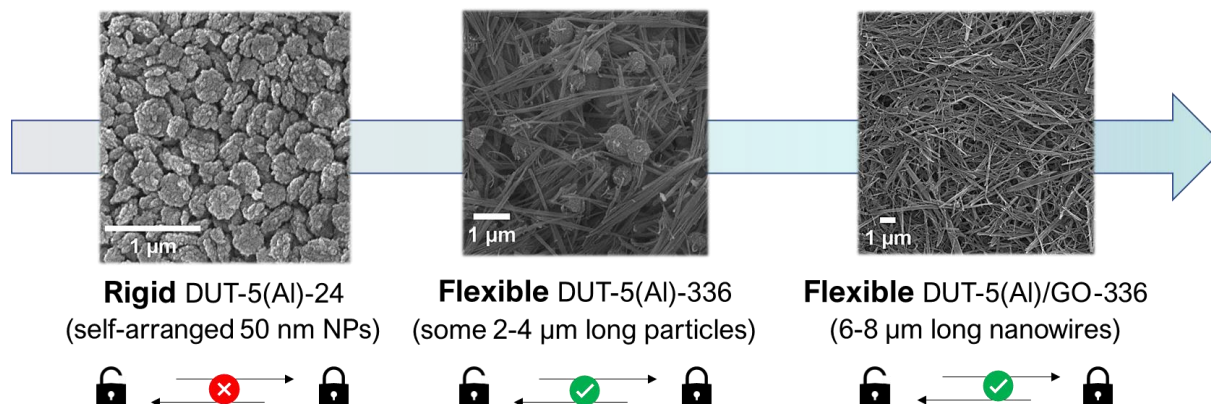


Figure 4-19: Graphical presentation of the observed structural behavior in DUT-5(Al)-24, DUT-5(Al)-336, and DUT-5(Al)/GO-336. The blue arrow presents the increase in flexible behavior with particle size.

Unfortunately, the assumed effect of size and morphology on the flexible behavior of the materials was not further tested in this PhD project. As mentioned in **chapter 3**, it is possible to control the size of DUT-5(Al)/GO-336 nanowires via controlling the reaction time. Thus, as a perspective, it would be of huge interest to test this concept by synthesizing DUT-5(Al)/GO-336 NWs of different sizes and comparing their flexible behavior. Finally, it is worth mentioning that to date, there is no clear explanation for the effect of particle size on flexibility in MOFs. In fact, even though models addressing size-dependent flexibility in MOFs are yet to be further developed, Erhling and co-workers suggested some hypotheses that can explain the energetics involved in this type of flexibility.^{31,32}

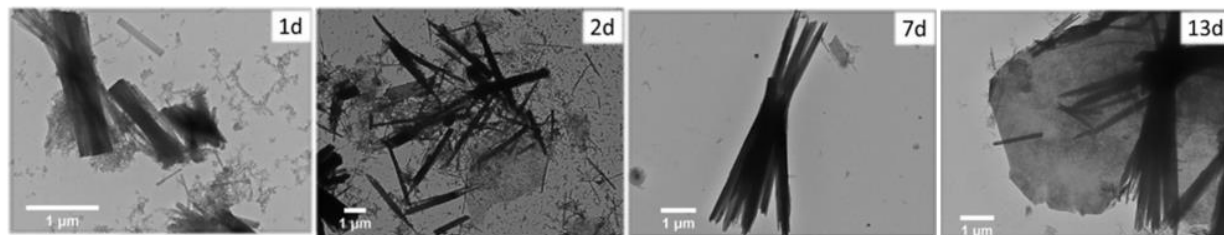


Figure 4-20: Evolution of DUT-5(Al)/GO-336 particle size with time under reflux (insert in days).

4.7 CONCLUSIONS AND PERSPECTIVES

Three samples were previously studied in **chapter 3**: DUT-5(Al)-24, DUT-5(Al)-336, and DUT-5(Al)/GO-336. It was shown that once DUT-5(Al)-336 and DUT-5(Al)/GO-336 were washed and heated, a contraction of the DUT-5(Al) framework occurs. This phenomenon was not observed for DUT-5(Al)-24. Herein, to better understand these results, the three samples were thoroughly studied. Based on literature, flexibility in MOFs was always correlated to the host/guest interactions inside the pores.¹³ Physical, or chemical stimuli have been considered necessary to trigger dynamic behaviors in MOFs. Thus, in this chapter, we have tested different stimuli to tune the observed contraction and understand the dynamic behavior of DUT-5(Al)-336 and DUT-5(Al)/GO-336. First, via comparing the results obtained by WAXS and PXRD, it was assumed that the contraction of the MOF frameworks is dependent on the pore content. This assumption was further confirmed by the observed gradual conversion in the PXRD patterns of DUT-5(Al)-336 and DUT-5(Al)/GO-336 from the (lp) to the (np) by guest removal at RT. The composite was chosen for a detailed study as it was the only sample to present reproducible PXRD patterns in the (lp) phase. Despite the poor quality of the recorded XRD data, it was possible to propose unit cell parameters of the (lp) and (np) phases of DUT-5(Al)/GO-336. Afterwards, it was critical to study the possibility of switching from one phase to another in a controllable manner. Therefore, the stimuli tested included heating and solvent exchange. *Ex-situ* (PXRD) and *in-situ* characterization techniques (Thermal FT-IR spectroscopy) were used, and it was concluded that the framework is flexible, and switching between the (lp) and (np) phases in a reversible manner is possible via simple procedures (soaking in DMF, heating, washing with ethanol). Moreover, to get better insights on both DUT-5(Al)-336 and DUT-5(Al)/GO-336, *in-situ* PXRD coupled with n-butane physisorption at 273 K was performed. Remarkably, it was observed that the studied frameworks both show

a flexible behavior, and that the switching between different phases (np1,lp1,np2, and lp2) was possible via n-butane adsorption/desorption. Further work needs to be performed in order to demonstrate the impact of crystal size and morphology on the flexible behavior of the different DUT-5(AI) based materials. Moreover, it should be highlighted that this is the first work to ever discuss an experimentally observed flexibility in the DUT-5(AI) framework.

4.8 REFERENCES

- (1) Millange, F.; Walton, R. I. MIL-53 and Its Isoreticular Analogues: A Review of the Chemistry and Structure of a Prototypical Flexible Metal-Organic Framework. *Israel Journal of Chemistry* **2018**, *58* (9/10), 1019–1035. <https://doi.org/10.1002/ijch.201800084>.
- (2) Schneemann, A.; Bon, V.; Schwedler, I.; Senkovska, I.; Kaskel, S.; A. Fischer, R. Flexible Metal-Organic Frameworks. *Chemical Society Reviews* **2014**, *43* (16), 6062–6096. <https://doi.org/10.1039/C4CS00101J>.
- (3) Seth, S.; Jhulki, S. Porous Flexible Frameworks: Origins of Flexibility and Applications. *Mater. Horiz.* **2021**, *8* (3), 700–727. <https://doi.org/10.1039/D0MH01710H>.
- (4) Kaur, J.; Kaur, G. Review on Flexible Metal-Organic Frameworks. *ChemistrySelect* **2021**, *6* (32), 8227–8243. <https://doi.org/10.1002/slct.202101524>.
- (5) Wieme, J.; Lejaeghere, K.; Kresse, G.; Van Speybroeck, V. Tuning the Balance between Dispersion and Entropy to Design Temperature-Responsive Flexible Metal-Organic Frameworks. *Nat Commun* **2018**, *9* (1), 4899. <https://doi.org/10.1038/s41467-018-07298-4>.
- (6) Krause, S.; Bon, V.; Senkovska, I.; Stoeck, U.; Wallacher, D.; Töbrens, D. M.; Zander, S.; Pillai, R. S.; Maurin, G.; Coudert, F.-X.; Kaskel, S. A Pressure-Amplifying Framework Material with Negative Gas Adsorption Transitions. *Nature* **2016**, *532* (7599), 348–352. <https://doi.org/10.1038/nature17430>.
- (7) Vanduyfhuys, L.; Rogge, S. M. J.; Wieme, J.; Vandenbrande, S.; Maurin, G.; Waroquier, M.; Van Speybroeck, V. Thermodynamic Insight into Stimuli-Responsive Behaviour of Soft Porous Crystals. *Nat Commun* **2018**, *9* (1), 204. <https://doi.org/10.1038/s41467-017-02666-y>.
- (8) Hoffman, A. E. J.; Senkovska, I.; Wieme, J.; Krylov, A.; Kaskel, S.; Speybroeck, V. V. Unfolding the Terahertz Spectrum of Soft Porous Crystals: Rigid Unit Modes and Their Impact on Phase Transitions. *J. Mater. Chem. A* **2022**, *10* (33), 17254–17266. <https://doi.org/10.1039/D2TA01678H>.

- (9) Senkovska, I.; Hoffmann, F.; Fröba, M.; Getzschmann, J.; Böhlmann, W.; Kaskel, S. New Highly Porous Aluminium Based Metal–Organic Frameworks: Al(OH)(Ndc) (Ndc=2,6-Naphthalene Dicarboxylate) and Al(OH)(Bpdc) (Bpdc=4,4'-Biphenyl Dicarboxylate). *Microporous and Mesoporous Materials* **2009**, *122* (1–3), 93–98. <https://doi.org/10.1016/j.micromeso.2009.02.020>.
- (10) Liu, Y.-Y.; Couck, S.; Vandichel, M.; Grzywa, M.; Leus, K.; Biswas, S.; Volkmer, D.; Gascon, J.; Kapteijn, F.; Denayer, J. F. M.; Waroquier, M.; Van Speybroeck, V.; Van Der Voort, P. New VIV-Based Metal–Organic Framework Having Framework Flexibility and High CO₂ Adsorption Capacity. *Inorg. Chem.* **2013**, *52* (1), 113–120. <https://doi.org/10.1021/ic301338a>.
- (11) Couck, S.; Van Assche, T. R. C.; Liu, Y.-Y.; Baron, G. V.; Van Der Voort, P.; Denayer, J. F. M. Adsorption and Separation of Small Hydrocarbons on the Flexible, Vanadium-Containing MOF, COMOC-2. *Langmuir* **2015**, *31* (18), 5063–5070. <https://doi.org/10.1021/acs.langmuir.5b00655>.
- (12) Depauw, H.; Nevjestić, I.; Wang, G.; Leus, K.; Callens, F.; Canck, E. D.; Buysser, K. D.; Vrielinck, H.; Voort, P. V. D. Discovery of a Novel, Large Pore Phase in a Bimetallic Al/V Metal–Organic Framework. *J. Mater. Chem. A* **2017**, *5* (47), 24580–24584. <https://doi.org/10.1039/C7TA08103K>.
- (13) Kitagawa, S.; Kitaura, R.; Noro, S. Functional Porous Coordination Polymers. *Angewandte Chemie International Edition* **2004**, *43* (18), 2334–2375. <https://doi.org/10.1002/anie.200300610>.
- (14) Hadjiivanov, K. I.; Panayotov, D. A.; Mihaylov, M. Y.; Ivanova, E. Z.; Chakarova, K. K.; Andonova, S. M.; Drenchev, N. L. Power of Infrared and Raman Spectroscopies to Characterize Metal–Organic Frameworks and Investigate Their Interaction with Guest Molecules. *Chem. Rev.* **2021**, *121* (3), 1286–1424. <https://doi.org/10.1021/acs.chemrev.0c00487>.
- (15) Salazar, J. M.; Weber, G.; Simon, J. M.; Bezverkhy, I.; Bellat, J. P. Characterization of Adsorbed Water in MIL-53(Al) by FTIR Spectroscopy and Ab-Initio Calculations. *J. Chem. Phys.* **2015**, *142* (12), 124702. <https://doi.org/10.1063/1.4914903>.
- (16) Titov, K.; Zeng, Z.; Ryder, M. R.; Chaudhari, A. K.; Civalleri, B.; Kelley, C. S.; Frogley, M. D.; Cinque, G.; Tan, J.-C. Probing Dielectric Properties of Metal–Organic Frameworks: MIL-53(Al) as a Model System for Theoretical Predictions and Experimental Measurements via Synchrotron Far- and Mid-Infrared Spectroscopy. *J. Phys. Chem. Lett.* **2017**, *8* (20), 5035–5040. <https://doi.org/10.1021/acs.jpcclett.7b02003>.
- (17) Jacob, M. M. E.; Arof, A. K. FTIR Studies of DMF Plasticized Polyvinylidene Fluoride Based Polymer Electrolytes. *Electrochimica Acta* **2000**, *45* (10), 1701–1706. [https://doi.org/10.1016/S0013-4686\(99\)00316-3](https://doi.org/10.1016/S0013-4686(99)00316-3).
- (18) Hoffman, A. E. J.; Vanduyfhuys, L.; Nevjestić, I.; Wieme, J.; Rogge, S. M. J.; Depauw, H.; Van Der Voort, P.; Vrielinck, H.; Van Speybroeck, V. Elucidating the Vibrational Fingerprint of the Flexible Metal–Organic Framework MIL-53(Al) Using a Combined Experimental/Computational Approach. *J. Phys. Chem. C* **2018**, *122* (5), 2734–2746. <https://doi.org/10.1021/acs.jpcc.7b11031>.

CHAPTER 4: Insights on the Induced Flexibility in the DUT-5(AI) Structure

- (19) S. Mowat, J. P.; R. Seymour, V.; M. Griffin, J.; P. Thompson, S.; Z. Slawin, A. M.; Fairen-Jimenez, D.; Düren, T.; E. Ashbrook, S.; A. Wright, P. A Novel Structural Form of MIL-53 Observed for the Scandium Analogue and Its Response to Temperature Variation and CO₂ Adsorption. *Dalton Transactions* **2012**, 41 (14), 3937–3941. <https://doi.org/10.1039/C1DT11729G>.
- (20) Millange, F.; Guillou, N.; I. Walton, R.; Grenèche, J.-M.; Margiolaki, I.; Férey, G. Effect of the Nature of the Metal on the Breathing Steps in MOFs with Dynamic Frameworks. *Chemical Communications* **2008**, 0 (39), 4732–4734. <https://doi.org/10.1039/B809419E>.
- (21) Felsner, B.; Bon, V.; Evans, J. D.; Schwotzer, F.; Grünker, R.; Senkovska, I.; Kaskel, S. Unraveling the Guest-Induced Switchability in the Metal-Organic Framework DUT-13(Zn). *Chemistry* **2021**, 27 (37), 9708–9715. <https://doi.org/10.1002/chem.202100599>.
- (22) Frentzel-Beyme, L.; Kolodzeiski, P.; Weiß, J.-B.; Schneemann, A.; Henke, S. Quantification of Gas-Accessible Microporosity in Metal-Organic Framework Glasses. *Nat Commun* **2022**, 13 (1), 7750. <https://doi.org/10.1038/s41467-022-35372-5>.
- (23) Sakata, Y.; Furukawa, S.; Kondo, M.; Hirai, K.; Horike, N.; Takashima, Y.; Uehara, H.; Louvain, N.; Meilikhov, M.; Tsuruoka, T.; Isoda, S.; Kosaka, W.; Sakata, O.; Kitagawa, S. Shape-Memory Nanopores Induced in Coordination Frameworks by Crystal Downsizing. *Science* **2013**, 339(6116), 193–196. <https://doi.org/10.1126/science.1231451>.
- (24) Ehrling, S.; Senkovska, I.; Bon, V.; Evans, J. D.; Petkov, P.; Krupskaya, Y.; Kataev, V.; Wulf, T.; Krylov, A.; Vtyurin, A.; Krylova, S.; Adichtchev, S.; Slyusareva, E.; Weiss, M. S.; Büchner, B.; Heine, T.; Kaskel, S. Crystal Size versus Paddle Wheel Deformability: Selective Gated Adsorption Transitions of the Switchable Metal–Organic Frameworks DUT-8(Co) and DUT-8(Ni). *J. Mater. Chem. A* **2019**, 7(37), 21459–21475. <https://doi.org/10.1039/C9TA06781G>.
- (25) Abylgazina, L.; Senkovska, I.; Engemann, R.; Ehrling, S.; Gorelik, T. E.; Kavooosi, N.; Kaiser, U.; Kaskel, S. Impact of Crystal Size and Morphology on Switchability Characteristics in Pillared-Layer Metal-Organic Framework DUT-8(Ni). *Frontiers in Chemistry* **2021**, 9.
- (26) J. Thompson, M.; L. Hobday, C.; Senkovska, I.; Bon, V.; Ehrling, S.; Maliuta, M.; Kaskel, S.; Düren, T. Role of Particle Size and Surface Functionalisation on the Flexibility Behaviour of Switchable Metal–Organic Framework DUT-8(Ni). *Journal of Materials Chemistry A* **2020**, 8 (43), 22703–22711. <https://doi.org/10.1039/D0TA07775E>.
- (27) Miura, H.; Bon, V.; Senkovska, I.; Ehrling, S.; Watanabe, S.; Ohba, M.; Kaskel, S. Tuning the Gate-Opening Pressure and Particle Size Distribution of the Switchable Metal–Organic Framework DUT-8(Ni) by Controlled Nucleation in a Micromixer. *Dalton Transactions* **2017**, 46 (40), 14002–14011. <https://doi.org/10.1039/C7DT02809A>.
- (28) Kavooosi, N.; Bon, V.; Senkovska, I.; Krause, S.; Atzori, C.; Bonino, F.; Pallmann, J.; Paasch, S.; Brunner, E.; Kaskel, S. Tailoring Adsorption Induced Phase Transitions in the Pillared-Layer Type Metal–Organic Framework DUT-8(Ni). *Dalton Transactions* **2017**, 46 (14), 4685–4695. <https://doi.org/10.1039/C7DT00015D>.

CHAPTER 4: Insights on the Induced Flexibility in the DUT-5(Al) Structure

- (29) Krause, S.; Bon, V.; Du, H.; Dunin-Borkowski, R. E.; Stoeck, U.; Senkovska, I.; Kaskel, S. The Impact of Crystal Size and Temperature on the Adsorption-Induced Flexibility of the Zr-Based Metal–Organic Framework DUT-98. *Beilstein J. Nanotechnol.* **2019**, *10*, 1737–1744. <https://doi.org/10.3762/bjnano.10.169>.
- (30) Dai, Z.; Lee, D. T.; Shi, K.; Wang, S.; Barton, H. F.; Zhu, J.; Yan, J.; Ke, Q.; Parsons, G. N. Fabrication of a Freestanding Metal Organic Framework Predominant Hollow Fiber Mat and Its Potential Applications in Gas Separation and Catalysis. *J. Mater. Chem. A* **2020**, *8* (7), 3803–3813. <https://doi.org/10.1039/C9TA11701F>.
- (31) Ehrling, S.; Miura, H.; Senkovska, I.; Kaskel, S. From Macro- to Nanoscale: Finite Size Effects on Metal–Organic Framework Switchability. *Trends in Chemistry* **2021**, *3* (4), 291–304. <https://doi.org/10.1016/j.trechm.2020.12.012>.
- (32) Ehrling, S.; Reynolds, E. M.; Bon, V.; Senkovska, I.; Gorelik, T. E.; Evans, J. D.; Rauche, M.; Mendt, M.; Weiss, M. S.; Pöppel, A.; Brunner, E.; Kaiser, U.; Goodwin, A. L.; Kaskel, S. Adaptive Response of a Metal–Organic Framework through Reversible Disorder–Disorder Transitions. *Nat. Chem.* **2021**, *13* (6), 568–574. <https://doi.org/10.1038/s41557-021-00684-4>.

CONCLUSIONS & PERSPECTIVES

The effectiveness of MOFs has been often constrained by their low chemical stability and processability. The combination of MOFs with carbon based functionalized surfaces such as graphene oxide sheets allows designing MOF based composites with an enhanced stability, processability, and conductivity, while inducing hierarchical pore characteristics and specific templating effects.^{1,2} The control over the size, morphology and surface structure of MOFs nanocrystals is a burgeoning scientific thematic due to its effect on the physico-chemical properties and the performance of these materials in different applications. During this project, we were able to extend the previously reported concept of using GO as a structural directing agent to the DUT-5(Al) MOF, allowing the formation of anisotropic 1D DUT-5(Al) based single crystals.³ The designed composite revealed interesting properties in terms of stability and structural switchability. Besides, it exhibited a dual micro- and mesoporosity due to the inherent porosity of the MOF and inter-particle spaces. This hierarchical porosity is prone to boost the diffusion of analytes and reactants towards the adsorption and/or active sites of MOFs, thereby enhancing the performance of MOFs in applications like catalysis and adsorption.^{4,5}

In chapter 2, an initial screening of the best candidate for designing nanostructured MOF/GO composites was first performed based on the results obtained with the previous MIL-69(Al)/GO project which led to MOF based single crystalline nanowires using GO nanoscrolls as a structural directing agent.⁶ The selection criteria were focused on targeting polycarboxylate aromatic Al/Zr based MOFs which can be obtained under reflux in DMF, water, or a mixture of the two solvents. The studied MOFs were: CAU-23(Al),⁷ DUT-5(Al),⁸ MOF-545(Zr),⁹ CAU-10-H(Al),¹⁰ and DUT-67(Zr)¹¹. For each of the MOFs, the synthesis protocol under reflux

(reported or optimized) was described. Afterwards, the design of the MOF/GO composite was reported, and the characterization of both the MOFs and their corresponding composites was presented. The samples were characterized first by PXRD and FT-IR spectroscopy, once proved crystalline, the samples were characterized by SEM to verify the presence of any templating effect by GO. Following this screening of the different candidates, DUT-5(Al) was selected as the corresponding DUT-5/GO presented the most promising microstructural properties.

DUT-5(Al) was then thoroughly studied in chapter 3. The reported synthesis was found to yield some extra aluminum oxide in the sample. This study thus focused on the synthesis optimization of both DUT-5(Al) nanoparticles and the DUT-5(Al)/GO composite, and their characterization by employing several advanced techniques (i.e., PXRD, FT-IR spectroscopy, TGA, N₂ physisorption, SEM, TEM, HAADF-STEM, SAED, EDX, XPS, ²⁷Al solid-state NMR, etc.). This optimization led to the formation of a pure DUT-5(Al) phase under reflux, and the preparation of anisotropic DUT-5(Al)/GO nanowires. Moreover, it was possible to obtain anisotropic DUT-5(Al) based nanostructures by tuning synthesis conditions, in absence of GO. Yet, the anisotropic nanostructures obtained in presence of GO (DUT-5(Al)/GO-336) were more well-defined and homogenous than those obtained without it (DUT-5(Al)-336). While DUT-5(Al)/GO-336 consists of an assembly of monodisperse nanowires of 70-90 nm in diameter and length up to 6-8 μm, DUT-5(Al)-336 is made of spherical and elongated aggregates constructed by the assembly of rod-like particles with a high size distribution. Interestingly, an induced dynamic behavior was observed for both materials comprising anisotropic nanostructures.

Hence, chapter 4 discussed the flexible behavior of the MOF found in the DUT-5(Al)/GO composite. Interestingly, the performed experiments (i.e., PXRD,

synchrotron XRD, in-situ FT-IR spectroscopy, and in-situ PXRD coupled with gas adsorption) revealed a switchable behavior in DUT-5(Al)-336 elongated rods and DUT-5(Al)/GO-336 composite between two distinct forms of DUT-5(Al): large pore (lp) and narrow pore (np) phase. Nevertheless, of huge importance in this PhD project was to thoroughly study the observed flexible behavior in the DUT-5(Al) sample of elongated rods and the DUT-5(Al)/GO nanowires. Knowing that MOFs with a flexible structure are prone to respond to different physical and chemical stimuli (e.g., guest adsorption/ desorption, thermal, mechanical, etc.), different tests were performed during this PhD project. It was concluded that the two flexible frameworks can switch in a controllable manner between the (lp) and (np) phase via solvent exchange (ethanol, DMF), gas guest molecules (n-butane), and temperature. These findings allow the later utilization of these samples in different selectivity demanding applications (e.g., gas adsorption/ separation, sensors, etc.).

To our knowledge, no works in literature have ever discussed an experimentally observed flexible behavior in the DUT-5(Al) framework, besides, no flexible MOF/GO composite has been reported to date. The structural flexibility present in some MOFs has been a hot topic to address in the last two decades. Contrary to rigid MOFs, MOFs with a robust and flexible structure have not yet been thoroughly understood. Such dynamic frameworks are intriguing for different research areas such as catalysis, adsorption, separation, etc. Therefore, the idea of shaping MOFs at the nanoscale while inducing structural flexibility in their rigid structure is an interesting research area to accentuate. For instance, the flexible behavior studied in this project was absent when DUT-5(Al) was obtained in the form of self-aggregated nanoparticles, suggesting a relationship between the crystallite size and morphology, and the dynamic behavior of MOFs. Yet, despite the continuous development during the last two decades in the domain of flexible MOFs, such hypothesis remains so far an open question for further study.

In terms of perspectives, considerable progress has been achieved for the development of conductive MOFs, allowing their use in diverse applications for electrochemical energy storage.¹² Among those applications, supercapacitors have received great interest because of their high-power density, fast charging/discharging ability, and excellent cycling stability.¹² Thus, in this frame, we have recently started a scientific collaboration with Pr. Christel LABERTY-ROBERT and Dr. Arvinder SINGH at the Laboratoire de Chimie de la Matière Condensée de Paris (LCMCP) since they have a strong expertise in supercapacitor applications. Experiments were conducted on the DUT-5(Al)/GO-336 composite in comparison to the pure DUT-5 samples (DUT-5(Al)-24 NPs, DUT-5(Al)-336 rods). DUT-5(Al)/GO-336 composite presents an interesting performance as a supercapacitor electrode due to its good electron conductivity and its hierarchical porosity. This work is still under progress and will be published once finished.

In conclusion, the design of tubular MOF nano- and superstructures is still in its infancy. However, we can envision that this research area will be continuously expanded towards the exploration of novel hierarchical MOFs architectures with a high level of morphological complexity. Moreover, the discovery of flexibility phenomena in MOFs plays a crucial role in the progress of industrially applicable science in MOFs. Yet, monitoring of structural and phase changes in these materials requires an understanding of intrinsic framework dynamics. Thus, the development of additional in-situ and theoretical characterization techniques remains crucial. The DUT-5(Al)/GO sample presented in this PhD project, grants an interesting prototype on the design of anisotropic structures with a dynamic behavior, allowing the control over the opening and closure of their pores, and thus over the exploited applications. Inducing flexibility in 1D MOF based composites remains a novel and challenging approach. We hope that this PhD project would provide some valuable insights in facilitating the use of MOF materials in energy related

applications, engineering dimensional MOF based structures, and a better understanding of the smart dynamic behaviors in MOFs.

REFERENCE LIST

- (1) Haeri, Z.; Ramezanzadeh, B.; Ramezanzadeh, M. Recent Progress on the Metal-Organic Frameworks Decorated Graphene Oxide (MOFs-GO) Nano-Building Application for Epoxy Coating Mechanical-Thermal/Flame-Retardant and Anti-Corrosion Features Improvement. *Progress in Organic Coatings* **2022**, *163*, 106645. <https://doi.org/10.1016/j.porgcoat.2021.106645>.
- (2) Xu, J.; Peng, Y.; Xing, W.; Ding, Z.; Zhang, S.; Pang, H. Metal-Organic Frameworks Marry Carbon: Booster for Electrochemical Energy Storage. *Journal of Energy Storage* **2022**, *53*, 105104. <https://doi.org/10.1016/j.est.2022.105104>.
- (3) Muschi, M.; Lalitha, A.; Sene, S.; Aureau, D.; Fregnaux, M.; Esteve, I.; Rivier, L.; Ramsahye, N.; Devautour-Vinot, S.; Sicard, C.; Menguy, N.; Serre, C.; Maurin, G.; Steunou, N. Formation of a Single-Crystal Aluminum-Based MOF Nanowire with Graphene Oxide Nanoscrolls as Structure-Directing Agents. *Angew. Chem. Int. Ed.* **2020**, *59* (26), 10353–10358. <https://doi.org/10.1002/ange.202000795>.
- (4) Saad, A.; Biswas, S.; Gkaniatsou, E.; Sicard, C.; Dumas, E.; Menguy, N.; Steunou, N. Metal-Organic Framework Based 1D Nanostructures and Their Superstructures: Synthesis, Microstructure, and Properties. *Chem. Mater.* **2021**, *33* (15), 5825–5849. <https://doi.org/10.1021/acs.chemmater.1c01034>.
- (5) Feng, L.; Wang, K.-Y.; Lv, X.-L.; Yan, T.-H.; Zhou, H.-C. Hierarchically Porous Metal-Organic Frameworks: Synthetic Strategies and Applications. *National Science Review* **2020**, *7* (11), 1743–1758. <https://doi.org/10.1093/nsr/nwz170>.
- (6) Muschi, M.; Lalitha, A.; Sene, S.; Aureau, D.; Fregnaux, M.; Esteve, I.; Rivier, L.; Ramsahye, N.; Devautour-Vinot, S.; Sicard, C.; Menguy, N.; Serre, C.; Maurin, G.; Steunou, N. Formation of a Single-Crystal Aluminum-Based MOF Nanowire with Graphene Oxide Nanoscrolls as Structure-Directing Agents. *Angew. Chem. Int. Ed.* **2020**, *59* (26), 10353–10358. <https://doi.org/10.1002/ange.202000795>.
- (7) Lenzen, D.; Zhao, J.; Ernst, S.-J.; Wahiduzzaman, M.; Ken Inge, A.; Fröhlich, D.; Xu, H.; Bart, H.-J.; Janiak, C.; Henninger, S.; Maurin, G.; Zou, X.; Stock, N. A Metal-Organic Framework for Efficient Water-Based Ultra-Low-Temperature-Driven Cooling. *Nat Commun* **2019**, *10* (1), 3025. <https://doi.org/10.1038/s41467-019-10960-0>.
- (8) Gotthardt, M. A.; Grosjean, S.; Brunner, T. S.; Kotzel, J.; Gänzler, A. M.; Wolf, S.; Bräse, S.; Kleist, W. Synthesis and Post-Synthetic Modification of Amine-, Alkyne-, Azide- and Nitro-Functionalized Metal-Organic Frameworks Based on DUT-5. *Dalton Trans.* **2015**, *44* (38), 16802–16809. <https://doi.org/10.1039/C5DT02276B>.

- (9) Paille, G.; Gomez-Mingot, M.; Roch-Marchal, C.; Lassalle-Kaiser, B.; Mialane, P.; Fontecave, M.; Mellot-Draznieks, C.; Dolbecq, A. A Fully Noble Metal-Free Photosystem Based on Cobalt-Polyoxometalates Immobilized in a Porphyrinic Metal–Organic Framework for Water Oxidation. *J. Am. Chem. Soc.* **2018**, *140* (10), 3613–3618. <https://doi.org/10.1021/jacs.7b11788>.
- (10) Lenzen, D.; Bendix, P.; Reinsch, H.; Fröhlich, D.; Kummer, H.; Möllers, M.; Hügenell, P. P. C.; Gläser, R.; Henninger, S.; Stock, N. Scalable Green Synthesis and Full-Scale Test of the Metal–Organic Framework CAU-10-H for Use in Adsorption-Driven Chillers. *Advanced Materials* **2018**, *30* (6), 1705869. <https://doi.org/10.1002/adma.201705869>.
- (11) Reinsch, H.; Waitschat, S.; Chavan, S. M.; Lillerud, K. P.; Stock, N. A Facile “Green” Route for Scalable Batch Production and Continuous Synthesis of Zirconium MOFs. *European Journal of Inorganic Chemistry* **2016**, *2016* (27), 4490–4498. <https://doi.org/10.1002/ejic.201600295>.
- (12) Niu, L.; Wu, T.; Chen, M.; Yang, L.; Yang, J.; Wang, Z.; Kornyshev, A. A.; Jiang, H.; Bi, S.; Feng, G. Conductive Metal–Organic Frameworks for Supercapacitors. *Advanced Materials* **2022**, *n/a* (n/a), 2200999. <https://doi.org/10.1002/adma.202200999>.



ANNEX 1

Metal–Organic Framework Based 1D Nanostructures and Their Superstructures: Synthesis, Microstructure, and Properties

Ali Saad, Subharanjan Biswas, Effrosyni Gkaniatsou, Clémence Sicard, Eddy Dumas, Nicolas Menguy, and Nathalie Steunou*

Cite This: *Chem. Mater.* 2021, 33, 5825–5849

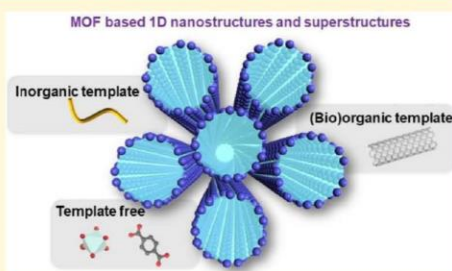
Read Online

ACCESS |

Metrics & More

Article Recommendations

ABSTRACT: Owing to their high and tunable porosity as well as great chemical diversity, metal–organic frameworks (MOFs) have shown great promise over the past 20 years for a wide range of applications, including gas storage/separation, catalysis, and biomedicine. To date, MOF nanoparticles (NPs) have mostly been obtained as polycrystalline powders or spherical nanocrystals while anisotropic MOFs nanocrystals have been less explored and are of interest in the fields of catalysis, sensing, and electronics. One of the main challenges for the practical application of MOFs is thus to control the crystal size, morphology, and multiscale porosity of these materials while developing adequate shaping strategies. In this review, we cover recent advances in the different synthetic strategies of one-dimensional (1D) MOF nanocrystals as well as hierarchical porous superstructures based on tubular MOFs. We describe the architectures based on MOFs nanotubes (NTs), nanowires (NWs), and nanorods (NRs). Our discussion is focused on the synthetic approaches that drive the structure, crystallinity, size, and morphology of these hierarchical porous hybrid materials. Finally, their potential for different applications is presented.



1. INTRODUCTION

The synthesis and application of hierarchically structured inorganic and hybrid materials have gained significant interest due to their high potential in different fields, including energy conversion and storage, life sciences, (photo)catalysis, adsorption, and separation.¹ As has been reported previously, the hierarchy of these materials at the composition, porosity, crystallite size/shape, and organization levels is crucial for their functionality, performance, and stability.^{1,2} In the past few years, novel synthetic strategies such as bioinspired approaches have been exploited to process nanostructured materials with tailored structural and physicochemical properties.^{1,3} Among those nanostructures, one-dimensional nanowires (NWs), nanotubes (NTs), and nanorods (NRs) have drawn significant attention, since the anisotropy of their crystal shape is prone to exposing functional or reactive crystal facets for optimal performance in applications such as catalysis and sensing.^{4,5} Such 1D nanostructures have been reported for a wide range of inorganic materials, including elemental materials (Si, B, etc.), metals (Au, Ag, etc.), metal oxides (TiO₂, VO_x, ZnO, etc.), metal chalcogenides (MoS₂, CdS), and nitrides (GaN, AlN, etc.), among others.^{1–9}

Metal–organic frameworks (MOFs), also termed porous coordination polymers (PCPs), are a class of porous crystalline hybrid materials constructed through the assembly of inorganic

nodes and organic polydentate ligands. A high diversity of two- and three-dimensional topologies with specific chemical functionalities can be designed by tuning the nature of the organic and inorganic building units.^{10,11} Moreover, due to their very high porosity and surface areas, MOFs have shown great promise for a myriad of applications, including gas storage and separation, catalysis, sensing, and biomedicine.^{12–19} To date, scientific research in the field of MOFs has mainly focused on the discovery of novel MOF structures, the evaluation of their physical properties, and the processing of MOF-based composites.^{19–26} However, since most of the MOFs reported to date are microporous (pore size <2 nm), MOF applications tend to be restricted to the adsorption, separation, and catalysis of small guest molecules (standard gases, organic molecules).^{12,13} This range of pore size is prone to decrease mass-transportation rates, limits the diffusion of substrates to catalytically active sites, and finally prevents the processing of MOF composites embedding large components

Received: March 24, 2021

Revised: July 3, 2021

Published: July 21, 2021





Figure 1. Schematic illustrations of the different strategies used to prepare tubular MOF-based nanostructures and superstructures.

such as nanoparticles (NPs) and proteins. To extend the porosity of MOFs in the mesoporous regime (pore size 2–50 nm), hierarchically porous (HP) MOFs have gained significant attention in the past few years for adsorption and catalytic applications.^{27–29} They were synthesized by using either a monodentate ligand as a modulator or soft templates.^{27–29} However, typical syntheses of microporous or HP MOFs generally produced fine powdered materials made of micrometer-sized particles or spherical nanocrystals. While powdered MOF samples are amenable to fundamental academic research, their transfer and implementation for real industrial applications is the current key challenge and requires shaping these materials and controlling their morphology.^{30,31} This issue was mainly addressed by combining MOFs with diverse supporting materials such as polymer membranes, oxides, textile fibers, carbon NTs, and graphene oxide, leading to the processing of multifunctional composites with a good synergism between the properties of the MOFs (porosity, crystallinity) and the supporting matrix (mechanical and chemical stability, processability).^{32–38} The typical preparation of MOF composites consists of combining preformed MOF particles with another component. However, in order to improve the physicochemical matching between the MOFs and the supporting substrate, MOFs can also be formed *in situ* in the presence of the supporting matrix, which not only served as a host matrix but also directed the nucleation and growth of MOFs through templating effects.^{39–41} Moreover, organic molecules or polymers could also act as modulators through their competitive interactions with the organic linkers, thereby affecting the kinetics of MOF crystallization.³³ By these approaches, tubular MOF nanostructures such as NWs and NTs were recently synthesized.^{42–46} These anisotropic MOF nanostructures have sparked interest, since they can potentially exhibit novel size- and dimensionality-dependent physicochemical properties (mass transport, adsorption), as previously demonstrated for low-dimensional nanostructured inorganic materials.^{4–8,47,48}

In view of developing MOFs that combine a hierarchical dimensionality and porosity, superstructures that consist of a mesoscale and oriented assembly of primary MOF crystals were also recently reported.^{39,49,50} These materials present a high level of morphological complexity with a specific (1D, 2D, or 3D) dimensionality of the primary crystals, their organized

assembly, and their interparticular porosity. This strategy was inspired by the observation of biological minerals of living organisms (diatom, leaf, dentine, etc.) and the scientific advances acquired in the bioinspired design of hierarchically nanostructured materials (oxides, metals, zeolites).^{2,3,51} In particular, it has been reported that superstructures such as NP arrays or mesocrystals can result from a strong interplay between aggregation and crystallization, leading to a self-assembly and reorganization of the organic and inorganic building units.

The present review is intended to give a useful survey of recent progress in the synthesis of tubular-structured MOFs as well as superstructures constructed through the assembly of nanotubular MOF units. We focus mainly on nano- and superstructures based on MOF NWs and NTs. MOF NWs are 1D nanostructures with diameters in the nanometer range and lengths of up to a few centimeters. Their aspect ratio (length to diameter ratio) varies to a large extent and is significantly higher than that of NRs. Note that several NWs have been reported with MOFs exhibiting 1D porous structures. Since the channels of the MOFs up to a few nanometers in diameter are lying parallel to the main axis of the NW, these 1D nanostructures have also been considered as MOF NTs as reported in the literature.⁵² In this review, we consider MOF NTs as cylindrical nanostructures characterized by an inner cavity of a few tens of nanometers in diameter. The MOF NTs reported so far can be categorized in the class of single-wall NTs, since they were obtained from MOFs with 3D crystallographic structures. The objective of this review is to describe the main synthetic routes of MOF NWs, NTs, and superstructures (Figure 1). Except for a few 1D MOF nanostructures obtained under template-free conditions as described in section 2, they were mainly prepared in the presence of inorganic or organic coreactants. As described in sections 3 and 4, MOF NTs and MOFs NT arrays were mainly formed through template-directed synthetic routes, by using two kinds of templates (positive or negative template). Some of these structure-directing agents were previously exploited for the synthesis of oxide NTs (Figure 1).⁵³ Positive templating consists of coating the outer surface of preformed 1D nanostructures (NWs or NRs) by the MOF, while negative templating consists of depositing the MOFs at the internal surface of a porous material. Finally, we present the potential

Table 1. Summary of the MOF Nanostructures and Superstructures with the Template or Modulator Employed for Their Syntheses, Dimensions, and Domains of Application

MOF	nanostructure	template	modulator	dimensions (diameter/length)	application	ref
MIL-110(Al)	NT			60 nm/a few μm	Fe ³⁺ ion sensing	59
MOF-74(Co)	NW			70 nm/25–30 μm	separation of dyes	52
HKUST-1	NT	Cu ₂ O NW		~250–400 nm/2–10 μm	adsorption of dyes	46
ZIF-67(Co)	hollow NR	Co ₂ (OH) ₂ (OAc) ₈ NR		~500 nm/a few μm		64
MOF-74(Co)	hollow NR	Co ₃ (OH)(OAc) ₅ NR		~200 nm/~500 nm	CO ₂ /N ₂ separation	62
Cd ₂ (btc) ₂ (H ₂ O) ₂	NT	Cd-btc NR		100–300 nm/>1 μm	Detection of nitroaromatic explosives	66
MOF-5	NW	graphene		~300 nm/a few μm	photoelectric transport properties	42
MIL-69(Al)	NW	graphene oxide		70 \pm 20 nm/>2 μm		45
ZIF-8(Zn)						
ZIF-67(Zn)						
ZIF-12(Co)	NT	PCTE@PDA		~250 nm/~10 μm	adsorption of dye	43
HKUST-1(Cu)						
ZIF-8(Zn)	NT, NW, and NR	PCTE@PVP		~30–100 nm/ ~2–6 μm		44
HKUST-1	NW	PCTE@Cu NWs		80–260 nm/a few μm		73
ZIF-67(Co)	NT	Co(CO ₃) _{0.5} (OH) NWs		100–200 nm/ 400–800 nm	precursors for Co ₃ O ₄ NT arrays	107
ZIF-67(Co)	hollow urchinlike superstructures	2CoCO ₃ ·3Co(OH) ₂ ·H ₂ O		~a few μm	precursors for SC cathode material	65
MOF-74-II(Zn)	microtubes/multichannel or flexible twisted tubular superstructures	PCN-74		microtubes: 5 μm / few tens of μm	heterogeneous catalysis	67
MOF-74-(Zn)-II-III-IV	spherulites based on MOF-74 NR			20–40 μm in diameter	adsorption of dyes and catalysis	94
MOF-74-(Zn)-II/III	multibranching treelike superstructures			a few 100 μm		88
MIL-47(V)	superstructures based on carbon NT fibers and MIL-47(V) NW			a few 10 μm	cathodes for Zn-ion batteries	90
[M ₂ (bdc) ₂ (dabco)] (M = Zn, Cu)	hexagonal rod mesocrystals (m _c -1h)		PEO ₆₈ -b-PMAA ₈	from 0.53 μm /2.9 μm to 64 μm /183 μm		91
[M ₂ (bdc) ₂ (dabco)] (M = Zn, Cu)	tetragonal mesocrystals (m _c -1t)	m _c -1h	PEO ₆₈ -b-PMAA ₈	a few μm		91
Cu-CAT	superstructures based on carbon fiber paper and NW arrays			200–250 nm/ 3–15 μm	SC electrode	89

applications of this class of nanostructured materials. A summary of the reported 1D MOF nano- and superstructures with their chemical compositions, morphologies, and domains of applications is given in Table 1.

2. TEMPLATE-FREE SYNTHESIS OF 1D MOF TUBULAR NANOSTRUCTURES IN SOLUTION

Various coordination polymers (CP) and a few MOF NWs^{54–56} were synthesized through the reaction between the metal precursors and the organic ligand in solution, either at RT or eventually under hydrothermal conditions. The crystal size and shape of these 1D nanostructures depend strongly on the physicochemical parameters (solvent, pH, metal source, reactant concentration, molar ratio of the reactants, temperature, pressure, etc.) of the synthesis. No clear general trend about the control of the crystal morphology could be extracted from the variation of these parameters, which are generally finely tuned for each nanostructure by trial and error. However, most of these coordination polymers and MOF NWs were typically obtained in alcohol (methanol, ethanol, isopropyl alcohol) or alcohol/water mixtures.^{54–56} The nucleation and growth processes of these 1D anisotropic nanostructures are generally explained by the Ostwald ripening

(OR) mechanism based on the growth of larger particles at the expense of smaller ones. It is known that the size and morphology of particles depend on the relative growth of the different crystallite facets. As previously reported for numerous inorganic and hybrid materials,^{47,57,58} the growth of primary particles may be strongly influenced by the surrounding medium (acidity, ligands, solvent, etc.), since the different crystal facets may present different surface chemistry and charge and thus different surface energy. The complexation or adsorption of one of these facets by complexing molecules such as alcohols may enhance their stability and drive the growth process of the nanocrystals. Moreover, the anisotropic growth of CP and MOF nanostructures may also be driven by the self-assembly of the amphiphilic organic ligand in water/EtOH solution. Note that a few 1D CP and MOF nanostructures were formed under hydro-/solvothetical conditions in the typical temperature range of 100–250 °C under autogenous pressure.^{53,54} Under these conditions, the solubilization and diffusion processes of organic and inorganic molecules are significantly enhanced as a result of the dependence of the physicochemical parameters of the solvent (dielectric constant, viscosity, ionization constant of water) with temperature and pressure, thereby affecting the degree of supersaturation of solutions and thus the nucleation step.⁵⁷

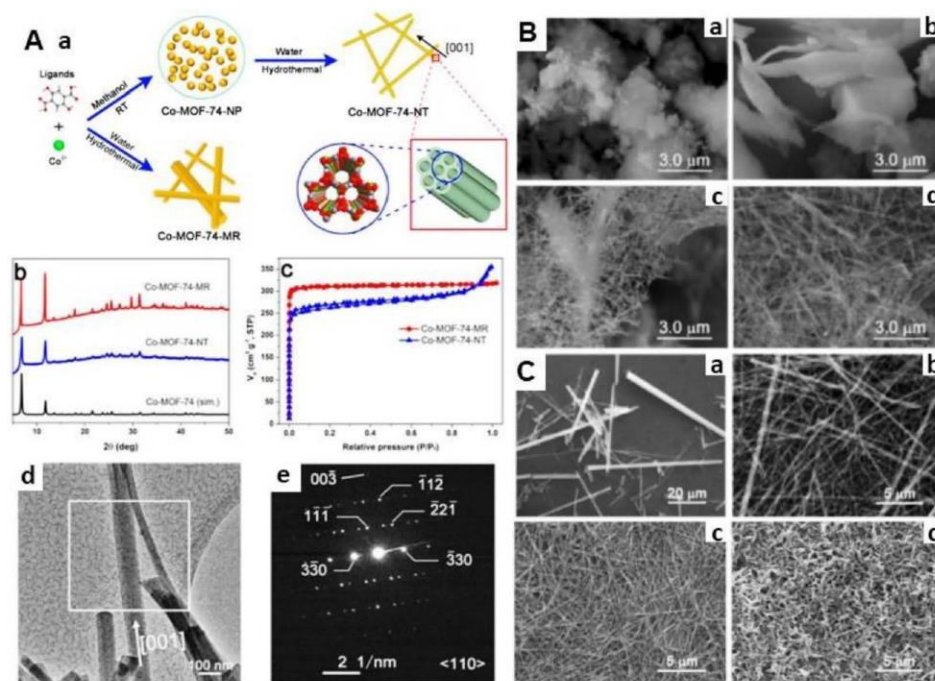


Figure 2. (A) (a) Synthesis of Co-MOF-74-NT and Co-MOF-74 rods (i.e., Co-MOF-74-MR). (b) Powder X-ray diffraction patterns of Co-MOF-74 and comparison with simulated patterns. (c) N_2 sorption isotherms for Co-MOF-74-NT and Co-MOF-74-MR. (d) TEM images and (e) SAED pattern of Co-MOF-74-NT. (B) SEM images of Co-MOF-74 prepared at 175 °C for 12 h in a water/methanol solvent (v/v), (a) 2:8, (b) 4:6, (c) 8:2, and (d) pure water, indicating that the water plays an important role in the formation of nanotubes. (C) SEM images of Co-MOF-74 prepared at pH (a) 4, (b) 5, (c) 9, and (d) 11. Adapted with permission from ref 52. Copyright 2018 American Chemical Society.

Moreover, ion pairs, complexes with low ionic charges, or aggregates can thus be formed under those conditions and can serve as structure-directing agents for the growth of 1D anisotropic nanostructures.

While numerous MOFs NRs have been synthesized in solution without any structure-directing agents, this synthetic approach only led to a limited number of MOF NTs and NWs.^{52,59} Note that the anisotropy of the crystallite morphology can be strongly related to the symmetry of the crystalline structure of the MOF or influenced by anisotropic bonding in the structures. The three-dimensional framework of the aluminum trimesate MIL-110(Al) (MIL = Materials Institute Lavoisier) is built up from the connection of inorganic aluminum octamers with a benzene-1,3,5-tricarboxylate (btc) organic linker.⁶⁰ This MOF exhibits a 1D porous structure that consists of hexagonal channels 1.6 nm in diameter. Dao et al.⁵⁹ have reported the synthesis of MIL-110(Al) NTs by mixing Na_3btc and $AlCl_3$ precursors at RT in a mixed ethanol/methanol solvent, followed by a final thermal treatment at 90 °C. As shown by TEM, these MIL-110(Al) NTs of about 60 nm in diameter and length of a few micrometers present a hollow tubular nanostructure with a wall thickness of about 20 nm and a central cavity with a diameter of 20 nm. However, the hollow feature of the cavity was not confirmed by cross-section TEM images, while their low BET

surface in comparison to the pure MOF (i.e., 390 vs 1400 $m^2 g^{-1}$) suggested quite a large amount of impurities. The MOF-74 type structure exhibits 1D honeycomb-like channels constructed by assembling helical chains of edge-sharing metal octahedra and a 2,5-dihydroxybenzene-1,4-dicarboxylate (H_4dobdc) organic linker (Figure 2).⁶¹ Zou et al.⁵² described the preparation of very long MOF-74(Co) NWs with a diameter of ~ 70 nm and length of 25–30 μm . As revealed by selected-area electron diffraction (SAED), the NWs are single crystals and grow along the [001] crystallographic direction, thereby showing that the nanochannels of the MOF framework are lying parallel to the long axis of the NWs (Figure 2). These MOF-74(Co) NWs were synthesized through a redissolution–crystallization process: amorphous MOF-74(Co) NPs were first formed at RT by reacting the cobalt acetate tetrahydrate precursor with H_4dobdc in methanol/water solvent mixtures.⁵² The subsequent redissolution of this kinetic phase at 175 °C led to single-crystalline MOF-74(Co) NWs. As shown by changing the solvents of the synthesis, the use of water was crucial for the formation of MOF-74(Co) NWs. Both the length and crystallinity of MOF-74(Co) increased with the amount of water in the reaction solvent, while the use of pure DMF, ethanol, or methanol did not lead to the formation of MOF-74(Co) NWs.⁵² The role of water in the construction of the 1D anisotropic nanostructure of MOF-74(Co) is certainly

related to the formation of the helical chains of Co octahedra that are parallel to the long axis of the MOF NWs. Such helical chains of Co octahedra are formed through hydrolysis and condensation reactions of Co precursors. The pH value of the original solution strongly affected the morphology of the NWs. The superlong MOF-74-NTs were typically obtained at a pH value between 6 and 10. At a pH of less than 5, MOF-74(Co) rods 60 μm in length and 5–6 μm in diameter were obtained, while at pH 11, shorter rods 3–4 μm in length were observed (Figure 2).⁵² At very high or low pH, the high solubility of the amorphous MOF-74(Co) kinetic phase presumably led to a high concentration of Co precursors and the formation of the MOF NWs could not be kinetically controlled. These multichannel MOF NWs were used as stationary phases in a column for the separation of large molecules such as methylene blue and rhodamine B in aqueous solution. Finally, their carbonization preserved the 1D morphology, leading to the production of 3D hierarchical carbon dendrites composed of carbon nanofibers, carbon NTs, and Co NPs that presented a very good electrocatalytic activity for the oxygen reduction reaction (*vide infra*, section 6).⁵²

3. INORGANIC TEMPLATE-DIRECTED SYNTHESIS OF 1D MOF HOLLOW TUBULAR STRUCTURES

The use of shaped metal oxides/hydroxides as sacrificial templates has been reported as an efficient and controllable strategy to design hierarchical porous MOFs, core–shell MOF/oxide composites and hollow tubular structures.^{46,62,63} This approach relies on the morphological replacement of a shaped sacrificial metal oxide used both as a metal source and as a structure-directing agent by a MOF with an analogous microstructure. This replication phenomenon is characterized by the preservation of the morphology and dimensions of the replaced parent oxide/hydroxide. It implies a kinetic and spatial coupling between the dissolution of a metastable oxide phase and the crystallization of the MOF.⁶³ $\text{Cu}_2\text{O}/\text{HKUST-1}$ core/sheath nanostructures were prepared through the direct immersion of Cu_2O NWs into an ethanol (EtOH)/*N,N*-dimethylacetamide (DMA) solution of H_3btc under optimized conditions (Figure 3).⁴⁶ This process involves the dissolution of Cu_2O , the oxidation of Cu^+ to Cu^{2+} in the reaction media with the presence of dissolved O_2 from the air, and the coordination of Cu^{2+} by the *btc* ligand. In a second step, the Cu_2O core of $\text{Cu}_2\text{O}/\text{HKUST-1}$ core/sheath nanostructures could be removed upon the addition of dilute acetic acid, thereby leading to HKUST-1 NTs. As revealed by coupling FESEM, TEM, and HAADF-STEM, $\text{Cu}_2\text{O}/\text{HKUST-1}$ core/sheath nanostructures consist of Cu_2O NWs wrapped by a layer of intergrown HKUST particles, the thickness of which increases with the reaction time.⁴⁶ The replication of the Cu_2O NW structure into HKUST-1-based nanostructures was found to be strongly dependent on the solvent used. A fast dissolution of Cu_2O was observed in pure water and precluded the use of Cu_2O as a template. In contrast, Cu_2O NWs are stable in DMA and no HKUST nuclei were observed. HKUST-1-based nanostructures could be formed by using a 1/4 v/v DMA/EtOH mixture, where the kinetics of Cu_2O dissolution and HKUST-1 growth could be controlled.⁴⁶

By a similar strategy, ZIF-67(Co) and MOF-74(Co) hollow NRs were prepared through the conversion of $\text{Co}_3(\text{OH})(\text{OAc})_5$ (OAc = acetate) NRs in a solution of the organic ligand of the corresponding MOF (i.e., 2-methylimidazole (miM) for ZIF-67(Co) and H_4dobdc for MOF-74(Co)).^{62,64}

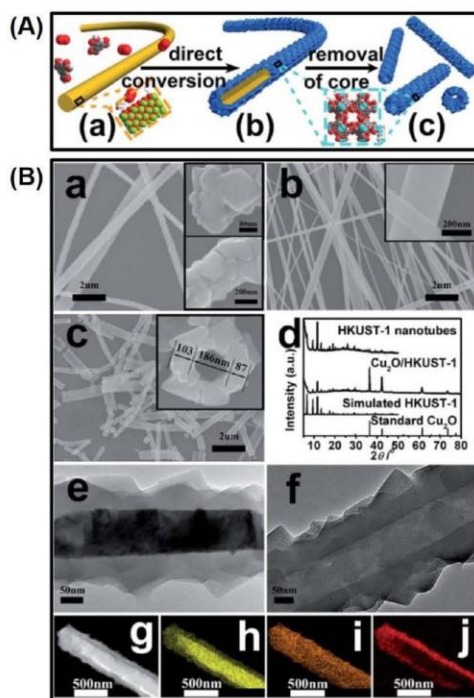


Figure 3. (A) Schematic illustration of direct conversion of (a) Cu_2O NWs into (b) $\text{Cu}_2\text{O}/\text{HKUST-1}$ core/sheath nanostructures and (c) HKUST-1 NTs. The structures of Cu_2O and HKUST-1 are illustrated in the orange and blue boxes, respectively (the atoms are shown as follows: Cu^+ , yellow-green; Cu^{2+} , light blue; O, red; C, gray). (B) FESEM images of (a) $\text{Cu}_2\text{O}/\text{HKUST-1}$ core/sheath nanostructures and their end (top inset), (b) Cu_2O NWs, and (c) HKUST-1 NTs and a cross-section (inset). (d) PXRD patterns of $\text{Cu}_2\text{O}/\text{HKUST-1}$ core/sheath nanostructures and HKUST-1 NTs. TEM images of (e) $\text{Cu}_2\text{O}/\text{HKUST-1}$ core/sheath nanostructures; (g) HAADF-STEM image of an individual $\text{Cu}_2\text{O}/\text{HKUST-1}$ core/sheath nanostructure. (h–j) Elemental maps of Cu, O, and C elements in the $\text{Cu}_2\text{O}/\text{HKUST-1}$ core/sheath nanostructure. Adapted with permission from ref 46. Copyright 2016 The Royal Society of Chemistry.

According to the TEM images, ZIF-67(Co) NRs are a few micrometers long with a diameter of about 500 nm, while the dimensions and aspect ratio of MOF-74(Co) NRs are lower (i.e., length of 500 nm and diameter of 200 nm). The difference in the dimensions between ZIF-67(Co) and MOF-74(Co) hollow NRs is mainly related to the size of the parent $\text{Co}_3(\text{OH})(\text{OAc})_5$ NRs used for their synthesis. From their high surface roughness observed by TEM, it can be inferred that these NRs are polycrystalline and their walls are constructed from numerous interconnected smaller rodlike crystals.^{62,64} In contrast to the previous HKUST-1 NRs,⁴⁶ the formation of hollow MOF-74(Co) nanostructures is mainly due to a difference in diffusion rates of the Co cations and deprotonated ligand anions, the diffusion of small cations being faster than that of ligand anions.⁶² During the chemical

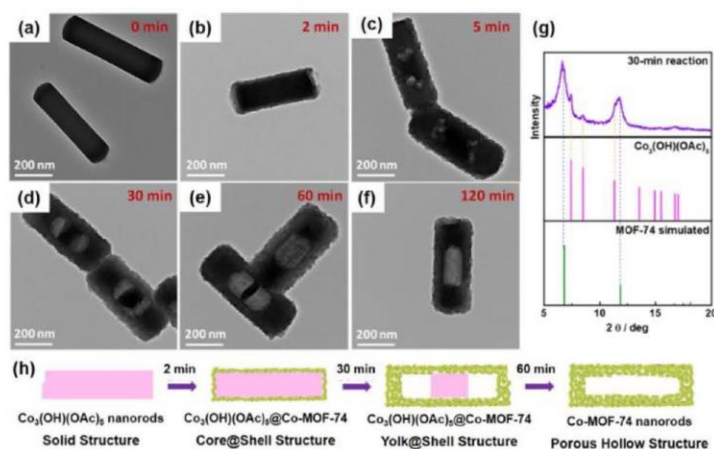


Figure 4. TEM images showing the evolution of $\text{Co}_3(\text{OH})(\text{OAc})_5$ NRs to Co-MOF-74 hollow NRs at (a–f) 0, 2, 5, 30, 60, and 120 min, respectively. (g) PXRD pattern of the product after 30 min conversion. (h) Scheme of the formation process of Co-MOF-74 hollow NRs. Adapted with permission from ref 62. Copyright 2018 American Chemical Society.

transformation, the outward diffusion of Co cations from $\text{Co}_3(\text{OH})(\text{OAc})_5$ can induce the nucleation and growth of a MOF shell at the surface of $\text{Co}_3(\text{OH})(\text{OAc})_5$ NRs. Time-dependent TEM experiments were performed to gain more insight into the formation process of MOF-74(Co) (Figure 4).⁶² For a short reaction time (i.e., 2 min of immersing $\text{Co}_3(\text{OH})(\text{OAc})_5$ in a solution of H_2dobdc in DMF), a MOF-74(Co) shell was formed *in situ* at the surface of $\text{Co}_3(\text{OH})(\text{OAc})_5$ NRs. Upon an increase in time, the thickness of the MOF shell increased at the expense of the $\text{Co}_3(\text{OH})(\text{OAc})_5$ core, thereby showing some voids in the center of the particles and thus the progressive consumption of Co cations from $\text{Co}_3(\text{OH})(\text{OAc})_5$. These observations showed that initial thin shell of MOF-74(Co) not only acted as a template to preserve the rodlike morphology but also limited the inward diffusion of ligand anions while the outward diffusion of Co cations from $\text{Co}_3(\text{OH})(\text{OAc})_5$ dominated.⁶² After a reaction time of 30 min, yolk-shell $\text{Co}_3(\text{OH})(\text{OAc})_5$ @MOF-74(Co) nanostructures with enlarged voids were obtained. Pure MOF-74(Co) NRs could be formed by tuning the reaction times and etching away the unreacted $\text{Co}_3(\text{OH})(\text{OAc})_5$ by using methanol.⁶² In comparison to the bulk MOF-74(Co), MOF-74(Co) hollow NRs exhibited a slightly lower surface area (804 vs 1049 $\text{m}^2 \text{g}^{-1}$ for NRs and bulk MOF-74(Co), respectively) and thus a lower CO_2 adsorption capacity at equilibrium. However, they showed much better CO_2/N_2 separation performance in comparison to the bulk crystals under dynamic flow conditions, as shown by chromatography. This can be explained by their hierarchical texture (interparticle pores, inner channel) that can provide fast diffusion pathways and thus facilitate adsorption/desorption of gas molecules in comparison to bulk crystals.⁶²

Urchin-like superstructures of ZIF-67(Co) composed of radially assembled ZIF-67(Co) NTs were synthesized following the replication strategy by using preformed urchin-like structures of a cobalt hydroxide carbonate phase as a sacrificial template.⁶⁵ This replicating approach was also extended to the use of coordination polymers as a sacrificial

template.^{66–68} Hexagonal-tube-type CPs with dimensions of 2.6 μm (outer hexagon) and a length of 2.2 μm were synthesized through the hydrothermal treatment of a mixture of carboxy-functionalized organic linkers (i.e., N',N' -phenylenebis(salicylideneimine)dicarboxylic acid and 1,4-benzenedicarboxylic acid (H_2bdc) and $\text{Zn}(\text{OAc})_2$ in DMF.⁶⁸ SEM experiments performed on different samples collected at different reaction times showed that these tubular CPs are produced through a redissolution–crystallization mechanism in which an initially formed metastable CP acted as a template and was fully converted to create new tubular CPs. This self-sacrificing template strategy was also explored for the synthesis of luminescent Cd^{2+} -based MOF NTs, taking advantage of both ultrasonic synthesis and vapor diffusion techniques.⁶⁶ Metastable Cd-based MOF NRs with an average diameter of 30–50 nm and a length of 300–500 nm were initially prepared through the reaction of CdCl_2 and H_3btc under ultrasonic conditions in the presence of triethylamine (TEA).⁶⁶ The removal of excess TEA and an ultrasonic treatment promote the dissolution of MOF NRs and their complete conversion into a large quantity of MOF NTs with inner diameters of 50–150 nm and outer diameters of 100–300 nm.⁶⁶ According to EDX and PXRD, the chemical composition of the initially formed MOF NRs is strongly different from that of MOF NTs corresponding to the thermodynamically stable 3D $[\text{Cd}_2(\text{btc})_2(\text{H}_2\text{O})_2]$ phase.⁶⁶ The Cd-based MOF NTs have shown a fast, highly sensitive, and selective response for the trace-level detection of nitroaromatic explosives. To conclude, this strategy of using preformed inorganic scaffolds (oxide, hydroxide, CP) to template the construction of MOF NTs and MOF hollow nanostructures was revealed to be efficient but succeeded mainly for the synthesis of MOFs based on divalent cations. Actually, this strategy requires a coupling between the dissolution of the parental template and the growth of the MOF. It might be expected that this approach would be more challenging with MOFs based on high-valent cations (i.e., Ti^{4+} or Zr^{4+}) due to the higher reactivity of these cations toward

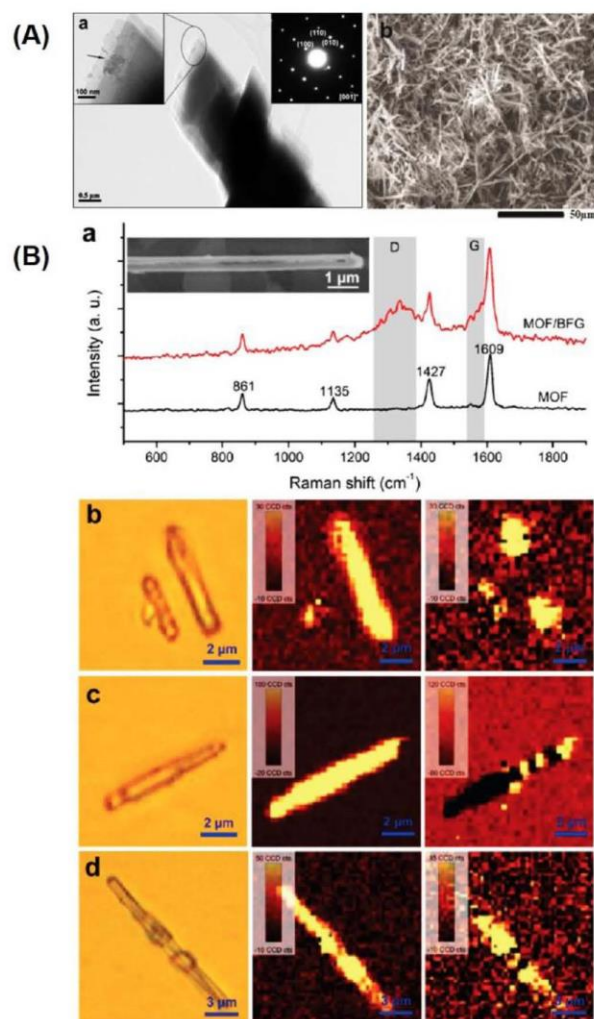


Figure 5. (A) (a) TEM images of MOF/BFG (5 wt %) NW. The upper-left inset shows a magnified image, and the arrow inside indicates BFG flake. The upper-right inset shows the SAED pattern. (b) SEM image of MOF/BFG (5 wt %) NWs. (B) (a) Raman spectra of MOF-5 and MOF/BFG (5 wt %). The inset shows an SEM image of an individual MOF/BFG NW. (b–d) Raman mapping of MOF/BFG NWs: (left) optical image; (middle) Raman maps integrated by the Raman band at 1609 cm^{-1} ; (right) Raman maps integrated by the D band of graphene. Adapted with permission from ref 42. Copyright 2010 American Chemical Society.

hydrolysis/condensation and complexation reactions.⁶⁹ This strategy can involve the formation of intermediate yolk–shell MOF nanostructures. Yolk–shell ZIF-8 particles were also reported but without the use of any sacrificial template.⁷⁰ The formation of such particles involved the slow growth of a polycrystalline ZIF-8 shell on poly(vinylpyrrolidone)-coated core particles. In the early growth stages, the shell is continuous but transforms to a yolk–shell due to geometrical frustration. Cavities are formed by shell deformation as a result of lattice mismatch during crystal growth. The localization and

size of such cavities are strongly dependent on the curvature of the core particle.⁷⁰ In the next section, the use of organic templates was considered to be a valuable approach for the preparation of 1D MOF nanostructures.

4. (BIO)ORGANIC TEMPLATE-DIRECTED SYNTHESIS OF 1D MOF TUBULAR NANOSTRUCTURES

Various organic templates were used to direct the synthesis of 1D tubular-structured MOFs.^{42–44,71–73} In addition to the

template types, different deposition methods (solution-based deposition, electrodeposition, etc.) were used to coat the template with the MOF precursors. This templating strategy is thus a versatile approach, although the morphology and size of the MOF nanostructures are limited by the dimensions of the templates. Graphene and graphene oxide (GO) were used for the fabrication of MOF NWs.^{42,45} GO is a chemically modified graphene containing several oxygen functional groups: epoxy and hydroxy groups are present on the basal planes of GO, while carboxylic acid groups are located on the edges of the GO sheets.⁷⁴ Since most of the MOFs are inherently electrically nonconductive, MOF/GO composites have attracted widespread attention in recent years, due to their good chemical stability and enhanced electrical conductivity and processability.^{72,75–79} They were thus explored in various applications including sensors, supercapacitors (SCs), batteries, gas storage, and catalysis.^{72,75–79} In 2010, Jahan and co-workers used benzoic acid functionalized graphene (BFG) as a structure-directing agent of MOF-5 NW.⁴² MOF-5 presents a cubic 3D porous structure by assembling tetramers of Zn tetrahedra and bdc ligands.⁸⁰ Due to the low density of carboxylate groups on the basal plane of GO and thus the expected limited metal-chelation capability of GO, the basal planes of GO were functionalized with benzoic acid functions with a high density thanks to diazonium grafting.⁴² Indeed, such carboxylate groups that possess a bridging bidentate coordination ability are prone to react with the Zn^{2+} cations and thus induce strong MOF-5/BFG interactions and a high degree of framework connectivity. In the second step, BFG was heated at reflux with the precursors of MOF-5 (zinc nitrate/bdc) in DMF, following the same protocol as that of MOF-5.⁸¹ The microstructure of the resulting NWs consists of the stacking of MOF-5 nanocrystals with a [220] growth direction and intercalated graphene sheets periodically distributed along the NWs, as shown by coupling multiple techniques (PXRD, SEM, TEM, SAED, micro-Raman spectroscopy) (Figure 5).⁴² Hence, this work demonstrated that BFG is not only a structure-directing agent of 1D MOF-5 NW but also an integral component of the MOF-5 framework (Figure 6).⁴² These BFG/MOF-5 NWs have a uniform shape, and their diameter of ~ 300 nm is consistent with the average diameter of the BFG sheets, in agreement with the structure-directing effect of BFG. Finally, it was shown that these BFG sheets impart new electrical properties such as a photoelectric transport property.⁴²

Recently, some of us and co-workers have reported the synthesis of single-crystal NWs of the microporous Al^{3+} dicarboxylate MIL-69(Al) MOF by using GO nanoscrolls as structure-directing agents.⁴⁵ The framework of this microporous Al 2,6 naphthalenedicarboxylate (2,6-ndc) based MOF is structurally analogous to the terephthalate-based MIL-53 and is built up from the connection of infinite chains of corner-sharing octahedral $AlO_4(OH)_2$ units with the 2,6-ndc ligand. Its hydrated form presents one-dimensional narrow rhombic channels with a window size of around 2.7×13.6 Å (see Figure 7).⁸² GO nanoscrolls can be formed by rolling GO sheets from one side or from the corner into Archimedean-type spirals and present open structures at both ends.⁸³ MIL-69(Al)/GO NWs were formed by mixing GO and the precursors of MIL-69(Al) (i.e., Al^{3+} salts, NaOH, and 2,6-ndc) under reflux. As shown by a combination of complementary characterization tools (PXRD, TEM, SAED, SEM, N_2 porosimetry), these NWs present a core-shell

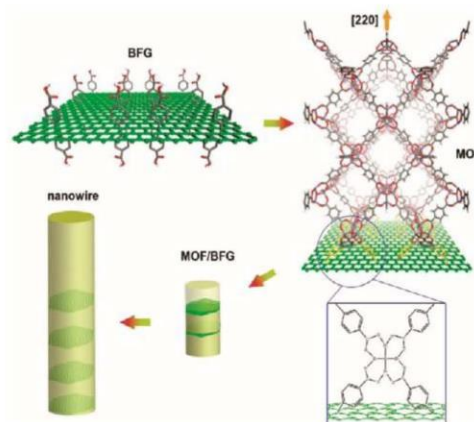


Figure 6. Scheme of proposed bonding between functionalized graphene and MOF-5 via $-COOH$ groups along the [220] direction and the assembly into a NW structure. Adapted with permission from ref 42. Copyright 2010 American Chemical Society.

porous microstructure with lengths up to $2 \mu m$ and an aspect ratio of up to 20. Their average diameter of 70 ± 20 nm is close to that of the GO nanoscrolls, which is in line with the templating role of GO. Note that this morphology contrasts strongly with that of polydisperse MIL-69(Al) NPs. According to SAED, each NW corresponds to a single crystal of MIL-69(Al) and was found to preferentially grow along the [001] crystallographic direction, which is parallel to the chain axis of the corner-sharing Al^{3+} octahedra in the structure of MIL-69(Al).⁴⁵ The interplay between multimodal characterization techniques and molecular modeling tools was exploited to unravel their mechanism of formation, which involves a mutual recognition between GO and MIL-69(Al).⁴⁵ GO directs the formation of the MOF, while conversely, the MOF drives the structuring of GO (Figures 7 and 8). The formation of MIL-69(Al) seeds, the self-scrolling of GO sheets, and the subsequent anisotropic growth of MIL-69(Al) NWs in the inner cavity of GO nanoscrolls were mainly mediated by specific GO sheet/MOF interactions, thereby limiting the crystal growth of MOF on certain facets (see Figure 8).⁴⁵ In the first stages of the growth process, the internal surface of GO nanoscrolls was decorated by numerous MIL-69(Al) NRs and NPs whose further growth and assembly were constrained in a confined space. This may drive the crystalline growth orientation in a direction parallel to the NW axis, gradually forming primary smaller aligned NWs (Figure 7).⁴⁵ Such a mechanism can involve redissolution-crystallization steps due to the highly reversible nature of coordination bonds of the MOF network. Finally, the lateral aggregation or crystallite fusion of these small NWs led to one single-crystalline NW, and this last step may proceed either through Ostwald ripening or the oriented attachment mechanism, as previously reported for the anisotropic growth of inorganic nanocrystals or biomineralization systems.^{45,51} In comparison to the pure MIL-69(Al) NPs, this MIL-69(Al)/GO composite presents a higher electrical conductivity. The structuring of MOF by using GO nanoscrolls can thus be considered as a valuable approach to integrate MOFs into GO without any agglomer-

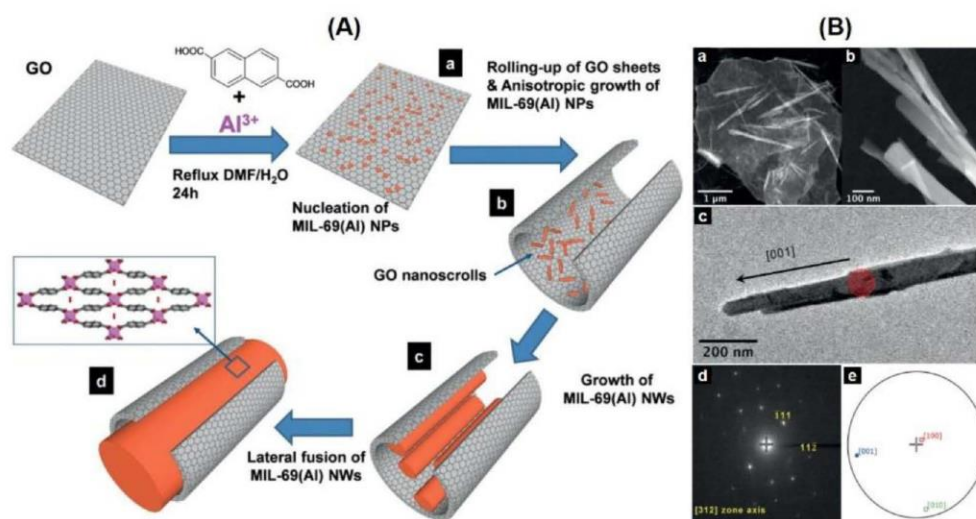


Figure 7. (A) Summary of the main stages of the MIL-69(Al) NWs formation. (B) (a, b) STEM-HAADF images and (c) TEM-BF image of MIL-69(Al) NWs. (d) SAED of the area highlighted by the red circle in (c). The stereographic projection (e) that is related to the crystallographic orientation deduced from (d) indicates unambiguously that the crystal growth proceeds along the [001] direction. Adapted with permission from ref 45. Copyright 2020 John Wiley and Sons.

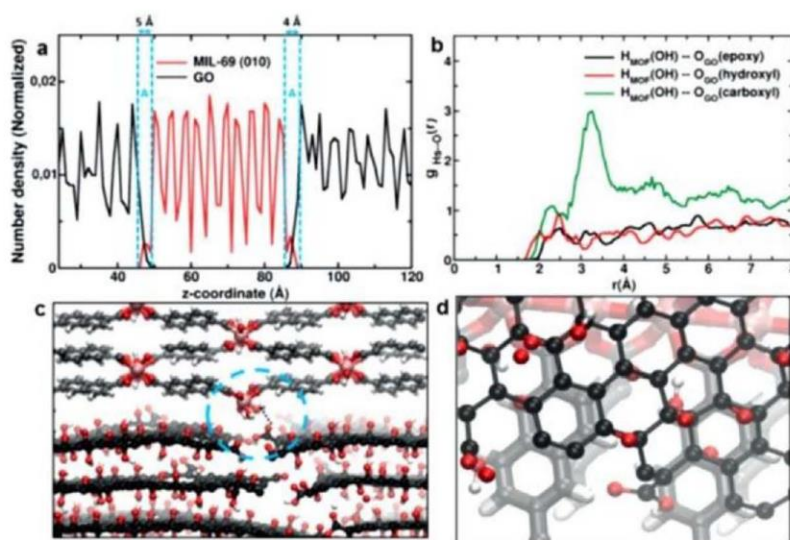


Figure 8. MIL-69(Al)(010)/GO model. (a) Representation of the normalized atomic density showing the interfacial region denoted A. (b) Radial distribution functions calculated between H_{OH} of MIL-69(Al) and the different O atoms of the functional groups of GO. (c) Illustrative snapshot showing the main interactions between the edge carboxylic acid groups of GO and H_{OH} of MIL-69(Al). (d) Snapshot showing preferential π - π interactions at the MIL-69(Al)(010)/GO interface. Color schemes are as follows. GO layers: C, black; O, red; H, white. MIL-69(010): C, gray; Al, pink; O, red; H, white. Adapted with permission from ref 45. Copyright 2020 John Wiley and Sons.

ation of MOF NPs or restacked GO layers while imparting electron transport properties.

Over the past few years, a series of recent studies investigated the use of polymeric macrostructural templates

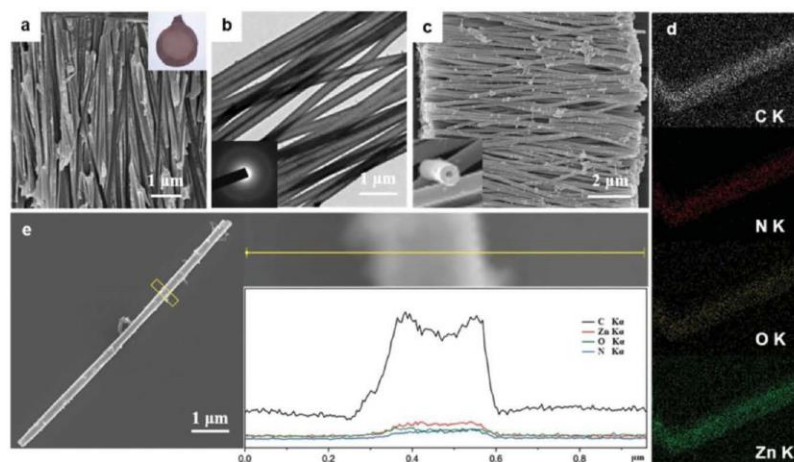


Figure 9. (a) Section view SEM image of ZIF-8 deposited on PCTM@PDA (PCTM = polycarbonate track-etched membrane). (b) TEM and (c) SEM images of self-supported hybrid ZIF-8 NTs after membrane dissolution. (d) TEM EDX elemental mapping of hybrid ZIF-8 NTs. (e) SEM image and the corresponding EDX spectrum profile scan of hybrid ZIF-8 NTs. Adapted with permission from ref 43. Copyright 2018 The Royal Society of Chemistry.

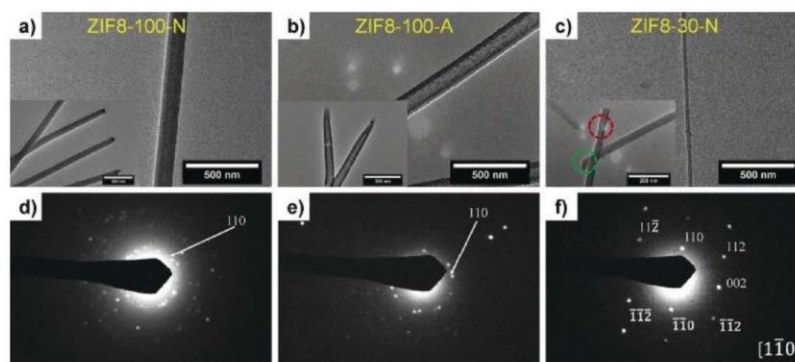


Figure 10. (a) TEM images (top row) and SAED patterns (bottom row) of (a, d) ZIF8-100-N, (b, e) ZIF8-100-A, and (c, f) ZIF8-30-N. The red circle in (c) defines the selected area from which the SAED pattern was obtained. The green circle shows one of the faceted ends of the NWs. Adapted with permission from ref 44. Copyright 2018 John Wiley and Sons.

to direct the nucleation and growth of MOFs into self-supported MOF NT arrays. Among the membrane templates, commercially available polycarbonate (PCTE) membranes with a tunable pore diameter (~ 20 nm to several micrometers) and pore density ($1-10^{10}$ pores/cm²) are produced by an ion-track technology involving a swift heavy-ion irradiation and subsequent chemical etching of the generated ion tracks.⁸⁴ They exhibit either parallel arrays of pores or highly interconnected pore networks. As shown previously, inorganic oxide NTs could be produced from these PCTE membranes and they were mostly freestanding due to the rapid dissolution of PCTE in organic solvents.⁵³ This is thus an advantage for the three-dimensional assembly of nanostructures and their integration into gas sensors and photocatalysis devices. Yu et al. used PCTE membranes to synthesize NTs based on

divalent (Zn^{2+} , Cu^{2+} , and Co^{2+}) MOFs that are capable of forming under mild conditions (i.e., ZIF-8, ZIF-67, ZIF-12, and HKUST-1).⁴³ The synthesis approach consisted of separating the ligand and metal precursor solutions in two different chambers by a piece of PCTE. This method leads to a concentration-gradient-driven diffusion across the membrane that results in the nucleation and growth of ZIF-8 crystals within the pore channels. After the template was dissolved, well-defined hollow and polycrystalline 1D ZIF-8 superstructures built from intergrown MOF crystals were obtained and were the replica of the parental PCTE porous membranes. The nucleation and growth of ZIF-8 are presumably promoted by a high concentration of deprotonated mIM ligands formed from the imidazole-catalyzed transesterification reaction of polycarbonate.⁴³ Although a continuous growth of ZIF-8

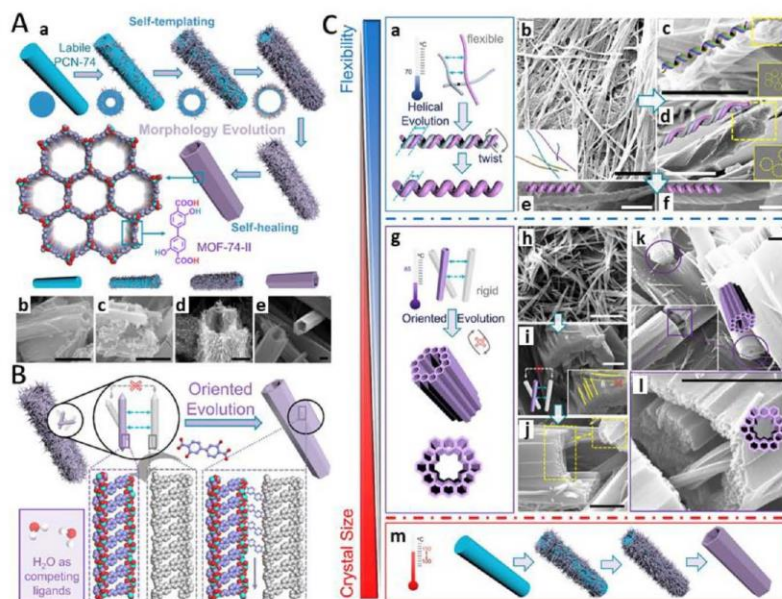


Figure 11. (A) (a) Illustration of self-templated growth of hollow MOF-74-II tubes and the structure of MOF-74-II with 1D channels. (b–e) SEM images showing the MOF-74-II tube evolution process. Scale bars: 2 μm . (B) Mechanism of self-healing via oriented evolution under solvothermal conditions: dynamic formation of Zn–O coordination bonds. (C) (a) Helical evolution of hierarchically porous MOF-74-II superstructures formed under 70 $^{\circ}\text{C}$. (b–f) Stepwise helical evolution of multiple MOF-74-II NWs into twisted tubular superstructures with two torsional directions. (g) Oriented evolution of hierarchically porous MOF-74-II superstructures. (h–j) Oriented evolution of multiple MOF-74-II crystallites into hierarchical multichannel superstructures at (h) 6 h, (i) 24 h, and (j) 48 h under 85 $^{\circ}\text{C}$. (k, l) SEM images of oriented superstructures at different scales. (m) Self-templated evolution of MOF-74-II tubes from PCN-74. Scale bars: 5 μm . Adapted with permission from ref 67. Copyright 2019 Elsevier.

crystals along the pore walls was observed, the 1D ZIF-8 superstructures did not exhibit uniform channels with homogeneous inner diameter, as the result of the nonuniform coating of ZIF-8 crystals on the template pores.⁴³ Moreover, cracks and fractures were also found in the isolated 1D ZIF-8 superstructures due to the poor interfacial properties of the ZIF-8/PCTE composite.⁴³ To address this issue, the heterogeneous nucleation and growth of ZIF-8 was tuned through the functionalization of the inner surface of the PCTE channels by polydopamine (PDA).⁴³ PDA chains bearing catechol and amine groups are prone to interact strongly with metal ions, thereby facilitating the nucleation and confined growth of MOFs. Moreover, they can serve as an interface strengthening agent for the fabrication of robust 1D MOF superstructures after template removal. Well-defined 1D hybrid ZIF-8 NTs spanning across the entire thickness of the template were successfully obtained with a high aspect ratio of up to 40 and length of 10 μm (Figure 9).⁴³

The versatility of the PDA-mediated synthesis approach was shown through the synthesis of other 1D MOFs superstructures based on ZIF-67, ZIF-12, and HKUST-1 with different morphologies.⁴³ In a similar approach, Qin et al. modified the pore walls of PCTE membranes by poly(*N*-vinylpyrrolidone) (PVP) to impart hydrophilicity, enhance their affinity to Zn^{2+} cations, and induce the nucleation of ZIF-8.⁴⁴ They used these PVP-modified PCTE membranes as a

structural template for the synthesis of ZIF-8 nanostructures. In a typical protocol, PCTE membranes were floated on top of Zn^{2+} solutions and left to soak for 24 h. Then, a 1-octanol solution of 2-methylimidazole (mIM) was put into contact with the membrane at the interface of the two solutions. Depending on the pore diameters of PCTE (i.e., 30 or 100 nm), the nature/concentration of the Zn^{2+} precursors ($\text{Zn}(\text{NO}_3)_2$ or $\text{Zn}(\text{Ac})_2$), and the experimental conditions, 1D ZIF-8 nanostructures of distinct morphologies were synthesized after dissolution of the PCTE template.⁴⁴ Polycrystalline ZIF-8 NRs (ZIF8-100-N) and NTs (ZIF8-100-A) having lengths of up to 6 μm were found to form within the 100 nm membrane pores while single-crystalline 2 μm long ZIF-8 NWs (ZIF8-30-N) grew inside the 30 nm pores (Figure 10). These three nanostructures possessed large aspect ratios of up to 60 and showed a preferential crystal orientation with the (110) planes stacking along the long axis of the NW.⁴⁴

In 2019, Caddeo and co-workers extended this approach by using an electrodeposition method to coat the PCTE template.⁷³ 3D interconnected NW networks of Cu-based MOFs (i.e., HKUST-1 and $\text{Cu}(\text{INA})_2$ with INA = isonicotinic acid) were produced by combining PCTE templating and electrochemical methods.⁷³ Cu NWs were first electrodeposited inside the PCTE membranes, followed by their subsequent conversion via electrochemical oxidation in a solution containing the required organic linker of each MOF.

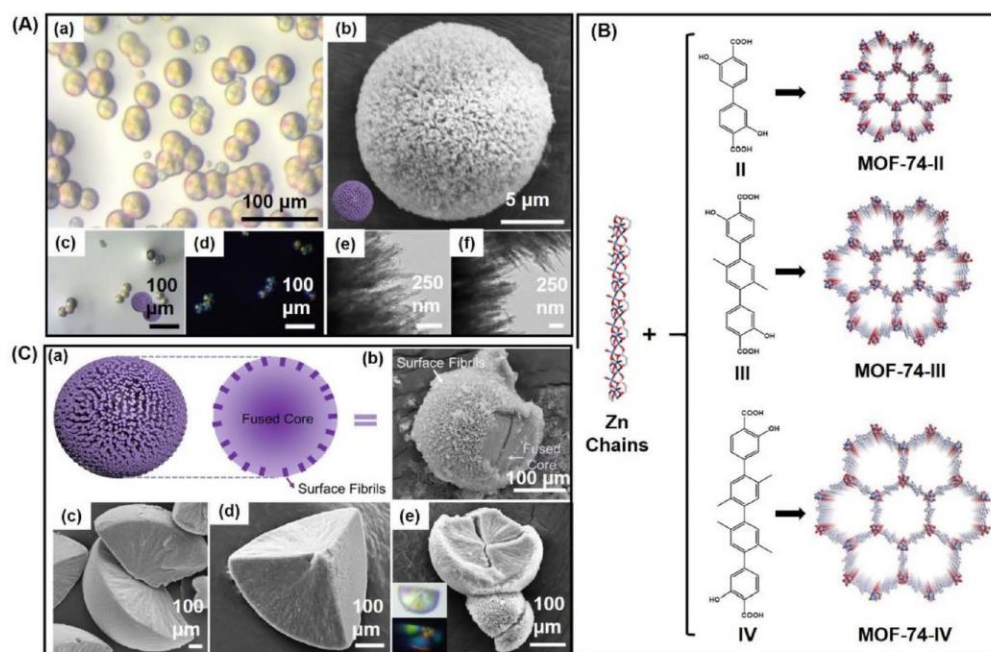


Figure 12. (A) (a) Optical images of MOF-74-III spherulites. (b) SEM images showing that MOF-74-III spherulites contain a large number of well-defined fibrils. (c, d) Optical image and the corresponding polarized optical image of MOF-74-III spherulites placed between crossed polarizers. The image displays a typical Maltese cross extinction pattern indicating spherulite superstructures under polarized light. (e) TEM image of a typical MOF-74-III spherulite showing the fibril size and arrangement. (f) TEM image of a peanutlike MOF-74-III spherulite showing the fibril size and arrangement. (B) Structural illustration of MOF-74-II, -III, and -IV and their respective organic ligands, L-II, -III, and -IV. (C) (a) Structural mode of MOF-74 spherulites with surface fibrils and a fused core. (b) SEM image showing well-defined fibrils on the surface of a spherulite and a fused core inside the spherulite. (c–e) SEM images of cracked MOF-74 spherulites. An optical image of a cracked MOF-74 spherulite is inserted in (e). Adapted with permission from ref 94. Copyright 2020 Elsevier.

The synthesized MOF NWs exhibit tunable diameters ranging between 80 and 260 nm, replicating the dimensions of the PCTE pore arrays. Moreover, the use of PCTE templates with three dimensionally interconnected nanochannels has led to the production of mechanically stable and 3D-ordered MOF NW networks that can be integrated into planar devices for sensing and photocatalysis applications.⁷³ The use of biological templates for the formation of 1D MOF NTs and NWs is quite scarce despite their low toxicity, biocompatibility, and low cost. However, rodlike biological templates such as bacteria (*E. coli*) and virus particles were used to grow a polycrystalline ZIF-8 shell on their surfaces and thus to prepare core–shell ZIF-8(Zn) microrods and NRs.^{85,86} Interestingly, the resultant *E. coli*@ZIF-8 not only presented micropores but also mesopores and macropores as a result of the ZIF-8 growth on the cell membrane.⁸⁶ Upon carbonization of the *E. coli*@ZIF-8 composite, hierarchical porous carbons were prepared with improved electrochemical capacity in comparison to carbonized pristine ZIF-8.⁸⁶ A similar bioinspired mineralization of ZIF-8(Zn) was conducted by using tobacco mosaic virus (TMV) as a biological template.⁸⁵ It was shown that the TMV–Zn interaction strongly affects the final morphology of TMV@ZIF-8 particles that are either core–shell particles or large ZIF-8 crystals with entrapped TMV, depending on the

synthesis conditions. The core–shell TMV@ZIF-8 particles can be used for the administration and controlled delivery of a therapeutic protein, since TMV is a preclinical vaccine platform.⁸⁷ It was shown that the ZIF-8 shell could protect the viral DNA and stabilize the encapsulated protein from denaturation. To conclude, a wide diversity of (bio)organic templates has been used to produce 1D MOF nanostructures with a high monodispersity in their diameter and length. One of the advantage of using PCTE membranes is the possible dissolution of the PCTE template, thereby leading to freestanding 1D MOF nanostructures. In addition, these MOF NTs and NWs could be assembled into 3D-ordered MOF superstructures which could be potentially applied as sensors or photoelectrodes. The next section will be devoted to the design of MOF superstructures with a higher microstructural complexity.

5. SYNTHESIS OF POROUS SUPERSTRUCTURES BASED ON TUBULAR MOF SUBUNITS

Hierarchical assemblies of low-dimensional MOFs crystallites have attracted great interest, since these superstructures might exhibit the physicochemical properties of the individual MOF crystallites together with those arising from the collective interactions of MOF nanocrystals and thus potentially

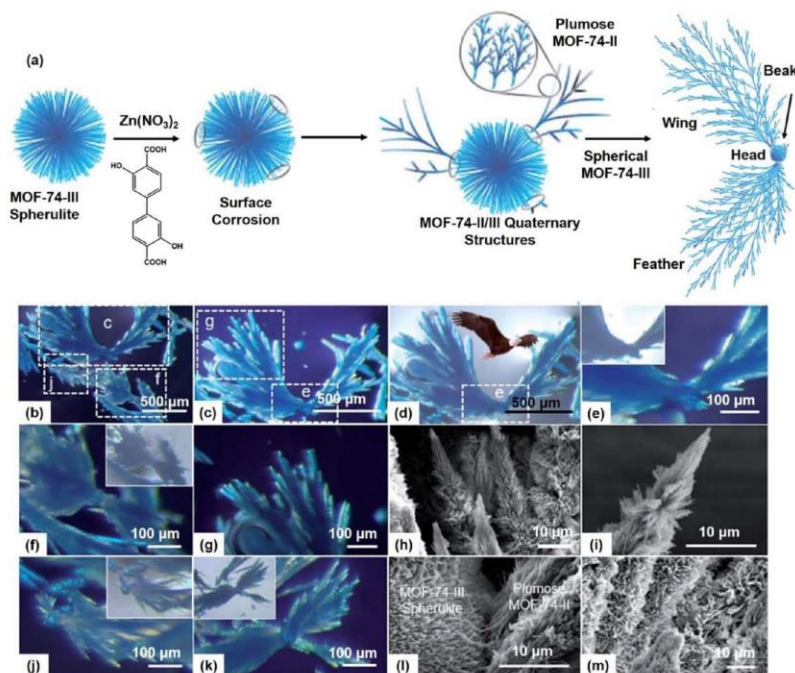


Figure 13. Evolution of spherical MOF-74-III/plumose MOF-74-II quaternary superstructures. (a) Schematic illustration of the stepwise evolution from MOF-74-III spherulites to spherical MOF-74-III/plumose MOF-74-II quaternary superstructures. (b–g, j, k) Optical images of MOF-74-III/plumose MOF-74-II crystals, showing fractal structures. The blue color of the crystals is visualized using a doped dye, a metal phthalocyanine ligand. (h, i, m) SEM images of plumose MOF-74-II fractal structures on the quaternary superstructures. (l) SEM images showing the junction interface between spherical MOF-74-III (left) and plumose MOF-74-II (right). Adapted with permission from ref 88. Copyright 2020 The Royal Society of Chemistry.

synergistic properties. The synthesis of MOF superstructures with a controllable 3D architecture is challenging, and very recently, a few studies have been dedicated to develop low-dimensional MOF-based superstructures.^{67,88–92}

Recently, tubular MOF-74(Zn) superstructures were prepared by Feng and co-workers under solvothermal conditions through the temperature-dependent evolution of MOF crystallites.⁶⁷ One well-studied structural feature of MOF-74 is the possibility of tuning the pore size by changing the length of the organic linker, and thus a series of isorecticular MOF-74 structures (see Figure 12B) was reported.⁹³ In this work, microtubes of MOF-74-II(Zn) were obtained through the reaction of zinc nitrate and the organic linker II (i.e., 3,3'-dihydroxy-[1,1'-biphenyl]-4,4'-dicarboxylic acid) in *N,N*-diethylformamide (DEF)/ethanol/water mixtures under solvothermal conditions at 100 °C. When the reaction products were monitored at different times by FESEM and TEM, microfibers 1–2 μm in diameter of a Zn coordination polymer (denoted PCN-74) were initially formed (Figure 11A).⁶⁷ When the reaction time was increased, the surface of these PCN-74 fibers was progressively covered by MOF-74(II) needles, leading to the formation of core–satellite structures. In a final stage, the PCN-74 core was dissolved and its complete removal led to crystalline hollow microporous tubes of MOF-74-II(Zn), as shown by combining TEM, HAADF-

STEM, and EDS mapping.⁶⁷ These results show that tubular MOF-74-II(Zn) results from the initial precipitation of the PCN-74 kinetic phase followed by its redissolution and conversion into the thermodynamically stable MOF-74-II(Zn) phase. Due to a negligible lattice mismatch between PCN-74 and MOF-74-II(Zn), the crystallization of primary MOF-74-II(Zn) needles at the surface of PCN-74 fibers may proceed through epitaxial growth and is followed by their subsequent growth through the coordination of unreacted precursors or through grain boundary consumption at the interfaces (Figure 11B).⁶⁷ The crystalline MOF tubular structure may finally result from the assembly and constrained growth of these spatially close MOF-74-II(Zn) needlelike crystals through Ostwald ripening involving highly reversible coordination bond formation and reconstruction.⁶⁷ The assembly and microstructural evolution of MOF-74-II(Zn) was strongly dependent on the temperature of its solvothermal synthesis. Decreasing the temperature below 100 °C slows down the decomposition of DEF solvent, the deprotonation of linker II, and thus the growth process of MOF-74(II). Therefore, smaller and more flexible primary MOF-74(II) tubular NPs were obtained that could assemble and evolve into different superstructures (Figure 11C).⁶⁷ Multichannel MOF-74-II(Zn) superstructures were prepared through a solvothermal treatment of zinc nitrate and the organic linker II in DEF/EtOH/

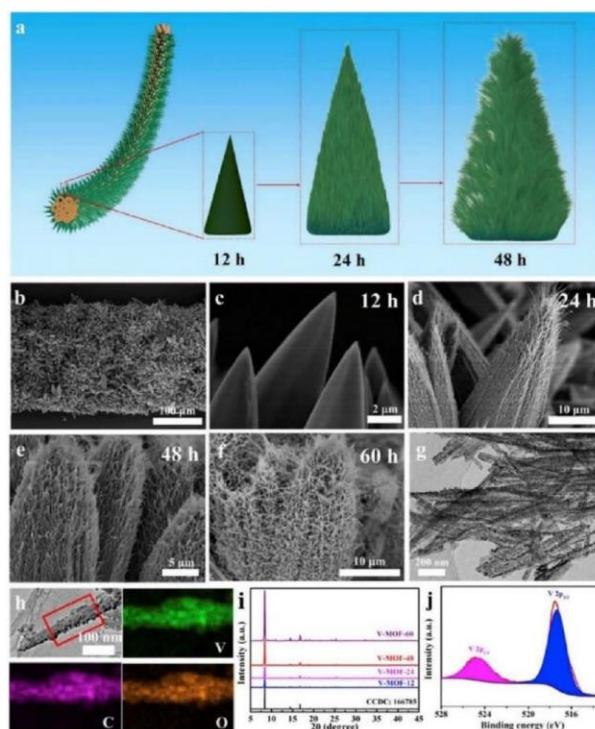


Figure 14. (a) Schematic illustration of the preparation process for the V-MOF@CNTF with a hierarchical NW structure. (b, c) SEM images of V-MOF-12@CNTF at different magnifications. (d–f) SEM images of (d) V-MOF-24, (e) V-MOF-48, and (f) V-MOF-60. (g) Low-magnification TEM image of V-MOF-48 NWs. (h) EDX mappings of the elements V, C, and O for a NW of V-MOF-48. (i) XRD patterns of the obtained V-MOF-12, V-MOF-24, V-MOF-48, and V-MOF-60 powders. (j) XPS spectrum of the V 2p region for V-MOF-48. Adapted with permission from ref 90. Copyright 2020 Elsevier.

water at 85 °C (Figure 11C(g)). These superstructures resulted from the self-assembly and crystal fusion of preformed MOF-74-II(Zn) microtubes. When the temperature of the solvothermal process was decreased to 70 °C, flexible twisted tubular MOF-74-II(Zn) superstructures 1–3 μm in width were formed and their microstructure resulted from the helical assembly of multiple MOF-74-II NWs (Figure 11C(a)).

MOF-74(Zn) was also used for the elaboration of a porous spherulite superstructure through the reaction of zinc nitrate and organic linker in DMF/water/EtOH mixed solvent under solvothermal conditions at 100 °C.⁹⁴ Such spherulite superstructures could be prepared with isorecticular MOF-74(Zn) materials (i.e., MOF-74(Zn)-II, -III, or -IV (see Figure 12)). They displayed a clear Maltese cross extinction pattern typical of spherulite structures under polarized light that had not been reported so far for porous materials (Figure 12A).⁹⁴ MOF-74(Zn)-III spherulites consisted of spherical particles 20–40 μm in diameter that result from the assembly and packing of radially aligned MOF-74(Zn) NRs with a diameter of 40–60 nm.⁹⁴ As indicated by FESEM images of the fractured spherulites, they presented a core–shell microstructure with a shell composed of radially arranged MOF NRs and an internal fused core without distinguishable individual MOF

fibrils (Figure 12C).⁹⁴ This microstructure shows that the close proximity of MOF-74(Zn) NRs in the core of spherulite can favor their aggregation and lateral growth through coarsening processes. The evolution behavior of MOF-74(Zn) spherulites was investigated by characterizing the solvothermal reaction products collected at different reaction times.⁹⁴ Spherulites about 15 μm in diameter were formed within 3 h, followed by the epitaxial growth of MOF-74(Zn)-III NRs, giving rise to the final spherical particles.⁹⁴ The growth of spherulites thus involves the branching of MOF-74(Zn)-III crystallites, whose crystallographic orientation deviates slightly from that of the parental NR. A radiating array of MOF-74(Zn)-III NRs was thus constructed as spherulites.⁹⁴ Due to their hierarchical superstructures, it was possible to prepare multicomponent materials through the encapsulation of metal precursors, organic dyes, or metal phthalocyanine into the MOF-74(Zn) spherulite.⁹⁴ Finally, PCN-222(Fe)@MOF-74(Zn)-II core–shell spherulites could also be prepared by using the porous PCN-222(Fe) MOFs as nuclei for the spherulite formation. Such a multifunctional material could exhibit an efficient catalytic activity for the olefin epoxidation with a high substrate selectivity as a result of its hierarchical porous architecture.⁹⁴ Note that analogous spherical superstructures composed of

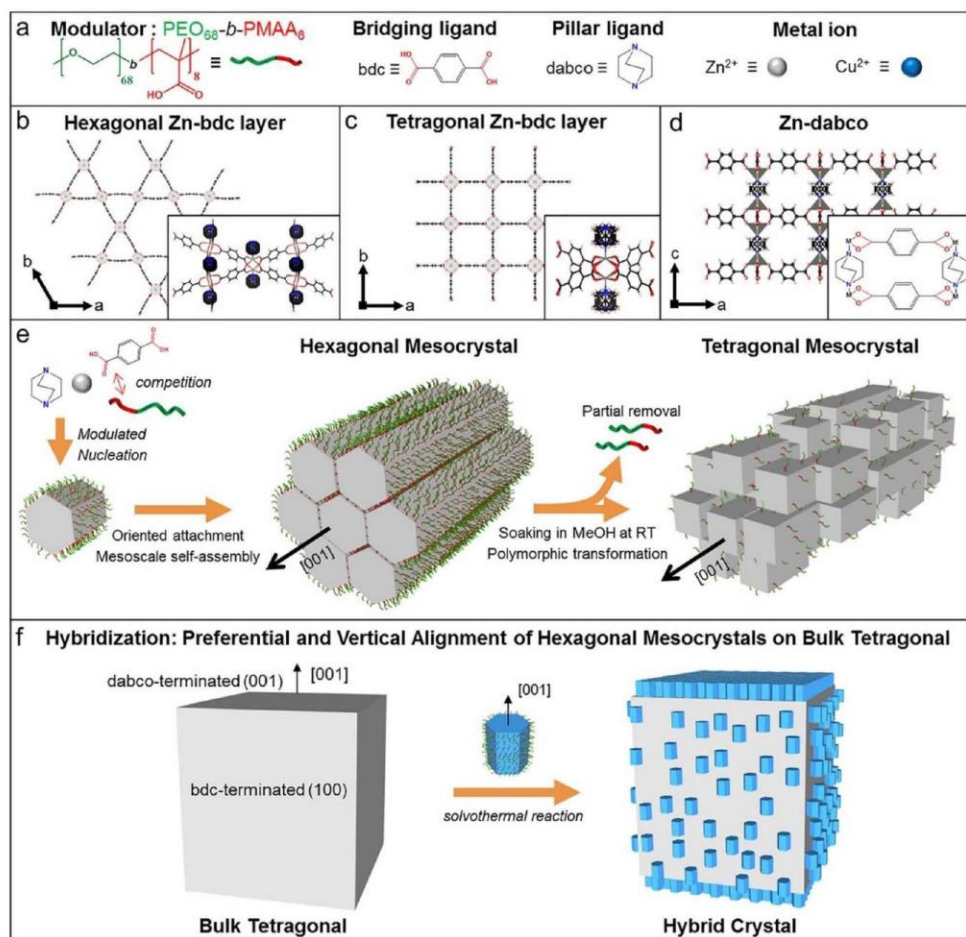


Figure 15. Morphogenesis of metal–organic mesocrystals mediated by $\text{PEO}_{68}\text{-}b\text{-PMAA}_8$ ($\text{EO}_{68}\text{MAA}_8$). (a) Chemical compositions of reactants. (b, c) Zn-bdc coordination mode: 2D layered conformational isomers of hexagonal (b) and tetragonal (c) frameworks. (d) Zn-dabco coordination mode. (e) Synthesis of hexagonal and tetragonal mesocrystals. (f) Hybridization of hexagonal mesocrystals and bulk tetragonal MOF crystals. Adapted with permission from ref 91. Copyright 2018 American Chemical Society.

radially assembled NRs were also obtained by using the same building blocks (Zn^{2+} and dobdc) as for $\text{MOF-74}(\text{Zn})\text{-II}$, but the NRs exhibited a different 3D nonporous CP architecture.⁹⁵

Following this pioneering work on MOF superstructures, Feng et al. increased further the level of complexity and hierarchy of MOF spherulites by designing quaternary superstructures composed of $\text{MOF-74}(\text{Zn})\text{-III}$ spherulites, the surfaces of which were decorated by plumose-like $\text{MOF-74}(\text{Zn})\text{-II}$ crystallites.⁸⁸ These complex architectures were formed by using $\text{MOF-74}(\text{Zn})\text{-III}$ spherulites as seeds that were mixed with the precursors of $\text{MOF-74}(\text{Zn})\text{-II}$ (zinc nitrate and organic linker II) in DMF at 100 °C. These plumose $\text{MOF-74}(\text{Zn})\text{-II}$ structures presented a multibranching treelike form and were characterized by a fractal pattern

(Figure 13). This nucleation and growth of fractal MOF structures is notably rare in MOF chemistry and may originate from the crystallographic mismatch between $\text{MOF-74}(\text{Zn})\text{-II}$ and $\text{MOF-74}(\text{Zn})\text{-III}$. Under solvothermal conditions, redissolution–crystallization processes could be expected to occur at specific regions of the $\text{MOF-74}(\text{Zn})\text{-III}$ spherulites, generating structural defects where the regioselective epitaxial growth of $\text{MOF-74}(\text{Zn})\text{-II}$ dendrites could take place.⁸⁸

Complex 3D multicomponent hierarchical MOF superstructures were designed by using carbon-based materials (polymers, carbon NT fibers, carbon papers, polymer membranes) as structure-directing agents or solid supports to induce the nucleation and growth of MOFs.^{89–92} The principle of the synthesis generally consists of directly growing the MOF

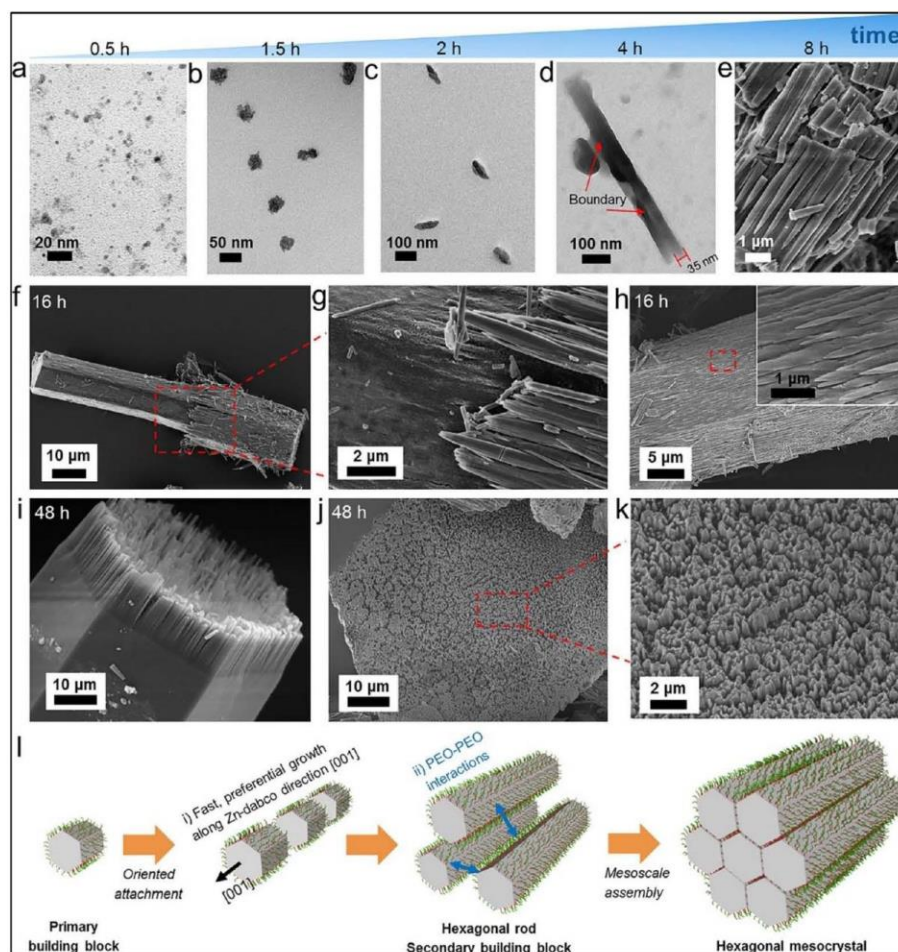


Figure 16. Growth processes of hexagonal rod mc-1h mediated by PEO₆₈-b-PMAA₃ at a [COOH of PEO₆₈-b-PMAA₃]/[Zn²⁺] molar ratio of 4, a PVP/PEO₆₈-b-PMAA₃ mass ratio of 1.5, and 120 °C. (a–k) Time-dependent TEM and SEM observations after reaction for 0.5 (a), 1.5 (b), 2 (c), 4 (d), 8 (e), 16 (f–h), and 48 h (i–k). (l) Proposed growth mechanism. Adapted with permission from ref 91. Copyright 2018 American Chemical Society.

nanocrystals on carbon-based materials by immersing these organic materials in the reaction solution containing the MOF precursors (metal salts and organic ligand), either at RT or under solvo-/hydrothermal conditions.^{89–92} This strategy led to the formation of MOF NW arrays grown on carbon papers or polymer membranes.^{89,92} In a similar approach, He et al. reported the synthesis of hierarchical composite electrodes (i.e., V-MOF@CNTF) composed of carbon NT fibers (CNTFs) decorated by an array of vanadium-based MOF (V-MOF) NWs.⁹⁰ This MOF corresponds to the V^{IV}(O)-bdc structure referenced in the literature as MIL-47(V). MIL-47(V) is built up from infinite chains of corner-sharing V^{IV}O₆ octahedra, interconnected by terephthalate groups to create a 3D framework containing 1D diamond-shaped channels.⁹⁰ The

solvothermal reaction products collected at different reaction times (between 12 and 60 h) were characterized by SEM. The formation of MIL-47(V) superstructures proceeds through a redissolution–precipitation process, involving the formation of egusi-shaped microcrystals for a short reaction time followed by their redissolution and crystallization of MIL-47(V) NWs (Figure 14).⁹⁰ These conductive CNTFs-MIL-47(V) composites were investigated as cathodes for aqueous Zn-ion batteries (*vide infra*, section 6).⁹⁰

Mesocrystals are colloidal crystals built up by assembling individual nanocrystals, which are aligned in a common crystallographic register.^{3,51} Therefore, a mesocrystal scatters like a single crystal and it is quite difficult to distinguish single crystals and mesocrystals, which means that mesocrystals are

probably much more common than is assumed in different families of inorganic and hybrid materials.^{3,51} Additionally, if the surface of the nanocrystals is not sufficiently stabilized, a crystallographic fusion of aligned nanocrystals is thermodynamically favored, leading to the transformation of mesocrystals into single crystals.^{3,51} Mesocrystals are very interesting self-assembled superstructures due to the anisotropic particle shape of the NP building units. Hwang et al. reported the synthesis of mesocrystals of nanoscale MOFs by using a double hydrophilic block copolymer (DHBC) as a crystal modulator.⁹¹ DHBCs were originally designed for mineralization purposes.⁹⁷ These bioinspired polymers consist of one functional block interacting with a mineral surface and one hydrophilic block promoting the solubilization of the polymer in water.^{3,51,97} Due to the separation of the binding and the solvating moieties, they were found to be effective in the crystallization control of various inorganic, inorganic/organic hybrid, or organic crystals.⁹⁷ Note that the morphosynthesis of inorganic crystals or MOFs mediated by DHBC is completely different from a template-directed synthesis.⁹¹ In contrast, DHBC could act as a crystal modulator of the MOF, thereby influencing the kinetic control of crystallization. The DHBC selected in this work, i.e. PEO₆₈-*b*-PMAA₈, consisted of one poly(methacrylic acid) block bearing complexing carboxylic acid functions prone to ionocovalently bind metal ions and one poly(ethylene oxide) block that may induce mesoscale assembly.⁹¹ This polymer was combined with a 3D MOF, [Zn₂(bdc)₂dabco] (dabco = 1,4 diazabicyclo[2.2.2]octane), whose framework consists of 2D layers of Zn-bdc connected by dabco pillars.⁹⁸ This MOF can crystallize into hexagonal **1h** (metastable kinetic phase) or tetragonal **1t** (thermodynamic phase) polymorphs (Figure 15). Due to its inherently metastable character, the size and morphology control of **1h** has rarely been achieved so far. Anisotropic hexagonal rod mesocrystals (**mc-1h**) were obtained by adding PEO₆₈-*b*-PMAA₈ into the conventional reaction mixture of bulk **1t**. As shown by SEM and TEM analyses on thin-sectioned rods, hexagonal rods with an average length and diameter of 2.9 and 0.53 μm, respectively, are composed of unidirectionally aligned hybrid nanocrystals along the long axis of the hexagonal rod. The electron diffraction of **mc-1h** is a characteristic pattern of a single crystal, indicating that the primary nanocrystals 30 nm in diameter are perfectly aligned to a joint crystallographic system.⁹¹ Similar results were obtained with the Cu structural analogue MOF [Cu₂(bdc)₂dabco]. While the kinetically metastable **2h** has never been isolated so far, the addition of PEO₆₈-*b*-PMAA₈ has not only stabilized and selected the **2h** metastable phase by slowing down the rate of crystal growth but also driven its anisotropic crystal growth into hexagonal NRs. The diameter of mesocrystals could be further increased by adding an amount of poly(vinylpyrrolidone) that slows down the nucleation step and thus allows the formation of larger MOF crystals.

According to the time-dependent TEM and SEM analyses carried out on different samples collected at different reaction times, it was possible to propose the growth mechanism of **mc-1h** (Figure 16). First, the mesocrystal formation involves the fast oriented attachment of small NPs formed at the first stages of the reaction (<8 h) into anisotropic secondary NRs with a length/width of 860/37 nm. PEO₆₈-*b*-PMAA₈ chains are presumably adsorbed on the Zn-bdc surfaces and stabilize the NRs of **mc-1h**. After 8 h, the NRs continuously grew and their mesoscale assembly mediated by favorable interactions

between PEO blocks led to the formation of hexagonal mesocrystals composed of aligned hexagonal microrods with a length/width of 183/64 μm (Figure 16). By an increase in the length of the PEO block, large hexagonal plates composed of aligned hexagonal MOF NRs were formed, thereby showing the role of the PEO block in the control of the mesoscale assembly as well as the particle aggregation. In the absence of PEO₆₈-*b*-PMAA₈, the kinetic phase **mc-1h**, which presents a higher solubility, evolves over time to the thermodynamic **mc-1t** phase through redissolution–crystallization processes, as commonly observed for numerous coordination polymers, MOFs, and oxides.⁵⁷ This indicates that the functionalization of **mc-1h** mesocrystals by PEO₆₈-*b*-PMAA₈ inhibited the conversion of **mc-1h** into **mc-1t**. Therefore, the partial dissolution of PEO₆₈-*b*-PMAA₈ chains of **mc-1h** by immersing **mc-1h** in methanol was conducted to induce the transformation of **mc-1h** into **mc-1t**.⁹¹ Mesocrystals of **mc-1t** composed of hexagonally arranged cubic NPs were thus formed by using the metastable **mc-1h** as a template (Figure 15e). This material presents a high morphological complexity with two levels of hierarchy in terms of porosity and dimensionality, since it exhibits not only micropores of the inherent MOF framework but also mesopores. Finally, in view of the preparation of multifunctional hybrid materials, bulk **1t** could be combined to mesocrystals of **mc-2h**, leading to hybrid crystals composed of **mc-2h** NRs vertically aligned on specific surfaces of bulk **1t** (Figure 15f).⁹¹ This work clearly demonstrated that DHBC could be very useful to tune the hierarchical dimensionality and porosity as well as the morphological complexity of MOFs by impacting the kinetics and thermodynamics of MOF formation. This control of crystallization exerted by DHBC, as previously reported for biominerals, oxides, and organic crystals, could thus be potentially extended to other MOFs by tuning the chemical functionality and structure of DHBC.⁹⁷

6. APPLICATIONS OF NANOSTRUCTURES AND SUPERSTRUCTURES BASED ON 1D TUBULAR MOFS

1D tubular MOF-based nano- and superstructures were investigated for different applications such as catalysis,^{55,67} sensing,^{59,66} and separation,^{73,99} as described in previous sections. Indeed, their hierarchical porosity and dimensionality can enhance the diffusion and mass transport efficiency of analytes toward the catalytic and adsorption sites of the MOF. As an example, MOF-74(Co) hollow NRs have shown a higher CO₂/N₂ separation performance in comparison to the bulk MOF-74(Co). (see section 3).⁶² The potential of 1D MOF nano- and superstructures was also explored in energy-related applications, especially for the development of electrochemical energy storage devices.^{100,101} Figure 17 summarizes the relationship between the physicochemical properties of 1D MOF nanostructures and their potential applications.

Energy storage devices are components of reliable renewable energy sources, but most of these systems are still not up to the desired standard levels of efficiency. An important class of such devices that could be used for the power supply of portable electronics, electric automobiles, and aerial vehicles constitutes rechargeable batteries and supercapacitors (SCs). However, batteries suffer from low power density and cyclic stability despite high energy densities. On the other hand, SCs can present very high power density and cyclic stability but can be limited by their low energy density.^{100,101} Therefore, neither of

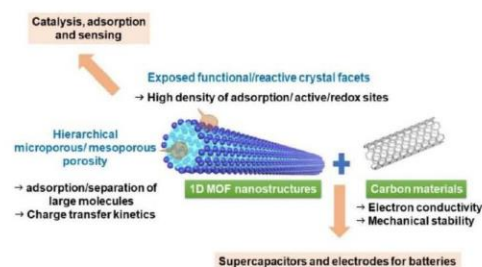


Figure 17. Schematic representation of the relationship between the structural and physicochemical properties of 1D MOF nanostructures and their potential applications.

these energy storage devices can independently fulfill the desirable needs of high energy and power density along with cyclic stability. In order to tackle these drawbacks, many efforts have been made to improve the electrode materials, which strongly affect the practical energy, power density, and overall stability of the devices.^{100,101} Suitable electrode materials should have high surface areas and tailored pore sizes for the electrolyte penetration and ion transportation, as well as excellent conductivity and electroactive sites for battery applications.^{100,101}

Due to their structural characteristics (hybrid nature, high tunability, high surface area, various pore sizes, etc.), MOFs have attracted much interest for energy-related applications such as SCs.¹⁰⁰ SCs store electric charge in electric double layers that are formed at the interface between the electrode and the electrolyte. These electrochemical capacitors present applications in memory backup systems, consumer electronics, and industrial energy/power management devices.¹⁰¹ Among them, solid-state SCs demonstrate all of the characteristics of traditional liquid electrolyte SCs, with the added benefits of easier handling, higher level of reliably and safety, and wider range of operating temperatures, constituting promising devices for next-generation energy storage.¹⁰¹ The electrode is a critical component of the SC, and the properties of the electrode material such as high conductivity, large specific surface area, high porosity, temperature stability, and good corrosion resistance are important parameters to optimize their energy storage capabilities and power densities.¹⁰¹ MOFs NPs with different morphologies (i.e., sphere, rods, sheets) have previously been tested as electrodes in two types of SCs

differing in their charge-storing methods: namely, electrical double-layer capacitors (EDLCs) and pseudocapacitors (see Figure 18).^{100–103} While the energy in EDLCs is stored by the electrostatic adsorption of charges on the surface of the electrodes, the energy in pseudocapacitors is stored by the reversible Faradaic redox reaction taking place at the surface of the electrodes.^{100,101,104} The controllable porous structure and high surface area of MOFs provide a significant advantage to enhance the electrolyte penetration, while the presence of redox-active metal centers has the potential to increase pseudocapacitance.^{100,101} Note that the vast majority of MOFs exhibit poor electron conductivity, which is the main limitation for the performance of SCs. However, an alternative strategy consists of integrating intrinsically conductive MOFs^{102,103} such as the Cu-CAT MOF as the sole electrode material into EDLC SCs.⁸⁹ This Cu-catecholate-based MOF was first synthesized by Hmadeh and co-workers and exhibits one of the highest conductivities (i.e., $2.1 \times 10^{-1} \text{ S cm}^{-1}$) reported so far for MOFs.^{103,105} This material is based on a redox-active linker, the highly conjugated tricatecholate 2,3,6,7,10,11-hexahydroxytriphenylene ($\text{H}_{12}\text{C}_{18}\text{O}_6$, HHTP). The structure of this MOF consists of two distinct types of alternatively stacked layers.¹⁰⁵ The first layer is an extended honeycomb structure with hexagonal pores, while the second layer is formed by trinuclear $\text{Co}_3(\text{HHTP})(\text{H}_2\text{O})_{12}$ units.^{92,105} These layers stack in a eclipsed fashion, giving rise to a hexagonal array of 1D channels along the *c* axis with a diameter of 12 Å.¹⁰⁵ Cu-CAT was directly grown onto carbon fiber paper—without using any conductive additives or binders—forming highly oriented NW arrays (NWAs), with 200–250 nm diameter and 3–15 μm length (Figure 19A).⁸⁹ Figure 19B(a) shows the typical CV curves of a Cu-CAT NWA electrode in a three-electrode cell. In comparison to Cu-CAT NWAs, the carbon paper did not exhibit any redox activity (Figure 19B(b)). The specific capacitance of Cu-CAT NWAs electrode remains as high as 66% ($202\text{--}134 \text{ F g}^{-1}$) when current densities increase 20 times ($0.5\text{--}10 \text{ A g}^{-1}$). As shown in Figure 19B(c), it retains 80% of its initial capacitance after 5000 cycles at 800 mV s^{-1} , which is comparable to other MOF-based supercapacitors.⁸⁹ In comparison, a Cu-CAT powder electrode obtained by mixing Cu-CAT crystallite powder with a polymer binder exhibited a 2 times lower capacitance in comparison to that of Cu-CAT NWAs (Figure 19B(d)). The ohmic resistance and charge transfer resistance of Cu-CAT NWAs are both lower than those of the Cu-CAT powder electrode. In the Cu-CAT powder electrode, the

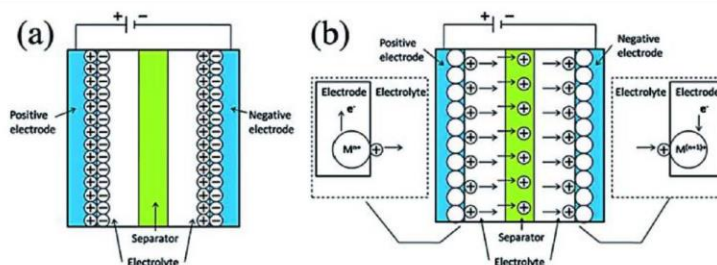


Figure 18. Representation of (a) electrical double-layer capacitors (EDLCs) and (b) pseudocapacitors (where M is a metal cation). Adapted with permission from ref 104. Copyright 2020 The Royal Society of Chemistry.

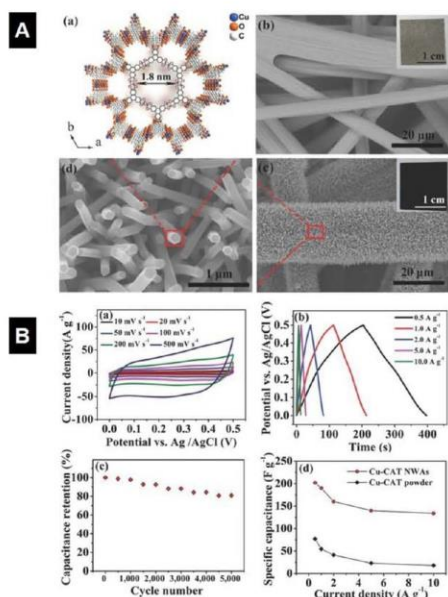


Figure 19. (A) (a) Crystal structure of Cu-CAT viewed along the *c* axis. (b) SEM and photographic image (inset) of the carbon fiber paper. (c, d) SEM and photographic images (inset in (c)) of the Cu-CAT NWAs growing on carbon fiber paper. (B) Electrochemical performance of a Cu-CAT NWA electrode in a three-electrode cell. (a) CVs at different scan rates. (b) Galvanostatic charge and discharge curves at different current densities. (c) Cycling performance. (d) Rate-dependent specific capacitance. Adapted with permission from ref 89. Copyright 2017 John Wiley and Sons.

presence of the polymer binder significantly induces large interparticle resistance and contact resistance between MOF NPs and the current collector.⁸⁹ In contrast, the intrinsic resistance and charge transfer resistance of Cu-CAT NWAs is significantly reduced, since their microstructure consists of highly oriented and packed single-crystal Cu-CAT NWs directly grown on carbon fibers.⁸⁹ This allows an effective charge/electron transport on the interface with the electrolyte.

Finally, the electrochemical performance of the conductive Cu-CAT NWAs was compared with a series of well-known MOFs (UiO-66, ZIF-8, ZIF-67, MIL-100, and MIL-101) that present a low electron conductivity. Cu-CAT NWs outperform this series of MOFs due to their good electron conductivity as well as hierarchical structure and porosity.

Finally, Cu-CAT NWA electrodes were also used for the construction of a symmetrical solid-state SC, using PVA/KCl (PVA = poly(vinyl alcohol)) gel as a solid electrolyte, and achieved a surface-area-normalized capacitance of 22 $\mu\text{F}/\text{cm}^2$, much higher than those reported for other MOF-based or most porous carbon-based symmetrical solid-state SCs.⁸⁹ Hou and co-workers employed the same intrinsically conductive Cu-CAT-NWAs for the development of all-solid-state flexible SCs, which could be exploited for the operation of flexible electronics.⁹² A uniform and ordered array of Cu-CAT-NWs with a diameter of 120–150 nm and length of 6 μm was

directly grown onto the self-supported polypyrrole (PPy) membrane through a facile hydrothermal synthesis without any inactive additive or binders. The Cu-CAT NWAs provided high conductivity and surface area for the accessibility of electrolytes, while the PPy membrane was selected due to its good mechanical stability, efficient charge transfer, and additional capacitance. This system affords self-supported and integrated electrodes for all-solid-state flexible SCs, with a high areal capacitance (252.1 mF cm^{-2}), an energy density of $22.4 \mu\text{Wh cm}^{-2}$, a power density of 1.1 mW cm^{-2} , a high cycling stability, and a high mechanical flexibility over a wide range of working temperatures (-20 to $+100$ °C).⁹² The energy density and power density of such an electrode is higher than that of numerous MOFs and several carbon materials. This capacitive behavior results from a combination of microstructural (porosity, 1D architecture of MOFs, flexibility) and electrochemical properties (conductivity) as a result of the synergistic assembly between Cu-CAT NWs and the PPy membrane.

However, the intrinsically low electrical conductivity of most MOFs is a main limitation for the development of high-performing electrochemical devices. Different strategies have been employed to improve the electrical conductivity of MOFs, including their combination with conductive carbon-based materials (graphene, graphene oxide, polymers, etc.).^{32,40,45} He et al.⁹⁰ used, as a cathode for Zn-ion batteries, a 3D conductive composite (i.e., V-MOF@CNTFs) composed of MIL-47 NWs and CNTFs, as explained in section 5 (*vide supra*).⁹⁰ The CNTFs were used due to their high electrical conductivity and good mechanical stability. The assembled V-MOF@CNTFs//Zn battery in aqueous electrolyte delivered a high volumetric capacity ($101.8 \text{ mAh cm}^{-3}$) at a current density of 0.1 A cm^{-2} and excellent rate capability in aqueous electrolyte.⁹⁰ Such an electrochemical performance could be ascribed to their unique porous 3D hierarchical superstructure that not only was prone to expose a large surface area of active material and active sites but also enhanced the diffusion of electrolyte ions. Moreover, to show the potential of these V-MOF@CNTF electrodes for wearable electronics, an all-solid-state fiber-shaped V-MOF@CNTFs//Zn battery was assembled using a PVA electrolyte and exhibited a maximum energy density of $30.71 \text{ mWh cm}^{-3}$ and a maximum power density of 1.46 W cm^{-3} . Such values are superior to those of most of the fiber-shaped all-/quasi-solid-state energy storage devices reported previously (SWNT/rGO//SWNT/rGO, graphene//Co₃O₄, aqueous sodium-ion battery, Zn//Co battery, etc.). Moreover, this battery exhibited an excellent flexibility and good cycle stability (81.5% retention of initial capacity after 300 cycles).⁹⁰

Another approach to circumvent the poor electrical conductivity of MOFs consists of converting these materials to highly conductive composites while keeping their high surface area and porosity. This strategy proceeds through the thermal decomposition of MOFs where organic linkers serve as carbon and heteroatom sources, as well as pore-forming agents, while inorganic species act as sacrificial porogens or can catalyze the *in situ* graphitization.^{30,101,105} Moreover, the inherent structure of MOFs with a well-defined periodic arrangement of metal nodes and organic motifs can induce the formation of composites with a homogeneous spatial distribution of (electro)active sites.^{30,101,106} This method can thus be efficient for the preparation of single-atom metal catalysts that are of high interest for catalytic and energy-

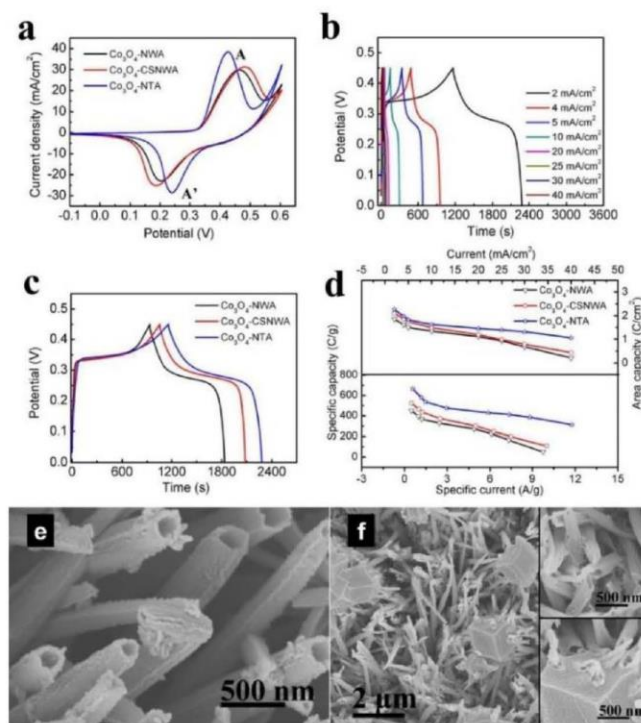


Figure 20. (a) CV plots of Co_3O_4 -NWAs, Co_3O_4 -CSNWAs and Co_3O_4 -NTAs at a scan rate of 2 mV s^{-1} . (b) Galvanostatic charge–discharge curves of Co_3O_4 -NTAs at current densities of 2, 4, 5, 10, 20, 25, 30, and 40 mA cm^{-2} . (c) Galvanostatic charge–discharge curves of Co_3O_4 -NWAs, Co_3O_4 -CSNWAs and Co_3O_4 -NTAs at a current density of 2 mA cm^{-2} . (d) Calculated area capacitance values from galvanostatic charge–discharge curves of Co_3O_4 -NWAs, Co_3O_4 -CSNWAs and Co_3O_4 -NTAs. (e) SEM images of ZIF-67 NTs formed from Co-NWs. (f) SEM image of Co_3O_4 -NTAs. The insets show the corresponding enlarged images of f). Adapted with permission from ref 107. Copyright 2015 The Royal Society of Chemistry.

related applications.³⁰ These MOF-derived composites thus present microstructural and physicochemical properties that could hardly be achieved by using other porous composites. Following this approach, 1D tubular MOFs were used as sacrificial templates for fabricating hierarchical porous composites based on carbon materials, metal oxides, and metal sulfides.^{52,64,65,107} Note that the textural and microstructural properties of the final carbon composites can be optimized by controlling the pyrolysis conditions (temperature, gas atmosphere, reaction time, etc.).^{52,64,65,107} Despite the severe calcination conditions ($700 \text{ }^\circ\text{C}$, Ar atmosphere), the carbonization of MOF-74(Co) NWs led to 3D hierarchical carbon dendrites composed of carbon nanofiber trunks and carbon NT branches in which Co NPs are immobilized.⁵² This composite exhibits a high electrocatalytic activity for the oxygen reduction reaction (ORR) and could also be used as a cathode in a Zn-air battery. By a similar approach, ZIF-67 NT arrays (NTAs) produced through the replication process (see section 3) were thermally converted to mesoporous Co_3O_4 NTAs (Figure 20).¹⁰⁷ The electrochemical properties of these Co_3O_4 NTAs were evaluated for their potential use as electrodes in batteries. As shown by the CV and galvanostatic

charge–discharge curves (Figure 20a,b), these ZIF-67-derived Co_3O_4 NTAs were characterized by a much higher specific capacity in comparison to Co_3O_4 NW arrays directly formed from Co NWs (i.e., Co_3O_4 -NWAs). At a current density of 2 mA cm^{-2} , it exhibited the highest area capacity of 2.26 C cm^{-2} in comparison to 1.85 C cm^{-2} for Co_3O_4 -NWAs (Figure 20c). Figure 20d displays the capacity values calculated from the galvanostatic charge–discharge curves. The area capacity (1.06 C cm^{-2}) of Co_3O_4 NTAs at a current density of 40 mA cm^{-2} is still maintained up to 46.9% of that measured at 2 mA cm^{-2} (2.26 C cm^{-2}).¹⁰⁷ These results show that Co_3O_4 NTAs are characterized by a high rate capability. The better electrochemical performance of Co_3O_4 NTAs in comparison to Co_3O_4 -NWAs can be ascribed to their peculiar microstructure with a high surface area, since Co_3O_4 NTs are composed of small NPs 10–20 nm in diameter.¹⁰⁷ This architecture is prone to provide a high number of electroactive sites while enhancing the ion diffusion rate and the charge transfer. Furthermore, Co_3O_4 NTAs exhibited comparable or better specific capacity and rate capability in comparison to those of previously reported Co_3O_4 -based materials. Finally, after 5000 cycles at a current density of 20 mA cm^{-2} , Co_3O_4 NTAs retained 96.9%

of the initial capacity (1.46 C cm^{-2}) while the overall capacitance loss of Co_3O_4 -NWAs was about 27.2%, thereby showing the excellent cycling stability of Co_3O_4 NTAs.¹⁰⁷

By a similar strategy, 3D hollow urchinlike superstructures of ZIF-67(Co) were transformed through a sulfuration and pyrolysis treatment to a $\text{Co}_{1-x}\text{S}@C$ composite with the preserved urchinlike architecture (Figure 21).⁶⁵ These composites that consist of Co_{1-x}S NPs homogeneously distributed in the carbon matrix present a high pseudocapacitive performance as a cathode material for SCs.⁶⁵

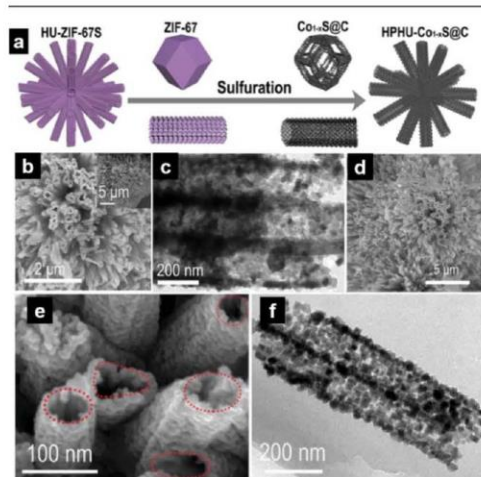


Figure 21. Morphological characterization of the $\text{Co}_{1-x}\text{S}@C$ superstructure. (a) Schematic preparation process. (b) SEM (inset: low-magnification SEM image) and (c) TEM images of $\text{Co}_{1-x}\text{S}@C$. (d, e) SEM and (f) TEM images of ZIF-67 superstructures. Adapted with permission from ref 65. Copyright 2019 The Royal Society of Chemistry.

8. CONCLUSIONS AND OUTLOOK

1D MOF based NTs and NWs with different compositions, microstructures (lengths, diameters), and organization levels have been prepared following different synthetic protocols. While the use of soft or hard templates has been revealed to be fruitful for the production of 1D MOF nanostructures, the number of MOF NWs and NTs produced in solution without any structure-directing agents is limited at the present time, however. This may be partially due to the key challenge in MOF synthesis to control the structure and the morphology of the material that will be formed under the specific experimental conditions. For numerous MOFs, the relationship between the synthetic parameters (precursor concentrations, temperature, time, etc.) and the structure/composition of MOF is hard to predict, such that the synthesis of a MOF with a tailored crystal morphology is typically accomplished on the basis of trial and error, rather than a rational design. Such a predictive understanding is of primary importance to master and upscale the production of these nanostructured materials by using reliable manufacturing protocols. It is worth noting that significant progress on the formation mechanisms of MOFs was achieved through *in situ* and time-resolved studies of MOF

crystallization and growth performed by using a broad range of complementary experimental (scattering methods, microscopy, and spectroscopy) and simulation techniques.⁵⁸ This valuable approach reported for a variety of MOFs has clearly shown that the processes of MOF nucleation and growth are highly system specific and proceed through diverse mechanisms (monomer addition, dissolution–recrystallization, solid-phase transformations, etc.).⁵⁸ Although SEM and/or TEM experiments have generally been performed to study the formation of MOFs NWs and NTs, time-resolved and *in situ* studies with a combination of multiple advanced characterization techniques would certainly provide insight into the anisotropic growth of MOF nanocrystals. This difficulty in predicting the crystalline growth of MOFs as well as their structural evolution during synthesis is also related to the surface structure of MOF nanocrystals, which is much more complex and heterogeneous in comparison other materials such as oxides due to the presence of a wide diversity of surface functional groups (organic linker, metal cations, surface defects, coordinating water molecules).¹⁰⁸

The control over the size, morphology, and surface structure of MOF nanocrystals is a burgeoning scientific theme due to its importance in the physicochemical properties and the performance of materials in applications. Hierarchical MOF superstructures and mesocrystals are recently reported in the literature and are currently sparking great interest, since they present NP characteristics together with those arising from the collective interactions of NPs.^{30,39,49,67,88,94} As was previously reported for inorganic mesocrystals (i.e., superparamagnetic magnetite assemblies or metal NP based superstructures),^{5,51} a synergy or amplification of properties would be expected if the mesocrystals are composed of aligned anisotropic nanocrystals with directional physicochemical properties. Moreover, these materials can potentially exhibit a dual micro- and mesoporosity due to the inherent porosity of the MOFs and interparticle spaces. This hierarchical multiscale porosity is prone to boost the diffusion of analytes and reactants toward the adsorption and/or active sites of MOFs, thereby enhancing the performance of MOFs in catalysis and adsorption.^{27,28} The design of tubular MOF nano- and superstructures is still in its infancy. However, we can envision that this research area will be continuously expanded toward the exploration of novel hierarchical MOF architectures with a high level of morphological complexity.

AUTHOR INFORMATION

Corresponding Author

Nathalie Steunou – Institut Lavoisier de Versailles, UMR CNRS 8180, Université de Versailles St Quentin en Yvelines, Université Paris Saclay, Versailles 78035, France;
 orcid.org/0000-0002-7049-7388;
 Email: nathalie.steunou@uvsq.fr

Authors

Ali Saad – Institut Lavoisier de Versailles, UMR CNRS 8180, Université de Versailles St Quentin en Yvelines, Université Paris Saclay, Versailles 78035, France
 Subharanjan Biswas – Institut Lavoisier de Versailles, UMR CNRS 8180, Université de Versailles St Quentin en Yvelines, Université Paris Saclay, Versailles 78035, France;
 orcid.org/0000-0002-1608-4240

Polymers and Templates; Naka, K., Ed.; Springer Berlin Heidelberg: 2007; pp 1–77.

(98) Dybtsev, D. N.; Chun, H.; Kim, K. Rigid and Flexible: A Highly Porous Metal–Organic Framework with Unusual Guest-Dependent Dynamic Behavior. *Angew. Chem., Int. Ed.* **2004**, *43* (38), 5033–5036.

(99) Yu, B.; Ye, G.; Chen, J.; Ma, S. Membrane-Supported 1D MOF Hollow Superstructure Array Prepared by Polycapamine-Regulated Contra-Diffusion Synthesis for Uranium Entrapment. *Environ. Pollut.* **2019**, *253*, 39–48.

(100) Kuyuldar, S.; Genna, D. T.; Burda, C. On the Potential for Nanoscale Metal–Organic Frameworks for Energy Applications. *J. Mater. Chem. A* **2019**, *7* (38), 21545–21576.

(101) Sundriyal, S.; Kaur, H.; Bhardwaj, S. K.; Mishra, S.; Kim, K.-H.; Deep, A. Metal-Organic Frameworks and Their Composites as Efficient Electrodes for Supercapacitor Applications. *Coord. Chem. Rev.* **2018**, *369*, 15–38.

(102) Dou, J.-H.; Arguilla, M. Q.; Luo, Y.; Li, J.; Zhang, W.; Sun, L.; Mancuso, J. L.; Yang, L.; Chen, T.; Parent, L. R.; Skorupskii, G.; Libretto, N. J.; Sun, C.; Yang, M. C.; Dip, P. V.; Brignole, E. J.; Miller, J. T.; Kong, J.; Hendon, C. H.; Sun, J.; Dincă, M. Atomically Precise Single-Crystal Structures of Electrically Conducting 2D Metal–Organic Frameworks. *Nat. Mater.* **2021**, *20* (2), 222–228.

(103) Xie, L. S.; Skorupskii, G.; Dincă, M. Electrically Conductive Metal–Organic Frameworks. *Chem. Rev.* **2020**, *120* (16), 8536–8580.

(104) Ahmad, R.; Khan, U. A.; Iqbal, N.; Noor, T. Zeolitic Imidazolate Framework (ZIF)-Derived Porous Carbon Materials for Supercapacitors: An Overview. *RSC Adv.* **2020**, *10* (71), 43733–43750.

(105) Hmadeh, M.; Lu, Z.; Liu, Z.; Gándara, F.; Furukawa, H.; Wan, S.; Augustyn, V.; Chang, R.; Liao, L.; Zhou, F.; Perre, E.; Ozolins, V.; Suenaga, K.; Duan, X.; Dunn, B.; Yamamoto, Y.; Terasaki, O.; Yaghi, O. M. New Porous Crystals of Extended Metal-Catecholates. *Chem. Mater.* **2012**, *24* (18), 3511–3513.

(106) Zhang, W.; Wu, Z.-Y.; Jiang, H.-L.; Yu, S.-H. Nanowire-Directed Templating Synthesis of Metal–Organic Framework Nanofibers and Their Derived Porous Doped Carbon Nanofibers for Enhanced Electrocatalysis. *J. Am. Chem. Soc.* **2014**, *136* (41), 14385–14388.

(107) Yu, D.; Ge, L.; Wu, B.; Wu, L.; Wang, H.; Xu, T. Precisely Tailoring ZIF-67 Nanostructures from Cobalt Carbonate Hydroxide Nanowire Arrays: Toward High-Performance Battery-Type Electrodes. *J. Mater. Chem. A* **2015**, *3* (32), 16688–16694.

(108) McGuire, C. V.; Forgan, R. S. The Surface Chemistry of Metal–Organic Frameworks. *Chem. Commun.* **2015**, *51* (25), 5199–5217.



ANNEX 2



Cite this: *J. Mater. Chem. A*, 2022, **10**, 8535

A robust eco-compatible microporous iron coordination polymer for CO₂ capture†

Marvin Benzaqui,^{ab} Mohammad Wahiduzzaman,^{ib} Heng Zhao,^b Md Rafiul Hasan,^{ib} Timothy Steenhaut,^{ib} Ali Saad,^a Jérôme Marrot,^a Périne Normand,^g Jean-Marc Grenèche,^{ib} Nicolas Heymans,^{ib} Guy De Weireld,^{ib} Antoine Tissot,^{ib} William Shepard,^{ib} Yaroslav Filinchuk,^f Sophie Hermans,^{ib} Florent Carn,^{ib} Magdalena Manlankowska,^{ib} Carlos Téllez,^{ib} Joaquín Coronas,^{ib} Guillaume Maurin,^{ib} Nathalie Steunou^{ib}*^{ab} and Christian Serre^{ib}*^{ab}

Iron(III) carboxylate based metal organic frameworks (MOFs)/porous coordination polymers (PCPs) have sparked great interest owing to their high structural diversity and tunable porosity, excellent stability, tailored functionality and their scalability as well as green synthesis associated with their biocompatible and biodegradable character. Herein, we present a new robust Fe(III) based PCP (labelled MIL-178(Fe)) built up from chains of corner sharing Fe octahedra interconnected by 1,2,4-benzene tricarboxylic acid, delimiting one dimensional narrow pore channels (pore diameter < 4.5 Å) decorated with polar groups (μ_2 -OH and $-\text{CO}_2\text{H}$ functions). These structural and chemical features are suitable for the selective adsorption of CO₂. MIL-178(Fe) was synthesized following a simple and green protocol in water under near ambient conditions using non-toxic reactants, allowing the production of sub-micrometer sized MIL-178(Fe) particles in a large amount (30 g). As shown by single-gas isotherms and CO₂/N₂ co-adsorption experiments as well as molecular simulations, this material exhibits a moderate CO₂ capacity at low pressure but a high CO₂/N₂ selectivity. This is fully consistent with the presence of μ_2 -OH groups acting as CO₂ adsorption sites, as revealed from both molecular simulations and *in situ* PXRD experiments. Finally, the good compatibility of this MOF with the elastomer block copolymer Pebax®-3533 allowed the processing of homogeneous and defect-free mixed matrix membranes with a MIL-178(Fe) loading of up to 25 wt% that outperformed pure Pebax®-3533 membranes for CO₂/N₂ separation.

Received 4th December 2021
Accepted 3rd March 2022

DOI: 10.1039/d1ta10385g
rsc.li/materials-a

Introduction

Metal organic frameworks (MOFs) and porous coordination polymers (PCPs) are a class of porous crystalline hybrid materials constructed through the coordination of multi-metallic units called secondary building units (SBUs) with organic multitopic ligands.^{1,2} They have gained widespread interest due to their high surface area, chemical diversity, unprecedented

variability of pore shape/size and topology.¹ Therefore, their physico-chemical properties can be finely tuned, making them promising materials for a myriad of applications including gas storage and separation, heterogeneous catalysis, sensing, biomedicine and so on.³⁻⁷ Remarkable advances have been made toward CO₂ capture and separation by using PCPs, MOFs and MOF based composites.^{4,8-10} The main advantages of MOFs over other porous materials are their high CO₂ sorption capacity

^aInstitut Lavoisier de Versailles, UMR CNRS 8180, Université de Versailles St Quentin en Yvelines, Université Paris Saclay, 78000 Versailles, France. E-mail: nathalie.steunou@wvsg.fr

^bInstitut des Matériaux Poreux de Paris, ENS, ESPCI Paris, CNRS, PSL University, 75005 Paris, France. E-mail: christian.serre@ens.fr

^cICGM, Univ. Montpellier, CNRS, ENSCM, Montpellier, France

^dInstituto de Nanociencia y Materiales de Aragón (INMA), CSIC-Universidad de Zaragoza, Zaragoza 50018, Spain

^eChemical and Environmental Engineering Department, Universidad de Zaragoza, Zaragoza 50018, Spain

^fInstitute of Condensed Matter and Nanosciences, Université Catholique de Louvain, 1348 Louvain-la-Neuve, Belgium

^gService de Thermodynamique et de Physique Mathématique, Faculté Polytechnique de Mons, Université de Mons, 7000 Mons, Belgium

^hInstitut des Molécules et des Matériaux du Mans (IMMM), UMR CNRS 6283, Université du Maine, 72085 Le Mans, Cedex 9, France

ⁱSynchrotron SOLEIL-URI, Orme des Merisiers, Saint-Aubin, BP 48, 91192, Gif-sur-Yvette, France

^jLaboratoire Matière et Systèmes Complexes (MSC), UMR CNRS 7057, Université Paris Diderot, Bât. Condorcet, 10 rue A. Domon et L. Duquet, 75013 Paris, France

† Electronic supplementary information (ESI) available. CCDC 2112974. For ESI and crystallographic data in CIF or other electronic format see DOI: 10.1039/d1ta10385g

and high CO₂ affinity.^{8–10} This largely stems from their potential high pore volume and large amount of CO₂-philic sites that can be introduced within their backbone. Typically, MOFs can integrate multiple CO₂ adsorption sites, e.g. open metal sites, Lewis basic sites and covalently-bound polar functional groups, that enables to achieve preferential CO₂ adsorption over other gas molecules such as N₂, CH₄ and H₂O.^{8–11} In addition, post-synthetic modification has been also employed to introduce novel CO₂ adsorption sites without altering or degrading the MOF structure.^{4,8–11}

While remarkable advances have been achieved for using PCPs and MOFs in CO₂ capture and separation, their large scale application in this field would require overcoming some challenges such as the limited chemical and thermal stabilities of some of them, particularly in the presence of harsh contaminants.^{8,12} Indeed, numerous MOFs reported so far for CO₂ capture still lack the requisite chemical stability. Note that moisture is a major concern in industrial gas separation as it is not economically feasible to use completely dry feed-gas streams. Therefore, only hydrothermally stable MOFs can be considered for real practical applications. Various strategies have been explored to design stable MOFs by privileging the formation of strong metal-ligand coordination bonds with the use of high valent metal cations (III/IV) according to Pearson's hard/soft acid/base principle, or alternatively the incorporation of hydrophobic and/or polydentate organic linkers.^{12,13}

In this context, Fe(III) carboxylates – denoted here as “Fe-MOFs” – were thus considered so far since the association of the Fe³⁺ cation with strong Lewis acid properties and carboxylate ligands can produce, although not systematically, water stable MOFs.^{14,15} Moreover, iron is widely distributed in nature and environmentally friendly. The abundance of iron and its low toxicity have promoted the development of Fe-MOFs, not only for gas separation but also for (photo)catalysis, heat reallocation, (bio)sensing or biomedicine due to their good chemical stability, high porosity and biocompatibility.^{14,16–19}

So far, Fe(III) MOFs of different architectures, such as the MIL-*n* (MIL-53, MIL-59, MIL-88, MIL-100, and MIL-101) series, the Fe-soc-MOF or Fe₂(μ₃-O)₂(BTB)_{8/3}(DMF)₂(H₂O)₂, have been designed by assembling either di-, tri-, tetranuclear clusters or Fe-hydroxy chains as SBUs and polycarboxylate aromatic moieties as organic linkers.^{18,20–23} Fe(III) sites were also introduced in the organic backbone of MOFs by using Fe(III) porphyrin ligands (PCN-223, PCN-224, and PCN-600).^{24–26} The Fe(III)-phosphonate MOFs such as Fe-CAU-53 were also recently reported.²⁷ However, not all of these MOFs exhibit a high hydrolytic stability that is not only driven by the type of SBUs but also the connectivity as well as the size and hydrophobic character of the organic linker.^{14–27} As an example, the good hydrothermal stability of MIL-53(Fe) is certainly due to its 1D micropore channel structure based on [Fe(OH)(COO)₂]_n chains while the mesoporous MIL-101(Fe) and PCN-333(Fe) based on the oxo-trimer SBU present a limited water stability. Due to the presence of CO₂ adsorption sites such as Lewis acid Fe³⁺ sites or polar functions (OH and F) and a high pore volume, a few Fe-MOFs such as MIL-100(Fe), MIL-88A(Fe), soc-MOF(Fe), Fe-BTB and Fe-BTC have been considered for CO₂ capture, and some of them have shown attractive CO₂ uptake at

low pressure (>2 mmol g⁻¹ at 1 bar, 298 K).^{14,15,28,29} Recently, an Fe-MOF (Fe₂(μ₃-O)₂(BTB)_{8/3}(DMF)₂(H₂O)₂), whose structure consists of two interpenetrating 3D skeletons, has shown a greater CO₂ uptake than that of several known MOFs with a larger pore volume as a result of its small pore and the presence of multiple CO₂ adsorption sites induced by the framework interpenetration.²³ Another property of MOFs and PCP that was exploited for CO₂ capture is their propensity for structural flexibility. In particular, a few Fe-MOFs or Fe-PCPs can undergo structural changes such as pore opening upon exposure to stimuli such as pressure or temperature.³⁰ In such cases, the CO₂ adsorption capacity of these MOFs such as MIL-53(Fe) can drastically increase at a definite gas pressure.³¹ Moreover, it was demonstrated that the structural flexibility and thus CO₂ adsorption capacity of MIL-53(Fe) could be modulated through the functionalization of the organic linker of the MOF.³² It was shown that the CO₂ adsorption capacity of MIL-53(Fe)-X could be enhanced through the introduction of groups with low polarity (X = Cl, Br, CH₃) that could modulate the μ₂-OH/CO₂ interactions instead of directly interacting with CO₂ molecules.³²

In spite of these interesting results, the number of Fe-MOFs and Fe-PCPs that combine all the properties required for CO₂ separation (high CO₂ adsorption capacity and selectivity; high chemical and thermal stabilities) is still limited. Moreover, many challenges regarding their synthesis remain unaddressed. Numerous Fe-MOFs are often prepared in the presence of toxic organic solvents and reactants and through a solvo/hydrothermal process leading to fine powdered materials made of micron-sized particles.^{14,15} This restricts their applications to a great extent. Therefore, the development of Fe(III)-MOFs using safer synthetic conditions allowing both the control of the crystal size and their large-scale production is still an open challenge for their future practical applications.³³

Herein, we report the synthesis and characterization of a novel PCP based on iron(III) and 1,2,4-benzene tricarboxylate (Fig. 1), named MIL-178(Fe) (MIL stands for Material of Institut Lavoisier), that exhibits a 1D architecture delimiting ultra-micropores ($\phi < 4.5$ Å) decorated with functional groups (-COOH, -OH). The structural behavior of this PCP under CO₂ pressure has been investigated by *in situ* powder X-ray diffraction and molecular modelling, thereby providing a detailed analysis of the preferential arrangement of the confined CO₂ molecules in the material pores and the host/guest interactions. Finally, co-adsorption CO₂/N₂ experiments and grand canonical Monte Carlo simulations were performed in tandem, revealing that this PCP presents an excellent CO₂/N₂ selectivity. Due to its high hydrothermal stability and scalability under room temperature green conditions, this PCP was used as an inorganic filler for the processing of mixed matrix membranes (MMMs). Its combination with the elastomeric block copolymer Pebax®-3533 led to defect-free composite membranes with an enhanced CO₂/N₂ post-combustion separation performance in comparison to the bare polymer. Pebax®-3533 was preferred over the most studied Pebax®-1657 due to the fact that the former is not water/ethanol soluble. Therefore, Pebax®-3533 based membranes are prone to be more stable in the separation of a realistic humid flue gas.³⁴

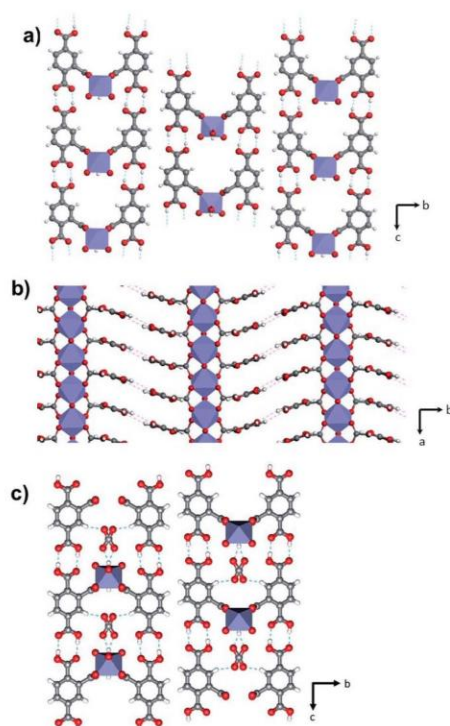


Fig. 1 Crystal structure of (a and b) MIL-178(Fe) along the (a) *a* axis and (b) *c* axis, and (c) CO₂ loaded-MIL-178(Fe) along the *a* axis. Fe octahedra, carbon, oxygen and hydrogen are in purple, gray, red and white respectively. Hydrogen bonds are represented as dotted lines.

Experimental

Chemicals

All chemicals were obtained commercially and used without further purification. The chemicals in this work were anhydrous FeCl₃ (Sigma Aldrich 99%) and 1,2,4-benzene tricarboxylic acid (1,2,4-BTC) (Sigma Aldrich, 95%). Pebax® MH 3533 was generously provided by Arkema, France.

Hydrothermal synthesis of MIL-178(Fe)-hyd. Single crystals of MIL-178(Fe)-hyd were synthesized *via* a hydrothermal route. 1,2,4-BTC (1.15 g, 5.5 mmol) was poured into a 125 mL Teflon-lined steel autoclave with anhydrous FeCl₃ (1.29 g, 8 mmol) and 10 mL of deionized H₂O. The mixture was stirred for 10 min and heated to 200 °C for 72 h under autogenous pressure. The resulting solution was then filtered, and a yellow powder was obtained after extensive washing with water and ethanol to remove the unreacted ligand.

Room temperature synthesis of MIL-178(Fe)-RT. 1,2,4-BTC (1.05 g, 5 mmol) and anhydrous FeCl₃ (0.81 g, 5 mmol) were poured into a 100 mL beaker with 50 mL of deionized H₂O and stirred at room temperature for 5 days. A bright yellow powder

was then recovered by filtration after extensive washings (H₂O & ethanol). For the scale-up synthesis of MIL-178(Fe)-RT, 150 mmol of both FeCl₃ and 1,2,4-BTC and 1.5 L of water were used.

Fabrication of the mixed matrix membrane. The MMMs were prepared following a two-step process. First, 6 wt% Pebax® MH 3533 (of a total weight of 3 g (polymer + solvent)) was dissolved in 1-propanol: 1-butanol (75/25 (v/v)) by stirring under reflux for 1 h. Afterwards, the dissolved polymer was used to cast bare polymeric membranes for comparison. In the case of MMMs, MIL-178(Fe)-RT was dispersed in the dissolved polymer. The required amount of the filler (5–25 wt%), which was calculated against the amount of Pebax® MH 3533 being used, was dispersed in 1.5 mL of 1-propanol/1-butanol (75/25 (v/v)) by repeated sonication and stirring at RT for 1 h. Next, both dispersions were mixed and kept under stirring overnight at RT. In the next step, the solution was poured into a Petri dish. At the end of the process, the membranes were dried for 48 h in a top-drilled box under a solvent-saturated atmosphere under ambient conditions. MMMs are labelled MIL-178(Fe)-Pebax-*X*, where *X* represents the weight fraction of MIL-178(Fe)-RT. MMMs were tested in the CO₂/N₂ separation through both single gas permeability (time lag) experiments and 15/85 CO₂/N₂ mixture measurements. Further details of these experiments are provided in the ESI†

Computational methods. MIL-178(Fe) structure models were optimized at the DFT level with the Quickstep module of the CP2K code using the PBE functional and the triple zeta basis set (TZVP-MOLOPT) for all atoms, except for the Fe centres, where double zeta functions (DZVP-MOLOPT) were employed. Semi-empirical dispersion corrections as implemented in the DFT-D3 method were considered. Force field based grand canonical Monte Carlo (GCMC) simulations were performed at 303 K to assess the single component CO₂ and N₂ and the binary mixture of CO₂/N₂ at 15 : 85 molar compositions in the DFT optimized MIL-178(Fe). The LJ parameters of the MOF atoms were taken from the universal force field (UFF), whereas CO₂ and N₂ molecules were described by the TraPPE potential models. The employed atomic partial charges were derived with the density-derived electrostatic and chemical charges (DDEC) method. Further details of these calculations are provided in the ESI†

Adsorption measurements. Pure CO₂ and N₂ adsorption measurements have been performed at 303 K up to 10 bars by a gravimetric technique using a high-pressure magnetic suspension balance Rubotherm GmbH.^{35,36} CO₂/N₂ co-adsorption measurements were performed on about 10 g of MIL-178(Fe) at 303 K and 1 and 3 bar by using an advanced homemade device that combines a volumetric apparatus and gas chromatography analysis (see the ESI† for more details).

Results and discussion

Synthesis of MIL-178(Fe), and structure resolution by single crystal X-ray diffraction

MIL-178(Fe) microcrystals were first synthesized through a hydrothermal route using the 1,2,4-BTC ligand and FeCl₃ as

an iron precursor. We did not consider Fe powder as a precursor due to its oxidation to Fe^{2+} that may thus lead first to the formation of the two-dimensional iron(II)-1,2,4 BTC phase (MIL-67(Fe)) as previously reported.³⁷ This material (*i.e.*, MIL-178(Fe)-*hyd*) was isolated as a yellow crystalline powder. The SEM images show that MIL-178(Fe) consists of uniform and anisotropic ellipsoidal microcrystals with a length and diameter of about 19 and 3 μm (Fig. 2a). The crystal structure of MIL-178(Fe) was determined by single crystal X-ray diffraction. Due to the small size of the crystals, the X-ray data acquisition was performed at SOLEIL synchrotron by using the PROXIMA 2A beamline equipped with a micro-focused beam. MIL-178(Fe) crystallizes in the orthorhombic space group *Pnma* with unit cell parameters of $a = 6.930(2)$ \AA , $b = 28.420(6)$ \AA and $c = 9.560(2)$ \AA and a unit cell volume of $1882.8(7)$ \AA^3 . The associated chemical formula of MIL-178(Fe) is $\text{Fe}(\text{OH})[\text{C}_9\text{O}_6\text{H}_5]_2(\text{C}_2\text{H}_5\text{OH})_{0.5}$. MIL-178(Fe) is made of 1D infinite chains of corner sharing Fe^{3+} octahedra along the *a*-axis (Fig. 1). According to the IUPAC definitions,³⁸ MIL-178(Fe) can thus be described as a 1D coordination polymer due to the presence of repeating coordination entities in one dimension. Each six-coordinated Fe^{3+} is covalently linked to two oxygen atoms of bridging μ_2 -OH groups and four oxygen atoms of the 1,2,4-BTC linker. The Fe–O distances range between 1.946 and 2.038 \AA . Interestingly, only one carboxylate group from the ligand bridges two Fe^{3+} centers holding the 1D chain together, the two other carboxylates being free –COOH groups. The free –COOH groups from two different ligands face each other and are thus involved in strong hydrogen bonds connecting the 1,2,4-BTC linkers in the *c* direction. Finally, 1,2,4-BTC linkers coordinated to Fe^{3+}

octahedra of different 1D chains also interact through hydrogen bonds in the *b*-direction. Remarkably, this structure possesses very narrow 1D channels following the *a*-axis, *i.e.* along the Fe infinite chains, that are occupied by ethanol molecules (Fig. 1). The dimensions of these channels of 3.5×4.3 \AA (see Fig. S8†) lie in the range of the CO_2 kinetic diameter (3.3 \AA), thereby suggesting that this material is of potential interest for CO_2 capture. Although the structure of MIL-178(Fe) presents free carboxylic acid groups, they are not exposed to the center of pores and may not strongly interact with adsorbed CO_2 molecules. However, the μ_2 -OH groups linked to Fe^{3+} octahedra decorate the internal surface of the channels and are known to be preferential adsorption sites for CO_2 . MIL-178(Fe)-*hyd* was then characterized by ^{57}Fe Mössbauer spectrometry (Fig. S1†). The ^{57}Fe Mössbauer spectra of MIL-178(Fe)-*hyd* at 300 and 77 K display a doublet that consists of two quadrupolar components Γ_1 and Γ_2 with relative amounts of 83 and 17%, respectively, according to the total absorption area. The hyperfine parameters of such components are consistent with high spin Fe^{3+} species in the octahedral environment. The ^{57}Fe Mössbauer spectra at 300 and 77 K obtained after evacuating and heating the MIL-178(Fe)-*hyd* sample at 60 and 100 $^\circ\text{C}$ (Fig. S1†) showed only the single quadrupolar Γ_1 component (see the ESI† for more details) while the spectra of the rehydrated MIL-178(Fe)-*hyd* sample are identical to those of the as-synthesized MIL-178(Fe)-*hyd*. According to these experiments, it can be inferred that both components can be assigned to six-fold coordinated Fe^{3+} centers with an identical first coordination shell (1,2,4-BTC and μ_2 -OH groups) but a different second coordination shell. In contrast to the non-hydrated Fe^{3+} site of the major Γ_1

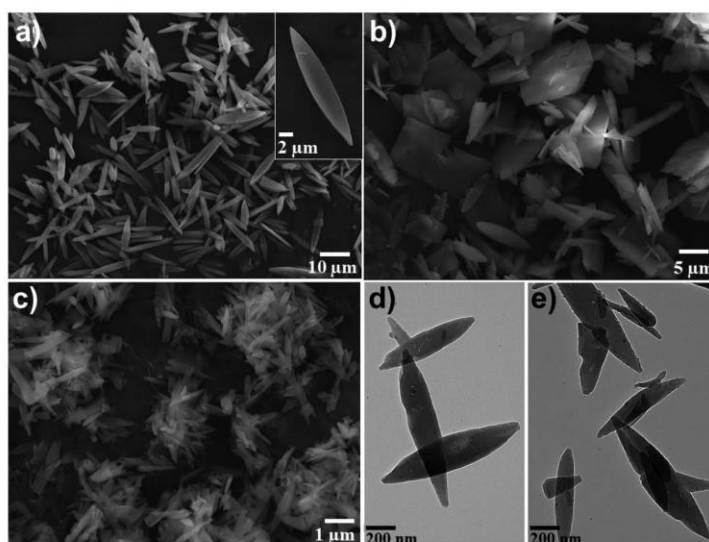


Fig. 2 SEM images of (a) MIL-178(Fe)-*hyd*. The inset shows a higher magnification image of MIL-178(Fe)-*hyd*, (b) MIL-178(Fe)-*re*, and (c) MIL-178(Fe)-*RT*; (d and e) TEM images of MIL-178(Fe)-*RT*.

component, the local environment of the Fe³⁺ site of the minor I_2 component contains water molecules that are located in the pores of this material. Similar results were previously reported for MIL-82(Fe).³⁹ MIL-178(Fe) was also characterized by thermogravimetric analyses (TGA) under O₂ (Fig. S2†). The first weight loss from 25 °C to 200 °C corresponds to the removal of free water and ethanol trapped in the pores. The second weight loss between 200 and 400 °C follows a two step process and corresponds to the degradation of the framework. The residual Fe₂O₃ content obtained at 400 °C (~15 wt%) is consistent with the chemical formula Fe(OH)[C₉O₆H₅]₂(C₂H₅OH)_{0.5}. Temperature-dependent PXRD experiments were performed, thereby confirming that MIL-178(Fe) is stable up to 200 °C (Fig. S3†). Moreover, the absence of any XRD peak shift upon increasing the temperature indicates that the framework of MIL-178(Fe) remains somehow rigid under these conditions. The FT-IR spectrum of MIL-178(Fe) shows the characteristic vibration bands of the coordinating carboxylate functions of 1,2,4-BTC (*i.e.* $\nu_s(\text{C}=\text{O}) = 1400 \text{ cm}^{-1}$ and $\nu_{as}(\text{C}=\text{O}) = 1543 \text{ cm}^{-1}$) and free carboxylate functions at 1703 cm^{-1} (Fig. S4†). Temperature-dependent FT-IR spectra of MIL-178(Fe)-hyd were recorded (Fig. S4†), showing the progressive increase of two vibration bands at 1852 and 1783 cm^{-1} from 125 °C to 225 °C. These two bands at 1852 and 1783 cm^{-1} can be respectively assigned to the asymmetric and symmetric carbonyl groups of the strained anhydride. The concomitant decrease of the vibration band of the free -CO₂H group at 1703 cm^{-1} upon increasing the temperature is in agreement with the condensation of the free carboxylic acid groups into the anhydride. Such a phenomenon was previously reported for other MOFs bearing a pending -CO₂H group grafted in the organic linkers such as UiO-66(Zr)-(CO₂H) and UiO-66(Zr)-(CO₂H)₂.⁴⁰ According to temperature-dependent PXRD experiments, the formation of anhydrides does not provoke any structural phase transition. Finally, the hydrothermal stability of MIL-178(Fe) was assessed by heating the material under reflux in deionized water for 72 h. The PXRD and TGA analyses of the hydrothermally treated MIL-178(Fe) are comparable to that of the initial MIL-178(Fe) (see Fig. S5†). These results show that MIL-178(Fe) presents a high chemical stability under hydrothermal conditions and does not show any significant flexibility upon water adsorption. Such a strong stability (chemical and thermal) was, in our opinion, rather unexpected as 1D coordination polymers are often thermally unstable and/or suffer from structural collapse upon desolvation while 3D chain related compounds such as MIL-53(Fe) exhibit a higher hydrothermal stability.¹² Most likely, the strong hydrogen bonds between the free -COOH groups lead to stabilization of the framework. The excellent stability of MIL-178(Fe) is therefore of utmost importance for the further practical use of this material for post-combustion CO₂/N₂ separation.

Scale up and control over the particle size of MIL-178(Fe)

The synthetic conditions were then transferred to reflux synthesis in water to tune the crystal sizes of MIL-178(Fe) and enable a multigram scale-up of this material. MIL-178(Fe) could

be obtained after heating an aqueous solution of FeCl₃ and 1,2,4-BTC under reflux (~100 °C) for 16 h (see the ESI† for details). The PXRD pattern of this phase (*i.e.*, MIL-178(Fe)-*re*) and TGA analysis are fully consistent with that of MIL-178(Fe)-*hyd* (Fig. 3 and S2†). The SEM images of MIL-178(Fe)-*re* show the presence of particles with a high polydispersity in diameter and shape (Fig. 2b). Ellipsoidal particles with the characteristic shape of MIL-178(Fe)-*hyd* are observed but are much smaller with a maximum length of about 5 μm and a diameter of about 3 μm. In addition, micrometer-sized platelets of about 5 × 5 μm are also obtained. Room temperature synthesis was then further explored to form particles with a lower diameter and a narrow particle size distribution. After stirring at room temperature an aqueous solution of FeCl₃ and 1,2,4-BTC for 5 days, a bright yellow powder (*i.e.* MIL-178(Fe)-*RT*) was obtained with a good yield ($m = 1 \text{ g}$; yield of 81% based on Fe). The PXRD pattern of MIL-178(Fe)-*RT* displays the characteristic Bragg peaks of MIL-178(Fe), but, as expected, are broader in comparison to those of MIL-178(Fe)-*hyd* (Fig. 3). As shown by SEM and TEM, MIL-178(Fe)-*RT* consists of sub-micrometer-sized elongated platelet crystals with a narrow size distribution (Fig. 2c-e). Their mean length, diameter and thickness of about 1 μm, 200 and 20 nm, respectively, are significantly lower than those of MIL-178(Fe) obtained at higher temperatures. Following this synthetic route, MIL-178(Fe)-*RT* could be produced at a large scale (*e.g.*, 30 g in one batch with a yield of 80% based on Fe) by increasing the amount of precursors and the solvent volume by about 30 times.

CO₂/N₂ gas sorption properties of MIL-178(Fe): single-gas adsorption, *in situ* PXRD, CO₂/N₂ coadsorption, and molecular simulations

The adsorption properties of this material were investigated. According to TGA (Fig. S2†), MIL-178(Fe)-*RT* needs to be activated by outgassing the sample to around 383 K in order to remove all the free water or residual ethanol. Single gas adsorption experiments were first performed on MIL-178(Fe)-*RT* samples. According to N₂ sorption at 77 K (Fig. S6†), MIL-178(Fe)-*RT* presents very small N₂ uptake at 77 K, which is consistent with the theoretically calculated small pore volume of $0.18 \text{ cm}^3 \text{ g}^{-1}$ and pore dimensions (<4.5 Å) of the cavities *vs.* the kinetic diameter of N₂ (3.64 Å). This PCP not only exhibits

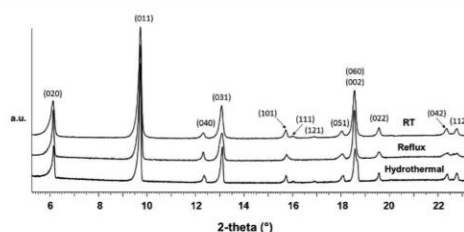


Fig. 3 Powder X-ray diffraction patterns of MIL-178(Fe) synthesized through a hydrothermal process (*i.e.* MIL-178(Fe)-*hyd*), under reflux (*i.e.* MIL-178(Fe)-*re*) or at room temperature (RT) (*i.e.* MIL-178(Fe)-*RT*).

very small pore apertures but also presents a good chemical stability and a framework bearing CO₂ adsorption sites (OH groups). It was thus further envisaged to address the CO₂/N₂ post-combustion separation. Fig. 4 shows the adsorption isotherms of single gas components CO₂ and N₂ obtained at 303 K. Both isotherms are of Type I with a steeper slope at low pressure for CO₂ as compared to N₂. The N₂ amount adsorbed in MIL-178(Fe) is low with a saturation capacity of 0.25 mmol g⁻¹ at 10 bar. For CO₂, the adsorption uptakes are 0.6 mmol g⁻¹ and 1.2 mmol g⁻¹ at 1 bar and 10 bar, respectively. Grand canonical Monte Carlo (GCMC) simulations were further carried out to confirm this experimental trend (see the ESI† for details). As shown in Fig. 4a, the calculated single component CO₂ and N₂ isotherms reproduce well the experimental isotherms at low pressure (<6 bar). The consideration of a fully rigid framework in our GCMC calculations cannot however capture the experimentally observed gradual increment of the uptake amount over a higher pressure range. The GCMC derived snapshots of the spatial arrangements of the adsorbed CO₂ and N₂ molecules at low pressure (Fig. 5a and S10†) show that μ₂-OH groups act as primary adsorption sites for both CO₂ and N₂ molecules. However, the corresponding radial distribution functions (RDFs) reported in Fig. S9† clearly indicate that CO₂ molecules interact much more strongly with the μ₂-OH

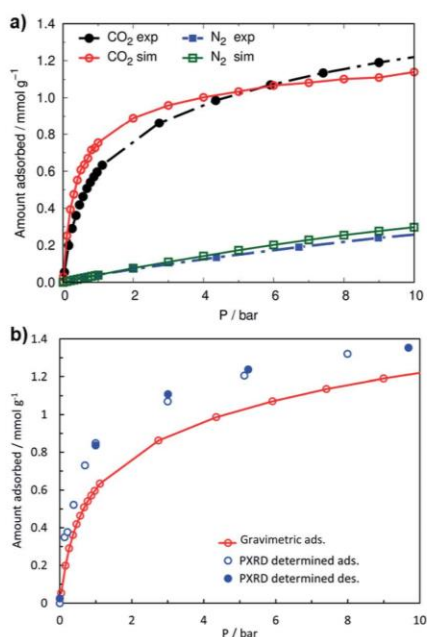


Fig. 4 (a) GCMC calculated and experimental adsorption isotherms for the single components CO₂ and N₂ in MIL-178(Fe)-RT at 303 K. (b) PXRD determined adsorption-desorption CO₂ isotherms of MIL-178(Fe)-RT in comparison to the experimental adsorption CO₂ isotherm.

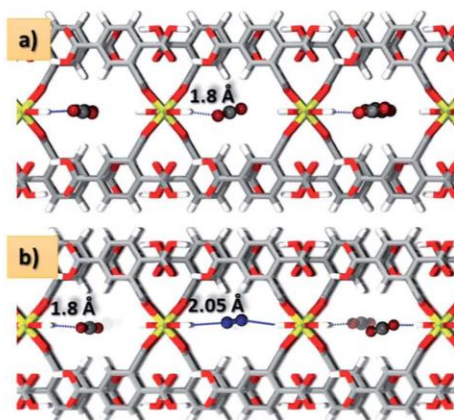


Fig. 5 Microscopic view of the GCMC derived preferential sittings at low pressure for (a) CO₂ molecules as single components and (b) both CO₂ and N₂ molecules in the binary mixture in the 1-D channel of MIL-178(Fe).

groups compared to N₂ molecules as evidenced by a shorter mean O(CO₂)...H(μ₂-OH) distance of 1.8 Å while the N(N₂)...H(μ₂-OH) mean distance is 2.05 Å. This preferential geometry is at the origin of a simulated adsorption enthalpy at low coverage for CO₂ (35 kJ mol⁻¹) much higher than the value obtained for N₂ (20 kJ mol⁻¹), in line with the experimental adsorption isotherm profiles observed at low pressure. Note that such a moderate adsorption enthalpy is prone to induce an easy reversibility of adsorption-desorption cycles. This is highly desirable for the adsorbent regeneration process as a balance between separation performance and energy cost is required in real adsorption processes. *In situ* PXRD experiments were then performed for various CO₂ pressures up to 10 bar in order to shed light on the possible structural changes of MIL-178(Fe) upon CO₂ adsorption. The whole patterns do not exhibit any drastic modification upon increasing the partial pressure of CO₂ with Bragg peaks showing only an intensity change. This indicates that the overall framework of the material is maintained upon loading with CO₂. A model of MIL-178(Fe) with empty pores was therefore created using the Fox simulated annealing software⁴¹ by starting from the structure solved from single crystal X-ray diffraction in which the solvent molecules were removed. CO₂ molecules were added, and their positions were optimized by using the pattern obtained under the highest CO₂ pressure. Once the position of CO₂ and occupancy at this loading were determined, Rietveld refinement was conducted using the Fullprof/Winplotr software (see the ESI† for details).⁴² Sequential Rietveld refinement was then performed at all the experimental CO₂ pressures. On the basis of these *in situ* PXRD data, adsorption/desorption CO₂ isotherms were calculated and compared to the gravimetric sorption data (see Fig. 4b). The good fit at each pressure point suggests that the CO₂ molecules progressively fill the pores without a major change of the host structure or a reorientation of the ligand. Diffraction data

suggest that the saturation with CO₂ is reached slightly above the half-filling of the site, and this CO₂ adsorption capacity is slightly higher than that found by gravimetric adsorption isotherm (see Fig. 4). As shown in Fig. 1c, CO₂ molecules could be located in the structure of MIL-178(Fe). The center of the guest CO₂ molecule is located on the mirror plane but the molecules are orientationally disordered outside the plane of symmetry. The closest contacts of CO₂ molecules with the host framework are defined by hydrogen bonds of the hydroxyl group, O(μ_2 O)-H \cdots O(C), having a H \cdots O distance of about 1.82 Å and an O-H \cdots O angle of 149 degree, which is fully consistent with the GCMC derived preferential sitting reported in Fig. 5.

Since MIL-178(Fe) shows a simulated adsorption enthalpy difference between CO₂ and N₂ of more than 15 kJ mol⁻¹, it is expected to be attractive for the selective adsorption of CO₂ over N₂. GCMC simulations were thus conducted on the binary mixture with a 15/85 CO₂/N₂ molar composition. The relatively high simulated CO₂/N₂ selectivity value \sim 80 at 1 bar (see Fig. S11†) confirms the promise of this material for CO₂ capture. Fig. 5b shows that the preferential adsorption site of CO₂ in MIL-178(Fe) remains the same for the CO₂/N₂ mixture as with the CO₂ single component. This prediction motivated us to perform binary mixture adsorption experiments by considering post-combustion CO₂ capture, *i.e.*, for a gas mixture CO₂/N₂ = 10/90 and 15/85 at 1.0 bar and 3.0 bar, *i.e.*, the typical industrial concentration and pressure conditions for the separation of flue gas emitted from power plants. Such real co-adsorption data were rarely reported in the literature.⁴³ Each mixture point was repeated 3 times giving an average selectivity. A high selectivity value of 116 ± 16 was obtained at 1 bar and 303 K for CO₂/N₂ = 10/90 and increases further to a value of 145 ± 15 upon increasing the CO₂ concentration (CO₂/N₂ = 15/85). This selectivity value is comparable with or greater than that of numerous well-known MOFs with low CO₂ heat of adsorption studied under the same conditions while it remains lower than that of a few MOFs recently reported (see Table S2†). By increasing the pressure to 3 bar, the selectivity values decrease but interestingly remain rather high (*i.e.* $S_{\text{EXP}} = 66 \pm 5$ for CO₂/N₂ = 10/90).

Processing of the mixed matrix membrane (MMM) for CO₂/N₂ separation

Since MIL-178(Fe) particles present a good colloidal stability in 1-propanol and 1-butanol solvents (see Fig. S14†), MMMs were prepared by dispersing MIL-178(Fe)-RT in a solution of Pebax@-3533 in a 1-propanol/1-butanol solvent mixture (see the Experimental part for details). Pebax@-3533 is a poly(amide-6-*b*-tetramethylene oxide) block copolymer composed of 70% of a rubbery poly(tetramethylene oxide) (PTMO) block with high affinity towards CO₂ molecules and 30% of a glassy polyamide (PA) block providing mechanical strength.⁴⁴⁻⁴⁶ This polymer has the advantage to be commercially available and soluble in non toxic alcohol solvents. In the past few years, the series of Pebax polymers was used as a continuous phase in MMMs owing to their promising separation performances resulting from their structural flexibility and solubility-selective gas separation.⁴⁷⁻⁵⁵

Moreover, a few rubbery Pebax-MOF MMMs have shown better MOF-polymer interfacial properties in comparison to numerous MMMs based on rigid glassy polymers.⁴⁷⁻⁵⁵ MIL-178(Fe)-Pebax-*X* MMMs with different MIL-178(Fe) contents (*X* = 5–25 wt%) were fabricated following a two-step protocol (polymer dissolution and filler dispersion followed by casting), as explained in the Experimental section. PXRD patterns of the different MIL-178(Fe)-Pebax-*X* MMMs display the characteristic Bragg peaks of MIL-178(Fe), the intensity of which increases with the amount of MIL-178(Fe) (Fig. 6). This indicates that the crystalline structure of MIL-178(Fe) is preserved upon their association with the polymer. The PXRD pattern of MMMs displays also a broad peak at $2\theta = 20^\circ$ corresponding to the crystalline region of PTMO. The FT-IR spectra of MIL-178(Fe)-Pebax-*X* MMMs (Fig. S15†) present the characteristic vibration bands of both MIL-178(Fe) and Pebax@-3533, in agreement with the incorporation of the PCP in the polymer matrix and with the prevalence of the PCP crystallinity upon the MMM preparation. The morphology of the membranes was investigated by SEM. In contrast to the pure Pebax@-3533 membrane that presents a smooth and homogeneous surface, the surface of MIL-178-Pebax-10 is rougher due to the embedding of well-dispersed MIL-178(Fe) platelets with a random orientation in the polymer matrix as shown in Fig. S16.† However, when the MOF content reached a loading of 15 wt%, the morphology of the MMMs changes drastically. As shown in Fig. 6, the top surface of MIL-178-Pebax-15 is smooth and exhibits a lamellar microstructure. Such layered structuration of the MIL-178-Pebax-15 MMM is also observed in cross-sectional SEM images and is certainly imparted by the stacking of MIL-178(Fe) platelets parallel to the substrate. A similar morphology was observed for the MMM with 25 wt% of MIL-178(Fe)-RT (Fig. S16†). The thickness of the MMMs lies between 40 and 45 μm . The thermal stability of MIL-178(Fe)-Pebax-*X* MMMs was evaluated by TGA in comparison to the pure MIL-178(Fe) and bare polymer (see Fig. S17†). First, negligible weight loss below 250 °C shows the removal of any residual solvent in the MMM. The onset decomposition temperatures of MIL-178(Fe)-Pebax-10 and MIL-178(Fe)-Pebax-15 MMMs are slightly higher than that of pure Pebax@-3533 (\sim 220 °C for the MMM *vs.* 180 °C for neat Pebax@-3533) as a result of the good thermal stability of MIL-178(Fe). In contrast, the thermal stability of MIL-178(Fe)-Pebax-25 is significantly lower than that of MMMs with a lower PCP content and pure polymer. This suggests that the interfacial interactions between the PCP and Pebax@-3533 in MIL-178(Fe)-Pebax-25 are presumably lower than that of MIL-178(Fe)-Pebax-*X* with *X* = 10 and 15. Nevertheless, the overall thermal stability of all MMMs is enough to meet the requirement for CO₂/N₂ separation. The residual amount above 500 °C of the MMMs is consistent with their respective MIL-178(Fe) contents. DSC experiments were performed to evaluate the impact of the MIL-178(Fe) filler on the degree of crystallinity of Pebax@-3533.⁴⁷ More precisely, as the DSC curves are characterized by a single endothermic peak corresponding to the melting of the PTMO phase ($T_m^{\text{PTMO}} \sim 10$ °C), we have quantified the degree of crystallinity of this phase. This was done for each MMM by calculating the ratio between the enthalpy of fusion (ΔH_f) obtained by integration of the peak

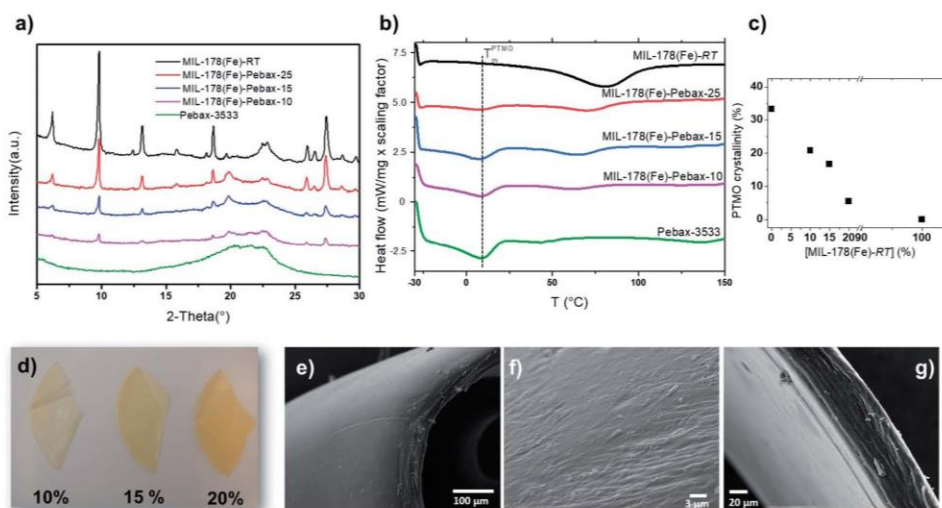


Fig. 6 (a) PXRD of MIL-178(Fe)-Pebax 3533 MMMs in comparison with the pure polymer and MIL-178(Fe)-RT, and (b) DSC curves of neat Pebax@-3533 and typical MIL-178(Fe)-Pebax-*X* MMMs. The curves are shifted vertically for clarity; (c) crystallinity degree of PTMO as a function of the content of MIL-178(Fe)-RT, and (d) photographs of MMMs with different MIL-178(Fe) contents. (e and f) SEM images of the top surface and (g) cross-sectional SEM image of the MIL-178-Pebax-15 MMM.

and the enthalpy of fusion corresponding to a purely crystalline PTMO phase as obtained from the literature ($\Delta H_f^* \approx 200 \text{ J g}^{-1}$)⁵⁶ (see the ESI† for details). The plot of the crystallinity degree as a function of the MIL-178(Fe)-RT concentration shows a continuous decrease from 33% to 5% when the MIL-178(Fe)-RT concentration varies from 0 to 20%. Thus, it appears that MIL-178(Fe)-RT inhibits the crystallization of the PTMO phase which should favor a significant softening of Pebax@-3533 considering that this polymer contains 70% of PTMO. Therefore, the addition of MIL-178(Fe) fillers to Pebax-3533 induces the presence of a larger amount of flexible PTMO chains. This is consistent with the mechanical properties of the membranes that were characterized at large deformation by performing tensile tests until failure. Fig. S19† shows the stress-strain curves for the MIL-178(Fe)-Pebax-*X* MMMs with *X* = 10 and 15 in comparison to the pure Pebax@-3533 matrix. Table S3† provides the values of Young's modulus (*E*), the stress at break (σ_{break}) and elongation at break (e_{break}). Compared to the pure Pebax@-3533 matrix, the mechanical properties of MIL-178(Fe)-Pebax-*X* MMMs are significantly enhanced. These materials are much more extensible, which is consistent with the presence of a larger amount of the rubbery PTMO phase as shown by DSC. Note that the deformability of MIL-178(Fe)-Pebax-15 is slightly lower than that of MIL-178(Fe)-Pebax-10. This can be imparted by the increasing amount of MIL-178(Fe) particles that can act as reinforcing fillers of the polymer as also shown by the higher value of Young's modulus of MIL-178(Fe)-Pebax-15 in comparison to those of the other MMMs. Finally, the long-term chemical stability of the MIL-178(Fe)-Pebax-*X* MMMs with *X* = 10, 15 and 25 was confirmed

by PXRD and FT-IR experiments after ageing the composite membranes, under humid ambient air for about 8 months, with no evidence of structural evolution (see Fig. S20†).

Gas separation measurements were carried out by feeding the post-combustion gaseous mixture of CO₂/N₂ (15/85 cm³(STP) min⁻¹) at an operating pressure of 3 bars to the feed side at 35 °C. A schematic representation of the GC module is given in Fig. S21.† Fig. 7 and Table S4† show the CO₂ permeability and CO₂/N₂ selectivity of MIL-178(Fe)-Pebax-*X* MMMs and pure Pebax@-3533. Remarkably, the addition of MIL-178(Fe) to Pebax@-3533 up to 10 wt% of MIL-178(Fe) led to

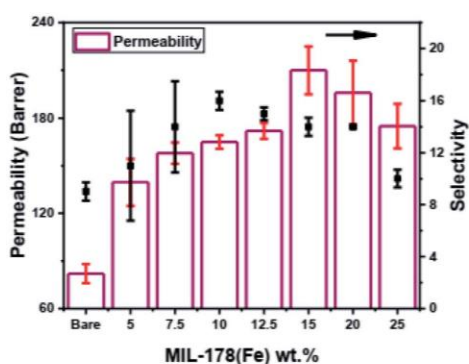


Fig. 7 Permeation analysis of MMMs, and their comparison with the bare polymer membrane.

a significant increase of both the CO₂ permeability and CO₂/N₂ selectivity. The CO₂ permeability of MIL-178(Fe)-Pebax-10 (165 ± 4 Barrer) increased by a factor of 2 compared to that of the pure Pebax®-3533 (83 ± 6 Barrer) while the CO₂/N₂ selectivity of MIL-178(Fe)-Pebax-10 (16.0 ± 0.7) was improved by about 80% in comparison to that of the pure polymer (9.0 ± 0.7). Further increase of MIL-178(Fe) content to 15 wt% led to membranes with the highest CO₂ permeability (210 ± 15 Barrer) at the expense of a slight decrease of the CO₂/N₂ selectivity (14.0 ± 0.7). These results indicate that the inclusion of MIL-178(Fe) fillers in the Pebax-3533 matrix can induce a high increase of both permeability and CO₂/N₂ selectivity values up to about 160% and 80%, respectively, in comparison to the bare membranes. The promising performance of these MMMs can be explained by the high CO₂/N₂ selectivity of the bare MIL-178(Fe) and the good compatibility of the MOF filler with the polymer matrix. Moreover, the ultra-micropores of MIL-178(Fe) are presumably fully accessible to CO₂ molecules since the penetration of polymer chains is not likely to occur in the MOF channels ($\phi < 4.5$ Å). To shed light on the solubility and diffusivity contributions of the gas permeation results, time lag experiments were carried out to obtain CO₂ and N₂ single gas permeabilities, and subsequently CO₂ and N₂ diffusivities and solubilities. It is worth mentioning that CO₂ permeability and CO₂/N₂ selectivity values of the bare membrane and MMM obtained by time lag and mixture separation analyses are in good concordance, as shown in Table S5.† Time lag experiments have demonstrated that the inclusion of the PCP in the polymer increases the CO₂ solubility (Table S5†). CO₂ solubility values are 7.3×10^{-2} and 3.3×10^{-1} (cm³(STP)/(cm³ cmHg)) for the pure polymer membrane and the MIL-178(Fe)-Pebax-10 MMM, respectively. In contrast, the CO₂ diffusivity decreases (and so does the N₂ diffusivity) from the pure polymer to the MIL-178(Fe)-Pebax-10 MMM from 1.3×10^{-7} to 3.8×10^{-8} cm² s⁻¹, in agreement with the narrow microporosity of MIL-178(Fe) and the tortuosity created in the MMM by the addition of the filler particles. Therefore, the enhanced permeability of the MMM in comparison to the pure Pebax®-3533 can be partly explained by the increased content of the more permeable amorphous PTMO (lower crystallinity degree) as was previously reported for a few MOF-Pebax MMMs.⁴⁷

Conclusions

A new water stable 1D microporous coordination polymer, MIL-178(Fe), was discovered, presenting interesting features for CO₂ capture such as hydrothermal and thermal stabilities as well as ultra-micropores decorated with polar OH groups acting as CO₂ adsorption sites. This material was synthesized through an easily-scalable and environmentally friendly protocol with non-toxic reactants, allowing the achievement of the production of a large amount of this material with high yield. Monodisperse MIL-178(Fe) sub-micrometer sized particles were synthesized at room temperature and were used for the preparation of MMMs. The complete characterization of the CO₂/N₂ gas sorption properties of MIL-178(Fe) by combining CO₂/N₂ adsorption/coadsorption experiments, *in situ* CO₂ PXRD and molecular

simulations revealed that MIL-178(Fe) presents a moderate CO₂ adsorption capacity at low pressure but retains a high CO₂/N₂ selectivity in the 1–3 bar pressure range due to the high affinity of CO₂ molecules toward μ_2 -OH groups located on corner-sharing Fe octahedral chains. MMMs based on MIL-178(Fe) and the Pebax®-3533 elastomer with a PCP loading up to 25 wt% were cast, showing significantly enhanced CO₂/N₂ separation performance in comparison to the pure Pebax®-3533. Such results are likely due to the excellent dispersion of MIL-178(Fe) particles in the polymer matrix with the absence of any interfacial microvoid defects, the enhancement of the MMM CO₂ solubility and the lower crystallinity degree of the Pebax matrix in comparison to the pure polymer. Finally, its excellent stability and cheap composition make this PCP interesting for other separation applications as well as sensing or catalysis.⁵⁷

Author contributions

MB performed the synthesis and characterization of MIL-178(Fe) by PXRD, TGA, FT-IR and N₂ sorption under the supervision of CS and NS. MW and GM performed the molecular simulations. HZ characterized MIL-178(Fe)-RT by TEM and the MMMs by PXRD, FT-IR and TGA under the supervision of NS and CS. MRH prepared the MMMs and studied their gas separation properties under the supervision of MM, CT and JC. AS characterized the MMMs by SEM under the supervision of NS. TS, YF and SH performed the CO₂ pressure-dependent PXRD experiments and related data analysis. JM, AT and WS characterized MIL-178(Fe) by single-crystal X-ray diffraction. JM determined its crystalline structure. JMG characterized MIL-178(Fe) by ⁵⁷Fe Mössbauer spectrometry. PN, NH and GDW performed the CO₂ and N₂ single gas and co-adsorption experiments. FC characterized the MMMs by DSC and performed the tensile tests on the MMMs. NS wrote the article with the contribution and help of all authors.

Conflicts of interest

There are no conflicts of interest to declare.

Acknowledgements

We acknowledge the European Community Seventh Framework Program (FP7/2007-2013) for funding the research presented in this article under Grant Agreement No. 608490 (Project M4CO2). The computational work was performed using HPC resources from GENCI-CINES (Grant A0100907613).

Notes and references

- Z. Ji, H. Wang, S. Canossa, S. Wuttke and O. M. Yaghi, *Adv. Funct. Mater.*, 2020, **30**, 2000238.
- S. Krause, N. Hosono and S. Kitagawa, *Angew. Chem., Int. Ed.*, 2020, **59**, 15325–15341.
- D. Zhao, P. K. Thallapally, C. Petit and J. Gascon, *ACS Sustainable Chem. Eng.*, 2019, **7**, 7997–7998.

- 4 J. Li, P. M. Bhatt, J. Li, M. Eddaoudi and Y. Liu, *Adv. Mater.*, 2020, **32**, 2002563.
- 5 P. Kanti Bharadwaj, P. Feng, S. Kaskel and Q. Xu, *Chem.–Asian J.*, 2019, **14**, 3450–3451.
- 6 J. W. M. Osterrieth and D. Fairen-Jimenez, *Biotechnol. J.*, 2021, **16**, 2000005.
- 7 F. Demir Duman and R. S. Forgan, *J. Mater. Chem. B*, 2021, **9**, 3423–3449.
- 8 M. Ding, R. W. Flaig, H.-L. Jiang and O. M. Yaghi, *Chem. Soc. Rev.*, 2019, **48**, 2783–2828.
- 9 Z. Hu, Y. Wang, B. B. Shah and D. Zhao, *Adv. Sustainable Syst.*, 2019, **3**, 1800080.
- 10 R. L. Siegelman, E. J. Kim and J. R. Long, *Nat. Mater.*, 2021, **20**, 1060–1072.
- 11 R. Luo, M. Chen, X. Liu, W. Xu, J. Li, B. Liu and Y. Fang, *J. Mater. Chem. A*, 2020, **8**, 18408–18424.
- 12 J. Duan, W. Jin and S. Kitagawa, *Coord. Chem. Rev.*, 2017, **332**, 48–74.
- 13 H. Assi, G. Mouchaham, N. Steunou, T. Devic and C. Serre, *Chem. Soc. Rev.*, 2017, **46**, 3431–3452.
- 14 Q. Xia, H. Wang, B. Huang, X. Yuan, J. Zhang, J. Zhang, L. Jiang, T. Xiong and G. Zeng, *Small*, 2019, **15**, 1803088.
- 15 S. Zhang, Y. Zhang, F. Baig and T.-F. Liu, *Cryst. Growth Des.*, 2021, **21**, 3100–3122.
- 16 A. Permyakova, S. Wang, E. Courbon, F. Nouar, N. Heymans, P. D'Ans, N. Barrier, P. Billefont, G. De Weireld, N. Steunou, M. Frère and C. Serre, *J. Mater. Chem. A*, 2017, **5**, 12889–12898.
- 17 S. Cui, M. Qin, A. Marandi, V. Steggles, S. Wang, X. Feng, F. Nouar and C. Serre, *Sci. Rep.*, 2018, **8**, 15284.
- 18 S. Patra, S. Sene, C. Mousty, C. Serre, A. Chaussé, L. Legrand and N. Steunou, *ACS Appl. Mater. Interfaces*, 2016, **8**, 20012–20022.
- 19 S. Sene, M. T. Marcos-Almaraz, N. Menguy, J. Scola, J. Volatron, R. Rouland, J.-M. Grenèche, S. Miraux, C. Menet, N. Guillou, F. Gazeau, C. Serre, P. Horcajada and N. Steunou, *Chem*, 2017, **3**, 303–322.
- 20 C. Serre, C. Mellot-Draznieks, S. Surblé, N. Audebrand, Y. Filinchuk and G. Férey, *Science*, 2007, **315**, 1828–1831.
- 21 D. Lenzen, J. G. Eggebrecht, P. G. M. Mileo, D. Fröhlich, S. Henninger, C. Atzori, F. Bonino, A. Lieb, G. Maurin and N. Stock, *Chem. Commun.*, 2020, **56**, 9628–9631.
- 22 M. Pang, A. J. Cairns, Y. Liu, Y. Belmabkhout, H. Chun Zeng and M. Eddaoudi, *J. Am. Chem. Soc.*, 2013, **135**, 10234–10237.
- 23 S. B. Choi, M. J. Seo, M. Cho, Y. Kim, M. K. Jin, D.-Y. Jung, J.-S. Choi, W.-S. Ahn, J. L. C. Rowsell and J. Kim, *Cryst. Growth Des.*, 2007, **7**, 2290–2293.
- 24 D. Feng, Z.-Y. Gu, Y.-P. Chen, J. Park, Z. Wei, Y. Sun, M. Bosch, S. Yuan and H.-C. Zhou, *J. Am. Chem. Soc.*, 2014, **136**, 17714–17717.
- 25 D. Feng, W.-C. Chung, Z. Wei, Z.-Y. Gu, H.-L. Jiang, Y.-P. Chen, D. J. Darensbourg and H.-C. Zhou, *J. Am. Chem. Soc.*, 2013, **135**, 17105–17110.
- 26 K. Wang, D. Feng, T.-F. Liu, J. Su, S. Yuan, Y.-P. Chen, M. Bosch, X. Zou and H.-C. Zhou, *J. Am. Chem. Soc.*, 2014, **136**, 13983–13986.
- 27 F. Steinke, A. Javed, S. Wöhlbrandt, M. Tiemann and N. Stock, *Dalton Trans.*, 2021, **50**, 13572–13579.
- 28 S. Wongsakulphasatch, W. Kiatkittipong, J. Saupsor, J. Chaiwisesphol, P. Piroonlerkgul, V. Parasuk and S. Assabumrungrat, *Greenhouse Gases: Sci. Technol.*, 2017, **7**, 383–394.
- 29 E. Soubeyrand-Lenoir, C. Vagner, J. W. Yoon, P. Bazin, F. Ragon, Y. K. Hwang, C. Serre, J.-S. Chang and P. L. Llewellyn, *J. Am. Chem. Soc.*, 2012, **134**, 10174–10181.
- 30 J.-J. Zheng, S. Kusaka, R. Matsuda, S. Kitagawa and S. Sakaki, *J. Am. Chem. Soc.*, 2018, **140**, 13958–13969.
- 31 F. Nouar, T. Devic, H. Chevreau, N. Guillou, E. Gibson, G. Clet, M. Daturi, A. Vimont, J. M. Grenèche, M. I. Breeze, R. I. Walton, P. L. Llewellyn and C. Serre, *Chem. Commun.*, 2012, **48**, 10237–10239.
- 32 T. Devic, F. Salles, S. Bourrelly, B. Moulin, G. Maurin, P. Horcajada, C. Serre, A. Vimont, J.-C. Lavalley, H. Leclerc, G. Clet, M. Daturi, P. L. Llewellyn, Y. Filinchuk and G. Férey, *J. Mater. Chem.*, 2012, **22**, 10266.
- 33 S. Wang and C. Serre, *ACS Sustainable Chem. Eng.*, 2019, **7**(4), 11911–11927.
- 34 A. S. Embaye, L. Martínez-Izquierdo, M. Malankowska, C. Télec and J. Coronas, *Energy Fuels*, 2021, **35**, 17085–17102.
- 35 G. De Weireld, M. Frère and R. Jadot, *Meas. Sci. Technol.*, 1999, **10**, 117.
- 36 N. Heymans, S. Vaesen and G. De Weireld, *Microporous Mesoporous Mater.*, 2012, **154**, 93–99.
- 37 M. Riou-Cavellec, C. Lesaint, M. Noguès, J.-M. Grenèche and G. Férey, *Inorg. Chem.*, 2003, **42**, 5669–5674.
- 38 S. R. Batten, N. R. Champness, X.-M. Chen, J. Garcia-Martinez, S. Kitagawa, L. Öhrström, M. O'Keefe, M. Paik Suh and J. Reedijk, *Pure Appl. Chem.*, 2013, **85**, 1715–1724.
- 39 M. Sanselme, J. M. Grenèche, M. Riou-Cavellec and G. Férey, *Solid State Sci.*, 2004, **6**, 853–858.
- 40 F. Ragon, B. Campo, Q. Yang, C. Martineau, A. D. Wiersum, A. Lago, V. Guillermin, C. Hemsley, J. F. Eubank, M. Vishnuvarthan, F. Taulelle, P. Horcajada, A. Vimont, P. L. Llewellyn, M. Daturi, S. Devautour-Vinot, G. Maurin, C. Serre, T. Devic and G. Clet, *J. Mater. Chem. A*, 2015, **3**, 3294–3309.
- 41 V. Favre-Nicolin and R. Cerny, *J. Appl. Crystallogr.*, 2002, **35**, 734–743.
- 42 J. Rodriguez-Carvajal, *Phys. B*, 1993, **192**, 55–69.
- 43 M. Benzaqui, R. S. Pillai, A. Sabetghadam, V. Benoit, P. Normand, J. Marrot, N. Menguy, D. Montero, W. Shepard, A. Tissot, C. Martineau-Corcoc, C. Sicard, M. Mihaylov, F. Carn, I. Beurroies, P. L. Llewellyn, G. De Weireld, K. Hadjiivanov, J. Gascon, F. Kapteijn, G. Maurin, N. Steunou and C. Serre, *Chem. Mater.*, 2017, **29**, 10326–10338.
- 44 L. Martínez-Izquierdo, M. Malankowska, J. Sánchez-Lainez, C. Télec and J. Coronas, *R. Soc. Open Sci.*, 2019, **6**, 190866.
- 45 L. Wang, Y. Li, S. Li, P. Ji and C. Jiang, *J. Energy Chem.*, 2014, **23**, 717–725.
- 46 J. H. Kim, S. Y. Ha and Y. M. Lee, *J. Membr. Sci.*, 2001, **190**, 179–193.

- 47 S. Meshkat, S. Kaliaguine and D. Rodrigue, *Sep. Purif. Technol.*, 2018, **200**, 177–190.
- 48 A. Sabetghadam, X. Liu, M. Benzaqui, E. Gkaniatsou, A. Orsi, M. M. Lozinska, C. Sicard, T. Johnson, N. Steunou, P. A. Wright, C. Serre, J. Gascon and F. Kapteijn, *Chem.–Eur. J.*, 2018, **24**, 7949–7956.
- 49 M. Mozafari, R. Abedini and A. Rahimpour, *J. Mater. Chem. A*, 2018, **6**, 12380–12392.
- 50 S. Meshkat, S. Kaliaguine and D. Rodrigue, *Sep. Purif. Technol.*, 2020, **235**, 116150.
- 51 N. Liu, J. Cheng, W. Hou, X. Yang and J. Zhou, *J. Appl. Polym. Sci.*, 2021, **138**, e50553.
- 52 J. Shen, G. Liu, K. Huang, Q. Li, K. Guan, Y. Li and W. Jin, *J. Membr. Sci.*, 2016, **513**, 155–165.
- 53 J. Deng, Z. Dai, J. Hou and L. Deng, *Chem. Mater.*, 2020, **32**, 4174–4184.
- 54 N. Habib, Z. Shamair, N. Tara, A.-S. Nizami, F. Hassan Akhtar, N. M. Ahmad, N. Amjad Gilani, M. Roil Bilad and A. Laeeq Khan, *Sep. Purif. Technol.*, 2020, **234**, 116101.
- 55 C. Song, R. Li, Z. Fan, Q. Liu, B. Zhang and Y. Kitamura, *Sep. Purif. Technol.*, 2020, **238**, 116500.
- 56 I. J. W. Bowman, D. S. Brown and R. E. Wetton, *Polymer*, 1969, **10**, 715–718.
- 57 M. Benzaqui, R. Semino, F. Carn, S. Rodrigues Tavares, N. Menguy, M. Giménez-Marqués, E. Bellido, P. Horcajada, T. Berthelot, A. I. Kuzminova, M. E. Dmitrenko, A. V. Penkova, D. Roizard, C. Serre, G. Maurin and N. Steunou, *ACS Sustainable Chem. Eng.*, 2019, **7**, 6629–6639.



ANNEX 3

Engineering of Metal–Organic Frameworks/Gelatin Hydrogel Composites Mediated by the Coacervation Process for the Capture of Acetic Acid

Subharanjan Biswas, Mohamed Haouas, Cátia Freitas, Carla Vieira Soares, Abeer Al Mohtar, Ali Saad, Heng Zhao, Georges Mouchaham, Carine Livage, Florent Carn, Nicolas Menguy, Guillaume Maurin, Moises L. Pinto, and Nathalie Steunou*

Cite This: <https://doi.org/10.1021/acs.chemmater.2c02704>

Read Online

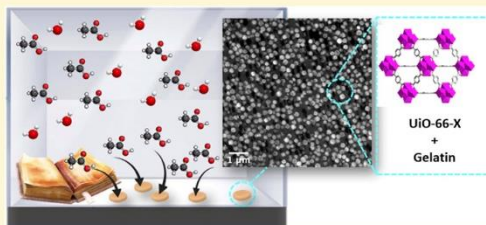
ACCESS |

Metrics & More

Article Recommendations

Supporting Information

ABSTRACT: A novel strategy is proposed to synthesize metal–organic framework (MOF)–gelatin bionanocomposites by taking profit of the thermo-reversible character of gelatin and the liquid–liquid phase separation process, that is, coacervation. This enables the formation of bionanocomposites based on a series of chemically stable Zr^{4+} dicarboxylate MOFs (UiO-66 and MOF-801) differing by their hydrophilic–hydrophobic balance and their chemical functionality. Bionanocomposites with homogeneous and uniform distribution of MOF particles in the gelatin matrix as well as a high MOF loading (up to 90%) without compromising their porosity were prepared as a result of an excellent physico-chemical matching between MOFs and gelatin. Finally, this series of bionanocomposites were shaped into films or monoliths, and they have shown high performance for the selective adsorption of acetic acid in the presence of humidity. These composites can be regarded as highly efficient adsorbents for cultural heritage preservation.



INTRODUCTION

Metal–organic frameworks (MOFs), a class of porous and crystalline hybrid materials, composed of metal ions and organic polydentate ligands have sparked tremendous research interest owing to their highly ordered pore structure, high internal surface areas, and chemical functionality.^{1,2} These unique properties make this class of materials very promising for a wide range of applications including gas storage and separation, sensing, catalysis, biomedicine, and energy storage, among others.^{3–6} However, MOFs still present some shortcomings that still limit their transfer and implementation in real industrial applications to a great extent. First, numerous MOFs have shown a limited chemical and thermal stability, although several efficient strategies have been reported to solve this issue and to construct chemically stable MOFs.⁷ Moreover, typical MOF syntheses generally produce brittle and powdered samples. The intrinsic fragility of MOF powders and their known poor processability and handling as well as low mass/heat transfer rate along with high pressure drop when being piled strongly hampers the potential of developing applications by using MOFs.⁸ To date, MOFs have been mainly processed in the forms of pellets, granules, beads, fibers, and membranes, but in many cases, the accessibility to the MOF porosity is lost after shaping.⁸ This issue was mainly addressed through the integration of MOFs with diverse

supporting materials such as carbon-based materials (polymers, carbon nanotubes, graphene, graphene oxide, textile fibers),^{9–15} thereby leading to multifunctional composites with a synergistic combination of the properties of MOFs (porosity, crystallinity) and the supporting matrix (mechanical stability, processability, etc.). Moreover, this strategy can also be efficient to impart novel functionalities such as enhanced stability and electron conductivity or extend their porosity in the meso- or macropore regime.^{9–14} This hybridization of MOFs with carbon-based materials led to a wide diversity of composites used in many applications, including gas adsorption and separation, sensing, water purification, catalysis, and biotechnology.^{9–16} However, these composites suffer frequently from a strong aggregation of MOF particles as a result of a poor interfacial compatibility between the MOF and the host matrix.^{9,10} In particular, this MOF particle agglomeration is a recurrent phenomenon reported for composites prepared by blending polymer or graphene oxide

Received: September 5, 2022

Revised: October 13, 2022

host matrices with preformed MOF particles.¹⁰ This issue becomes even more critical at higher MOF loadings that are usually required to optimize the performance of composites. Therefore, various alternative strategies have been explored to enhance the physico-chemical matching between MOF and carbon-based materials and thus to prepare homogeneous shaped composites without losing the porosity of MOFs. These approaches include the surface modification of MOFs,¹⁷ the covalent grafting of polymers onto the outer surface of MOF particles,^{10,18,19} the in situ formation of MOF within the polymer matrix,²⁰ the in situ polymerization of polymers on the surface of MOF particles,²¹ the polymers templating MOF growth,^{10,22} or MOF synthesis using polymer ligands (polyMOF).²³ However, numerous MOF–polymer composites still present significant shortcomings such as a low surface area as a result of the MOF pore clogging by polymer chains and/or a poor distribution of MOF particles in the polymer matrix. In addition, the preparation of these composite implies time-consuming multi-step synthetic procedures, and the use of synthetic polymers derived from petrochemical products can lead to serious toxicity and environmental and health concerns.

This work reports a novel and easy-handle strategy for the synthesis of hydrogel composites combining gelatin and a series of Zr⁴⁺-dicarboxylate MOFs with the UiO-66 (UiO = University of Oslo) type structure bearing different functional organic linkers and the Zr⁴⁺-fumarate MOF-801.²⁴ Gelatin is one of the most commonly used protein biopolymers in industry for drugs and cosmetics microencapsulation because of its low cost, biodegradability, nontoxicity, and renewability.²⁵ Its combination with a wide range of inorganic materials including (hydr)oxides, hydroxyapatite, clays, zeolites, and metals was mainly explored for regenerative medicine, drug vectorization, or biosensing.^{26,27} Gelatin was also shown to exert a remarkable control over the nucleation and growth of biogenic inorganic materials such as fluoroapatite mesocrystals.²⁸ Such ability of gelatin for morphogenesis in soft conditions was mainly ascribed to its self-organization properties into triple helices and the existence of attractive interactions at the fluoroapatite/gelatin interface. Recently, the synthesis of MOF–gelatin hydrogels was mainly reported for bioapplications related to tissue engineering, wound healing, drug delivery, or bioimaging.^{29–36} These composites were mainly prepared through the impregnation of preformed MOF particles into functionalized gelatin-based scaffolds or hybrid hydrogels or the physical gelation of gelatin in the presence of MOF particles eventually associated to electrospinning.^{29–36} Although these hydrogels present interesting performance, the large majority of these composites suffers from a low porosity as a result of the very low amount of MOF (<10 wt %) and this strongly limits the exploitation of their physico-chemical properties and drug delivery properties.^{29–36} A MOF–gelatin composite was also used for water purification with however a low MOF content and/or a low porosity.³⁷ It should be noted that MOFs based on divalent cations (ZIF-8, ZIF-67, and HKUST) were mainly used for the processing of gelatin-based hydrogels while interfacing gelatin with MOFs of higher chemical stability such as the series of UiO-66(Zr) was only rarely described.³³ Therefore, the processing of MOF/gelatin hydrogel with a high porosity, high chemical stability, and high MOF content would be most desirable to further optimize their performance. Herein, the thermo-reversible character of gelatin associated to a liquid–liquid phase separation process, that is, coacervation,^{38,39} was

exploited to prepare a series of gelatin/UiO-66-X (X = H, CF₃, and NH₂) and gelatin/MOF-801 composites that combine attractive features such as high MOF loading (>80 wt %), large porosity, homogeneous MOF distribution in the host matrix, and a tunable hydrophobic–hydrophilic balance. It should be noted that the main advantage of using biomacromolecules such as gelatin is related to its chemical complexity, multifunctionality, and polyelectrolyte nature to which no synthetic equivalent is available. This enables the integration of hydrophilic as well as hydrophobic MOFs into the water-soluble gelatin.

Finally, these MOF–gelatin composites were shaped in different forms (films or monoliths) on a large scale, and remarkably, they showed high performance for the selective capture of acetic acid (AA) under humid ambient conditions. The emission of AA is a major concern in cultural heritage (CH) for the preservation of cellulose-based artifacts such as papers, books, photographic films, and so forth.⁴⁰ More than 75 years of visual and audio memories are actually in serious danger because of the hydrolysis and oxidation of cellulose acetate into AA.^{41,42} A viable solution to protect CH artifacts consists of using adsorbents such as activated carbons, zeolites, silica, and pillared clays to efficiently capture AA.^{43,44} However, AA raises additional challenges compared to other less-hydrophilic molecules because of its potential competitive adsorption with water under relative humidity (RH) above 30%. Zeolites, such as NaY or NaX, are strongly hydrophilic, which makes them readily saturated by water even at very low RH,⁴⁴ thus considerably reducing their AA adsorption efficiency. On the contrary, activated carbons, usually more hydrophobic, generally suffer from a low AA uptake capacity owing to their relatively poor affinity to AA. Therefore, the search of alternative and more efficient adsorbents that combine large AA adsorption capacity and high AA/water selectivity is still a great challenge for the CH conservation. Recently, some of us considered for the first time MOFs for this application and demonstrated that Zr⁴⁺ polycarboxylate MOFs present good performance for the selective capture of AA in the presence of water.⁴⁵ However, as other pure MOFs, these materials are obtained as powdered samples and cannot be used at the vicinity of CH artifacts in museums or storerooms. It is thus of primary importance to shape MOFs without losing their porosity and their AA uptake capacity. In the present article, we reveal that UiO-66-X/gelatin composites can be considered as a novel type of highly efficient adsorbents in CH preservation.

■ EXPERIMENTAL SECTION

Chemicals. All chemicals were commercially available and used without further purification. Commercial gelatin extracted from porcine skin (type A with a bloom of 175 g) corresponding to an average molecular weight of 40,000 g mol⁻¹ and an isoelectric point (I.E.P) of about 8 (according to the supplier) was purchased from Sigma-Aldrich. Other chemicals were purchased from Sigma-Aldrich or Merck.

Preparation of Gelatin Solutions. Gelatin solutions (1–10 wt %, in aqueous solution) were prepared by swelling the gelatin granules in an aqueous solution for a minimum period of 3 h at a temperature of 5 °C. Gelatin was then dissolved at a temperature of 50 °C using a magnetic stirrer for 30 min at 300 rpm.

Synthesis of MOF–Gelatin Hydrogel Composites by Coacervation. The MOFs were formed in situ in the presence of a gelatin coacervate.

B

<https://doi.org/10.1021/acs.chemmater.2c02704>
Chem. Mater. XXXX, XXX, XXX–XXX



Figure 1. Schematic drawing of (A) room-temperature synthesis of UiO-66-X ($X = \text{H}, \text{NH}_2, (\text{CF}_3)_2$) and MOF-801, (B) synthesis approach of the UiO-66-X ($X = \text{H}, \text{NH}_2, (\text{CF}_3)_2$)/gelatin and MOF-801/gelatin composites. (C,D) Photographs of UiO-66/gelatin hydrogels obtained just after the addition of ethanol (C) and after aging at RT for 24 h (D). Zr polyhedral, carbon, oxygen, nitrogen, fluoride, and hydrogen are in pink, gray, red, blue, green, and white, respectively.

- Step 1. To a 20 mL scintillation vial were added 71 μL of a 70% zirconium propoxide $[\text{Zr}(\text{OPr})_4]$ solution in 1-propanol (0.0519 g, 0.158 mmol), 7 mL of DMF, and 4 mL of acetic acid (4.196 g, 70 mmol). The solution was heated in an aluminum block on a hot plate at 130 $^\circ\text{C}$ for 2 h, during which a noticeable change in solution color from colorless to yellow was observed. Then, the solution was cooled at RT.
- Step 2. To 11 mL of the $\{\text{Zr}_6\}$ oxo-cluster solution (0.158 mmol) obtained from step 1, 0.5 mmol of any one of the ligands (84 mg of 1,4 benzene dicarboxylic acid (bdc), 151 mg of bdc- $(\text{CF}_3)_2$, 90.5 mg of bdc- NH_2 , and 58 mg of fumaric acid (FA) was added. The mixture was stirred for 15 min until a homogeneous dispersion was obtained. Then, 2 mL of 10 wt % gelatin was added to this solution and stirred for 10 min followed by the addition of 2 mL of ethanol. Finally, the mixture was stirred at room temperature (RT) (25 $^\circ\text{C}$) for 24 h to obtain the hydrogel composites.

Processing of the MOF–Gelatin Composite Films and Tablets. After macroscopic phase separation, the composite hydrogels were heated with their supernatant solution at 70 $^\circ\text{C}$ for 15 min and then 90 $^\circ\text{C}$ for 5 min before being poured without their supernatant solution into molds thermalized at 70 $^\circ\text{C}$. Then, the molds are immediately capped in an almost hermetic manner. Using different molds, coatings and tablets were finally formed by cooling at RT for 15 min and then kept at 2 $^\circ\text{C}$ for 1 day. Prior to the adsorption experiments, all materials were activated in high vacuum (10^{-6} mbar; HiCube 80, Pfeiffer Vacuum) for 4 h at 150 $^\circ\text{C}$.

RESULTS AND DISCUSSION

Synthesis of UiO-66-X ($X = \text{H}, \text{NH}_2, (\text{CF}_3)_2$) and MOF-801 Nanoparticles. For the design of MOF/gelatin composites, we first considered a series of microporous MOFs with the UiO-66 type framework. The idealized structure of UiO-66 can be described by the assembly of the $\{\text{Zr}_6\text{O}_4(\text{OH})_4\}$ secondary building unit (SBU) with 12 ditopic 1,4 benzene dicarboxylate (1,4-bdc) linkers, resulting in a crystalline structure with face-centered cubic (fcc) topology

(Figure 1).²⁴ We have selected a series of isostructural UiO-66-X functionalized derivatives ($X = \text{NH}_2, (\text{CF}_3)_2$) that can be obtained by using bdc linker grafted with either $-\text{NH}_2$ or $-\text{CF}_3$ groups,^{45–47} as well as the FA analogue MOF-801.^{48–50} This whole series of MOFs was synthesized following a two-step RT protocol previously reported by Farha et al.⁵¹ (see the Supporting Information (SI) for details.). First, it implies the synthesis of the $[\text{Zr}_6\text{O}_4(\text{OH})_4(\text{OAc})_{12}]$ (OAc = acetate) oxo clusters, which react in a second step with the organic linker (bdc-X ($X = \text{H}, \text{NH}_2, (\text{CF}_3)_2$), or FA). These materials were characterized by combining powder X-ray diffraction (PXRD), thermogravimetric analysis (TGA), Fourier transform-infrared (FT-IR) spectroscopy, N_2 porosimetry, scanning and transmission electron microscopy (SEM, TEM, HAADF-STEM, and STEM-XEDS) (see the SI for details). The PXRD pattern of these MOFs display the characteristic Bragg peaks of the UiO-66 type structure (Figure S3). UiO-66 consists of spherical nanocrystals with an average particle diameter of 70 nm and a quite large distribution in diameter between 40 and 200 nm (Figures S7, S8). In contrast, UiO-66-X ($X = \text{NH}_2, (\text{CF}_3)_2$) and MOF-801 samples are made of nanocrystals whose diameters (~ 30 nm for UiO-66- NH_2 and MOF-801, ~ 15 nm for UiO-66- $(\text{CF}_3)_2$) are significantly lower than that of UiO-66 (Figures S10, S11, S13, and S14), in agreement with the presence of broad Bragg peaks on their PXRD patterns. This series of MOFs was synthesized by using a high concentration of modulator (i.e., acetic acid, AA, 443 eq) that not only affords control over the crystal size but also the density of defects.^{52–54} Moreover, this addition of a modulator can strongly affect the porosity, the hydrophilic–hydrophobic balance of the MOFs, and their adsorption or catalytic properties, as previously reported.^{55–60} Defects arise when an organic linker (linker defects) or an entire zirconium cluster and its 12 associated linkers (cluster defects) are missing

C

<https://doi.org/10.1021/acs.chemmater.2c02704>
Chem. Mater. XXXX, XXX, XXX–XXX

resulting in the creation of open coordination sites on SBUs. As previously reported, charge-compensation of these sites is mainly achieved through the capping of these uncoordinated Zr sites with either OH/H₂O or the modulator (here, acetate).^{51–57} The composition and amount of structural defects of this series of MOF was determined by combining TGA, ¹H and ¹³C MAS NMR spectroscopy (see the SI for details), as previously reported for defective UiO-66.^{55–57} Table 1 indicates the chemical composition of the MOFs as well as their defect level which can be defined as the average number of missing linkers per Zr₆ node. These MOF shows a quite large amount of defects because the connectivity of the {Zr₆} clusters ranges between 10 (UiO-66 and UiO-66-NH₂), 9 (MOF-801), and 8 (UiO-66-(CF₃)₂) while this connectivity is 12 for an ideal defect-free UiO-66. UiO-66 and UiO-66-NH₂ present an amount of defects which is comparable to that previously reported for these MOFs prepared with a similar amount of modulator.^{51,58,61} Neither TGA nor ¹H and ¹³C MAS NMR are able to differentiate between missing-linker and missing-cluster defects. However, correlated missing-cluster defects can result in a defected reo phase that exhibits one broad peak at a low angle, typically 3–8° 2θ range.⁵⁶ Such a broad peak was not observed in the PXRD pattern of these MOFs. Therefore, if these MOFs contain missing clusters defects, their density is presumably quite low and/or they are randomly distributed in the MOFs. These MOFs were also characterized by N₂ adsorption/desorption isotherms (see Figure 2) at 77 K. UiO-66 presents a type-I isotherm which is consistent with the microporous structure of this MOF (cages of 8 and 11 Å in diameter). In contrast, the isotherms of the other MOFs are combinations of type I and type IV isotherms, indicating that these MOFs contain both micropores and mesopores. As indicated by the pore size distribution (PSD) derived from the Barrett–Joyner–Halenda (BJH) pore-size model (see Figure S6), UiO-66-(CF₃)₂ exhibits a distribution of mesopores of approximately 3.5–12 nm in diameter that correspond presumably to interparticle voids as a result of strong aggregation of the MOF nanoparticles (NPs) while we cannot distinguish any contribution in the 2–3 nm range likely excluding the presence of mesopores created by missing cluster defects.⁶²

Similarly, UiO-66-NH₂ and MOF-801 contain not only intercrystallite mesopores of about 20 nm in diameter but also small mesopores of about 2 nm, most probably associated with the presence of missing cluster defects.^{61,63}

Synthesis of MOFs/Gelatin Hydrogel Composites through Coacervation. Gelatin/MOF composites were prepared through the blending of these preformed MOF particles into physical gel of gelatins. Indeed, gelatin is soluble in water above the temperature of gelification (close to 27 °C for a mammalian gelatin) but forms reversible physical gels below this temperature.⁶⁴ The UiO-66-gelatin hydrogels were prepared by mixing UiO-66 NPs and gelatin aqueous solutions at 40 °C (see the SI for details) and pH 3, followed by cooling to 4 °C to induce the physical gelation of gelatin. Unfortunately, these hydrogels present a very low amount of UiO-66 whatever the initial amount of gelatin and MOF, as revealed by the very low intensity of the characteristic PXRD Bragg peaks and FT-IR vibrations of UiO-66 (Figure S2). Moreover, the UiO-66 content of hybrid hydrogels remains low, even though MOF and gelatin were mixed in pH conditions (pH 7) for which they exhibit opposite electrostatic charge (the point of zero charge of UiO-66 NPs is close to 6

Table 1. Structural Properties and Chemical Composition of MOFs and MOF/Gelatin Composites

hybrid material	AcO/L ^a	molecular formula of MOF ^b	defect level (%) ^c	MOF content (wt %) ^d	connectivity of {Zr ₆ } oxo cluster	S _{BET} (m ² g ⁻¹)	total pore volume (cm ³ g ⁻¹)
UiO-66(Zr)	0.20	Zr ₆ O _{5.2} (OH) _{2.8} (bdc) _{4.9} (AcO) _{1.0}	18.3	88	10	1560	0.60
UiO-66(Zr)/G	0.20	Zr ₆ O _{5.2} (OH) _{2.8} (bdc) _{4.9} (AcO) _{1.0}	18.3	88	10	1083	0.49
UiO-66(Zr)-NH ₂	0.45	Zr ₆ O ₄ (OH) ₄ (bdc-NH ₂) _{3.5} (AcO) _{2.5}	16.6	70	10	1243	0.51
UiO-66(Zr)-NH ₂ /G	0.30	Zr ₆ O ₄ (OH) ₄ (bdc-NH ₂) _{3.5} (AcO) _{2.5}	16.6	70	10	790	0.42
UiO-66(Zr)/(CF ₃) ₂	0.70	Zr ₆ O _{4.65} (OH) _{3.4} (bdc-(CF ₃) ₂) _{4.2} (AcO) _{1.8}	30	91	8.4	649	0.27
UiO-66(Zr)/(CF ₃) ₂ /G	0.43	Zr ₆ O _{4.65} (OH) _{3.4} (bdc-(CF ₃) ₂) _{4.2} (AcO) _{1.8}	30	91	8.4	397	0.16
MOF-801(Zr)	0.62	Zr ₆ O _{4.3} (OH) _{3.7} (FA) _{4.5} (AcO) _{2.7}	25	51	9	1020	0.43
MOF-801(Zr)/G	0.62	Zr ₆ O _{4.3} (OH) _{3.7} (FA) _{4.5} (AcO) _{2.7}	25	51	9	572	0.23

^adetermined by ¹H and ¹³C MAS NMR, L = organic linker (bdc, bdc-NH₂, bdc-(CF₃)₂, FA), AcO = acetate. ^bDetermined by combining TGA and ¹H and ¹³C MAS NMR. ^cThe defect level is the average number of missing linkers per Zr₆ node and thus the average number of defects divided by the ideal number of linkers per formula unit (6 for UiO-66). ^dDetermined by combining TGA and ICP-AES.

D

<https://doi.org/10.1021/acs.chemmater.2c02704>
Chem. Mater. XXXX, XXX, XXX–XXX

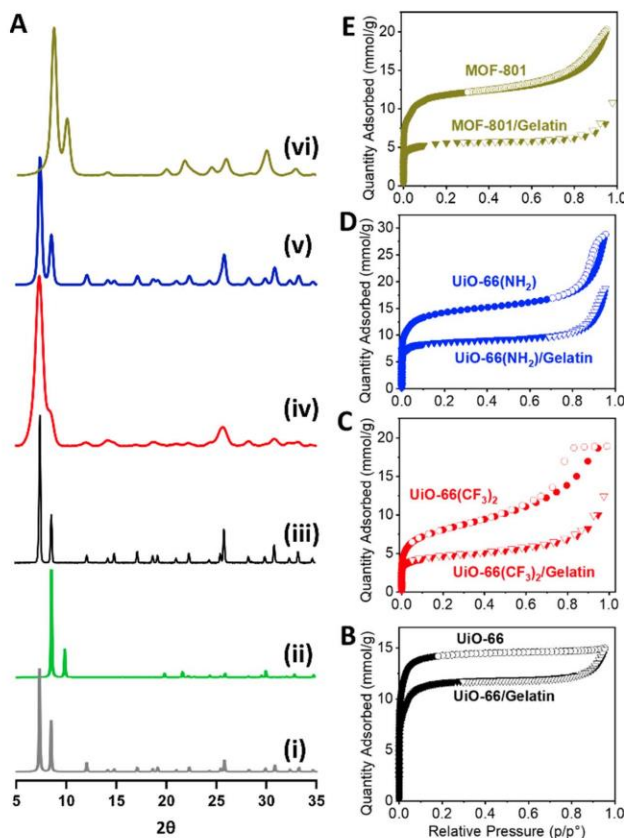


Figure 2. (A) Calculated PXRD patterns of (i) UiO-66 and (ii) MOF-801. Experimental PXRD patterns of (iii) UiO-66/G, (iv) UiO-66-(CF₃)₂/G, (v) UiO-66-(NH₂)/G, (vi) MOF-801/G, (B–E) N₂ adsorption–desorption isotherms (adsorption, filled symbols; desorption, empty symbols) at 77 K (*p*° = 1 atm) of (B) UiO-66 and UiO-66/G, (C) UiO-66-(CF₃)₂ and UiO-66-(CF₃)₂/G, (D) UiO-66-(NH₂) and UiO-66-(NH₂)/G and (E) MOF-801 and MOF-801/G.

(Table S1) while the isoelectric point of gelatin is equal to 8).⁶⁴

In order to enhance the MOF rate in the hydrogels, we took profit of the coacervation process which is widely used as an efficient formulation tool for the microencapsulation of drugs and cosmetics.^{38,65,66} This is a liquid–liquid phase separation process that takes place by adding a “nonsolvent” to the polymer solution. Herein, the phase separation of gelatin was induced by adding ethanol (nonsolvent) to an aqueous solution of gelatin.⁶⁷ Gelatin is a polyampholyte, containing both positively and negatively charged amino acid residues in the polymer backbone. In the presence of the nonsolvent, sequential intermolecular charge neutralization of gelatin molecules occurs, leading to the aggregation of gelatin molecules in the aqueous phase.⁶⁷ This phenomenon thus gives rise to the formation of a gelatin-rich and gelatin-lean solution phase. This coacervation process is thus particularly useful to increase the gelatin concentration in hydrogels.^{68,69} As previously reported, the gelatin concentration of gelatin coacervate can reach up to a value of 45 wt % while it does not exceed 15 wt % for hydrogels prepared through simple gelatin

dissolution (physical gelation).^{68,69} In this study, the simple coacervation process of gelatin was coupled with in situ formation of UiO-66(Zr) NPs (see Figure 1). The two-step synthesis of UiO-66(Zr) NPs at RT as previously used for the synthesis of pure MOF⁵¹ was thus conducted by reacting the {Zr₆} oxo-cluster and the bdc linker with gelatin aqueous solution (10 wt %, pH 7) and nonsolvent ethanol (Figure 1C, see the Experimental section). Keeping this dispersion stirring at RT for 24 h leads to a phase separation between a white viscoelastic hydrogel (Figure 1D) and an organic solution. To the best of our knowledge, the present article is the first study dealing with the synthesis of MOF-based hydrogels via a coacervation process. The PXRD pattern of the UiO-66/gelatin composite (UiO-66/G) displays sharp and intense Bragg peaks of UiO-66 in agreement with the formation of highly crystalline UiO-66(Zr) (Figure 2A). According to TGA and inductively coupled plasma atomic emission spectroscopy (ICP-AES), the composite contains a large amount of UiO-66 (~88 wt %). Similar syntheses of UiO-66-X/G (X = NH₂, (CF₃)₂) and MOF-801/G composites were performed by keeping constant all the physico-chemical parameters of the

E

<https://doi.org/10.1021/acs.chemmater.2c02704>
Chem. Mater. XXXX, XXX, XXX–XXX

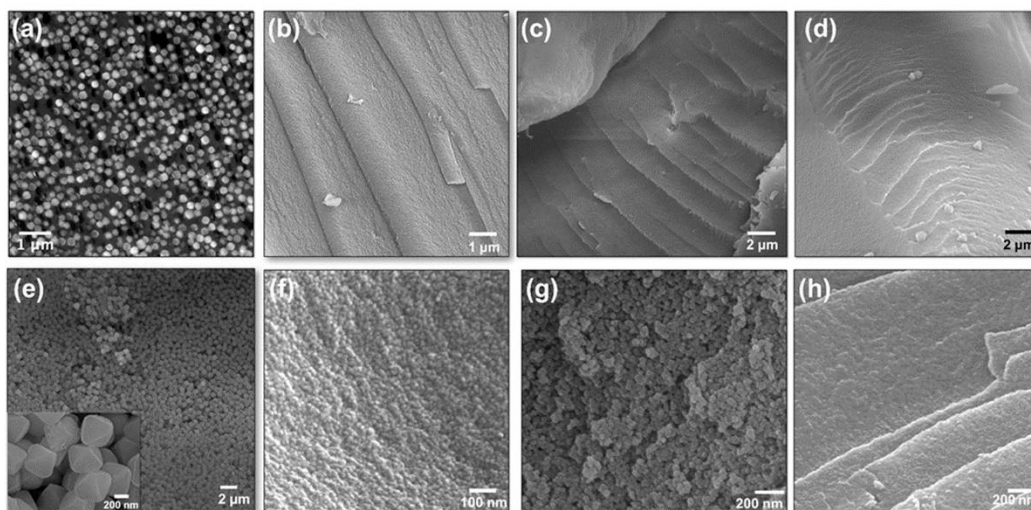


Figure 3. (a) TEM image of 80 nm ultramicrotomed slice of the UiO-66/G hydrogel, (e) SEM images of the UiO-66/G hydrogel after washings in water, (b,f) SEM images of UiO-66-(CF₃)₂/G, (c,g) SEM images of UiO-66-(NH₂)/G, (d,h) SEM images of MOF-801/G.

preparation of hydrogel composites (concentrations of precursors, pH, duration, etc.) in order to compare the affinity of gelatin with different functionalized MOFs. The PXRD patterns of the composite hydrogels present the characteristic Bragg peaks of the parental MOFs, in agreement with the formation of these MOFs under the coacervation conditions (Figure 2A). However, while the PXRD pattern of UiO-66/G displays sharp and intense Bragg peaks, the peaks of the other composites are much broader. This suggests that the MOF particles in UiO-66-X/G (X = NH₂, (CF₃)₂) and MOF-801/G composites are smaller than that of UiO-66/G (Figure 2 and S3), as shown by SEM and TEM (vide infra). According to TGA and ICP-AES, these bionanocomposites also present a high MOF loading (>50 wt %) (see Table 1).

These MOF/G hydrogel composites consist presumably of MOF particles distributed in physically cross-linked gelatin gels that can be described as an entangled assembly of rigid triple helices connected by flexible links. Indeed, the sol-gel transition of gelatin and thus the partial renaturation of collagen triple helices is likely to take place during the coacervation process by decreasing the temperature.^{26,64} The presence and relative quantification of gelatin triple helices in the composites was thus determined by differential scanning calorimetry (DSC). For the whole series, the DSC thermograms (Figure S16a,b) are characterized by a broad endothermic peak corresponding to two superimposed phenomena related to the water vaporization and the melting of gelatin triple helices. By assuming the heat of water vaporization of 100 J g⁻¹, it was possible to extract the heat of gelatin triple helices melting that qualitatively reflects the amount of gelatin triple helices.^{69,70} As shown in Figure S16c, the amount of gelatin triple helices linearly increases with the amount of gelatin, and this tendency is fully consistent with that observed for previously reported gelatin hydrogels.⁶⁹ Because the gelatin concentration varies from 9, 12, 30, and 49 wt % for UiO-66-(CF₃)₂/G, UiO-66/G, UiO-66-(NH₂)/G, and MOF-801/G, respectively, the gelatin triple helices

content is significantly higher for UiO-66-(NH₂)/G and MOF-801/G than that for UiO-66/G and UiO-66-(CF₃)₂/G. The acetate/organic linker molar ratio of the MOFs in the MOF/G hydrogels evaluated by ¹H/¹³C solid state NMR (Figures S22–S33) was compared to that of pure MOFs. Prior to NMR acquisition, MOF/G hydrogels were thoroughly washed in water to partially remove gelatin. However, the quantification of FA and acetate in the MOF-801/G sample was not possible because of the remaining large amount of gelatin. For the other MOF/G hydrogels, the acetate/organic linker molar ratio and thus the amount of defects in the MOF/G composites are comparable (UiO-66/G) or significantly lower (UiO-66-X/G (X = NH₂, (CF₃)₂)) than those of the parental MOFs. These results show that gelatin is prone to affect the creation of defects in the MOF framework. As shown by N₂ sorption at 77 K, the Brunauer-Emmett-Teller (BET) area of UiO-66/G composite decreases by ~30% to 1083 m² g⁻¹ in comparison to the pure UiO-66 (1560 m² g⁻¹). To exclude the weight percentage of the nonporous gelatin (i.e., 12 wt %), the adsorption isotherm of UiO-66/G was normalized to the weight of the MOF only, giving a normalized BET area close to ~1230 m² g⁻¹. This indicates that the UiO-66/G composite is highly porous and still retains 79% of the BET area of the parent MOF. Similar to UiO-66/G, the normalized BET area of UiO-66-X/G (X = NH₂, (CF₃)₂) and MOF-801/G calculated by considering the MOF content of these composites show that these materials keep more than 68% of the BET area of the pristine MOF (see Table 1). Accordingly, the normalized micropore volumes of MOF/G composites are similar to those of the parental MOFs, indicating that the micropores of the MOFs are thus not infiltrated by gelatin. In contrast, one can observe a strong decrease in the mesopore volume of UiO-66-(CF₃)₂/G and MOF-801/G in comparison to the parental MOFs (Table S5). The normalized mesopore volume decreased by 57 and 15% for UiO-66-(CF₃)₂/G and MOF-801/G, respectively. This observation can be explained by a partial penetration of gelatin

F

<https://doi.org/10.1021/acs.chemmater.2c02704>
Chem. Mater. XXXX, XXX, XXX–XXX

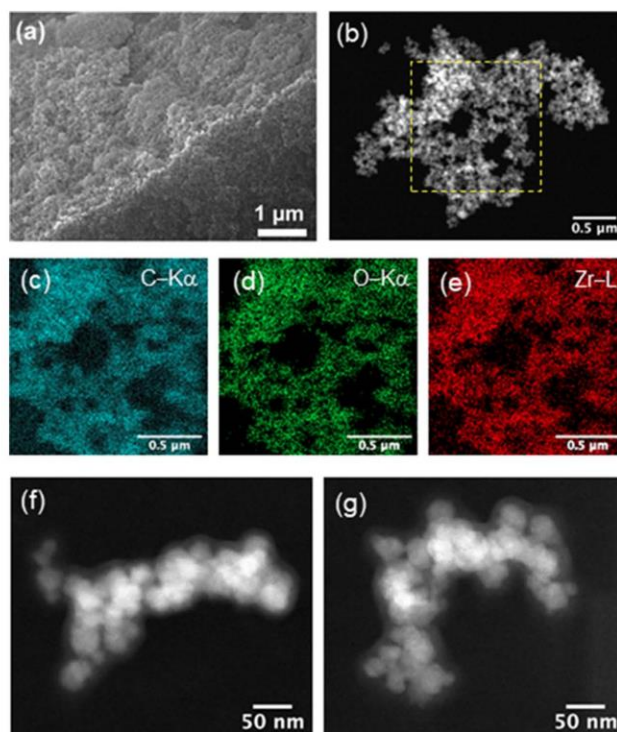


Figure 4. (a) Cross-section SEM image of the UiO-66-(NH₂)/G composite, (b,f,g) HAADF-STEM images of the UiO-66-(NH₂)/G composite, and (c–e) STEM-XEDS elemental mapping of the area related to the yellow dashed square in (b). For images (b–g), the composite was washed in water to remove gelatin partially.

chains and triple helices in MOF interparticle voids because such mesopores are accessible to the gelatin triple helices with a diameter and length of 1.5 and 300 nm, respectively.⁷¹ The high accessibility of micropores in MOF/G and partial mesopores clogging by gelatin in UiO-66-(CF₃)₂/G and MOF-801/G composites is confirmed by BJH-PSD analysis (see Figure S6). The microstructure of composites as well as the morphology of entrapped MOF particles were investigated by combining SEM and TEM experiments. First, prior to the SEM and HAADF-STEM observations, the MOF/G composites were washed in water in order to remove a large amount of gelatin. The SEM and TEM images (see Figures 3e and S9a,b) clearly show that UiO-66/G consists of highly monodisperse and well-defined octahedral crystals with an average diameter of 350 nm. In contrast, UiO-66-X (X = NH₂, (CF₃)₂) and MOF-801/G composites are made of spheroidal and much smaller MOF NPs with a diameter of about 30 nm for UiO-66-NH₂/G and MOF-801/G and 15 nm for UiO-66-(CF₃)₂/G, as shown by HAADF-STEM images (see Figures 4 and S15). Remarkably, the MOF NPs formed within gelatin present a homogeneous morphology and low size distribution, as shown by HAADF-STEM and STEM-XEDS (Figure 4). The spatial distribution of MOF particles in the as-prepared MOF/G hydrogels was also characterized by combining TEM and SEM of fractured samples. The top surface and cross-section SEM images of UiO-66-X (X = NH₂, (CF₃)₂) and

MOF-801/G composites show an excellent dispersion of MOF NPs in the gelatin matrix with the absence of any significant aggregation and phase separation (see Figures 3 and 4a). Remarkably, UiO-66-X (X = NH₂, (CF₃)₂) and MOF-801/G exhibit an organized lamellar texture as revealed by the presence of oriented steps (Figure 3). This gelatin organization was typically observed for pure physical gelatin hydrogels, as previously shown.⁶⁸ The distribution of MOF particles in the UiO-66/G sample was difficult to observe by classical SEM observations because of the larger diameter of MOF particles. We thus relied on the TEM observation of ultramicrotomed hydrogel samples with a fixed thickness (80 nm). This allows MOF particles to be clearly visualized in the entire volume of the composite. It is known that MOF particles are prone to aggregate upon drying, and this phenomenon is even more pronounced as the MOF particle size increases and the MOF/polymer interactions are weak. However, according to the TEM images of ultrathin slices of UiO-66/G (Figures 3a and S9c, d), MOF particles are remarkably well distributed in the gelatin matrix with the absence of phase separation and particle aggregation despite the high diameter of UiO-66 particles. These observations reveal high compatibility between gelatin and this series of functionalized MOFs. It should be noted that the highest MOF content of about 91 wt % is obtained with the hydrophobic UiO-66-(CF₃)₂ MOF while gelatin is a hydrophilic and water-soluble biopolymer. In contrast, despite

G

<https://doi.org/10.1021/acs.chemmater.2c02704>
Chem. Mater. XXXX, XXX, XXX–XXX

the hydrophilic character of MOF-801, the corresponding MOF-801/G hydrogel contains the lowest MOF amount (~51 wt %).

This indicates that the hydrophilic-hydrophobic balance of the MOF is not the driving force for the incorporation of MOF with gelatin. The good compatibility of gelatin with this series of UiO-66-X/MOF-801 materials is certainly related to the high chemical functionality of the gelatin backbone that consists of about 20 different amino acid residues with charged, polar, and coordinative groups able to interact with the MOF NPs as discussed below.

Characterization of the Interfacial Properties of MOF/Gelatin Composites: FT-IR/Solid-State NMR Spectroscopies and Molecular Modeling. To unravel the origin of the good compatibility between MOFs and gelatin, the bionanocomposites were characterized by combining FT-IR and multinuclear solid-state NMR (^1H , ^{13}C , ^{19}F , ^{15}N) spectroscopies, and the gelatin/MOF surface interactions were computationally explored using Density Functional Theory (DFT) calculations. The FT-IR spectra of composites display the characteristic vibration bands of the parental MOFs and gelatin, with only a slight shift of their position as a result of noncovalent interactions between MOFs and the amino acid residues of gelatin (see Figure S4 and Table S3). Similarly, the ^1H MAS and $^{13}\text{C}\{^1\text{H}\}$ CP MAS spectra (Figures S17 and S19) of MOF/G composites display the characteristic signals of the parental MOF and gelatin with similar ^1H and ^{13}C chemical shifts than those of the pure components, thereby showing the absence of any covalent cross-linking between gelatin and the MOFs. In addition, ^{19}F MAS and $^{15}\text{N}\{^1\text{H}\}$ CP MAS NMR spectra of UiO-66-(CF_3) $_2$ /G and UiO-66-(NH_2)/G, respectively (Figures S20 and S21), indicate also that the functional groups (CF_3 and NH_2) of the organic linkers of UiO-66-X (X = NH_2 , (CF_3) $_2$) do not strongly interact with gelatin. The MOF/G interfacial interactions were finally assessed by molecular modeling considering that gelatin presents a repetitive amino acid sequence (Gly-Xaa-Yaa) $_n$.

In a mammalian gelatin, every third amino acid is thus glycine (Gly), while Xaa is often proline and Yaa is mostly hydroxyproline (Hyp) or alanine (Ala).^{26,71} Therefore, cluster models that mimic the surfaces of UiO-66 and UiO-66-(CF_3) $_2$ were put into contact with either a Gly-Pro or Gly-Ala dipeptide sequence (Figure S34). The termination scheme of these cluster models cleaved from the periodic DFT-optimized bulk structures involves the capping of the Zr atoms by the OH group.⁷² Several initial configurations for Gly-Ala and Gly-Pro in interaction with both clusters were considered and further geometry-optimized. The most stable configurations are presented in Figure 5. Figure 5c shows that the amino and carboxyl functions of Gly-Ala interact via their hydrogen and oxygen atoms, respectively, with the terminal hydroxyl groups of UiO-66(Zr) forming hydrogen bonds with associated short separating distances ranging from 1.5 to 1.7 Å. The oxygen atom of the peptide function equally forms a hydrogen bond with the terminal hydroxyl groups of UiO-66(Zr). In the case of the UiO-66(Zr)-(CF $_3$) $_2$, the presence of the grafted functions to the organic linkers substantially changes the preferential orientation of the Gly-Ala motif as compared to the scenario encountered for UiO-66(Zr) and favors hydrogen bond interactions between the amino function of the molecule and the -CF $_3$ group (Figure 5e). Notably, this additional dipeptide/MOF surface interaction might induce proton shuttling between the terminal NH_3^+ to the neighbor terminal

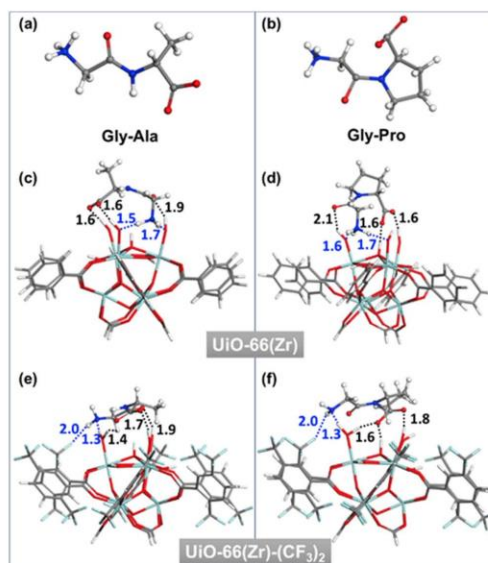


Figure 5. (a,b) Molecular structure of Gly-Ala and Gly-Pro dipeptides, (c–e) illustration of the main interactions between (c) UiO-66(Zr) and Gly-Ala, (d) UiO-66(Zr) and Gly-Pro, (e) UiO-66(Zr)-(CF $_3$) $_2$ and Gly-Ala, and (f) UiO-66(Zr)-(CF $_3$) $_2$ and Gly-Pro. Color code: C, gray; N, blue; O, red; H, white; F, green; Zr, dark green. Characteristic separating distances (expressed in Å) between the amino groups and carbonyl groups of the dipeptides and the MOF atoms are reported in blue and black, respectively.

hydroxyl groups of the MOF surface, as illustrated in Figure 5e with the formation of HO-H...NH $_2$ bridging species with a distance between H and N of 1.3 Å. The resulting interaction energy between Gly-Ala and UiO-66(Zr)-(CF $_3$) $_2$ (−138.6 kcal mol $^{-1}$) is therefore substantially higher compared to the scenario with the pristine UiO-66(Zr) (−93.9 kcal mol $^{-1}$). Remarkably, Gly-Pro behaves similarly, as illustrated in Figure 5d–f. One can observe that this molecule adopts preferential conformations in such a way to form hydrogen bonds between its terminal carboxyl, amino, and peptide functions with the MOF hydroxyl groups for both UiO-66(Zr) and UiO-66(Zr)-(CF $_3$) $_2$ while the additional interaction with the -CF $_3$ group might favor the formation of the same HO-H...NH $_2$ bridging species with the terminal group of UiO-66(Zr)-(CF $_3$) $_2$. This results in a significantly higher interaction energy for UiO-66(Zr)-(CF $_3$) $_2$ (−112.5 kcal mol $^{-1}$) as compared to UiO-66(Zr) (−85.4 kcal mol $^{-1}$). This set of predictions supports stronger overall interactions between gelatin and the functionalized UiO-66(Zr)-(CF $_3$) $_2$. This high compatibility between MOFs and gelatin leads to the enrichment of MOF in the gelatin-rich aqueous phase during the coacervation process, as observed experimentally. Gelatin, being a polyampholyte, could thus act as a MOF NP stabilizer and buffer.

Influence of Gelatin on the Nucleation and Growth of MOFs. As a further stage, to investigate the impact of gelatin on the nucleation and growth of MOF, the diameter and morphology of MOF particles in MOF/G composites were compared to those of pure MOFs. It should be noted that the presence of gelatin induces the formation of UiO-66 with a

H

<https://doi.org/10.1021/acs.chemmater.2c02704>
Chem. Mater. XXXX, XXX, XXX–XXX

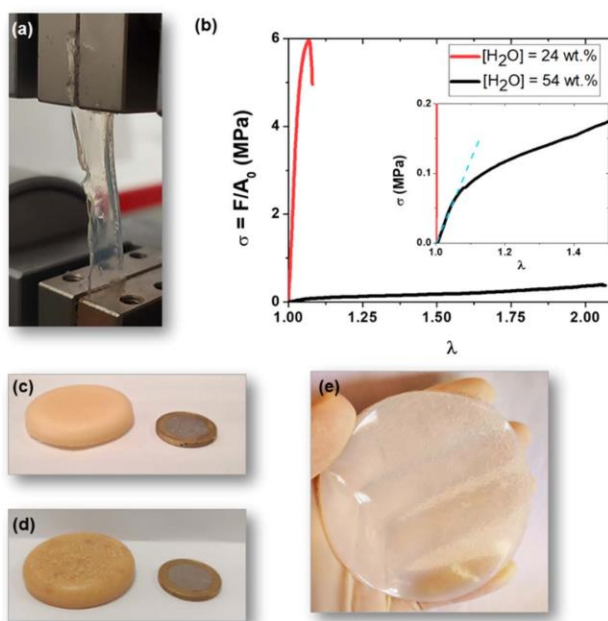


Figure 6. (a) Photograph of the UiO-66-(CF₃)₂/G composite under tensile test measurement. (b) Representative stress–stretch (σ – λ) curves obtained by tensile testing to failure for samples prepared at different hydration rates (24 and 54 wt %). Stress corresponds to the ratio of the elongation force to nondeformed cross-section. Inset shows the curve at small deformation. Dotted blue segment shows the linear behavior used to estimate the Young's modulus (E) of the most hydrated sample; (c–e) photographs of shaped MOF/G composites: tablet of (c) UiO-66/G, (d) UiO-66-(CF₃)₂/G, and (e) coating of UiO-66/G.

much larger particle size (average diameter 350 versus 70 nm for the pure UiO-66) and a narrow diameter distribution. In contrast, UiO-66-X (X = NH₂, (CF₃)₂) and MOF-801/G samples are made of nanocrystals whose morphology and diameter (~ 30 nm for UiO-66-NH₂ and MOF-801, ~ 15 nm for UiO-66-(CF₃)₂) are comparable to those present in pure MOF (Figures 3 and 4, S7–S15). These results show that gelatin acts as a molecular modulator for the formation of UiO-66 while this biopolymer exerts no kinetic control of the crystallization of UiO-66-X (X = NH₂, (CF₃)₂) and MOF-801. Polymers and biopolymers have already sparked a great interest as modulators for the morphogenesis of MOFs.^{9,73} In particular, a concentration-dependent influence of gelatin on the nucleation/growth of HKUST-1 was previously observed.²⁹ In the present work, MOF NPs are synthesized by using an excess of AA, which served as a complexing ligand for the formation of the [Zr₆O₄(OH)₄(OAc)₁₂] oxo cluster and as a modulator for controlling the crystal growth of MOFs. As previously reported, the MOF nanocrystal size results from a subtle interplay between different equilibria such as linker deprotonation, linker complexation, modulator deprotonation, and termination.^{74,75} It was clearly shown that the presence of monocarboxylic acid such as AA can increase or reduce the crystal size of UiO-type MOFs depending on whether these molecules can limit the organic linker deprotonation or act as the surface capping ligand.^{61,74,75} An acid modulator with a significant amount has the effect of limiting the deprotonation of the ligand upon decreasing pH and can also compete with

the organic linker for the metal coordination, thereby slowing down the metal–ligand complexation and leading to large particle sizes.^{74,75} The role of gelatin as a modulator of UiO-66 compares thus very well with that of monocarboxylic acids. It should be noted that the role of L-proline as an efficient modulator was shown for the formation of Zr and Hf MOFs.⁷⁶ In the case of gelatin, this is certainly due to the presence of the carboxylate side chains of the glutamate (Glu) and aspartate (Asp) residues.²⁹ It should be noted that AA as well as the carboxylate side chains of the Asp and Glu residues exhibit a similar pK_a value than that of the organic linker of UiO-66 ($pK_a(\text{AA}) = 4.20$ and $pK_a(1,4\text{-bdc}) = 4.82$ and 3.5 , $pK_a(\text{Asp}) = 3.71$ $pK_a(\text{Glu}) = 4.15$), and this may explain the high level of coordinative competition between modulators (AA and gelatin) and the organic linker. It should be noted that these literature pK_a values are measured in aqueous solution while MOF/G composites were synthesized in a mixture of aqueous/organic solvents. However, they can qualitatively explain the observed trends. In comparison, UiO-66-NH₂/MOF-801 and UiO-66-(CF₃)₂ NPs in the hydrogel composites are 11 and 23 times smaller than that of UiO-66 NPs, respectively, which means that the addition of gelatin interferes to a less extent with linker deprotonation. The strong acidity of the (CF₃)₂-bdc linker ($pK_a = 1.1$) may induce a fast nucleation process, leading to very small MOF nanocrystals. Therefore, gelatin is not able to impede the deprotonation of the (CF₃)₂-bdc linker even at high concentrations. In summary, gelatin exerts mainly a kinetics

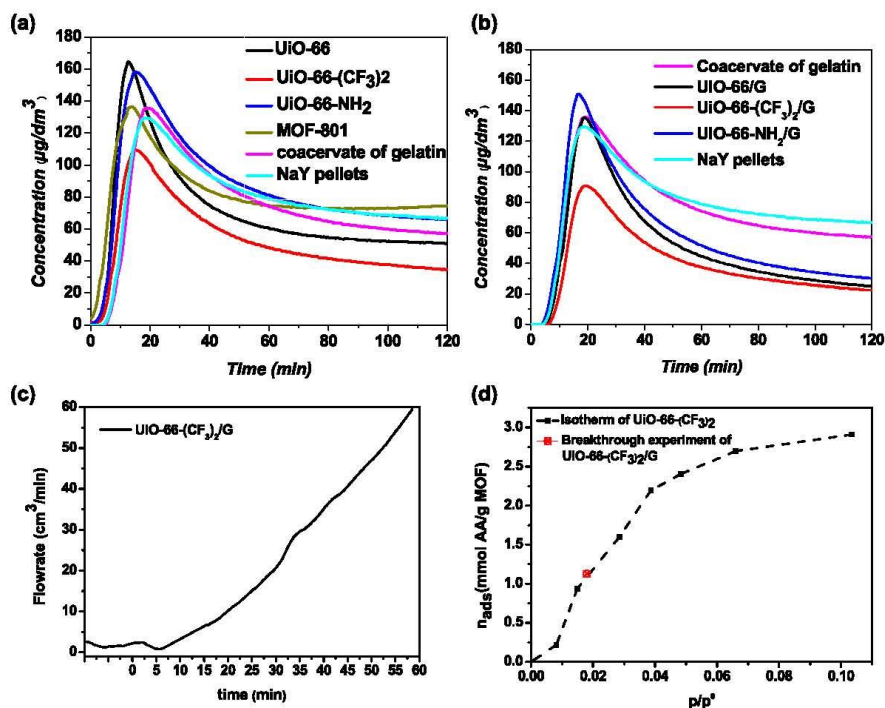


Figure 7. (a,b) AA concentration profiles inside a closed chamber after the injection of 1 μL of AA, at 25 $^\circ\text{C}$ and 40% RH in the presence of 50 mg of different adsorbents including (a) MOFs and (b) UiO-66-X/G ($X = \text{H}, \text{NH}_2, (\text{CF}_3)_2$) composites. These AA concentration profiles are compared to that obtained with pure gelatin coacervate or NaY pellets. The mean accuracy of the AA concentration ($\mu\text{g}/\text{dm}^3$) is $\pm 1\%$. (c) Breakthrough curve for AA (concentration 500 ppm in N_2) on UiO-66-(CF_3)₂/G composite under 40% RH and (d) AA isotherm for the UiO-66-(CF_3)₂ (black curve). The value of the AA adsorbed amount in UiO-66-(CF_3)₂/G obtained from the breakthrough experiment is indicated in red. This value was given by taking into account the UiO-66-(CF_3)₂ content in the UiO-66-(CF_3)₂/G composite.

control on the formation of the nonfunctionalized UiO-66 nanocrystals. The absence of any covalent cross-linking between these UiO-66-type MOFs and gelatin despite the presence of free carboxylate functions on the gelatin backbone is certainly due to the strong metal–bdc bond. This result is fully consistent with the absence of any postsynthetic ligand exchange previously observed by adding poly(amic acid) to UiO-66.⁷⁷

Processing of MOF/Gelatin Composites as Adsorbents for the Capture of Acetic Acid under Humid Ambient Conditions. In the final step, MOF/G composites were evaluated for the selective capture of AA under ambient humid conditions. For their processing and practical use as AA adsorbents, we have first characterized their mechanical properties at large deformation by performing tensile tests until failure (Figure 6a). Figures 6 and S35 show, respectively, the stress–strain curves of both the UiO-66-(CF_3)₂/G composite and pure gelatin coacervate while Tables S7, S8 provide the values of the Young's modulus (E), the stress at break (σ_{break}), and elongation at break (λ_{break}) for both materials. As previously reported, the physical hydrogels of gelatin exhibit very poor mechanical properties and this largely limits their application.^{68,69} In contrast, both pure gelatin coacervate and the UiO-66-(CF_3)₂/G composite exhibit very good mechanical properties characterized by high deform-

ability under humid ambient conditions ($T \approx 25$ $^\circ\text{C}$ and $\text{HR} \approx 40\%$) (Figure S35 and the black curve in Figure 6b). Tensile tests were also performed on pure gelatin coacervate after drying in an open humid environment. We have observed that pure gelatin coacervate evolves upon drying to a glassy material with a classical brittle failure which is in complete agreement with that previously reported.^{68,69} As shown in Table S7, the Young's modulus E and stress at break (σ_{break}) increase notably while the elongation at break λ_{break} decreases with increasing the drying rate. This observation can be explained by an increase in the glass transition temperature (T_g) of gelatin with dehydration, as previously demonstrated.⁷⁸ It means that the hydration rate of gelatin strongly impacts its mechanical properties because water molecules play the role of plasticizer of gelatin.

Similar to pure gelatin coacervate, the UiO-66-(CF_3)₂/G composite evolves also to a glassy and fragile material upon dehydration in an open humid environment ($T = 20$ $^\circ\text{C}$, 40% RH, 24 h) (red curve of Figure 6b). It should be noted that these drying conditions are more drastic in an open environment than those operating in a closed humid environment as targeted by the application. Indeed, the water evaporation capacity of the air is optimal in an open environment. Therefore, we have also evaluated the kinetics of water desorption of such composites in comparison to pure

J

<https://doi.org/10.1021/acs.chemmater.2c02704>
Chem. Mater. XXXX, XXX, XXX–XXX

gelatin coacervate in a humid closed chamber ($T = 20\text{ }^{\circ}\text{C}$, 40% RH). The water content of UiO-66/G, UiO-66-(CF₃)₂/G, and pure gelatin coacervate has thus been measured as a function of the aging time, as shown in Figure S36. It is noteworthy that the drying kinetics of UiO-66/G and UiO-66-(CF₃)₂/G are considerably slowed down compared to that of pure gelatin coacervate. Moreover, the hydration rate of both UiO-66/G and UiO-66-(CF₃)₂/G composites is significantly higher than that of pure gelatin coacervates and reach a value of 43 and 56 wt %, respectively, after 8 h of drying. It should be noted that the water content of these UiO-66/G and UiO-66-(CF₃)₂/G composites is also significantly higher than that of the glassy UiO-66-(CF₃)₂/G (24 wt % of water) composite dried in an open environment (Figure 6). Therefore, in contrast to pure gelatin coacervates, the MOF/G composites behave as solvated hydrogels and do not evolve to brittle glassy materials upon aging in a closed humid chamber ($T = 20\text{ }^{\circ}\text{C}$, 40% RH) for about 8 h. Such an observation is consistent with the good mechanical properties of the UiO-66-(CF₃)₂/G composite under humid ambient conditions (see Figure 6b). It should be noted that the transition between the “dried” and “hydrated” state of UiO-66-(CF₃)₂/G composite is fully reversible because of the thermo-responsivity of gelatin. The glassy dried UiO-66-(CF₃)₂/G composite can evolve to an extensible hydrogel after immersion in water whose mechanical properties are comparable to that of the hydrated UiO-66-(CF₃)₂/G composite stored at RH \sim 40% (see Figure 6b). According to their good mechanical properties, MOF/gelatin hydrogels could be processed in different forms including thick coatings and tablets (see Figure 6c–e) by taking advantage of the temperature-dependent sol–gel transition of gelatin (see the Experimental Section). It is noteworthy that these shaped UiO-66/G composites could be used in real conditions and thus inserted in archive boxes of photographic films. To assess the performance of MOF/G composites for the capture of AA under real conditions, experiments were conducted by using an environmental chamber in the presence of water (Figure S38a), that is, 40% RH typically present in museums. Minor amounts of AA were injected in the closed chamber (corresponding to 362 $\mu\text{g dm}^{-3}$) with controlled RH, allowing the measurement of comparative profiles of AA removal by the MOFs (100 $\mu\text{g dm}^{-3}$ is equivalent to 40 ppm in volume). There is an initial increase in the AA concentration in the chamber because of the evaporation and diffusion of AA molecules to the sensor followed by a decrease due to the adsorption of AA by the adsorbents. The increase in the AA concentration observed in the first minutes of the experiment is not relevant for our envisaged application and is dictated by various parameters such as the shape of the AA droplet, the positioning of the adsorbent in the chamber, the particle size distribution of the adsorbent, and so forth. The region of interest in the AA concentration profiles of the adsorbent lies after 1 to 2 h of injection. The real performance of the adsorbents is thus evaluated by its capacity to remove the highest amount of AA after 2 h of exposure when a quasi-static condition is established. In the absence of an adsorbent, a fast increase in the AA concentration as high as 260 $\mu\text{g dm}^{-3}$ is observed and maintained during 2 h (see Figure S38b). The AA co-adsorption properties of pure UiO-66-X ($X = \text{H}, \text{NH}_2, (\text{CF}_3)_2$) NPs were first evaluated in the chamber. MOF-801 presents a poor AA/water adsorption selectivity in line with its very high affinity for water. The MOF-801/G composite was thus not considered as an AA adsorbent. As shown in Figure

7a, the UiO-66-X ($X = \text{H}, \text{NH}_2, (\text{CF}_3)_2$) materials show very good AA adsorption capacity under humid conditions, in agreement with results previously reported.⁴⁵ Then, the performance of UiO-66-X ($X = \text{H}, \text{NH}_2, (\text{CF}_3)_2$)/G composites for the selective capture of AA under humidity was tested in comparison to the corresponding pure MOFs, pure gelatin coacervates, as well as the benchmark Na-Y zeolite (Figure 7b). This series of UiO-66-X/G led to very interesting results outperforming the benchmark NaY adsorbent by decreasing the AA concentration down to 24.9, 30.2, and 22.4 $\mu\text{g dm}^{-3}$ for UiO-66/G, UiO-66-(NH₂)/G, and UiO-66-(CF₃)₂/G, respectively, after 2 h of exposure (Figure 7b). It is interesting to note that the pure gelatin coacervate adsorbs AA but with considerably less efficiency (57.3 $\mu\text{g dm}^{-3}$ after 2 h). To demonstrate the reproducibility of these experiments and validate the performance of the MOF/G composites, the AA co-adsorption experiments were repeated four times with the UiO-66/G composite under the same operating conditions (50 mg of adsorbent, 1 μL of acetic acid, 25 $^{\circ}\text{C}$, and 40% RH) (see Figure S38c). For the four experiments, the measurements converge to a very close AA concentration after an adsorbent exposure time of 60 min while almost the same AA concentration of $24.9 \pm 0.2\ \mu\text{g dm}^{-3}$ was reached after 120 min of exposure. These experiments are consistent with a high homogeneity of the UiO-66/G composite and can yield the standard deviation error of the measurements. It should be noted that these co-adsorption experiments using the environmental chamber have been repeated for the different adsorbents that were stored for two months under humid ambient conditions. These experiments show that the MOF/G composites keep their AA adsorption selectivity upon aging under humid ambient conditions. These results show also that the residual AA concentration measured in the presence of the benchmark NaY after 2 h is almost three times higher than the one in the presence of UiO-66-(CF₃)₂/G. The best material was thus found to be UiO-66-(CF₃)₂/G for which the fastest decrease was observed, reaching 22.4 $\mu\text{g dm}^{-3}$ after 2 h. To confirm the potential of this composite for the selective capture of AA, we have also recorded breakthrough experiments (see the SI for more experimental details). Breakthrough experiments were performed using the set up shown in Figure S37 of the SI. The column was packed with the best performing composite, UiO-66-(CF₃)₂/G. After activation, the sample was hydrated using a flow of nitrogen with 40% RH. The flow of gas was then switched to the AA and nitrogen mixture at an AA concentration of 500 ppm. The output of the column was continuously analyzed using a mass spectrometer, giving the breakthrough curve shown in Figure 7c. More details on the experimental procedure are given in the SI. The adsorbed AA amount calculated from the breakthrough curve yielded 1.13 mmol AA/g MOF. It is noteworthy that the MOF content in UiO-66-(CF₃)₂/G of 91 wt % was taken into account. The used concentration (500 ppm) corresponds to a p/p_0 of 0.0174 (details are provided in the SI). The AA adsorbed amount calculated from the breakthrough curve is in perfect agreement with the AA adsorption isotherm of the pure UiO-66-(CF₃)₂, as shown in Figure 7d (red circle). This experiment shows that the AA adsorption capacity and selectivity of UiO-66-(CF₃)₂ are fully preserved once combined with gelatin. In the UiO-66-(CF₃)₂/G composite, the pores of the MOF are thus fully accessible to AA under humid ambient conditions, in agreement with the absence of any clogging of the MOF pores by gelatin (see vide supra). It should be noted that a similar

K

<https://doi.org/10.1021/acs.chemmater.2c02704>
Chem. Mater. XXXX, XXX, XXX–XXX

AA adsorption capacity was also measured by the breakthrough experiments by using a UiO-66-(CF₃)₂/G that was stored under humid ambient conditions for about 18 months. This result demonstrates that the performance of UiO-66-(CF₃)₂/G for the selective capture of AA is highly stable with time. The high AA/water adsorption selectivity of this composite can be mainly imparted by the parental MOF which shows a comparable profile for the AA removal (Figure 7a). As shown by the AA adsorption isotherm (Figure S39), UiO-66-(CF₃)₂ presents a very good AA adsorption capacity. Compared to UiO-66, UiO-66-(CF₃)₂ presents a higher affinity to AA because of the presence of hydrogen bonds between the MOF framework and AA (CH₃-C(=O)OH...μ₃(OH) and CH₃-C(=O)OH...CF₃) and its higher hydrophobicity, as previously shown by molecular modeling.⁴⁵ It should be noted that the AA adsorption of pure gelatin and MOF/G composites measured by gravimetric isotherms is almost negligible (Figure S39) and this may be due to their activation at 150 °C under vacuum prior to the isotherm acquisition. Under those conditions, gelatin and MOF/G composites are completely dehydrated and evolve to glassy rigid materials, as shown previously (see Figures 6 and S35). As previously shown by advanced characterization tools and molecular modeling, we may expect that the MOF NPs are coated by gelatin chains because of the good compatibility between both MOF and gelatin. Therefore, we may thus expect that gelatin chains at the surface of MOF NPs present a very low flexibility and mobility in the absence of water (after activation at 150 °C), and this may prevent the diffusion of AA in the MOF pores. Actually, pure gelatin coacervates are also nonporous to AA, as shown in Figure S39. Therefore, the evaluation of the performance of adsorbents is more relevant by using the environmental chamber that fairly reproduces the conditions of the application (RH between 40 and 60%). Finally, the high chemical stability of the UiO-66-X (X = H, NH₂, (CF₃)₂)/G composites was shown by collecting characterization experiments (PXRD, N₂ porosimetry, FT-IR, SEM) after aging the composites for 30 days under humid ambient conditions with no evidence of MOF degradation (see Figure S41). A series of hydrogels labeled as p-UiO-66-X/G were also prepared by using preformed UiO-66-X NPs (see the SI for details) and then tested in similar conditions for the AA capture in humid conditions. However, their AA adsorption efficiency is significantly lower in comparison to the first set of UiO-66-X/G hydrogels (see Figure S40). This clearly indicates that the synthetic approach integrating the coacervation process and the in situ formation of MOFs can lead to UiO-66-X/G adsorbents with excellent microstructural and textural properties for the selective capture of AA. Finally, the potential use of these composites for removing organic dyes from contaminated water was also evaluated. The shaped UiO-66/G composite was thus immersed in an aqueous solution of 0.5 mM Reichardt's dye. After soaking for 15 min, the solution became colorless while the UiO-66/G composite became purple. The efficiency of UiO-66/G for the dye adsorption was confirmed by recording UV-vis spectra of the supernatant solutions (Figure S43). The high water stability of UiO-66-X (X = H, (CF₃)₂)/G composites was also confirmed by recording the PXRD pattern and FT-IR spectra on composites soaked in aqueous solution for about 48 h (see Figure S42).

CONCLUSIONS

In summary, we report here a new and versatile approach for the synthesis at RT of green and eco-compatible hydrogel composites combining gelatin and Zr(IV) MOFs. This approach benefits from the thermo-reversible properties of gelatin and its phase separation by coacervation associated to the RT in-situ formation of UiO-66-type MOFs. This strategy was successfully applied to a series of Zr(IV) dicarboxylate and fumarate MOFs (UiO-66-type MOFs and MOF-801, respectively) differing by their hydrophobic-hydrophilic balance and the functionalization of the organic linker. This enabled the production of hydrogel composites with interesting features such as a high MOF content (>50 wt %), large porosity, and a homogeneous MOF NP distribution in the matrix. This arises from an excellent compatibility between gelatin and MOF NPs, as evidenced by a combination of advanced characterization techniques and molecular modeling. Such composites could be shaped at the gram scale in different forms such as coatings and thick tablets because of their very good mechanical properties under ambient conditions. Finally, these shaped composites have shown high performance for the selective capture of AA under humid conditions. This paves the way toward the use of these composites as adsorbents in CH preservation. Interestingly, our synthetic approach could be extended to other complex fluids whose combination with MOFs may lead to a wide range of MOF-based composites with a hierarchical porous structure.

ASSOCIATED CONTENT

Supporting Information

The Supporting Information is available free of charge at <https://pubs.acs.org/doi/10.1021/acs.chemmater.2c02704>.

Further details on the synthesis of MOFs and MOF-gelatin composites and structural characterization (PXRD, FT-IR, TGA, SEM, TEM, HAADF-STEM, STEM-EDX, DSC, solid-state NMR, etc.); computational modeling; tensile test; acetic acid adsorption; and dye adsorption (PDF)

AUTHOR INFORMATION

Corresponding Author

Nathalie Steunou – Institut Lavoisier de Versailles, UMR CNRS 8180, Université de Versailles St Quentin en Yvelines, Université Paris Saclay, 78000 Versailles, France; Institut des Matériaux Poreux de Paris, UMR CNRS-ENS-ESPCI 8004, PSL Research University, 75005 Paris, France; orcid.org/0000-0002-7049-7388; Email: nathalie.steunou@uvsq.fr

Authors

Subharanjan Biswas – Institut Lavoisier de Versailles, UMR CNRS 8180, Université de Versailles St Quentin en Yvelines, Université Paris Saclay, 78000 Versailles, France

Mohamed Haouas – Institut Lavoisier de Versailles, UMR CNRS 8180, Université de Versailles St Quentin en Yvelines, Université Paris Saclay, 78000 Versailles, France;

orcid.org/0000-0002-2133-702X

Cátia Freitas – CERENA, Departamento de Engenharia Química, Instituto Superior Técnico, Universidade de Lisboa, 1049-001 Lisboa, Portugal; orcid.org/0000-0003-0325-691X

Carla Vieira Soares – ICGM, CNRS, Université Montpellier, ENSCM, 34293 Montpellier, France

L

<https://doi.org/10.1021/acs.chemmater.2c02704>
Chem. Mater. XXXX, XXX, XXX–XXX

Abeer Al Mohtar – CERENA, Departamento de Engenharia Química, Instituto Superior Técnico, Universidade de Lisboa, 1049-001 Lisboa, Portugal; orcid.org/0000-0002-9212-1269

Ali Saad – Institut Lavoisier de Versailles, UMR CNRS 8180, Université de Versailles St Quentin en Yvelines, Université Paris Saclay, 78000 Versailles, France

Heng Zhao – Institut des Matériaux Poreux de Paris, UMR CNRS-ENS-ESPCI 8004, PSL Research University, 75005 Paris, France

Georges Mouchaham – Institut des Matériaux Poreux de Paris, UMR CNRS-ENS-ESPCI 8004, PSL Research University, 75005 Paris, France

Carine Livage – Institut Lavoisier de Versailles, UMR CNRS 8180, Université de Versailles St Quentin en Yvelines, Université Paris Saclay, 78000 Versailles, France

Florent Carn – Laboratoire Matière et Systèmes Complexes, UMR CNRS 7057, Université Paris-Cité, 75013 Paris, France; orcid.org/0000-0002-7842-3658

Nicolas Menguy – Institut de Minéralogie, de Physique des Matériaux et de Cosmochimie, UMR CNRS 7590, Sorbonne Université, MNHN, IRD, 75005 Paris, France

Guillaume Maurin – ICGM, CNRS, Université Montpellier, ENSCM, 34293 Montpellier, France; orcid.org/0000-0002-2096-0450

Moises L. Pinto – CERENA, Departamento de Engenharia Química, Instituto Superior Técnico, Universidade de Lisboa, 1049-001 Lisboa, Portugal; orcid.org/0000-0003-3061-9632

Complete contact information is available at: <https://pubs.acs.org/10.1021/acs.chemmater.2c02704>

Notes

The authors declare no competing financial interest.

ACKNOWLEDGMENTS

S.B., C.F., A.A.M., M.L.P. and N.S. acknowledge the financial support from the European Union's Horizon 2020 program (Nemosine Project, grant agreement N°760801). S.B. and N.S. acknowledge the financial support from the ANR-11-LABEX-0039 (LabEx charmmmat). Fundação para a Ciência e a Tecnologia (FCT-MCTES) is acknowledged for the funding to the Projects UIDB/04028/2020 and UIDP/04028/2020 (CERENA). The computational work was performed using HPC resources from GENCI-CINES (Grant A0100907613). S.B. and N.S. would like to acknowledge Christine Pechoux and the facilities of MIMA2 (MET – GABI, INRA, Agroparitech, Jouy-en-Josas, France MIMA2: <https://doi.org/10.15454/1.5572348210007727E12>) for the preparation of ultramicrotomed MOF/gelatin samples. S.B. and N.S. would like to acknowledge Bertrand Lavédrine (Muséum National d'Histoire Naturelle) and Christian Serre (ENS/ESPCI/PSL) for fruitful discussions. G.M. (IMAP) would like to acknowledge Shyamapada Nandi for his technical assistance.

REFERENCES

- Ji, Z.; Wang, H.; Canossa, S.; Wuttke, S.; Yaghi, O. M. Pore Chemistry of Metal–Organic Frameworks. *Adv. Funct. Mater.* **2020**, *30*, No. 2000238.
- Krause, S.; Hosono, N.; Kitagawa, S. Chemistry of Soft Porous Crystals: Structural Dynamics and Gas Adsorption Properties. *Angew. Chem., Int. Ed.* **2020**, *59*, 15325–15341.
- Li, J.; Bhatt, P. M.; Li, J.; Eddaoudi, M.; Liu, Y. Recent Progress on Microfine Design of Metal–Organic Frameworks: Structure Regulation and Gas Sorption and Separation. *Adv. Mater.* **2020**, *32*, No. 2002563.
- Osterrieth, J. W. M.; Fairen-Jimenez, D. Metal–Organic Framework Composites for Theragnostics and Drug Delivery Applications. *Biotechnol. J.* **2021**, *16*, No. 2000005.
- Duman, F. D.; Forgan, R. S. Applications of Nanoscale Metal–Organic Frameworks as Imaging Agents in Biology and Medicine. *J. Mater. Chem. B* **2021**, *9*, 3423–3449.
- D'Ans, P.; Courbon, E.; Permyakova, A.; Nouar, F.; Simonnet-Jegat, C.; Bourdreux, F.; Malet, L.; Serre, C.; Frère, M.; Steunou, N. A New Strontium Bromide MOF Composite with Improved Performance for Solar Energy Storage Application. *J. Energy Storage* **2019**, *25*, No. 100881.
- Duan, J.; Jin, W.; Kitagawa, S. Water-Resistant Porous Coordination Polymers for Gas Separation. *Coord. Chem. Rev.* **2017**, *332*, 48–74.
- Liu, X.-M.; Xie, L.-H.; Wu, Y. Recent Advances in the Shaping of Metal–Organic Frameworks. *Inorg. Chem. Front.* **2020**, *7*, 2840–2866.
- Schmidt, B. V. K. J. Metal–Organic Frameworks in Polymer Science: Polymerization Catalysis, Polymerization Environment, and Hybrid Materials. *Macromol. Rapid Commun.* **2020**, *41*, No. 1900333.
- Kalaj, M.; Bentz, K. C.; Ayala, S., Jr.; Palomba, J. M.; Barcus, K. S.; Katayama, Y.; Cohen, S. M. MOF-Polymer Hybrid Materials: From Simple Composites to Tailored Architectures. *Chem. Rev.* **2020**, *120*, 8267–8302.
- Ma, K.; Idrees, K. B.; Son, F. A.; Maldonado, R.; Wasson, M. C.; Zhang, X.; Wang, X.; Shehayeb, E.; Merhi, A.; Kaafarani, B. R.; Islamoglu, T.; Xin, J. H.; Farha, O. K. Fiber Composites of Metal–Organic Frameworks. *Chem. Mater.* **2020**, *32*, 7120–7140.
- Saad, A.; Biswas, S.; Gkaniatsou, E.; Sicard, C.; Dumas, E.; Menguy, N.; Steunou, N. Metal–Organic Framework Based 1D Nanostructures and Their Superstructures: Synthesis, Microstructure, and Properties. *Chem. Mater.* **2021**, *33*, 5825–5849.
- Muschi, M.; Lalitha, A.; Sene, S.; Aureau, D.; Fregnaux, M.; Esteve, I.; Rivier, L.; Ramsahye, N.; Devautour-Vinot, S.; Sicard, C.; Menguy, N.; Serre, C.; Maurin, G.; Steunou, N. Formation of a Single-Crystal Aluminum-Based MOF Nanowire with Graphene Oxide Nanoscrolls as Structure-Directing Agents. *Angew. Chem., Int. Ed.* **2020**, *59*, 10353–10358.
- Benzaqui, M.; Semino, R.; Carn, F.; Tavares, S. R.; Menguy, N.; Giménez-Marqués, M.; Bellido, E.; Horcajada, P.; Berthelot, T.; Kuzminova, A. I.; Dmitrenko, M. E.; Penkova, A. V.; Roizard, D.; Serre, C.; Maurin, G.; Steunou, N. Covalent and Selective Grafting of Polyethylene Glycol Brushes at the Surface of ZIF-8 for the Processing of Membranes for Pervaporation. *ACS Sustainable Chem. Eng.* **2019**, *7*, 6629–6639.
- Jin, P.; Tan, W.; Huo, J.; Liu, T.; Liang, Y.; Wang, S.; Bradshaw, D. Hierarchically Porous MOF/Polymer Composites Via Interfacial Nanoassembly and Emulsion Polymerization. *J. Mater. Chem. A* **2018**, *6*, 20473–20479.
- Mahdi, E. M.; Tan, J.-C. Mixed-Matrix Membranes of Zeolitic Imidazolate Framework (ZIF-8)/Matrimid Nanocomposite: Thermo-Mechanical Stability and Viscoelasticity Underpinning Membrane Separation Performance. *J. Membr. Sci.* **2016**, *498*, 276–290.
- Li, C.; Liu, J.; Zhang, K.; Zhang, S.; Lee, Y.; Li, T. Coating the Right Polymer: Achieving Ideal Metal–Organic Framework Particle Dispersibility in Polymer Matrixes Using a Coordinative Crosslinking Surface Modification Method. *Angew. Chem., Int. Ed.* **2021**, *60*, 14138–14145.
- Dai, D.; Wang, H.; Li, C.; Qin, X.; Li, T. A Physical Entangling Strategy for Simultaneous Interior and Exterior Modification of Metal–Organic Framework with Polymers. *Angew. Chem., Int. Ed.* **2021**, *60*, 7389–7396.
- Zimpel, A.; Preiß, T.; Röder, R.; Engelke, H.; Ingrisch, M.; Peller, M.; Rädler, J. O.; Wagner, E.; Bein, T.; Lächelt, U.; Wuttke, S. Imparting Functionality to MOF Nanoparticles by External Surface

M

<https://doi.org/10.1021/acs.chemmater.2c02704>
Chem. Mater. XXXX, XXX, XXX–XXX

- Selective Covalent Attachment of Polymers. *Chem. Mater.* **2016**, *28*, 3318–3326.
- (20) Lim, J.; Lee, E. J.; Choi, J. S.; Jeong, N. C. Diffusion Control in the In Situ Synthesis of Ironic Metal–Organic Frameworks within an Ionic Polymer Matrix. *ACS Appl. Mater. Interfaces* **2018**, *10*, 3793–3800.
- (21) Liu, Y.; Gong, C. S.; Dai, Y.; Yang, Z.; Yu, G.; Liu, Y.; Zhang, M.; Lin, L.; Tang, W.; Zhou, Z.; Zhu, G.; Chen, J.; Jacobson, O.; Kiesewetter, D. O.; Wang, Z.; Chen, X. In Situ Polymerization on Nanoscale Metal–Organic Frameworks for Enhanced Physiological Stability and Stimulus-Responsive Intracellular Drug Delivery. *Biomaterials* **2019**, *218*, No. 119365.
- (22) O'Neill, L. D.; Zhang, H.; Bradshaw, D. Macro-/Microporous MOF Composite Beads. *J. Mater. Chem.* **2010**, *20*, 5720–5726.
- (23) Zhang, Z.; Nguyen, H. T. H.; Miller, S. A.; Cohen, S. M. PolyMOFs: A Class of Interconvertible Polymer–Metal–Organic–Framework Hybrid Materials. *Angew. Chem., Int. Ed.* **2015**, *54*, 6152–6157.
- (24) Cavka, J. H.; Jakobsen, S.; Olsbye, U.; Guillou, N.; Lamberti, C.; Bordiga, S.; Lillerud, K. P. A New Zirconium Inorganic Building Brick Forming Metal Organic Frameworks with Exceptional Stability. *J. Am. Chem. Soc.* **2008**, *130*, 13850–13851.
- (25) Jonker, A. M.; Löwik, D. W. P. M.; Van Hest, J. C. M. Peptide- and Protein-Based Hydrogels. *Chem. Mater.* **2012**, *24*, 759–773.
- (26) Steunou, N. Interfacing Gelatin with (Hydr)Oxides and Metal Nanoparticles: Design of Advanced Hybrid Materials for Biomedical Engineering Applications. In *Adv. Mater. Interfaces*, Tiwari, A., Patra, H. K., Wang, X., Eds.; John Wiley & Sons: Hoboken, NJ, USA, 2016; pp 275–324.
- (27) Utech, S.; Boccaccini, A. R. A Review of Hydrogel-Based Composites for Biomedical Applications: Enhancement of Hydrogel Properties by Addition of Rigid Inorganic Fillers. *J. Mater. Sci.* **2016**, *51*, 271–310.
- (28) Cölfen, H. Bio-Inspired Mineralization Using Hydrophilic Polymers. In *Biomaterialization II. Topics in Current Chemistry*, Naka, K., Ed.; Springer: Berlin, Heidelberg, 2006; Vol. 271; pp 1–77.
- (29) Garai, A.; Shepherd, W.; Huo, J.; Bradshaw, D. Biomimetic-Inspired Growth of Metal–Organic Frameworks in Gelatin Hydrogel Matrices. *J. Mater. Chem. B* **2013**, *1*, 3678–3684.
- (30) Deng, Z.; Li, M.; Hu, Y.; He, Y.; Tao, B.; Yuan, Z.; Wang, R.; Chen, M.; Luo, Z.; Cai, K. Injectable Biomimetic Hydrogels Encapsulating Gold/Metal–Organic Frameworks Nanocomposites for Enhanced Antibacterial and Wound Healing Activity under Visible Light Actuation. *Chem. Eng. J.* **2021**, *420*, No. 129668.
- (31) Hsieh, C. T.; Ariga, K.; Shrestha, L. K.; Hsu, S. H. Development of MOF Reinforcement for Structural Stability and Toughness Enhancement of Biodegradable Bioinks. *Biomacromolecules* **2021**, *22*, 1053–1064.
- (32) Jiang, Y.; Pan, X.; Yao, M.; Han, L.; Zhang, X.; Jia, Z.; Weng, J.; Chen, W.; Fang, L.; Wang, X.; Zhang, Y.; Duan, R.; Ren, F.; Wang, K.; Chen, X.; Lu, X. Bioinspired Adhesive and Tumor Microenvironment Responsive NanoMOFs Assembled 3D-Printed Scaffold for Anti-Tumor Therapy and Bone Regeneration. *Nano Today* **2021**, *39*, No. 101182.
- (33) Ji, H.; Wang, X.; Wang, P.; Gong, Y.; Wang, Y.; Liu, C.; Ji, G.; Wang, X.; Wang, M. Lanthanide-Based Metal–Organic Frameworks Solidified by Gelatin-Methacryloyl Hydrogels for Improving the Accuracy of Localization and Excision of Small Pulmonary Nodules. *J. Nanobiotechnol.* **2022**, *20*, 60.
- (34) Li, J.; Lv, F.; Li, J.; Li, Y.; Gao, J.; Luo, J.; Xue, F.; Ke, Q.; Xu, H. Cobalt-Based Metal–Organic Framework as a Dual Cooperative Controllable Release System for Accelerating Diabetic Wound Healing. *Nano Res.* **2020**, *13*, 2268–2279.
- (35) Sun, Y.; Liu, X.; Zhu, Y.; Han, Y.; Shen, J.; Bao, B.; Gao, T.; Lin, J.; Huang, T.; Xu, J.; Chai, Y.; Zheng, X. Tunable and Controlled Release of Cobalt Ions from Metal–Organic Framework Hydrogel Nanocomposites Enhances Bone Regeneration. *ACS Appl. Mater. Interfaces* **2021**, *13*, 59051–59066.
- (36) Tang, L.; Gong, L.; Xu, Y.; Wu, S.; Wang, W.; Zheng, B.; Tang, Y.; Zhang, D.; Tang, J.; Zheng, J. Mechanically Strong Metal–Organic Framework Nanoparticle-Based Double Network Hydrogels for Fluorescence Imaging. *ACS Appl. Nano Mater.* **2022**, *5*, 1348–1355.
- (37) Pei, R.; Fan, L.; Zhao, F.; Xiao, J.; Yang, Y.; Lai, A.; Zhou, S. F.; Zhan, G. 3D-Printed Metal–Organic Frameworks within Biocompatible Polymers as Excellent Adsorbents for Organic Dyes Removal. *J. Hazard. Mater.* **2020**, *384*, No. 121418.
- (38) Veis, A.; Aranyi, C. Phase Separation in Polyelectrolyte Systems. I. Complex Coacervates of Gelatin. *J. Phys. Chem.* **1960**, *64*, 1203–1210.
- (39) Martin, N.; Tian, L.; Spencer, D.; Coutable-Pennarun, A.; Anderson, J. L. R.; Mann, S. Photoswitchable Phase Separation and Oligonucleotide Trafficking in DNA Coacervate Microdroplets. *Angew. Chem., Int. Ed.* **2019**, *58*, 14594–14598.
- (40) Gibson, L. T.; Watt, C. M. Acetic and Formic Acids Emitted from Wood Samples and Their Effect on Selected Materials in Museum Environments. *Corros. Sci.* **2010**, *52*, 172–178.
- (41) Dupont, A. L.; Tétreault, J. Cellulose Degradation in an Acetic Acid Environment. *Stud. Conserv.* **2000**, *45*, 201–210.
- (42) Al Mohtar, A.; Nunes, S.; Silva, J.; Ramos, A. M.; Lopes, J.; Pinto, M. L. First-Principles Model to Evaluate Quantitatively the Long-Life Behavior of Cellulose Acetate Polymers. *ACS Omega* **2021**, *6*, 8028–8037.
- (43) Al Mohtar, A.; Pinto, M. L.; Neves, A.; Nunes, S.; Zappi, D.; Varani, G.; Ramos, A. M.; Melo, M. J.; Wallaszkovits, N.; Lahož Rodrigo, J. L.; Herlt, K.; Lopes, J. Decision Making Based on Hybrid Modeling Approach Applied to Cellulose Acetate Based Historical Films Conservation. *Sci. Rep.* **2021**, *11*, 16074.
- (44) Cruz, A. J.; Pires, J.; Carvalho, A. P.; Brotas de Carvalho, M. Adsorption of Acetic Acid by Activated Carbons, Zeolites, and Other Adsorbent Materials Related with the Preventive Conservation of Lead Objects in Museum Showcases. *J. Chem. Eng. Data* **2004**, *49*, 725–731.
- (45) Dedecker, K.; Pillai, R. S.; Nouar, F.; Pires, J.; Steunou, N.; Dumas, E.; Maurin, G.; Serre, C.; Pinto, M. L. Metal–Organic Frameworks for Cultural Heritage Preservation: The Case of Acetic Acid Removal. *ACS Appl. Mater. Interfaces* **2018**, *10*, 13886–13894.
- (46) Biswas, S.; Van Der Voort, P. A General Strategy for the Synthesis of Functionalised UiO-66 Frameworks: Characterisation, Stability and CO₂ Adsorption Properties. *Eur. J. Inorg. Chem.* **2013**, *2013*, 2154–2160.
- (47) Hu, Z.; Peng, Y.; Kang, Z.; Qian, Y.; Zhao, D. A Modulated Hydrothermal (MHT) Approach for the Facile Synthesis of UiO-66-Type MOFs. *Inorg. Chem.* **2015**, *54*, 4862–4868.
- (48) Furukawa, H.; Gandara, F.; Zhang, Y. B.; Jiang, J.; Queen, W. L.; Hudson, M. R.; Yaghi, O. M. Water Adsorption in Porous Metal–Organic Frameworks and Related Materials. *J. Am. Chem. Soc.* **2014**, *136*, 4369–4381.
- (49) Iacomi, P.; Formalik, F.; Marreiros, J.; Shang, J.; Rogacka, J.; Mohmeyer, A.; Behrens, P.; Ameloot, R.; Kuchta, B.; Llewellyn, P. L. Role of Structural Defects in the Adsorption and Separation of C₃ Hydrocarbons in Zr-Fumarate-MOF (MOF-801). *Chem. Mater.* **2019**, *31*, 8413–8423.
- (50) Choi, J.; Lin, L.-C.; Grossman, J. C. Role of Structural Defects in the Water Adsorption Properties of MOF-801. *J. Phys. Chem. C* **2018**, *122*, 5545–5552.
- (51) DeStefano, M. R.; Islamoglu, T.; Garibay, S. J.; Hupp, J. T.; Farha, O. K. Room-Temperature Synthesis of UiO-66 and Thermal Modulation of Densities of Defect Sites. *Chem. Mater.* **2017**, *29*, 1357–1361.
- (52) Schaate, A.; Roy, P.; Godt, A.; Lippke, J.; Waltz, F.; Wiebecke, M.; Behrens, P. Modulated Synthesis of Zr-Based Metal–Organic Frameworks: From Nano to Single Crystals. *Chem. – Eur. J.* **2011**, *17*, 6643–6651.
- (53) Xiang, W.; Zhang, Y.; Chen, Y.; Liu, C.-J.; Tu, X. Synthesis, Characterization and Application of Defective Metal–Organic Frameworks: Current Status and Perspectives. *J. Mater. Chem. A* **2020**, *8*, 21526–21546.

- (54) Firth, F. C. N.; Cliffe, M. J.; Vulpe, D.; Aragonés-Anglada, M.; Moghadam, P. Z.; Fairen-Jimenez, D.; Slater, B.; Grey, C. P. Engineering New Defective Phases of UiO Family Metal–Organic Frameworks with Water. *J. Mater. Chem. A* **2019**, *7*, 7459–7469.
- (55) Vermoortele, F.; Bueken, B.; Le Bars, G.; Van de Voorde, B.; Vandichel, M.; Houthoofd, K.; Vimont, A.; Daturi, M.; Waroquier, M.; Van Speybroeck, V.; Kirschhock, C.; De Vos, D. E. Synthesis Modulation as a Tool to Increase the Catalytic Activity of Metal–Organic Frameworks: The Unique Case of UiO-66 (Zr). *J. Am. Chem. Soc.* **2013**, *135*, 11465–11468.
- (56) Shearer, G. C.; Chavan, S.; Bordiga, S.; Svelle, S.; Olsbye, U.; Lillerud, K. P. Defect Engineering: Tuning the Porosity and Composition of the Metal–Organic Framework UiO-66 Via Modulated Synthesis. *Chem. Mater.* **2016**, *28*, 3749–3761.
- (57) Shearer, G. C.; Vitillo, J. G.; Bordiga, S.; Svelle, S.; Olsbye, U.; Lillerud, K. P. Functionalizing the Defects: Postsynthetic Ligand Exchange in the Metal Organic Framework UiO-66. *Chem. Mater.* **2016**, *28*, 7190–7193.
- (58) Kondo, Y.; Kuwahara, Y.; Mori, K.; Yamashita, H. Dual Role of Missing-Linker Defects Terminated by Acetate Ligands in a Zirconium-Based MOF in Promoting Photocatalytic Hydrogen Peroxide Production. *J. Phys. Chem. C* **2021**, *125*, 27909–27918.
- (59) Feng, X.; Jena, H. S.; Krishnaraj, C.; Leus, K.; Wang, G.; Chen, H.; Jia, C.; Van Der Voort, P. Generating Catalytic Sites in UiO-66 through Defect Engineering. *ACS Appl. Mater. Interfaces* **2021**, *13*, 60715–60735.
- (60) Chen, Z.; Feng, L.; Liu, L.; Bhatt, P. M.; Adil, K.; Emwas, A.-H.; Assen, A. H.; Belmabkhout, Y.; Han, Y.; Eddaoudi, M. Enhanced Separation of Butane Isomers Via Defect Control in a Fumarate/Zirconium-Based Metal Organic Framework. *Langmuir* **2018**, *34*, 14546–14551.
- (61) Gibbons, B.; Bartlett, E. C.; Cai, M.; Yang, X.; Johnson, E. M.; Morris, A. J. Defect Level and Particle Size Effects on the Hydrolysis of a Chemical Warfare Agent Simulant by UiO-66. *Inorg. Chem.* **2021**, *60*, 16378–16387.
- (62) Shan, B.; McIntyre, S. M.; Armstrong, M. R.; Shen, Y.; Mu, B. Investigation of Missing-Cluster Defects in UiO-66 and Ferrocene Deposition into Defect-Induced Cavities. *Ind. Eng. Chem. Res.* **2018**, *57*, 14233–14241.
- (63) Mileo, P. G. M.; Cho, K. H.; Chang, J.-S.; Maurin, G. Water Adsorption Fingerprinting of Structural Defects/Capping Functions in Zr–Fumarate MOFs: A Hybrid Computational-Experimental Approach. *Dalton Trans.* **2021**, *50*, 1324–1333.
- (64) Joly-Duhamel, C.; Hellio, D.; Djabourov, M. All Gelatin Networks: 1. Biodiversity and Physical Chemistry. *Langmuir* **2002**, *18*, 7208–7217.
- (65) Bungenberg de Jong, H. G. Crystallisation-Coacervation-Flocculation. In *Colloid Science*, Kruyt, H. G., Ed.; Elsevier Publishing Company: Amsterdam, 1949; Vol. 2, pp 232–258.
- (66) Carn, F.; Steunou, N.; Djabourov, M.; Coradin, T.; Ribot, F.; Livage, J. First Example of Biopolymer-Polyoxometalate Complex Coacervation in Gelatin-Decavanadate Mixtures. *Soft Matter* **2008**, *4*, 735–738.
- (67) Khan, S. A.; Schneider, M. Improvement of Nanoprecipitation Technique for Preparation of Gelatin Nanoparticles and Potential Macromolecular Drug Loading. *Macromol. Biosci.* **2013**, *13*, 455–463.
- (68) Carn, F.; Durupthy, O.; Fayolle, B.; Coradin, T.; Mosser, G.; Schmutz, M.; Maquet, J.; Livage, J.; Steunou, N. Assembling Vanadium(V) Oxide and Gelatin into Novel Bionanocomposites with Unexpected Rubber-Like Properties. *Chem. Mater.* **2010**, *22*, 398–408.
- (69) Baroudi, I.; Simonnet-Jégat, C.; Roch-Marchal, C.; Leclerc-Laronze, N.; Livage, C.; Martineau, C.; Gervais, C.; Cadot, E.; Carn, F.; Fayolle, B.; Steunou, N. Supramolecular Assembly of Gelatin and Inorganic Polyanions: Fine-Tuning the Mechanical Properties of Nanocomposites by Varying Their Composition and Microstructure. *Chem. Mater.* **2015**, *27*, 1452–1464.
- (70) Coppola, M.; Djabourov, M.; Ferrand, M. Unified Phase Diagram of Gelatin Films Plasticized by Hydrogen Bonded Liquids. *Polymer* **2012**, *53*, 1483–1493.
- (71) Gelse, K.; Pöschl, E.; Aigner, T. Collagens—Structure, Function, and Biosynthesis. *Adv. Drug Delivery Rev.* **2003**, *55*, 1531–1546.
- (72) Semino, R.; Moreton, J. C.; Ramsahye, N. A.; Cohen, S. M.; Maurin, G. Understanding the Origins of Metal–Organic Framework/Polymer Compatibility. *Chem. Sci.* **2018**, *9*, 315–324.
- (73) Hwang, J.; Heil, T.; Antonietti, M.; Schmidt, B. V. K. J. Morphogenesis of Metal–Organic Mesocrystals Mediated by Double Hydrophilic Block Copolymers. *J. Am. Chem. Soc.* **2018**, *140*, 2947–2956.
- (74) Forgan, R. S. Modulated Self-Assembly of Metal-Organic Frameworks. *Chem. Sci.* **2020**, *11*, 4546–4562.
- (75) Marshall, C. R.; Staudhammer, S. A.; Brozek, C. K. Size Control over Metal-Organic Framework Porous Nanocrystals. *Chem. Sci.* **2019**, *10*, 9396–9408.
- (76) Marshall, R. J.; Hobday, C. L.; Murphie, C. F.; Griffin, S. L.; Morrison, C. A.; Moggach, S. A.; Forgan, R. S. Amino Acids as Highly Efficient Modulators for Single Crystals of Zirconium and Hafnium Metal–Organic Frameworks. *J. Mater. Chem. A* **2016**, *4*, 6955–6963.
- (77) Pastore, V. J.; Cook, T. R.; Rzaev, J. Polymer–MOF Hybrid Composites with High Porosity and Stability through Surface-Selective Ligand Exchange. *Chem. Mater.* **2018**, *30*, 8639–8649.
- (78) Coppola, M.; Djabourov, M.; Ferrand, M. Phase Diagram of Gelatin Plasticized by Water and Glycerol. *Macromol. Symp.* **2008**, *273*, 56–65.

Titre : Conception de composites flexibles et nanostructurés en associant des MOFs à base d'Al³⁺ et de l'oxyde de graphène pour des applications en adsorption

Mots clés : MOFs, oxyde de graphène, flexibilité

Résumé : Malgré le nombre croissant de travaux portant sur les matériaux hybrides poreux de type Metal Organic Frameworks (MOF) dans l'état de l'art, les recherches dans ce domaine portent essentiellement sur la découverte de nouvelles structures de MOF et l'étude de leurs propriétés physico-chimiques pour des applications. Cependant, la plupart des MOFs décrits jusqu'à aujourd'hui sont microporeux, et ces matériaux sont capables d'adsorber et de convertir des petites molécules, ce qui représente une limitation pour leurs applications potentielles en adsorption ou en catalyse. Pour améliorer les performances de ces matériaux, la conception de composites en combinant les MOFs avec des matériaux à base de carbone a été développée et ces matériaux peuvent présenter des propriétés fonctionnelles intéressantes et une porosité hiérarchique à différentes échelles (micro- et mésoporosité). Parmi les différents matériaux à base de carbone étudiés dans la littérature, l'oxyde de graphène (GO) s'est avéré jouer un rôle intéressant en contrôlant la nucléation et la croissance de certains MOFs. Ainsi, l'objectif de cette thèse était de développer de nouveaux composites MOF/GO nanostructurés qui combinent de manière synergique les propriétés du GO (e.g., mise en forme, conductivité électronique, etc.) et d'un polycarboxylate d'Al³⁺ poreux (e.g., cristallinité, porosité, etc.). Nous avons montré que ces composites consistent en l'assemblage de nanofils monocristallins de MOF et de feuillets de GO. Nous avons montré que la nucléation et la croissance de ces nanofils sont contrôlées par l'autoassemblage des feuilles de GO en nanoscrolls de GO. La conception de composites à base de nanocristaux de MOF anisotropes est assez difficile et a été rarement décrite dans la littérature. Pourtant, ces composites sont intéressants dans les domaines de la catalyse, de la détection, du transport de gaz et de l'électronique, car la

dimensionnalité et la morphologie des cristaux de MOF peuvent avoir un impact sur la diffusion et l'efficacité du transport des analytes vers les sites catalytiques et d'adsorption du MOF. La synthèse de ces composites a été optimisée en ajustant les différents paramètres physico-chimiques de la synthèse. Ils ont été caractérisés en combinant plusieurs outils de caractérisation avancés (diffraction des rayons X sur poudre (DRX), MEB, MET, HAADF-STEM, diffraction électronique, porosimétrie de N_2 , RMN à l'état solide) tandis que nous avons étudié leur mécanisme de formation en combinant des expériences diffusion des rayons X, DRX, MEB et MET. Nous avons également étudié leurs propriétés d'adsorption de gaz et de liquides. Un comportement flexible de ces composites a été mis en évidence alors que le MOF pur ne présente aucun comportement dynamique. Nous avons observé que le MOF du composite peut présenter une transition structurale d'une forme larges pores (lp) à une forme petits pores (np) sous l'application de différents stimuli (solvants, température...). Ces résultats permettent de valider davantage le rôle du GO comme agent structurant des MOFs, et de mieux comprendre le comportement dynamique des MOFs.

